European Cells and Materials Vol. 3. Suppl. 2, 2002 (pages 1-4) ISSN 1473-2262

THE NATIONAL HIGH MAGNETIC FIELD LABORATORY: A NATIONAL RESOURCE IN SUPPORT OF BIO-MEDICAL SCIENCE AND TECHNOLOGY

J. E. Crow

National High Magnetic Field Laboratory, Tallahassee, FL 32310, USA

INTRODUCTION: The National High Magnetic Field Laboratory (NHMFL) is an international user facility supported by the United States National Science Foundation and the State of Florida. The laboratory is operated by Florida State University, the University of Florida, and Los Alamos National Laboratory and charged to develop and maintain facilities in support of magnet-related research that are open to all qualified scientists and engineers through a peer-review proposal process. The laboratory has developed and supports unique facilities responding to the scientific challenges in biology, biomedicine, chemistry, engineering, geo-chemistry, materials science, and physics. In addition to supporting magnet-related science, the NHMFL has established unique capabilities in nearly all areas of magnet science and technology that respond to the wide and varied challenges from the diverse communities served by the laboratory. There are only a limited number of facilities similar to the NHMFL worldwide and the NHMFL is the only magnet laboratory in the western hemisphere. The NHMFL is the largest and highest powered magnet laboratory in the world and provides access to the highest magnetic field in almost all magnet areas including continuous powered, resistive magnets; pulsed magnets; and specialized superconducting magnets. Unique magnets are only one of the components required to drive new science and technology at high magnetic fields. The faculty and staff of the NHMFL in collaboration with users from other institutions have been committed to the development of new approaches to measurement science. These efforts have led to high field magnetometry with sensitivities approaching and often exceeding that available with commercial magnetometers, e.g., superconducting quantum interference devices, and novel high pressure cells for high pressure research that are compatible with the high magnetic fields and the small volumes often associated with reaching the highest magnetic fields.

In response to the challenges in biology, biomedicine, chemistry, and environmental sciences, the laboratory has established magnetic resonance programs in electron magnetic resonance (EMR), nuclear magnetic resonance (NMR), magnetic resonance imaging (MRI) and in Ion Cyclotron Resonance Mass Spectroscopy (ICRMS). The NHMFL is the only laboratory in the world that supports such a diverse approach to magnetic resonance and the complementary and synergistic nature of these techniques has helped to drive new research areas. This paper will provide an overview of the NHMFL current capabilities followed by a more detail discussion of some of the areas where the NHMFL is going to respond more effectively to new scientific challenges that may be of interest in biological, medical, chemical and environmental sciences areas. A much fuller summary of the research accomplishments of the users of this national facility is presented in the *NHMFL Annual Research Review* which is available on the NHMFL web site (www.magnet.fsu.edu). In addition, the NHMFL publishes the *NHMFL Annual Programs Report* that is also available on the web and provides an overview of the programs, user activities, and outreach programs for the NHMFL.

NHMFL-OVERVIEW: The main facilities of the NHMFL are located in Tallahassee, Florida and are housed in a 330,000 sq. ft complex dedicated to magnet-related research and technology. Additional facilities are located at two other sites including the High B/T Facilities and Advanced Magnetic Resonance Imaging and Spectroscopy (AMRIS) facilities located at the University of Florida in Gainesville, Florida, and the NHMFL Pulsed Field Facility located at Los Alamos National Laboratory, Los Alamos, New Mexico. The NHMFL in Tallahassee provides user access to continuous fields in resistive ($B \leq 33$ T), hybrid ($B \leq 45$ T) and superconducting ($B \leq 20$ T) magnets. At the center of the continuous field facilities is a very low ripple, 40 MW DC power supply and a high pressure, high

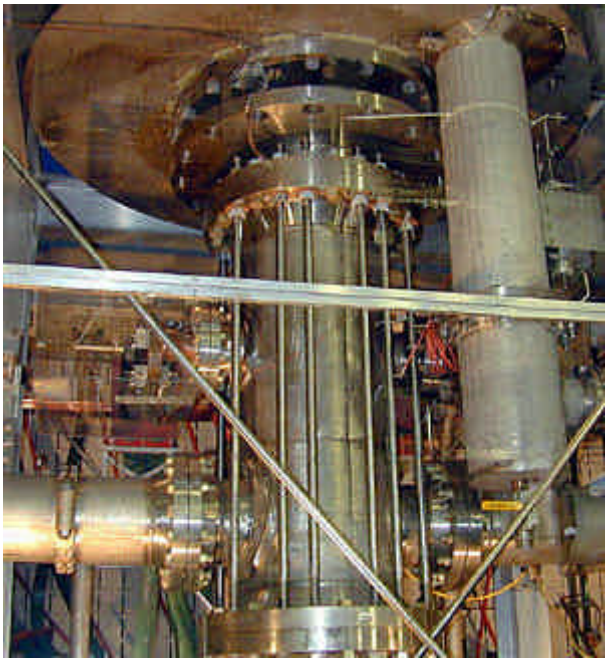

Fig. 1: 45 T Hybrid magnet at the NHMFL.

volume cooling system. Shown in Fig. 1 is the 45 T Hybrid. This magnet provides user access to field up to 45 T in a 32 mm warm bore and is composed of a superconducting magnetic capable of providing 14 T with a powered resistive magnet at the center providing the balance of the field. This is the highest continuous field system in the world. In addition to the Hybrid, the NHMFL also operates several resistive magnets configured to meet a variety of needs including a 25 T, 52 mm warm bore magnet with a homogeneity approaching 10 ppm. In the near future this magnet's homogeneity will be improved with a target of ~1 ppm. This coupled with a NMR field lock on the DC power and compensation coils will permit research with both temporal and spatial homogeneities approaching and, in some cases, exceeding 1 ppm. Such a system opens new opportunities unique in the world for high field NMR at and beyond 1 GHz. The NHMFL is currently studying a new design for the next generation hybrid, which will place the superconducting outsert and resistive insert in series. This system may offer much greater stability and hopefully will open new research opportunities in the 30 T to 35 T range for high field NMR with temporal and spatial homogeneities exceeding 1 ppm.

At the NHMFL Pulsed Magnet Facilities located at Los Alamos National Laboratory, the laboratory provides higher magnetic fields approaching 75 T for short durations, i.e., for a few 10's milliseconds. Within the next few years, the NHMFL hopes to offer short-pulsed fields approaching 100 T. Under redevelopment is a new powered magnet that can provide controlled pulses up to 60 T with a variety of pulse shapes. The controlled waveform for this pulsed magnet includes a nearly constant 60 T for 100 msec. and represents an absolutely unique capacity in the world. The High B/T Facility at the University of Florida combines low temperatures, i.e., ~ few 100 μK, and high magnetic fields, B ≤ 16 T. The upper limit on the magnetic field will soon be increased to ~20 T with the procurement of a new super-conducting magnet for this facility.

In addition to the powered and pulsed magnets, the NHMFL provides a variety of specialty systems to support magnetic resonance including EMR, ICRMS, NMR and MRI. Because of the demanding requirements for homogeneity and stability for most of these systems, superconducting technology is exclusively used here. For all the magnetic resonance techniques, increased magnetic field increases resolution and signal to noise with the details of the resonance technique dictating the level of improvement.

Under development testing at the NHMFL is a 21.1 T (900 MHz), high-resolution, NMR magnet, i.e., a homogeneity ~1 ppb and a warm bore of 100 mm. This magnet is shown in Fig. 2 as it is prepared to be installed in a test dewar for high field testing prior to installation in its final cryostat and commissioning for users. This system will be one of the world's highest field, largest bore, high-resolution NMR systems.

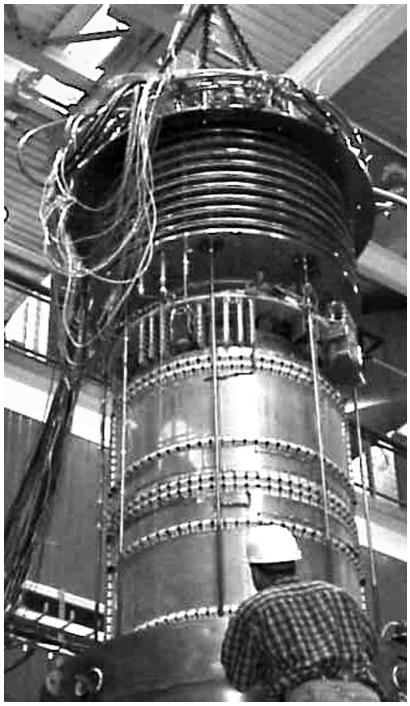

Fig. 2: NHMFL 900 MHz magnet system.

In addition to the high field NMR facilities, the NHMFL in collaboration with the McKnight Brain Institute at the University of Florida also provides access to a 12 T, 400 mm warm bore, small animal imaging system. In mass spectroscopy, the NHMFL offers the highest precision mass spectrometers in the world. The unique ICRMS facilities will soon be augmented by the highest field ICRMS system in the world, i.e., a 15 T, 100 mm bore magnet that is under development. The EMR facilities offer unique capabilities including a Bruker W-band and X-band spectrometer with many unique features along with a high field, time resolved, EMR spectrometer permitting time resolved EMR spectroscopy with solution approaching nanoseconds. Most of these facilities have been developed specifically to open new research opportunities in the biological and chemical sciences.

BIOLOGY AND CHEMISTRY AT HIGH MAGNETIC FIELDS: High magnetic fields enhance all the magnetic resonance techniques but nowhere is the drive to high magnetic field stronger than in NMR. Here the quest for high fields is driven by improved resolution and reductions in signal to noise. Much of this attention is focused on structural biology where the commercial sector is aggressively pushing systems to the 900 MHz range. It is anticipated that soon this drive may even extend to efforts to produce a 1 GHz high resolution NMR system. New probe development focused at cryo- and superconducting probes will also have a significant impact on improved sensitivity for the future. Much of this effort will continue to be driven by structural biology and drug development.

ICRMS offers unparalleled precision along with the capability to analyze unknown mixtures. Diesel fuel is a very good example of an unknown mixture where there is a keen interest in having more detailed knowledge about those components that negatively impact the environment, e.g., sulfur bearing compounds. Show in Fig. 3 is a trace of abundance vs. mass to charge ratio for a typical diesel fuel. Capitalizing on the two key aspects of ICRMS, researchers can examine very complex unknown mixtures and because of the extremely high resolutions of this approach, a unique chemical identification is often possible. It is quite clear that these two features of ICRMS can be extended to a

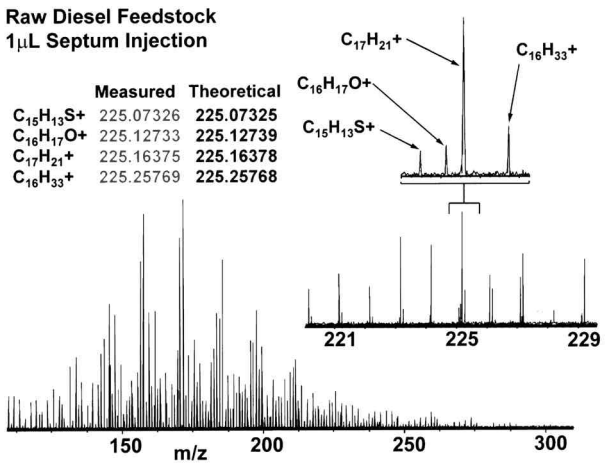

Fig. 3: ICRMS analysis of diesel fuel.

host of interesting problems in both the biological and chemical sciences, including environmental analysis, forensics, and protein sequencing.

The background information presented above is only a very brief glimpse into the vast impact that high magnetic fields can have on the biological and chemical sciences. There are other areas where magnetic fields are making an impact, e.g., processing and growth of biological systems which take advantage of the ability to use high magnetic fields to levitate diamagnetic materials and also to

provide a preferred direction for growth due to the anisotropy in the magnetic susceptibility. The impact of higher magnetic fields on MRI, e.g., increased spatial resolution with increase fields, and the extension of MRI to functional brain imaging and non-invasive chemical diagnosis has not even been mentioned. The presentation will explore these areas along with an overview of the NHMFL capabilities and examples of applications of high magnetic fields to various scientific challenges in the biological and chemical sciences.

POTENTIAL DEPARTMENT OF DEFENSE (DOD) APPLICATIONS OF MAGNETIC CARRIERS

V.M. Browning

Defense Advanced Research Project Agency (DARPA), 3701 North Fairfax Drive, Arlington, VA 22203, USA

ABSTRACT: Novel developments in biocompatible magnetic carrier and magnetic sensor technologies will likely have a pervasive, enabling impact on many areas of biotechnology. It is likely that the development of these technologies could also significantly impact the development of a number of future DoD mission capabilities in biological warfare defense, personnel monitoring, and diagnostic and therapeutic treatments for military personnel. It is believed that magnetics is particularly suited to address many DoD requirements in that it offers the promise of a portable, robust, and highly sensitive transduction mechanism for monitoring and controlling biological activity at all levels. This presentation will discuss some of the perceived future military uses of biotechnology and will also speculate on how future investments in bio-magnetics might greatly enable the transition of many exciting developments in biotechnology out of the laboratory and into the hands of the military.

Living cells and tissues exhibit an extraordinary range of functionalities including highly selective biochemical sensing (even in chemically noisy environments), protein synthesis, information processing, and color change. Recent developments in biotechnology offer the promise of exploiting these functionalities for sensing, diagnostic, therapeutic, and other DoD and commercial applications. However, exploitation of these functionalities in devices that can be taken out of a laboratory environment will require the development of biochemical signal transduction mechanisms that are robust, portable, and highly reliable in noisy environments. A transduction mechanism based on a bio-magnetic interface would meet these requirements and offers solutions to outstanding technical issues that continue to keep many innovative developments in biotechnology from being fielded for DoD use. Some specific examples of expected DoD payoff areas include: 1) rapid, robust, hand-held bio-detection devices with multi-analyte capability, high sensitivity (on par with current reagent based PCR and ELISA techniques), and minimal sample preparation requirements; 2) portable, magnetics based micro total analysis (μTAS) or "lab on a chip" diagnostic devices; 3) novel, magnetically targeted therapeutics for attacking infected cells and tissues without harmful side effects to surrounding healthy cells and tissues; and 4) new capabilities for initiating and monitoring intracellular functions such as apoptosis, mitosis, protein expression, and color change.

The realization of biomagnetics as a portable, robust transduction mechanism for monitoring and/or initiating biological activity will require research and development in several core areas. These core areas include the following: 1) novel, biocompatible ferrofluids, or magnetic "tags", with superior magnetic properties that are capable of attaching to a wide range of single biomolecules and cells with a high degree of specificity; 2) novel, biocompatible, high sensitivity magnetic sensors capable of detecting single magnetic nanoparticles with diameters ranging from < 100nm to > 1 μm; and 3) high density magnetic field gradient architectures that are biocompatible and capable of manipulating single magnetic nanoparticles, attached to single biomolecules or cells, with nanoscale precision.

Biological applications of today's commercially available magnetic beads are primarily aimed at bio-separations and image contrast agents. These applications do not require high moment particles or a high degree of uniformity in the particles' magnetic properties. A new class of biocompatible magnetic particles with superior magnetic and physical properties would enable many new applications. For example, the ability to selectively attach a well defined magnetic moment to a single bio molecule or cell could enable a high sensitivity, *quantitative* bio detection mechanism. However, this would require an order of magnitude increase in the magnetic moment of the beads as well as a high degree of uniformity in particle size and moment. This is a tremendous research challenge. Today's beads are primarily ferrite-based due largely to the fact that ferrites are easily stabilized in fluid solutions. The disadvantage of ferrites is their relatively small magnetic moment as compared to ferromagnetic materials such as pure iron, iron cobalt, etc. Developing the surface chemistries to stabilize and functionalize ferromagnetic particles

(as opposed to ferrites) for biological applications is one of the technical hurdles that will require additional research investment. Another technical challenge will be control of the uniformity of magnetic moment between particles. This will likely require controlling compositional and size distribution of magnetic particles to better than 5%. The development of stable, bio-functionalized, highly uniform ferromagnetic particles will require considerable future research investment in order to realize new applications such as quantitative biodetection.

In addition to developing superior magnetic beads or carriers, many future applications will require better magnetic sensors that are biocompatible and capable of detecting and quantifying magnetically tagged bio-molecules and cells. Today's state-of-the-art GMR sensors can easily detect micron size or larger ferrite beads. However, extending the sensitivity of magnetic sensors down into the nanoscale range will be non trivial since for a given magnetic material each order of magnitude reduction in particle diameter results in three orders of magnitude reduction in particle moment. The development of next generation magnetic sensors for biological applications is another area that will require considerable research investment.

Finally, some of the most intriguing and futuristic applications of magnetics in biotechnology involve the use of magnetic forces to control and monitor biological activity at the cellular and sub-cellular level. In addition to requiring novel magnetic particles and sensors, realization of these capabilities will require the development of high-density magnetic field gradient architectures that are capable of generating sufficient forces to manipulate multiple magnetic nanoparticles with nanoscale precision. Once again, developing these high density, high precision, magnetic "tweezers" will require a significant research effort in order to enable a biomagnetics transduction mechanism capable of monitoring and initiating a wide range of biological activity in cells.

MAGNETIC LABELING AND TRACKING OF CELLS USING MAGNETODENDRIMERS AS MR CONTRAST AGENT

J.W.M. Bulte[1], T. Douglas[2], B. Witwer[3], S-C. Zhang[3], B.K. Lewis[1], P. van Gelderen[1], Ian D. Duncan[3], & J.A. Frank[1]

[1] Johns Hopkins University School of Medicine, Baltimore, MD 21205, [2] Montana State University, Bozeman, MT 59717, [3] University of Wisconsin, Madison, WI 53706

INTRODUCTION: During the last few years, the therapeutic use of stem and progenitor cells as a substitute for malfunctioning endogenous cells has received much attention. Unlike their use in animal models, the introduction of therapeutic cells in patients will require techniques that can monitor their tissue biodistribution non-invasively. Among the different imaging modalities, magnetic resonance (MR) imaging offers both near-cellular (i.e. 50 μm) resolution and whole-body imaging capability. In order to be visualized, cells must be labeled with an intracellular marker that can be detected by MR imaging. Superparamagnetic iron oxide nanoparticles provide currently the highest sensitivity when used as MR contrast agent. Following their covalent linking to anti-transferrin receptor internalizing monoclonal antibodies [1] or small HIV-tat peptides [2], they can be used as cellular contrast agent allowing MR tracking of magnetically labeled progenitor cells following transplantation. We have recently developed a new type of iron oxide nanoparticle, magnetodendrimers, that has excellent magnetic and NMR relaxation enhancing properties [3] and, due to its coating with a dendrimer as transfection agent, is effciently taken up by a variety of mammalian cells [4].

METHODS: Magnetodendrimers (MD-100) were synthesized with a stochiometric ratio of 100:1 of Fe:dendrimer as described [3]. Transmission electron microscopy revealed an oligocrystalline structure of 7-8 nm crystals separated by a somewhat smaller distance (see Figure 1).

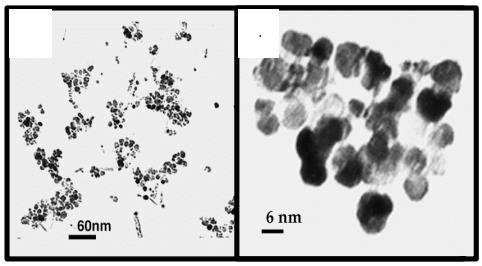

Fig. 1: TEM results for magnetodendrimer oligomers from synthesis with 100:1 Fe:dendrimer stochiometry (MD-100). The higher magnification on the right shows a cluster with individual iron oxide crystals.

MD-100 has a high saturation magnetization of 94 emu g/Fe, no magnetic hysteresis at 300 K, and exhibits T2 relaxivities of 200 $mM^{-1}s^{-1}$ (at 37 °C), with a rapid approach to saturation at magnetic field strengths well below 1.5 Tesla.

Cells were magnetically labeled by simply adding MD-100 to the culture medium at concentrations of 10-25 μg Fe/ml, and incubation of 1-2 days. This included mouse 3T3 fibroblasts, mouse C2C12 muscle progenitor cells, rat CG-4 oligodendrocyte progenitors, rat neural stem cell (NSC)-derived oligodendroglial progenitors, human HeLa cervix carcinoma cells, human GLC-28 small cell lung carcinoma cells, human endothelial progenitor cells, human NSCs, and human mesenchymal stem cells. Approximately 5 x 10^4 MD-100 labeled NSC-derived rat oligodendroglial progenitors were transplanted into the ventricles of neonatal (P=0) Long Evans shaker (*les*) rats. Cells were co-transfected with the LacZ gene (encoding for the enzyme β-galactosidase), in order to track them histochemically by incubating with the X-gal enxyme substrate. Animals were imaged on a weekly to biweekly basis using a clinical 1.5 Tesla clinical imager and a 4.7 Tesla animal imaging system.

RESULTS AND DISCUSSION: Prussian blue staining of magnetically tagged cells showed a remarkably high degree of intracellular labeling, with the cytoplasm containing large numbers of iron-containing vesicles or endosomes (Figure 2).

Achievement of intracellular labeling is a critical requirement, since a membrane-bound magnetic probe is likely to interfere with cell-tissue interactions (membrane recognition processes), may detach easily from the cell membrane, or may be taken up and transferred to other cells *in vivo*. All cells showed a comparable degree of uptake, demonstrating that the MD-100 uptake is non-specific and not dependent on the cell type or species.

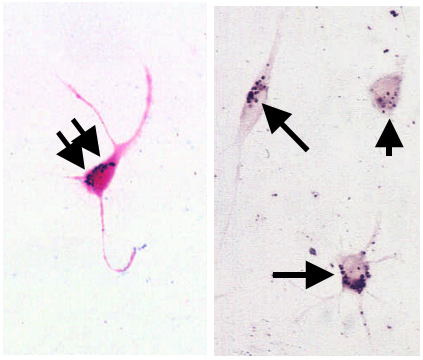

Fig. 2: Non-enhanced (left) and DAB-enhanced (right) Prussian Blue stains of MD-100 labeled, NSC-derived oligodendroglial precursor cells show the presence of numerous iron-containing vesicles in the cytoplasm.

The total iron content of cells labeled with 25 µg Fe/ml MD-100 for 2 days is approximately 10 pg Fe/cell, whereas unlabeled cells contained about 1 pg Fe endogenous iron. Magnetic labeling with MD-100 appeared irreversible, that is, the label is not excreted from the cells *in vitro* for at least 1 week following labeling. Labeled cells appeared unaffected in their proliferation capacity and viability, and an MTT-based toxicity assay showed no difference between unlabeled cells and MD-100 labeled cells. Furthermore, MD-100 labeled human NSCs showed comparable formation of neuronal processes when replated and grown for an additional 10 days, and differentiated normally into glial cells and neurons.

Following transplantation, migration of labeled cells into the brain parenchyma could be observed at the earliest time points (between 2 and 3 weeks) throughout the latest time points of imaging (6 weeks following transplantation). There was a good gross anatomical correlation with the macroscopic distribution of β-galactosidase-expressing cells. Moreover, the transplanted and labeled cells were also found to be able to form myelin that overlapped with the area of MR contrast. Figure 3 demonstrates an example of a 3D-reconstructed MR image obtained *in vivo* at the latest time point of imaging (6 weeks). While this image was obtained at high resolution using a dedicated high field (4.7 Tesla) animal scanner, the labeled cells could also be readily identified *in vivo* using a conventional 1.5 Tesla clinical imaging system. A comparison of several pulse sequences demonstrated that T2* weighted gradient echo imaging, that does not compensate for the induced dephasing of protons, was most sensitive to the presence of labeled cells. From the number of cells injected, and the overall area of contrast, we estimate that it should be possible to detect only a few cells when using T2* weighted imaging techniques.

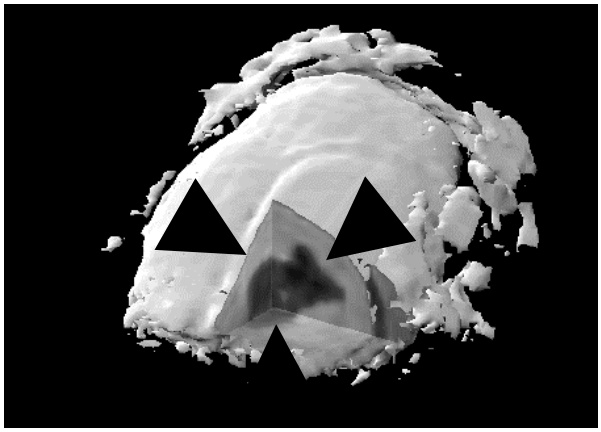

Fig. 3: 3-D Reconstructed in vivo MR image of les rat brain showing distribution of magnetically tagged oligodendroglial progenitors at 6 weeks following transplantation. Note the migration of cells into the parenchyma away from the ventricle (arrowheads).

CONCLUSIONS: Magnetodendrimers represent a new class of cellular MR contrast agents that can be used for a high degree of magnetic cellular labeling regardless of animal species. Following transplantation of MD-100 labeled oligodendrocyte progenitors, cells can be followed in vivo for at least 6 weeks following transplantation, with a good histopathologic correlation including the formation of myelin. The prospect of MR tracking of labeled cells appears attractive not only as a tool to perform longitudinal cell migration studies in the same animal, but also because of its potential to help guide future clinical studies involving the use of therapeutic stem and progenitor cells.

REFERENCES: [1]J.W.M. Bulte, S-C. Zhang, P. van Gelderen et al., (1999) *Proc Natl Acad Sci USA* **96**:15256-15261. [2]M. Lewin, N. Carlesso, CH Tung et al., (2000) *Nature Biotechnol* **18**:410-414. [3]E. Strable, J.W.M. Bulte, B. Moskowitz et al (2001) *Chem Mater* **13**:2201-2209. [4]J.W.M. Bulte, T. Douglas, B. Witwer et al (2001) *Nature Biotechnol* **19**:1141-1147.

IN-VITRO BLOCKAGE OF A SIMULATED VASCULAR SYSTEM USING MAGNETORHEOLOGICAL FLUIDS AS A CANCER THERAPY

G. A. Flores & J. Liu

California State University, Department of Physics and Astronomy, Long Beach, CA 90840 USA

INTRODUCTION: Tumors need a constant blood supply to keep them alive. Therapies to eradicate the tumor include chemotherapy, radiation and surgical removal and often result in toxic doses to the patient and side effects. New developments are underway to aim at more effectively eliminating cancer cells with minimal side effects, such as anti-angiogenesis drugs to prevent the growth of new blood vessels, and brachytherapy to localize radioactive "pellets" to kill the tumor [1].

Here we report a cancer therapy whose effect is similar to anti-angiogenesis drugs with lower cost and easy to produce, and to brachytherapy with localized treatment. We use magnetorheological (MR) fluids injected into the blood vessels leading to a tumor and apply an external magnetic field over the tumor area to localize the magnetizable (iron oxide) particles in MR fluids. These micrometer-sized particles will form a solid seal near the magnetic poles and thus block the blood flow to the tumor, leading to tumor necrosis.

In-vitro experiments, as a continuation of our earlier work [2-4], were done using silicone tubes to simulate human blood vessels. We have reported in the last two conferences the relationship between seal formation time and seal strength as a function of significant controlling parameters, such as magnetizable particle volume fraction, size and types, as well as magnetic field strength and fluid flow rate. We also compared different carrier fluids such as water, human plasma and blood [2-4].

Last year, we performed simulation experiments for four branches of "blood vessels" connected to a 3- and 5-mm diameter cavity cell to simulate a tumor [4]. We used both water and sheep blood as our carrier liquid. Seals were formed immediately after the magnetic field was turned on for water–based MR fluids. However, the seal was unstable for our sheep blood-based MR fluid in a 5-mm cavity cell where the magnetic field was 0.43 – 0.48 T. For this paper, we report experimental simulations for up to six branches of "blood vessels" encased in a cavity cell simulating a tumor. The magnetic field has been increased to between 0.6 – 1.1 T. Water is still used as a carrier fluid, but future tests will include whole human blood. The tube diameter and the fluid flow rate have been decreased to be more realistic in simulating a human circulatory system.

METHODS: A suspension of pure magnetite particles (MAG) from Chemicell GmbH, Germany is used with water as the carrier liquid. The magnetite particles are coated with a hydrophilic starch derivative to make them biocompatible and to reduce electrostatic repulsive interactions with red blood cells (RBC). Two different diameters (**2*a***) of MAG particles are used: 0.25-μm particles are designed for intra-venous applications, while 1.0-μm particles are intended for increasing the efficiency of mechanical blockage of the fluid flow and are suited for an intra-arterial application. Based on our earlier study, a particle volume fraction (***F***) of 1.0% is chosen in order to seal the tubes within a reasonable time frame (~ 30 min.) and with the minimum number of particles [3].

The simulated vascular system consists of a network of silicone tubes with various inner diameters (***D***) ranging from 1.6 mm in the "arteries" and "veins", to 0.8-mm and 0.4-mm branches. Finally, they divide down to 0.2 mm, simulating human arterioles. As seen in Fig. 1, a 1.6-mm tube is placed inside the MR source beaker to draw the sample toward a peristaltic pump from Manostat ("SARAH" model, Barnant Company, USA) that will send the fluid through the system. The fluid flow rate (***Q*** ~ 0.007 ml/min per tube) is similar to that within a human arteriole, but with a lower fluid flow velocity (~3.7 mm/s for ***D*** = 0.2 mm, compared to ~7.5 mm/s for ***D*** = 0.050 mm arteriole).

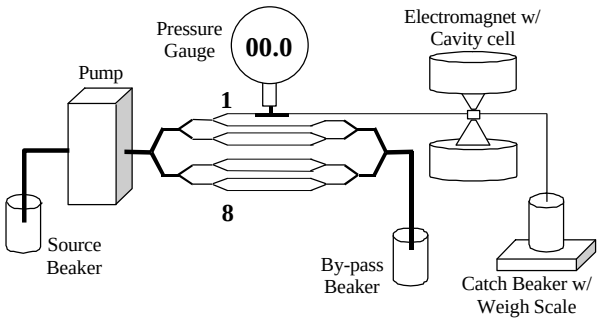

Fig. 1: Experimental setup for 2-branch cavity connection. In 4- and 6- branch cavity connection, tubes Nº. 2 and 3 also connect to the cavity cell and pass through the magnetic poles.

The top tube (***D*** = 0.2 mm), labeled Nº. 1, leads to a DSF26 digital pressure gauge, manufactured by Kolbold USA, Inc. to measure the resistive pressure (***P***) exerted on the tube wall. The gauge is connected

to a PC computer through a Data Acquisition (DAQ) board from National Instruments Inc. The incoming data is sent as a voltage from 0 to 10 V as set by the factory, which corresponds to a pressure range from 0 to 200 mm Hg. Due to the use of multiple tubes, the pressure in any tube is not very sensitive to the seal formation. The remaining tubes Nº. 2-8 (***D*** = 0.2 mm each) are sent to the By-pass beaker to "complete" our circulatory system.

From the pressure gauge and tube Nº. 1 are our cavity cells of diameters (***S***) 3.0 mm or 5.0 mm, which are used to "simulate" a Stage II and III breast cancer or melanoma [4]. Once the tube is inside the cavity cell, it is not connected the same way as before [4]. Instead, in order to simulate the complex capillary patterns within a tumor, the 0.2-mm tube is looped or coiled a few turns, as seen in Figs. 2 and 3. Thus, the fluid travels inside the confines of the tube and do not accumulate inside the cavity as before. For multiple tubes, i.e. using two or three tubes, these tubes are connected the same way. The number of loops within the cavity cells, and the number of tubes connected to the cells vary. The following table shows how long these tubes are within the cavity cells.

Table 1: Tube lengths for each 0.2-mm tube within the cavity cells used for the experiment.

3-mm cavity		End-cap thickness = 6 mm	
Nº. of tubes	Nº. of loops/tube	Tube length inside cell (mm)	Total tube length (mm)
1	2	18.8	30.8
2	1	9.4	21.4

5-mm cavity		End-cap thickness = 5 mm	
Nº. of tubes	Nº. of loops/tube	Tube length inside cell (mm)	Total tube length (mm)
1	4	62.8	72.8
2	2	31.4	41.4
3	1	15.7	25.7

To create the seals, a pair of electromagnets with 1150 turns each, and two poles made of 1018 steel of maximum diameter 25.4 mm and a pole diameter of 16 mm generates and focuses an external magnetic flux density (***B***) to the cavity cell. This ***B***-field, which is driven by a current of 5.0 A (DC), gives us 0.6 T for the 5-mm cell, and 1.1 T for the 3-mm cell, measured at the center.

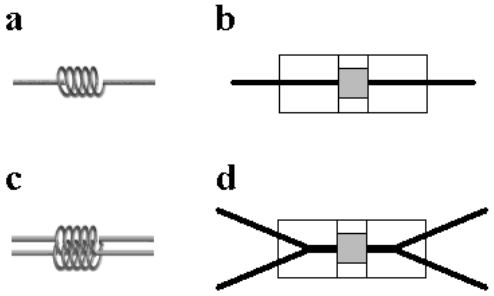

*Fig. 2: Looping of 0.2-mm tubes for a 3-mm cavity cell. Figs. 2a, c show the new configuration, while Figs b, d show the old configuration. The old tubes (**D** = 0.4 mm) filled the cavity (shown in gray) to form the seal. Overall length of the cavity cell is 15 mm.*

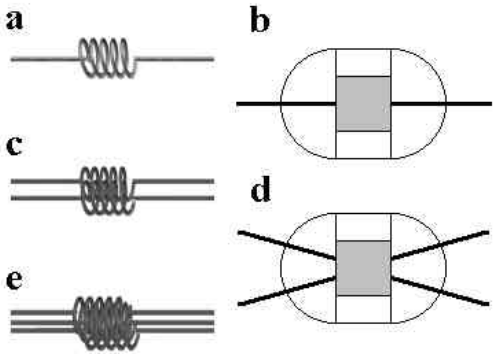

Fig. 3: Looping of 0.2-mm tubes for a 5-mm cavity cell. Figs. 3a, c, e show the new configuration, while Figs b, d show the old configuration. Previously, only 2- and 4-branches were done. Overall length of the cavity cell is 15 mm.

The fluid leakage downstream from the magnetic poles is used to monitor the seal formation. To measure the fluid weight (***W***), we used a Mettler-Toledo PB-153 balance connected to the computer via a RS-232 port. This data from the balance, as well as the data from the pressure gauge was analyzed using the software LabVIEW.

RESULTS: Figure 4 shows the result of ***W*** vs. time for water-based MAG fluids. The magnetic ***B***-field is switched on at ***t*** = 15 minutes. It is clear that ***W*** has saturated once the field is on. Thus a seal has formed within the tubes inside the cavity cell for all cases for our water-based MAG sample. Visually, we observed the seal formation since the particles are brown-gray and the tube is transparent. This extended seal (covering the 16-mm pole diameter plus 3-5 mm in some cases after the pole) is concentrated near the poles with a clear water area of about 15–20 mm in length on both ends of the seal that separate the seal from the rest of the MAG fluid. This is due to the ***B***-field near the poles that attracts nearby particles to the poles.

a (3-mm cell, 0.25 mm particles)

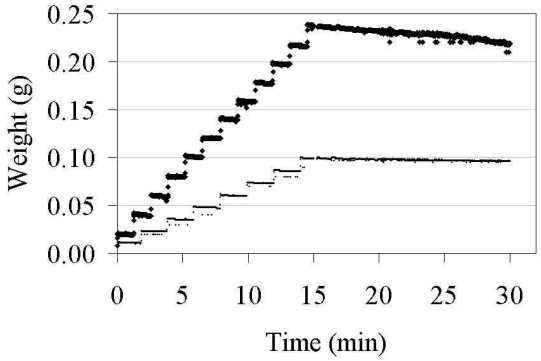

b (3-mm cell, 1.0 mm particles)

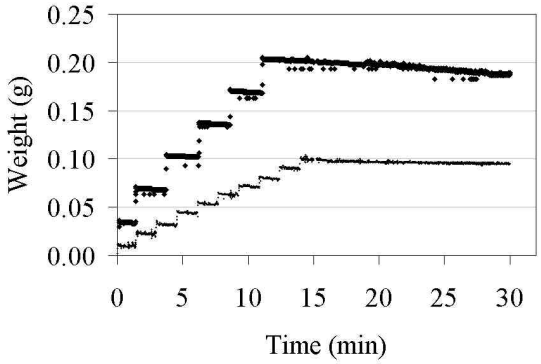

c (5-mm cell, 0.25 mm particles)

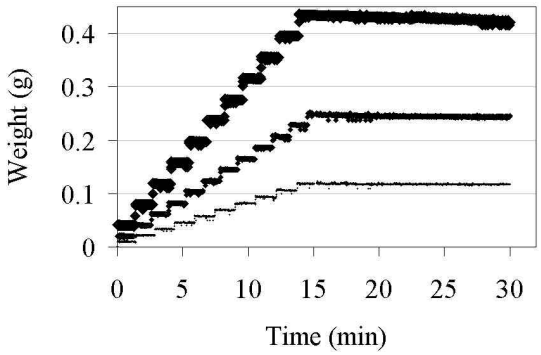

d (5-mm cell, 1.0 mm particles)

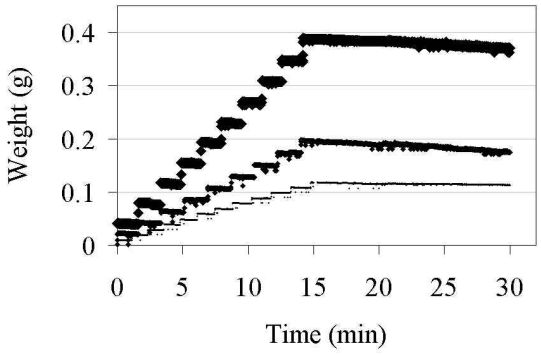

*Fig. 4: Graph showing fluid weight vs. time within the cavity cell. Magnetic **B**-field for the 3-mm cell is 1.1 T at the center of the cell, while the **B**-field for the 5-mm cell is 0.6 T. Lighter points show 2-branch construction, medium points show 4-branch construction, while heavier points show 6-branch construction.*

The seal formation increases ***P*** so that no more particles are pushed toward the poles.

In most cases, ***P***, which was initially 3-5 mmHg in the beginning, rose to nearly 8-12 mmHg once the field was active. Thus the clear region shows the range of the magnetic force.

DISCUSSION & CONCLUSIONS: In a multiple-branch vascular simulation, a fluid flow blockage was simulated. We used 0.2-mm tubes looped inside 3-mm and 5-mm cavity cells to simulate a Stage II and III tumor. To facilitate this blockage, two different-sized magnetite particles were tested: 1.0 μm for intra-arterial treatments, and 0.25 μm for intravenous treatments. Using water as our carrier liquid and an external magnetic field of between 0.6 and 1.1 T, the MR fluid forms a stable seal for both cell sizes and for both particle sizes almost immediately after the field is turned on. This seal formation prevents the carrier liquid from passing through our cavity cell. Previously, we used 2- and 4-branch connections to the cavity cells which led to the fluid being deposited directly into the cells. This did not result in a tight seal for the larger 5-mm cells. When sheep blood was used, the seal would often collapse [4]. It is much easier to block a river than a lake. Because of this, we decided to use a new approach of looping the tubes inside the cell. One concern is to balance the magnetic field availability against the tumor size. Further work is needed to understand the details of the seal strength when using blood as a carrier liquid as compared to using water.

REFERENCES: [1]T.J. Dilling, J. W. Goldwein (2001) *The Treatment of Cancer*, OncoLink - The University of Pennsylvania Cancer Center www.oncolink.com. [2]G.A. Flores, R. Sheng, J. Liu. (2000) Proceedings of the 7th Int'l Conference on Electrorheological Fluids and Magnetorheological Suspensions, World Scientific, Inc., 716. [3]J. Liu, G.A. Flores, R. Sheng (2001) J. Magnetism and Mag. Mat. **225**:209-217. [4]G.A. Flores, J. Liu. To be published in the Proceedings of the 8th Int'l Conference on Electrorheological Fluids and Magnetorheological Suspensions, World Scientific, Inc.

ACKNOWLEDGEMENTS: We would like to thank Chemicell GmbH, Germany, for the MAG particles, and Leslie T. Ferro for her helpful discussions. This work was partially supported by a grant from Research Corporation (CC4801), NASA (NAG3-1830), and from California State University, Long Beach.

THE MTC TECHNOLOGY: A PLATFORM TECHNOLOGY FOR THE SITE-SPECIFIC DELIVERY OF PHARMACEUTICAL AGENTS

Jacqueline Johnson, Thomas Kent, Joy Koda, Caryn Peterson, Scott Rudge, Gilles Tapolsky

FeRx Inc., 12635 E. Montview Blvd. - Suite 300, Aurora, CO 80010, USA

Magnetic Targeted Carriers (MTCs) are microparticles composed of metallic iron and activated carbon and are prepared by a high-energy milling process. Very pure elemental iron comprises approximately 75% of the microparticle mass while high surface area activated carbon comprises the remaining. The synergy between these two components creates a magnetically susceptible particle capable of carrying therapeutic quantities of a wide range of pharmaceutical agents which may be targeted and localized at the desired site. MTCs range in size from 0.5 μm to 5 μm with an average diameter of approximately 1 μm [1-3].

Using a small, externally positioned magnet to create a localized magnetic field within the body, MTCs can be targeted to specific sites following intra-arterial administration as illustrated in Fig. 1 [4]. Having a higher magnetic susceptibility and saturation than particles made of iron oxides (including magnetite, Fe_3O_4, and hematite, Fe_2O_3), the iron containing MTCs are captured by the external magnetic field more efficiently and at depths up to 14 cm, a clinically relevant depth for most solid tumors. In response to the magnetic field, the MTCs are pulled out of the circulation through the vasculature by a physical process of extravasation leading to the localization of the particles in the surrounding tissue.

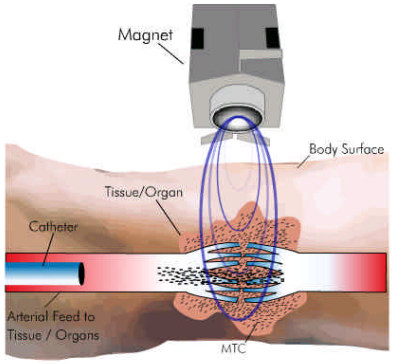

Fig. 1: Schematic Representation of the targeting of the MTCs

The pharmaceutical agent to be delivered to solid tumors is simply adsorbed onto the microparticles (activated carbon component) at the hospital pharmacy just prior to administration. As illustrated in Fig. 2, a commercial formulation of the chemotherapeutic agent doxorubicin, is combined with the MTCs and the mixture is allowed to incubate for 30 minutes at room temperature to ensure complete absorption. The MTC-DOX complex is then diluted with a vehicle that provides a homogeneous suspension for administration. The MTC-DOX suspension is administered intra-arterially by placing a catheter proximal to the selected tumor site and a magnet positioned on the surface of the body over the desired site. The MTC-DOX is then slowly infused with the magnet in place for an additional 15 minutes following administration [4]. MTCs are localized within the interstitial space, thus providing a retention mechanism that does not allow for redistribution.

In vivo characteristics of the MTCs have been investigated in preclinical animal studies as well as in ongoing human clinical trials. These studies defined the preliminary safety profile of MTC-DOX and the efficiency of magnetic targeting and retention of the MTCs.

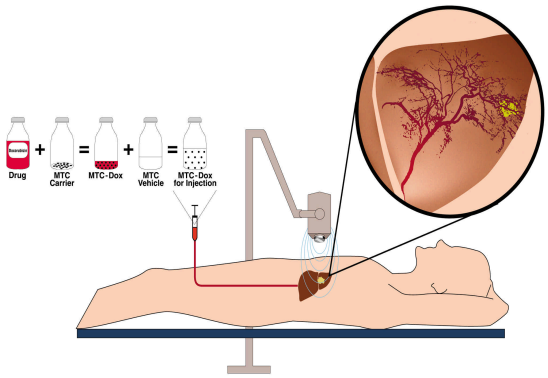

Fig. 2: Administration of the microparticles.

Preclinical Studies

MTCs can be selectively targeted in a large animal model to specific sites. Targeting was assessed through the use of gamma camera images following adsorption of ^{99m}Tc to MTCs. ^{99m}Tc is a gamma emitting radionuclide widely used for imaging purposes. Results showed that the MTCs can be targeted to the desired site (4). Targeting has been shown in lung, liver, pancreas, kidney, brain, and breast [5].

Clinical Investigation

The lead product developed by FeRx, MTC-Doxorubicin (MTC-DOX), is under investigation in the U.S. in a phase I/II clinical trial in patients with hepatocellular carcinoma. In humans, the efficiency

of the targeting and the fate of the MTCs over time are assessed by MRI. To date, 32 patients have been enrolled and clinical results confirm the preclinical findings, highlighting the efficiency of tumor targeting and the retention of MTCs at the targeted site. An angiogram taken immediately after administration of MTC-DOX to a tumor lesion in the liver of a patient with hepatocellular carcinoma is shown in Figure 3. It demonstrates that the mechanism for retention is extravasation of the MTCs and not embolization.

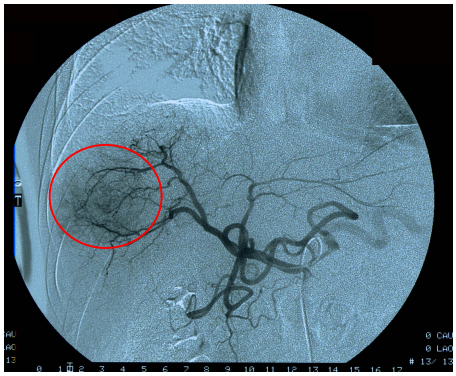

Fig. 3: Angiogram taken immediately after administration of MTC-DOX.

In addition, a MRI scan is done in order to verify the targeting efficiency. As shown in Figure 4, the MTCs are localized only in the tumor where they are retained [6].

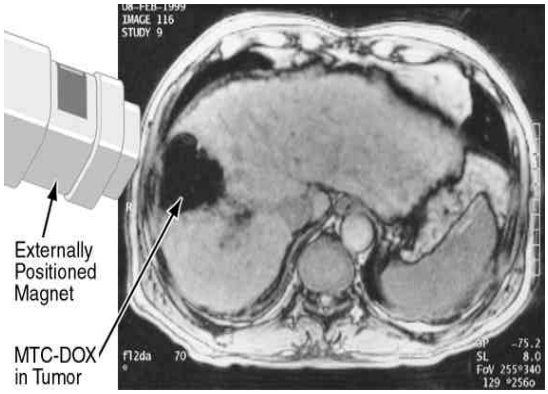

Fig. 4: MRI scan of an HCC lesion in a patient following targeted delivery of MTC-DOX.

Finally, in this Phase I/II clinical trial designed to determine the tolerability and safety profile of this product, a Maximum Tolerated Dose of 60 mg Doxorubicin and 600 mg MTCs was reached.

Platform Technology

The platform nature of the MTC technology has been demonstrated by the wide range of pharmaceutical agents that can be adsorbed onto the MTCs, the control of the release rate, and the targeting to many different organs [5].

Chemotherapeutic drugs

The use of systemic chemotherapeutic agents, alone or in combination is a common treatment against many cancers. However, the efficacy of the systemic administration of current chemotherapies has been limited by the low effective concentration at the tumor site and from the systemic toxicity of these drugs. FeRx's lead product is based on doxorubicin, a widely used chemotherapeutic agent. Many other chemotherapeutic drugs have been shown to adsorb onto the MTCs, such as mitomycin C, etoposide, paclitaxel, oxaliplatin. The adsorption of the drug onto the MTCs is done at room temperature. The release characteristics are studied in human plasma and the cytotoxicity profile is investigated by combining with an appropriate cell line either the MTCs drug complex or the solution of the drug after release from the MTCs. A complete study of MTC-DOX and MTC-Taxol are described in Rudge *et al.* [1] and Allen *et al.* [2].

Radioisotopes

External beam radiation is a widely used treatment in solid tumors with good efficacy. However, radiation exposure to normal tissue surrounding the tumor or in the path to a tumor is the limiting step of this therapy [7]. The MTC technology could overcome these limitations by direct localization of MTCs labeled with radionuclides inside the tumor. *In vitro* labeling studies with various radionuclides have shown that irreversible binding with simple chemistry modifications. Efficiency and stability of the labeling in human plasma at 37°C are shown in Figure 5 for Rhenium 188 labeled MTCs [8,9]. Investigation of ^{90}Y, ^{131}I, and ^{111}In is underway and results will be reported soon [10]. These *in vitro* results indicate that MTCs are well suited for local radiation therapy and animal experiments are underway to evaluate the feasibility of using MTCs for the localized radiation therapy of solid tumors.

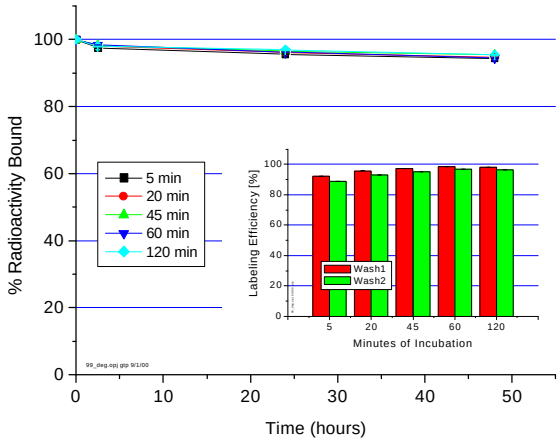

Fig. 5: Labeling Efficiency and Stability of ^{188}Re perrhenate labeled MTCs.

Peptides

We selected a peptide being developed for the radioimmunotherapy of neuroendocrine tumors as a model peptide. Octreotate is a synthetic eight amino acid peptide that binds to somatostatin receptor subtypes 2. This peptide has been further functionalized and includes a chelator moiety, DOTA. Octreotate can thus be radiolabeled with radionuclides such ^{177}Lu or ^{90}Y for the therapy of neuroendocrine tumors [11].

The radiolabeled peptide binds quantitatively to MTCs (99.5 $\pm$ 0.1%) at room temperature. The desorption of Octreotate from MTCs in human plasma at 37ºC is shown in Fig. 6. Three types of MTCs that were prepared with activated carbons having different characteristics show different rates of release. The MTC-HP particles prepared with the carbon HP have the most desirable set of properties with the preferred release profile in human plasma.

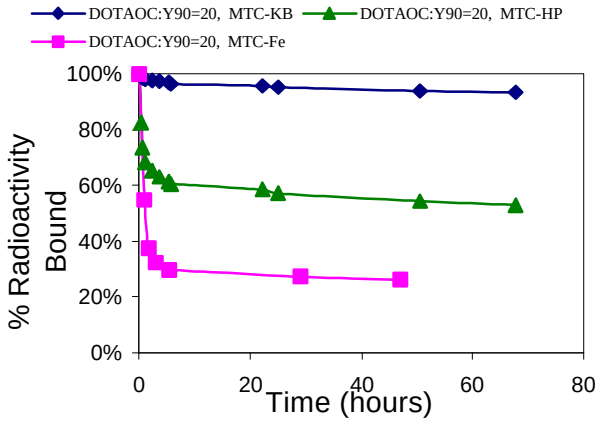

Fig. 6: Release profiles in human plasma at 37ºC.

These results indicate that therapeutic peptides can be adsorbed and desorbed from MTCs. Peptides with molecular targeting function could also benefit from the physical targeting of MTCs by increasing their local concentration and eventually improving the percentage of peptide being efficiently targeted by pre-localizing them at the desired site.

Proteins

Tumor Necrosis Factor alpha (TNF-α) is a 17 kDa macrophage derived cytokine that has been shown to have anti-tumor activity against a variety of malignancies in murine models [12]. However, its clinical development has been hampered because of its systemic side effects such as hypotension, which severely limits the systemic use of this drug. High doses of TNF-α administered by intra-tumoral injections or isolated limb perfusion have shown dramatic regression in some patients. Therefore, achieving adequate local concentrations of TNF-α may reduce or eliminate the systemic toxicities while increasing the efficacy through site specific delivery of the therapeutic agent.

Adsorption of TNF-α was rapid and quantitative with more than 95% being adsorbed after 1 hour. The desorption from MTCs in human plasma was investigated: 10 µg of TNF-α in aqueous solution at neutral pH was mixed with 1 mg of MTCs. After binding at room temperature for 1 hour, the MTC/TNF-α complex was washed once with phosphate buffer at pH 7.4. Human plasma was then added to investigate the desorption at different time points. Results shown in Figure 7 indicated that TNF-α is desorbed from MTCs slowly under the conditions studied.

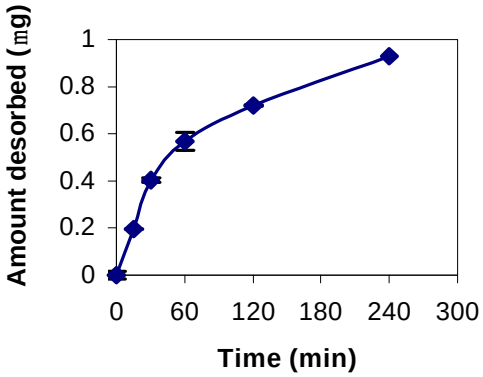

Fig. 7: Release profiles in human plasma at 37ºC.

Furthermore, the cytotoxicity of TNF is unchanged throughout this adsorption/desorption process. The preliminary *in vitro* cytotoxicity of MTC/TNF-α was investigated using the WEHI-13Var cell line (Fig. 8). Results indicate that the biological activity of TNF-α adsorbed onto and then desorbed from MTCs is retained.

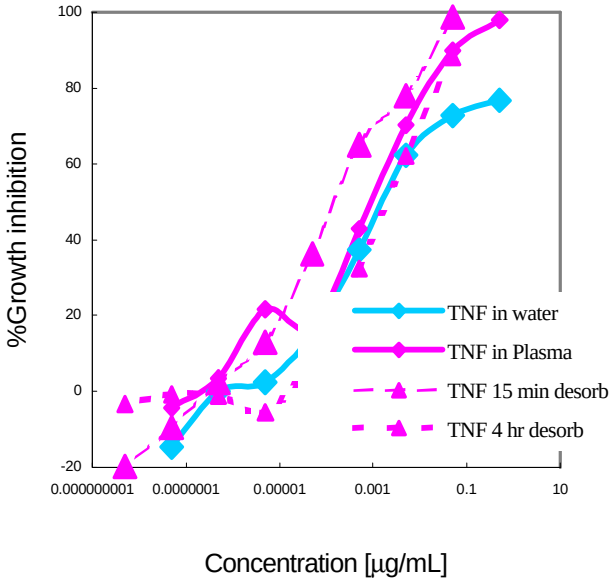

Fig. 8: Cytotoxicity of TNF, shown as growth inhibition, before and after adsorption to MTC.

Conclusions

The MTC technology is an innovative technology with well-characterized *in vitro* and *in vivo* properties. Because of their unique properties, these microparticles are targeted to the desired sites, extravasated into the tissue, and do not redistribute over time. They can reversibly bind chemotherapeutic drugs, peptides, and proteins or irreversibly bind radionuclides. Thus, MTCs could be used for the site-specific delivery of chemotherapeutic agents or localized radiation therapy. On-going human clinical trials with MTC-DOX show that these microparticles are efficiently targeted to liver tumors. Expansion to other clinical indications and intra-tumoral radiation therapy are planned for the near future.

ACKNOWLEDGMENTS

Results presented in this paper are the work of FeRx's personnel and especially Jacqueline Johnson, Caryn Peterson, Joy Koda, Scott Rudge, Tom Kent, Yuhua Li, Sarah Failing, and collaborators including Scott Goodwin (PHS Grant # 5M01 R00865-25), Jennifer Hill, Urs Häfeli, and Marion de Jong.

BIBLIOGRAPHY

[1]Rudge, S., T. Kurt, and C. Vessely, "Preparation, characterization and performance of magnetic iron/carbon microparticles for chemotherapy", *Biomaterials* 21, 1411, (2000). [2]Allen, L.R., Kent, T., Wolfe, C., Ficco, C., and Johnson, J. "A magnetic targetable drug carrier for paclitaxel" *Scientific and Clinical applications of magnetic carriers.* New York, Plenum, 481 (1997). [3]Volkonsky, V. A., S. D. Dvukhsherstnov, S. V. Chernyakov, *US 5,705,195.* [4]Goodwin, S., C. Peterson, C. Hoh, and C. Bittner, "Targeting and retention of magnetic targeted carriers (MTCs) enhancing intra-arterial chemotherapy", *J. MMM*, 194, 132 (1999). [5]Hill, J., Bittner, C., Bonilla, S., Bonneville, A., Melinek, J., Goodwin, S. *Proceedings American Association of Cancer Research 41*, #1646, March 2000. [6]Goodwin, S., Hill J., Gordon, R., Kerlan, R., Walser, E., Suhocki, P., *25th Annual Meeting of the Society of Cardiovascular and Interventional Radiology*, April 2000. [7]Gaze, Mark N., "The current Status of Radiotherapy in Clinical Practice", *Phys. Med. Biol.* 41, 1895 (1996). [8]Knapp, F.F. "A generator for cancer therapy". *Cancer Biother. Radiopharm*. 13, 337 (1998). [9]Häfeli, U., Pauer, G., Failing, S., Tapolsky, G. " Radiolabeling of Magnetic Particles with Rhenium188 for Cancer Therapy", *Journal of Magnetism and Magnetic Materials*, **225**: 73-8 (2001). [10]Yu, Y., Häfeli, U., Li, Y., Tapolsky, G. "Radiolabeling of Magnetic Targeted Carriers with Indium 111" manuscript in preparation. [11]deJong M., Breeman W., Kooij P., Valekame E., and Krenning E., "Therapy of neuroendocrine tumors with radiloabeled somatostatin analogs", *Q. J. Nucl. Med.* , 43, 356 (1999). [12]Corti, A. and Marcucci, F., "Review: Tumor Necrosis Factor: Strategies for Improving the Therapeutic Index", *J. Drug Targeting*, 5, 403 (1998).

RADIOLABELING OF MAGNETIC TARGETED CARRIERS WITH SEVERAL THERAPEUTIC AND IMAGING RADIOISOTOPES

J.F. Yu[1], U. O. Häfeli[1], Y. Dong[1], M. J. Sands[1], Y.H. Li[2], S. Failing[2], T. Leakakos[2], G. Tapolsky[2]

[1] *The Cleveland Clinic Foundation, 9500 Euclid Ave. T28, Cleveland, OH 44195, USA*
[2] *FeRx Inc., 12635 E. Montview Blvd. - Suite 300, Aurora, CO 80010, USA*

INTRODUCTION: Magnetic Targeted Carriers (MTCs) are magnetic microparticles made from metallic iron and activated carbon [1]. The average microparticle diameter is approximately 1 μm (0.5-5 μm). The activated carbon component of the MTCs is capable of adsorbing a wide variety of pharmaceutical agents including chemotherapeutic drugs such as doxorubicin. This technology is under clinical investigation in a Phase I/II clinical trial in patients with hepatocellular carcinoma investigating the safety and tolerability profile of MTC-Doxorubicin in human patients [2].

The efficacy of a chemotherapeutic treatment depends on the tumor sensitivity to the drug as well as the effective intra-tumoral drug concentration. Radiation therapy is a good alternative for some chemoresistant tumors. Furthermore, local or intra-tumoral radiotherapy could be a better therapeutic approach as it would minimize side effects typically associated with external beam radiation therapy. We recently prepared MTC microparticles labeled with the therapeutic radioisotope ^{188}Re [3]. The labeling efficiency was higher than 95% and the *in vitro* characteristics satisfactory. However, due to the limited availability of Re generators, we chose to study other commercially available radionuclides. We investigated the radiolabeling of MTCs with ^{90}Y, ^{111}In, ^{125}I and ^{131}I. The physical properties of these radioisotopes are summarized in Table 1. These radioisotopes have been used for many years in diagnostic and therapeutic radiopharmaceuticals.

The aim of this paper is to report the optimal conditions for the radiolabeling of MTCs with these radioisotopes and testing their stabilities *in vitro*.

Table 1. Physical properties of radioisotopes used for MTC radiolabeling.

Isotope	Decay mode	Half-life	Max. Particle Energy (%)	Max. Range	γ Energy (%)
^{90}Y	β	2.67 d	2.29 MeV (100)	11.9 mm	-
^{111}In	γ	2.83 d	-	-	171 keV (90) 245 keV (94)
^{131}I	β, γ	8.0 d	807 keV(1) 606 keV(86) 336 keV(13)	2.4 mm	364 keV (81)
^{125}I	EC	60 d	-	0.02 mm	35 keV (7)

METHODS: Several methods to bind ^{90}Y, ^{111}In, ^{125}I and ^{131}I to MTCs were investigated. Direct incubation of MTCs with the radioisotopes were studied as well as adsorption using different radiolabeled chelators or molecules (1,4,7,10-tetraazacyclododecane-1,4,7,10-tetraacetic acid = DOTA; 2-p-aminobenzyl-1,4,7,10-tetraazacyclo-dodecane-1,4,7,10-tetraacetic acid = ABz-DOTA), oxine for ^{90}Y and ^{111}In; iodogen, MIBG, and Iodohippurate. The parameters investigated were concentration, mole ratios, temperature, buffers and incubation time, were investigated. Thin Layer Chromatography (TLC) was used to analyze the chelation efficiency. The binding stability of the radiolabeled MTCs was determined in human plasma at 37 °C for 7 days for ^{90}Y or ^{111}In and for 28 weeks for ^{131}I by measuring the activity released in human plasma and comparing it to the activity still bound on the MTCs

RESULTS: The chelation and binding efficiencies of MTCs labeled with different radioisotopes after optimization of the reaction parameters are summarized in Table 2.

Table 2. Optimized chelation and binding efficiencies.

Radiolabeled MTC	Chelation efficiency	Binding effiency
^{90}Y-MTC		98.5% ± 1.2% (n=3)
^{90}Y-DOTA-MTC	97.0%	100% (n=3)
^{90}Y-ABz-DOTA-MTC	99.7%± 0.4% (n=4)	100% (n=12)
^{90}Y-oxine -MTC	97.6%± 0.1% (n=10)	100% (n=5)
^{111}In-MTC		83.7 ± 1.2% (n=3)
^{111}In-DOTA-MTC	95.1 ± 2.5% (n= 5)	84.9 ± 2.6% (n=3)
^{111}In-ABz-DOTA-MTC	96.9%± 2.2% (n= 5)	97.7 ± 0.9% (n=3)
^{111}In-oxine -MTC	100%	100% (n=3)
^{125}I-MTC	-	10.8% ± 5.2% (n=3)
^{125}I-Iodogen-MTC		88.1% ± 2.0% (n=3)
^{131}I-iodohippurate-MTC		76.1% ± 0.8% (n=3)
^{131}I-MIBG-MTC		97.9% ± 0.1% (n=3)

Binding stability profiles of these different radiolabeled MTC products in human plasma at 37°C are shown in Figures 1 through 3.

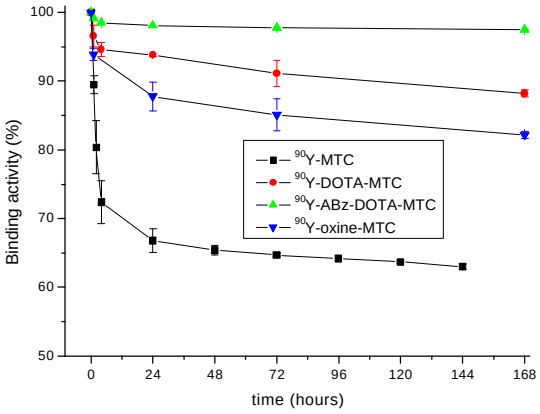

Fig. 1: Plasma stability of ^{90}Y-MTC, ^{90}Y-DOTA-MTC, ^{90}Y-ABz-DOTA-MTC, and ^{90}Y-oxine-MTC.

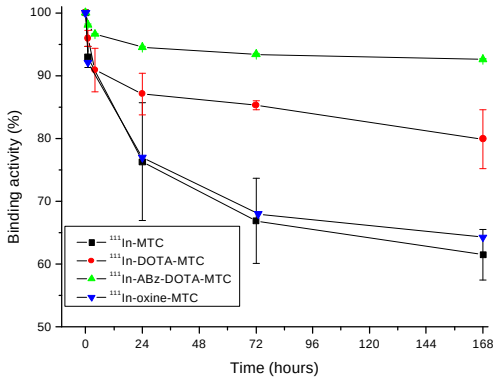

Fig. 2: Plasma stability of ^{111}In-MTC, ^{111}In-DOTA-MTC, ^{111}In-ABz-DOTA-MTC and ^{111}In-oxine-MTC.

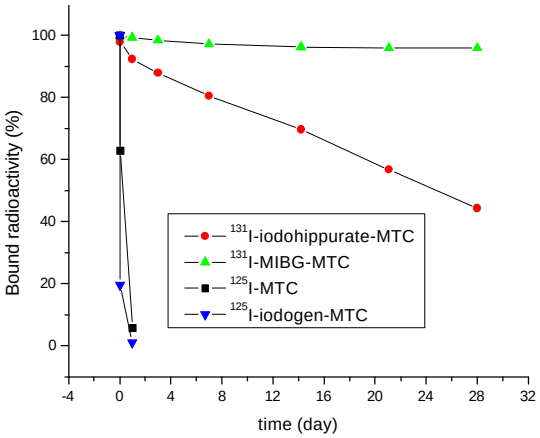

Fig. 3: Plasma stability of ^{125}I-MTC, ^{125}I-iodogen-MTC, ^{131}I-iodohippurate-MTC and ^{131}I-MIBG-MTC.

The TLC system consisting of Sil G/UV$_{254}$ as stationary phase and 8:2 of 10% NH_4Ac (pH 4): methanol as the mobile phase is appropriate for the analysis of ^{90}Y-labeled compounds (Figure 4). In this system, free $^{90}Y^{3+}$ migrates with the solvent front (R_f: 0.8-1.0) while ^{90}Y-MTC (or ^{90}Y colloid) stays at the origin (R_f: 0). The R_f of ^{90}Y-DOTA is 0.2-0.4 and ^{90}Y-ABz-DOTA 0.3-0.5. This system is also suitable for the characterization of the ^{111}In-compounds.

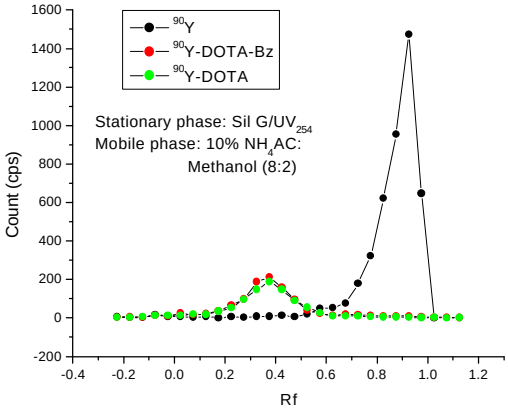

Fig. 4: TLC system for analysis of ^{90}Y-DOTA, ^{90}Y-ABz-DOTA and ^{90}Y-ABz-DOTA-MTC.

However, not every radiopharmacy uses a radiation scanner, and analysis should also be made possible by cutting the TLC in two pieces and counting them with a γ- or β-counter. We therefore evaluated additional TLC systems. The Tec-strip and ITLC systems with methanol as solvent, or Whatman 17 paper with water as solvent also separated free and chelated ^{111}In (^{90}Y) (Figure 5). The strips can both be cut into two pieces at 1 cm from origin and counted in a γ-counter. As In colloids could be counted together with free ^{111}In, a control should be run to determine the eventual concentration of colloids *vs* free when using these three TLC systems.

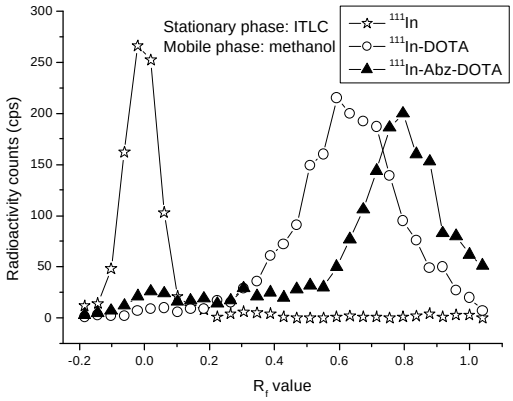

Fig. 5: TLC system for analysis of free ^{111}In, ^{111}In-DOTA and ^{111}In-ABz-DOTA.

DISCUSSION & CONCLUSIONS: *In vitro* results described here indicate the potential for the MTC technology to be used for the site-specific targeting of therapeutic and imaging radioisotopes. The chelation and binding efficiencies, and stability profiles in human plasma for ^{90}Y-ABz-DOTA-MTC and ^{131}I-MIBG-MTC are particularly encouraging.

MTCs can be targeted to specific sites in the human body using a small, externally positioned permanent magnet which creates a localized magnetic field within the body at the desired site. MTCs are administered intra-arterially with the catheter positioned proximal to the targeted area. The physical force created by the magnetic field pulls the MTCs out of circulation through the endothelial wall (extravasation) into the interstitial space, resulting in

localization and retention of the microparticles at the targeted site. The magnet is removed approximately 15 minutes after infusion of MTCs [2]. In the Phase I/II clinical trial investigating safety and tolerability profile in patients with primary liver cancer, MTC-Doxorubicin microparticles have been shown to be efficiently targeted to liver tumors. In addition, it had been previously demonstrated in healthy swine that MTCs were efficiently and selectively targeted to different organs using ^{99}Tc labeled MTCs [5].

Therefore, the development of MTCs labeled with therapeutic radioisotopes could lead to radiopharmaceuticals suited for the intra-tumoral radiotherapy of solid tumors.

Preliminary *in vivo* investigation of the binding stability and localization was performed in normal swine. Eleven mCi of ^{90}Y-ABz-DOTA-MTC was administered intra-arterially to a swine liver via catheterization of the hepatic artery. Blood samples were taken following the administration, which indicated that less than 3% of the total injected activity was circulating 30 minutes following the administration and decreased over time. In addition, a γ-camera image taken 24 hours after the injection using the Bremsstrahlung emission associated with ^{90}Y. While purely qualitative, the picture shows a single source of emission in the region of the liver where the ^{90}Y-ABz-DOTA-MTCs were targeted (Fig. 6).

In conclusion, *in vitro* results suggest that the MTC technology may be used for the site-specific delivery of radioisotopes. ^{90}Y-ABz-DOTA-MTCs is potentially a good candidate for the intra-tumoral radiotherapy of solid tumors.

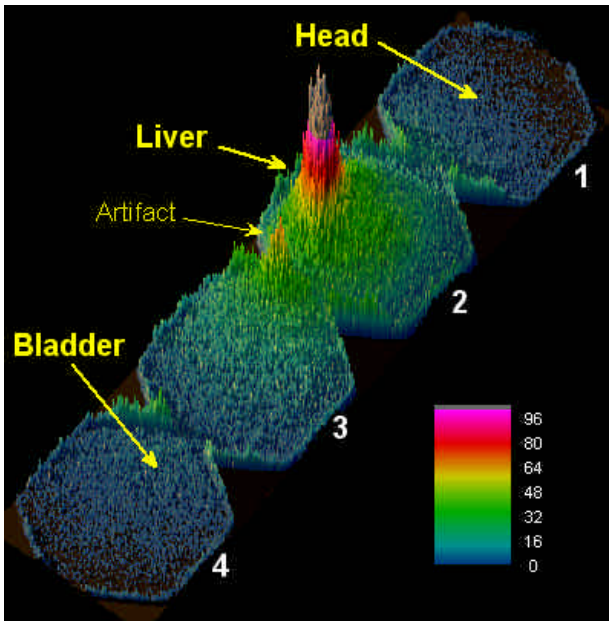

Fig. 6: Bremsstrahlung image taken 24 hours after intra-arterial delivery of ^{90}Y-ABz-DOTA-MTCs to the right liver lobe of a swine. The animal was lying on its back. Four consecutive scans were taken and combined in this figure. The artifact is due to imperfect alignment of the scans 2 and 3 (they were taken too close together).

REFERENCES:

[1]S.R. Rudge, T.L. Kurtz, C.R. Vessely, et al (2000) *Biomaterials* **21**: 1411-20. [2] S. Goodwin, C. A. Bittner, C.L. Peterson, G. Womg (2001) *Toxicological Sciences* **60**: 177-83. [3]U.O. Häfeli, G.J. Pauer, S. Failing, et al (2001) *Journal of Magnetism and Magnetic Materials* **225**: 73-8. [4]F.F. Knapp (1998). *Cancer Biotherapy and Radiopharmaceuticals* **13**: 337-49. [5] S. Goodwin, C. A. Bittner, C.L. Peterson, C. Hoh, (1999) *Journal of Magnetism and Magnetic Materials* **194**: 132.

ACKNOWLEDGEMENTS: We are thankful to FeRx Inc. and NIH (SBIR # CA 88597-01) for funding this study and to Draximage for providing us with ^{131}I-iodohippurate and ^{131}I-MIBG.

USE OF THE PHOTOACOUSTIC SPECTROSCOPY IN THE INVESTIGATION OF IONIC MAGNETIC FLUIDS

P.C. Morais, A.L. Tronconi, & A.C. Oliveira

Universidade de Brasília, Instituto de Física, Núcleo de Física Aplicada, 70919-970 Brasília-DF, Brazil

INTRODUCTION: High-resolution microscopy, magnetization, and static magnetic birefringence are traditional magnetic fluid (MF) characterization techniques. Magnetic resonance and Raman spectroscopy were introduced more recently as extremely useful tools in the investigation of MF properties. However, the wide range of applications of MFs, as for instance in the biomedical field, requires more detailed investigation of their properties. In particular, the nature and interaction of the nanoparticle surface coating layer with both the surrounding medium and the nanoparticle core has attracted much attention in recent years. Photoacoustic (PA) spectroscopy is a well-established, surface-based experimental technique [1] with a wide range of application in material science. Nevertheless, only recently, has PA spectroscopy been used in the investigation of MF samples [2]. Briefly, the PA effect measures the non-radiative de-excitation processes that occur in a system after it has been optically excited by wavelength-variable modulated light. In this study, features in the PA signal obtained from thin liquid films of ionic MF samples deposited on top of inert substrates are used to draw conclusion about the suspended magnetic nanoparticles and the corresponding surface coating layer.

METHODS: Similarly to the standard procedure described in Ref. [3] three preparations containing $MnFe_2O_4$ nanoparticles, with different mean diameter values (3.8, 6.6, and 10.7 nm), were used to produce stable ionic MF samples. The $MnFe_2O_4$-based MF samples were stabilized around pH3 and labeled samples 1, 2, and 3, corresponding to mean diameter values of 3.8, 6.6, and 10.7 nm, respectively. PA spectra were taken from the three MF samples prepared as a thin liquid film on top of a polished quartz substrate. The MF samples were enclosed in a sealed, high-performance, PA cell at atmospheric pressure, coupled to a sensitive microphone. The light from a 150 watt Xe lamp was dispersed by a 0.22 m double monochromator (Spex model 1680) and used as the variable wavelength light source. The light was chopped at a frequency of a few hertz, to improve the signal-to-noise ratio. Figure 1 shows a schematic representation of the PA experimental setup. All the PAS spectra of the samples were normalized to the spectra of a highly absorbing film. For the three samples investigated, several PA features were observed in the wavelength range of 0.3 to 1 μm. In the range of 0.35 to 0.45 μm an intense band (band-C) was observed in the PA spectra. A less intense structure (band-S) was observed around 0.47 μm. Finally, in the 0.65 to 0.90 μm region a complex structure (band-L), identical in the three samples investigated, was observed in the PA spectra.

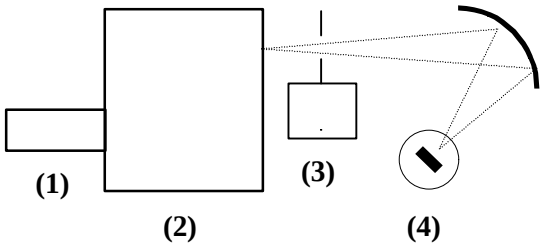

Fig. 1: Typical experimental setup of the photoacoustic experiment. (1) is the lamp, (2) is the monochromator, (3) is the chopper, and (4) is the PA cell.

RESULTS & DISCUSSION: Figure 2 shows the PA spectra of samples 1, 2, and 3 in the range of 0.3 to 1 μm. The features occurring in bands L, S, and C will be discussed as follows. Band-L shows identical features in all ferrite-based ionic MF samples we have investigated so far, including samples with divalent metal-ions as different as Fe^{2+}, Co^{2+}, Ni^{2+}, Zn^{2+}, and Cu^{2+} (data not shown). It is claimed that band-L is related to the characteristics of the MF stabilizing coating layer, thus explaining the similarities observed in the PA spectra of all ionic MF samples investigated to date. The main peak (around 0.47 μm) of band-S is quite intense in manganese-ferrite-based ionic MF samples, similar to what has been observed in cobalt-ferrite-based ionic MF samples [2]. As previously stated [2], band-S is related to the metal-polyoxy-hydroxy surface layer built up at the ferrite-based nanoparticle surface, which is particularly enriched by hydroxyl groups [4]. Furthermore, the strong peak around 0.47 μm, observed in all ionic MF samples investigated, indicates the expected high surface hydroxyl grafting coefficient. Note that the PA band around 0.47 μm is typical of the crystal field band of transition-metal ions in a distorted octahedral environment [5]. Finally, the spectral features observed in band-L and band-S could be associated

to higher-order Raman overtones due to molecular species in the coating layer and in the nanoparticle surface, respectively.

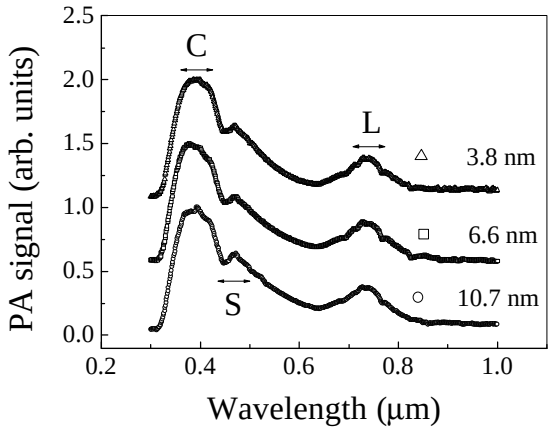

Fig. 2: PA spectra of ionic magnetic fluid samples based on $MnFe_2O_4$ nanoparticles with different average sizes.

Whereas band-L and band-S have been respectively ascribed to the stabilizing coating layer and the nanoparticle surface layer, band-C has been related to the absorption of the incident light by the core nanoparticle [2]. At this point we should emphasize that the PA signal scales with the optical absorption coefficient and, under low optical excitation intensities, the PA signal scales linearly with the optical absorption coefficient. Further, the optical absorption edge of most bulk ferrite-based crystals falls in the range of 0.3 to 0.4 μm. It is important to mention that a semiconductor quantum dot model has been successfully used to explain the charge-discharge mechanism as well as the stability of aqueous colloids based on ferrite nanoparticles. Moreover, the PA signal represented by band-C has been previously attributed to a charge-transfer band [5]. Therefore, the main features of band-C in the PA spectra shown in Figure 2, namely, the presence of structures and the rapid rise of the PA signal at decreasing wavelength, are the signatures of optical processes near the semiconductor absorption edge. One aspect that deserves attention with regard to band-C (see Figure 2) is the presence of structures. A more detailed analysis of the features appearing in Figure 2 can be performed after imaging the PA signal in the the wavelength window of 0.41 to 0.46 μm. Figure 3 shows the first derivative of the PA signal in the 0.41-0.46 μm range. The first derivative of the PA signal, probably gaussian in shape, does improve the band deconvolution procedure into several components. The right-hand side arrows in each PA spectrum (see Figure 3) are claimed to be signal fundamental optical transitions in the band-C region, quoted at 0.432, 0.436, and 0.439 μm for samples 1, 2, and 3, respectively. This is exactly the wavelength order one should expect for the size-dependence of the fundamental optical transition in quantum-confined semiconductor systems. In Figure 3 extra arrows are pointing to features occurring at higher energies. These features are claimed to be due to optical transitions between excited energy states. In support to the view described above, the PA features in sample 1 (3.8 nm particle size) appear much more widely spaced in energy, compared to those for samples 2 and 3. This is due to the quantum confinement effect, which is expected to be stronger in sample 1 in comparison to samples 2 and 3.

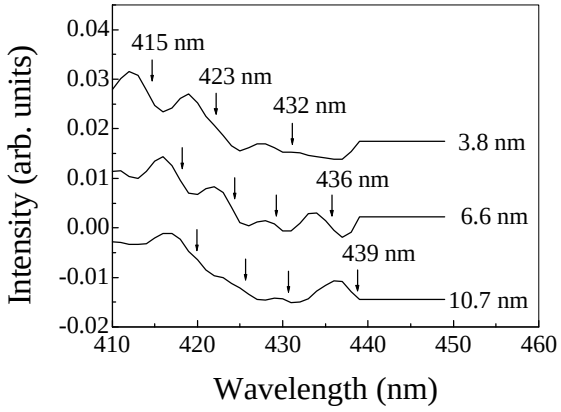

Fig. 3: First derivative of the PA spectra, in the range of 0.41 to 0.46 mm.

At this point it is important to stress that a more detailed analysis (a quantitative analysis) of the PA features revealed in Figure 3 requires knowledge of several parameters, not only for the nanoparticle core but also for the nanoparticle surface layer. Among the parameters are the electron and hole effective masses, conduction and valance band offsets, dielectric constants, and fundamental band-gaps. In addition to these parameters the pH of the magnetic fluid sample is extremely important in order to include the surface charge density and thus the effects due to band-bending and band-gap renormalization. Not only is such analysis far beyond the scope of the present study, but to date the required parameters are not available.

CONCLUSIONS: In summary, this study shows that PA spectroscopy emerges as a powerful technique to investigate magnetic fluid samples. Three main bands (L, S, and C) were identified in the 0.3 to 1 μm spectral range. Bands L, S, and C were ascribed to the coating layer, to the metal-

polyoxy-hydroxy thin layer at the nanoparticle surface, and to the nanoparticle core, respectively. Features in band-C were associated with the fundamental and excited optical transitions in the quantum-confined semiconductor system (quantum dot). Indeed, PA spectroscopy requires relatively low-cost instrumentation and most of the systems in operation are home made.

REFERENCES: [1]A. Rosencwaig and A. Gersho (1975), *Science* **190**:556-557. [2]A.C. Oliveira, A.L. Tronconi, N. Buske, and P.C. Morais, *J. Magn. Magn. Mater.* (in press). [3]P.C. Morais, V.K. Garg, A.C. Oliveira, L.P. Silva, R.B. Azevedo, A.M.L. Silva, and E.C.D. Lima (2001), *J. Magn. Magn. Mater.* **225**:37-40. [4]P.C. Morais, S.W. da Silva, M.A.G. Soler, and N. Buske (2001), *Biomol. Eng*. **17**:41-49. [5]A. Rosencwaig (1977) *Solid State Photoacoustic Spectroscopy* in Optoacoustic Spectroscopy and Detection (ed Y-H. Pao) Academic Press, pp. 193-239.

ACKNOWLEDGEMENTS: This work was supported by the Brazilian agencies FAP-DF, CNPq, and FINATEC.

MAGNETO-OPTICAL RELAXATION OF FERROFLUIDS

C. Groß[1], E. Romanus[1,2], G. Glöckl[1], P. Weber[2], and W. Weitschies[1]

[1]*Institute of Pharmacy, Ernst-Moritz-Arndt-Universität Greifswald, Jahnstr.17, D-17487 Greifswald, Germany,* [2]*Institute of Solid State Physics, Friedrich-Schiller-Universität Jena, Helmholtzweg 5, D-07743 Jena, Germany*

Introduction: A variety of different methods for the determination of biological binding reactions are available due to the great interest in biology, biochemistry and medicine. One approach to the determination of biological binding reactions is based on the use of single domain magnetic nanoparticles (MNP) as signal generators conjugated with one of the components of the binding reaction [1-3]. The measured signal is the relaxation of the magnetization of the magnetic nanoparticles after switching off a magnetizing field. As the concentrations of the binding partners are usually very low, the measured magnetic relaxation signals are extremely weak. Therefore, the detection of such magnetic relaxation signals requires a sophisticated measurement setup based on superconducting quantum interference devices (SQUIDs) as the currently most sensitive, magnetic field sensors.

Ferrofluids become birefringent when a magnetic field is applied perpendicular to the optical axis of light impinging the fluid, as the magnetic nanoparticles contained in the ferrofluid tend to align in the direction of the external field. This causes an optical anisotropy (Cotton-Mouton-effect) [4]. After switching off the magnetizing field a relaxation of the optical birefringence can be observed due to Brownian motion. Recently, it has been demonstrated that magneto-optical relaxation measurements can be used for the determination of binding reactions of biological molecules attached to magnetic nanoparticles [5]. The aim of the present study was to evaluate this novel approach for the determination of biological binding reactions of antibody-conjugated MNP.

METHODS: Magnetic nanoparticles. Magnetic nanoparticles with a core of iron oxide (DDM 128N, Meito Sangyo, Japan) and a shell of carboxydextran were magnetically fractionated at 50 mT, as described elsewhere [6]. The coupling of streptavidin onto the nanoparticles was achieved by oxidation of the carboxydextran molecules on the surface of the nanoparticles and reaction of streptavidin with the aldehyde groups formed during oxidation of the carboxydextran shell. Briefly, 15 mg sodium periodate were dissolved in a citrate/phosphate buffer (pH 5.0) and added to 2 ml of the magnetic nanoparticles. The mixture was incubated at 4°C for 40 min. Thereafter, the buffer was exchanged to 10 mM phosphate buffer pH 7.4 by size exclusion chromatography. Then, 2 mg of streptavidin were added. After 2 h incubation at 4°C dimethylborane (150 mM) and ethanolamine (0.5 M) were added. Finally, the magnetic nanoparticles were purified via magnetic separation and stored in 0.1 % BSA/PBS at 4°C. For the determination of the binding reaction between an antibody and its antigen the biotinylated antibody was attached to the nanoparticles via the binding between biotin and streptavidin.

Measurement setup. The measurement setup for the determination of the magneto-optical relaxation of ferrofluids (MORFF) consists of a laser (L), a polarizer (P), a λ/4 plate (R), a cuvette (C) containing the sample, an analyzer (A) and a detector (D) mounted on an optical bench. Figure 1 shows a scheme of the measurement setup. The polarizer and analyzer are aligned orthogonally and at 45° to the magnetic field axis (or, more precisely, the axis of birefringence). The polarizer is parallel to the slow axis of the λ/4 plate. The cuvette is placed into a magnetization coil generating a pulsed magnetic field with a magnetic flux density of 10 mT at a frequency of 20 Hz and with a duty cycle of 25 % corresponding to a magnetization time of 12.5 ms. The relaxation of the birefringence is recorded by a photodiode. The measurement runs continuously without any delay between magnetization and detection.

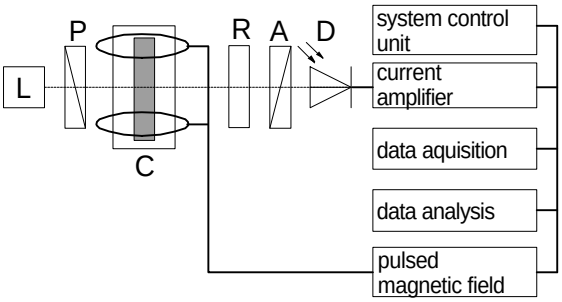

Fig. 1: Measurement setup for the detection of the magneto-optical relaxation in ferrofluids.

Results: The mean hydrodynamic particle diameters obtained by MORFF measurements for the binding experiments are shown in Figure 2. The data show that during the observed incubation time of 6 h the mean particle sizes of the samples incubated with 10 ng, 100 ng, 1 µg and 10 µg of hIgG are increasing. The maximum increase in particle size was found for an added amount of 1 µg. For higher amounts of hIgG an increasing number of binding sites becomes saturated and, thus, cannot further contribute to the crosslinking.

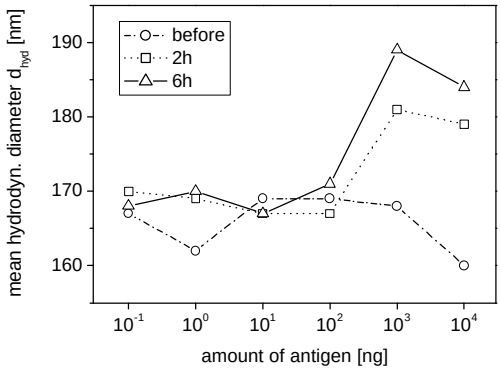

Fig. 2: Hydrodynamic particle diameters calculated from magneto-optical measurements before, 2 h and 6 h after addition of different amounts of antigen (hIgG) to magnetic nanoparticles conjugated with an antibody against hIgG.

Discussion and Conclusions: The presented experiments confirm that the determination of the relaxation of the transient field-induced birefringence of magnetic nanoparticles can be used as a novel tool for the investigation of biological binding reactions, as long as these reactions result in an increase of the particle size of magnetic nanoparticles due to aggregation. Compared to magnetic nanoparticle relaxation measurements the separation of stimulation (magnetic) and signal detection (optical) is of great advantage, as the optical measurement system is comparatively simple, robust and compact. The application of optical measurements is restricted by optical properties of the sample due to scattering or absorption of the laser beam. Nonetheless, magneto-optical nanoparticle relaxation measurements seem very feasible for *in vitro* investigations of binding reactions.

Acknowledgments: This research project is supported by the Deutsche Forschungsgemeinschaft (DFG), No. WE 2555/2.

References: [1]Weitschies, R. Kötitz, T. Bunte, and L. Trahms (1997) *Determination of relaxing or remanent nanoparticle magnetization provides a novel binding-specific technique for the evaluation of immunoassays* Pharm. Pharmacol. Lett. **7**: 5-8. [2]R. Kötitz, H. Matz, L. Trahms, H. Koch, W. Weitschies, T. Rheinländer, W. Semmler, and T. Bunte (1997) *SQUID Based Remanence Measurements for Immunoassays* IEEE Trans. Appl. Supercond **7**: 3679-3681. [3]Y.R. Chemla, H.L. Grossman, Y. Poon, R. McDermott, R. Stevens, M.D. Alper, and J. Clarke (2000) *Ultrasensitive magnetic biosensor for homogeneous immunoassay* PNAS **97** 14268-14272. [4]A. Cotton, H. Mouton (1907) *Nouvelle propriété optique (biréfringence magnétique) de certains liquides organiques non colloïdaux* Comptes Rendus hebdomadaires des Séances de l'Académie des Sciences Paris **45**: 229-231 [5]E. Romanus, C. Groß, R. Kötitz, S. Prass, J. Lange, P. Weber, and W. Weitschies (2001) *Monitoring of biological binding reactions by magneto-optical relaxation measurement* Magnetohydrodynamics **3:** 328-333 [6]T. Rheinländer, J. Justiz, A. Haller, R. Kötitz, W. Weitschies, W. Semmler (1999) *Dynamic properties of fractions yielded by magnetic fractionation of magnetic fluids* IEEE Trans. Magn. **35**: 4055-4057

CHARACTERIZATION OF MAGNETIC PARTICLES AND MICROSPHERES AND THEIR MAGNETOPHORETIC MOBILITY USING A DIGITAL MICROSCOPY METHOD

U. O. Häfeli [1], R. Ciocan[2], J.P. Dailey[3]

[1] *The Cleveland Clinic Foundation, 9500 Euclid Ave. T28, Cleveland, OH 44195, USA,*
[2]*University of Akron, Electrical Engineering Department, Akron, OH 44325,*
[3]*Division of Ophthalmology, Hamot Medical Center, 300 State Street, Suite 200A, Erie, PA 16507*

INTRODUCTION: Although direct measurements of the magnetic susceptibility of magnetic microspheres can be made with a magnetic Faraday balance [1-3], as well as with MRI techniques [4], the results only hint at the microspheres' behavior in vivo, as for example after injection into a person's blood system. For such applications, magnetic susceptibilities only give an approximate indication of magnetic 'responsiveness' because magnetic microspheres, nanospheres and particles not only span a large range of sizes, but are also made from many different matrix materials incorporating different types and amounts of magnetic compounds [5]. In addition, these magnetic compounds can be distributed quite differently within the microsphere. Other factors such as the solvent system, the particle's porosity, its density, surface coating and aggregation tendencies can further influence its overall magnetic responsiveness. For clinical applications in the blood circulation of a person [6], an all-inclusive test would be advantageous that allows to choose the most appropriate magnetic microspheres for a certain application.

In addition to the direct methods, more elaborate but indirect systems have been applied to measure the magnetic susceptibility of magnetic microspheres in suspension. One of these systems is field flow fractionation (FFF) where an external magnetic field is applied perpendicular to the flow direction [7, 8]. The interaction of hydrodynamic and magnetic forces separates the particles. The particles' retention ratio then allows for the calculation of their magnetic susceptibility.

A further improvement in analysis was reached by a 'cell tracking velocimetry' system. In this system, the movement of magnetic microspheres or magnetically labeled cells in a well-defined magnetic field is videotaped [9]. The velocity of each particle passing the camera in laminar flow was determined by tracking its movement. By comparing the data to magnetic particles of calibrated magnetic susceptibility [10], information about their magnetic mobility and susceptibility was obtained.

The aim of the current work is to determine the magnetophoretic mobility (overall 'magnetic responsiveness' or amount of velocity for a given magnetic field and field gradient) of different types of magnetic microspheres so that their behavior in a patient's circulation can be predicted. For this purpose, we developed a stationary setup, similar to the just described cell tracking velocimetry system, which can be used on a standard microscope equipped with a digital camera and computer system. The main difference to the above system is that there is no flow of the suspension liquid containing the magnetic particles. The geometry and size of the setup and the magnets used can thus be reduced considerably (see Fig. 1). Furthermore, the close combination of the microscope setup with a computer allows fully automated data acquisition and processing.

METHODS: In order to analyze the movement of the magnetic microparticle in a static magnetic field we assumed that (1) there is no interaction between particles, (2) the particles are perfect spheres, (2) the gravity force does not affect the movement of the analyzed microspheres, (4) the product $H\frac{dH}{dy}$ in the measurement area is constant across the capillary, (5) the magnetic field in x-direction (along the capillary, Fig. 1) is constant ($\frac{dH}{dx}=0$), and (6) the particle's Reynold number is less than 1 (i.e., the friction force becomes the Stoke's force). The particle movement in this hypothetic situation thus becomes unidimensional and constant and is equal to

$$v=\frac{V_m c m_0 H\frac{dH}{dy}}{3phD} \qquad (1)$$

This relationship was demonstrated by Senyei et al [11]. The movement of a magnetic microsphere in a well defined magnetic field is determined by (1) the magnetic properties of the particle (volume of the magnetic component, V_m; and magnetic susceptibility, χ), (2) the hydrodynamic properties

of the medium (viscosity, η), and (3) the dimensions (diameter, D) and physical properties (mass, m).

When analyzing magnetic microspheres of the same type with identical shape and homogeneous distribution of the magnetic component, but different particle diameter, then the velocity v can be expressed as a function of the changing radius r or diameter D as

$$v = \frac{2r^2 f_m c m_0 H \frac{dH}{dy}}{9h} = \frac{D^2 f_m c m_0 H \frac{dH}{dy}}{18h} \qquad (2)$$

Magnetic fields were measured with a gaussmeter and the field gradients calculated.

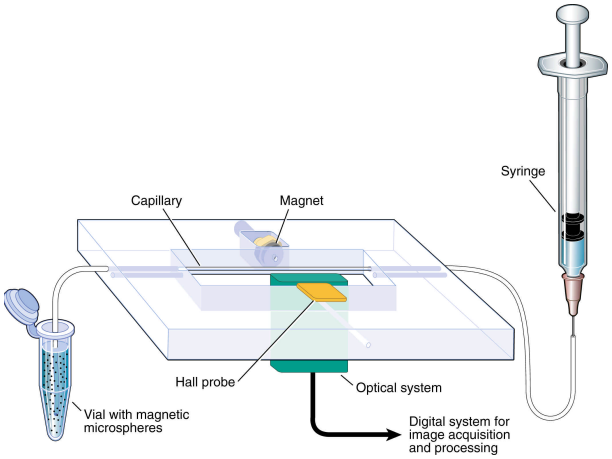

Fig. 1: Schematic setup of the microscopy table for magnetic microsphere measurement.

A Nikon TMS optical microscope was used together with a table moveable in x and y direction with finger screws. A supplementary custom-made piece of acrylic (9×13 cm^2) was placed on the microscope table (Fig. 1). A 1.0 mm inner diameter glass capillary was filled with a well-mixed microsphere suspension (about 0.2 to 1 mg/ml, depending on microsphere size) using a 1 ml syringe. During the filling, the magnet was 18 mm away from the capillary (magnetic field <2 mT). The microscope was then manually focused so that the DC-330 3CCD color video camera (Dage-MTI, Michigan City, IN) mounted on the microscope and connected to a computer displayed a clear picture of the microspheres on the screen. The images were captured using a Flashpoint 128 video capture card (Integral Technologies, Indianapolis, IN). The magnet was moved close to the capillary, to a magnetic field of ~12 mT and a magnetic field gradient of ~5 mT/mm, and the automated system for image acquisition was started. A sequence of 10 images was saved per sample at an interval of one frame per second. The images were saved directly in digital form using the imaging software ImagePro Plus from Media Cybernetics (Silver Spring, MD). The difference of two succesive images was obtained directly with a built-in software function, resulting in a differential picture of only the moving particles (Fig. 2). The initial microsphere position is shown in white, the final position in black. From these differential pictures, individual parameters for each moving microsphere were automatically determined, such as their X,Y-coordinates, roundness, and median diameter for each of frame 1 through frame 10.

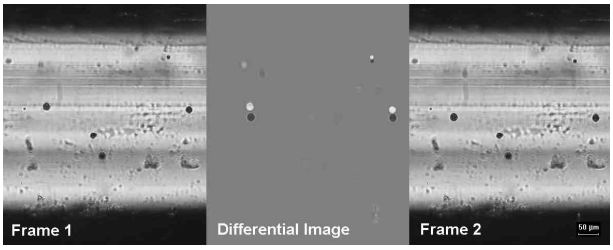

Fig. 2: Typical microscopic images captured during the analysis. The first frame is the first of a set of 10 images, separated by 1 second from frame 2. The differential image of the magnetic poly(lactic acid) microspheres in these two frames is shown in-between. All static elements such as unfocused or stopped microspheres, reflections, light artifacts and the capillary disappear.

Before particles can be counted and their movement calculated, they must satisfy certain criteria: (1) The roundness has to be equal to 1.0 ± 0.3, thus excluding microsphere clusters from investigation. (2) The particle diameter cannot be less than 1.3 µm. This is the minimal pixel size for the optical configuration used with a magnification of 10x. (3) The maximum distance of allowed movement from one frame to the next is the capillary's diameter of 1.0 mm. And finally (4), the maximum traveling distance accepted in the X direction, which is the axis perpendicular to the magnet cannot exceed ± 1.3 µm (1 pixel). This excludes from analysis any movements due to remaining flow or magnetic interactions between particles. The velocities and diameters were determined for all microspheres that satisfied these criteria using the software program Labview V5.0 (National Instruments, Austin, TX). Seven different types of microspheres were investigated. Their main characteristics are listed in **Table 1**.

Description	Composition	Size (µm)	Density (g/cm^3)	Velocity in water (cm/s)	Velocity in CMC or glycerol* 5% (cm/s)	Magnetization at 1 kOe / saturat. (emu/cm^3)
Magnetic glass microspheres[4]	Iron lanthanum silicate with ~15% Fe_3O_4 (8-10 nm sized)	2 - 20	4.6	8.80 ± 3.01	6.95 ± 4.06	18.1 / 29.2
Dynabeads M280[1]	Polystyrene microspheres with 12% γ−Fe_2O_3	2.8 ±0.2	1.3	13.41 ± 3.74	5.48 ± 3.12	~12 / ?
Micromer-M[2]	Polystyrene micro-spheres (3% Fe_3O_4)	12	1.2	10.24 ± 4.51	3.29 ± 2.62	3.0 / 3.6
Albumin-M[2]	Albumin microspheres with 30% Fe_3O_4	2	1.2	12.31 ± 4.10	8.84 ± 3.71	10.3 / 13.5
PLA-M[2]	Poly(lactic acid) micro-spheres (48% Fe_3O_4)	2.0	1.3	12.36 ± 5.11	6.67 ± 2.55	13.7 / 21.1
MMS	Poly(lactic acid) micro-spheres (10% Fe_3O_4)	15-21	1.3	11.19 ± 4.04	8.19 ± 3.80*	8.8 / 11.7
Estapor[3]	Polystyrene micro-spheres (39% Fe_3O_4/Fe_2O_3)	2.6	~1.6	15.68 ± 2.85	11.09 ± 3.61*	? / 13.2

Table 1. Properties of the analyzed microspheres. [1]Dynal, [2]micromod, [3]Merck, [4]MO-SCI Corp., [5]FeRx.

RESULTS: The feasibility of the newly developed microscopy method was tested with different magnetic microspheres adequate for in vivo application. Testing up to about 300 microspheres in one experiment is very fast. In fact, the preparation of a homogeneous microsphere suspension takes just as long as the entire measurement and analysis of a sample. The raw pictures as for example frame 1 and 2 in Fig. 2 are automatically stored, the differential images extracted and X,Y-coordinates, roundness, and median diameter of all allowed features automatically determined using a macro. The data points are then extracted into a special program written to analyze the microspheres' movement parameters. Fig. 3 shows the control panel of this program with the trajectories and main parameters determined for the Micromer-M microspheres. A total of 321 microspheres was analyzed in this measurement. The color-coding of the microspheres makes even overlapping trajectories possible and analyzable.

Initial results with our method are given in Table 1. The results are not as diverse as we expected, something that is very likely due to the fact that microspheres with higher density sink immediately to the ground of the capillary and thus escape the analysis. A more viscous medium such as 5% carboxymethyl cellulose (CMC) seems to help to get an analysis with statistically appropriate numbers of microspheres. As expected from eq. 1, the higher viscosity of the medium decreases the velocity by the factor "viscosity of water / viscosity of the medium".

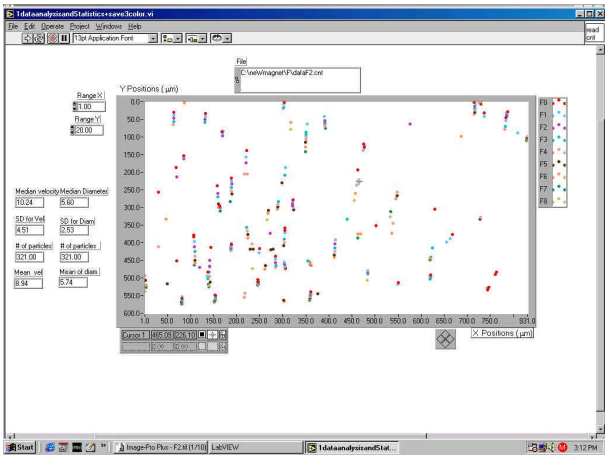

Fig. 3: Control panel of the program written for data analysis. The screen shows the trajectories and the main parameters determined for the Micromer-M microspheres.

Some limitations are connected to the optical system. For example, we used a 10x objective on the microscope to analyze all samples. At this magnification, one pixel equals 1.3 µm, and anything smaller than that will be detected only with difficulty. The determination of the size of smaller particles is difficult and will be inaccurate, although

the determination of the particle dimension might not be that critical in cases where the microspheres are highly uniform, as is the case with the magnetic polystyrene microspheres. On the other hand, our setup allows up to a 40x lens for the determination of the magnetic responsiveness. In combination with shorter intervals between frames, this would allow to analyze magnetic nanospheres down to a diameter of about 500 nm. Also, the use of square capillaries instead of round ones might increase the number of microspheres that can be analyzed per measurement, because less particles will fall outside the stringent 'scoring' criteria. In addition, square capillaries would prevent distortions in the optical measurements and increase the accuracy of the microsphere size measurements.

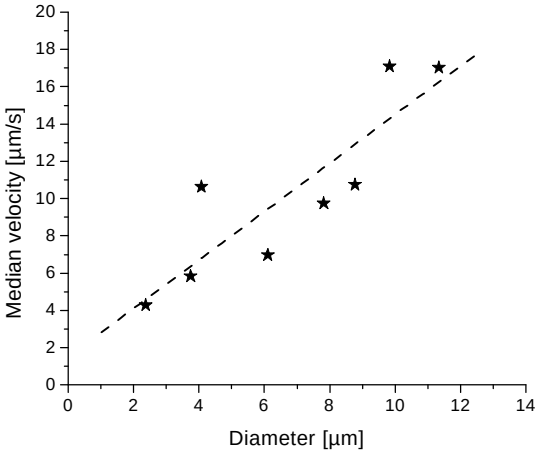

Fig. 4: Dependence of median velocity versus diameter for magnetic glass microspheres.

The analysis of single trajectories from our different tested magnetic microspheres confirmed that the velocity of the particles stays constant over the 10 seconds of measurement time. The speed of the microspheres stayed generally within better than ±15%. The constant velocity also demonstrates that many of the particles remained in the horizontal (focal) plane during the measurement. This seems to confirm that gravity can be neglected with high enough frame rates, although we plan to integrate this factor into a later version of our program.

The dependence of the velocity on the particle diameter could be determined directly for samples that showed a broad size distribution. Larger magnetic microspheres, as shown in **Fig. 4** using the magnetic glass microspheres showed a more or less linear increase in velocity with increase in diameter. This is less than the theoretically expected four-fold increase in velocity when the diameter is doubled (see eq. 2), but confirms the potential of the system.

Future work will repeat the measurements with well characterized solutions and microspheres, use larger numbers of microspheres to get good statistical conditions, and from there calculate the magnetic susceptibility of newly synthesized magnetic microspheres with improved properties. In vivo conditions can be simulated relatively easily by employing a solvent such as blood plasma, spinal fluid or ascites, as well as by adjusting the magnetic field to levels which can be reached in vivo with current setups. For this reason, we plan to replace the currently used permanent magnet with a small electromagnet. Quick comparisons of different magnetic microsphere batches are thus possible using a readily available microscope with digital camera in a standardized fashion. This simple method performed under static, no-flow conditions should thus help to choose the optimal magnetic particle for the application at hand.

REFERENCES: [1] S.J. Gill, C.P. Malone, M. Downing (1960) *Rev. Sci. Instrum.* **31**, 1299-303. [2] L.F. Lindoy, V. Katovic, D.H. Busch (1972) *J. Chem. Ed.* **49**, 117-20. [3] L. Petersson, A. Ehrenberg (1985) *Rev. Sci. Instrum.* **56**, 575-80. [4] O. Beuf, A. Briguet, M. Lissac et al (1996) *J. Magn. Resonance, Series B* **112**, 111-18. [5] R. Arshady (2001) *Microspheres, Microcapsules & Liposomes: Magneto- and Radiopharmaceuticals* (Citus Books, London, ed. 1st), vol. 3. [6] W. Schütt, C. Grüttner, U. Häfeli et al (1997) *Hybridoma* **16**, 109-17. [7] C.B. Fuh, S.Y. Chen (1999) *J. Chromat. A* **857**, 193-204. [8] Y. Jiang, M.E. Miller, M.E. Hansen et al (1999) *J. Magn. Mag. Mat.* **194**, 53-61. [9] S. Reddy, L.R. Moore, L. Sun et al (1996) *Chem. Eng. Sci.* **51**, 947-56. [10] L.R. Moore, M. Zborowski, M. Nakamura et al (2000) *J. Biochem. Biophys. Methods* **44**, 115-30. [11] A. Senyei, K. Widder, G. Czerlinski (1978) *J. Appl. Physiol.* **49**, 3578-83.

ACKNOWLEDGEMENTS: This work was made possible by an AFOSR/DARPA seedling grant and the financial support of the Lord Foundation in Erie, Pennsylvania.

PRELIMINARY STUDIES ON THE DETECTION OF HUMAN ALBUMIN USING ANTIGEN SPECIFIC PRECIPITATION OF MAGNETIC PARTICLES AND MAGNETIC PERMEABILITY MEASUREMENTS

Kirstin Kriz[1,2], Min Lu[1] & Dario Kriz[1,2]

[1]European Institute of Science, Research Park IDEON, SE-223 70, Lund, Sweden and [2]Lund University, Department of Pure and Applied Biochemistry, Box 124, SE-221 00, Lund, Sweden

INTRODUCTION: A novel method for the specific detection of human albumin using magnetic permeability measurements and antigen-specific precipitation of magnetic particles, is presented. Earlier our group has presented the detection of proteins using magnetic permeability detection in direct and competitive sandwich assays [1]. Recently, we have reported the detection of Concavalin A [2,3] and DNA [4] using sandwich assays and nonspecific electrostatic interactions in combination with magnetic permeability measurements. Now we present the immunospecific detection of human albumin.

METHODS: Magnetic particles (100 nm) coated with protein A were obtained from Micromod GmbH in Rostock, Germany. Conjugation of polyclonal anti-human albumin IgG (goat) to the magnetic particles was carried out by incubating 0.45 ml magnetic particles with 90 µl of a 1 mg/ml IgG solution in 162 mM PBS buffer, pH 7.4. Incubation was carried out for 3 hours at room temperature. Non-bound IgG was removed by washing the magnetic particles in PBS buffer using a high-gradient magnetic field device.

The measuring instrumentation used in the experiment, the MPM-100 (magnetic permeability meter), was obtained from the European Institute of Science in Lund, Sweden and is shown in Figure 1. The measuring principle is based on the fact that in the presence of human albumin, the magnetic particles will crosslink via antigen-antibody interactions, and these precipitates will sediment to the bottom of the vial in the presence of a magnetic field. The magnetic permeability of the precipitate is directly proportional to the amount of human albumin present in solution.

Precipitation studies for the detection of free human albumin in solution, were carried out by placing 200 µl (0.25 mg/ml) of magnetic particles conjugated with polyclonal anti-human albumin IgG in a measuring vial. Subsequently, free human albumin was added to solution and the vial was allowed to stand at room temperature for 1 hour. After the 1-hour incubation, the vial was placed on a permanent magnet for 30 minutes. Lastly, the vial was placed in the magnetic permeability meter, and the magnetic permeability of the precipitate was measured. Various amounts of human albumin (0.005, 0.01, 0.1, 0.5, 1.1, 2, 5, 10 and 15 µg) were added and the samples were analyzed using this technique.

Fig. 1: The magnetic permeability meter used for the detection of human albumin.

RESULTS: The magnetic permeability of the precipitate formed by the magnetic particles in the presence of various concentrations (0.5 nM - 1.23 µM) of human albumin was carried out. There is a linear increase in magnetic permeability of the precipitate up to about 840 nM. At 1.23 µM nearly all the magnetic particles had been precipitated from solution. The linear range of the detection curve is shown in Figure 2. The equation of the line obtained is $y = 10.142 + 4.95 \times 10^6 x$, $R = 0.99015$. The limit of detection is 50 nM.

DISCUSSION & CONCLUSIONS: The detection of human albumin in solution was carried out using the antigen-specific precipitation of magnetic particles and magnetic permeability detection. We observed a linear response in the range of 0.5 - 840 nM human albumin. The limit of detection was 50 nM. Further studies on the kinetics of the system and the concentration of magnetic particles need to be conducted. However, our preliminary study

indicates that, for the detection of proteins, the antigen-specific precipitation of magnetic particles is a viable alternative to sandwich format assays.

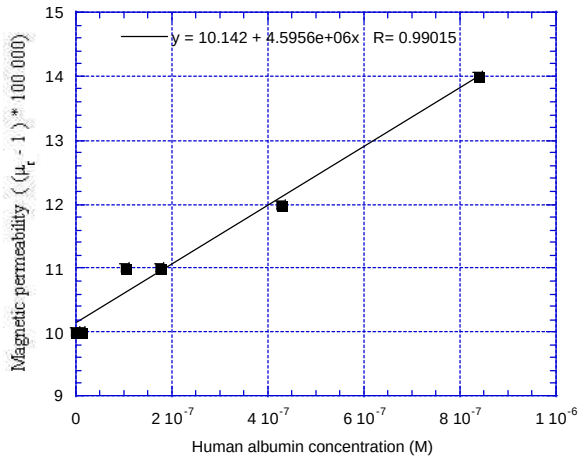

Fig. 2: The linear range (0.5 - 840 nM) for the detection of human albumin.

REFERENCES: [1]Kriz, C.B., Rådevik, K., Kriz, D., 1996. Magnetic permeability measurements in bioanalysis and biosensors. Analytical Chemistry 68, 1966-1970. [2]Kriz, K., Gehrke, J., Kriz, D., 1998. Advancements toward magneto immunoassays. Biosensors & Bioelectronics 13, 817-823. [3]Larsson, K., Kriz, K., Kriz, D., 1999.Mangetic transducers in biosensors and bioassays. Analysis 27, 617-621. [4]Lu, M., Kriz, K., Kriz, D, 2002. DNA detection based on magnetic permeability measurements and electrostatic interactions. Manuscript submitted for publication.

INFLUENCE OF MAGNETIC PARTICLE AGGREGATION ON CYTOMAGNETOMETRY

Winfried Möller[1], Iku Nemoto[2] and Joachim Heyder[1]

[1]*Institute of Inhalation Biology, GSF National Research Center, Gauting, Germany and*
[2]*Department of Mathematical Sciences, Tokyo Denki University, Hatoyama, Japan*

INTRODUCTION: Cytomagnetometry is a novel method to measure cytoskeleton-associated cell functions by the use of ferromagnetic beads. In our studies macrophages ingest ferromagnetic microparticles, which are incorporated into phagosomes. First the particles are magnetized and aligned by a short magnetic field pulse. After that a remanent magnetic field (rmf) of the cell probe can be detected. Intracellular phagosome transport causes stochastic disorientations of the dipole particles, resulting in a decay of the magnetic cell field (relaxation). Relaxation proves motile macrophage functions. Magnetic particle twisting is used to investigate the mechanical integrity and viscoelastic properties of the cytoskeleton. The studies are performed *in vitro* using macrophage cell lines (cytomagnetometry) [1, 2] or *in vivo* after voluntary inhalation of ferromagnetic aerosol particles (magnetopneumography, MPG) [3] In human studies, ~1 mg of ferromagnetic particles are inhaled and the retained particles are detected by a superconducting magnetic field sensor (SQUID) [3]. J774A.1 macrophages and primary alveolar macrophages, obtained by bronchoalveolar lavage, were used for *in vitro* studies. After 24 h incubation of particles with macrophages, more than 90 % of the particles were phagocytized. The purpose of this study is to investigate the influence of magnetic bead aggregation on cytomagnetometric measurements.

METHODS: Spherical ferromagnetic beads of narrow size variation (monodisperse) were produced by centrifugal nebulisation of a colloidal iron oxide (Fe_2O_3) solution [4]. In an atmosphere containing 1-2 % H_2-gas the non-magnetic Fe_2O_3 particles are reduced to ferrimagnetic Fe_3O_4. As long as the particles are not exposed to a strong magnetic field, they are non-magnetic. The particles can be magnetized in a short magnetic field pulse of at least 100 mT strength. The saturation magnetic moment m_{sat}, related to the mass of material, was S_m ~ 3-5 Am^2/kg. The increase of remanent magnetic moment in increasing external fields B_M was approximated by [4]:

$$\frac{m(B_M)}{m_{sat}} = \frac{1}{2}\left\{\tanh\frac{\ln(B_M / B_{50})}{\ln(b_S)} + 1\right\} \quad (1)$$

where B_{50} is the field producing 50% saturation and b_S describes the gradient at B_{50}. Typical parameters of Eq. (1) are B_{50} = 60.3±1.2 mT and b_S = 1.82±0.07.

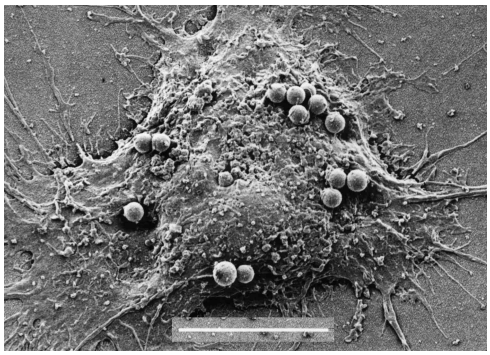

Figure 1: 1.4 µm spherical ferromagnetic microspheres on top of a J774A.1 macrophage (bar = 10 µm)

Figure 1 shows 1.4 µm spherical monodisperse magnetite particles on top of a J774A.1 macrophage after 3 hours of incubation. After that time a large amount of particles can also be found inside (within phagosomes) of the cell. The particles do not aggregate as long as they are not magnetized.

Particle aggregates of defined size were prepared using small magnetic steel spheres. Before forming the aggregate the single spheres were first magnetized in a strong magnetic field. Their remanent magnetic moment was detected by a fluxgate sensor.

RESULTS:

Forces between magnetic dipoles

After magnetization every particle has a remanent magnetic moment m, which produces a magnetic field B. In this magnetic field a force arises to another dipole m according to:

$$\vec{F} = grad(\vec{m}\vec{B}) \quad (2)$$

The field is strongest when the dipole m is parallel to the field lines B. Therefore, besides attraction, an alignment between the dipoles takes place. The force is strongest when both dipoles are aligned along a common z-axis and we get:

$$F = \frac{m_0 m^2}{4p} \frac{6}{z^4} \qquad (3)$$

For example a 2 µm diameter magnetic particle has a remanent magnetic moment of m = 6×10^{-14} Am^2 and the force between two particles having a distance equal to their radius is ~27 pN. This force is higher than the mean force acting on magnetic phagosomes during intracellular transport, which is ~10 pN [5]. The magnetic force exceeds the intracellular transport force and causes the aggregation of the particles. The attractive force decays very rapidly with increasing distance and can be neglected if the distance exceeds about two particle diameters. This shows that significant aggregation only takes place when using high particle concentrations, which are not suitable for cell studies.

Magnetic properties of aggregates

Experimental studies have shown that the formation of magnetic particle multiplets implies more than a superposition of single particles, i.e. a doublet has not double, but four times the magnetic moment of a single particle. When two particles approach one another, they each come into the magnetic field of the neighbor. Besides the arisal of attractive forces between the particles, each particle is in the magnetic field of the neighbor and gets further magnetized. The adherence of remanent magnetic particles causes a mutual magnetization, resulting in an increase of m.

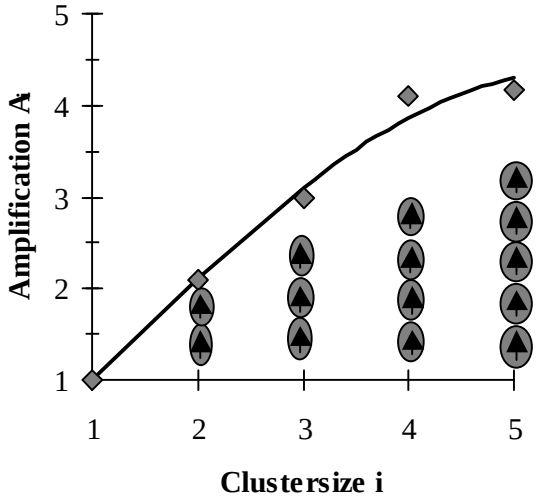

Fig. 2: Effect of aggregated microspheres on rmf. The amplification factor A_i is the relation between the rmf of an aggregate with i subunits and the rmf of i single spheres.

This mutual amplification increases with increasing aggregate size, as shown in Fig. 2, and has significant influence on the cytomagnetometric data evaluation, which will be discussed in the following paragraphs. In macrophage probes containing magnetic particles, the formation of aggregates is seen by an increase of the rmf after multiple pulse magnetizations and the application of twisting fields.

Distribution of particles in macrophages

The number of particles being phagocytized per macrophage is not equally distributed. J774A.1 macrophages are a permanent cell line and therefore a fraction of cells is in the state of cell division. Those cells are not active in phagocytosis and remain free from particles while other cells can phagocytize more particles, even at a particle to cell ratio of 1:1.

Table 1: Percent of cells having no (0), 1, 2, 3, 4 or more particles per cell for a total mean number of particles per cell.

mean	0	1	2	3	>=4
0.5	61	30	8	1	0
1	37	37	18	6	2
1.5	22	33	25	13	7
2	14	27	27	18	14
3	5	15	22	22	35

We describe the number of particles per cell by a Poisson distribution, where the mean denotes the mean number of particles per cell. Results of this relation are shown in Table 1 for 0.5 particles per cell (one particle in every second macrophage) up to 3 particles per macrophage in the mean. For one particle per macrophage in the mean, 37% of the cells remain free from particles, 37% have one particle phagocytized, 18% have two and 10% have more than two particles ingested. But not all particles in multiple loaded macrophages are necessarily aggregated. If we correlate this distribution with the above amplification of multiplets, the rmf of the cell/particle probe increases. The particle multiplets can only be formed after the first pulse magnetization. Longer and multiple application of twisting fields enhances the formation of multiplets, because the particles are aligned in a way that north and south pole of two adjacent particles face to each other. These are optimal conditions for the attraction of the particles.

Relaxation

We use the rotational Brownian motion model to describe relaxation, which implies a randomization energy E_r as driving force [6]. Experimental studies have shown, that E_r is more than 1000 times higher than thermal energy (kT ≈ 4×10^{-21} Joule at 37 °C) and correlates with the intracellular ATP concentration [7]. Rotational Brownian motion of monodisperse spherical particles in a Newtonian viscosity predicts an exponential decay.

$$\frac{B(t)}{B_0} = \exp(-\frac{t}{t}),\ t = \frac{kVh}{2E_r}, \qquad (4)$$

where κ is the rotational shape factor (κ = 6 for spheres), V is the volume of the particles and η is the surrounding viscosity. In order to calculate the relaxation behavior of aggregated particles, we approximate the aggregates as rotational ellipsoids having the same volume, which implies a short axis length equal to the diameter of a single particle and a long axis equal to the aggregate size times the diameter of a single particle. According to Eq. 4 the relaxation time constant τ increases, as shown in Table 2, due to an increase of both the shape factor κ and the volume V.

Table 2: Dependence of rotational shape factor and relaxation time constant (normalized to the time constant of single spheres) on aggregate size.

Aggr-size	1	2	3	4
κ	6	9.03	14.04	20.37
τ/τ_1	1	3.01	7.022	13.58

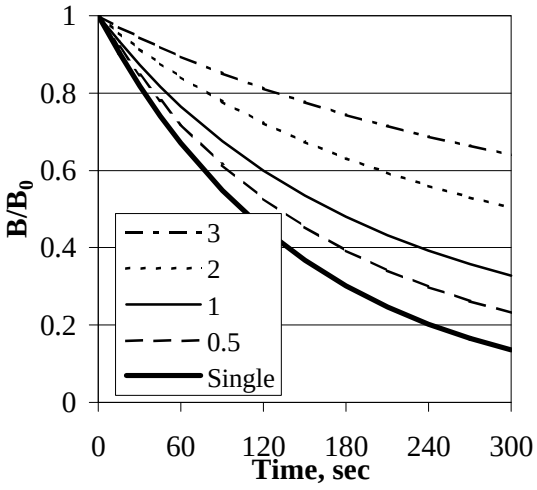

Figure 2: Relaxation behavior of single particles in comparison to a distribution of particles with a mean of 0.5, 1, 2 and 3 particles per macrophage, which are aggregated.

If the particle aggregates are distributed according to Table 1, then we obtain relaxation behavior as shown in Figure 2. Relaxation is significantly slower and does not follow purely exponential decay when particle aggregates are present. Even for a mean of one particle per cell, relaxation differs from that of single particles. Only after the first pulse magnetization of the cell probe can we assume to measure a single particle relaxation. Repeated pulse magnetizations and relaxation measurements always shows a slower decay.

In living macrophages relaxation shows two phases with an initially fast decay followed by a slow exponential decay. Viscoelastic properties of the cytoplasm are the main reason for this two-phase decay [8]. A retarded decay is seen after multiple pulse magnetizations, which results from particle aggregates and which can be visualized microscopically.

Measurement of the randomizing energy E_r

Magnetic dipole (m) realignment in a weak magnetic field B_M depends on the relation between magnetic twisting force (mB_M) and randomization energy (E_r) and can be described by the Langevin function [6]:

$$L(a) = \coth a - \frac{1}{a},\ a = \frac{mB_M}{E_r}. \qquad (5)$$

This method provides a direct measure of E_r from the degree of magnetic particle alignment. Because of mutual magnetization and strong enhancement of m, particle aggregates induce large errors in estimation of E_r.

Figure 3 illustrates the influence of particle aggregates on the degree of alignment and the estimation of E_r. Because of the stronger magnetic moment of aggregates they obey a higher level of alignment $L(\alpha)$ in a given external twisting field. The dotted curve in Fig. 3 shows that single particles would reach 75% alignment, while doublets would reach 92% alignment. Assuming that the particle aggregation is unknown, doublets would result in a four times higher α and a lower E_r. In the case of a mixed distribution (curve 'Mix' in Fig. 3), where 70% are singlets, 20% are doublets and 10% are triplets, the error is less pronounced. A measurement of 75% alignment implies a 33% higher α of the aggregate mix compared to single particles and, according to Eq. 5, a 33% underestimation of E_r.

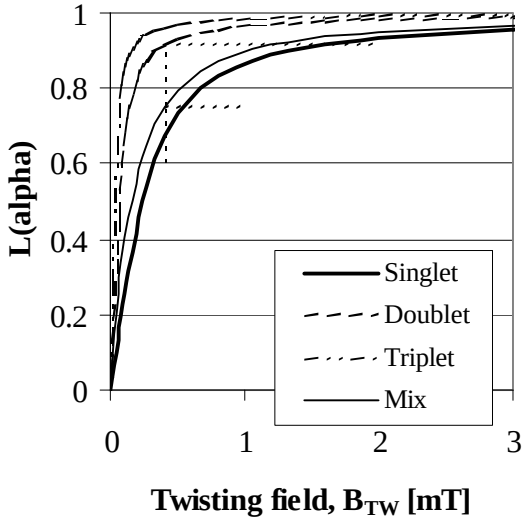

Figure 3: Influence of particle aggregates (doublets and triplets in comparison to singlets) on the level of alignment in increasing strength of twisting field (B_{TW}) under the influence of randomization energy E_r. Mix describes a distribution of 70% singlets, 20% doublets and 10% triplets.

Magnetic particle twisting

Particles twisting in an external weak magnetic field yield the viscoelastic properties of the cytoplasm. According to Stokes law, the external stress s is proportional to the shear rate dq/dt:

$$-h\, dq/dt = s \sin q\,, \quad s = \frac{mB_M}{kV},$$

and the Newtonian viscosity η is the factor of proportionality (q is the angle between m and B_M). For spherical single particles the magnetization of the particles ($M_T = m/V$) and therefore the shear stress is independent of particle size. In the case of particle aggregates the stress σ varies with the size of the aggregate because of the shape factor κ and the increase of m according to the mutual magnetization. Table 3 summarizes the results of estimation of the stress for increasing number of particles being incorporated into the aggregate. The influence of particle clustering on twisting is less significant compared to relaxation and seems to decrease for bigger aggregates.

Table 3: Increase of stress factor s (normalized to stress of a single sphere, s_1) with increasing number of spheres incorporated in the aggregate.

Aggr-size	1	2	3	4
k	6	9.03	14.04	20.37
s/s_1	1	1.33	1.28	1.18

CONCLUSIONS: The aggregation of magnetic spheres has a significant influence on cytomagnetometric measurements. The mutual magnetization of particles is the dominant factor influencing the measurements. Besides the increase in volume, the change of rotational shape factor significantly influences the hydrodynamic behavior.

ACKNOWLEDGEMENTS: This work was supported by the EC under FIGD-CT-2000-00053.

REFERENCES:

1. P.A. Valberg, Butler J.P. Biophys. J. 1987;52:537-50.
2. W. Möller, Guzijan V., Pohlit W., Stahlhofen W., Wenisch T., Wiegand J. J. Aerosol Sci. 1992;23:S519-S520.
3. W. Stahlhofen, Möller W. Radiat. Environ. Biophys. 1993;32:221-38.
4. W. Möller, Scheuch G., Sommerer K., Heyder J. J. Magn. Magn. Mater. 2001;225:8-16.
5. W. Möller, Nemoto I., Matsuzaki T., Hofer T., Heyder J. Biophys. J. 2000;79:720-30.
6. I. Nemoto. IEEE Trans. Biomed. Eng. 1982;29:745-52.
7. I. Nemoto, Ogura K., Toyotama H. IEEE Trans. Biomed. Eng. 1989;36:598-607.
8. I. Nemoto, Möller W. IEEE Trans. Biomed. Eng. 2000;47:170-82.

CHARACTERIZATION/QUANTIFICATION OF THE FACTORS INVOLVED IN THE IMPARTING A MAGNETOPHORETIC MOBILITY ON CELLS AND PARTICLES

H. Zhang[1], M. Nakamura[1], K. Comella[1], L. Moore[2], M. Zborowski[2] & J. Chalmers[1, 3, *]

[1] *Department of Chemical Engineering, The Ohio State University, 140 W 19th Ave., Columbus, OH 43210,* [2] *The Cleveland Clinic Foundation, Department of Biomedical Engineering, 9500 Euclid Avenue, Cleveland, OH 44195,* [3] *Director, University Cell Analysis and Sorting Core*

** corresponding author.*

INTRODUCTION: Numerous published studies indicate the direct relationship between cell surface antigen expression level and cell function. Thus, it is important to obtain quantitative information on certain cell surface antigen expression level. In our laboratory, we have developed an instrument named Cell Tracking Velocimetry (CTV) based on the concept of magnetophoresis. The CTV system has been used to measure the "degree to which" a cell is immunomagnetically labeled, which is referred to as magnetophoretic mobility, m_c [1].

Popular magnetic reagents in immunomagnetic cell labeling are of particle (such as Dynal™ beads, Dynal AS, Oslo, Norway) and colloidal (such as MACS™ beads, Miltenyi Biotec, Germany) sizes. In our application, colloid-sized magnetic beads are used because the number of beads bound to the cell surface is directly proportional to cell surface antigen expression level due to their small size.

The magnetic force acting on a labeled cell in a magnetic field can be expressed as:

$$F_m = (n_1 q_1 l_1)(n_2 q_2 l_2) n_3 F_b \equiv N_b \cdot F_b \qquad (1)$$

where n_1 is the total number of antigen molecules per cell, q_1 is the fraction of antigen molecules on the cell surface bound by primary antibodies, and l_1 is the valence of the primary antibody. This pattern is repeated when n_2 is the total number of secondary antibody binding sites on the primary antibody, q_2 is the fraction of binding sites on the primary antibodies that are occupied by the secondary antibodies, l_2 is the valence of secondary antibody, and finally, n_3 is the number of magnetic beads conjugated to a secondary antibody. When antibodies are used, $n_1 q_1 l_1$ corresponds to **Antibody Binding Capacity** (ABC), and when $q_1 = q_{\max}$ it corresponds to the maximum number of primary antibodies bound to the cell surface. Parameters $n_2 q_2 l_2 n_3$ can also be combined into one term β, and β represents the number of magnetic beads bound to one primary antibody. b can be thought of as an amplification factor. Alternatively, the term N_b can be used which corresponds to the amount of magnetic beads bound to the cell (or particle) surface [2].

The magnetic force acting on a magnetic bead is expressed as:

$$F_b = \Delta c V \cdot \nabla\left(\frac{B^2}{2m_0}\right) \equiv k \cdot \nabla\left(\frac{B^2}{2m_0}\right) \qquad (2)$$

where B is the imposed magnetic field induction; m_0 is the magnetic permeability of free space; Δc is the difference in volumetric magnetic susceptibility between the magnetic bead c_b and the medium c_f, V is the volume of a magnetic particle; $k \equiv \Delta c \cdot V$ is defined as "the magnetic bead-field interaction parameter".

If the labeled cell moves relatively slowly in the medium, Stoke's law can be applied, and the drag force is given as:

$$F_d = 3\pi u_c D_c h \qquad (3)$$

where D_c is the diameter of the cell, η is the viscosity of the medium and u_c is the induced velocity in the field.

By applying force balance in the magnetic field direction, we can solve the induced velocity u_c as expressed in equation (4).

$$u_C = \frac{n_1 q_1 l_1 \cdot b \cdot k}{3\pi D_C h} \cdot \nabla\left(\frac{B^2}{2m_0}\right) \qquad (4)$$

We can further normalize u_C into magnetic mobility m_C, by dividing u_C by magnetic energy density S_m, which is defined as $S_m \equiv \nabla\left(\frac{B^2}{2m_0}\right)$, so that:

$$m_C = \frac{N_b \cdot b \cdot k}{3\pi D_c h} \qquad (5)$$

where N_b is a function of the amount of magnetic beads used in labeling process.

Magnetic bead-field interaction parameter k is a parameter of the magnetic nanobeads.

In the content of this paper, our work is composed of two parts:

- Studying the relationship between mobility and amount of labeling reagents;
- Determination of k value

METHODS:

The CTV measures magnetophoretic mobility m_c of a particle or cell, using a well-defined magnetic field [3,4]. The diagram of our CTV system is shown in Figure 1.

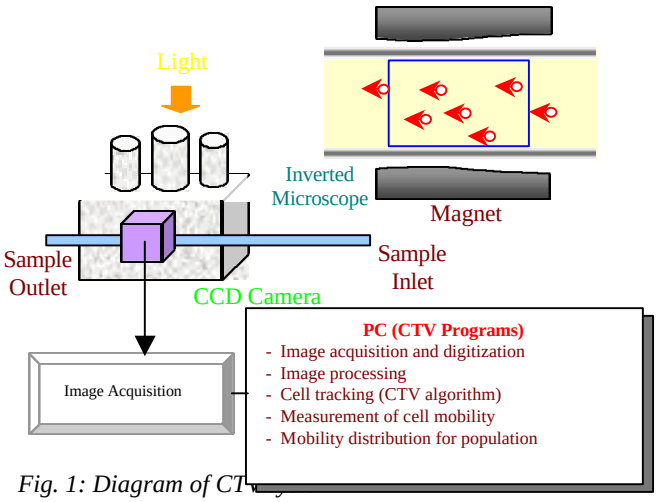

Fig. 1: Diagram of CTV

ProActive® Biotin-coated microspheres (Bangs Laboratories, IN, USA) and Streptavidin MACS™ beads (Miltenyi Biotec, CA, USA) were used in our study. Biotin-coated microspheres are uniformly sized polystyrene particles (5.12 μm) with certain amount of biotin molecules bound to the surface. Streptavidin MACS™ beads are colloidal super-paramagnetic nano-beads (50 nm) conjugated to streptavidin. Biotin-streptavidin interaction is one of the strongest non-covalent bonds (Ka =10^{15}/M vs. 10^{7}-10^{11}/M for antibody-antigen interactions).

A water solution of Gadolinium (Gd^{3+}) salt (Optimark®, Mallinckrodt Inc.) was used as suspending fluid. Gadolinium salt is a paramagnetic chemical, and it was used to change the volumetric magnetic susceptibility of the medium, c_f , to study the induced change in mobility.

In our work, we labeled 10^6 biotin-coated microsphere with certain amount of streptavidin MACS™ beads at 4°C for 30 minutes. Then washed with x20 water three times by centrifuge. After discarding the supernatant, we added gadolinium-containing medium and measured mobility using CTV.

RESULTS:

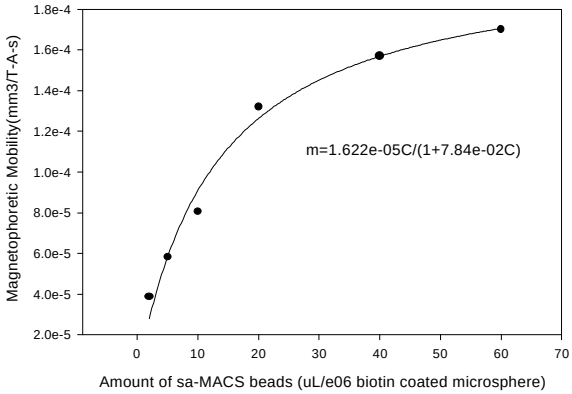

Fig. 2. Saturation curve of magnetophoretic mobility versus amount of labeling agents.

By changing the concentration of gadolinium salt in the solution, magnetophoretic mobility will change. When $c_f = c_b$, microspheres will not move in the magnetic field (zero mobility). Based on Figure 3, we can determine c_b value as shown.

DISCUSSION & CONCLUSIONS:

Following the concept of antibody-antigen interaction, we can deduct equation (6).

$$q_1 = \frac{K_a C}{1 + K_a \cdot C} \qquad (6)$$

where Ka is the association constant between the receptor (usually proteins) and antibody, and C is the free concentration of antibodies in the solution.

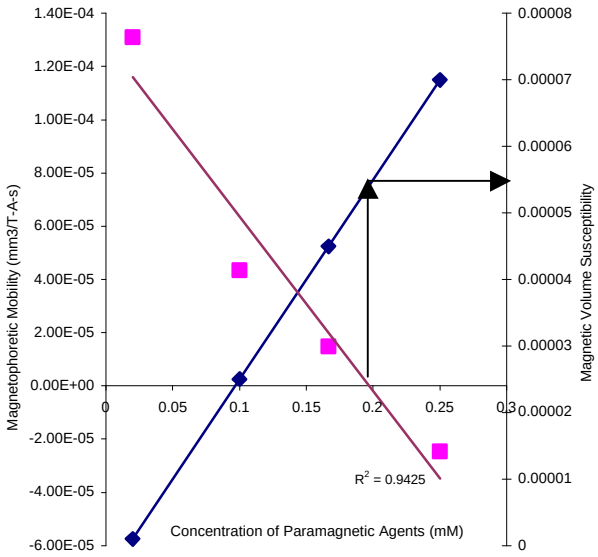

Fig. 3: Relation between mobility and concentration of paramagnetic agents

By combining equation (5) and (6), we obtain the following expression:

$$m_c = \frac{k b l_1}{3p D_c h} \cdot \frac{n_1 \cdot K_a \cdot C}{1 + K_a \cdot C} \qquad (7)$$

In Figure 3, we used above equation to fit the data. We used the total amount of labeling reagents instead of free concentration of labeling reagents in equation (7) by assuming the total amount of labeling reagents is a reasonably large value. Significant agreement between the data and equation (7) is observed.

Future work will focus on further verification of equation (7). If this equation is the appropriate expression of the relation between mobility, surface antigen, and labeling agents, work will continue to use the CTV system to measure the **true** surface antigen expression level, n_1 in equation (7).

Measuring magnetic bead-field interaction parameter k is a necessary step to quantitate cell surface antigen using our CTV system. However, It is rather challenging to measure the volumetric magnetic susceptibility of nano-paramagnetic particles c_b . Figure 4 shows when $c_f = 0.00007$, some microspheres have the positive mobility while others have negative mobility, which implies that there is a concentration gradient of paramagnetic salts in the monitored area.

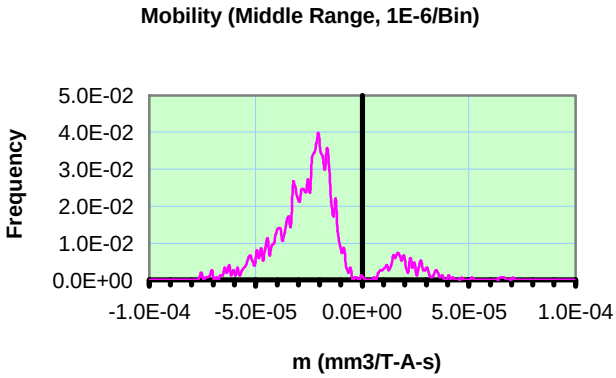

Fig. 4: Output of CTV (when $c_f = 0.00007$).

ACKNOWLEDGEMENTS:

This work was supported by the National Cancer Institute (R33 CA81662-01 to JJC, RO1 CA62349 to M.Z., and CA16058-25 to OSU) the National Science Foundation (BES-9731059 to J.J.C).

REFERENCES:

[1] Chalmers, J. J., Zhao, Y., Nakamura, M., Melnik, K., Lasky, L., Moore, L., Zborowski, M., (1999), J. of Magnetism and Magnetic Materials **194**: 231-241.

[2] McCloskey, K. E., Chalmers, J. J., and Zborowski, M., (2000), Cytometry **40**:307-315.

[3] Moore, L. R., Zborowski, M., Nakamura, M., McCloskey, K., Gura, S., Zuberi, M., Margel, S., Chalmers, J. J., (2000), J. of Biochemical and Biophysical Methods **44**: 115-130.

[4] Nakamura, M., Zborowski, M., Lasky, L. C., Margel, S., Chalmers, J. J. (2001), Experiments in Fluids **30**: 371-380.

THERAPEUTIC APPLICATIONS OF IMMUNOMAGNETIC CELL SELECTION: A REVIEW

S. S. Farag, M.D. Ph.D.

The Ohio State University Comprehensive Cancer Centre, Division of Hematology and Oncology, Columbus, OH 43210

INTRODUCTION: With the explosion in the development of monoclonal antibodies and the improved characterization of lineage and tumor specific antigens, it is now possible to separate many specific cell types from mixed populations in blood, bone marrow and other tissue fluids. Immunomagnetic technology has greatly facilitated this process, particularly in the research laboratory where certain cellular subtypes can be separated with high purity for further investigations. Cell selection for therapeutic use, however, is a growing field that places more stringent demands on immunomagnetic technology.

Cellular therapy finds its greatest application in the field of stem cell graft engineering and adoptive immunotherapy of cancer. The main applications include purging of malignant cells from autologous stem cell products, depletion of T cells, and selection of specific lymphocyte subsets with potential antileukemic activity.

PURGING OF STEM CELL PRODUCTS: Autologous bone marrow or peripheral blood stem cells may be used to support high dose chemotherapy for a variety of malignancies. One limitation of this technique is the contamination of the stem cell product with residual malignant cells. Eradication of these cells may reduce the chance of relapse following transplantation. Purging strategies have been investigated in leukemia, lymphoma, neroblastoma and breast cancer. For example, monoclonal antibodies against B lymphocyte specific antigens, such as CD10, CD19 and CD20, have been used with complement for the ex-vivo purging of lymphoma cells from autologous bone marrow prior to transplantation [1,2]. More recently, monoclonal antibodies to the CD34 antigen, present on the surface of hematopoietic progenitor cells, have been captured on solid substrates such as immunomagnetic beads or avidin coated columns and used for the positive selection of CD34+ cells. Positive CD34 selection has been used as a means of negative purging of lymphoma, myeloma, and breast cancer cells from autologous bone marrow and peripheral blood stem cell products [3-8]. Although 2-3 $\log_{10}$ purging can be achieved, the biological and clinical significance of purging in the autologous stem cell transplantation remains controversial.

T CELL DEPLETION : T cells are the major cell type responsible for the development of graft versus host disease (GvHD) following allogeneic stem cell transplantation. Clinically significant GvHD (grade II or higher) occurs in 29-42% of recipients of HLA-identical sibling stem cells and >75% of recipients of HLA-mismatched grafts [9], and is the primary cause of failure of allogeneic stem cell transplantation. Development of severe GvHD is the major obstacle to successful transplantation across the HLA barrier, thereby limiting the procedure to only 40% of patients who can benefit from the treatment by having a suitable HLA-matched donor. Engineering the graft to deplete T cells can completely abrogate GvHD, even in mismatched bone marrow transplants. In the mismatched setting, T cell depletion has been associated with graft rejection, which may, however, may be overcome by the use of large doses of CD34+ cells [10,11], and potentially by the infusion of NK cells [12]. Technologies that consistently produce 5-log depletion of T cells with minimal loss of stem cells are needed.

A number of methods for T cell depletion have been investigated. Mostly, these have included monoclonal antibody-based negative selection techniques, separation based on lectin-mediated agglutination, and physical separation by size and density. The majority of these methods result in depletion of 2-4 $\log_{10}$ of T cells, which is not sufficient to prevent severe GvHD in unrelated donor or haplotype-mismatched SCT. Furthermore, these methods frequently result in the loss of more than half of hematopoietic progenitors as assessed by granulocyte monocyte colony forming units (CFU-GM) or CD34+ cells.

More recently, positive selection of CD34+ cells has been used to eliminate T cells. The first positive CD34 selection system developed for clinical scale purification of CD34+ cells was the **Ceprate SC stem cell collection system** (Cellpro, Bothell, WA). Using an avidin-biotin immunoadsorption technique, biotinylated anti-CD34 antibody-labeled stem cells are passed through a column containing avidin-coated beads. Unbound cells are washed away, and then the

bound CD34 cells are eluted using mechanical agitation. The extent of T cell depletion achieved with this system is approximately 3 $\log_{10}$, which is insufficient for abrogating GvHD in the haplotype-mismatched transplant setting, and the mean CD34 recovery has varied between 31-79% [13-15]. Additional steps, including further depletion T cells by rosetting with sheep red blood cells have been used but are extremely tedious and result in significant loss of stem cells.

More recently, immunomagnetic methods of cell selection have been developed. The **Isolex 300i** cell selection technology (Baxter, Irvine, CA) involves specific binding of target cells by a mouse anti-CD34 monoclonal antibody, 9C5. The target cells-9C5 complexes are then captured by sheep anti-mouse IgG-coated paramagnetic ***microspheres*** (diameter 3-4 μm). Unbound CD34- cells are removed by magnetic washes on the Isolex Magnetic Cell Separator. In a final step, target cells are released from the 9C5-microspheres by a peptide that binds competitively to the 9C5 monoclonal antibody. This method is reported to achieve a mean CD34+ cell recovery between 41-69% [16-18]. T cell depletion is between 3 and 4 $\log_{10}$ [19], thus resulting in T cell doses in the allograft lower than those suggested to cause acute GvHD in the T-depleted stem cells in the HLA-matched setting. However, a higher level of T cell depletion is required in the haplotype-mismatched setting. A recent up-grade of software (version 2.5) is reported to improve the extent of T cell depletion to a median of 4.5 $\log_{10}$, with a range of 3.5 to 4.8 $\log_{10}$ [20]. However, to further improve T cell depletion, a negative selection step has been added following positive CD34 selection. In this modification, CD4 and CD8 monoclonal antibodies bound to microspheres are automatically added to the primary chamber at various times indicated by the device to bind residual contaminating T cells and retain them in the magnetic field. Combined with +/- cell selection technology has, this device is been reported to result in median 5.1 (range 4.4-5.6) $\log_{10}$ T cell depletion, with median 57% (range 39%-68%) CD34+ recovery [20]. The currently available Isolex 300i version 2.0 with +/- technology uses anti-CD2 for the negative selection step; the performance of this antibody compared to the combination of anti-CD4 and anti-CD8 has yet to be determined. None of the Isolex 300i devices are currently approved for T cell depletion in the United States.

The other available immunomagnetic positive CD34 selection technology is the **CliniMACS** device. In this system, the stem cell product is incubated with a monoclonal anti-CD34 antibody conjugated to iron-dextran ***nanobeads*** (50-100 nm). After washing, the bound cells are captured by passage through a tube with a ferromagnetic core, attached to a permanent magnet. The tube is washed to remove unbound cells. After removal of the magnet, the retained cells are eluted and passed through a newly prepared tube. The reported mean T cell depletion is 4 $\log_{10}$ [21,22], with a reported median CD34+ cell recovery of 71% (range 24% to 105%) [22]. The CliniMACS device is not currently approved in the United States.

Overall, the major limitation of the available technology, the Isolex 300i with +/- selection and the CliniMACS, is the significant loss of CD34+ cells associated with the procedure. Up to 50% of stem cells may be lost during T cell depletion. When it is considered that successful engraftment in this setting may require infusion of $\geq 10 \times 10^6$ CD34+ cells/kg, a total of 20×10^6 CD34+ cells will need to be mobilized and collected. In a study of 112 normal donors mobilized in a standard manner with granulocyte-colony stimulating factor (G-CSF), the median number of CD34+ cells collected per apheresis procedure was 7.58 (range 2.05-27.96) $\times 10^6$/kg recipient weight [23]. This means that in more than half of donors, several apheresis procedures, and in some cases, several mobilization attempts will be required to achieve the required cell dose. Optimizing the cell separation procedure to achieve 4-5 $\log_{10}$ T cell depletion with minimal loss of CD34+ cells (e.g. >90% recovery) will result in major cost saving and comfort to the donors.

SELECTION OF SPECIFIC LYMPHOCYTE SUBSETS: While depletion of T cells can eliminate GvHD, the process is also associated with delayed immune reconstitution post-transplant with a consequent increased risk of infection. Cell selection techniques may also allow the depletion of specific subsets of T cells that mediate GvHD (alloreactive T cells) while preserving other T cells are also under investigation.

Natural killer cells are lymphocytes that do appear to mediate GvHD, but have potent alloreactive activity against malignant cells. There is growing interest in the use of purified NK cells for cellular therapy. A major obstacle to the development of treatment protocols of adoptive immunotherapy with NK cells has been the lack of clinical scale technology for the isolation of these cells from peripheral blood. There is currently no commercially available device for the clinical

scale isolation of NK cells, and most clinical protocols have used lymphokine activated killer (LAK) cells, which are >90% polyclonal nonspecific T cells. Recently, Frohn et al. have used the SuperMACS, a large scale CD56 column designed for laboratory research use, for the purification of NK cells from allogeneic donors for adoptive therapy of 11 patients with renal cell carcinoma [24]. They were able to infuse 1.02±0.265x109 cells, with NK cell purity of 85-95%. However, a significant number of residual T cells remained in the cellular product, which would have been capable of causing severe GvHD in an HLA-mismatched setting. Large scale isolation of NK cells from haploidentical donors for posttransplant immunotherapy has also been reported by Koehl et al. who initially depleted T cells with magnetic bead conjugated CD3 antibodies using the CliniMACS, followed by a second step with magnetic bead conjugated CD56 antibody [25]. Although NK cell purity was reported to be high at 96.2±4.4% (range 91.0-98.1%), recovery of NK cells was suboptimal at 45.9±11.7%. CD3 cell contamination was <0.08%. Overall, there is need a major need to develop clinical scale systems for the rapid and efficient isolation of NK cells for adoptive immunotherapy.

Other application include the selection of CD34 cells for ex-vivo expansion, the selection of lymphoid cells for expansion of T cell clones reactive against certain infectious agents (e.g. cytomegalovirus and Epstein-Barr virus), and selection of cells for the generation of dendritic cells for vaccine generation. Many of these are still in the preclincial phase of development. Overall cell selection techniques that result in a favorable balance between the depletion of unwanted cells without the concomitant loss of important cell populations will greatly enhance the field of cellular therapy.

REFERENCES:

1. Gribben JG, et al. 1991. Immunological purging of marrow assessed by PCR before autologous bone marrow transplantation for B cell lymphoma. N Engl J Med 325: 1525-33.
2. Feedman A, et al. 1997. Long term prolongation of disease free survival and overall survival following autologous bone marrow transplantation in patients with advanced relapsed follicular lymphoma. Proc Am Soc Clin Oncol 89 (abstract 304).
3. Di Nicola M, et al. 1996. Combined negative and positive selection of mobilized CD34 blood cells. Br J Hematol 94: 716-21.
4. Lopez M, et al. 1997. Bone marrow versus peripheral blood progenitor cell CD34 selection in patients with non-Hodgkin's lymphomas: different levels of tumor cell reduction. Imnplications for autografting. Blood 90: 2830-38.
5. Lemoli RM, et al. 1999. Selection and transplantation of autologous CD34+ B-lineage negative cells in advanced-phase multiple myeloma patients: a pilot study. Br J Hematol 107: 419-28.
6. Abnour R, et al. 1998. Autologous transplantation of mobilized peripheral blood CD34+ cells selected by immunomagnetic procedures in patients with multiple myeloma. Bone Marrow Transplant 22: 957-63.
7. Cancelas JA, et al. 1999. peripheral blood CD34+ cell immunomagnetic selection in breast cancer patients: effect on hematopoietic progenitor content and hematologic recovery after high-dose chemotherapy and autotransplantation. Transfusion 38: 1063-70.
8. Yanovich S, et al. 2000. Transplantation of CD34+ peripheral blood cels selected using a fully automated immunomagnetic system in patients with high-risk breast cancer: results of a prospective randomized clinical trial. Bone Marrow Transplant 25: 1165-74.
9. Przepiorka D. Prevention of acute graft versus host disease. 2000. In Ball ED, Lister J, Law P (Eds). Hematopoietic Stem cell therapy. Churchill Livingston, NY, pp 452-69.
10. Reisner Y, Martelli MF. 2000. Tolerance induction by 'megadose' transplants of CD34+ stem cells: a new option for leukemia patients without an HLA-matched donor. Current Opinion in Immunol 12: 536.
11. Aversa F. et al. 1998. Treatment of high-risk acute leukemia with T-cell depleted stem cells from related donors with one fully mismatched HLA haplotype. N Engl J Med 339: 1186.
12. Ruggeri L, Capanni M, Aristei C, et al. 2000. Mini mismatched transplantation in the mouse by the use of alloreactive NK cells for conditioning. Blood 96: 473a.
13. Handgretinger R, et al. 1997. Positive selection and transplantation of peripheral CD34+ progenitor cells: feasibility and purging efficacy in pediatric patients with neuroblastoma. J Hematother 6: 235-42.
14. Hassan HT, Zeller W, Stockschlader M, et al. 1997. Comparison between bone marrow and G-CSF-mobilized peripheral blood allografts

undergoing clinical scale CD34+ cell selection. Stem Cells 14: 419-29.
15. Johnson RJ, et al. 1996. Peripheral blood stem cell transplantation in myeloma using CD34 selected cells. Bone Marrow Transplant. 17: 723-7.
16. Lane TA, et al. 1995. Harvesting and enrichment of hematopoietic progenitor cells mobilized into the peripheral blood of normal donors by granulocyte-macrophage colony-stimulating factor (GM-CSF) or G-CSF: potential role in allogeneic marrow transplantation. Blood 85: 275-82.
17. Civin CI, et al. 1996. Highly purified CD34-positive cells reconstitute hematopoiesis. J Clin Oncol. 14: 2224-33.
18. Mapara MY, et al. 1997. Monitoring of tumor cell purging after highly efficient immunomagnetic selection of CD34 cells from leukapheresis products in breast cancer patients: comparison of immunocytochemical tumor cell staining and reverse transcriptase-polymerase chain reaction. Blood 89: 337-44.
19. Martin-Henao GA, et al. 2000. Isolation of CD34+ progenitor cells from peripheral blood by use of an automated immunomagnetic selection system: factors affecting the results. Transfusion 40: 35-43.
20. Martin-Henao GA, et al. 2001. Combined positive and negative cell selection from allogeneic peripheral blood progenitor cell (PBPC) by use of immunomagnetic methods. Bone Marrow Transplant 27: 683-87.
21. McNiece I, et al. 1997. Large-scale isolation of CD34+ cells using the Amgen cell selection device results in high levels of purity and recovery. J Hematother 6: 5-11.
22. Schumm M, et al. 1999. Isolation of highly purified autologous and allogeneic peripheral CD34+ cells using the CliniMACS device. J Hematother 8: 209-18.
23. Korbling M. 1999. Collection of allogeneic peripheral blood stem cells. Balliere's Clinical Haematology 12: 41-45.
24. Frohn C, et al. Feasibility of the adoptive transfusion of allogeneic human leukocyte antigen-matched natural killer cells in patients with renal cell carcinoma. J Immunother 23: 499-504.
25. Koehl U, Barting T, Esser R, et al. 2000. Large scale isolation of natural killer cells from haploidentical donors for posttransplant immunotherapy. Bone Marrow Transplant 25 (Suppl 1): S123.

MAGNETIC IMMUNOASSAY FOR RAPID ASSESSMENT OF ACUTE MYOCARDIAL INFARCTION (AMI)

Y. Haik [1], M. Cordovez [1], C.-J. Chen [1] & J. Chatterjee [1]

[1] *Biomagnetic Engineering Lab, FAMU-FSU College of Engineering, Tallahassee, FL 32310*

INTRODUCTION: Cardiac disease, especially acute myocardial infarction (AMI) affects a growing number of people in the United States and other parts of the world. A complication of current diagnosis procedures is that a number of ambulatory AMI patients are discharged with negative findings only to have recurrent and often more serious complications at home. Of the more than 5 million individuals with acute chest pains admitted to emergency rooms in the U.S., about 3 million are admitted to an intensive care unit or telemetry ward because traditional methods of diagnosis are not sensitive enough. More importantly, 2-8% of patients with chest pains who are discharged from emergency departments develop acute myocardial infarctions resulting in adverse events and malpractice actions [1]. The development of a simplified cost–effective and accurate procedure to diagnose AMI would greatly aid medical care providers, especially those in emergency rooms where the majority of AMI patients are initially evaluated. Additionally, the use of improved myocardial injury markers would improve detection in patients with minor or silent MI. Furthermore, the ability to perform such diagnostic tests at the point of care (POC) allows for the timely evaluation of patients within the emergency room or even in an ambulance. Care can then be delivered immediately, based on the results of these assays.

Our study presents a magnetic immunoassay that was developed to simultaneously test for two markers of AMI (Myoglobin and Fatty Acid Binding Protein).

Myoglobin (MYO), a single polypeptide chain (17 kDa), and Fatty Acid-Binding Protein (FABP, 15 kDa) are two small cardiac proteins that show elevated serum levels soon after the infarction, significantly increasing their concentration within 2 hours and peaking after 4-6 hours. The levels of myoglobin and FABP in plasma rise from about 32 μg/L and 3 μg/L to over 200 μg/L and 100 μg/L, respectively, often within less than 5 hours after an AMI [1]. Recent studies have shown that the combined measurement of Myoglobin and FABP in plasma allows for discrimination between myocardial and skeletal muscle injury with the ratios for these markers differing between heart (MYO/FABP ratio 4:5) and skeletal muscle (MYO/FABP ratio 20:70, depending on muscle type) [2].

Regardless of the cardiac marker, measurement of marker concentrations has relied on various types of immunoassays. The most common methods are radioimmunoassay, latex agglutination, and two-site immunoassay.

Current immunological methods have the dual drawbacks of often being time consuming, with determination ranges of 3-4 hours, and requiring special equipment, which limits their usefulness in emergencies. Today, with increased emphasis on cost-effective decision-making and rapid treatment, hospitals are in need of the rapid and efficient determination of an AMI for patients admitted to the emergency department (ED) room with acute chest pain.

The use of magnetic particles in immunological assays has grown considerably, as the particles' magnetic properties permit their easy separation and/or concentration in large volumes, allowing for faster assays and in some cases improved sensitivity over currently available commercial methods. We chose a standard solid-phase ELISA (Enzyme Linked Immunoassay), consisting of the formation of a complex or "sandwich" by attaching two different antibodies to different epitopes on the same target antigen or protein. One antibody was attached to a solid surface (superparamagnetic microsphere), and the other to a small chemical enzyme (Alkaline Phosphates). The first antibody, attached to a surface, is used for the separation of the antigen from the background, while the second antibody, labeled with a enzyme, reacts with an introduced chemical reagent to give a relative indication of the concentration of the antigen (the extent of this reaction is proportional to the concentration of the antigen).

METHODS: Albumin superparamagnetic particles with a magnetic core made of γ-Fe_2O_3 (maghemite) were prepared [3]. The magnetic particles were prepared in-house with diameters ranging from 6-10 nm. These magnetic particles were then coated with albumin. Figure 1 shows albumin coated magnetic microspheres. Protein coupling efficiency was measured for the composite particles. Avidin was used as a model ligand due to its strong bond-

forming ability with various ligands used in immunoassays. It was found that only 30% of the calculated amount of avidin required for monolayer formation on particles was used to coat the particles and the remaining portion was not adsorbed. Measurements with a Superconducting Quantum Interface Device (SQUID) showed that the particles were superparamagnetic. They can thus be easily separated from a solution with a small magnet and immediately re-dispersed into the liquid phase, without clumping, by removal of the magnet.

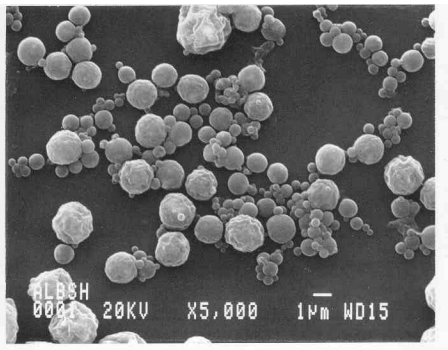

Fig. 1: SEM of albumin microspheres.

The immunoassay developed follows a standard solid-phase ELISA, consisting of the formation of a complex or "sandwich" by attaching two different antibodies to different epitopes. The main difference to the standard method is the use of superparamagnetic microspheres for the separation and concentration of the antibodies-antigen complex from the background. The antibodies conjugate with the myoglobin protein forming the microsphere-myoglobin-enzyme complex. Using an external magnet, the superparamagnetic properties of the microspheres allow for the repeated washing of the sample, separating the complex from all background media. After the complex has been isolated, a chemical reagent is introduced that reacts with the enzyme label in the complex to give a relative measurement of myoglobin concentration in a sample.

Biotin serves as the bridging link between the microspheres and the antibodies and the Alkaline Phosphatase (AP) and the antibodies. The antibodies used are two complementary clones of monoclonal mouse anti-human cardiac myoglobin (mouse isotope IgG1: 908 and 4E2) chosen because their epitopes are placed widely apart on the myoglobin protein. They were obtained from Research Diagnostics Inc. delivered in 1 mg antibody/ml PBS, pH 7.4 containing 0.1% sodium azide as preservative.

Both antibodies were coupled to two different labels: the avidin coupled superparamagnetic microspheres and the streptavidin coupled alkaline phosphatase enzyme marker. Coupling was achieved by biotinylating the antibodies and incubating them with the avidin and streptavidin coupled labels.

Calf intestinal Alkaline Phosphatase (MW 140kD), an enzyme that hydrolyzes pNPP (para-nitrophenolphosphate MW 371) to produce a yellow substrate, was used. The reaction is easily measured with a Spectrophotometer at 405nm and can be stopped at any time with the addition of 2M NaOH, which makes it possible to store results for later comparisons and verifications. While measurements using calf intestinal Alkaline Phosphatase (AP) can be affected by the presence of endogenous alkaline phosphates activity, the markers used in the immunoassay can be easily substituted.

Antibodies were biotinylated using a Sulfo-NHS-LC-Biotinylation Kit from Pierce Chemicals. The long chain (LC) arm biotin, containing a 22 Å spacer arm between the reacted primary amine and the biotin moiety, was used to minimize the possible effects of steric hindrance when conjugating the Biotin to the much larger paramagnetic microspheres and to increase the sensitivity. After the antibodies were biotinylated and the microspheres coupled with avidin, the procedure for conjugating the antibodies to their respective labels was carried out.

Human Serum Albumin (HSA) was added to the antibody-label conjugates to block all other possible binding sites for biotin and/or avidin in both the microsphere-antibody conjugate and on the Alkaline Phosphatase-Antibody conjugate. The addition of HSA (a major soluble protein in human blood) can also partially mimic the conditions in the whole blood samples for clinic use. We found HSA did not interfere with our AMI-marker measurements. Since there is a high concentration of HSA in human blood, we expect that no additional blocking agents are needed in our AMI assay system in clinic use [4].

RESULTS: Experiments to establish the myoglobin calibration curve based on the absorbance levels for the reaction of pNPP to AP at 405 nm were conducted. Myoglobin (obtained from Sigma) concentration samples of (0.0 μg/ml, 0.05 μg/ml, 0.10 μg/ml, 0.15 μg/ml, and 0.20 μg/ml) were incubated with labeled antibodies test amounts previously incubated with HSA solution using 4 ml cuvettes and 9 ml washes. Incubated the materials for 5 minutes before applying the magnetic immunoassay.

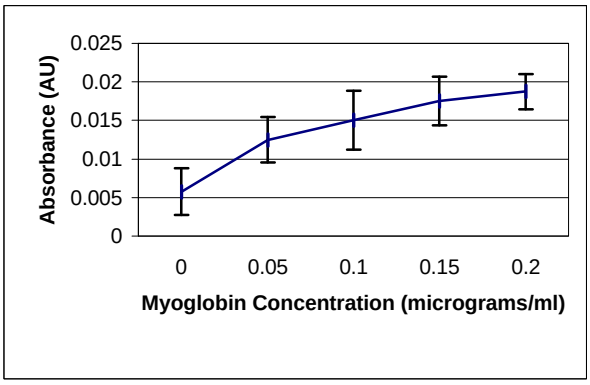

Fig. 2: Calibration curve for myoglobin based on the reaction of pNPP to AP following coupling with labeled antibodies and magnetic separation using the magnetic immunoassay.

Figure 2 shows the calibration curve for myoglobin with error bars representing the standard deviation for each data set. Each data point represents the average absorbance of 4 separate experiments. The center point concentration of 0.10 µg/ml represents a discriminator value for AMI, a myoglobin concentration used by previous researchers as indicative of AMI, and values both above and below that value were used in the curve to demonstrate the validity of the magnetic immunoassay in the concentration ranges of most likely use. The validation of the magnetic immunoassay is supported by the data of figure 2 allowed us to modify the magnetic immunoassay to target other cardiac proteins to support the assumption that the magnetic immunoassay used could be modified to a variety of proteins.

Using the same magnetic immunoassay methodology and simply modifying the antibody labels with the appropriate anti-FABP antibodies, samples for 4 different concentrations of FABP were used to create a concentration curve based on the absorbance levels for the reaction of pNPP to AP. Figure 3 shows the values for absorption for different concentrations of FABP based on the pNPP-AP reaction. Notice in Figure 3 the significant difference between the reading with no FABP present and all the others, but little difference between the samples containing FABP. A possible reason for this was the low concentration of superparamagnetic microspheres, which caused the saturation of antibody binding.

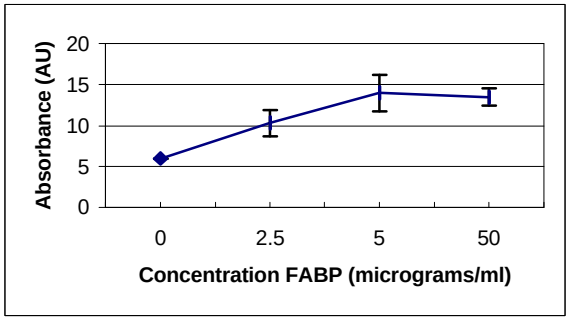

Fig. 3: Calibration curve for FABP.

A laboratory scale magnetic immunoassay was used to prototype a self-enclosed POC device for the measurement of diagnostic proteins. Figure 4 shows a schematic of translating the steps used in the immunoassay into a workable device. The device consists of a mechanism to introduce the sample into the testing chamber (a syringe is currently used). Mixing is obtained by manually shaking the sample. A set of magnets is being used to attract the coupled magnetic microspheres to the AMI marker and the Alkaline Phosphatase. Cyclic washing is used to decant the unwanted solution while maintaining the magnets to capture the microspheres. *Para*Nitrophenolphosphate is then added to the solution to react with AP for 1 min, followed by stopping the process with 2 M NaOH and measuring the AMI marker concentration in a spectrophotometer. The process is currently being automated.

Fluorescence labels were additionally used instead of the chemical reagent because (a) fluorescence could be adequately measured using at 499 nm in any standard spectrophotometer as a function of light absorption, and (b) using fluorescein as the quantifying label simplifies the process, as there is

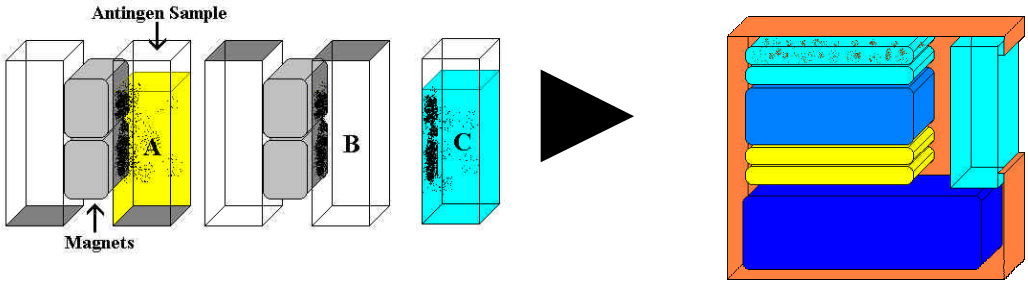

Fig. 4: Translating the constitutive steps of the magnetic immunoassay into a self-enclosed POC device.

no separate reaction step needed as in the case of most chemical enzyme tags. Fluorescein SMCC-BSA was used as the antibody label for quantifications.

A simple calibration curve for a single series of 7 different concentrations ranging from 0 to 0.063 μg/ml was performed. This test was done to asses the ability of absorbance measurements of fluorescein by the equipment, and to evaluate sample handling and initial testing procedures. Figure 5 shows the calibration curve for fluorescein.

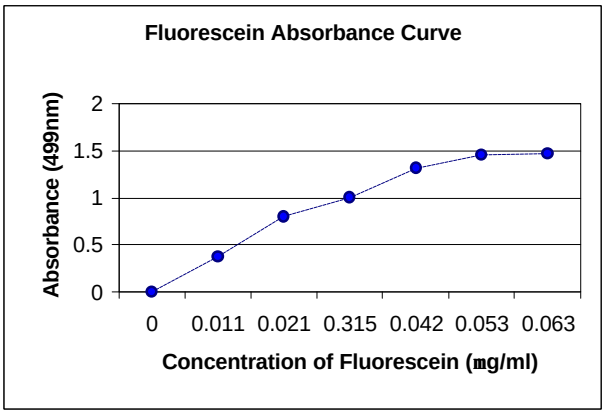

Fig. 5: Calibration curve for fluorescein SMCC-BSA.

Measurements were found to not be stable. The absorbance values for absorption increased with time, making it necessary for all the measurements to be conducted after exactly the same time intervals. Measurements could thus not be reread at a later time point.

Using Alkaline Phosphatase has proven adequate to predict AMI markers concentration.

DISCUSSION & CONCLUSIONS: According to the American College of Cardiology/American Heart Association guidelines for the management of patients with AMI, a proper goal for an emergency department AMI protocol would be a targeted clinical examination and a door-to-needle (as in treatment for AMI) time that is less than 30 minutes. Current immunological methods have the dual drawbacks of often being time consuming, requiring determination ranges of 3-4 hours, and requiring special equipment, which limits their usefulness in emergencies. This study presents the development of a magnetic immunoassay that has been used for detecting for two cardiac markers simultaneously. The time needed to present a result for both markers is less than 3 minutes. The magnetic immunoassay uses a standard solid-phase ELISA that consists of the formation of a complex or "sandwich" by attaching two different antibodies to different epitopes on the same target antigen or protein. One antibody is attached to a nanomagnetic particle, and the other is attached to a chemical enzyme (AP). Current work includes transforming the developed immunoassay into a miniaturized point of care device.

REFERENCES: [1] M. Hudson, R. Christenson, L. Newby et al. (1999) *Clin Chim Acta* **284**:223-237. [2] J. Monique, K. Wodzig, M. Simoons, et al (1999) *Cardiovascular Res*. **44:**315-324. [3] J. Chatterjee, Y. Haik and C-J. Chen (2001), *Coll. Poly.Sci*., **279**:1073-1081. [4] Cordovez, M. (2001) "Point of Care Diagnosis of Acute Myocardial Infarction Using Magnetic Immunoassays," Master Thesis, FSU.

ACKNOWLEDGEMENTS: This project was sponsored by the FSU Research Foundation.

IMMUNO-MAGNETIC SEPARATION FOLLOWED BY SOLID-PHASE CYTOMETRY FOR THE RAPID DETECTION AND ENUMERATION OF PATHOGENS IN SURFACE WATER

B. Pourima[1], C. Pougnard[2], C. Josson[1], P. Le Baron[3], E. Pringuez[2], J.L. Drocourt[4], P.A. Cabanes[2], & S. Legastelois[1]

[1] Indicia Biotechnology, 33 avenue de la Californie, 69600 Oullins, France, [2] Electricité de France, Division Recherche et Développement, 6 quai Watier, 78401 Chatou Cedex, France, [3] Observatoire Océanologique, Centre National de la Recherche Scientifique CNRS-UMR7621, Université Paris VI, 66651 Banyuls-sur-Mer, France, [4] Chemunex, 3 allée de la Seine, 94854 Ivry-sur-Seine Cedex, France

INTRODUCTION: Contamination of surface waters with pathogens such *Naegleria fowleri*, *Cryptosporidium parvum*, *Legionella pneumophila* is a major public health concern worldwide. Detection and enumeration methods for these pathogens in water are based on culture enrichment to increase the concentration of viable organisms, followed by immunofluorescence assay, enzyme-immunoassay, polymerase-chain reaction, latex agglutination test, flow cytometry, or enzyme electrophoresis for identification and, to some extent, enumeration.

There are two major drawbacks for simple and rapid detection of pathogens in water. First, most of the current methods are not sensitive enough to detect small numbers of pathogens in their original environment. Second, technologies that could reach the required level of sensitivity are limited by the fact that large volumes of water (1 to 100 liters) must be processed for one single analysis. Membrane filtration often used is laborious, time-consuming and non-selective, leading to the presence in the filtrated samples of undesired contaminants such PCR inhibitors, auto-fluorescent events or cross-reactive unrelated organisms.

The Chem*Scan*™ system (Chemunex, Ivry, France) is a recently developed solid-phase cytometer that allows the identification of rare events and their enumeration down to one pathogen or cell per analysis [1]. The Chem*Scan*™ combines a fluorescent detection of membrane-filtered organisms with an automated counting system. To perform the detection of pathogens in large volumes with the Chem*Scan*™ device, it is essential to use a simple and adapted sample preparation method in which contaminating elements are efficiently removed. To this end, immuno-magnetic separation (IMS) was utilized to recover pathogens directly from their water habitat, concentrating and selecting the organisms in a suitable volume for subsequent detection and enumeration by solid-phase cytometry.

However, procedures using IMS also present a major obstacle: detaching pathogens from magnetic beads prior to detection is generally not completely achieved. A significant number of captured organisms are likely to remain on the beads after the detaching step, leading to an erroneous enumeration. Using stronger elution conditions often has an impact on the integrity of the membrane of the pathogen, making the immuno-labelling uncertain.

Due to their low steric effects and their easy filtrability, the use of small sized magnetic particles (< 350 nm) makes possible the direct fluorescent detection of the whole complex bead-pathogen with the Chem*Scan*™ system, so that a detaching step is not required.

In this report, we describe the development of an IMS technique for the rapid and efficient separation of *Naegleria fowleri*, a free-living amoeba found in various freshwater environments, known as the causative agent of a rare but almost always fatal meningo-encephalitis [2].

Several sizes and two natures of magnetic (ferrofluid and polystyrene) particles were compared for their compatibility with solid-phase cytometry analysis and their efficiency in amoeba recovery.

Both experimental (amoeba from culture) and natural samples were assayed.

Preliminary results on the detection and enumeration of *Cryptosporidium parvum* using the same technology are also discussed.

METHODS:

Samples: (*Naegleria fowleri)*: Contaminated water samples were collected in the cooling system of nuclear power plants at different sites. Liquids were fixed with formaldehyde 2% and stored at +4°C. Experimental samples were obtained by adding amoeba harvested from cultures dishes in Ringer's solution.

Immunomagnetic separation of Naegleria fowleri: Both indirect and direct immunoseparation were investigated. Magnetic particles from different origins (diameter 0.05 (ferrofluid), 0.19, 0.34, 1.05 and 2.8 µm) were sensitized with anti-*Naegleria fowleri* monoclonal antibody [3] or anti-*Cryptosporidium parvum* polyclonal antibody (Waterborne Inc., USA) for direct immunocapture. Indirect immunocapture was performed by using magnetic particles (0.34 µm) sensitized with anti-rabbit IgG polyclonal antibody.

Direct immunoseparation: 50 µl of each suspension of particles at 1% solid were added to 10 ml of contaminated water and incubated for 30 min. at room temperature. Particles were separated by using a Neodyn-Iron-Bore magnet of 1 tesla, washed twice with PBS, and filtered through a polycarbonate membrane (porosity 2 µm, diameter 25 mm).

Indirect immunoseparation: 10 µl of rabbit polyclonal antibody to *N.fowleri* (4.2 µg/ml) was added to 10 ml of contaminated water, and incubated for 30 min at room temperature. 50 µl of anti-rabbit IgG magnetic particles at 1% solid was added to the suspension and incubated for 15 min. After washing, the particles were filtrated through the 2 µm membrane. The immobilized *N.fowleri* were then revealed as described below.

Controls: Supernatants resulting from magnetic particle separations (containing non-captured organisms) were analyzed. Water samples not incubated with magnetic particles were also filtered and analyzed as positive controls.

Immunofluorescence staining: [4] Amoeba were revealed by incubating the membrane with biotinylated monoclonal antibody to *N.fowleri* (5D12), followed by incubation with streptavidin conjugated to R-phycoerythrin-Cy5.

Detection and counting: [4] All information regarding the Chem*Scan*™ system can be obtained from the manufacturer. Briefly, the labelled membrane was transferred onto the sample holder of the Chem*Scan*™, and scanned by a water-cooled argon laser emitting at 488 nm. Emission was collected in the red channel (655-705 nm) for *Naegleria fowleri,* and in the green channel (500-530 nm) for *Cryptosporidium parvum*. After scanning the whole membrane, a set of discriminants was applied, allowing the differentiation between labelled amoeba and autofluorescent elements. Additionally, all positively selected events were manually validated by microscopic examination.

RESULTS:

Table 1. Comparison of direct and indirect immunocapture (0.34 µm particles).

	Direct	Indirect
Recovery (exp[al] sample)	100%	96%
Recovery (natural sample)	73%	1%

Table 2. Effect of particle size on the efficiency of the recovery of amoeba from experimental samples.

Particle size (µm)	0.05	0.19	0.34	1.05	2.8
Recovery	100%	99%	100%	100%	60%

Table 3. Effect of particle size on the efficiency of the recovery of amoeba from natural samples

Particle size (µm)	0.05	0.19	0.34	1.05	2.8
Recovery	89%	69%	67%	NI	NI

NI – Non Interpretable (no filtration possible)

Table 4. Effect of antibody coverage on the efficiency of the immunocapture (ferrofluid 50 nm).

Ratio Antibody/Particle	5	10	15
Recovery	50%	89%	71%

Table 5. Influence of particle binding on fluorescence intensity (ferrofluid 50 nm).

	Peak Intensity
Free amoeba	5.720 +/- 1487
Particle-bound amoeba	11.017 +/- 3811

DISCUSSION & CONCLUSIONS: Finalizing an immuno-magnetic separation method depends on numerous parameters such antibody coverage, coupling procedure, nature and size of the particle, type of sample, ratio of particle/pathogen, etc. As shown in this paper, most of the difficulty comes from the fact that, unlike experimental samples containing cultured organisms, natural samples are complex and often not suitable for immunoassay.

The first example is given by the comparison of direct and indirect immunocapture. Table 1 clearly demonstrates that, although the percentages of recovery are acceptable when using experimental samples, the indirect method is not suitable for the capture of amoeba in their natural environment (1% versus 96 %). This is partially due to the fact that the free monoclonal antibodies, when diluted in natural water, do not easily reach their target, due to unphysiological conditions. All other experiments were undertaken with the direct procedure.

As previously mentioned, most of the IMS reagents commercially available require a detachment step to separate the particles from the pathogen prior to identification. This often results in a significant loss of pathogens. In our example (Tables 2 and 3), the suspensions containing both particles and pathogens were filtered and labelled.

This requires small-sized particles. Indeed, during the filtration through a 2 µm membrane, the non reactive particles must pass through the membrane, while only particles bound on pathogens remain on the membrane. In this way, large volumes of sample can be processed.

One other condition that must be considered when doing IMS without a detachment step is that the binding of particles onto the membrane of the pathogen leaves sufficient antigenic sites open for subsequent immunofluorescent labelling. Table 5 surprisingly shows that when using 50 nm particles, the level of the fluorescent intensity is higher that that of free amoeba. One explanation that can be put forward is that the interaction of small size particles with cells may protect their integrity during the filtration step, thus giving a higher apparent immuno-reactivity.

Our study demonstrates that IMS coupled to Chem*Scan*™ analysis is efficient in recovering and detecting amoeba as well as cryptosporidium from their water environment. The preliminary performance of this method appears to be sufficient for its future use in routine monitoring of surface waters.

REFERENCES: [1] K. Mignon-Godefroy, J.G. Guillet and C. Butor (1997) *Cytometry* **27:** 336-344. [2] F. Marciano-Cabral (1988) *Microbiol.Rev.* **52:** 114-133. [3] F. Reveiller, F. Marciano-Cabral, P.Pernin et al. (2000) *Parasitol. Res*. **86:** 634-641. [4] C. Pougnard, P. Catala, J.L Drocourt et al. (2001) submitted to *Appl. Env. Microbiol*.

ACKNOWLEDGMENT: This work was supported by a grant from Electricité de France.

SELECTIVE EXTRACTION OF LANTHANIDES AND ACTINIDES BY MAGNETIC SILICA PARTICLES WITH CMPO-MODIFIED CALIX[4]ARENES ON THE SURFACE

C. Grüttner [1], S. Rudershausen[1], S.E. Matthews[2], P. Wang[2], V.Böhmer[2], & J.-F.Dozol[3]

[1] *micromod Partikeltechnologie* GmbH, Friedrich-Barnewitz-Str.4, D-18119 Rostock, Germany [2] Fachbereich Chemie und Pharmazie, Johannes-Gutenberg-Universität, Duesbergweg 10-14, Mainz, D-55099, Germany [3] CEA Cadarache, DCC/DESD/SEP/LPTE, St. Paul lez Durance, F-13108, France

INTRODUCTION:

The recovery of lanthanides and actinides from high level nuclear waste is an area of world-wide concern. Current approaches are based on the TRUEX process which utilizes the highly efficient, neutral, organophosphorous ligand; octyl phenyl *N*,*N*-diisobutyl carbamoylmethyl phosphine oxide (CMPO).[1] Previously, we have reported on calix[4]arene based extractants which incorporate CMPO moieties at the wide[2] or narrow rim. Such pre-organisation of the chelating ligands leads to a 100 fold increase[2] in extraction efficiency combined with an enhanced selectivity for actinides and lighter lanthanides.

Solvent extraction methods using either simple or calix[4]arene-based systems, despite being highly efficient, do not lead to a marked decrease in waste volume. Recent interest has been focused on the use of magnetic fluidised bed separation technology and the development of magnetically assisted chemical separation (MACS) systems for nuclear waste remediation. These combine the selectivity of a solvent exchange ligand system with improved separation, resulting in a system that can be used at low concentrations and provides only a small volume of high level waste. The magnetic particles can then be stripped, to enable re-use, or vitrified. Adsorption of CMPO to magnetic acrylamide particles enhances extraction of americium and plutonium through a synergistic relationship between the extractant and magnetic particle.[3]

Here we report on magnetic silica particles with covalently attached CMPO derivatives on the surface, which allow for the evaluation of the pre-organisation effect of chelating ligands through direct comparison of calixarene and single ligand CMPO derivatives.

METHODS: As previously reported[4] non-porous magnetic silica particles with a diameter of 6 µm and carboxylic acid functionalities on the surface were modified by covalent attachment of suitably amine derivatised ligands. The simple ligand (**1**) was easily synthesised by mono acylation of 1,7-diaminoheptane with *p*-nitrophenyl(diphenylphosphoryl)acetate.[2] In contrast, a calix[4]arene-based system[4] (**2**) was designed to allow chelation at the wide rim and attachment *via* a two-point interaction at the narrow rim (Figure 1).

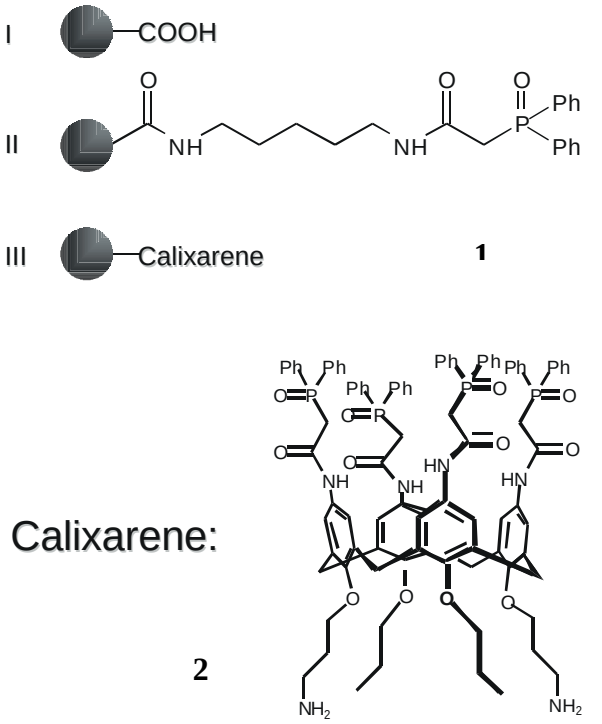

Fig. 1: Immobilization of the CMPO-derivative (1) and the CMPO-calix[4]arene (2) on the surface of non-porous magnetic silica particles (I).

The carboxylic acid groups of the particles were first activated by treatment with DCC, then washed by magnetic separation before being treated with the amino CMPO derivatives (**1**) and (**2**). The concentration of carboxylic acid groups (50 µmol/g) on the surface of the particles was determined by polyelectrolyte titrations. A 50 µmol/g concentration of CMPO ligands on the surface was achieved through stoichiometric treatment of the particles with either 50 µmol/g of (**1**) or 12.5 µmol/g of (**2**).

Highly porous magnetic silica particles with a diameter of 100 µm have a larger area for the immobilization of chelators per g of particles than corresponding non-porous particles. The density of functional groups on the surface of porous magnetic silica particles increases to about 800 µmol per g of particles in comparison to about 50 µmol per g of non-porous particles. The calix[4]-arenes (**3**) and (**4**) were covalently attached on the surface of highly porous magnetic silica particles to study the influence of the effective area for chelator binding on the surface of magnetic particles (Figure 2).
Furthermore, the very important influence of the spacer length between the calixarene moiety and the particle surface was studied. This spacer length increases from three carbon atoms in calixarene (**2**) to 5 in calixarene (**3**) and to 10 carbon atoms in (**4**).

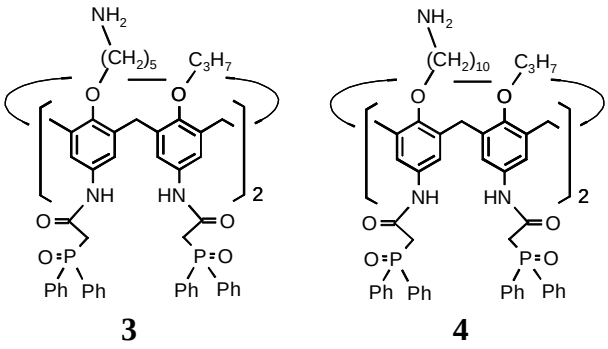

*Fig. 2: CMPO-calix[4]arenes (**3**) and (**4**)*

Solid-liquid extraction experiments were performed under conditions that simulate European nuclear waste streams (4M $NaNO_3$, 1M HNO_3). Separation of europium or americium as representatives of the early lanthanides and actinides, was initially evaluated. γ-Ray spectroscopic measurements of the initial nuclide activity in the aqueous phase and the activity after shaking with the particles were used to calculate the percentage extraction.

The covalent binding of the CMPO-calix[4]arenes (**3**) and (**4**) on the surface of the porous magnetic silica particles was followed by spectrophotometric determination of the decrease of the calix[4]arene concentration in the supernatant after magnetic separation of the particles. In contrast to the high density of functional binding sites on the particle surface of about 800 µmol per g of particle, a calix[4]arene binding capacity of about 25 µmol per g of particles was obtained. This is due to the corresponding space requirement of the large calix[4]arene molecules.
Solid-liquid extraction experiments were carried out to determine the percentage extraction and distribution coefficients K_D of europium and americium separation with the highly porous magnetic silica particles. The porous particles (**IV**) have the CMPO-calix[4]arene (**3**) on the surface, and the particles (**V**) the CMPO-calix[4]arene (**4**).
For comparison of different solid-liquid extraction experiments, the volume of the aqueous phase and the mass of particles were included in the calculation of the distribution coefficient K_D.

The porous magnetic silica particles with the highest percentage extraction (**IV**) of europium were used to study the possibility of recycling the magnetic particles by back extraction of the europium from the particle surface. Therefore 5 mg of magnetic particles (**IV**) were incubated for one hour with 5 ml europium nitrate solution (10^{-4} mol/l, 1 mol/l HNO_3). After magnetic separation the supernatant was removed and stored. The particles were incubated for 30 min with HEDPA solution (1-hydroxyethane-1,1-diphosphonic acid, 10^{-3} mol/l). Then the particles were washed with water for three times and again incubated with 5 ml europium nitrate solution (10^{-4} mol/l, 1 mol/l HNO_3) for one hour. The complexation – back extraction – washing cycle was repeated for three times. The europium concentration remaining in the supernatants after the complexation process was monitored spectrophotometrically using Arsenazo III as reagent (Figure 3).

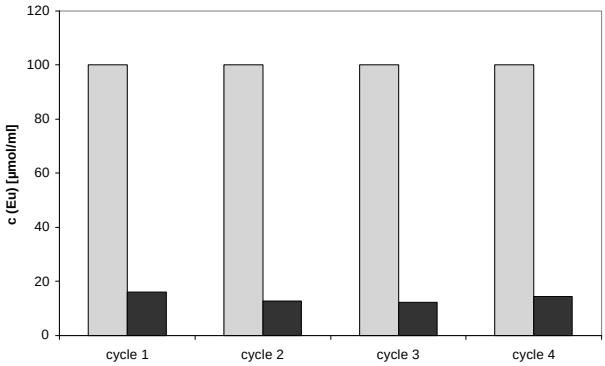

*Fig. 3: Complexation of europium cations on the surface of porous magnetic silica particles with CMPO-calix[4]arene (**4**) on the surface. The initial europium concentration in each cycle is 100 µmol/l (light columns). The europium concentration in the supernatant after incubation with particles (cycle 1), after complexation – back extraction – com-plexation (cycle 2) etc. is shown as dark columns.*

RESULTS: Attachment of the simple CMPO ligand (**1**) directly onto the surface of magnetic particles (**II**) enables extraction of europium and americium albeit at a low level. However, with the calix[4]arene(**2**)-based particles (**III**) there is significant enhancement in extraction, with a preference for americium (Table 1) as previously seen with non-particulate calixarene systems.[2] Comparable partition coefficients for europium extraction to the chemically sorbed systems are obtained. However, larger K_D values per mass of ligating function are found for americium. Thus covalently bound ligand particles show greatly enhanced extraction of americium over europium and offer the potential of selective extraction systems. Interestingly, preliminary results on the extraction of ^{139}Ce are in marked contrast to those found previously for the flexible wide rim CMPO-calix[4]arenes. The minimal extraction of cerium, by CMPO-calix[4]arenes, has been rationalised by the oxidation of Ce^{3+} to the smaller radius Ce^{4+} in the extremely acidic conditions used. However, with the solid-liquid extraction conditions reported here, 90% extraction of cerium is achieved within 19 hours of shaking, offering an opportunity for effective and selective separation.

*Table 1. Percentage extraction (%E) of lanthanides and actinides by CMPO and CMPO-calix[4]arene non-porous magnetic silica particles after 19 h shaking (**I-III**, figure 1). (%E = 100(A_0 - A) / A_0 where A_0 and A symbolise the initial and final activity of the aqueous phase)*

Magnetic particles	% E		
	^{152}Eu	^{241}Am	^{139}Ce
I	4	0	9
II	2	1	9
III	78	82	92

The highly porous magnetic silica particles have a higher density of CMPO-calix[4]arenes (**3**) or (**4**) on their surface (25 µmol per g of particles) than the non-porous particles (12.5 µmol / g). The percentage extraction of europium and americium with particles (**IV**) and (**V**) demonstrates the very high separation level for both cations in connection with a high selectivity for americium over europium (Table 2). The distribution coefficients K_D for europium and americium are dependent on the length of the spacer between the particle surface and the calixarene moiety. A prolongation of the spacer length from 3 to 10 carbon atoms decreases the K_D values for both cations (Table 3).

Table 2. Percentage extraction (%E) of lanthanides and actinides by CMPO-calix[4]arene porous magnetic silica particles after 1 h shaking.

Magnetic particles	^{152}Eu	^{241}Am
IV	80	90
V	63	80

Table 3. Distribution coefficients for lanthanides and actinides by CMPO-calix[4]arene magnetic silica particles (III-V). (KD = 100(A0 -A)x V / A / m where A0 and A symbolise the initial and final activity of the aqueous phase, V the volume of aqueous phase and m the mass of magnetic particles).

Magnetic Particles	K_D [ml / g]	
	^{152}Eu	^{241}Am
III (nonporous)	261	335
IV (porous)	129	310
V (porous)	57	132

The possibility of re-using the magnetic particles after the primary cation separation is very important for the cost reduction of a magnetic particle based separation process of lanthanides and actinides.

The back extraction experiment of europium from magnetic particles (**IV**) with HEDPA has shown that there is no significant loss of separation capacity for europium after stripping (Figure 3). This enables the re-use of the CMPO-calix[4]arene modified magnetic silica particles.

DISCUSSION & CONCLUSIONS: The importance of pre-organisation of chelating ligands onto a calix[4]arene scaffold was demonstrated by

experiments on magnetic particles (Table 1 and 2). We have developed a magnetic particle based process which applies a pre-organized calix[4]arene-CMPO ligand covalently attached on the particle surface. Efficient extraction of americium and europium from simulated nuclear waste conditions has been achieved together with surprisingly high levels of cerium extraction.

Highly porous magnetic silica particles allow for a higher density of CMPO-calix[4]arenes than do corresponding non-porous particles. In combination with the optimal spacer length between the particle surface and the calixarene moiety, the extraction properties of these particles can be further increased. Initial studies have shown that spacer lengths of 3 to 5 carbon atoms lead to a more effective extraction of europium and americium than the highly flexible C10 spacer. This can be explained by additional intermolecular interactions between the CMPO units of neighboring calixarenes. But the increasing spacer length to C5 and C10 results in an increasing selectivity of the particles for americium over europium (K_D (Am) / K_D (Eu)) from 1.28 for the C3 spacer to 2.3 – 2.4 for the longer C5 and C10 spacers. This higher selectivity is due to the complex formation of europium or americium cations with CMPO units from single calixarenes. Thus the optimal spacer length for calixarene attachment on a particle surface must prevent interactions between the CMPO units of different calixarenes for a complete exploitation of the pre-organisation effect of chelating CMPO ligands onto a calix[4]arene scaffold. This is the crucial factor for a high complexation capacity and selectivity of cation binding.

The possibility of recycling the magnetic particles was demonstrated by back extraction of europium from the particle surface. The complexation capacity of the particles did not change within four complexation – back extraction cycles. This allows for the use of magnetic particles with CMPO-calix[4]arenes on the surface in industrial applications.

REFERENCES: [1] E. P. Horwitz, D. G. Kalina, H. Diamond, D. G. Vandegrift, W. W. Schultz (1985) *Solv Extr Ion Exch* 75:3. [2] F. Arnaud-Neu, V. Böhmer, J-F. Dozol, C. Grüttner, R. A. Jakobi, D. Kraft, O. Mauprivez, H. Rouquette, M-J. Schwing-Weill, N. Simon, W. Vogt (1996**)** *J Chem Soc, Perkin Trans 2*: 1175-1182. [3] L. Nuñez, B. A. Buchholz, G. F. Vandegrift (1995**)** *Sep. Sci. Tech.* 30, 1455-1471. [4] S. E. Matthews, P. Parzuchowski, A. Garcia-Carrera, C. Grüttner, J-F. Dozol, V. Böhmer (2001**)** *Chem Commun*: 417-418.

ACKNOWLEDGEMENTS: This work is financially supported by the European Commission in the framework of the research program “Selective extraction of minor actinides from high activity liquid waste by organized matrices”, CONTRACT N° FIKW-CT2000-00088.

ADSORPTION OF DYES ON MAGNETICALLY LABELED BAKER'S YEAST CELLS

I. Safarik, L. Ptackova, & M. Safarikova

Laboratory of Biochemistry and Microbiology, Institute of Landscape Ecology, Na Sadkach 7, 370 05 Ceske Budejovice, Czech Republic

INTRODUCTION: Textile industry (and especially its part focused on the dyeing process) belongs among important sources of contamination responsible for the continuous pollution of the environment. The production of textile industry, as well as the volume of waste water containing processed textile dyes, steadily increases. The release of dyes into the environment constitutes only a small proportion of water pollution, but dyes are visible in small quantities due to their brilliance. Many dyes reaching the water sources are difficult to decompose and may cause problems due to their possible carcinogenicity etc. That's why the control of water pollution has become more important in the last years [1].

Textile dyes differs in their chemical composition and stability and that's why different approaches have to be used to lower their content in water sources. In general, chemical, physical and biological treatment procedures can be used for this purpose. The individual procedures differ in their efficiency to remove or degrade the dyes and also in the cost required for the treatment of the comparable volumes of polluted water.

Various adsorbents have been tested and used for the removal of dyes from polluted water, such as activated carbon, silica gel, natural clay, peat, wood chips, rice husk ash (a waste from rice mills), living or dead microbial biomass etc.

Biologically based procedures use low-cost materials, namely living or died microorganisms. Both adsorption on the surface of the cells (biosorption) and exploitation of cell's enzymes for biodegradation can be used for removal of textile dyes from wastewater. Interactions between microorganisms (yeast, bacteria, fungi, algae) and dyes depend on chemical properties of all the reaction partners. Each dye can have affinity to various microorganisms and on the other side one microorganism is able to bind more types of dyes.

Currently an extensive research is perform in many laboratories to find optimal (and as cheap as possible) microbial biomass and reaction conditions in order to develop an optimal technological processes enabling to separate contaminating dyes from large volumes of polluted water.

Magnetic adsorbents can be efficiently used for the separation of various types of compounds both from solutions and suspensions. During our experiments we have observed that yeast cells efficiently interact with some types of water based ferrofluids, leading to the formation of magnetically labeled cells which could be easily separated from the system using an appropriate magnetic separator. This material might be a promising adsorbent for various xenobiotics present in water sources. Magnetic properties of the adsorbent could be useful in the course of loaded adsorbent removal.

Adsorption characteristics of this new type of biological adsorbent, based on its interaction with selected model dyes are described in this paper.

METHODS: Baker's yeast (*Saccharomyces cerevisiae*) was obtained locally. Water based ionic ferrofluid (stabilized with perchloric acid) was prepared using the standard Massart procedure [2]. The relative ferrofluid concentration (32.0 mg/mL) is given as the magnetite content determined by a colorimetric method [3]. Acridine orange (C.I. 46005; Loba Chemie, Austria), aniline blue, water soluble (Water Blue; Methyl Blue; C.I. 42755; Lachema, Czech Republic), crystal violet (Basic Violet 3; C.I. 42555; Loba Chemie, Austria), malachite green (C.I. 42000; Roth, Germany) and safranine O (C.I. 50240; Sigma, USA) were used as model dyes.

The following optimized procedure was used for the magnetic modification of yeast cells. The compressed baker's yeast (2 g) was suspended in saline (6 mL), centrifuged and again resuspended in 6 mL 0.1 M acetate buffer (pH 4.6). After next centrifugation the sediment was resuspended in acetate buffer again to obtain ca 33 % yeast suspension (v/v; yeast cells volume determined after sedimentation for 24 h at 1 g). Three ml of the yeast suspension were added to 1 mL of ferrofluid, the suspension was mixed and then incubated at room temperature for one hour without mixing. After this time period the majority of yeast cells was magnetically modified by the added ferrofluid

(the cells responded to external magnetic field). Non-magnetic yeast cells and residual ferrofluid were removed by repeated static magnetic separation using acetate buffer (once) and saline as washing liquids, respectively, until the supernatant was clear. Magnetically modified yeast cells were then heated in a boiling water bath for 15 minutes. Heated magnetically modified yeast cells were washed with saline and stored at 4 °C. This material was used for further experimental work.

The adsorption experiments were performed in the following way. The suspension of magnetically modified yeast cells (200 μL; the settled volume of the adsorbent was 50 μL) in 15-mL test tube was mixed with 4.8 mL of water. Then 0.01 - 5.0 mL portion of stock water solution (1 - 2 mg/mL) of a tested dye was added and the total volume of the suspension was made up to 10.0 mL with water. In the same manner water solution of the tested dye, used for the construction of a calibration curve, was prepared; instead of 200 μL of magnetic cell suspension 200 μL of water were used. The suspension was mixed for 3 h at room temperature. Then the magnetic yeast cells were separated from the suspension using a magnetic separator (MPC-1 or MPC-6, Dynal, Norway) and the clear supernatant was used for the spectrophotometric measurement. The concentration of free (unbound) dye in the supernatant (C_{eq}) was determined from the calibration curve, and the amount of dye bound to the unit volume of the adsorbent (q_{eq}) was calculated by difference, using the following formula (Eq. (1)):

$$q_{eq} = (D_{tot} - 10\ C_{eq})/50 \quad (\mu g\ mm^{-3} \text{ or } mg\ cm^{-3}) \quad (1)$$

where D_{tot} is the total amount of dye used in an experiment.

RESULTS: Several types of water based ferrofluids were tested for the modification of baker's yeast cells to become magnetic. It was observed that ionic water-based ferrofluid stabilized with perchloric acid enabled rapid magnetic derivatization of the yeast cells. The magnetically modified cells could be easily separated using commonly used permanent magnets or commercially available magnetic separators.

Magnetically modified yeast cells were then tested as possible dye adsorbents. In order to have stabilized product enabling work for a long period of time, dead yeast cells are preferred. That's why heating of cells in boiling water bath was used in the course of the adsorbent preparation.

The order of heating and magnetic modification of yeast cells is important from the point of view of cells adsorption capacity. It was observed that cells at first magnetically modified with the ferrofluid and then heated (i.e., procedure described in METHODS) exhibit substantially higher dye adsorption capacity than the cells at first heated and subsequently magnetically modified (see Fig. 1). In all experiments the adsorbent prepared by an optimized procedure was used.

The period of heating of magnetically modified cells also influences the adsorption capacity of the adsorbent. As shown in Fig. 2, significantly lower adsorption capacity was observed for preparations heated for 2 minutes, while prolonged cells heating (5 – 15 min) lead to the adsorbents with higher and almost equal adsorption capacity. In all experiments magnetically modified yeast cells heated for 15 min were used.

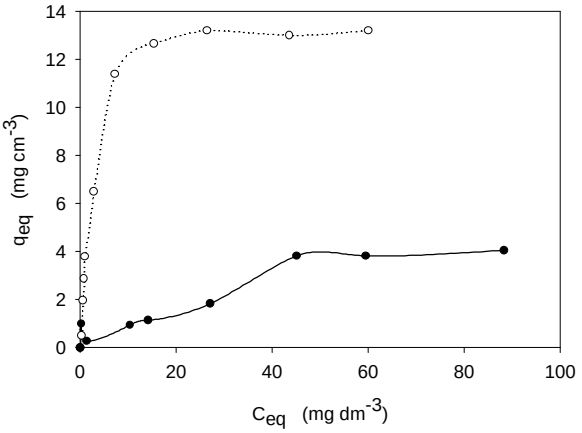

Fig. 1: Equilibrium adsorption isotherms of safranine O using magnetically modified baker's yeast cells as an adsorbent. Bottom curve, the cells were at first heated and then magnetically modified. Top curve, the cells were at first magnetically modified and then heated (15 min in both cases). C_{eq} – equilibrium liquid-phase concentration of the unadsorbed (free) dye (mg dm^{-3}); q_{eq} – equilibrium solid-phase concentration of the adsorbed dye (dye uptake) (mg cm^{-3}).

Preliminary experiments indicated that the adsorption of the dyes reached equilibrium in approximately 90 minutes (see Fig. 3). In the subsequent experiments, the adsorption of the tested dyes was performed for three hours.

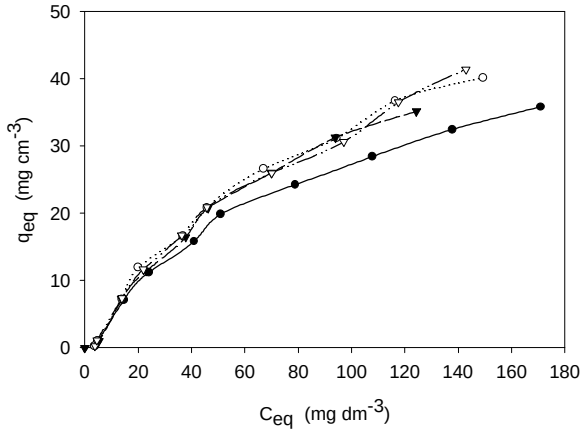

Fig. 2: Equilibrium adsorption isotherms of aniline blue using magnetically modified baker's yeast cells as an adsorbent. Various time of heat treatment of magnetically modified yeast cells was used (● , 2 min; ○, 5 min; ▼, 10 min; ▽, 15 min). The legends are the same as in Fig. 1.

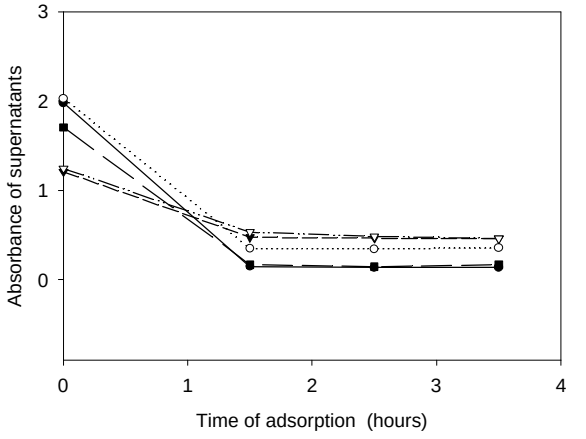

Fig. 3: Time dependence of the adsorption of tested dyes on magnetically modified yeast cells. ●, acridine orange; ■, aniline blue; ○, crystal violet; ▽, malachite green; ▼, safranine O.

Two types of dyes were used for adsorption experiments. Triphenylmethane dyes are represented by aniline blue, crystal violet and malachite green, while heteropolyaromatic dyes are represented by acridine orange and safranine O. Fig. 4 shows the equilibrium adsorption isotherms for unbuffered aqueous solutions of tested dyes. Adsorption isotherms represent the equilibrium distribution of the dyes molecules between the aqueous and solid phases as the dye concentration increases. The isotherms follow the typical Langmuir adsorption pattern as shown by the linear transformation of the experimental data (see Fig. 5).

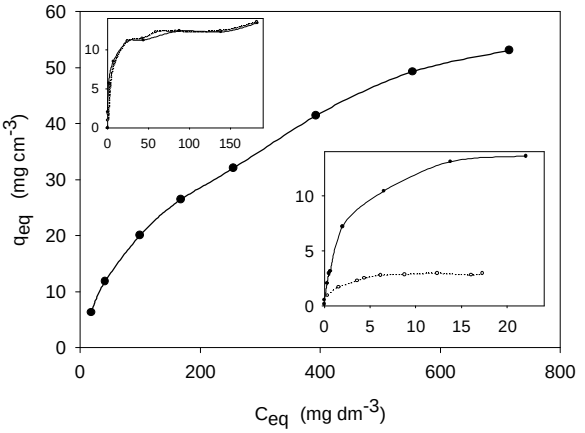

Fig. 4: Equilibrium adsorption isotherms of tested dyes using magnetically modified baker's yeast cells as an adsorbent. Main graph, aniline blue. Top insert, acridine orange and crystal violet. Bottom insert, malachite green (bottom curve) and safranine O (top curve). The legends are the same as in Fig. 1.

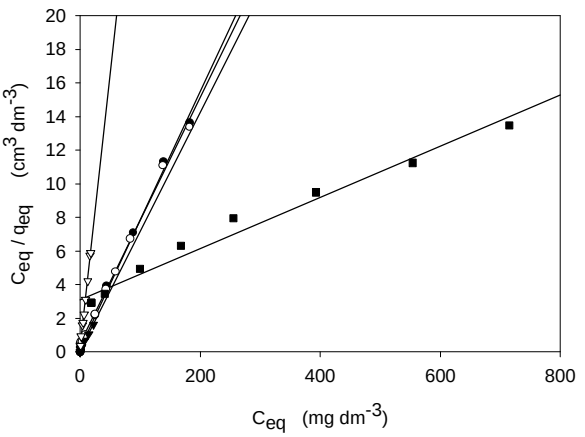

Fig. 5: Langmuir transformation of equilibrium adsorption isotherms of tested dyes. The symbols are the same as in Fig. 3; the legends are the same as in Fig. 1.

The linearized form of the Langmuir isotherm was used to calculate maximum adsorption capacity of the adsorbent (Eq.2):

$$C_{eq} / q_{eq} = 1 / b.Q + C_{eq} / Q \qquad (2)$$

where q_{eq} is the amount of dye adsorbed per unit of adsorbent ("adsorbed dye"), C_{eq} is the concentration of dye remaining in solution at equilibrium ("free dye"), Q is maximum adsorption capacity (number of mol or g of the dye adsorbed per unit of adsorbent, forming a continuous monolayer on adsorbent surface) and b is a constant.

The values of magnetic adsorption capacities are shown in Table 1.

Table 1. *Maximum adsorption capacities of magnetically modified baker's yeast cells for the tested dyes. Q is calculated using the settled volume of the magnetic adsorbent (mg ml^{-1}) while Q' is calculated using the dry weight of the adsorbent (mg g^{-1}).*

Dye	Q	Q'
Acridine orange	13.1	82.8
Aniline blue	68.1	430.2
Crystal violet	13.6	85.9
Malachite green	3.1	19.6
Safranine O	14.3	90.3

DISCUSSION & CONCLUSIONS: Modification of baker's yeast cells with the perchloric acid stabilized ferrofluid lead to the formation of magnetically responsible material which could be used as an efficient adsorbent for the removal of various dyes. The maximum adsorption capacity observed is relatively high, so magnetically modified yeast cells can be a promising dye adsorbent.

It seems that even small changes in the dye structure may significantly influence the adsorption capacity. Very different maximum adsorption capacities were observed for three triphenylmethane dyes (aniline blue, crystal violet and malachite green). The highest adsorption capacity for aniline blue could be caused by the presence of two aromatic rings with sulfonic acid groups present in the molecule while in crystal violet and malachite green four methyl groups are present.

Magnetic modification of other yeast cells and their possible application is currently studied.

REFERENCES: [1] T. Robinson, G. McMullan, R. Marchant, and P. Nigam (2001) *Bioresource Technol* **77:**247-255. [2] R. Massart (1981) *IEEE Trans Magn* **17**:1247-1248. [3] H. Kiwada, J. Sato, S. Yamada, et al (1986) *Chem. Pharm. Bull.* **34:** 4253- 4258.

ACKNOWLEDGEMENTS: The research is a part of ILE Research Intention No. AV0Z6087904. The experimental work was supported by the NATO Science Programme (Collaborative Linkage Grant No. LST.CLG.977500), Ministry of Education of the Czech Republic (grant project No. OC 523.80) and Grant Agency of the Czech Academy of Sciences (Project No. S6087204).

MAGNETIC FLOW SORTING USING SUSCEPTIBILITY-MODIFIED CARRIER FLUIDS

L.R. Moore[1], P.S. Williams[1], J.J. Chalmers[2], & M. Zborowski[1]

[1]*The Cleveland Clinic Foundation, 9500 Euclid Ave. ND20, Cleveland, OH 44195, USA*
[2]*The Ohio State University, Columbus, OH 43210 USA*

INTRODUCTION: Continuous flow magnetic cell sorting with a Quadrupole Magnetic Flow Sorter (QMS) has been successfully applied to the isolation of cells of biological interest, and is particularly relevant to stem cell isolation. Specific cell populations are labeled with magnetic nanosphere-antibody conjugates, rendering them magnetic compared with non-binding negative cells. Our QMS device consists of an annular channel placed in the bore of a permanent quadrupole magnet, which generates a radial magnetic force. The theory specific to this system is validated by experiments with cells and calibration microspheres [1,2]. The positive cell recovery is predicted once the mobility distribution is known, with the aid of our novel device, the Cell Tracking Velocimeter (CTV). CTV generates mobility histograms of cell populations by sequentially tracking their motion in a well-characterized magnetic field [3].

Enriched fraction purities are difficult to predict and control. Due to a combination of flow non-idealities and geometric imperfections, negative cell "crossover" into the enriched fraction inevitably occurs in the QMS. Even a low fractional crossover can have a large impact when target cells are rare in the feed, as in the case of progenitor cells in apheresis product or umbilical cord blood. An attractive solution is the introduction of magnetic material into the carrier. Since transverse migration is governed by the difference in magnetic susceptibility between the cell and medium, raising the susceptibility of the medium has the effect of repelling the unlabeled - and therefore, non-magnetic - cells from the increasing magnetic field gradient, while only slightly retarding the motion of the magnetically-labeled cells.

The magnetic contrast agent, MAGNEVIST® (gadopentetate dimeglumine) (Berlex Laboratories, Wayne, NJ), used for MRI imaging of the central nervous system, is desirable for producing magnetic carrier due to its biocompatibility, chemical stability and high molar susceptibility. CTV measurements of non-magnetic polystyrene microspheres (PSMs) in dilute Gd^{3+} solution, confirm the predicted effects and serve as a basis to validate the assumptions of magnetic particle tracking. QMS studies of red blood cells (RBCs) and PSMs show that crossover is significantly reduced by the addition of Gd^{3+} to the carrier medium. This allows selection of flow conditions to yield greater throughput, purity and resolving power.

METHODS: A thorough description of the fluid dynamic and magnetic theory applicable to the QMS is given [1]. The separation element of the QMS lies in the annulus between a coaxial core rod 2, and an outer cylinder 3, as illustrated in Fig 1. This is surrounded by four pole pieces 1, generating a magnetic quadrupole field. Coaxial cylindrical splitters 4, separate inlet and outlet streams, where the feed and carrier streams are *a'* and *b'*, and depleted and enriched streams are *a* and *b*. Three or four independent syringe drives control the flow components. The source of the magnetomotive force is four Nd-Fe-B permanent magnets.

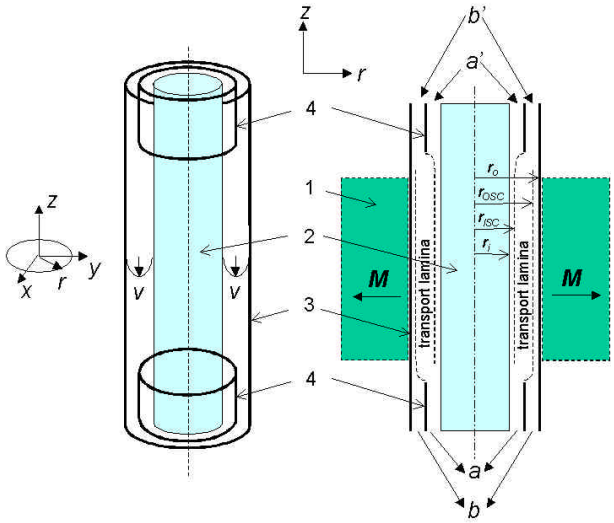

Fig. 1: Perspective view not showing magnet (left) and axial section (right) of QMS.

The component flows converge just beyond the inlet splitter, and the virtual boundary separating the fluids and extending down the column, is called the inlet splitting surface (ISS); see Fig. 1. The radial position of the ISS depends non-linearly on the ratio of the feed component flow to the total flow, Q_a/Q:

$$\frac{Q_{a'}}{Q} = \frac{\left[2r^{2} - r^{4} + 2A_2 r^{2}\ln r - A_2 r^{2}\right]_{r_i}^{r_{ISS}}}{A_1\left(1 - r_i^{2}\right)}$$

(1)

A_1 and A_2 are constants which depend on the channel geometry, $\tilde{n}$ is the dimensionless ratio r/r_o, r_o is the radial distance to the inside surface of the cylinder, and $\tilde{n}_i$ is defined at the core rod radius r_i. A similar outlet splitting surface (OSS) extends upward from the outlet splitter and separates the flow components *a* and *b*. Analogously to eq. 1, the position of the OSS, $\tilde{n}_{OSS}$ depends on Q_a/Q. The transport lamina thickness, *d*, is the distance between the splitting surfaces, OSS and ISS.

The numerical values of the QMS parameters are maximum field, B_o = 1.344 T, r_o = 4.53 mm, r_i = 2.38 mm, inlet flow rate ratio, $Q_{a'}/Q$ = 0.2, variable outlet flow rate ratio, Q_a/Q = 0.1 … 0.35, and total flow rate, Q = 4 ml/min.

Magnetically labeled cells in a magnetic field experience a magnetic drift velocity, $u_m = mS_m$, where *m* is the cell magnetophoretic mobility and S_m is the field strength parameter. In the general case, and applicable to the field of CTV, S_m is described for a particle of inducible magnetization, as

$$S_m = \left|\frac{\nabla B^2}{2m_0}\right|$$

(2)

where m_0 is the permeability of free space. In the ideal quadrupole system, S_m is related to the system parameters by:

$$S_m = \frac{B_o^2}{m_0 r_o}\frac{r}{r_o}$$

(3)

B_o, in this case, is the flux density at the inner surface of the outer cylinder, r_o. Note that S_m depends on the radius *r*, but not on the angular coordinate, *è*. The mobility is independent of the magnetic environment and relates to properties of the cell, label and medium by:

$$m = \frac{2}{9}\frac{R^2 \Delta c}{h}$$

(4) (3)

R is the particle radius, *ç* is the medium viscosity and Ä÷ is the difference between the volumetric susceptibilities of the cell and the medium. Neglecting the slight contribution of water, the volumetric susceptibility of a gadolinium solution, in SI units, is:

$$c = \frac{4p}{1000}\left[Gd^{3+}\right]c_{M,Gd3+}^{CGS}$$

(5)

where $c_{M,Gd3+}^{CGS}$ is the molar susceptibility of Gd^{3+} in CGS units, 0.027. For an unlabeled cell or non-magnetic particle of approximately zero susceptibility, suspended in a Gd^{3+} solution, eqs. 4 and 5 become:

$$mh = -\frac{8p}{9000}R^2 c_{M,Gd3+}^{CGS}\left[Gd^{3+}\right]$$

(6)

It is clear that a plot of mh vs. $[Gd^{3+}]$ should yield a straight line of slope given by the constant parameters.

CTV, a device for measuring the mobility of cell or particle suspensions, comprises a permanent magnet circuit with pole pieces shaped to produce a nearly constant S_m within the field of view of a microscope [3]. The induced magnetic particle velocity u_m is, therefore, constant for paramagnetic particles. The CTV analysis area is 1.27 x 1.72 mm. Assuming that a uniform probability distribution governs the uncertainty of positioning the viewing area in the magnetic field, the weighted mean of the horizontal component of $\tilde{N}B^2$ is 376.8 ± 2.5 T^2/m, giving rise to a mean S_m of 1.499 x 10^8 TA/m^2.

A microscope with a mounted CCD camera with a frame speed of 30 Hz, is used to observe particle migrations in a glass channel in the magnetic field. A µ-Tech Frame Grabber is used to convert the analog camera image into a binary 480x640 pixel array, where each pixel contains eight bits of gray-level. To improve low-mobility sensitivity, frame speeds less than 30 Hz are used by selectively skipping frames during the acquisition. The particle tracking and velocity calculation is performed using a computer algorithm consisting of two parts: determination of particle location and 2-D tracking. The output of CTV gives location and velocity data, for multiple particles, over the observed frames. These velocities, combined with the known S_m, give mobilities. Typically, hundreds of particles are analyzed in a sample, enabling the construction of mobility histograms and the calculation of population statistics.

The CTV computational algorithm has been tested for self-consistency and sensitivity by tracking the sedimentation of polystyrene microspheres. Validation of the magnetic assumptions has been explored by tracking magnetite-coated polystyrene

beads, which were separately measured with a magnetometer [4]. The results were affected by the large degree of dispersion of magnetite content and the non-constant velocities of ferromagnetic materials in the field of the CTV magnet. An improved method of validation, described below, applies to the tracking of monodisperse PSMs suspended in a solution of paramagnetic salt, in which the expected direction of migration opposes the field gradient.

RESULTS & DISCUSSION: Figure 2 gives distributions, obtained by CTV, for monodisperse PSMs of diameter 6.992 ± 0.050 μm (Duke Scientific Corp., Palo Alto, CA) suspended in various dilutions of MAGNEVIST®, expressed as the concentration of Gd^{3+}. The abscissa combines mobility with medium viscosity, whose dependence on contrast agent concentration was determined with a plate-and-cone viscometer. The peak relative dispersions remain fairly constant, and the control peak is statistically distinct from that of the lowest concentration. Fig. 3 gives the experimental data and theoretical plot of $m\eta$ versus $[Gd^{3+}]$, with the aid of eq. 6. The data from Fig. 2 are plotted with regression line and confidence interval. Because the regression line fits the measured data with a high degree of confidence, the disparity with the theoretical curve indicates that an unknown systematic error may be involved. Nonetheless, the slopes compare favorably: -8.195×10^{-16} (regression) compared with -9.215×10^{-16} (theoretical).

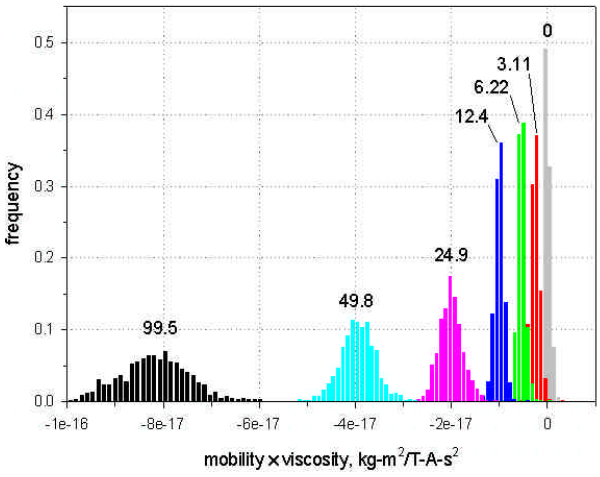

Fig. 2: CTV analyses of monodisperse PSMs suspended in various millimolar concentrations of Gd^{3+}.

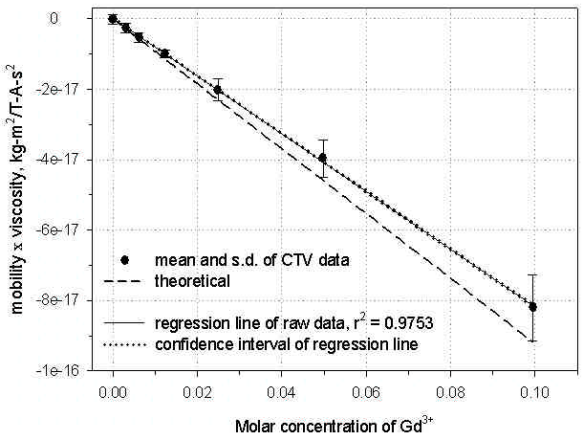

Fig. 3: Data reduction of PSMs in Gd^{3+} medium.

The non-specific crossover of 15.8 μm PSMs in the QMS was investigated, as shown in Fig. 4. Data were obtained by injecting 3-5 samples into the column, for each flow condition, and monitoring the light attenuation with a UV detector at outlet b, as described [2]. The dashed line shows the position of the ISS relative to the core rod and outer wall of the channel. The ISS is calculated for a constant inlet flow rate ratio of 0.2, with the use of eq. 1. The outlet flow rate ratios Q_a/Q were varied, corresponding to various positions of the OSS and transport lamina thicknesses given on the abscissa. Under control conditions the particles have no significant magnetization relative to the medium (0.5% fetal bovine serum in Plasmalyte™ (Baxter Healthcare, Deerfield, IL). And under ideal behavior - no geometric imperfections or external forces - their fractional recovery F_b, at and beyond the ISS, must be zero.

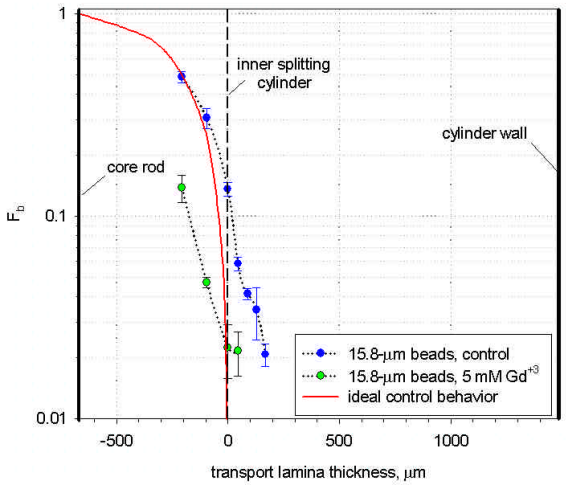

Fig. 4: The crossover PSMs in the QMS. Bold lines of the core rod and cylinder wall bound the annulus.

The ideal control curve is generated by the simple relationship, $F_b = 1 - Q_a/Q_{a'}$, with Q_a ranging from 0 to $Q_{a'}$. Evidence of non-ideal behavior is seen by the non-zero recoveries at positive transport lamina.

For a practical QMS separation, a suitable outlet flow rate ratio is found from the transport lamina which meets a low crossover criterion, e.g. 2%. If this criterion can be satisfied while reducing the outlet flow rate ratio, theoretically, the resolving power and recovery can be improved. Likewise, reducing crossover for the same outlet flow rate ratio improves the purity in the enriched fraction. Either aim might be achieved when gadolinium salt is added to the medium, as seen in Fig. 4.

These experiments were repeated with red blood cells (RBC's) replacing PSMs; Fig. 5. RBCs, whose mean hydrodynamic diameter is 5.52 μm, are important in that they are a frequent contaminant in leukocyte separations involving human blood, bone marrow and apheresis product. Comparison of Fig. 5 with Fig. 4 gives evidence that RBCs have a higher crossover, under the same conditions, than PSMs, probably due to the bi-concave shape of the RBCs. Further, the effect of 5 mM Gd^{3+} in reducing crossover is greater for the PSMs, because of the effect of size in eq. 3. Still, the possibility of adding gadolinium salt to the medium in practical separations of leukocytes is indicated.

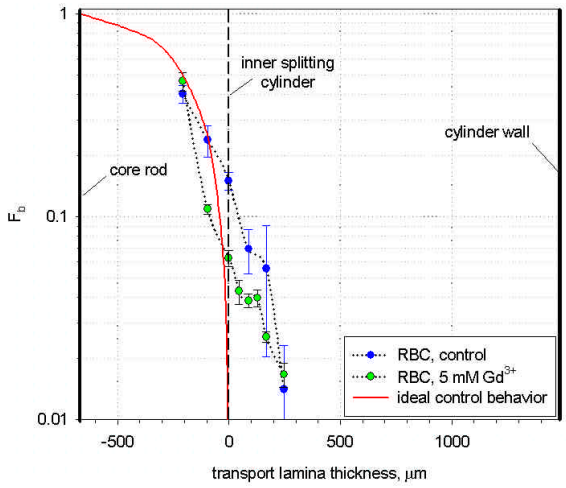

Fig. 5: The crossover of RBCs in the QMS.

REFERENCES: [1]P.S. Williams, M. Zborowski, and J.J. Chalmers (1999) *Flow rate optimization for the quadrupole magnetic cell sorter*, Analytical Chemistry **71**: 3799-3807. [2]M. Hoyos, L.R. Moore, K.E. McCloskey, S. Margel, M. Zuberi, J.J. Chalmers, and M. Zborowski (2000) *Study of magnetic particles pulse-injected into an annular SPLITT-like channel inside a quadrupole magnetic field*, J Chromatography A **903**: 99-116. [3]J.J. Chalmers, Y. Zhao, M. Nakamura, K. Melnik, L. Lasky, L. Moore, and M. Zborowski (1999) *An instrument to determine the magnetophoretic mobility of labeled, biological cells and paramagnetic particles*, J Magnetism and Magnetic Materials **194**: 231-241. [4]L.R. Moore, M. Zborowski, M. Nakamura, K.E. McCloskey, S. Gura, M. Zuberi, S. Margel, and J.J. Chalmers (2000) *The use of magnetite-doped polymeric microspheres in calibrating cell tracking velocimetry*, J Biochem Biophys Methods **44**: 115-130.

ACKNOWLEDGMENTS: These studies were supported by the grants from the NIH (R01 CA62349 to M.Z., R33 CA81662 to J.J.C.), and the NSF (BES-9731059 to J.J.C. and M.Z.). The RBC specimens were provided by Dr. G. Ostera, National Institute of Diabetes, Digestive and Kidney Disease, NIH, Bethesda, MD.

HIGH GRADIENT MAGNETIC SEPARATION (MACS) FOR ISOLATION AND MODIFICATION OF BIOMOLECULES

A. Cremer, C. Reinhard, S. Müller, G. Günther, M. Köhler, M. Köster, N. Braß-Heckel, C. Biervert, I. Johnston, D. Merkel, V. Nölle, S. Miltenyi

Miltenyi Biotec GmbH, Friedrich-Ebert-Str. 68, 51429 Bergisch Gladbach, Germany

INTRODUCTION: High gradient magnetic separation is not only applicable to cells, but also offers advantages in the isolation of biomolecules, such as nucleic acids or proteins (see Fig. 1). The small size of the particles involved gives rise to fast binding kinetics similar to a solution state reaction, which in turn reduces the time of separation. Low nonspecific binding as well as rigorous washing steps on the column lead to high purity products which can be used after elution or even processed further on the column. On-column reactions would add the benefits of solid phase reactions such as easy exchange of reaction media and efficient removal of excess reagent to the MACS system. The small void volume (25µl) of the µMACS column allows for economic use of reagents. To extend the possibilities of on-column reactions further, a heated magnet (ThermoMACS) was developed in order to enable reactions above room temperature. The following investigations were performed to evaluate in principle the possibilities of on-column modifications of magnetically immobilized biomolecules.

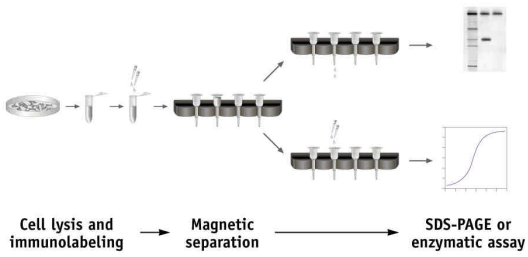

Fig. 1: Example for a reaction on the column: enzymatic activity assay after immunoprecipitation.

METHODS: Restriction digestion on the column: 5' biotinylated DNA (700 bp PCR product) is isolated with µMACS Streptavidin Kit. Restriction enzymes EcoRI, HindIII, SacI, SalI are used to cut the DNA on-column in a ThermoMACS (1 h / 37° C). After elution of the unbiotinylated fragment, release reagent is applied and the biotinylated fragment is isolated.

Activity of enzymes immobilized on the column after immunoprecipitation with µMACS Protein G or –A MicroBeads: An immunoprecipitation from Jurkat cell lysate is performed with anti v-src antibody (clone 327) and µMACS protein G MicroBeads. For assessing enzyme activity a nonradioactive kinase assay (Roche) is used. The substrate is applied to the column where the immunoprecipitated enzyme is magnetically immobilized. After elution the degree of phosphorylation is quantified by ELISA according to protocol.

cDNA synthesis on the column: mRNA is isolated from Jurkat cells with the µMACS mRNA Isolation Kit. Instead of eluting the mRNA according to protocol, a cDNA synthesis mix containing reverse transcriptase and dNTPs is incubated on the column in the ThermoMACS (50 min / 37° C). After RNAseH digest and release from the beads the cDNA is eluted.

RESULTS: Restriction digestion on the column: In order to show that efficient enzymatic reactions of magnetically immobilized molecules on the column are possible, digests with several restriction enzymes were performed on a biotinylated 700 bp PCR product. The amount of enzyme needed is the same as in a corresponding digest in a tube. Unbiotinylated and biotinylated fragments are eluted separately (see Fig. 2).

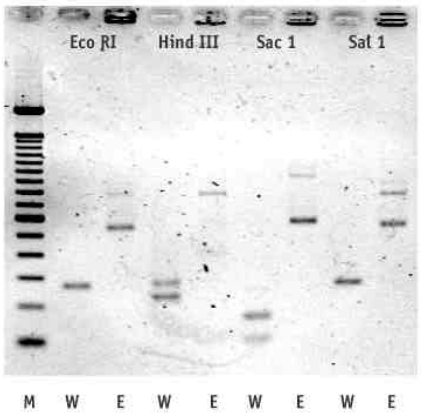

Fig. 2: ***Restriction digestion of 700bp DNA.*** *Agarose gel electrophoresis of the isolated fragments. Lanes W, unbiotinylated fragments; lanes E, biotinylated fragment eluted after release. Used enzymes: see above lanes.*

Activity of immunoprecipitated enzyme immobilized on the column: A kinase (81 kDa) could be isolated from Jurkat cells. A peptide substrate for v-

src was incubated on the column. ELISA of the eluted substrate showed that the peptide was phosphorylated.

cDNA synthesis on the column: mRNA from Jurkat cells was used for synthesizing cDNA. All steps were performed on the column in a heated magnet. The final eluate contained cDNA, which was confirmed by agarose gel electrophoresis.

Digestion experiments with DNAse and RNAse showed that the nucleic acid isolated is cDNA and not mRNA. A PCR amplification of housekeeping gene GAPDH showed that the resulting products were amplified from cDNA and not from genomic DNA, which would give larger PCR products with the used primer pair due to an intron present.

DISCUSSION & CONCLUSIONS: The examples above show that MACS enables not only fast and highly pure isolations of biomolecules, but also can be utilized to facilitate subsequent reaction steps by performing them on the column. The µMACS columns have a void volume of 25 µl which serves as the reaction volume. Through capillary forces the column matrices do not run dry, but stay filled even during prolonged incubation steps. Together with easy washing steps and exchange of reagents inside the matrix simply by applying the appropriate solutions, this contributes to the suitability of the columns as convenient reaction vessels. The ThermoMACS further broadens the range of possible applications by enabling reactions above room temperature.

In summary, the MACS system offers the possibility to switch between solid phase style and solution style steps simply by reversible magnetic immobilization on the column or use of the colloidal solution. So the benefits of both worlds can be used depending on the application. Isolations of biomolecules are done in the colloidal state which offers the advantage of fast binding kinetics. Modifications of isolated molecules can be done on-column, which offers the advantages of a small reaction volume for economic reagent use and efficient washing steps without the danger of losing precious material.

NEGATIVE DEPLETION CELL SORTING USING A QUADRUPOLE MAGNETIC CELL SORTER

O. Lara[1], M. Nakamura[1], M. Zborowski[2], J.J. Chalmers[1]

[1] *Ohio State University, Columbus, OH 43210, USA*
[2] *Cleveland Clinic Foundation, Cleveland, OH 44195, USA*

INTRODUCTION: Immunomagnetic cell sorting is a suitable technique for many therapeutic applications. Positive depletion using a Quadrupole Cell Sorter (QMS) has proved to effectively sort cells of interest in a short time with high throughput (Moore, et al. 2001, Nakamura, et al. 2001). Improvements made to the separation device have led to the application of the same apparatus to negative depletion.
Operating the QMS for negative depletion can be applied to depletion of T-cells for bone marrow transplant and to detection of cancer cells in circulating peripheral blood.
From the basic theory developed for QMS separation (Hoyos, et al., 2000) it is understood that parameters such as cell concentration, transport lamina thickness, and magnetization level, among others, govern cell separations. Therefore, it is necessary to evaluate each of those parameters to optimize separation to a desired cell purity level in the negative outlet.
We are showing partial results on negative depletion, and the effect of various parameters that govern this separation.

OBJECTIVE: The present study aims to evaluate and optimize the separation parameters governing negative depletion for future clinical application. The model cell system is composed of a human breast cancer cell line (MCF-7) and peripheral blood leucocytes (PBL).

METHODS: Peripheral blood buffy coats from apparently healthy donors were purchased from the American Red Cross, Central Ohio Region. Ficoll–Hypaque density gradient centrifugation (1.077 g/ml) was used to separate mononuclear cells from the buffy coat. No red cell lysis was carried out since we have found that leukocytes tend to clump after this treatment. Leukocytes were resuspended in calcium- and magnesium-free PBS buffer containing 2mM EDTA and 0.5 % bovine serum albumin (BSA). In addition, monocytes and macrophages were removed by allowing them to adhere to plastic for two hours at 37 C in 5% CO_2. Non-adherent cells were collected and resuspended in PBS buffer.
MCF-7 cells were grown to confluence on Eagle medium supplemented with 10% fetal bovine serum (FBS). MCF-7 cells were harvested using trypsin-EDTA for 5 minutes and then washed and resuspended in PBS buffer.
Cell number and size analysis was carried out using a Coulter Multisizer II system ((Beckmann-Coulter, Miami, FL). PBL cells were accounted in the range from 5.92 μm to 12.57 μm and MCF-7 cells were accounted from 12.57 μm to 40.1 μm. The great size difference allows us to obtain the ratio of MCF-7/PBL cells.
Cell mixture was prepared to a desired MCF-7 ratio by mixing calculated volumes of cell suspensions and adjusting to a desired concentration with PBS buffer. Final concentration of the mixture was determined before each set of experiments.
Leukocytes were labeled using a two-step labeling technique. Since we wanted to deplete our mixture of leukocytes, we chose anti-CD45-PE (Beckmann Coulter, Cat # IM2078) as primary antibody and Anti-PE microbeads (Miltenyi Biotech, Cat # 488-01) as a secondary antibody.
Cell separation was carried out using a QMS system with the latest version of separation column, MarkV1b.
Separation buffer was calcium- and magnesium-free PBS supplemented with 0.5 % of BSA and 2mM EDTA final concentration. Cells were pulsed using an injection valve with 500 μl capacity. Fig. 1 depicts the QMS column used for this separation.

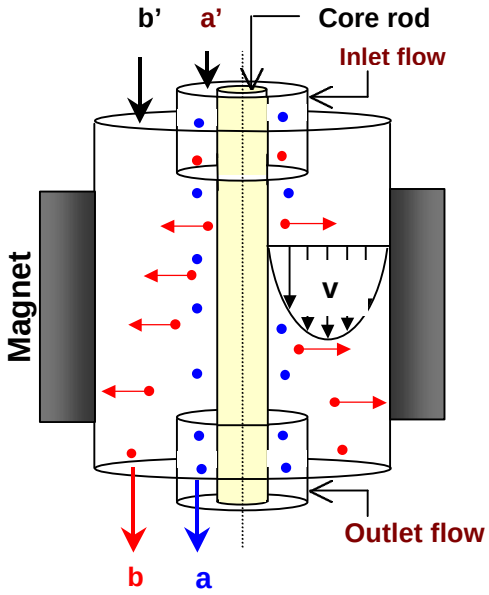

Fig. 1: QMS column showing flow distribution and cell path during separation.

Inlet ports **a'** and **b'** receive cell suspension to be separated and carrier buffer respectively. Immunomagnetically labeled cells migrate toward outlet **b** whereas non-labeled cells elute at outlet **a**.
All experiments were performed on a closed system, using a syringe pump to inject buffer and a syringe pump for suction from the outlets.
Effluents were analyzed using a Coulter Multisizer II (Beckmann Coulter, Miami, FL), relating size distributions, ratio, purity and recovery percentages of both cell types in each effluent.

RESULTS: To accumulate representative results, each experiment was performed three times on different days so as to minimize donor variability. Total cell number on each fraction was calculated by knowing the total volume in calibrated tubes.
There were control samples for this type of separation; labeled leukocytes were the positive control and non-labeled MCF-7 cells as the negative control. In the case of the positive control, 8 % of injected cells went to outlet **a**, 45.4 % went to outlet **b**, and the remaining cells presumably hit the column wall. For negative control (MCF-7), 97 % of the injected cells went to outlet **a**, and 1 % were found in outlet **b**.
Results are shown in such a way that they represent the fraction of the originally injected cells that appear in either outlet **a** or **b**. Then, $Fe_{,tg}$ means fraction of target cells in enriched fraction (outlet a) $Fd_{,tg}$ means fraction of non-target cells in depleted fraction (outlet **b**). The same definition applies for non-target cells, which are designated by the subscript **nt**.
Summarized results can be found in Tables 1 and 2.

Table 1. Effect of transport lamina thickness on QMS performance. Cell concentration » $1x10^7$ cells/ml. Amount of primary and secondary antibody is constant at 5ml per 10^6 cells.

Transport Lamina (µm)	Feed MCF-7 (%)	$Fe_{,tg}$ %	$Fd_{,tg}$ %	$Fe_{,nt}$ %	$Fd_{,nt}$ %
32	1.27	17.50	57.72	2.09	23.45
42	5.78	23.96	59.91	8.38	42.57

Table 2. Effect of cell concentration. Primary and secondary antibody maintained to 20 ml per 10^6 cells. Transport lamina thickness constant at 42mm

Cell conc. (10^6/ml)	Feed MCF-7 (%)	$Fe_{,tg}$ %	$Fd_{,tg}$ %	$Fe_{,nt}$ %	$Fd_{,nt}$ %
5.06	4.69	44.23	42.78	8.75	47.19
3.38	3.19	25.37	54.28	13.15	39.92

DISCUSSION AND CONCLUSIONS: A saturation study previously carried out (data not shown) indicates that 5 µl/10^6 cells of antibody is insufficient for saturation. In fact, 20 µl/10^6 cells is required.
The QMS system is still under development and it is necessary to improve the design of the column as well as to include in the current mathematical model some phenomena we have observed with other apparatus also developed in our laboratory. From results obtained when running the control samples, we have noticed that when there is a single cell population inside the column, the effluent compositions are very close to the theoretical predictions. However, when two different cell populations are present, the theory does not closely match the effluents.
This effect has been observed during Cell Tracking Velocimetry (CTV) experiments and it is apparently related to cell concentration (McCloskey, K., et al 2001). The higher the cell concentration, the greater this effect seems to be. We are attributing those results to a drafting effect occurring inside the column. This drafting effect occurs due to the large number of immunomagnetically labeled cells susceptible to the magnetic field. Consequently, we have reduced the number of cells injected into the column. We expected to obtain better results by this measure; however, we did not find any improvement in the results. This can be attributable to the low cell concentration in each effluent. It is necessary to try methods such as filtration to obtain a measurable cell concentration with low variation.
Our results suggest that there may be cell interaction (PBL-MCF-7) inside the column and

that this plays an important role in cell separation. It is necessary to run experiments using different cell lines, since MCF-7 cells are known to form clumps, making quantitation rather difficult.
It is important to mention that it is necessary to perform more experiments in order to completely characterize the instrument for different cell systems and begin clinical applications that will show its relevance in the field.

REFERENCES: Moore, Lee R., et al. (2001) *J. Magnetism Magnetic Materials* **44**:115-130. Nakamura, M., et al. (2001) *Biotechnol Bioeng* **17**(6):1145-1155. Hoyos, et al. (2000) *J Chromatography A* 903:99-116.

ACKNOWLEDGEMENTS:
This work was supported by the National Cancer Institute (R33 CA81662-01 to JJC, RO1 CA62349 to M.Z., and CA16058-25 to OSU) the National Science Foundation (BES-9731059 to J.J.C).

CARRIERS FOR EXTRACORPOREAL BLOOD PURIFICATION: FROM BASIC RESEARCH TO HEALTH CARE

W.Schuett[1], W. Ramlow[2], & D. Falkenhagen[3]

[1]Institute for Applied Biosciences e.V. and [2]Apheresis Service Gesellschaft e.V., Rostock, Germany, [3]Danube University Krems, Austria

The concept of removing pathogenic agents from the body by blood purification procedures is certainly one of the oldest therapeutic approaches in the history of medicine starting in ancient time with therapeutic bloodletting.

Traditional ways for the removal of targeted substances from the blood by means of extracorporeal devices are centrifugation, membrane permeation such as hemodialysis and hemofiltration and adsorption.

The extracorporeal centrifugation system has certain limitation to separate among macromolecule, needs appropriate and physical alteration to produce aggregates, is technical complicated and very costly.

Due to modern membrane and electronic technology dialysis and filtration are biocompatible, efficient and safe. On the other hand the membranes used in those procedures do not enable the possibility of the specific removal of substances. As an example in hemodialysis or even in hemofiltration the elimination of mostly hydrophilic and not or only weakly protein-bound substances is based on diffusive or convective transport due to semiconductive and porous properties of the membrane. Dialysis treatment started 60 years before and is now a well-established procedure for the removal of uremic toxins having a relative molecular mass below 12,000.

Plasmapheresis or continuous plasma exchange was developed with the invention of cell separators and plasma filters in the early 1970s. A large number of meanwhile published reports suggest that plasma exchange has been performed in desperate cases of almost every systemic disease. Controlled clinical studies, however, are rare, although some indications are supported by a substantial body of evidence. Plasma exchange can be very efficient in acutely removing pathogenic plasma constituents until a relative molecular mass of 2 to 2,500,000, such as autoantibodies (AAB) and circulating immune complexes (CIC), if a sufficient blood volume is processed. One has to remember, however, that clinical relevant side effects especially upon substitution with human plasma protein solutions are frequent. Although of minor relevance in cases of life threatening disease, the risk of transmission of infectious diseases has also to be taken into account.

Treatment using plasmapheresis or modified procedures in combination with adsorption based on modified microspheres is very useful for the removal of albumin bound toxins in patients with liver diseases [1-3]. So far young companies have developed successful liver support systems in order to use combined membrane-adsorption systems as successful liver support systems especially for bridging to transplantation.

The specific or even selective removal of substances of different relative molecular mass requires the use of functionalized surface either the membrane and their pores or of adsorbent particles.

Adsorption processes are based on different binding forces such as hydrophobic interaction due to van der Waal's forces, hydrogen, electrostatic or covalent binding. Nevertheless the surface area is almost of highest importance. For example, 1 µm particles in a volume of the space of 1 mm particle have a 1000 times larger surface.

But more substantial is the inner surface, which is very characteristic for substances such as activated charcoal, resins or other polymers. The total surface area can reach 2000 m^2/g. The amount of 50-100 g of particles with such a surface is enough to remove the pathological toxins e.g. bilirubin from one patient. The advantage of the smaller particle with pores in comparison with normally used 100-300 µm porous particle is the much shorter diffusion time, as demonstrated for different adsorbents and target molecules.

Especially adsorbent technologies based on functionalized surfaces using immobilized antibodies or specific peptides, spacer linked aromatic groups for he removal of IgG or even cationic groups such as DEAE (diethyl-aminoethyl) - groups for the removal of endotoxins are very efficient in case of using microparticle technology. Of course, in case of highly porous adsorbents there is no difference of the adsorption capacity comparing to the same volume of adsorbent of the given diameter. But for many substances investigated the adsorption could be reached after hours using particle in the range of 200 µm in comparison to the microparticles of 1-5 µm. Their adsorption capacity normally is reached after minutes at a given concentration.

Extracorporeal immunoadsorption (IA) is a form of plasmapheresis based on affinity chromatography [2,3] with particles sized 100 – 250 µm.
In comparison to plasma exchange, IA allows more or less selective elimination of pathogenic substances from plasma without disposal of valuable plasma proteins. The profile of adsorbed plasma constituents depends on the nature of interaction with the respective ligand. A number of systems are approved and available on the market. For instance CIC and AAB can be eliminated by columns with either tryptophan or phenylalanine immobilized to a polyvinyl ethanol gel [4]. These columns have been used successfully in the treatment of SLE patients eliminating anti-dsDNA antibodies and CIC. Considerable data from clinical queries have been also accumulated for protein A coupled to Sepharose (Immunosorba, Excorim AB, Lund, Sweden) or to silica (Prosorba, Fresenius HemoCare / Cypress Bioscence Inc., San Diego, California) [5]. The affinity of protein A columns to CIC is much higher than to single IgG molecules because of IgG cluster formation in CIC.
The removal of AAB and CIC from the circulation has been postulated as primary mechanism of action of IA. Newer clinical studies, however, show beneficial effects of IA in disorders that appear to be mainly T-cell-mediated. One might place IA into the new context of being a modulator of immune response.

The patient-specific immunoadsorber (psIA) is capable to selectively remove CIC. The adsorber filling consists of a carrier material derivatized with a protein A-purified patient plasma fraction as ligand. The individualized column appears to have binding properties selective for plasma constituents of the individual patient. The choice of a suitable carrier material, optimization of the activation method (ONB-activation; ONB: 5-norbornene-2,3-dicarboximido carbonochloridate) and immobilization of dissociated antigen/antibody-complexes on activated support were important milestones in the development of the psIA. They were underlined by studies of immune complex models like human IgG/anti-human IgG, human serum albumin/anti-human serum albumin, and human transferrin/anti-human transferrin. Analytical data from in vitro experiments carried out in parallel by FPLC and batch procedures show surprising elimination characteristics.

REFERENCES: [1]Falkenhagen D (1996) *Microspheres Based Detoxification System: A New Method in Convective Blood Purification.* Artificial Organs **20**:420-425. [2]Nose Y, Yamaji K, Sueoka A, Yamane S. (1997) Membrane apheresis technology: historical perspective and new trends toward bioincompatible systems [editorial]. Ther.Apher: 1:5-12. [3]Smith JW. (1999*) Therapeutic apheresis in the United States: current indications and directions [editorial]*. Ther. Apher. 3:1-3. [4] Higgins RM, Bevan DJ, Carey BS, Lea CK, Fallon M, Buhler R, Vaughan RW, O'Donnell PJ, Snowden SA, Bewick M, Hendry BM. (1996) *Prevention of hyperacute rejection by removal of antibodies to HLA immediately before renal transplantation.* Lancet 348:1208-11. [5]Matic G, Schütt W, Winkler R, Tiess M, Ramlow W (2000). *Extracorporeal removal of circulating immune complexes: From non-selective to patient-specific.* Blood Purification: 18:156-160.

HYPERTHERMIA AND CANCER

Kurt G. Hofer

Department of Biological Science, Florida State University, Tallahassee, Florida 32306

HISTORICAL DEVELOPMENT: The use of hyperthermia (heat) in the treatment of malignant tumors is as old as medicine itself. For example, the 5000-year old Edwin Smith Surgical Papyrus mentions heat as potential treatment for breast cancer [1]. Hippocrates, the father of medicine, proposed that surface tumors should be cauterized by application of hot iron. In modern times, more advanced methods (hot water bath, pyrogens such as mixed bacterial toxins, perfusion heating, high frequency radiation, magnetic fluid hyperthermia) were employed to heat, and hopefully destroy, tumors.

Use of hyperthermia in cancer patients is based on two different principles. Mild hyperthermia (up to 42°C) is used to stimulate the immune response for non-specific immunotherapy of cancers. Higher temperatures (around 45°C) are used with the hope of inducing regression or outright disappearance of the cancer by direct cell destruction with heat. Unfortunately, the use of hyperthermia by itself to control malignant tumors under clinical conditions has proved to be an elusive goal. In part, this was due to the difficulties encountered in delivering sufficient thermal energy to cancer cells. Whole-body heating could overcome this problem, but the temperatures required to kill cancer cells by heat alone are usually higher than can be tolerated by normal body tissues.

To overcome these limitations, attempts have been made to use hyperthermia in combination with other treatment modalities such as chemotherapy and radiation therapy [1]. This approach was based on growing knowledge about microenvironmental conditions within the tumor, in particular the fact that many tumors contain a significant fraction of hypoxic (poorly oxygenated) cells. Hypoxic cells are much more resistant to radiation than euoxic (well oxygenated) cells, so the presence of hypoxic cells in tumors may constitute a major obstacle to successful radiation therapy of cancers. For heat the situation is reversed, that is, hypoxic cells are more heat-sensitive than euoxic cells. Therefore, it seemed logical to combine these two modalities in cancer therapy.

WORK IN OUR LABORATORY: Based on the principles outlined above, we developed and tested a combination technique where hyperthermia is used in conjunction with chemical agents that enhance the radiation response of cancers [2].

We had previously shown that radiation exposures of cancer cells at temperatures of 41°C or higher resulted in strongly enhanced tumor cells death. Figure 1 shows the results of an experiment where euoxic and hypoxic BP-8 murine sarcoma cells grown in mice were irradiated at normal (37°C) or elevated (41.5°C) body temperatures. In this study, whole-body heating was performed by placing the mice in perforated plastic holders and immersing them for 1 h in a precision-controlled water bath. Hypoxic cells exhibited significantly greater heat enhancement of radiation death than euoxic cells. With euoxic cells the D_0 (the dose that reduces cell survival along the exponential part of the survival curve to 37% of the control value) was 1.8 Gy at 37°C and 1.4 Gy at 41.5°C, yielding a DMF (dose modifying factor, that is, the ratio of the two D_0 values) of 1.29. With hypoxic cells the D_0 declined from 5.2 to 3.0 Gy (DMF 1.73). The oxygen enhancement ratio (the ratio of the D_0 values for euoxic vs. hypoxic cells) was 2.89. Thus, heating at 41.5°C was effective in enhancing radiation-induced cell death in hypoxic cancer cells, but not as effective as full oxygenation.

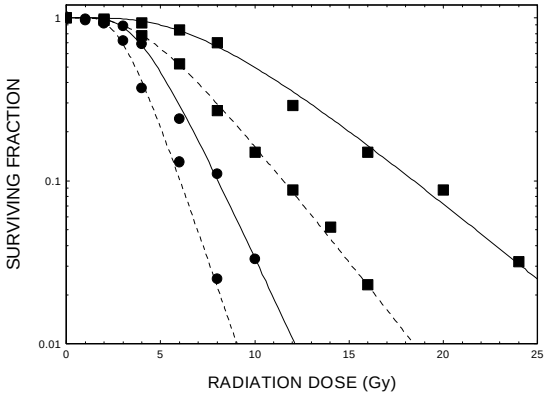

Fig. 1: X-ray response of euoxic (circles) and hypoxic (squares) BP-8 murine sarcoma cells irradiated at either 37°C (solid lines) or 41.5°C (dashed lines).

In another series of radiosensitization experiments, euoxic and hypoxic BP-8 cells were irradiated at 37°C in the presence or absence of misonidazole, a chemical radiosensitizer that mimics the action of oxygen. As illustrated in Figure 2, administration of misonidazole (0.5 mg/g body weight) had little effect on the radiation response of euoxic cells (DMF of 1.13), but did reduce the D_0 of hypoxic cells from 5.2 Gy to 2.4 Gy (DMF of 2.17).

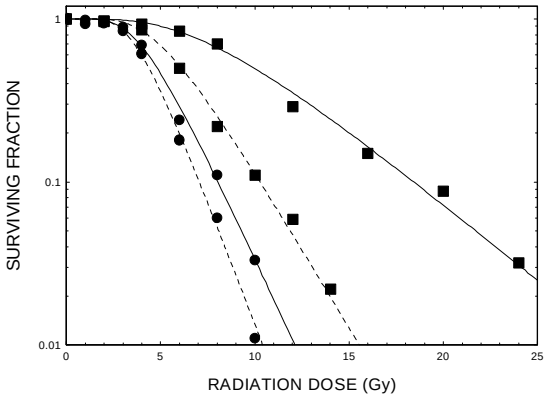

Fig. 2: X-ray response of euoxic (circles) and hypoxic (squares) BP-8 murine sarcoma cells. Solid lines show the radiation response of control groups, dashed lines the response of misonidazole groups.

From the data in Figures 1 and 2 it is apparent that heat and misonidazole are effective in potentiating radiation death in hypoxic cancer cells, but neither mode of

radiosensitization is as effective as full tumor oxygenation. However, when the two agents are used in combination with each other, they produce synergistic potentiation effects on hypoxic cells that far exceed the action of oxygen. As shown by the data in Figure 3, the D_0 of hypoxic BP-8 cells subjected to heat and misonidazole during irradiation was reduced from 5.2 Gy to 1.2 Gy (DMF of 4.33). In other words, the degree of radiosensitization by combination treatment was such that the hypoxic cancer cells actually became more radiosensitive than euoxic cells. Even euoxic cells subjected to combination therapy were not as radiosensitive as hypoxic cells irradiated in the presence of heat and misonidazole. Similar results were obtained with other tumors (Figure 4), so it would appear that synergistic radiosensitization of hypoxic cancers by combination therapy may be a general phenomenon, not a unique event observed only in BP-8 murine sarcoma [2].

However, no radiosensitizer (or combination of sensitizers) will be of any clinical value unless it can be shown that normal body tissues are not sensitized to the same extent as tumors. Lethality experiments on mice and studies on three normal body tissues (Table 1 and Figure 5) indicated that radiosensitization by combination treatment was relatively minor or completely absent in normal tissues of mice (DMF of 1.3 for skin, 1.0 for bone marrow and intestine). These results suggest that simultaneous administration of hyperthermia and oxidizing agents should be an effective adjuvant for clinical radiation therapy of cancers.

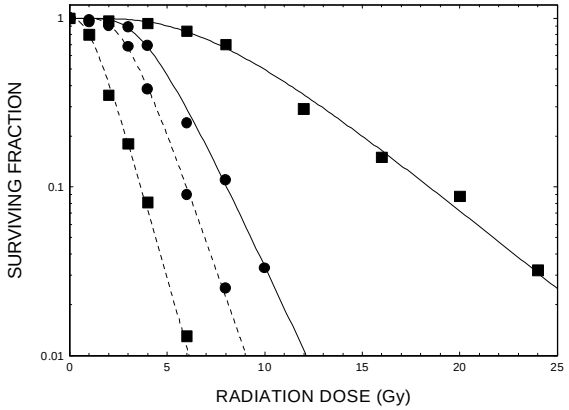

Fig. 3: X-ray response of euoxic (circles) and hypoxic (squares) BP-8 murine sarcoma cells. Solid lines show the response of control groups, dashed lines the response of euoxic and hypoxic cells subjected to heat and misonidazole.

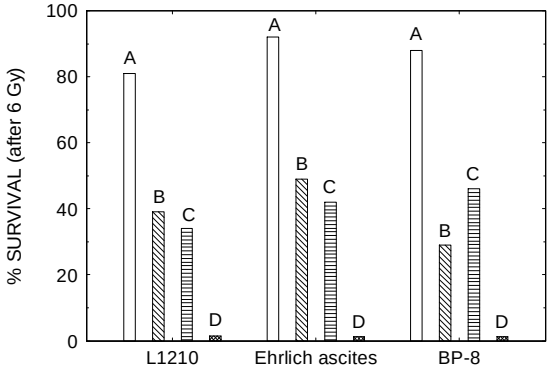

Fig. 4: Radiation response of hypoxic L1210, Ehrlich ascites and BP-8 cells after exposure to 6 Gy under the following conditions: A: 37°C, no misonidazole; B: hyperthermia (41.5°C for L1210 and Ehrlich ascites, 42°C for BP-8), no misonidazole; C: 37°C, misonidazole; D: 41.5°C, misonidazole.

CLINICAL CONSIDERATIONS: The findings reported above were subsequently confirmed by three other laboratories working on a variety of different tumor systems. Thus, there is no longer any doubt that combination therapy does in fact yield radiosensitization effects that exceed those of oxygen. The sensitization effects are selective for hypoxic cancers, that is, normal body tissues are not sensitized to the same extent.

Table 1: $LD_{50(30)}$ (lethal dose to 50% of the mice within 30 days after radiation exposure) for ICR mice irradiated at 37°C or 41.5°C in the absence or presence of misonidazole.

Treatment	$LD_{50(30)}$ (Gy)
Control (37°C, no Misonidazole)	5.6
Heat (41.5°C, no Misonidazole)	5.5
Misonidazole (0.5 mg/g, no Heat)	5.5
Heat plus Misonidazole	5.4

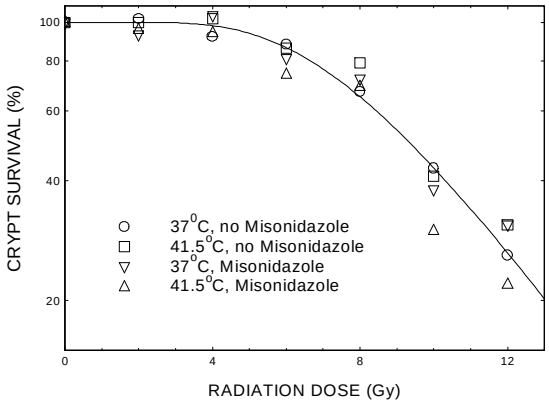

Fig. 5: Radiation response of the intestine after whole body irradiation of mice at 37°C or 41.5°C with of without misonidazole. The percent figures refer to percent survival of the intestinal crypts after radiation exposure.

In spite of enormous magnitude of the sensitization obtained in mice, at least two improvements are required before this treatment regimen can be used in clinical radiotherapy. First, we need better methods for selective tumor heating. The studies described above were performed on mice that were subjected to whole-body heating in a water bath. This is not optimal for clinical application because whole-body heating limits the heat dose that can be given to the cancer. It seems likely that the hyperthermia component of combination therapy can be significantly improved by heating tumors selectively with magnetic particles subjected to external AC magnetic fields.

A second important improvement would be the development of a more selective method of drug delivery into the tumor. Nitroimidazoles such as metronidazole and misonidazole are usually well tolerated in mice, but clinical use of these agents in human patients can result in severe peripheral neuropathy. One promising approach to deal with this obstacle is to encapsulate the radiosensitizing agents in heat-sensitive liposomes [3]. Ideally, the liposomes should also contain magnetic particles, so they can be guided to the tumor by a magnetic field. After the liposomes reach the interior of the tumor, they could be subjected to heating by an external AC magnetic field [4]. This would cause the liposomes to burst and selectively release the radiosensitizing agent in the interior of the tumor. Such a system may also facilitate selective local tumor heating. If successful, this procedure could offer an elegant method to realize the promise of combination radiosensitization in the clinical radiotherapy of cancers.

REFERENCES: [1]O.S. Nielsen, M. Horsman, and J. Overgaard (2001) *Eur J Cancer* **37**: 1587-89. [2]K.G. Hofer, A.R. MacKinnon, A.L. Schubert, et al (1981) *Radiol* **141**: 801-9. K.G. Hofer, M.G. Hofer, J. Ieracitano et al (1977) *Radiat. Res.* **70**: 362-77. K.G. Hofer, D.A. Choppin, and M.G. Hofer (1976) *Cancer* **38**: 279-87. [3]D. Needham, and M.W. Dewhirst (2001) *Adv. Drug Deliv. Reviews* **53**: 285-305. [4]A. Jordan, P. Wust, R. Scholz, et al (1997) in Scientific and Clinical Applications of Magnetic Carriers (eds. U. Häfeli, W. Schütt, J. Teller, and M. Zborowski) Plenum, New York.

EVALUATION OF FERRIFLUIDS CONTAINING PHOTOSENSITIZER

Nikolai A. Brusentsov,[1] Lubov Kh. Komissarova,[2] Anatoly A. Kuznetsov,[2] Andrey F. Mironov,[3] Alexander V. Lubeshkin,[3] Tamara G. Nikolaeva,[1] Felix S. Bayburtskiy,[4] Elena Yu. Filinova,[1] Leonid I. Shumakov,[5] Tatiana N. Brusentsova,[6] Anatoly Yu. Baryshnikov [1]

[1] Russian N.N. Blokhin Memorial Cancer Research Center RAMS, Moscow 115478, Kashyrskoyesh., 24; [2] Institute of Biochemical Physics RAS, Moscow, 117977, Kosygin 4;
[3] Lomonosov State Academy of Fine Chemical Technology Moscow, 117571, Pr. Vernadsky 86;
[4] All-Russian Research Institute of Chem. Technology, Moscow, 115320, Kashyrskoye shosse, 33;
[5] All-Russian Radiotechnical Research Institute, Moscow;
[6] Mendeleev University Chemical Technology Russia, Moscow 125047, Russia

INTRODUCTION: We have developed magnetic dextran-ferrite (DF) nanoparticles [1] and photogem (PG) [2] for tumor cell induction DF AC magnetic field hyperthermia (ACH) [3] and PG magneto- [4] and thermosensitization [5] in the dark (MTS). DF ferrifluids (DFFs), that had been prepared from DF, may be ideal magnetic carriers [1,3,6]. DF dissipates AC magnetic field energy and therefore causes hyperthermia in the area of their confinement [3]. PG in analogy to hematoporphyrin [4] may generate singlet oxygen or superoxide radicals and cause the destruction of tumor cells in the dark.

The inevitable technical problem of photodynamic therapy is the initiation of the absorbency of visible light by a tumor that has been injected with photo-sensitizing agent, because incident light at wavelengths between 600 and 1000 nm reacts with the photosensitizing agent only at shallow depth (0.1-1 cm) of tissue.

The purposes of this work were: to evaluate PG-containing dextran-ferrite ferrifluids for the combination of an ACH with MTS; to analyze the influence of AC magnetic field and hyperthermia on cell death and lysis in the presence of PG; to obtain further insights into the mechanisms of these processes.

METHODS AND MATERIALS: We have tested five water-based dextran-ferrite (DF) ferrifluids (DFFs): 12.0; 0.6; 0.2; 0.02 and 0.002%, that were prepared by a procedure modified from [6]. The sample of the initial DFF was lyophilized. DF specific saturation magnetization (*ó*) and DFF zeta-potential (ζ); specific power absorption rates (*SAR*); saturation magnetization (M_s), other physical and chemical characterizations and biological properties were determined as presented in [3,6]. The analytical fractionation of the samples of ferrimagnetic particles was performed by stepwise passage of their 1% aqueous sols through membrane filters (100 nm, 45 nm, 20 nm, XM300, XM100, XM50, UM20 – UM05u) at a nitrogen pressure of 0.1–0.3 atm on an Amicon TSF-10 thin-channel ultrafiltration system or in Model 12 and Model 202 cells, and using a column gel-filtration system. Gaussian/Nicomp and volume-weighted Gaussian distribution analysis of particles in the diluted DFFs and PG sols was performed by dynamic light scattering laser particle sizing system, Submicron Particle Sizer NICOMP™ 380/DLS (Particle Sizing Systems, Inc., Santa Barbara, Calif., USA).

PG was obtained by treatment of haemin with a 50% solution of hydrogen bromide in acetic acid followed by sequentially adding acetic acid, sodium acetate, and water. Hematoporphyrin diacetate, precipitated from solution, was filtered and treated with 0.1 M sodium hydroxide for 1 hour. PG was precipitated by acetic acid followed by filtering, washing with water, and drying in air. PG prepared as a deep-violet crystal powder represents a complex half-synthetic mixture of monomeric and oligomeric porphyrins. The solution of this substance in 0.5% sodium hydroxide and adjustment to pH 7.4 with 1 M hydrochloric acid, produced the PG sol.

For biotesting in vitro, two types of tumor cells were used: adherent human carcinoma ovarii (CaOv) and murine ascitic limpholeukosis P388 cells. The latter were obtained from tumor-bearing DBA_2 mice on the 7^{th} day after intraperitoneal transplantation of 10^6 P388 cells. The survival of CaOv and P388 cells, as a result of exposure to increased temperature and a concentration of DF alone, PG alone, histidine (His) alone, DF in combination with PG (DF+PG), PG in combination with His (PG+His) was investigated. Magneto- and thermosensitization of tumor cells by PG in the dark and heating DFFs achieved simultaneously by an AC magnetic field or by a flow thermostat. For the CaOv and P388 cell survival study, the previously used experimental setup [3] was modified. An AC magnetic field 0.88 MHz, 9.3 kA/m, 0.15 kW was achieved inside a water-cooled copper induction coil of 4.5cm radius (20 turns with turn-to-turn distance of 0.9 cm). The tumor cells (concentration 10^6 cells/ml) alone and with reagents: DF, PG, His, PG+DF, PG+His were

placed in the center of the coil and exposed for 30 min to the AC magnetic field in the dark. To 6 test tubes (TTs) containing 2 ml of fresh peritoneal ascitic limpholeukosis P388 or CaOv cells (2×10^6/ml) were added respectively: 2 ml of 12% (w/v) DFF (net γ-Fe_2O_3 weight: 60 mg); 2 ml of 0.6% DFF; 2 ml of 0.2% DFF; 2 ml of 0.02% DFF; 2 ml of 0.002% DFF; and 2 ml of 0.9% saline to the sixth as a control. The TTs then were exposed to the AC magnetic field as described above, and the selected temperature in the range of 37 to 44°C was maintained for 30 minutes (Table 1). The cell temperature was measured during the AC magnetic field treatment using an alcohol thermometer. Alternatively, the cells were exposed to the AC magnetic field in the dark in the presence of PG alone, His alone, PG+DF, and PG+His. For the control, the cells were incubated at 37°C in the laboratory thermostat. To 6 isolated TTs were added 0.1 ml of fresh P388 or CaOv cells (2×10^6/ml) and 0.1 ml of reagents as listed above (Table 3-5); in the sixth (control TT, Tables 1,2) 0.1 ml 0.9 % saline was added. The volume of reaction mixture in the TTs, containing tumor cells and reagents, was 4 ml (Table 1) and 0.2 ml (Tables 2-6); the concentration in all the TTs was 10^6 cells/ml. The temperature of the reaction mixtures from 37 to 41°C was achieved using a flow thermostat (Tables 3 and 5); from 37 to 44°C (Table 1) and from 37 to 41°C (Tables 4 and 6) was achieved by the AC magnetic field. The survival of P388 and CaOv cells as a result of the exposure to concentrations of DF, PG, His, PG+DF and PG+His at 37 to 41°C during tumor cell PG magneto- and thermosensitization (MTS) achieved by AC magnetic field in the dark was fixed. After CaOv or P388 cells exposure to AC magnetic field, DFFs, PG, PG+DF, PG+His at various conditions, the survival of the cells was analyzed by a hemocytometer counting and by intraperitoneal injection of 0.1 ml analyzed compositions of P388 cells to DBA_2 mice. The interaction of DF with the cells was investigated, taking account of the recommendations in [7]. The results represent the mean ±SD from the four independent experiments.

RESULTS AND DISCUSSION: DF appeared as dark-brown leaflets and contained about 27 % of γ-Fe_2O_3, 71 % dextran and 2% H_2O; the value of σ was 18 $A\cdot m^2/kg$, LD_{50} 5 g/kg. 12% DFF appeared as a dark-brown sol, pH 7, ζ 15 mW, M_s 1.5 kA/m, SAR 240 W/g Fe. TEM data allowed evaluation of the DF particles size: the maxima of the microcrystal and microsphere diameters were 12 and 240 nm, respectively; in a good accordance with the results of analytical fractionation and dynamic light scattering analysis of the DF particle samples and Gaussian/Nicomp and volume-weighted Gaussian distribution analysis of the particle diameter in diluted DFFs that appeared as 2 peaks at 205 and 220 nm (Fig. 1).

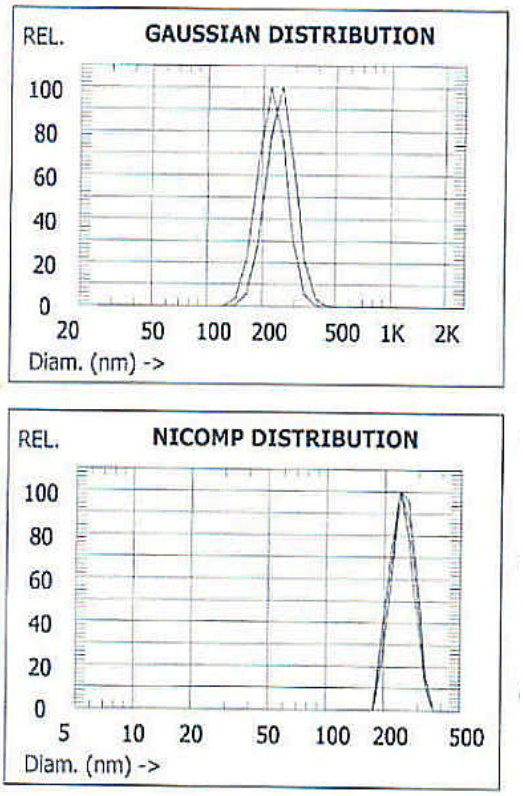

Fig. 1: Particle sizing analysis of DFF.

PG sol particle diameter distribution was in 3 peaks: peak 1 at 5 to 7 nm; peak 2 at 50 to 70 nm and peak 3 at 300 to 400 nm, and was in good accordance with PG gel-chromatography results. The obtained DFFs were resistant to gravitational forces, magnetic fields and liophylising. Determinations showed direct proportional decrease of $\dot{I}_s$ and heat production to decrease of DF concentration. Under the chosen conditions, the heating of a 0.9% NaCl solution was always below the detection limit. DFFs showed satisfactory heating to 2°C/mg Fe min. The experimental results are presented in Tables 1 and 4. No long-term toxicity or acute cell death was detected when cells were exposed to DFFs (up to 60 mg DF/ml) alone, or to AC magnetic field alone for periods of time up to 6 hours at +37°C. However, when P388 or CaOv cells were exposed to ACH at 41 to 44°C for 30 minutes in the presence of DFFs, the high hyperthermia effect was observed (Table 1).

Table 1. Influence of DF on CaOv cells during 30 min of AC magnetic field exposure.

Test tubes	Surviv. cells, %	Dead cells, %	DF, mg/ml	T, °C
1	0.0	100±6	60.0	43-44
2	4±0.8	96±5.8	6.0	42-43
3	48±3.4	52±3.6	1.00	41-42
4	91±5.5	9±1.4	0.10	39-40
5	95±5.8	5±1.0	0.01	37-38
6	96±5.8	4±0.8	0.00	37

Table 1 shows: the temperatures in TTs 1-6 were proportional to DF concentration. The cell death fractions were proportional to DF concentration: the cell survival fractions at 37 to 41°Ñ were high, at 42 to 43°Ñ were insignificant, and at 43-44°Ñ were absent.

Table 2. Influence of PG on CaOv cells during 30 min of AC magnetic field exposure at 37°Ñ.

T. T.	Surviv. cells, %	Dead cells,%	Cell lysis, %	PG (µg/ml)
1	0.0	0.0	100±6	325.00
2	9.5±1.5	60±4.0	30.5±2.5	32.50
3	54±3.7	28±2.5	18±1.9	3.25
4	87.3±5.5	5.7±1.0	7.0±1.3	0.65
5	91±5.5	5±1.0	4±0.8	0.06
6	95±5.8	4±0.8	1±0.1	0.00

Table 2 shows PG cytotoxicity obtained by magnetosensitization at 37°C for 30 minutes: the cell lysis and death rate fractions at the low PG concentrations were surprisingly high.

Table 3. Influence of PG on CaOv cells during 30 min exposure in the flow thermostat at 37°Ñ (TTs 1-3) and at 41°Ñ (TTs 4-6).

T. T.	Surviv. cells,%	Dead cells, %	Cell lysis, %	PG, (µg/ml)
1	3±0.6	6±1.1	91±5.5	325
2	29±2.5	50±3.5	21±2.0	32.5
3	66±4.3	16±1.8	18±2.4	3.25
4	10±1.5	55±3.8	35±2.8	32.5
5	38±2.9	39±3.0	23±2.2	3.25
6	82±5.1	14±1.7	4±0.8	0.32

Table 3 shows of PG cytotoxicity obtained as a result of CaOv cell thermosensitization at 41°C for a 30 minute period. The cell lysis and death fractions were proportional to PG concentration and increased with increasing temperature. The cell survival fractions at 37°Ñ, PG concentration 325 µg/ml, and at 41°Ñ, PG concentration 32.5 µg/ml, were insignificant.

Table 4. Influence of DF and PG on CaOv cells during 30 min of AC magnetic field exposure at 41 to 43°Ñ (TTs 1-3) and at 37°Ñ (TTs 4-6).

T. T.	Surv. cells (%)	Dead cells (%)	Cells lysis (%)	DF, mg/ml	PG, (µg/ml)
1	0	91±5.5	9±1.4	9.0	0.80
2	0	88±5.4	12±1.6	6.0	1.60
3	3±1	52±3.6	45±3.3	3.0	32.50
4	20±2	45±3.3	35±2.8	0.10	3.25
5	10±1	50±3.5	40±3.0	0.01	32.50
6	0.0	0.00	100±6	0.001	325.0

Table 4 shows PG+DF cytotoxicity that were obtained at 41 to 43°C and at 37°C for a 30 minute period; the cell lysis and death fractions were proportional to the concentrations of PG and DF. As the result of combination ACH with MTS at the moderate concentrations of PG (0.8-32.5 µg/ml) and the high concentrations of DF (3-9 mg/ml) the cell survival fraction was absent; at the moderate PG concentrations (3.25-32.5 µg/ml) and the low DF concentrations (0.001-0.1 mg/ml) the cell survival fractions were average; at the high PG concentration (325 µg/ml) and the low DF concentration the cell survival fraction was absent.

Table 5. Influence of PG on P388 cells during 30 min flow thermostat exposure at +41°Ñ (test tubes 1-3) and at +37°Ñ (test tubes 4-6).

T. T.	Surviv. cells, %	Dead cells, %	Cells lysis, %	PG (µg/ml)
1	9±1.4	54±3.7	37±2.9	32.5
2	39±3.0	36±2.8	25±2.3	3.25
3	70±4.5	18±1.9	12±1.6	0.325
4	29±2.5	40±3.0	31±2.5	32.50
5	88±5.4	8±1.2	4±0.8	3.25
6	91±5.5	5±1.0	4±0.8	0.325

Table 5 shows PG cytotoxicity that was obtained by the incubation of P388 cells at 41°Ñ and 37°Ñ for a 30 minutes period, the cell lysis and death fractions were proportional to the concentrations of PG and temperature. As a result of hyperthermia at 41°Ñ for 30 minutes with PG thermosensitization of P388 cells at concentrations of PG (0.325-32.5 µg/ml) the cell survival fractions were proportional to the concentrations of PG; at 37°Ñ and the same PG concentrations the cell survival fractions were three times as high.

Table 6. Influence of PG and His on P388 cells during 30 min of AC magnetic field exposure at 37°C (test tubes 1-3) and at 41°Ñ (test tubes 4-6).

T. T.	Surv. Cells, %	Dead cells, %	Cells lysis, %	PG, µg/ml	His, mg/ml
1	94±5.7	6±1.2	0.00	0.00	1.6
2	9±1.4	51±3.5	40±3.0	32.5	0.0
3	77±4.9	12±1.6	11±1.5	32.5	1.6
4	84±5.2	16±1.8	0.00	0.00	1.6
5	3±0.6	51±3.5	46±3.3	32.5	0.0
6	63±4.2	20±2	17±1.8	32.5	1.6

Table 6 shows that substantial inhibition of cell lysis and death by PG in the presence of 1.6 mg/ml His was observed. AC magnetic field cell damage enhancement by PG at 37°Ñ (TT 2) and simultaneous thermal- and AC magnetic field cell damage enhancements by PG at 41°Ñ (TT 5) was effectively suppressed by the addition of singlet oxygen scavenger, His (TTs 3,6).

We investigated the role of: DF, PG, His, PG+DF, PG+His alone; hyperthermia, AC magnetic field induction, DF AC magnetic field hyperthermia (ACH) alone; PG magneto- and thermo-sensitization in the dark (MTS) to increase the destruction of tumor cells. Two types of tumor cells: adherent human carcinoma ovarii (CaOv) and murine ascitic limpholeukosis P388 cells were incubated in the presence or absence of the enumerated reagents and physical factors. The cells were successively heated at 41 to 44°Ñ by AC magnetic field treatment with the 0.88 MHz, 9.3 kA/m, 0.15 kW induction coil. The combined effects of ACH and MTS were then examined and tested for statistical significance. Significant differences between cytotoxic effects produced by ACH, MTS and the combination of ACH with MTS were found. PG at nontoxic doses at 37°Ñ significantly enhanced magneto- and thermal tumor cell damage at 41°Ñ and above in a dose-dependent manner. Magneto- and thermal cell damage enhancement by PG was effectively suppressed by the addition of His, singlet oxygen and a superoxide scavenger. In the presence of PG+His non-toxic doses, the cell survival fractions were proportional to the temperature. Significant differences between cytotoxic effects produced by PG at 37°Ñ and 41°Ñ at the same concentrations of PG were found. Therefore the cytotoxicity of ACH should be attributed to the effects of heat itself. Combination of PG with DF have potential as a magneto- and thermosensitizer because of the following advantages: their dose-dependent enhancement of magneto- and thermal cell damage; lack of toxicity at physiological parameters, AC magnetic field (frequency, induction, strength, power and temperature), and at the non-toxic doses of PG+DF required for tumor cell magneto- and thermosensitization. Combination of ACH with MTS is the summary method. These data confirm the feasibility of using induction DF AC magnetic field hyperthermia in combination with tumor cell PG magneto- and thermosensitization. The advantage of this method is the much deeper penetration of the magnetic field into body tissues as compared to light. Further in vitro and in vivo investigations allow choosing of the PG+DF optimal doses and AC magnetic field range intensity and continuity.

CONCLUSIONS: Dissolution of dextran-ferrite in water results in formation of dextran-ferrite ferrifluids useful for the magnetically controlled combination of AC magnetic field induced hyperthermia with photogem magneto- and thermosensitization of tumor cells. The mechanism of ferrimagnetic heating most likely involves the magnetization relaxation loss process, and tumor cells photogem magneto- and thermosensitization most likely involves free-radical processes with a key role of superoxide radical.

REFERENCES: [1]A.I. Autenshlyus, N.A. Brusentsov, A. Lockshin (1993) *J. Magn. and Magn. Mater.* **122**:360-363. [2]A.F.Mironov, A.N. Nizhnik, A.Yu. Nockel (1990) *J. Photochem. Photobiol.* **4**:297-306. [3]N.A. Brusentsov, V.V. Gogosov, T.N. Brusentsova, A.V. Sergeev, N.Y. Jurchenko, A.A. Kuznetsov, O.A. Kuznetsov, L.I. Shumakov (2001*) J. Magn. and Magn. Mater.* **225**:113-117. [4]M. Babincova, D. Leszczynska, P. Sourivong, P. Babinec (2001) *J. Magn. and Magn. Mater*. **225**:194-196. [5]A. Saito, R. Tanaka, H. Takahashi, K. Kakimura (1998) Int. J. Hyperthermia **14**:503-511. [6]O.A. Kuznetsov, N.A. Brusentsov, A.A. Kuznetsov. N.Y. Jurchenko, N.E. Osipov, F.S. Bayburtskiy (1999*) J. Magn. and Magn. Mater.* **194**:83-89. [7]U.O. Häfeli, G.J. Pauer (1999) *J. Magn. and Magn. Mater*. **194**:76-82.

A SYSTEM FOR THE TREATMENT OF LIVER CANCER BY TARGETED HYPERTHERMIA USING MAGNETIC MICROSPHERES

S. K. Jones[1] P. Moroz[2] and B. N. Gray[1]

[1]*Sirtex Medical Ltd, North Ryde, NSW 1670, Australia,*
[2]*University of Western Australia, Crawley, WA 6009, Australia*

ABSTRACT: Sirtex Medical Limited is developing new technology to treat liver cancer by induced hyperthermia using magnetic microspheres. Eighty to ninety percent of patients presenting with primary or secondary liver cancer have inoperable disease and a poor prognosis [1-4]. The median survival for patients with non-resectable hepatocellular carcinoma is three to six months [5,6], and six to 12 months for patients with non-resectable hepatic colorectal metastases [7]. These patients must rely largely on various forms of chemotherapy, radiotherapy and other local or novel treatments. Although these treatments have at times shown promising response rates and symptom palliation and have occasionally down staged hepatic tumours to allow surgical resection, they have not improved five year survival rates which remain in the order of less than 1% [8]. The persisting poor survival among the vast majority of patients with hepatic malignancies has stimulated interest in the development of other treatment options, such as targeted hyperthermia.

In current clinical practice, hyperthermia therapy is mostly used as an adjunct to radiotherapy in the treatment of superficial and other easily accessible tumour sites. Restrictions to the wider application of hyperthermia to the treatment of tumours located at deep body sites are technological in nature. There are presently no reliable non-invasive techniques that can be used to deliver an adequate heat dose to a localized tumour in a deep body organ such as the liver without risking unacceptable heating of overlying and surrounding normal tissue.

The Sirtex technology uses the heat generated in small magnetic microspheres when exposed to a high frequency magnetic field to heat these tumours. It is well known that macroscopic liver tumours derive virtually all their blood supply from the hepatic artery, while normal liver tissue is predominantly supplied by the portal venous system [9]. Hence, an infusion of the magnetic microspheres through the hepatic artery results in embolisation of the tumour vasculature with an enhanced concentration of microspheres around any tumours in the liver. This concentration differential ensures only the diseased tissue is heated once the high frequency magnetic field is applied.

We have used a rabbit model of liver cancer to investigate different aspects of this new system, including the successful demonstration of tumour heating to therapeutic temperatures with minimal heating of the surrounding parenchyma and the consequent collapse of tumour growth [10]. Analysis of the distribution of the magnetic material shows a clear concentration around the edge of the tumour and this is reflected in the measured heating patterns which show the tumour core temperature generally lagging behind that of the tumour rim. This is in direct contrast to the situation in conventional hyperthermia where it is often much easier to heat the necrotic core of a tumour with energy deposition from an external beam (e.g. microwave or ultrasound) than it is the highly vascular tumour rim which can be left with a sub-therapeutic thermal dose. Further analysis to compare the heating rate achieved in large and small tumours with the same average concentration of magnetic material showed that it is relatively easier to heat larger tumours compared to smaller ones using the arterial microsphere technique [11].

In another recently published study [12] we have compared the therapeutic efficacy of tumour heating via arterially infused microspheres against heating from magnetic material directly injected into the tumour milieu. Despite the generally inferior heating from the arterial microspheres, the therapeutic effect was clearly superior to the direct injection result.

These results highlight several unique advantages that this new form of hyperthermia may offer compared to more conventional methodologies. This paper reviews this research and discussed its implications for future clinical application of the technology.

REFERENCES: [1]H.M. Hoogewoud (1993) *Hepatocellular Carcinoma and Liver Metastases: Diagnosis and Treatment*, Springer Verlag. [2]S. Cascinu S, V. Catalano, A.M. Baldelli, et al (1998) *Cancer Treatment Reviews* **24**: 3-14. [3]L. Ellis, J. Chase, Y. Patt, et al (1998) *Hepatic arterial infusion chemotherapy for colorectal cancer metastasis to the liver* in Liver Cancer (ed S. Curley) Springer Verlag, pp 150-172. [4]J. Sitzmann and R. Abrams (1993) *Annals of Surgery* **217**: 149-154. [5]K. Lewin, M.A. Burton, B.N. Gray and G. Self (1987) *Europ J Cancer Clin Oncol* **23**: 37-41. [6]G. Rosenbusch, N. Smits and J. Reeders (1989) *Ultrasonography in hepatobiliary and pancreatic malignancies* in Hepatobiliary and Pancreatic Malignancies, Diagnosis, Medical and Surgical Management (eds N. Lygidakis and G. Tygat). Thieme Medical Publishers Inc, pp 51-65. [7]Y. Fong, J. Fortner, R.L. Sun, et al (1999) *Annals of Surgery* **230**: 309-321. [8]J.S. Wagner, M.A. Adson, J.A. van Heerden, et al (1994) *Annals of Surgery* **199**: 502-508. [9]C. Breedis and G. Young (1954) *American J Pathology* **30**: 969-977. [10]S.K. Jones, J.G. Winter and B.N. Gray (2002) *Int J Hyperthermia*, In Press. [11]P. Moroz, S.K. Jones and B.N. Gray (2002) *Int J Hyperthermia*, In Press. [12]P. Moroz, S.K. Jones and B.N. Gray (2002) *J Surg Oncol*, In Press.

"SMART" MEDIATORS FOR SELF-CONTROLLED INDUCTIVE HEATING

A.A. Kuznetsov[1], O.A. Shlyakhtin[2], N.A. Brusentsov[3], O.A. Kuznetsov[1,4].

[1]Institute of Biochemical Physics, Russian Academy of Sciences, 117977 Moscow, Russia; [2]Chemistry Dept., Moscow State University, 119899 Moscow, Russia; [3]Blokhin Oncological Research Center RAMS, 115478, Moscow, Russia; [4]University of Louisiana at Lafayette, LA 70504-2451, USA

INTRODUCTION: Hyperthermia is a rapidly developing technique in cancer therapy. It takes advantage of the higher sensitivity of tumor tissue to heat and typically involves heating of the affected organ to 43 – 45 °C. Magnetic fluid hyperthermia [1] attracts increasing attention, since it allows minimizing side effects by the localized heating of only desired parts of the organism, including tumors located deep inside the patient's body. The method involves introduction of ferromagnetic particles (mediators) into the desired part of the organism and heating them with an alternating electromagnetic field of radio-frequency range (***RF***). Magnetic fluids based on nanocrystalline Fe_3O_4, stabilized by biocompatible surfactants [2-6], are typically used as mediators. Unfortunately, it is impossible to control the local temperature near the mediator particles, possibly causing local overheating and necrosis of normal tissue. This problem could be solved with ferromagnetic particles of high ***RF*** absorption and a Curie temperature (T_c) of ca. 42 - 45 °C. Thus, local temperature control can be ensured even with a nonuniform distribution of mediator particles throughout the tissue, variable ***RF*** intensity and uneven dissipation of the evolving heat. If T_c of this material can be purposefully varied, mediators could be adapted to the particular medical application.

Similar approach is used in cancer thermal therapies, which utilize implantable "thermoseeds" with a particular Curie temperature [7,8]. These macroscopically sized solid units are surgically inserted in the affected organ and are heated by an external ***RF***. The T_c of the "thermoseed" determines the temperature of the heating. Significant limitations of these methods are the necessity of a stressful surgical intervention and a relatively small volume around each "thermoseed" which can be effectively heated. The reduction of size of the heat-producing elements so that they can be delivered as a suspension via catheter into the bloodstream of the tumor and spread throughout its capillaries, is the obvious solution of these problems. Sato et al [9,10] reported using 50 μm flakes of an amorphous ferromagnetic metal alloy with T_c of ca. 45 °C for intratissue hyperthermia in dogs. However, these relatively large electrically conducting particles are heated in an ***RF*** field by eddy currents even above T_c and do not penetrate into small capillaries. Numerous studies [1-6,12,13] have shown that submicron-sized non-conducting particles are most effective for hyperthermia. The goal of this work was to produce biologically compatible, electrically non-conductive nanoparticles with T_c in the range of 40-50°C.

Individual ferromagnetic substances with T_c in this range do not exist, but by combining several elements and by varying the composition of the mixture it is possible to produce alloys, amorphous structures, ferrites and other multi-component systems consisting of metals and metalloids. We used several synthesis techniques to produce a variety of ultradisperse particles with suitable T_c and tested their behavior in an ***RF*** field.

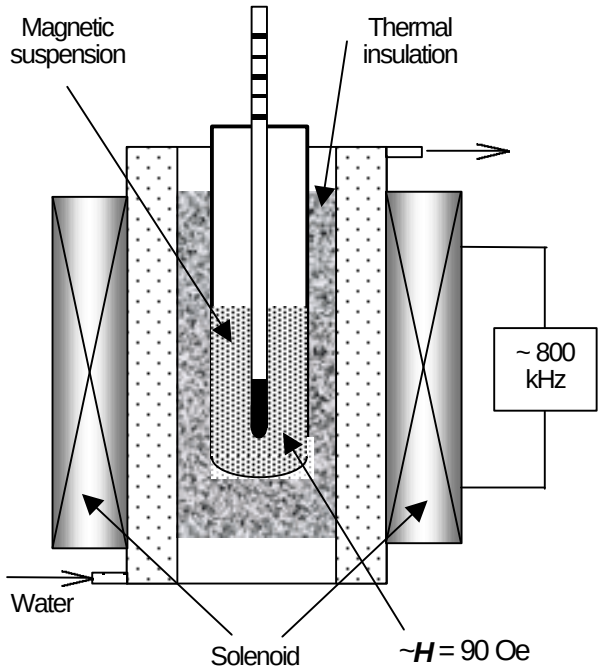

Fig.1: Scheme of the experimental setup.

MATERIALS AND METHODS: In order to study their ***RF*** absorption rate, fine powders of $ZnFe_2O_4$ (T_c = 100 - 102°C), $La_{0.8}Sr_{0.2}MnO_3$ (T_c = 48°C) and $La_{0.75}Sr_{0.25}MnO_3$ (T_c = 56°C) have been prepared by the freeze-drying synthesis technique [11]. During absorption studies 0.5 g of each powder has been ultrasonically dispersed in 3 ml of water and placed in a glass test tube inside an air-cooled inductor (inner diameter 60 mm; length 200 mm) with a matching high-Q-resonator fed with ***RF*** power [12](Fig. 1). To avoid ***RF*** absorption by metal parts, the temperature of the fluid was monitored with an alcohol thermometer. A sample of magnetic fluid containing dextran-coated nanocrystalline Fe_3O_4 [4,12] was used for comparison. Previous studies have confirmed the absence of ***RF*** absorption in this frequency range by water or by components of the measuring cell [12].

RESULTS AND DISCUSSION: Experimental heating curves are presented in Fig.2. Fe_3O_4 - based magnetic fluid demonstrates a fast, almost linear heating rate, close to that shown in [13], without any significant decrease in the tested experimental conditions. ***RF*** irradiation of the $ZnFe_2O_4$ suspension leads to significant, but less intense heating with no obvious temperature limit over the time of the experiment. This curve, taking into account the lower absorption rate of $ZnFe_2O_4$, is also similar to those of typical magnetic ferrofluids [13]. Both samples of La-Sr manganite powders demonstrate intense heating during the initial stages of the process, followed by temperature stabilization at 46.3°C and 37.8°C, respectively. These temperatures correspond rather well with the T_c of the samples. The observed difference between T_c and the temperatures of ***RF*** absorption termination can be attributed to the sharp decrease of saturation magnetization M - usual for ferromagnetics in the vicinity of T_c and predicted by ferromagnetic exchange theory - and to the heat exchange balance. These results create many prospective applications of magnetic particles with predetermined T_c for heating of biological tissues and other objects to the optimum temperature using the demonstrated parametric feedback.

Absorption of ***RF*** by ferromagnetic particles of various diameters is known to involve several physical mechanisms, including different types of remagnetization processes [5]. Usually ***RF*** absorption strongly depends on the crystallite size. Absorption rates of superparamagnetic nanoparticles are usually much higher than those of multi-domain crystallites, mostly due to Neel's losses. Powders produced by freeze-drying, are usually substantially agglomerated [14]. Intense milling of $La_{0.75}Sr_{0.25}MnO_3$ powders in a high-energy planetary ball mill resulted in a decrease of average aggregate size from 2 to 0.15-0.2 microns, as measured by light scattering. This is close to the average crystallite size observed by SEM (0.1-0.2 microns, Fig. 3). Meanwhile, this treatment did not affect the ***RF*** absorption rate of this powder, with the heating curve being practically the same as that of the initial sample (data not shown). Since the observed size of crystallites even after milling is still much larger than the typical size of superparamagnetic particles, the most probable dominating absorption mechanism for these powders is scattering by displacement of magnetic domain walls. However, ***RF*** absorption rates of polycrystalline manganites are anomalously high compared to those of Fe_3O_4 polycrystals.

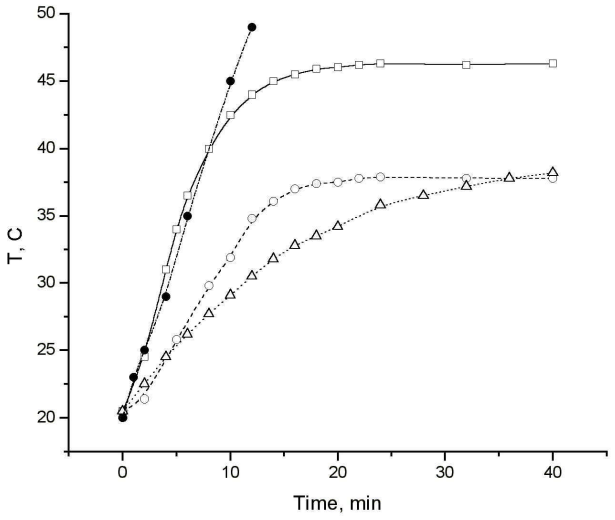

Fig. 2: Time course of the temperature inside the measuring cell during RF (800 kHz) heating using the following mediators: • Dextran-coated Fe_3O_4 (commercially available); □ $La_{0.75}Sr_{0.25}MnO_3$; ❍ $La_{0.8}Sr_{0.2}MnO_3$; Ä $ZnFe_2O_4$..

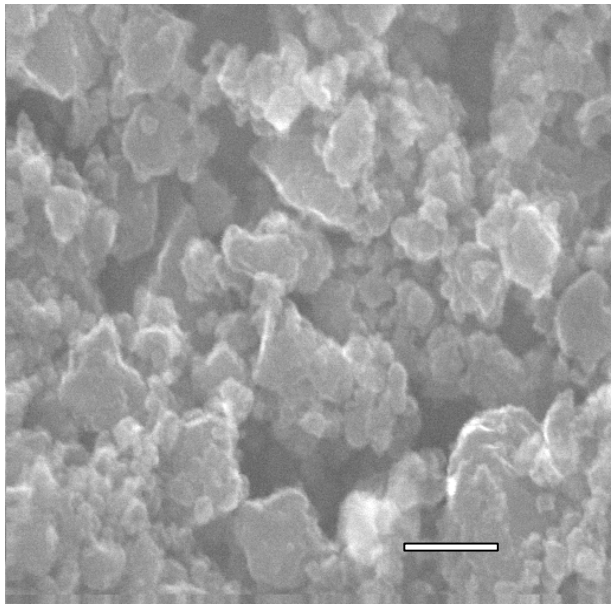

Fig.3: SEM micrograph of $La_{0.75}Sr_{0.25}MnO_3$ powder after milling. The bar is 500 nm.

From our results we can conclude, that powders of La-Sr manganites make it possible to heat a sample by ***RF*** to the necessary temperature without exceeding it. Further heating will be automatically switched off at T_{lim}, which is closely related to T_c. T_c of La-Sr manganites strongly depends on the content of Me in $La_{1-x}Me_xMnO_3$ (where Me = Sr, Ba, Pb, Ag, Na). By varying the composition of the manganite it is possible to create materials with T_c ranging from 20 to 90°C [15]. Thus, ***RF*** heating to any desired temperature in this range without overheating can be achieved without any external temperature control. Application of $ZnFe_2O_4$ for these purposes is less attractive due to severe dependence of T_c on the metastable, poorly reproducible cation distribution between sub-lattices of the spinel structure, and a lower absorption rate, while no advantages over existing Fe_3O_4-based ferrofluids were observed. The prospects of a direct manganites application in ***RF*** hyperthermia of tumors will depend on the results of the ongoing medical compatibility studies.

We have proven that the freeze-drying synthesis technique permits the production of ultradisperse particles with the predetermined composition and Tc. The particles have a high absorption rate at lower temperature and abruptly stop absorbing RF energy at a particular temperature, preventing further heating of the sample. We continue searching for more biologically compatible nanoparticles for self-regulating hyperthermia.

The proposed ***RF*** heating with parametric feedback can be useful not only in medicine, but also in solving technological problems, e.g., for precise localized temperature control in chemical and biochemical reactors. Coating of finely dispersed magnetic particles with a catalyst (including enzymes) combined with RF heating could ensure constant temperature at the reaction zone even in intense mass flows and strongly varying heat supply.

REFERENCES: [1]A. Jordan, R. Scholz, P. Wust, H. Faehling & R. Felix (1999) Magnetic fluid hyperthermia (MFH): Cancer treatment with AC magnetic field induced excitation of biocompatible superparamagnetic nanoparticles. *J. Magn.*

Magn. Mater. **201**: 413-419. [2]R.K. Gilchrist, *et al* (1957) Selective inductive heating of lymph nodes. *Ann. Surgery* **146**: 596-606. [3]M. Shinkai, *et al* (1999) Intracellular hyperthermia for cancer using magnetic cationic liposomes. *J. Magn. Magn. Mater*. **194**: 176-184. [4]O.A. Kuznetsov, *et al* (1999) Correlation of the coagulation rates and toxicity of biocompatible ferromagnetic microparticles. *J. Magn. Magn. Mater*. **194**: 83-89. [5]R. Hergt, *et al* (1998) Physical Limits of Hyperthermia Using Magnetite Fine Particles. *IEEE Trans. Magnetics* **34**: 3745-3754. [6]D.C.F. Chan, D.B. Kirpotin & P.A. Bunn (1997) in Sci. Clin. Appl. Magn. Carriers, Proc.1st Int. Conf., Plenum, New York, pp 607-618. [7]J.A. Paulus, *et al* (1997) Thermal ablation of canine prostate using interstitual temperature self-regulating seeds: new treatment for prostate cancer. *J. Endourology* **11**: 295-300. [8]T.C Cetas, E.J. Gross & Y. Contractor (1998) A ferrite core metallic sheath thermoseed for interstitial thermal therapies. *IEEE Trans. Biomed. Engineering* **45**: 68-77. [9]T. Sato, *et al* (1993) The development of anticancer agent releasing microcapsule made of ferromagnetic amorphous flakes for intratissue hyperthermia. *IEEE Trans. Magnetics* **29**: 3325-3330. [10]H. Matsuki, *et al* (1994) Temperature sensitive amorphous magnetic flakes for intratissue hyperthermia. *Mater. Sci. & Engineering A* **182**: 1366-1368. [11]O.A. Shlyakhtin, Y.J. Oh & Yu.D. Tretyakov. (2000) Preparation of dense $La_{0.7}Ca_{0.3}MnO_3$ ceramics from freeze-dried precursors. *J. Eur. Ceram. Soc.* **20**: 2047-2054. [12]N.A. Brusentsov, *et al* (2001) Evaluation of ferromagnetic fluids and suspensions for the site-specific radiofrequency-induced hyperthermia of MX11 sarcoma cells in vitro. *J. Magn. Magn. Mater*. **225**: 113-117. [13]R. Hiergeist, *et al* (1999) Application of magnetic ferrofluids for hyperthermia. *J. Magn. Magn. Mater*. **201**: 420-422. [14]Yu.D. Tretyakov, N.N. Oleynikov & O.A. Shlyakhtin (1997) *Cryochemical Technology of Advanced Materials*, Chapman&Hall, London. [15]C.N.R. Rao, R. Mahesh, A.K. Raychaudhuri, R. Mahendiran (1998) Giant magnetoresistance, charge ordering and other novel properties of perovskite managanates. *J.Phys.Chem Solids* **59**: 487-502.

NOVEL THERMO-RESPONSIVE MAGNETIC NANOPARTICLES

Hirotaka Furukawa[1*], Noriyuki Ohnishi[1], Kazunori Kataoka[2] and Akihiko Kondo[3**]

[1]Chisso Corporation Yokohama Research Center, 5-1 Ookawa, Kanazawa-ku, Yokohama, 236-8605, Japan; [2]Department of Materials Science, Graduate School of Engineering, The University of Tokyo, 7-3-1 Hongo, Bunkyo-ku, Tokyo 113-8656, Japan; [3]Department of Chemical Science and Engineering, Faculty of Engineering, Kobe University, 1-1 Rokkodaicho, Nada-ku, Kobe, 657-8501, Japan

INTRODUCTION: Magnetic support materials have been widely used in the field of biotechnology such as bioseparations, immunoassay, immobilization of enzymes and drug carriers. Previously, we have reported on thermo-responsive magnetic nanoparticles showing lower critical solution temperature (LCST), which could be flocculated and separated quickly from solution under magnetic field by elevating the temperature [1,2]. However, for the separation of unstable proteins, high temperature should be avoided. Recently, we have developed novel thermo-responsive copolymers showing upper critical solution temperature (UCST). They were synthesized by copolymerizing *N*-substituted acrylamide such as acrylamide or methacrylamide and *N*-acetylacrylamide or *N*-formylacrylamide, respectively [3]. In this report, we describe novel thermo-responsive magnetic nanoparticles and their applications.

METHODS: In our UCST polymer, we have chosen the copolymer composed of *N*-acryloylglycineamide and biotin monomer because biotin is useful for various biological experiments. The biotin monomer was synthesized as shown in Figure 1.

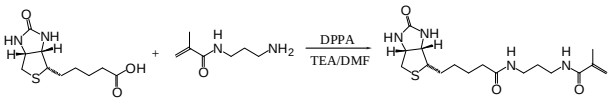

Fig. 1: Synthesis procedure for biotin monomer.

Monomers were copolymerized in the presence of magnetic nanoparticles to prepare thermo-responsive magnetic nanoparticles.

RESULTS AND DISCUSSION: The thermo-responsive magnetic nanoparticles coated by UCST copolymer show the same properties as the copolymer. The particles were dispersed in water at higher temperature than the UCST. On cooling the solution below UCST, the particles were aggregated and collected quickly by the magnet (Figure 2).

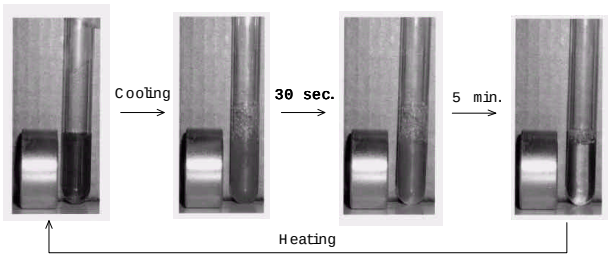

Fig. 2 : Response of modified magnetic nanoparticles to a magnetic field after lowering the temperature below the UCST.

The particles modified by biotin bound avidin in egg white solutions and could easily be separated with a magnetic field after lowering the temperature (Figure 3).

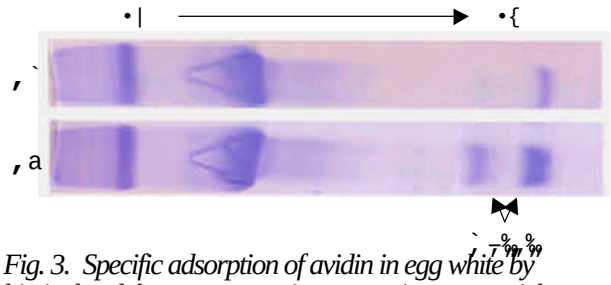

Fig. 3. Specific adsorption of avidin in egg white by biotinylated thermo-responsive magnetic nanoparticles. Lane A: Supernatant after flocculation and collection of particles. Lane B: Egg white solution before addition of particles.

Our results suggest that the magnetic nanoparticles provide various applications employing the avidin-biotin binding system. We are going to report methods of adding new functions to the particles and their applications in enzyme immobilization and cell separations.

REFERENCES: [1] Kondo et al (1994) *Appl. Microbiol. Biotechnol.*, **41**:99-105. [2]Kondo et al (1997) *J. Ferment. Bioeng.*, **84**:337-341. [3]Ohnishi et al. (2002) in press.

MAGNETOFECTION: ENHANCING AND TARGETING GENE DELIVERY BY MAGNETIC FORCE

C. Plank [1], F. Scherer[1], U. Schillinger [1], M. Anton [1], & C. Bergemann [2]

[1] *Technische Universität München, D-81675 Munich,* [2] *Chemicell, D-10777 Berlin, Germany*

INTRODUCTION: The true benefits of gene therapy are only realized if the limitations posed by insufficient gene transfer efficacy and specificity can be overcome. Moreover, assigning function to the recently decoded primary sequences of vertebrate genomes affords rapid and highly efficient gene transfer techniques *in vitro* amenable to high throughput automation. The objectives of this study were to exploit the attractive forces of magnetic gradient fields on superparamagnetic particles to potentiate the efficacies, improve the kinetics and dose response profiles of gene transfer processes, and target gene delivery with applied magnetic fields. Similar approaches have been described previously in magnetic targeting of classic drugs and have been used with some success in the treatment of cancer patients [1-2].

METHODS: Superparamagnetic iron oxide nanoparticles were manufactured with polyelectrolyte surface coatings to allow their association with gene vectors by salt-induced colloid aggregation. State-of-the-art gene vectors were associated with these particles by simple mixing in salt-containing buffers. Association was evaluated by dynamic light scattering, zeta potential measurements and electron microscopy, and was quantified with radioactively labeled components. Magnetic devices with neodymium-iron-boron (NdFeB) permanent magnets (remanence Br = 1080 - 1150 mT) matched the dimensions of cell culture dishes, under which the magnets were placed for *in vitro* gene delivery. For *in vivo* gene delivery, rectangular-shaped NdFeB magnets were positioned in direct contact with the target tissue of gene transfer, such as blood vessels, the intestine or the stomach followed by luminal injection of superparamagnetic gene vectors.

RESULTS: Synthetic and viral gene vectors associated quantitatively with polyelectrolyte-coated superparamagnetic nanoparticles by salt-induced aggregation. The magnetic gradient fields of the devices constructed for cell culture experiments were sufficient to sediment superparamagnetic gene vectors on target cells quantitatively within a few minutes. As a consequence, the required process times of gene transfer decreased from hours to minutes (Fig. 1, left). Also, the dose-response profiles were greatly improved (Fig. 1, right), and gene transfer efficiencies were raised up to 5 orders of magnitude.

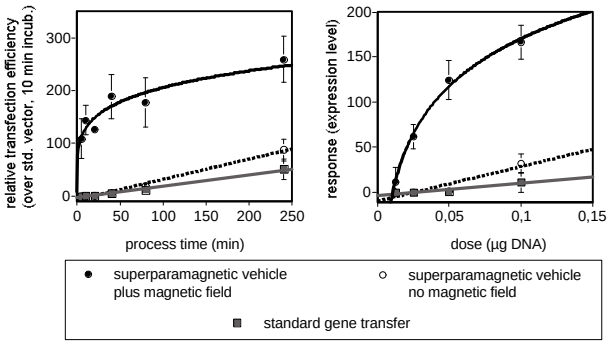

Fig. 1: The transfection reagents GenePorter (left) and Lipofectamine (right) were incubated with plasmid DNA (squares) containing the luciferase gene as reporter according to the instructions of the manufacturers or with plasmid DNA previously mixed with polyethylenimine-coated superparamagnetic iron oxide nanoparticles (circles). NIH3T3 mouse fibroblasts were incubated with these preparations in the presence (filled circles) or the absence of a magnetic field for the specified durations (left) or with serial dilutions of these preparations for 15 min (right). Reporter gene expression was determined after 24 hrs by measuring the luminescence arising upon substrate (luciferin) addition to cell extracts.

Notably, gene transfer was confined ("targeted") to an area defined by the shape of the magnetic fields of the applied magnetic devices (Fig. 2). This held true for any gene transfer technique examined (viral and nonviral). Gene delivery even to otherwise non-permissive cells and tissues was achieved. Most importantly, magnetic field-guided local transfection *in vivo* in the gastrointestinal tract and in blood vessels was feasible. The principle of magnetic drug targeting is universally applicable to gene vectors.

DISCUSSION & CONCLUSIONS: The drastically lowered vector dose, the short incubation times required to achieve high transfection / transduction efficiency, and the possibility of gene delivery to otherwise non-permissive cells make magnetofection an ideal tool for ex vivo gene therapy approaches and for screening purposes where the available vector dose, the required process time, and the sustainable costs of the procedure are limiting factors. For in vivo gene- and nucleic acid-based therapies, magnetofection may become a good choice where local treatment is required. Specific and efficient magnetic targeting of interior body regions upon systemic vector administration will require the generation of focused strong magnetic fields, a challenge for physical and medical sciences.

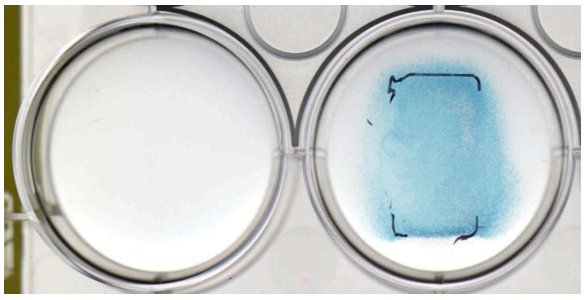

Fig. 2: NIH3T3 cells were incubated for 5 min with a recombinant adenovirus carrying the lacZ reporter gene at a multiplicity of infection (MOI) of 200 with a NdFeB magnet attached under the culture dish (right) or without magnet (left). The virus preparation was previously associated with polyethylenimine-coated superparamagnetic iron oxide nanoparticles. NIH3T3 cells are non-permissive for adenovirus infection, as they do not

express the virus receptor (CAR). By magnetofection, this limitation can be overcome, and gene transfer is confined to an area defined by the shape of the magnet attached under the dish (rectangular area in the right dish).

REFERENCES: [1] A.S. Lübbe, C. Bergemann (1998) *Cancer J.* 11:104-105; [2] A.S. Lübbe et al. (1996) *Cancer Res* 56:4686-4693.

ACKNOWLEDGEMENTS: This work was supported by German government grants 01GE0002 and 13N8186.

MULTIFUNCTIONAL SUPERPARAMAGNETIC NANOPARTICLES FOR LIFE SCIENCE APPLICATIONS

S. Rudershausen, C. Grüttner, M. Frank, J. Teller, & F. Westphal

micromod Partikeltechnologie GmbH, Friedrich-Barnewitz-Str. 4, 18119 Rostock, Germany

INTRODUCTION: Superparamagnetic nanoparticles have a high potential as carriers for oligonucleotides and biomolecules (e.g. proteins, antibodies, enzymes, and nucleic acids) in different life science applications (e.g. immunoassays, magnetic resonance imaging, magnetic cell separation, magnetic oligonucleotide and nucleic acid separation). Beside the magnetic separation and targeting of nanoparticles, different methods for their detection become more and more important. Up to now the detection of magnetic nanoparticles was mainly realized by their magnetic relaxation properties in resonance techniques. A multifunctional fluorescent superparamagnetic nanoparticle separable with a conventional permanent magnet and tagged with a biomolecule (Fig. 1) allows for magnetic separation and magnetic targeting in life science applications in combination with the sensitive method of fluorescence detection.

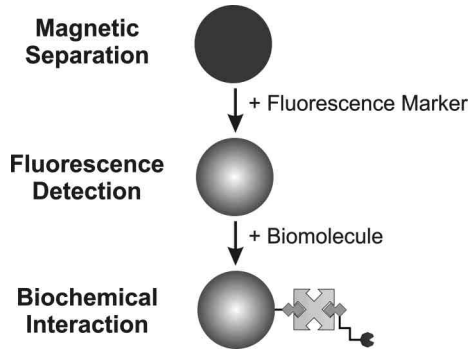

Fig. 1: Synthesis principle of multifunctional magnetic nanoparticles for life science applications (schematic view)

Here we report on the synthesis, magnetic properties, and the chemical and biochemical functionalization of superparamagnetic nanoparticles. In a modular way the magnetic properties of the particles are combined with the introduction of fluorescence and the immobilization of proteins, antibodies, enzymes, nucleic acids and oligonucleotides on the particle surface.

METHODS: Magnetic nanoparticles can be divided in two sections given by the kind of application: nanoparticles separable by permanent magnets (a) and nanoparticles separable by a high gradient magnetic field (b). Nanoparticles with the magnetic properties (a) or (b) can be synthesized via two different synthesis strategies: either by precipitation of iron oxide in the presence of polymers or by coating of iron oxide with polymers according to the core-shell principle (Fig.2) [1].

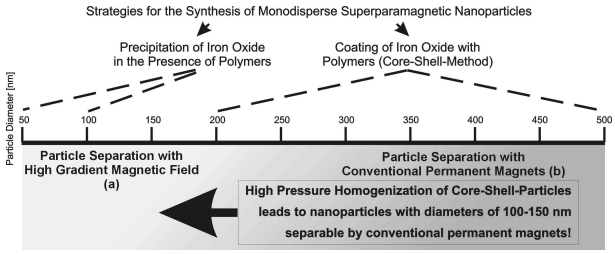

Fig. 2: Strategies for the synthesis of monodisperse superparamagnetic nanoparticles and resulting size ranges.

Furthermore, the technique of high pressure homogenization can be used to move the borderline between (a) and (b) to smaller nanoparticle diameters.

Fluorescence labelling of superparamagnetic nanoparticles can be done by covalent coupling of fluorescent dyes to the matrix polymer covering the magnetic core of the particle. Regarding the applications of our nanoparticles, we used the biocompatible and biodegradable biopolymer dextran as a matrix polymer benefitting additionally by its huge number of functionalities (hydroxyl groups) for the covalent coupling of fluorescence markers and biochemical compounds. For instance three commonly used fluorescence markers like aminofluorescein (employed as the reactive dichlorotriazinyl derivative DTAF), rhodamine B or DAPI (4',6-diamidino-2-phenyl-indol) can be attached covalently to the surface of the superparamagnetic dextran nanoparticle nanomag®-D (Fig.3). In the case of DAPI a bifunctional carboxylic acid spacer is used to

couple the fluorescent dye via one of its amino functionalities to the dextran.

In a typical experiment, a suspension of nanomag®-D in borate buffer (pH = 9) is shaken with DTAF overnight. Unreacted dye is then removed by repeated magnetic washing (principle of separation and resuspension) of the particles with water.

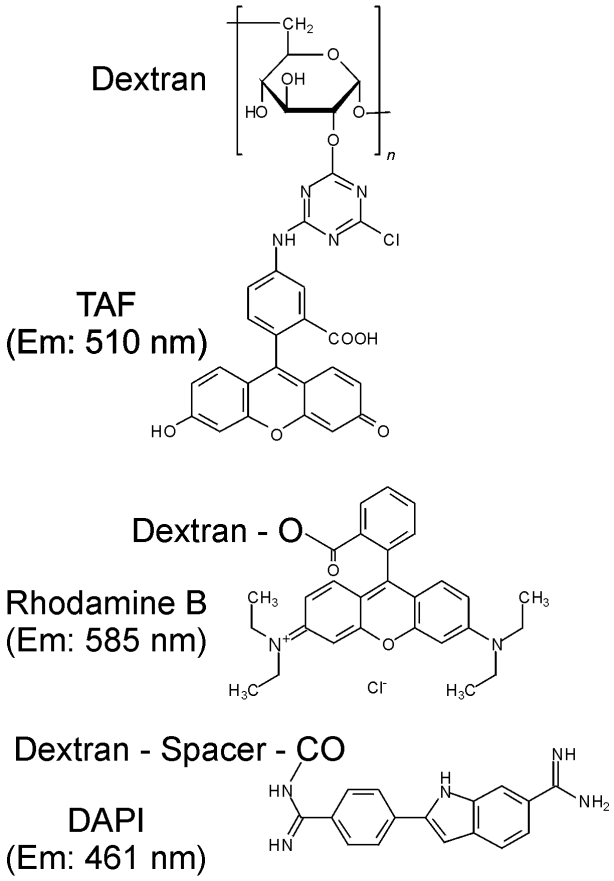

Fig. 3: Covalent coupling of aminofluorescein, rhodamine B and DAPI to the biodegradable particle matrix polymer dextran

To use nanomag®-D as a carrier biomolecules like proteins, antibodies, enzymes, nucleic acids and oligonucleotides can be immobilized additionally to the fluorescence marker on the surface of the superparamagnetic dextran nanoparticle because of the high number of hydroxyl groups of the dextran matrix polymer. In general three activation procedures were applied for the coupling of biomolecules to the dextran matrix of the nanoparticle: periodate activation (a), cyanogen bromide activation (b) and NHS (N-hydroxysuccinimide) / carbodiimide activation (c) (compare Fig.4). The appropriate method can be chosen depending on the desired application and the special kind of biomolecule.

RESULTS & DISCUSSION: Superparamagnetic nanoparticles having a matrix of the biodegradable and biocompatible polymer dextran (nanomag®-D) were synthesized in three different sizes: 50 and 100 nm (separable by high gradient magnetic fields) and 250 nm (separable by conventional permanent magnets) according to Grüttner et al [1].

To get the advantages of smaller superparamagnetic nanoparticles like prolonged blood circulation and higher surface area, and to keep the advantage of separability by a permanent magnet, we applied high pressure homogenization on nanomag®-D with a diameter of 250 nm. The resulting nanoparticles had a diameter of about 130 nm - and were still separable by a conventional permanent magnet - which speeds up different coupling procedures of biomolecules on the particle surface with many washing steps and allows for magnetic targeting, for example.

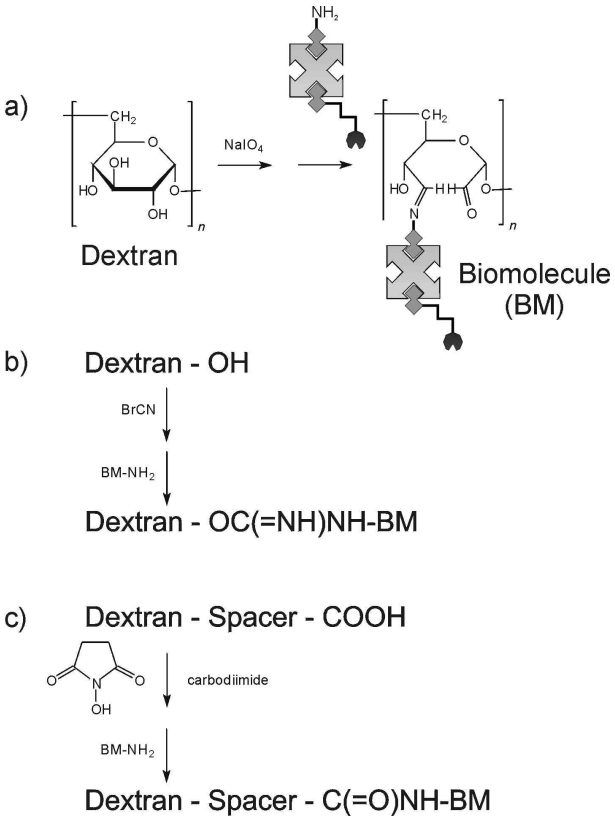

Fig. 4: Covalent coupling of biomolecules to the biodegradable particle matrix polymer dextran

Fluorescence detection is a very common method and is highly sensitive. Lots of devices for the detection of fluorescently-labelled compounds,

already established on the market, can also be used for the fluorescence detection of superparamagnetic nanoparticles nanomag® -D labelled with a fluorescent dye. Fluorescence filters are available, which are compatible for the emission wavelengths of aminofluorescein, rhodamine B and DAPI. So we coupled these dyes covalently to the dextran matrix polymer of nanomag® -D benefitting from the large number of hydroxyl groups on the particle surface deriving from the dextran. Aminofluorescein was employed as its reactive trichlorotriazinyl derivative DTAF, which easily reacts with the hydroxyl groups under alkaline conditions. Rhodamine B was coupled via its carboxylic acid group by using the method of carbodiimide activation. The attachment of DAPI took place after the introduction of a bifunctional carboxylic acid spacer on the particle surface. Spacer and DAPI were both coupled by using carbodiimide activation. Because of the covalent bonding of the fluorescent dyes to the matrix polymer dextran, no leakage of the dye from the nanoparticle surface into the surrounding medium is observed.

Since dextran has so many hydroxyl groups a biochemical functionalisation of already fluorescently-labelled nanomag® -D can additionally be done giving a nano-carrier. For instance antibodies or proteins like streptavidin or protein A were covalently bound to nanomag® -D using coupling methods a) to c). The method of choice depends on the kind of the biomolecule and also on the application of the carrier. We applied a periodate activation (a in Fig.4), a cyanogen bromide activation (b) and a NHS / carbodiimide activation with good results.

In first experiments multifunctional fluorescent superparamagnetic nanoparticles nanomag® -D were loaded with biomolecules, moved into cells, and were visualized there because of their fluorescence emission and had a special effect on cell growth and behavior, for example.

CONCLUSIONS: Superparamagnetic nanoparticles of different adjusted sizes from 50-250 nm were fluorescently-labelled with commonly used dyes and tagged with biomolecules like antibodies or streptavidin. This allows for complex applications in life sciences combining magnetic separation and targeting with fluorescence detection and a specific biological effect, for example.

REFERENCES: [1]C. Grüttner, J. Teller, W. Schütt, F. Westphal, C. Schümichen, and B.R. Paulke (1997) *Preparation and Characterization of Magnetic Nanospheres for In Vivo Application* in Scientific and Clinical Applications of Magnetic Carriers (eds U.O. Häfeli, W. Schütt, J. Teller, and M. Zborowski) Plenum Press, New York, pp 53-68.

CARBON NANOTUBES FOR MEDICAL APPLICATIONS

A.R. Harutyunyan[1], B.K. Pradhan[1], G.U. Sumanasekera[1], E.Yu. Korobko[2], A.A. Kuznetsov[3]

[1] *Dept. of Physics, The Pennsylvania State University, University Park, PA 16802, USA*
[2] *Dept. of Pharmacy, People Friendship University of Russia, Moscow, 117513 Russia*
[3] *Institute of Biochemical Physics RAS, Moscow V-334, 117977, Russia*

INTRODUCTION: Recent discoveries of various forms of carbon nanostructures have stimulated research on their applications in diverse fields. They hold promise for applications in medicine, drug and gene delivery areas [1]. For instance, carbon nanotubes have the potential to carry drugs in the organism as they are hollow and much smaller than the blood cells. The methods were developed for attaching DNA and protein molecules to the inside and outside of the nanotubes. This gives one the ability to target and destroy individual cells that may be cancerous or infected by a virus. Nanotubes with attached enzymes might, in the long term, be used as enzymatic biosensors that could simultaneously detect and measure a variety of biological molecules [2]. Carbon nanotubes arrays can play a key role in the artificial cochlea development (JPL in Pasadena, CA). It has been established that growing of the carbon nanotubes requires use of small metal catalyst particles (~5-100 nm). Usually 3d metals (Fe, Co, Ni) or their combinations with other metals are very effective as catalysts. Carbon nanofibers/nanotubes grow through or from the surface of such metal catalyst particles. A combination of carbon nanotubes and the magnetic, metal catalyst particles may allow one using carbon nanofibers/nanotubes for the magnetically guided drug delivery purposes.

A successful application of such a nanotube-magnetic particle combination depends significantly on the physical, chemical and biological properties of the material. The particles must be biologically inert and biodegradable, they must have high sorption capacity, the sorption selectivity must be adjustable, convenient binding with antibodies must be possible, and high magnetization and magnetic susceptibility in the relatively weak magnetic fields should also be achievable (particularly if such particles are designed for the guided drug delivery). Iron particles with combination of different carbon nanostructures meet all these requirements. Therefore, they are likely candidates for medical applications. Proposed medical applications of the carbon nanotubes require pure nanotube material. However, it has been established that beside nanotubes, the reaction product contains a mixture of different carbon forms, such as amorphous carbon (which covers the nanotubes), multi-shell carbon, as well as metal catalyst residues. The impurities affect the properties of the carbon nanotube reaction product and make its application problematic. Therefore, a controlled synthesis of different kinds of carbon nanofibers/nanotubes, their purification and the property modification became a very important object of materials research investigations.

The growing interest in basic research on carbon nanotubes and in their applications require new, flexible approaches to their synthesis. Many researchers consider chemical vapor decomposition (CVD) method as the only viable approach to a controlled, large-scale production of carbon nanotubes, and in particular, the single wall nanotubes.

In this work we present CVD synthesis of different forms of carbon nanofibers and nanotubes, their purification and modification by filling the nanotubes with different metals and large molecules like the fullerene (a “peapod” structure). Also we discuss problems that can become a serious barrier to the nanotubes applications.

METHODS: The catalyst powders for synthesis of carbon nanofibers *(CNFs*) were prepared by the conversion of metal carbonates to oxides with further reduction of pure metal particles. The precipitate of the metal carbonates was obtained from the solution of calculated amounts of analytical-grade reagents in the form of respective metal nitrates, using ammonium bicarbonate. After drying in the oven at 105-110^{o}C for 24 hours, the precipitate was sintered in the air for 4 hours at a 400^{o}C to convert the carbonate to oxides. The apparatus used in this work consisted of a quartz flow reactor (38 mm i.d. and 90 cm long) located in a horizontal tube furnace. After reduction of catalyst (Fe) powders in a 10%H_2/He gas at 500^{o}C, the temperature was raised to 600^{o}C and carbon fibers were grown by passing a mixture of C_2H_4 and H_2 gases over the catalysts for 90 min.

In the case of growing single wall carbon nanotubes **(***SWNTs***),** the aluminum oxide-supported iron catalyst particles were prepared by adding iron nitrite aqueous solution into methanol solution containing ~2 μm diameter Al_2O_3 particles. After reduction of the aluminum oxide-supported Fe ox-

ide catalyst in the H_2 gas at 500°C, the gas was replaced by argon and the temperature was raised to the nanotube growth temperature. SWNTs were grown by passing a mixture of CH_4 diluted in Ar over the catalyst at a temperature in the range 700-900°C for ~60 min. The reactor was then allowed to cool to room temperature with the Ar gas flowing

The **"***peapod*" structures were prepared by a diffusion of C_{60} molecules inside the preliminary purified SWNTs with opened ends at 420° C in an evacuated (10^{-6} Torr) and sealed glass ampoule. SWNTs were first subjected to selective oxidation to remove amorphous carbon, which covers the SWNTs and the metal catalyst particles, followed by refluxing of nitric acid, which digests the residual metal and opens the tube ends; it also creates defects or a hole on the sidewall of SWNTs. With the opening of the nanotube ends, and the creation of the hole in the nanotube wall, the internal pore or channel is accessible to foreign materials such as C_{60}.

The inclusion of iron oxide nanoparticles into template-synthesized carbon nanotubes was also possible when MOCVD (metal organic chemical vapor deposition) technique was employed. A carbon-deposited film was subjected to MOCVD of ferrocene $Fe(C_5H_5)_2$ in the following manner. Ferrocene was vaporized at 90 °C (corresponding to the vapor pressure of 0.1 kPa) and the vapor was introduced into the film in the quartz reactor with H_2 gas (50% in N_2) at a total flow rate of 100 cm^3 (STP)/min. The feed line was wrapped with heating tapes and maintained at a high temperature (150°C) to avoid the condensation of ferrocene vapor. In order to prepare Ni/carbon nanocomposites, metal-organic chemical vapor deposition (MOCVD) of nickelocene $Ni(C_5H_5)_2$ was employed in the following manner. Nickelocene was vaporized at 105 °C (corresponding to the vapor pressure of 0.6 kPa) and the film was exposed to the vapor with H_2 gas (50% in N_2) at a total flow rate of 100 cm^3 (STP)/min at 275 °C for 0.25 or 1 h. After the metal loading, the films were treated with 10 M NaOH solution at 150 °C in an autoclave for 6 h to dissolve the anodic aluminum oxide. Metal/carbon nanotube composites were obtained as an insoluble fraction.

RESULTS & DISCUSSION: From the first derivative of the temperature programmed oxidation (TPO) profile (50-100°C, rate 3°C/min, under dry air), the preferential oxidation temperatures of the different phases of carbon in the sample were determined. Existence of a more than one peak is connected with the inhomogeneity of the sample (with amorphous carbon and different morphologies of carbon fibers present); this was also correlated with the microscopic measurement results. The mild HCl acid treatment and selective oxidation were carried out to remove the catalyst particles not connected with fibers and the undesirable carbon structures. The DTPO profile after post synthesis treatment showed mainly one peak, which we associate with certain carbon structure. In Fig. 1a the TEM image of the "herringbone" fiber is shown after post synthesis treatments. TEM studies have shown that after selective oxidation, the amorphous carbon phases are removed from carbon nanofibers, and as a result, the BET surface area increases (for given sample from 170 to 580 g/m^2). The studies of the BET surface area modification showed that by changing the synthesis conditions (H_2/C_2H_4 ratio) and the subsequent oxidation procedure, it is possible to control pore size distribution and to achieve a relatively high surface area of ~ 800g/m^2. By changing the catalyst particle size (from 20-150nm) and its composition (e.g. Fe/Ni with different ratio), we were able to synthesize different morphologies of carbon nanofibers ("tubular", "spiral", "platelet") with modified magnetic properties (H_c~120-300G and M_s~20-30 emu/g). The resulting GNFs have a potential for applications as magnetic adsorbents.

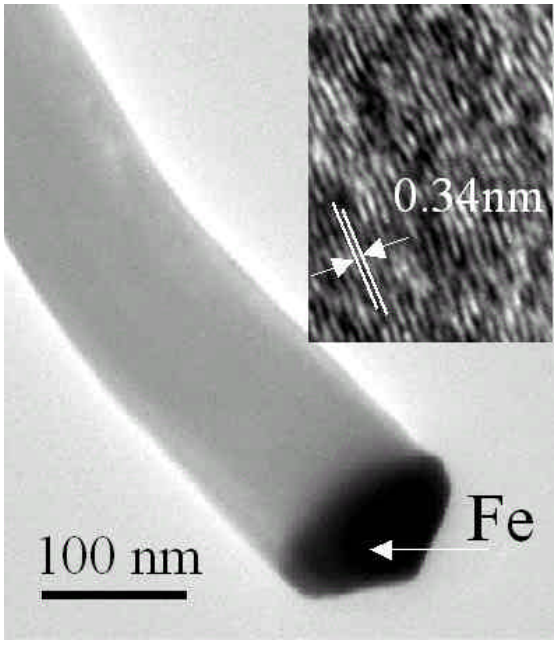

Fig 1: TEM images of carbon nanofiber.

TEM studies of raw samples showed that the SWNTs are a minority constituent in the reaction product. Also present, for example, was amorphous carbon, which coated the bundle walls, the residual metal catalyst, and the multi-shell sp^2 carbon, which covered the metal catalyst residue. The images of SWNTs bundles exhibit an average bun-

dle diameter of 10 nm; also, many individual SWNTs with average diameter of ~1.5nm were observed. Further application of SWNTs in medicine requires purification of the reaction product. Aluminum oxide powders were removed after HF acid treatment of the raw sample. Initial selective oxidation to remove amorphous carbon, followed by a reflux in HNO_3 acid to remove the metal catalyst (Fe) particles, was conducted. In Fig. 2 the TEM image of the SWNTs after purification is shown.

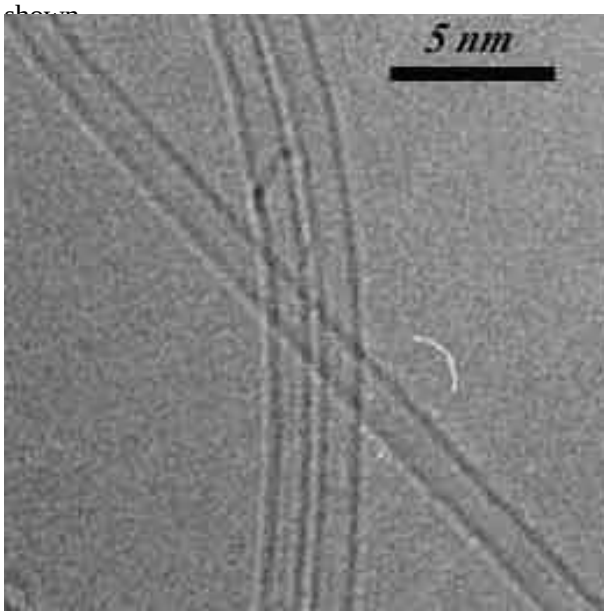

Fig. 2: TEM image of purified SWNTs.

It is important to mention that the refluxing in HNO_3 acid can induce wall damage in the tubes, which changes the electronic structure of the SWNT; this, in turn, can affect the binding energy and can limit the proposed applications in the medicine. Also, as a result of the purification procedure, most of the Fe particles were removed (<0.2wt%), which made it impossible to use these tubes for the magnetically guided drug delivery. Moreover, one must consider the potential interaction of the purified SWNTs with certain gases and chemical species, which adds additional limitations on their medical applications. Electrical and thermal transport studies reveal that the raw SWNTs are extrinsically p-type due to O_2 doping. By stripping O_2 molecules from the nanotube walls with high temperature degassing in vacuum, the nanotubes become n-type (as determined by thermoelectric power measurements) and considered to be intrinsic. The intrinsically n-type SWNTs show measurable, reversible changes in their transport properties when exposed to gases like He, N_2, and H_2. Gases like O_2, NH_3 induce irreversible changes implying charge transfer reactions leading to changes in electronic structure of the nanotubes. More interestingly, chemical vapors such as alcohol and aromatics in contact with nanotube walls induce huge swings in transport/electronic properties and thus modify the binding energy.

TEM image of the **"***peapod***"** structure is shown in Fig. 3. As one can see, the C_{60} molecules formed a chain inside the SWNTs.

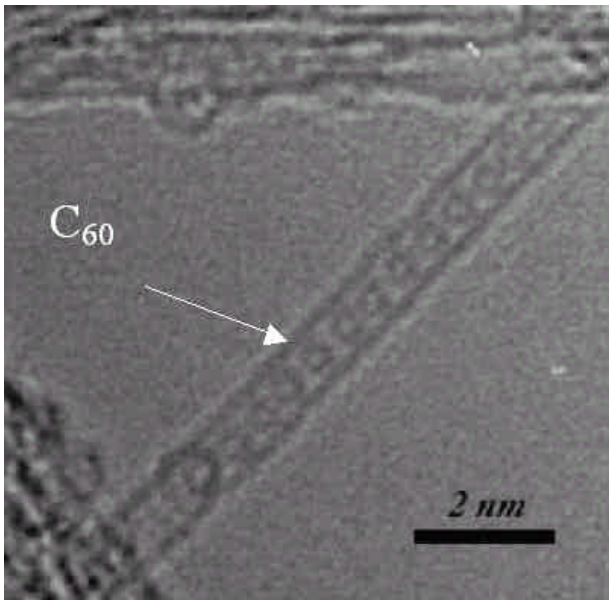

Fig. 3: TEM image of C_{60}@SWNT.

Therefore, it is possible to fill SWNTs with relatively large molecules, which may lead to applications of some specific properties of such molecules, in combination with SWNTs, to particular problems in medicine.

Figure 4a shows the TEM bright field image of the Fe/carbon tube composites prepared by the MOCVD at 400 °C for 3 h with 0.1 kPa ferrocene vapor. These images exhibit the presence of uniform carbon nanotubes with the outer diameter of 30 nm and the wall thickness of about 5 nm. Although some of the tubes are empty, the others contain many dark particles. It should be noted that there are no metal deposits on the outside wall of the nanotubes. The high magnification image shows that the shape of some particles looks like a cube, implying high crystallinity of these particles. Figure 4b shows a TEM bright field image of the nickel/carbon nanotube composite prepared by the MOCVD of nickelcene for 1 h. The image exhibits a carbon nanotube with a diameter of about 30 nm, containing a single nanowire of 500 nm in length and 4 nm in diameter. Energy dispersive X-ray spectrum taken from this nanowire confirms the presence of nickel element with no signal corresponding to oxygen. Silver, platinum and gold filling are also possible by an impregnation method.

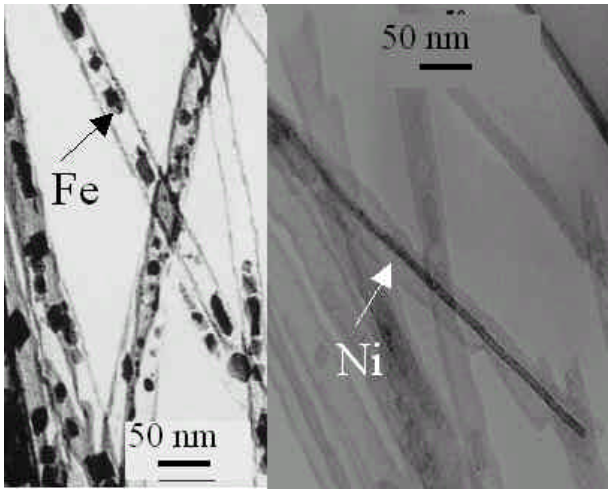

Fig. 4: TEM images of MWNTs filled with Fe (left) and Ni (right).

CONCLUSIONS: Carbon nanotubes (purified/modified) have a high potential of finding unique applications in wide areas of medicine. Also, the encapsulation of other materials in the carbon nanotubes would open up a possibility for their applications in medicine. There remains a number of fundamental issues that need to be resolved, however, such as homogeneity of the material that contains different nanostructures, wide distribution of the nanotube's diameters, presence of residual metals; separation of the individual nanotubes; and a sensitivity to the different gases and species. Also, purification of the nanotubes without inducing wall defects remains a challenging problem.

REFERENCES: [1]C. N. R. Rao and A. K. Cheetham (2001), J.of Materials Chemistry, **11**, 2887-94, [2]M. Freemantle (1996) Chem. & Eng. News, **July 15**, 62-64.

STATISTICAL ANALYSIS OF WEAKEST LINK IN CHAINS OF MAGNETIC PARTICLE CARRIERS FOR APPLICATIONS IN PRINTING BIOCHEMICAL ARRAYS

B. Yellen, G. Friedman

Drexel University, ECE Department, Magnetic Microsystems Laboratory, Philadelphia, PA 19104

INTRODUCTION: Magnetic particle chains have been studied in the past as a means for delivering magnetic particles to surfaces. In situations where the magnetic energy of the particles is comparable with the energy of thermal fluctuations, chain structures have been analyzed using statistical methods [1]. For relatively large diameter particles (i.e. greater than 100-nm), magnetic energy dominates thermal fluctuations, and therefore the deterministic approaches taken by Harpavat [2] and Alward [3] are justified. Previous authors have analyzed the force between each joint in a linear chain of permeable magnetic spheres to determine the weakest link [2,3]. In both these approaches, the particles in the chain were magnetized by a magnetic source at one end without considering the saturation magnetization of the particles. By contrast, this paper considers a situation in which the external magnetic field completely saturates the particles, and the weakest link is determined for a chain in contact with a magnetized substrate at both ends.

The main motivation for this analysis is to better understand the conditions that promote deposition of a specific number of particles onto a magnetized substrate. The ability to control the number of particles deposited has great potential for biochemical printing applications, where the goal is to control the amount of material deposited and maximize the density of the array. An example of an array that is printed with labeled magnetic particles is shown in Fig 1.

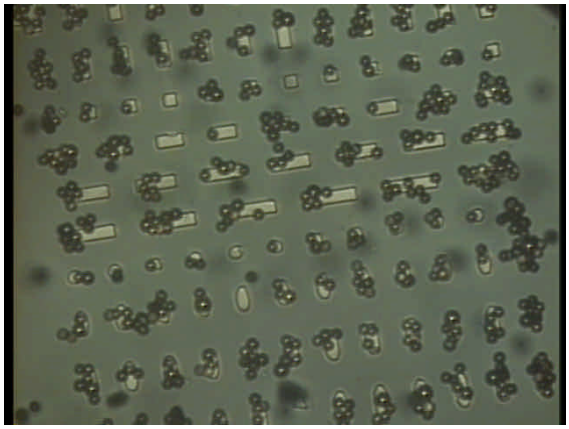

Fig 1: Magnetic particles (5 µm diameter) deposited onto an array of magnetic islands of different shapes and sizes magnetized in planar direction.

In this paper, we consider a situation in which a magnetic island, whose magnetization is perpendicular to the substrate, interacts with a chain of magnetic particles held by a larger magnet at the opposite end. Both the island and external magnets are modeled as cylindrical bodies that are magnetized along their axis perpendicular to the substrate and separated by the length of the chain. It is also assumed that all particles in the chain are magnetized to saturation by external magnetic fields directed along the chain axis.

In an attempt to model a more realistic situation, the particles are treated as having random saturation magnetization and random sizes. The distribution of radii is chosen to be consistent with currently available materials, whereas the distribution of magnetic moments is chosen to be log normal according to a frequently used assumption. In addition, several assumptions are made to simplify calculations. One is that the presence of magnetic particles does not influence the magnetization of the substrates. This assumption is justified for substrates composed of a relatively hard magnetic material. Another assumption is that the particles are treated as constant dipoles.

This paper will be organized as follows. First, a brief overview of the computational method will be provided. Then, calculation results for the deterministic case will be shown and general trends described. Subsequently, the radii and magnetic moments of the particles are given random probability distributions, and the expected force and standard deviation at each joint in the chain will be calculated for varying circumstances. With the breaking range of a joint considered to be within one standard deviation of the expected value, the question of how reliably the particles are deposited will be answered. Finally, a brief conclusion will be provided.

COMPUTATIONAL METHOD: The force on a magnetic dipole of moment m due to a magnetic field with flux density component in the z-direction denoted by B_z is given by

$$F = -m\frac{\partial B_z}{\partial z} \qquad (1)$$

Assuming that saturation flux density of a cylindrical magnet that is magnetized along its

own axis is B_s, then the z-component of the flux density of this magnet along its axis is

$$B_z(z) = \frac{B_s}{2}\left(1 - \frac{z}{\sqrt{z^2 + r^2}}\right) \qquad (2)$$

where r is the magnet's radius whose length is assumed to be many times greater than its radius, thereby allowing us to neglect the field contribution due to the furthest pole face of the magnet. In this paper, the magnetic field of the island B_{isl} and the magnetic field of the magnet B_{mag} will be computed according to (2).

A chain of magnetic dipoles is aligned along the z-axis, attached to the magnet at the $z = 0$ end and to the magnetic island at the $z = L$ end. The force that the magnet exerts on the entire chain of magnetic dipoles and island (i.e. the force on the 0^{th} joint in the chain) can be found from (1) and (2) as follows:

$$F_0 = -q_{isl} B_{mag}(L) + \sum_{i=1}^{N} m_i \frac{\partial B_{mag}(z_i)}{\partial z} \qquad (3)$$

where q_{isl} is the magnitude of the effective magnetic charge on the pole face of the island, m_i is the magnetic moment of the i^{th} particle, and z_i is the z-position of the center of the i^{th} particle of radius r_i given by:

$$z_i = -r_1 + \sum_{j=1}^{i} 2r_j \qquad (4)$$

Note that in deriving (3) it was assumed that the island diameter is much smaller than the magnet diameter justifying the use of an effective magnetic charge representing the effect of the island.

To determine the force at any joint in the chain, one needs also to account for forces between magnetic particles located on opposite sides of the joint. The interaction force between the i^{th} and j^{th} magnetic dipoles in the chain is given by:

$$F_{ij} = -\frac{m_0}{2p} m_i m_j \frac{\partial}{\partial z_i} \frac{1}{(z_i - z_j)^3} \qquad (5)$$

Using (1-5), the force at the n^{th} joint in the chain can be calculated:

$$F_n = F_0 - \sum_{i=1}^{n} m_i \frac{\partial B_{mag}(z_i)}{\partial z} - \sum_{i=n}^{n} m_i \frac{\partial B_{isl}(z_i)}{\partial z} + \sum_{i=1}^{n} \sum_{j=n+1}^{N} F_{ij} \qquad (6)$$

The force at each joint in the chain is thus computed, first deterministically, and then with statistical variations for 1000 trials using randomly generated values of particle radius and magnetic moment. The particle radius is treated as a random variable with uniform distribution between 90-110% of a chosen mean value, while the magnetic moment is treated as a random variable with log normal distribution and with 90% of its probability density occurring between 0.85 and 1.2 times the expected value. Using this method, the expected force and standard deviation is calculated for each joint and the weakest links are determined.

RESULTS: The above computational method for finding the average weakest link in a chain was implemented with MATHCAD software. Magnetic flux densities of the magnetic substrates are chosen to be in the range of 0.2 – 1.0 Tesla, which is consistent with the remnant magnetization of available magnetic materials, such as Fe and Co [4]. The diameter of the island was fixed at 1-ìm, while the particle and external magnet diameters are referenced against the island diameter. In this paper, the particle diameters were limited to a range of 0.1 to 10.0 times the island diameter, and the external magnet's diameter in most cases was limited to a range of 100 to 1000 times the island diameter. These values were chosen because they are experimentally realistic and consistent with available materials and methods.

Current photolithographic tools can produce 2-D patterns in thin films in the sub-micron range, and external magnets with millimeter and sub-millimeter diameter are relatively easily to manufacture. Additionally, magnetic particles in the micron range are currently being used in various biochemical labeling and bio-sensing applications.

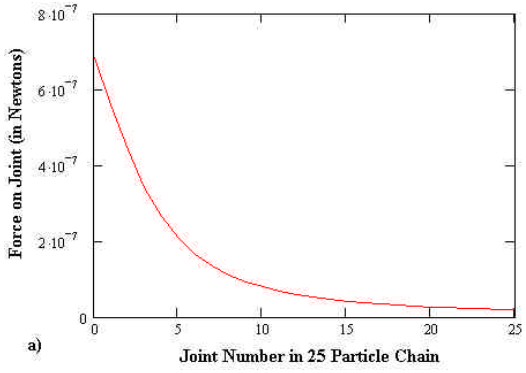

Fig. 2: Illustration of the weakest link in a 25-particle chain where the external magnet diameter is 100 times the island diameter and both magnetic substrates have 1 Tesla flux density. The particle diameter is 10 times the island, and the minimum force occurs at the joint in contact with the island.

The weakest link in the chain was first calculated deterministically, and certain trends were observed for varying chain lengths, particle and external magnet sizes. For chains composed of large particles with diameter exceeding 10 times the

island's diameter, for example, the island's magnetic field gradient is too weak to retain massive particles. In these circumstances, the weakest joint is frequently at the island surface, as is shown in Figure 2.

For chains composed of very small particles with diameter less than 0.1 times the island diameter, the gradient due to the island is felt much more strongly throughout the chain. In these circumstances, the weakest joint is frequently at the external magnet surface, as shown in Fig 3.

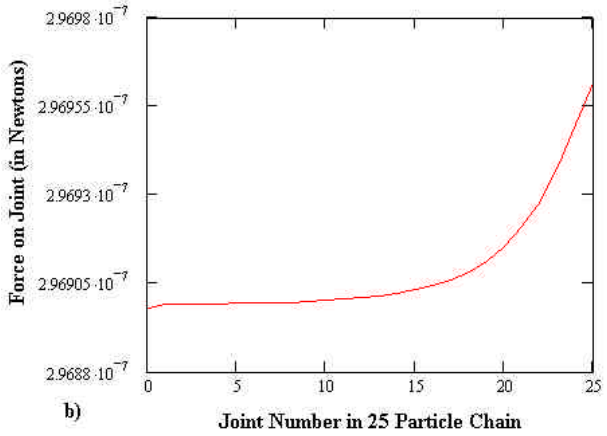

Fig. 3: Illustration of the weakest link in a 25-particle chain where the external magnet diameter is 100 times the island diameter and both magnetic substrates have 1 Tesla flux density. The particle diameter is 0.1 times the island, and the minimum force occurs at the joint in contact with the external magnet (i.e. the 0th joint).

In contrast, situations in which particles and island have equal diameters show that the weakest link in the chain is frequently one of the interior joints. The reason the break occurs in the interior is that the island exerts a stronger force on the nearest few particles due to its similarity in size. However, the island's field gradient decreases very quickly, in contrast with the external magnet's field gradient, which decreases slowly. As a result, it can be seen intuitively that the energy minimum occurs at a joint closer to the island side.

Among the joints closest to the island, the exact weakest link is strongly influenced by the length of the chain as well as particle and external magnet diameters, as is shown in Fig 4. For example, in 10-particle chains with equal particle and island diameters, the weakest link is usually within the first three joints from the island side. In short chains, a small magnet can exert greater forces on each particle than can a large magnet, due primarily to the fact that a smaller magnet has stronger local magnetic field gradient.

For long chains, however, the field gradient due to a small magnet dies out very quickly. A large diameter magnet, by contrast, has a slowly decreasing magnetic field gradient, which exerts a strong influence much farther down the chain, as is shown in Fig 4b. A general conclusion for printing applications, which requires printing relatively few particles onto a magnetic island, would be that a smaller magnet should be used with shorter chains and a larger magnet with longer chains.

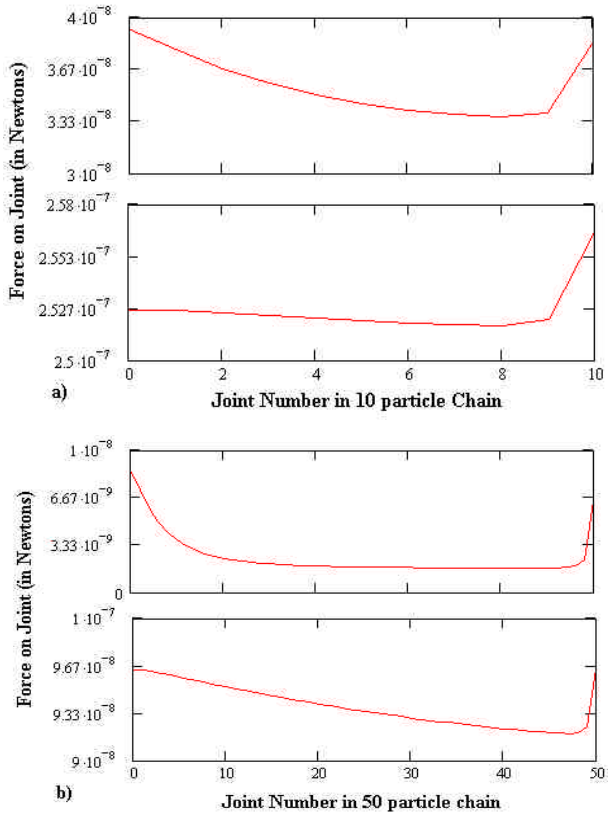

Fig. 4: Illustration of the effects of varying external magnet diameter on a) 10 particle chains and b) 50 particle chains with equal particle and island diameter and magnetic field densities of both substrates equal to 1 Tesla. The top graph for a) and b) represents the effect of a small diameter external magnet (10 times the island diameter), whereas the bottom graph represents the effect of a large diameter magnet (100 times the island diameter).

Next, the weakest link in the chain was computed probabilistically to determine how reliably the chain breaks at a specific joint. The particle radii and magnetic moments were treated as random variables, and the expected force and variance were calculated at each joint. The breaking range at each joint was designated to be within one standard deviation of the expected value, as is shown in Fig 5. Using these ranges, it is possible to determine not only the weakest joint, but also if the breaking range of another joint intersects the breaking range of the weakest joint. If the two ranges intersect, then the chain may break at either joint when a force within that range is applied.

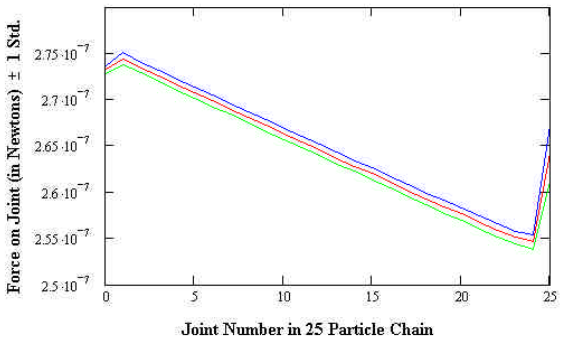

Fig. 5: Illustration of the force on each joint in a 25-particle chain (red), as well as one standard deviation to the plus (blue) and minus (green) sides. The particle and external magnet diameters are 4 and 500 times the island diameter, respectively; and both magnetic substrates have1.0 Tesla magnetic field density. There is clearly a minimum at the joint between the first and second particles from the island side.

In general, it is beneficial to know what circumstances are conducive to printing 1-4 particle chains onto a magnetic island.

Table 1. Number of Particles Deposited with Varying Parameters.

Trial	P:M	Chain	B_{isl}	B_{mag}	Part.
1	5:250	14-20	1.0	1.0	1
2	4:200	8-17	0.75	1.0	1
3	3:200	2-14	0.4	1.0	1
4	2:200	3-12	0.2	1.0	1
5	5:500	17-45	1.0	1.0	1,2
6	4:500	7-28	1.0	1.0	1,2
7	4:500	20-58	0.5	1.0	1,2
8	3:500	4-32	0.5	1.0	1,2
9	3:1000	6-47	0.25	1.0	1,2
10	2:200	13-38	0.2	1.0	1,2
11	5:1000	46-77	1.0	1.0	1,2,3
12	4:500	29-49	1.0	1.0	1,2,3
13	3:500	33-65	0.5	1.0	1,2,3
14	3:100	29-38	0.5	1.0	1,2,3
15	2:200	39-63	0.2	1.0	1,2,3
16	2:200	12-25	0.4	1.0	1,2,3
17	5:500	72-78	1.0	1.0	1,2,3,4
18	4:500	50-66	1.0	1.0	1,2,3,4
19	3:500	66-87	0.5	1.0	1,2,3,4
20	2:200	25-45	0.4	1.0	1,2,3,4
21	5:500	3-36	0.5	1.0	0,1
22	5:500	37-47	0.5	1.0	0,1,2
23	4:200	4-22	0.5	1.0	0,1
24	1:200	50	1.0	0.5	Any
25	0.5:200	50	1.0	1.0	Any

With all the potential variations in particle size, chain length, island and magnet radii and field densities, it is unclear how to demonstrate the effects of all these variables in a graph. Therefore, Table 1 will be used to represent some of the circumstances in which only a few particles will be deposited on the magnetic island substrate. In Table 1, the variable *P:M* represents ratio of particle to external magnet size, *Chain* is the chain length in terms of number of particles, B_{isl} and B_{mag} are the magnetic field densities of the island and external magnet in Tesla, and *Part* represents the number of particles remaining on the island given the intersecting probability ranges. The table can be read as follows. In trial 6, when the particle is 4 island diameters, the external magnet is 500 island diameters, and the magnetic field density of the island and external magnet are both 1.0 Tesla, then the chain will break at either the first or second particles away from the island for chain lengths between 7 and 28 particles long

CONCLUSIONS: A set of chains attached to a large magnet can be idealized as a "magnetic brush". If the chain bristles of the brush come into direct contact with a magnetic island whose diameter is on the same order as the particle, then in some situations a few particles will remain attached to the islands when the brush is pulled away. Assuming all parameters including chain length, particle size, magnet diameter and magnet strengths can be tuned appropriately, this magnetic brush may potentially be used to paint a specific number of particles onto an island.

For sufficiently long chains with average particle diameter between 2 and 5 times the island diameter, it was found that the chain consistently deposited between 1 and 4 particles onto the islands. Such situations are considered to be desirable; moreover, it is shown that system parameters can be varied to make extreme situations, in which a large number of particles or no particles are deposited, statistically unlikely.

REFERENCES: [1] P.C. Jordan (1979) *Mol. Phys* **38**: 769. [2] G. Harpavat (1974) *IEEE Trans. Magn.* **Mag-10**: 919-922. [3] J. Alward, W. Imaino (1986) *IEEE Trans. Magn.* **Mag-22**: 128-134. [4] G. J. Parker, C. Cerjan (2000) *J. Appl. Phys*. **87**: 5514-5516.

SELF-STABILIZED AQUEOUS FERROFLUIDS PROPERTIES AND CHARACTERISTICS

R. F. Ziolo

University of Barcelona Xerox Laboratory, Av. Diagonal 647, 08028 Barcelona, Spain

INTRODUCTION: Ferrofluids are very stable colloidal dispersions of ultra-fine particles of a magnetic material, such as magnetite, in a liquid, which may be chosen to conform to a particular application. A stabilizer or surfactant is usually added at the time of preparation to prevent aggregation of the nanoscale particulate. As a result of their composition, magnetic fluids possess a unique combination of fluidity and the capability to interact with a magnetic field. For magnetic carrier applications, ferrofluids may be thought of as being bi-functional materials with both a magnetic particle and magnetic fluid component.

PERSPECTIVE: S. S. Papel made the first ferrofluids by grinding magnetite in a ball mill in the presence of oleic acid (surfactant) and kerosene (U. S. Patent 3,215,572, 1965). The preparations required many months of milling and commercial ferrofluids soon followed. Their development and eventual understanding were pioneered by such researches as R. E. Rosensweig, then at Exxon Corp, and K. Raj, then at Ferrofluidics Corp.

The early preparations followed a “top down” strategy starting with the grinding of micron or sub-micron sized magnetite in the presence of a hydrocarbon and a small amount of surfactant. The grinding usually lasted in excess of six months. Rapid recombination of the nascent nanoscale particles probably contributed to the very long grinding times.

Significant advances in the preparation of ferrofluids, and thus in the understanding and creation of new ferrofluids, came when researchers realized that magnetic fluids could be made from a “bottom up” rather than “top down” strategy. Thus, precipitation reactions to produce magnetic nanoparticles in the presence of a stabilizing agent led directly to the formation of ferrofluids and eliminated the need to mill. The new approach decreased the preparation time from months to days.

The technological development of the hydrocarbon ferrofluids outpaced that of the water based ferrofluids, partly as a result of practical need, and partly as a result of the extraordinary stability of the former and instability of the latter. In non-polar carrier liquids, such as the hydrocarbons, the particulate is stabilized by steric repulsion.

It wasn’t until ionic stabilization was introduced by R. Massart that water based fluids took hold [1]. The electrostatic repulsion was achieved by the preferential adsorption of ions of one type on the magnetic particles and resulted in a relatively stable water-based fluid.

In general, practical ferrofluids are black or very dark brown liquids and are not very suitable for optical applications. Some of the more important uses of ferrofluids today are for heat exchange and mechanical damping in loudspeakers, as seals in hard disk drives and as vacuum seals in general.

To date, applications of ferrofluids in the biomedical and biotech communities have been driven mainly by the diverse and specific needs of those communities. Many excellent examples of applications can be found in the published proceedings of former conferences such as the present one, *Scientific and Clinical Applications of Magnetic Carriers*, and the *International Conference on Magnetic Fluids*.

Although ferrofluids involve nanoscale materials, their community and technologies evolved long before the emergence of nanoscience and nanotechnology. In an academic sense, the study of ferrofluids would qualify as a subset of the later and present a research area rich in challenges for the newcomer. Interdisciplinary research on ferrofluids as nanomaterials could lead to more ‘user-friendly’ ferrofluid designs that may in turn help drive the biomedical and biotechnical applications. Two such series of water-based ferrofluids will be discussed in the present talk along with their properties, characteristics and unusual effects.

SULFONATED POLYSTRENE AS MATRIX: One series of ferrofluids is formed by a technique of matrix milling a nanocomposite containing maghemite, ë-Fe_2O_3, in water or a water miscible solvent. In this case, a solid matrix, a DVB cross-linked sulfonated polystyrene, is used to synthesize the nanoparticles and keep them isolated to prevent aggregation [2]. The composite is then milled for a few hours to yield the ferrofluid.

In order to increase the magnetization (M) of the ferrofluids after centrifugation, the fluids are subjected to ultrafiltration, which effectively increases the volume fraction of the maghemite. Volume reductions of between 80% and 96% result in stable ferrofluids containing between 15% and 55% by weight solids, as determined by oven drying the fluids at 110 C.

Analysis of the solids showed that the iron oxide to polymer ratio was not constant. The mass ratio increased from 1:1 for the pre-concentrated ferrofluids to about 6:1 for the most concentrated ferrofluids, demonstrating that only a portion of the original polymer was necessary for colloidal stabilization of the nanocrystalline ë-Fe_2O_3. Moreover, there was no apparent effect on the stability of the ferrofluids over this mass ratio range, unlike that reported for aqueous ferrofluids of magnetite, Fe_3O_4, stabilized with sodium oleate. In the latter case, deviation on either side of the optimal magnetite-to-stabilizer ratio, 7:5, resulted in a drastic reduction of either the magnetic properties of the fluid or its stability.

Capillary electrophoretic analysis (see below) established that ultrafiltration served not only to concentrate the ferrofluids by carrier loss but also to purify them by removal of non-bonded or degraded polymer with both losses contributing to the increase in magnetization.

Zeta potential determinations on the particulate in the diluted ferrofluids yielded values of from – 65 to – 85 mv. Solution studies of the hydrodynamic particle size by quasi-elastic light scattering techniques and by SAXS measurements suggested particles of a very narrow size distribution with diameters of either 47 or 100 nm. The particle size analyses and general behavior of the ferrofluids suggest a solvent swollen, three-dimensional polymer network stabilizing the nanocrystalline ë-Fe_2O_3. The behavior of the particles appears to mimic the comb-like grafted hydro gels that show rapid de-swelling response to temperature changes or to gels as described earlier by Y. Li and T. Tanaka. For the most part, the present ferrofluids, which are water-based, are stabilized by steric repulsion.

MAGNETIC AND OPTICAL PROPERTIES:

Room temperature magnetization values (M) for the present ferrofluids range from <2 to 52 kA/m, depending on the preparative history of the sample and the applied field. In general, the magnetization of the fluids increases proportionally with the mass loading of iron oxide. A representative ferrofluid at 300 K in the present series is nearly saturated with a magnetization 35.8 kA/m in an applied field of 800 kA/m. The magnetic remanence and coercivity are zero, consistent with superparamagnetic behavior and the nanoscale dimensions of the particles. Below 50 K, a small hysteresis loop appears. At 10 K, the ferrofluid has a sizable coercive field of 22 kA/m. The hysteresis loop appears symmetric about the center for both the field-cooled and zero field cooled cases. Superparamagnetic behavior was observed for all of the ferrofluids in the present series, as well as for the solid nanocomposite parent.

One of the magnetically strongest ferrofluids in the present group is a very viscous fluid with a saturation magnetization of 52.3 kA/m in an applied field of 800 kOe. Magnetization versus applied field curves at 300 K showed virtually no hysteresis consistent with superparamagnetic behavior. The fluid contained 53% by weight solids and had a density of 1.55 g/cc.

In the proximity of a one Tesla permanent magnet, the ferrofluids with an M of about 12 kA/m and higher show the familiar spiking or tooth pattern that represents the surface structure of a ferrofluid in the presence of a magnetic field. The surface instability results from the interaction of magnetic, gravitational and viscous forces and the surface free energy of the ferrofluid. Spike heights in the strongest ferrofluids can reach several centimeters.

Optical data on bulk ferrofluids has been quite limited. Magnetite-base ferrofluids, for example, are black and opaque except in very thin layers. Optical data for the present ferrofluids were identical to those reported for the solid nanocomposite [2], consistent with our observation of no detected physical or chemical change in the crystallite after milling. As a result, the ferrofluids have a color similar to that of the solid composite parent and appear amber or amber red in color except for the strongest fluids. Because of their relative transparency, the ferrofluids may be used as an optical diagnostic tool in fluid dynamic and fluid mechanical studies For example, use of the present fluids aboard MIR has enabled the first observation and study of convection currents *inside* of a suspended drop of ferrofluid in microgravity experiments using simple optical diagnostic techniques. In the presence of an applied field, the stronger ferrofluids exhibit optical birefringence.

Changing the alkali metal hydroxide used in the preparation of the starting material can significantly

change the color of the ferrofluids. The use of Li, K, Rb, Cs and ammonium hydroxides instead of NaOH causes the ferrofluids to go from lighter to darker red through a significant shift in the optical absorption edge of the nanocrystalline ë-Fe_2O_3. The role of the cation in changing the optical properties of the mesoscopic oxide appears to be more complex than a simple doping phenomenon since K, Rb and Cs cations presumably do not fit into a normal ë-Fe_2O_3 lattice. The observed shifts support the possible effects of the pressure hypothesis as suggested earlier [2] involving different size cations located between the sulfonated resin and the Fe_2O_3 particles.

The optical transparency of the nanocrystalline ë-Fe_2O_3 along with the relatively high initial permeability, magnetization and stability of the ferrofluids also enables the existence of machine-usable colored magnetic inks at room temperature. To our knowledge, nanotechnology has been the only approach to successfully provide simultaneous color and magnetism in the same material at room temperature.

ALGINATE AS MATRIX: Alginate is a naturally occurring polysaccharide that finds heavy use in the pharmaceutical and food industries. The availability of magnetic forms of the polysaccharide can offer new avenues for materials management and control.

In the form of alginic acid, alginate forms cross-linked gels in the presence of various cations. Magnetic forms of alginate have been made by incorporating micron scale iron oxides into the calcium cross-linked gel. Magnetic gels are the subjects of current research for applications in medical diagnostics, drug delivery and cell sorting systems.

We have produced alginate based ferrofluids by first forming the magnetic gel [3]. This was accomplished by using Fe as the cross-linking ion and using it as the reaction center for the in situ formation of nanocrystalline iron oxides.

Two mm diameter Fe(II) cross-linked beads were formed by dropping an aqueous solution of sodium alginate at room temperature through a 17-gauge stainless steel needle into a degassed solution of iron(II) chloride. Excess ferrous ions were removed by washing with 1:1 MeOH/water solutions under nitrogen. The beads, which were kept in the MeOH/water mix and under nitrogen, were then treated with a sodium hydroxide solution to effect the conversion of Fe(II) ion to ë-Fe_2O_3. This two-step synthesis was repeated up to four times to increase the loading of iron oxide in the gel. This technique led to gels that on a dry basis contained between 10 and 50% iron.

Aqueous alginate ferrofluids were then formed by oxidative depolymerization of the beads in water with air bubbled through the suspension to evaporate the methanol, which acts as an inhibitor to the depolymerization of the alginate.

The physical properties of the alginate ferrofluids are similar to those of the sulfonated polystyrene fluids. Gels obtained after five consecutive loading cycles and then dehydrated have a room temperature saturation magnetization of 30 kA/m at 20 kOe. Magnetization curves of M vs. applied field and temperature (4.2 K to 300 K) suggest superparamagnetic behavior consistent with the small size of the iron oxide.

ANALYSIS: The effective characterization of water-based ferrofluids is as important as their design. Conventional methods of analyzing these materials include transmission electron microscopy and quasi-elastic light scattering techniques for particle size. Microelectrophoresis is also used and yields data on the *average* electrophoretic mobility and the zeta-potential of the colloid. None of these methods allows for the fast detection of impurities. Methodology reported by Morneau et al. [4] on the application of capillary electrophoresis (CE) to the analysis and characterization of magnetic fluids will also be discussed. In the study, CE was coupled with diode array UV-visible detection to provide a new, efficient and sensitive method to characterize water-based ferrofluids in terms of surface charge, electrophoretic mobility and the level of purity. The method has also proved useful in quality control of ferrofluid production.

REFERENCES: [1]See, for example, S. W. Charles (1992) *Magnetic Fluids (Ferrofluids)* in Magnetic Properties of Fine Particles (eds J. L. Dormann and D. Fiorani) North-Holland Elsevier, pp 267-374. [2]R. Ziolo, et al. (1992) *Science* **33**:1471-77. [3]E. Kroll, et al. (1996) *Chemistry of Materials*, **8**:1594-1596. [4]A. Morneau, et al. (1999) *Colloids & Surfaces A: Physicochemical & Engineering Aspects* **154**:295-301.

ACKNOWLEDGEMENT: I would like to acknowledge the contributions of my colleagues and students to the understanding and development of these ferrofluids.

COOKING WITH NANOPARTICLES: A SIMPLE METHOD OF FORMING ROLL, PANCAKE, AND BREADED POLYSTYRENE MICROPARTICLES

J.N. Anker[1], T.D Horvath[1], & R. Kopelman[1]

[1] *The University of Michigan, Chemistry Department, Ann Arbor, MI 48109-1055 USA*

INTRODUCTION: We report here simple methods of forming roll and disc-shaped (pancake) microparticles that require no unusual reaction conditions, templates, or molds. In addition, we have physically embedded small "breading" particles into the surface of larger particles to form hybrid particles of various compositions. We have breaded fluorescent nanospheres into rolled magnetic polystyrene particles. We have also breaded magnetic material into fluorescent polymer pancakes. Such magnetic particles align in magnetic fields due to their magnetic anisotropy. Since a particle's shape and composition affects its magnetic, optical, chemical, and mechanical properties, our non-spherical particles may prove useful in a variety of optical, chemical and biomedical applications.

Nagy and Keller describe a physical method of forming elliptical polymer microparticles [1]. They formed a suspension of polystyrene microspheres in a polyvinyl alcohol (PVA) solution, and allowed it to dry into a thin film. The film was then stretched at a temperature above the glass transition temperature of both the polystyrene (T_g 94°C), and the PVA (T_g 85°C). The embedded microspheres were deformed into ellipses while the film was stretched. The PVA was then dissolved leaving elliptical microspheres. The amount that the film was stretched controlled the aspect ratio of the particles.

Wang et al expanded Nagy and Keller's method and formed oblate elliptical particles by compressing particles in a PVA matrix above the glass transition temperature [2]. Jaing et al invented a method of forming a polystyrene mold around microspheres, dissolved the microspheres, and stretched the mold at an elevated temperature so that it had elliptical holes. They then filled the holes with a variety of polymers and sol gels to form solid and shell shaped elliptical microparticles [3]. However, we are unaware of any room temperature deformations. In addition, we are unaware of any previous deformation of magnetic microspheres, although Gabrielson and Folkes tried unsuccessfully to deform magnetic polystyrene microspheres [4].

METHODS: Fluorescent polystyrene microspheres 3.4 μm in diameter were purchased from Bangs labs. Polystyrene microspheres containing ferromagnetic chromium dioxide 2 μm and 4.4 μm in diameter were purchased from Spherotech. Iron oxide nanoparticles were obtained from Magnox. Fluorescent decyl methacrylate and silica sol gel nanospheres were polymerized in our lab. Glass microscope slides were from Fisher Scientific.

A simple method of deforming microspheres into rolls and multirolls is illustrated in Fig. 1. Polystryrene microspheres were deposited onto a microscope slide and the slide was clamped to a laser table. A second slide was placed on top to sandwich the particles. The top slide is then moved laterally while applying pressure with the fingers. With a low concentration of particles and small lateral motions, single particle rolls are formed, while with a high concentration of particles and large lateral motions, the rolls form together into multirolls as shown in Fig. 4. The rolling procedure can be performed with microspheres that are either suspended in solution, or dry. The preferred procedure was to suspend the microspheres in ethanol and deposit them on a microscope slide to dry before rolling.

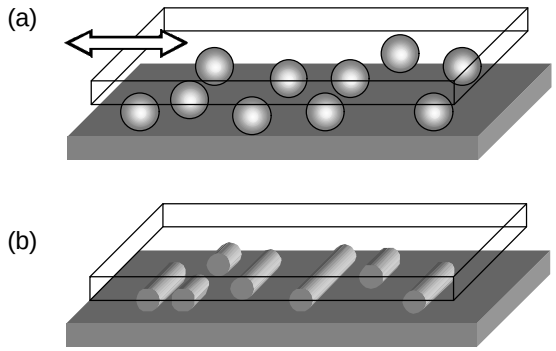

Fig. 1: Method of rolling microspheres into rolls and multirolls. Microspheres are deposited onto a microscope slide and the slide is clamped to a laser table. A second slide is placed on top to sandwich the particles. The top slide is then moved laterally while applying pressure with the fingers as shown in (a). With a low concentration of particles and small lateral motions, single particle rolls are formed, while with a high concentration of particles and large lateral motions, the rolls form together into multirolls (b).

Pancake-shaped microparticles are formed using a rolling pin (a ¼" diameter glass tube with a metal pin through it) to flatten deposited microspheres, as

shown in Figure 2. This method can also be used to form coupled pancakes and flattened rolls and multirolls.

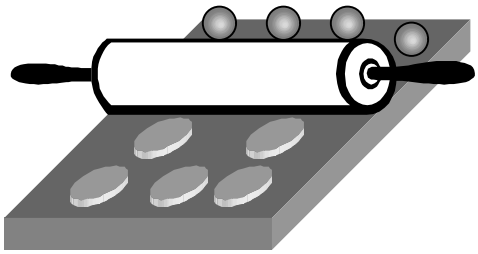

Fig. 2: Method of flattening microspheres into "micropancakes." A rolling pin, comprising a ¼" glass tube with a metal pin through it, is rolled over particles deposited on a microscope slide.

Smaller particles could be breaded onto larger particles by applying small "breading" particles to the microscope slide before the larger microspheres are added. The breading particles are implanted into larger particle rolls or pancakes during the normal rolling or flattening procedure.

RESULTS: The rolling process works remarkably well for a process literally done by hand. It works wet or dry, with large concentrations of particles or small concentrations, with polystyrene particles, and magnetic polystyrene particles, and in the presence of breading. However, hand rolling has its limitations. The shape of particles formed by hand is hard to control; for example, rolled particles tend to be thinner and longer where direct pressure from the fingers is applied, than elsewhere. When the particles begin to deform, one feels the rolling resistance decrease, but otherwise one has to check under the microscope to see particle shape. If too much pressure is applied, the particles are crushed into pancakes, and then smeared instead of rolled. When wet rolling particles, it is important to use a sufficient volume of water: insufficient water leads to droplets that shrink with evaporation, causing particles to aggregate. This aggregation interferes in the rolling process as shown in Fig. 3. However, we have demonstrated that particles can be rolled and breaded. We are designing simple machines to apply uniform pressure and control the shape of the particles formed.

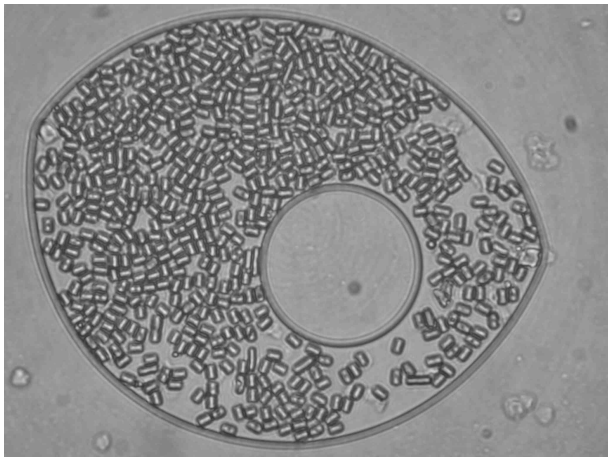

Fig. 3: Wet-rolled 3.4μm polystyrene microspheres forced together in an evaporating droplet containing a soap bubble.

Rolls and multirolls of magnetic polystyrene particles breaded with fluorescent polystyrene, sol gel, and decyl methacrylate have been formed. Fig. 4 shows a CCD image of fluorescently breaded magnetic microspheres. Due to their magnetic shape anisotropy, these rolls align with external magnetic fields when placed in solution.

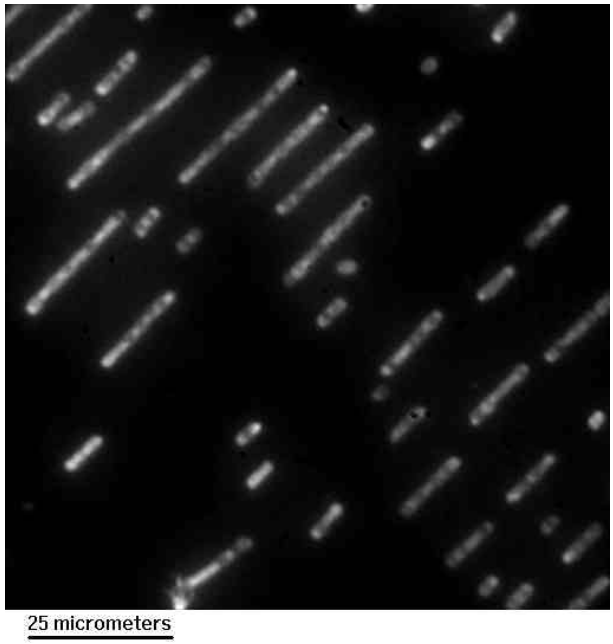

Fig. 4: Fluorescent image of breaded multirolls. They were formed from 2 μm CrO_2 containing magnetic polystyrene microspheres and breaded with ~500 nm decyl methacrylate nanospheres containing a fluorescent dye. These particles were rolled dry.

Fluorescent polystyrene pancakes have also been formed, and pancakes have been breaded with magnetic material. The magnetically breaded fluorescent pancakes align with external magnetic fields, as shown in Fig. 5. These magnetically

breaded pancakes were stable in water for at least five days.

(a) (b) (c)

Fig. 5: Fluorescent 3.4 mm polystyrene microspheres were flattened onto iron oxide nanoparticles (magnetic breading). The magnetically breaded fluorescent pancakes align with external magnetic fields. a), b), and c) show fluorescent images of one particle aligned in three different magnetic field orientations.

DISCUSSION & CONCLUSIONS: We have discovered a method of forming non-spherical particles that requires no template, unusual reaction conditions, or elevated temperatures. Our early efforts have used polystyrene microspheres and polystyrene containing chromium dioxide nanoparticles. We expect the method to apply to a number of other polymer and metal micro/nanospheres. Non-spherical magnetic particles can be oriented in magnetic fields due to their shape anisotropy. We plan to elucidate the effects of temperature, solvent, stress, and rate of strain on particle formation, and to develop a machine to uniformly deform particles.

REFERENCES: [1]M. Nagy, and A. Keller (1989) *Polymer Communications* **30 (5)**: 130-132. [2]S. Wang, P Xu, and J.E. Mark (1991) *Macromolecules* **24** (22):6037-6039. [3]P. Jiang., J.F. Bertone, and V.L. Colvin (2001) *Science* **291** (5503):453-457. [4]L. Gabrielson, M.J. Folkes (2001) *Journal of Materials Science* **36** (1):1-6.

ACKNOWLEDGEMENTS: We wish to thank Murphy Brasuel for providing the fluorescent Decyl methacrylate nanosphere breading, and Yong-Eun Koo for providing fluorescent silica based sol gel nanosphere breading. This research was supported by NSF grant DMR 9900434 and NIH/NCI contract N01-CO-07013.

SYNTHESIS OF POLYETHYLENE MAGNETIC NANOPARTICLES

J. Chatterjee [1], Y. Haik [1] & C.-J. Chen [1]

[1] *Biomagnetic Engineering Lab, FAMU-FSU College of Engineering, Tallahassee, FL 32310*

INTRODUCTION: Polymer-based nanoparticles have been synthesized in the last few decades for biomedical applications, mostly in drug delivery, immunoassay and cell separation. Non-magnetic and water-insoluble polyethylene, polypropylene and polystyrene particles are being used as components in cleansing agents in the cosmetic industry and to study the effect of body fluids on polymer particles in vitro. In most cases polymer composite particles and encapsulated particles are prepared by emulsion polymerization, solvent evaporation, hot melt method etc. A convenient way of forming encapsulated particles is to dissolve the polymer and the inorganic particles in a solvent or water and then forming an oil in water emulsion and stabilizing the particles either by chemical crosslinking or by heat. Recently a method has been described by Wunder et al [1] to prepare UHMWPE particles to be used for in vitro study. Their method was based on the concept of nonsolvent and temperature induced crystallization. This method is much easier and less complicated for the preparation of particles with crystalline polymers. In this study the above method is modified to produce composite particles. A method of solvent-nonsolvent temperature induced crystallization, coupled with ultrasonication using an ultrasound probe is reported in this paper. No direct interaction of sound field with molecular species takes place during ultrasound application; moreover, the acoustic cavitations at the transient high temperature and high pressure cause chemical effects and give rise to nanostructured materials. Ultrasound mixing of the polymer with maghemite in the solvent and further mixing with the nonsolvent caused the formation of a homogeneous emulsion with a well-dispersed phase of polymer with maghemite. Initially, the emulsion was formed by mixing the solvent, polymer with maghemite and nonsolvent at high temperature using ultrasound. The ultrasonication caused the formation of micro-droplets, which formed a microphase-separated system while cooled rapidly and consequently a macrophase-separated system was formed separating two liquids. Polymer crystallized with lowering of temperature and the polymer along with magnetic particle was distributed in the nonsolvent medium separating two liquids.

Our study focuses on the effect of different solvents and amplitudes of sonication during particle formation. The two solvents with high boiling points were Decalin and OMCTS and the nonsolvent was tetraglyme. The polymer used in this study was low molecular weight polyethylene with broad distribution. The polymer had a wax like appearance and softness. The particles formed with this polymer are non-toxic and can be used for in vitro applications and also as an efficient medium for transdermal drug delivery. These polyethylene magnetic particles were further modified to bind avidin for biomedical applications such as cell separation and immunoassays. The protein coupling efficiency was measured. The magnetic properties were also investigated, since these submicron composite particles are designed for biomedical applications where an external magnetic field will induce a force to separate them.

METHODS: Very low molecular weight polyethylene wax (number average molecular weight 700 g/mole) was obtained from the Honeywell Corporation. This product is not hazardous under OSHA Hazard communication. Decalin and tetraglyme were obtained from Sigma-Aldrich, octamethylcyclotetrasiloxane from Dow Chemical Company, sodium oleate from Sigma-Aldrich. All solvents and nonsolvents were used as received.

Iron oxide particles with an average diameter range of 5 nm -10 nm were synthesized by a combination of the widely used coprecipitation method along with ultrasonication [2]. These particles were modified with sodium oleate (an anionic surfactant) to attach them to polyethylene. Iron oxide powder was mixed with sodium oleate (30% of weight of polymer) in water, stirred at moderate speed for about 2 hours, dried and then used in a mixture with the polyethylene wax.

A dilute (0.05% w/w) solution (10 ml) of the polyethylene wax and iron oxide mixture was made using Decalin at 150^{o}C in a 25 ml screw cap scintillation vial by ultrasonication. Ten ml of tetraglyme at same temperature was added and sonicated at 50% amplitude for 30 seconds. After dissolution and mixing at 150^{o}C, the mixture was immediately cooled at 0^{o}C temperature. An emulsion formed within a few minutes. Within 45 minutes to one hour at room temperature,

polyethylene particles along with maghemite formed. The suspension was then kept at –10°C in the refrigerator for about half an hour. A very thin reddish brown layer was observed in the junction of two liquids. The top and the bottom layer of liquids were extracted with the help of micropipette and syringe. The particles were then centrifuged in a microcentrifuge to isolate it from rest of the solvent mixture. The remaining solvent was removed and particles were washed with acetone. Six different batches of particles were made using two solvents at two different speeds of sonication and with two different concentrations of polymers in each of two solvents.

Appropriate amounts of the ligand avidin were dissolved in the adsorption buffer (sodium acetate/ acetic acid, pH 5). The polyethylene magnetic particle suspension (in the same buffer, 10% solid) was added to above protein solution and mixed gently for 1-2 hours. After 2 more hours at room temperature, the mixture was centrifuged and the protein concentration in the supernatant was measured using a Turner spectrophotometer (SP 830) at a wavelength of 562 nm, using BCA protein assay kit.

One drop of polyethylene composite particles in acetone was placed on a carbon coated copper grid, dried and observed under a JEOL 2010 Transmission Electron Microscopy microscope operated at 200 KV. Bright field imaging technique was used to image the samples by selecting the transmitted diffraction spot to form the image.

A D 3000 Nanoscope from Digital Instruments was used in tapping mode. One drop of sample was placed on cleaved Mica surface and observed under the microscope. Micrographs were taken in both height and amplitude mode.

A Quantum Design MPMS5 DC Superconducting Quantum Interference Device (SQUID) was used to study the magnetic properties of the maghemite particles and the polyethylene magnetic particles. Weighed amount of sample were packed in gel capsules and placed tightly in the glass tube ensuring no movement in either direction and the magnetic properties were measured.

A Perkin Elmer DSC 7 equipped with a 3700 data station was used for Differential Scanning Calorimeter and the instrument was calibrated with an Indium standard. Approximately 4 mg of pure polyethylene wax sample was heated first to a temperature of 150°C then quenched to room temperature and kept there for 10 minutes to ensure complete crystallization and then reheated at a rate of 10°C/min to 150°C. Similarly pure polyethylene particles and polyethylene composite particles both formed by solvent-nonsolvent and temperature induced crystallization when heated in aluminum pans from 40°C to 150°C at same heating rate. The peak temperature in the endotherm was considered as the melting temperature and the crystallinity values were calculated based on the standard heat of fusion value of polyethylene (ΔH_u = 290J/g).

RESULTS AND DISCUSSION: The polyethylene magnetic composite particles were formed under the experimental conditions summarized in Table 1. High boiling solvents and nonsolvent were chosen in order to increase the undercooling, which enhanced the crystallization process. Particle morphology is dependent on the choice of solvent as evident from the micrographs.

Table 1: Experimental conditions and results.

Polymer conc (w/v) %	Solvent: Nonsolvent	% maghemite	Morphology (av. diameter (mm))
0.05	Decalin/TG	50	Spherical/elliptical ~300 nm
0.05*	Decalin/TG	50	Spherical/elliptical ~370 nm
0.1	Decalin/TG	30	Spherical/elliptical ~200 nm
0.1*	Decalin/TG	30	Spherical/elliptical ~360 nm
0.05	OMCTS/TG	50	Spherical ~300 nm
0.1	OMCTS/TG	30	Spherical ~250 nm
0.1*	OMCTS/TG	30	Not well formed

**Amplitude of sonication was set at 80%, while all other samples were set at 50%*

Transmission electron micrographs (Figures 1 and 2) obtained for particles formed under different experimental conditions showed that the particles have diameters in the range of 50 - 500 nm with two types of distinct morphology, spherical and elliptical. It was found that an increase in the amplitude of ultrasonication produced smaller particles after crystallization. However, there was a lack of attachment for the iron oxide particles with the polymer and the mostly irregular shaped particles were formed under that condition irrespective of the type of solvent. Most particles were nicely formed using 50% amplitude with both types of solvents.

The polymer concentration had no significant effect on particle size. In fact, when polymer crystallized from the solvent in the nonsolvent medium, it had maghemite on the surface, which affects the particle growth and final shape.

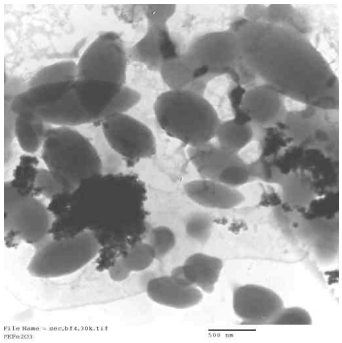

Fig. 1. TEM of polyethylene particles.

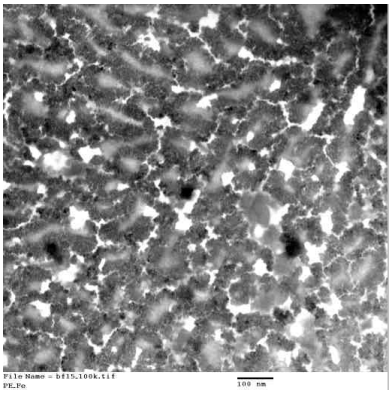

Fig. 2. TEM of polyethylene composite.

Particles formed from the OMCTS/tetraglyme emulsion showed mostly spherical morphology under different experimental conditions (Fig. 3), but the particles formed from the decalin/tetraglyme system have both elliptical and spherical morphology. The low molecular weight polyethylene used in this study has a very wide distribution of molecular weights (300-700 g/mole). It has been reported [3] that fractionations occur for solution grown crystals of polyethylene with shorter molecules concentrated towards the edges of lamella within the crystal. This could be one of the reasons for the changes in particle morphology. The solvent effects on particle morphology are still under investigation. The whole system after addition of a nonsolvent becomes a phase-separated system, which leads to precipitation of a swollen polymer and is used in fractionation and recystallization. The lower value of crystallinity for the solution crystallized pure particles and composite particles as obtained from differential scanning calorimetry studies might be additional evidence for fractionation and recrystallization. The effect of ultrasonication at the dissolution and mixing step where interparticle collision occurred due to ultrasonication needs to be considered. Particles are not well formed when used 80% amplification.

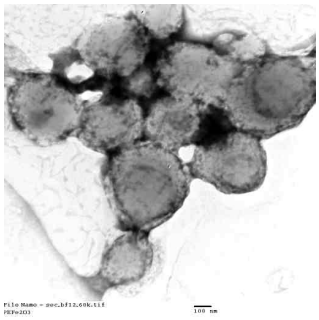

Fig. 3. TEM of polyethylene particles.

An atomic force micrograph for the polyethylene avidin-coated particles is shown in Figure 4. Particles are found to be agglomerated after protein adsorption on their surface due to protein-protein interaction. In these micrographs, both spherical and elliptical particles were observed.

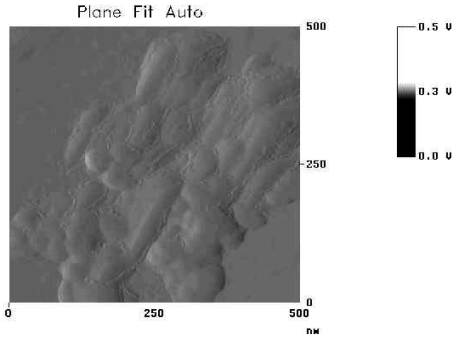

Fig. 4. AFM of avidin coated polyethylene particles.

Degree of crystallinity values for the pure polymer, polymer crystallized from solvent-nonsolvent emulsion (without iron oxide) and composite particles were obtained from their heat of fusion values. As expected the composite particles showed lowest value of crystallinity indicating the presence of another material with the polymer. Polymer particles formed without maghemite also showed lower crystallinity compared to the pure polymer indicating fractionation by the effect of dissolution and recrystallization process. Their crystallinity values are tabulated in Table 2 along with the melting points.

Table 2. Degree of Crystallinity

Sample	Melting point (^{o}C)	Degree of Crystallinity (%)
PE wax	85.3	74.2
PE particles (nonmagnetic	87.5	53.4
PE particles (magnetic)	85.4	16.7

Magnetization was measured using a SQUID at 5 K and at 300 K (Figures 5 and 6). It was found at 5

K that the hysteresis was rather large with a coercive field. The hysteresis loop is symmetric, showing the characteristics of superparamagnetic behavior. Magnetization curves at 300 K showed no hysteresis and the typical superparamagnetic behavior of the composite particles.

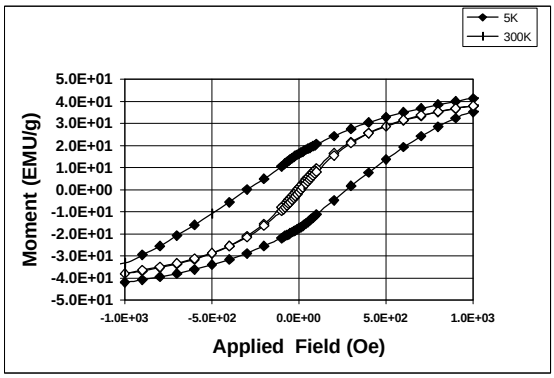

Fig. 5. Hysteresis curve at 5 K and 300 K.

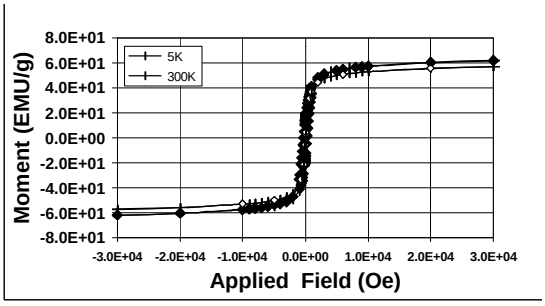

Fig. 6. Hysteresis curve at 5 K and 300 K.

The protein coupling efficiency was measure for the composite particles. Avidin was used as ligand as it has strong bond forming ability with various ligands used in immunoassays. Composite particles were coated with avidin. It had been found only 30% of the calculated amount of avidin required for monolayer formation on polyethylene particles is used to coat the particles and remaining portion remained unadsorbed.

CONCLUSIONS: Polyethylene magnetic composite particles have been fabricated in submicron range using nonsolvent-temperature-induced crystallization coupled with ultrasonication. The particles formed have spherical and elliptical morphology depending on the nature of solvent for a certain time of crystallization. Polymer concentration and amplitude of ultrasonication have large effects on the size of the microdroplets of polymer with iron oxide in solvent-nonsolvent emulsion. The final size of the particles is dependent on the size of the microdroplet formation. Smaller particles (30-50 nm) with irregular shapes are formed at high amplitude of ultrasonication. Unmodified maghemite showed no coupling with polyethylene under any of the reaction conditions. The decrease in crystallinity for the composite particles shows the presence of iron oxide in the polymer. Lower magnetic moments support the above conclusion. Lower blocking temperatures show that the particles are coated with polymer, as has been also shown in the transmission electron micrographs. Composite particles are superparamagnetic in nature as observed in the magnetization experiment. Composite particles can be effectively coated with ligands such as avidin and could thus be used for biomedical applications.

REFERENCES: [1] Y. Yaravoy, G. Baran, S. Wunder and R. Wang (2000) *J. Biomed. Mat. Res*. **53**:152. [2] J. Chatterjee, Y. Haik, and C.-J. Chen (2001) *J. Mag. Magn. Mat.* **225**:21. [3] D. Bassett in Principles of Polymer Morphology. R. Cahn, M. Thompson and I. Ward Eds. (1981) Cambridge University Press.

ACKNOWLEDGEMENTS: This project was sponsored by Therakos Inc.

POLYSILOXANE FLUID DISPERSIONS OF COBALT NANOPARTICLES IN SILICA SPHERES FOR USE IN OPHTHALMIC APPLICATIONS

M. Rutnakornpituk[1], V.V. Baranauskas[1], J.S. Riffle[1], J. Connolly[2], T.G. St. Pierre[2] and J.P. Dailey[3]

[1]Department of Chemistry, Virginia Polytechnic Institute and State University, Mail Code 0212, Blacksburg, VA 24061-5976, U.S.A., [2]Department of Physics, The University of Western Australia, Crawley, WA 6009, Australia, [3]Dept. of Ophthalmology, Case Western Reserve University, Cleveland, OH, U.S.A.

INTRODUCTION: Cobalt nanoparticles are of interest for biomedical applications because of their inherent higher magnetization relative to magnetite or maghemite. The bulk saturation magnetization of cobalt is theoretically 1400 emu/cm^3 while magnetite or maghemite is about 400 emu/cm^3 [1]. We have previously reported that nanophase-separated PDMS-PCPMS-PDMS triblock copolymers (Figure 1) can be effective

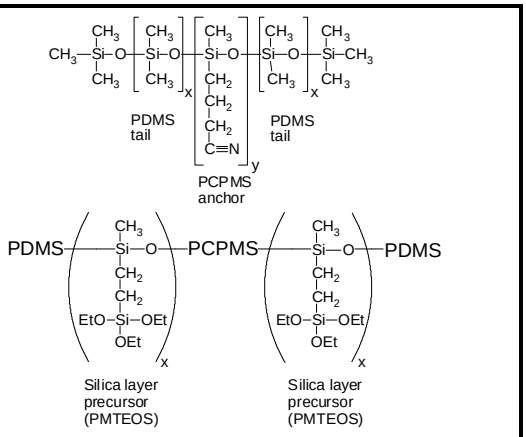

Fig. 1: Top – PDMS-PCPMS-PDMS triblock stabilizer showing the PCPMS cobalt anchoring segments and the PDMS stabilizing structures; Bottom – PDMS-PMTEOS-PCPMS-PMTEOS-PDMS pentablock stabilizer showing the anchor, tails and the silica layer precursors.

steric dispersion stabilizers for colloidal cobalt particles in polydimethylsiloxane (PDMS) carrier fluids [2-3]. The central nitrile-functional blocks coordinate with the cobalt surface as a so-called "anchor" block and the polydimethylsiloxane "tail" blocks extend into the PDMS to stabilize the particles in the dispersion. These fluids have saturation magnetizations of approximately 100 emu/g of cobalt, but magnetic measurements made over time show that their magnetic susceptibility decreases with aging for dispersions in contact with an air-containing atmosphere. This has been attributed to surface oxidation [3].

This paper describes our work on inhibiting environmental oxidation of magnetic cobalt nanoparticles by coating them with silica shells (Figure 2). Dicobalt octacarbonyl has been thermolyzed in the presence of PDMS-PMTEOS-PCPMS-PMTEOS-PDMS pentablock copolymers (figure 1). The PCPMS central block binds the cobalt and the PDMS tail blocks sterically stabilize the cobalt dispersion as described previously [2-3].

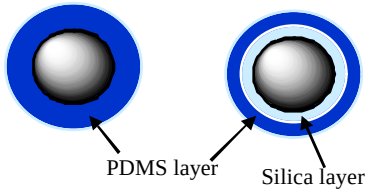

Fig. 2: Model for cobalt nanoparticles coated with a thin "pseudo-silica" interlayer, and surrounded with a PDMS steric stabilizer. These protected cobalt nanoparticles disperse readily in biocompatible PDMS carrier fluids to provide cobalt ferrofluids.

The PMTEOS blocks serve as precursors for the nanoparticle coating process. Since these precursor blocks are covalently bound to the segment which is coordinated to the cobalt nanoparticle surfaces, these silica precursors are uniquely positioned to form a tight "pseudo-silica" protective interlayer. After forming the nano-cobalt, the PMTEOS blocks are condensed to form a thin protective layer at the nanoparticle surfaces. Oxidative aging studies are underway, and will be reported in a separate paper in this symposium [4]. It appears that coating the particles with silica can retard any oxidation kinetics significantly.

METHODS: *Synthesis of PDMS-PMVS-PCPMS-PMVS-PDMS pentablock copolymers (PMVS is poly(methylvinylsiloxane).* A procedure for preparing a copolymer with 15000 g/mol PDMS, 2000 g/mol PMVS and 2000 g/mol PCPMS blocks is provided. The first part of the copolymer synthesis involves preparing controlled molecular weight PCPMS oligomers with terminal lithium siloxanolates. D_4CN (12.5 g) and 0.24 g (0.01 mol) lithium hydroxide were charged to a 500-mL roundbottom flask equipped with a mechanical stirrer and nitrogen purge. The mixture was stirred at 140 °C for at least 48 hours to reach thermodynamic equilibrium. The ratio of cyclics to linear species at equilibrium monitored by GPC was 27 wt% small cyclics and 73 wt% linear chains. After equilibrium was achieved, 250 mL

of dichloromethane was added to the macroinitiator via cannula. Twenty-two mL of trimethyltrivinylcyclotrisiloxane (D_3-vinyl) was added along with 12.5 mL THF as a reaction rate promoter (≈5 vol.% of the total volume). Five volume percent of the promoter was added to all block copolymer reactions irrespective of the block molecular weights. ^{1}H NMR was used to monitor the reaction progress by observing the disappearance of the signals at 0.23 ppm from the methyl protons in D_3-vinyl and the appearance of the signals at 0.14 ppm owing to methyl protons in linear PMVS blocks. After the reaction reached 85% conversion, the solution was transferred to a flame dried 1000-mL roundbottom flask filled with argon via cannula. A 200-mL aliquot of a D_3-dichloromethane solution (0.85 g D_3 per mL) was added along with an additional 20 mL THF. Another 150 mL of dichloromethane was added to bring the reaction volume to ≈600 mL and to obtain a clear solution. The disappearance of the D_3 protons at 0.14 ppm was monitored by ^{1}H NMR. The reaction was allowed to proceed at room temperature to obtain 85% monomer conversion. The pentablock copolymer was terminated with an excess of trimethylchlorosilane (4.4 mL) via syringe and stirred for 30 minutes. The solution clouds upon termination due to precipitation of LiCl. The excess trimethylchlorosilane and the dichloromethane solvent were removed under reduced pressure. The viscous copolymer was diluted with chloroform and washed repeatedly with water to remove the lithium chloride. The copolymer-chloroform solution was precipitated into methanol to remove nitrile containing siloxane cyclics (from the central block equilibration step) and the THF promoter. The methanol phase was decanted, and the polymer was dried at 80 °C under vacuum overnight. The block molecular weights and the total molecular weights of the triblock copolymers after purification were established using a combination of titration and NMR measurements.

Synthesis of PDMS-PMTEOS-PCPMS-PMTEOS-PDMS protective steric stabilizers. An exemplary procedure describes a hydrosilation reaction of a pentablock copolymer containing 2000 g/mol PMVS, 2000 g/mol PCPMS, and 15000 g/mol PDMS blocks with triethoxysilane in a 2000 g/mol PDMS carrier fluid. Variations of this reaction were conducted in either toluene, octamethylcyclotetrasiloxane (D_4), hexamethyldisiloxane or cyclohexane as reaction media. An important advantage of using low molecular weight solvents over using 2000 g/mol PDMS is that the sol-gel reactions can be conducted under relatively dilute conditions, then they can be removed in vacuo to concentrate the magnetic component in the mixture.

The reaction apparatus consisting of a 250-mL 2-neck roundbottom flask equipped with a mechanical stirrer and argon purge was flame-dried under argon. Twenty mL of 2000 g/mol PDMS and 1g of a PDMS-PMVS-PCPMS-PMVS-PDMS pentablock copolymer were charged with stirring. Triethoxysilane (0.25 mL) and 0.09 mL (0.5 wt%) platinum divinyltetramethyldisiloxane complex catalyst (Karstedt's catalyst) in xylene (2.1–2.4 wt % Pt) were charged to the reaction flask with stirring to hydrosilate the vinyl-containing blocks with Si-H groups from triethoxysilane. A stoichiometric ratio of triethoxysilane to vinylsilane units was used in all cases. The reaction was allowed to proceed for 2-3 days at 55 ^{o}C. ^{1}H NMR was used to monitor the reaction progress by observing the disappearance of vinyl peaks (δ=5.8-6.1 ppm) and the Si-H peak (δ=4.3 ppm). Approximately 2000 g/mol PDMS carrier fluids were prepared by the equilibrium ring-opening polymerization of D_4 with triflic acid as a catalyst. The detailed discussion of the carrier fluid synthesis has been reported previously [2].

Synthesis of a cobalt nanoparticle dispersion and formation of the silica protective layer. One gram of $Co_2(CO)_8$, 1 g of a PDMS-PMTEOS-PCPMS-PMTEOS-PDMS pentablock copolymer and 20 mL of solvent were dissolved at room temperature irrespective of the reaction medium. The reaction proceeded at 45 °C for 45 min. The reaction temperature was raised to 120 °C to yield a greenish-brown solution and maintained at this temperature for 16 h for reactions conducted in 2000 g/mol PDMS or 2 h for the reactions conducted in other solvents. Upon reaction completion, the mixture was slowly cooled to room temperature under an argon purge. The reaction mixture was diluted with 80 additional mL of solvent when using hexamethyldisiloxane, D_4 or toluene, but was not diluted for the case of using PDMS as the solvent. Thirty-five μl of O_2-free water was added along with 21 μl of dibutyltin diacetate (DBTA) catalyst to condense ethoxysilanes and form a "pseudo-silica" network. The dispersion was stirred at room temperature under argon for a week. The concentration of water added to the reaction was estimated from the concentration of ethoxy groups in the copolymers. One mole of water was used for every two moles of ethoxy groups.

Specified cobalt concentrations of the reactions conducted in 2000 g/mol PDMS carrier fluids were

achieved by introducing an appropriate amount of PDMS at the beginning of the reaction to obtain the targeted cobalt concentration. For reactions conducted in other solvents, dispersions with specified cobalt concentrations in PDMS carrier fluids were prepared by transferring an aliquot of the silica-coated cobalt dispersion in the original solvent to a vial, diluting the sample with the desired amount of PDMS, and then removing the solvent under reduced pressure.

Characterization: TEM micrographs were obtained using a Philips 420T TEM run at 100kV. The TEM samples of the cobalt dispersions were prepared by diluting the dispersions with toluene to obtain the color of "weak tea." The solutions were cast onto a carbon-coated grid and the toluene was evaporated. Magnetization measurements of the cobalt fluids with specified cobalt concentrations were made on a Standard 7300 Series Vibrating Sample Magnetometer (VSM) System (Lake Shore Cryotronics, Inc.). Measurements were made in applied fields ranging from 8000 Oe to –8000 Oe with 0.1 emu sensitivity.

RESULTS AND DISCUSSION: The materials have been developed to function in specific clinical applications. The first application is for a silicone magnetic fluid for use in retinal detachment surgery. This application requires long-term placement of the nanocobalt dispersion in the eye. The silica coating is necessary to provide protection against local and systemic toxicity, and to provide stable magnetic properties over time. The second application for coated cobalt nanoparticles is magnetic field-directed drug delivery. The polymer dispersants in this case will require modification to make them hydrophilic. This application requires the same protection against toxicity, and also requires strict size regimentation into the 10nm range to facilitate renal excretion of the nanoparticles.

The formation of silica-protected cobalt nanoparticle dispersions in PDMS fluids can be considered in three steps: (1) Formation of the magnetic cobalt nanoparticles, (2) Condensation of the "pseudo-silica" protective interlayer at the cobalt surface, and (3) Transfer of the protected cobalt particles to PDMS with concurrent concentration of the cobalt as the reaction solvent is removed. One principle in the cobalt formation step was to design reaction conditions whereby the organocobalt precursor would diffuse into the core of block copolymer micelles (formed by the stabilizer in solution) and would react within that core. This yields well-coated, non-aggregated cobalt nanoparticles [2-3]. Ethoxysilane groups in the copolymers were then condensed essentially to form silica shells around the particles and inhibit oxidation. It is important to conduct this step in a reaction medium that allows the PMTEOS precursor block of the stabilizer to contract, tightly condense, and form a "pseudo-silica" thin film on the particle surfaces. We hypothesize that the nature of the interaction between the blocks comprising the silica layer precursor (PMTEOS) with the solvent for this step is an important consideration to achieve "tight" protective layers. If these blocks extend too far into the solvent, inter-particle condensation rather than the desired intra-particle condensation may be significant.

Toluene is a good solvent for PDMS but a poor solvent for PCPMS. We have previously conducted both surface tension measurements and dynamic light scattering of toluene solutions of PDMS-PCPMS-PDMS triblock copolymers and the results suggest the desired micellar structures which are probably the reaction sites for particle formation [2]. It is hypothesized that the pentablock copolymers also form micellar solutions in D_4, hexamethyldisiloxane, and 2000 g/mol PDMS, where the PCPMS is concentrated in the micelle cores and long PDMS tail blocks protrude outward into the media to form the micelle coronas. PMTEOS blocks located between PDMS and PCPMS blocks are able to form a silica layer around the particles during the sol-gel process.

Dicobalt octacarbonyl was dissolved in pentablock micellar solutions at room temperature, then the mixtures were heated to evolve the carbon monoxide ligands. In all cases, this step of the reactions was conducted using 1g of copolymer and 1g of $Co_2(CO)_8$ in 20 mL of the reaction medium. Further discussion of similar cobalt dispersion reactions using triblock stabilizers have been reported previously [2-3]. Thermolysis of the dicobalt octacarbonyl to form magnetic cobalt nanoparticles encased in pentablock copolymers was successful in hexamethyldisiloxane, PDMS, D_4 and toluene, but not in cyclohexane. These cobalt dispersions were transparent, dark red-brown liquids.

The cobalt nanoparticles prepared in toluene, hexamethyldisiloxane and PDMS have an average particle diameter of 10 nm with relatively narrow size distribution. As will be further described below, D_4 appears to be a particularly promising solvent for these reactions, but early results show a somewhat bimodal particle size distribution, and further investigation will be required (figure 3).

One objective has been to investigate effects of the nature of the solvent in the sol-gel condensation step (step 2) with respect to how tightly the silica layer forms around the particle surfaces. Small (stoichiometric) amounts of O_2-free water and DBTA catalyst were introduced into the stable cobalt dispersions (in toluene, D_4, hexmethyldisiloxane and 2000 g/mol PDMS) to condense ethoxysilane pendent groups. Quantitative reaction conditions were established by monitoring the elimination of ethanol using ^{1}H NMR. Some aggregation was observed when the sol-gel reactions were conducted in hexamethyldisiloxane, but the other solvents produced stable silica-protected cobalt nanoparticle dispersions.

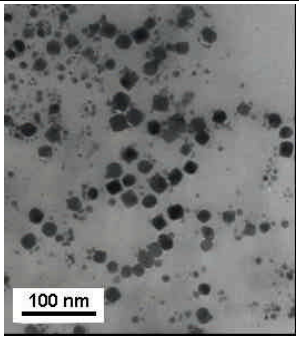

Fig. 3: A TEM micrograph of the dispersions prepared in D_4..

The final step in the process is to concentrate the dispersions as they are transferred to PDMS to increase the magnetic response of the desired PDMS fluids. While PDMS is an effective solvent for forming the particles, it cannot be easily removed due to its polymeric nature. Early results from this phase of the research show that aggregation occurs during the concentration step if the particles are produced in toluene, but that no aggregation occurs when the protected particles are synthesized in D_4 (Figure 3). Early studies suggest that a bimodal particle size distribution can form, and control over this aspect will require further investigations. A significant decrease in magnetic susceptibility of the dispersions prepared in toluene was also observed upon concentration, whereas the magnetic susceptibility of those prepared in D_4 is promising. Consequently, the use of D_4 as a reaction solvent may allow for a significant increase in the magnetic susceptibility of a material since higher cobalt concentrations can be achieved.

Magnetic properties of the cobalt dispersions conducted in PDMS were monitored during the sol-gel reactions. Approximately 10% loss in saturation magnetization occurs during the process (Figure 4). The dispersions containing silica-coated particles prepared in 2000 g/mol PDMS were sealed under argon or air-containing atmospheres to study their oxidative stability over time. These early magnetic measurements indicate that coating the particles with silica thin films inhibits oxidation. Results suggest some loss in magnetic properties in the first two months, then the materials appear to stabilize. These aspects will undoubtedly require longer-term aging studies. The aging characteristics of stable dispersions containing higher concentrations of cobalt prepared in D_4 are also under investigation.

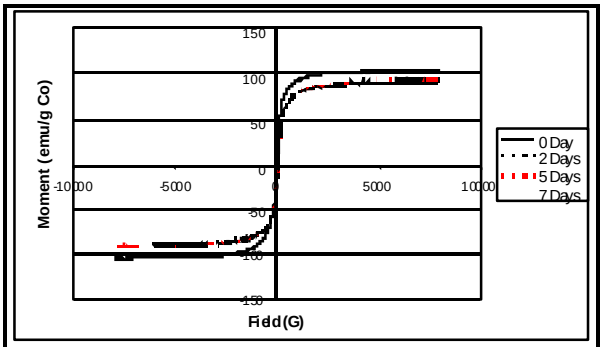

Fig. 4: Specific magnetization vs applied field curves during the sol-gel silica coating process conducted in 2000 g/mol PDMS.

CONCLUSIONS: Well-defined cobalt nanoparticle dispersions have been successfully prepared in D_4 and 2000 g/mol PDMS carrier fluids in the presence of PDMS-PMTEOS-PCPMS-PMTEOS-PDMS pentablock copolymer micelles. This copolymer fills the dual role of both a dispersion stabilizer and a precursor for a protective nanoparticle coating process. Nanoscale particles (on the order of 10-20 nm in diameter) result. Magnetic measurements suggest that coating the nanoparticles with silica thin films slows the oxidation process significantly.

REFERENCES: [1]B. Berkovski and V. Bashtovoy, eds., Magnetic Fluids and Applications Handbook. 1996, Begell: New York. [2]J.P. Stevenson, M. Rutnakornpituk, M. Vadala, A.R. Esker, J.S. Riffle, S.W. Charles, S. Wells, and J.P. Dailey, J. Magn. Magn. Maters., 225(1-2), 47-58 (2001). [3]M. Rutnakornpituk, M.S. Thompson, L.A. Harris, K.E. Farmer, A.R Esker, J.S. Riffle, J. Connolly and T.G. St. Pierre, Polymer, 43, 2337-2348 (2002). [4]J. Connolly, T.G. St. Pierre, M. Rutnakornpituk and J.S. Riffle, "Silica Coating of Cobalt Nanoparticles Increases their Magnetic and Chemical Stability for Biomedical Applications," Proc. 4th Int'l Conf. On Scientific and Clinical Applications of Magnetic Carriers.

ACKNOWLEDGEMENTS: The authors gratefully acknowledge the financial support of the Orris C. and Beatrice Dewey Hirtzel Memorial Foundation, the Carilion Biomedical Institute and the Lord Foundation.

SILICA COATING OF COBALT NANOPARTICLES INCREASES THEIR MAGNETIC AND CHEMICAL STABILITY FOR BIOMEDICAL APPLICATIONS

J. Connolly[1], T.G. St. Pierre[1], M. Rutnakornpituk[2], J.S. Riffle[2]

[1]*Department of Physics, The University of Western Australia, Crawley, WA 6009, Australia*

[2]*Department of Chemistry, Virginia Polytechnic Institute and State University, Mail Code 0212, Blacksburg, VA 24061-5976, U.S.A.*

INTRODUCTION: Cobalt-based magnetic fluids designed for possible use in medical applications have been synthesized. The magnetic properties of silica-coated and non-silica-coated cobalt particles are compared and used to probe the chemical nature of the particles. Measurement of the magnetic properties of frozen ferrofluids gives insight into the chemical stability and structure of their particles and enables comparisons of the properties of magnetic fluids prepared by different methods.

METHODS: The magnetic fluids studied consist of a suspension of metallic cobalt nanoparticles in polydimethylsiloxane (PDMS) carrier fluid[1]. In two of the magnetic fluids, the particles are stabilised against aggregation by a triblock copolymer: poly[dimethylsiloxane-b-(3-cyanopropyl)methylsiloxane-b-dimethylsiloxane] (15kPDMS-2kPCPMS-15kPDMS). The central polymer block binds to the cobalt particles through CN-Co coordination and the two outer blocks act as tails to increase stability. The remaining two magnetic fluids were prepared in PDMS fluids using a pentablock copolymer: 15k PDMS-2kPMTEOS-2kPCPMS-2kPMTEOS-15kPDMS[2]. Following the cobalt nanoparticle formation, the additional PMTEOS blocks were condensed to form a silica coating at the nanoparticle surface. In both methods, the cobalt particles are prepared through thermal decomposition of $Co_2(Co)_8$ in copolymer micelles using toluene as the solvent fluid. The particles are then transferred to a PDMS carrier fluid. After production, one sample produced by each method was exposed to air for the duration of the experiments and another sealed under an argon atmosphere. The differences in production are summarised in Table 1.

Magnetic measurements were performed using a magnetic susceptometer incorporating a superconducting quantum interference device sensor (MPMS-7, Quantum Design). The freezing point of the fluids was approximately 222 K and initially magnetic fields were not applied above this temperature so the particles would not be exposed to field gradients which may cause aggregation of the particles in the fluid. Magnetisation in a 100 Oe field was measured from 5-220 K after the fluids had been cooled from 220 K (i) in zero field and (ii) in a 70 kOe field.

Table 1. Production method, exposure to atmosphere after production, and final composition of each fluid.

Fluid Label	Production Method	Exposure	% cobalt
A	no coating	air	1.9
B	no coating	argon	1.6
E	silica coating	air	2.0
F	silica coating	argon	2.0

Cobalt specific magnetization (σ) vs. applied field (H) behaviour of the fluids was measured from -70 kOe to 70 kOe at 5 K. The σ vs H responses were measured both after cooling from 220 K in a zero field and a 70 kOe field.

The σ vs H behaviour at 5 K was studied over time for all samples to measure the chemical stability of the particles. After this series of measurements, σ vs H behaviour at fields up to 1 kOe at 298 K was measured. Particle size was studied with electron microscopy.

RESULTS: The zero-field-cooled and field-cooled temperature dependent cobalt specific magnetisations in 100 Oe are shown in Figure 1. The two families of particles have different peak zero-field cooled magnetisation temperatures, the temperatures of the peaks representing a characteristic magnetic blocking temperature for the sample. The silica-coated particles have lower characteristic blocking temperatures than the non-silica-coated particles. The characteristic blocking temperatures of the non-silica-coated particles appear to be above the freezing points of their fluids. Measurement of the temperature dependent magnetisation of the fluid above this point provides no further information about the size

distribution of the particles as they rapidly rotate into the field direction.

There is a second clear peak at 15 K in the curves of the silica-coated particles. This is not evident in the curves for the non-silica-coated particles. For the non-silica-coated particle dispersions, A and B, the bifurcation temperature of the field-cooled and zero-field-cooled magnetization in 100 Oe is above the melting temperature. The bifurcation temperature for samples E and F is 160 K.

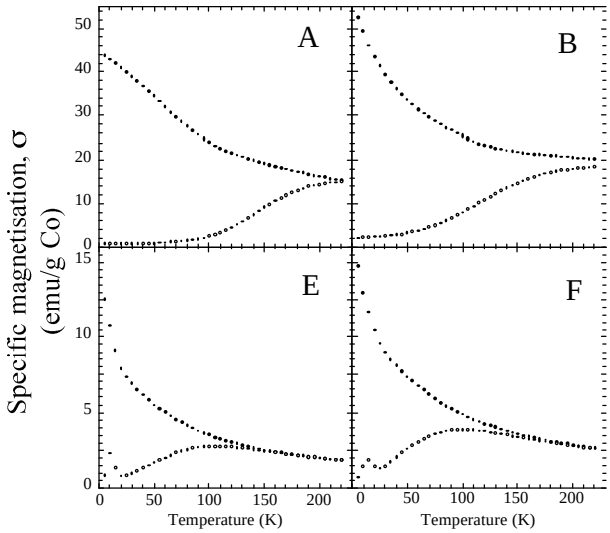

Fig. 1: Temperature dependent specific magnetisation of cobalt particles. Filled dots are field-cooled measurements, empty dots are zero-field cooled measurements. The letters on the plots refer to the sample measured

The zero-field-cooled and field-cooled magnetic hysteresis behaviour of samples at 5 K is shown in Figure 2. The centres of the field-cooled magnetic hysteresis loops at 5 K are shifted to negative fields for all samples. Sample B is almost magnetically saturated at 70 kOe and has a smaller negative bias field than sample A. The silica-coated samples (samples E and F) have loop shifts which are similar to that of the argon-sealed non-silica-coated sample (B). However, the maximum specific magnetisation is much less than that of sample B.

It is clear from the hysteresis loops that the samples have not reached magnetic saturation at 70 kOe. The behaviour of the magnetization at high fields has been modelled by fitting the sum of a Brillouin function (representing magnetization of paramagnetic species) and a constant (representing the expected saturated magnetization of metallic cobalt particles, $\sigma_{s\text{-}met}$) to the magnetisation for fields greater than 30 kOe. The constant, $\sigma_{s\text{-}met}$, and the atomic angular moment quantum number J were allowed to vary freely during the fitting procedure. The value of J from the fit ranged from 0.35 to 0.84.

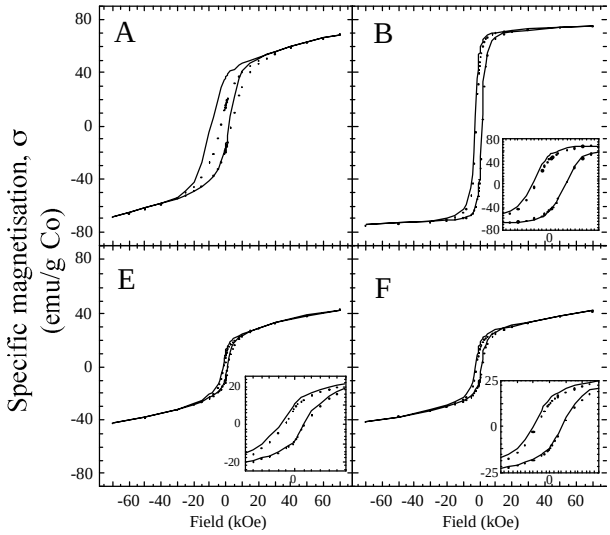

Fig. 2: Magnetic hysteresis loops of cobalt particles measured at 5K after cooling in zero field (closed circles) and in 70 kOe field (line). The letters on the plots refer to the sample measured. The inset plots are from -6 kOe to 6 kOe.

The magnetisation loss per day is calculated from a linear fit to $\sigma_{s\text{-}met}$ against time (Figure 3). The non-silica-coated particles exposed to air (sample A) clearly lose more specific magnetisation per day than the other particles. A linear fit to the $\sigma_{s\text{-}met}$ vs time data using a Levenberg-Marqhardt algorithm yields the uncertainties on the rates of saturation magnetisation decay (shown as error bars in Figure 3).

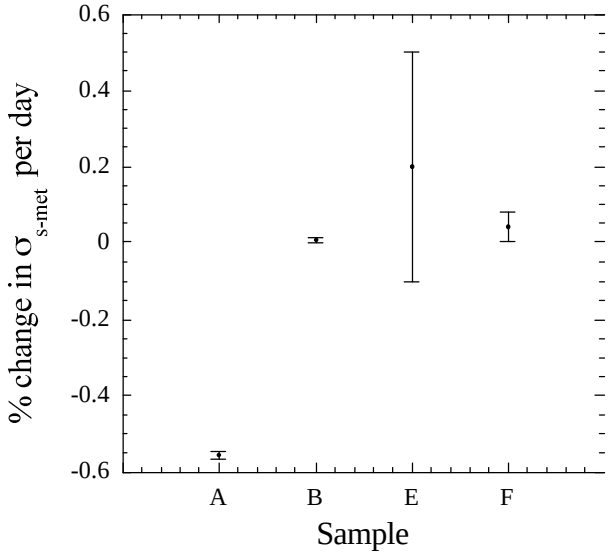

Fig. 3: Change in $\sigma_{s\text{-}met}$ per day for all samples.

All fluids show non-hysteretic σ vs H behaviour at 298 K. There is no remanent magnetisation observable and the particles do not reach saturation at the fields studied. Electron microscopy images show the non-silica-coated particles cluster into

groups of 2-4, while the silica-coated particles do not appear to cluster. The silica-coated particles are smaller than the non-silica-coated particles.

DISCUSSION & CONCLUSIONS: The peak in the zero-field-cooled temperature dependent magnetisation of an ensemble of particles gives an indication of the average size of the magnetic core of the particles[3]. The temperature of bifurcation of the zero-field and field-cooled curves is related to the volume of the largest particles in the ensemble. The lower temperature of peak magnetisation and bifurcation for the silica-coated particles indicates a smaller average magnetic core size of the particles. The smaller overall size of the particles as observed by electron microscopy supports this. Particle size differences alone may not entirely account for the much higher temperature of the peak in the zero-field-cooled magnetisation of the non-silica-coated samples. The electron microscopy images of the particles clearly show clustering of the non-silica-coated particles into groups of 3-5. This clustering will have a demagnetising effect on each of the particles in a cluster. The energy needed to align the magnetization of each particle with the magnetic field will be greater for particles in a cluster than for an isolated particle. This means that in the case of clustered particles the temperature of the maximum in the zero-field-cooled peak may not be simply related to particle size. Although the non-silica-coated particles have both a characteristic blocking temperature and a bifurcation temperature above the measurement range this does not necessarily mean there will be a remanent magnetisation at room temperature. It is unclear whether the clustering observed by electron microscopy is present when the particles are in the fluid state. Nevertheless, the time for rotation of a cluster of particles is still less than the measurement time. From the 298 K σ vs H measurements, the measured remanence of Samples A and B above the freezing point of the liquid is zero.

The significant loss of specific saturation magnetisation $\sigma_{s\text{-}met}$ with time for the air-exposed non-silica-coated particles (A) indicates a chemical change in the particles over time. This observation strongly suggests that the particles are steadily oxidizing. This sample also has a larger shift of the centre of its field-cooled magnetic hysteresis loop than any other samples. Field-cooled magnetic hysteresis loops can exhibit a shift in the centre of the loop when antiferromagnetic surface states on the particle are coupled to the core[4]. The susceptibility of cobalt to oxidation is well known so the shell is most likely cobalt oxide. As neither a significant loss of saturation magnetisation nor a large field-cooled hysteresis loop shift are evident in the argon-sealed non-silica-coated sample (B), an oxidation effect is the most likely explanation for these observations rather than particle-particle interaction effects.

The air-exposed and argon-sealed silica-coated particles (samples E and F respectively) and the argon-sealed non-silica-coated particles (sample B) all have similar loop shifts. The similar loop shifts for air-exposed and argon-sealed silica-coated particles confirm that the silica coating does protect the cobalt particle from oxidation when the reaction process is complete and the particles are in the carrier fluid. As the production mechanism of silica-coated particles is very similar to that for the non-silica-coated particles, the stability of these particles against oxidation must be attributed to their silica coating. The antiferromagnetic ordering of the surface layer is probably a result of oxidation occurring at some point in the production process. However as yet it is unclear when or why these particles become oxidised.

The measurements give substantial evidence for multiple forms of cobalt in the suspensions. Together, the clear peak at 15 K in the zero-field-cooled magnetisation of the silica-coated particles, the paramagnetic signal in all the 5 K σ vs H measurements and the shift of the centre of all the field-cooled 5 K magnetic hysteresis loops suggest additional non-metallic cobalt species in the fluids. The second species may be a chemically different form of cobalt or a metallic cobalt with a different magnetic ordering. The chemical form of cobalt responsible for this component may be reaction intermediates or fully reacted species which have formed amorphous cobalt compounds instead of metallic cobalt particles. Alternatively, the second species may be surface cobalt with a different magnetic ordering and so different magnetic properties to the cobalt particle core.

The peak at approximately 15 K in the zero-field-cooled curves of the silica-coated particles may indicate a second population of particles with a much smaller core size in these samples. It is possible that clusters of cobalt, which have not formed into larger particles, are producing this peak. It is also possible that the silica coating produces a range of surface states which are not present on the non-silica-coated particles. The surface atoms involved in these states could be weakly magnetically coupled and so be observable as a peak in the zero-field-cooled curve at much

lower temperatures than that associated with the magnetically ordered core. They also may contribute to the paramagnetic signal observed in the σ vs H measurement at 5 K.

The value of J obtained from the Brillouin fit to the σ vs H measurement is lower than expected from theory. The reduced J value suggests that the magnetic moment of the paramagnetic cobalt atoms which contribute to this signal are quenched through interaction with other atoms. The binding of a ligand to a surface is known to quench the magnetic moment of the atoms on the surface. It may be these bound cobalt atoms which are contributing to the paramagnetic signal with a reduced magnetic moment as compared to bulk cobalt. The reduced J value may also be due to a surface spin structure where interactions between the spins prevent the paramagnetic magnetic moment reaching the bulk value. The shifted field-cooled hysteresis loops are usually a result of antiferromagnetic surface states on a particle. Possibly the particles are oxidised at some point in the production process and portions of the surface are antiferromagnetically ordered. The antiferromagnetically ordered states may force other surface atoms into partially antiferromagnetically aligned states, reducing their J value.

It is most likely that there is more than one form of cobalt which contributes to the observed magnetic behaviour. The measurements suggest some effects from the surface of the cobalt particles, as well as the possibility of amorphous paramagnetic cobalt species in the fluids. As yet, the contribution from each form of cobalt cannot be separated.

From this work it is clear that coating the cobalt particles with a polysiloxane based copolymer does not fully prevent oxidation of the particles. A shell of silica surrounding a cobalt core can be used to protect the particles against oxidation. The silica-coated particles have a lower specific saturation magnetisation and magnetic susceptibility, most probably because of an increase in antiferromagnetic or paramagnetic cobalt. The reduced volume of the magnetic core of the silica-coated particles ensures that they are superparamagnetic well below room or body temperature. The increased chemical stability of the silica-coated particles as compared to the non-silica-coated particles makes them more suitable for use in the human body.

REFERENCES: [1]M. Rutnakornpituk, M. S. Thompson, L. A. Harris, et al, (2002) *Polymer* **43:** 2337-2348. [2]M. Rutnakornpituk, V.V. Baranauskas, J.S. Riffle, et.al. (2002) Proc. 4th Int'l Conf. On Scientific and Clinical Applications of Magnetic Carriers. [3]M. Hansen, C. Johansson, M. S. Pedersen, et al, (1995) *J. Phys.: Condens. Matter*. **7**: 9267-9277. [4]J. Nogués and I. K. Schuller, (1999) *J. Magn. Magn. Mater*. **192**: 203-232.

MAGHEMITE@SILICA NANOPARTICLES FOR BIOLOGICAL APPLICATIONS

S. Mornet, F. Grasset*, J. Portier and E. Duguet

*Institut de Chimie de la Matière Condensée de Bordeaux ICMCB-CNRS, Université Bordeaux-1, 87 avenue du Dr Albert Schweitzer, F-33608 Pessac, France * Current address: Laboratoire des Verres et Céramiques, Institut de Chimie de Rennes, Université Rennes-1, Campus de Beaulieu, F-35042 Rennes, France*

INTRODUCTION

There is a great deal of interest in investigating new synthetic routes, controlling the size and the morphology, and understanding the overall behavior of nanoparticles. Magnetic nanoparticles are being studied in particular for their current and future applications in biology and medicine, including magnetic cell separation, magnetic resonance imaging contrast enhancement, magnetic transport of anti-cancer drugs [1].

In this field and especially for *in vivo* applications, the main challenges currently consist in (i) reducing the nanoparticle size for going through the majority of biological membranes, (ii) ensuring their stability in pH conditions of biological fluids and (iii) tailoring their surface in order to functionalize and/or develop strong interactions with specific biological components (dye, drug or effector grafting).

The magnetic nanoparticles, which are the most frequently studied, belong to the ferrite family, especially magnetite (Fe_3O_4) and maghemite (γ-Fe_2O_3). Many studies focused on ferrofluids, which are colloidal aqueous solutions (sols) of monodomain magnetic particles. Ferrofluids necessitate a sufficient electrostatic repulsion between particles [2]. Nevertheless, the zero point of charge (ZPC) of these iron oxides is close to 7. Aqueous ferrofluid dispersions therefore flocculate in the pH range of 5 to 9 and are stable only under highly acidic or basic conditions. On the other hand, the ZPC of SiO_2 is about 2-3 and therefore silica nanoparticles are negatively charged at pH 7 and consequently their dispersions in biological media would be stable.

For this reason we investigated the route consisting of encapsulating preformed maghemite nanoparticles in the ferrofluid state into silica. We hoped to obtain core-shell nanoparticles, denoted γ-Fe_2O_3@SiO_2, which (i) would form a stable dispersion in the pH conditions of biological fluids, (ii) would have sufficiently powerful magnetic properties and (iii) would have an easy surface chemistry thanks to the well-known reactivity of silica towards coupling agents, such as the numerous commercially available alkoxysilane derivatives.

The synthetic method was derived from the Stöber process of silica nanoparticles synthesis (based on the base-catalyzed polycondensation of tetraalkoxysilane) and developed in reverse microemulsion conditions [3]. This technique relies on the self-assembly nature of surfactants to push aqueous reactant into micelles. Due to the dynamic nature of micelles, aqueous components (including maghemite nanoparticles) can come together and react to form particles, which are constrained to the micelle size.

The goals of the present study are to (i) control the γ-Fe_2O_3@SiO_2 morphology thanks to the synthesis conditions, (ii) investigate their stability in water, their thermal behavior and their magnetic properties and (iii) use them, secondarily, as precursors for silica hollow nanospheres, obtained by a discriminatory dissolution of the magnetic cores.

METHODS

Materials: all the chemicals (from Aldrich) were of reagent grade and used without further purification.

Ferrofluid synthesis: cationic γ-Fe_2O_3 aqueous sols were prepared according to the Massart's method [2]. The Fe_3O_4 precipitate, obtained by alkalizing $FeCl_2$ and $FeCl_3$ (Fe^{2+}/Fe^{3+} = 1/2) aqueous mixture, was oxidized successively with 2 M HNO_3 and 0.33 M $FeNO_3$ solutions until the Fe^{2+}/Fe^{3+} ratio in the particles was lower than 0.05 and therefore until magnetite was converted to maghemite. After removing by centrifugation, the particles were peptized in 2 M HNO_3 solution under vigorous stirring in order to create positive surface charges. The acidic precipitate was isolated by decantation on a magnet, washed in acetone and dispersed in pure water at pH ≈ 2.5 in order to obtain an iron concentration of 0.125 M.

g-Fe_2O_3@SiO_2 synthesis: both types of surfactants were simultaneously used: an ionic one which is dioctyl sulfoccinate, sodium salt (AOT) and a nonionic one, which is polyoxyethylene (4) lauryl

ether (Brij®30). W/O microemulsions were prepared by adding the aqueous ferrofluid (whose pH was first adjusted with KOH in the range of 2.5-4.5) into a stirred solution of Brij®30/AOT (weight ratio 1/2) in heptane. Then, tetraethoxysilane (TEOS) was added. TEOS is an organophilic molecule and therefore is more readily dissolved in heptane than in aqueous micelles. Nevertheless, the presence of the acidic ferrofluid catalyzes TEOS hydrolysis. We supposed that after 15 min, the main part of TEOS has been pre-hydrolyzed and consequently has migrated into the micelles. Lastly, ammonia solution (30 wt.%) was added to catalyze the polycondensation of the prehydrolyzed TEOS into silica. The weight ratio of ferrofluid/TEOS/ammonia used in all experiments was 2.2/5.3/3. After 20 h, nanoparticles were washed with ethanol and chloroform to remove heptane and surfactant. The powder was dried at 60°C under vacuum for thermal, magnetic and BET studies.

g-Fe_2O_3@SiO_2 aqueous dispersion preparation: microemulsions were washed as previously described, but without the drying operation. Then, a 0.5 M KOH aqueous solution was added on the flocculate and mixed in a vortex agitator. The addition of 10 volumes of acetone allowed the mixture to flocculate. In order to obtain the alkaline dispersion, the flocculate was peptized, after centrifugation, by addition of water.

SiO_2 hollow spheres synthesis: the flocculates of γ-Fe_2O_3@SiO_2 were leached by 10 M HCl solution in order to dissolve the maghemite cores. The flocculates were washed with water and centrifuged to remove the $FeCl_3$, until the yellow color vanished. The so-neutralized flocculate was then peptized the alkaline way as for the γ-Fe_2O_3@SiO_2 flocculates.

Characterization techniques: transmission electron microscopy (TEM) experiments were performed with a JEOL 2000 FX operating at an accelerating voltage of 200 kV. Samples for TEM were prepared on copper grids coated with a carbon support film (Pelco International) by evaporating a drop of particles dispersion. Specific surface areas were measured by nitrogen adsorption (BET method) using a Micromeritics ASAP 2010. The zeta potential titrations were obtained using a Zetasizer instrument of Malvern Corporation. Magnetic measurements were achieved using a susceptometer MANICS and SQUID 5MPMS.

RESULTS AND DISCUSSION

Shape and size of nanoparticles: the morphology of the pristine γ-Fe_2O_3 nanoparticles was observed by transmission electron microscopy (TEM). It was observed that maghemite particles are spherical with a diameter ranging between 5-10 nm (Fig. 1). BET measurements gave a specific surface area of 130 m^2/g. The X-ray diffraction pattern at room temperature (not shown here) is consistent with the spinel structure.

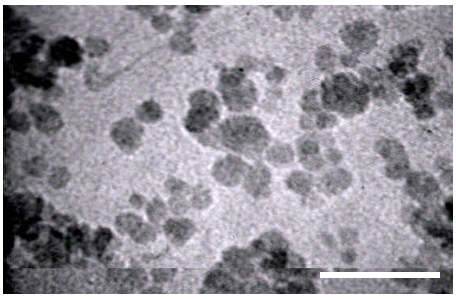

Fig. 1: TEM micrograph of g-Fe_2O_3 nanoparticles extracted from the ferrofluid (scale bar: 50 nm)

Fig. 2 displays TEM pictures of γ-Fe_2O_3@SiO_2 nanoparticles vs. the initial pH of maghemite ferrofluids. It can be noticed that, in the studied pH range, the lower the pH value, the best dispersed the maghemite nanoparticles and therefore the lower the number of magnetic cores per silica shell. So, when the value of pH is close to the flocculation pH of 5, the aggregates of maghemite form chains and the morphology of core-shell particles is less well-defined (Fig. 2e).

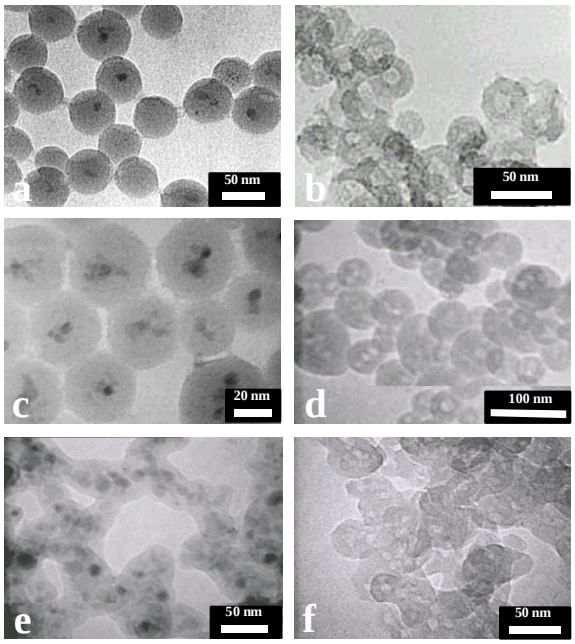

Fig. 2: TEM micrographs of g-Fe_2O_3@SiO_2 nanoparticles vs. the initial pH of maghemite ferrofluids (a : pH 2.5; c : pH 3.5; e : pH 4,5) and their corresponding silica hollow spheres (b, d and f, respectively).

For the particular condition of the ternary system (water/surfactant/heptane) used in this study, it appears that pH is the main parameter that governs the morphology of the γ-Fe_2O_3@SiO_2 nanoparticles and the number of maghemite cores per silica shell.

BET measurements gave a specific surface area of 440 m^2/g for core-shell particles displayed on Fig. 2a, which suggests that the silica shell is highly porous. This feature might allow the dissolution of the maghemite core.

The electron microscopy pictures of the silica hollow spheres confirm that the maghemite cores have disappeared (Fig. 2b, 2d and 2f). Their diameter is close to that of their parent core-shell particles (in the range of 50 nm), demonstrating the discriminatory mechanism of the dissolution process. The size and number of holes seem to depend directly on the size and number of maghemite cores. Their specific surface area is higher than that of their parent core-shell particles (480 m^2/g versus 440 m^2/g).

Properties of g-Fe_2O_3@SiO_2 ferrofluids: Zeta potential titrations as a function of pH (obtained by adding 0.01 M HNO_3 or KOH solutions) allowed to verify the value of 7 for maghemite ZPC and the flocculation of the nanoparticles in the pH range from 5 to 9 (Fig. 3). The presence of the silica shell decreased this value close to the silica ZPC (*i.e.* 2.5) and γ-Fe_2O_3@SiO_2 dispersions are stable for a pH higher than 5. However, it is well known that silica will readily dissolve under highly basic conditions.

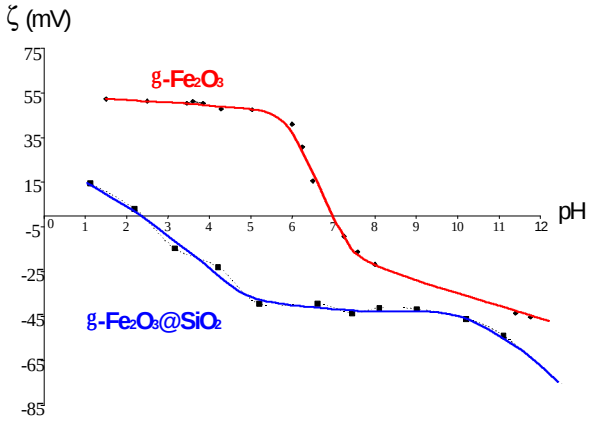

Fig. 3: Zeta potential titration as a function of pH of the g-Fe_2O_3 dispersion and g-Fe_2O_3@SiO_2 dispersion (synthesized from the ferrofluid in Fig. 2a with initial pH of 2.5).

Thermal behavior: As already observed for nanoparticles embedded in silica monoliths [4], the γ-Fe_2O_3 nanoparticles, obtained by drying the aqueous sol, transform into hematite (α-Fe_2O_3) at around 673 K, whereas the γ-Fe_2O_3 cores in the γ-Fe_2O_3@SiO_2 materials remain unaltered until 1273 K (100° step and aging at this temperature for 1 h ; X-ray diffraction patterns not shown here). α-Fe_2O_3 appears only at 1473 K, which is a further proof of the maghemite encapsulation by silica.

Magnetic properties: Typical zero field cooled (ZFC) and field cooled magnetization (FC) are plotted vs. temperature in Fig. 4. Such a behavior is characteristic of superparamagnetism and is due to the progressive blocking of the magnetization of smaller and smaller particles when temperature is decreasing. The temperature at which the ZFC and the FC curves get separated indicates the onset of blocking for the largest γ-Fe_2O_3 particles, while the maximum temperature in the ZFC curve can be related to the blocking temperature with the average volume.

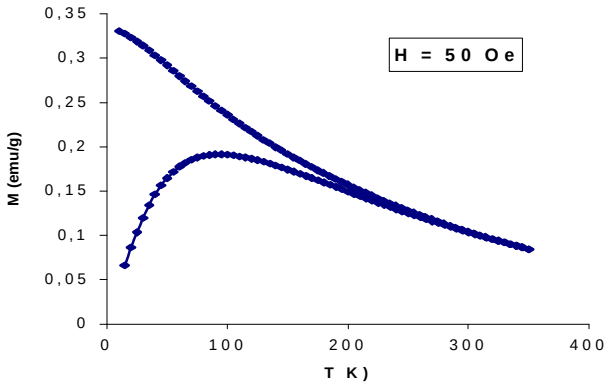

Fig. 4: ZFC and FC curves vs. temperature of g-Fe_2O_3@SiO_2 (synthesized from the ferrofluid in Fig. 2a with initial pH of 2.5).

The field dependent hysteresis loops were measured at temperatures both below and above the blocking temperature. Fig. 5 shows the hysteresis curves at 15 K and 150 K. The magnetization vs. data at 15 K displays some hysteresis and confirms that the γ-Fe_2O_3 nanoparticles are ferrimagnetic below the blocking temperature. The absence of coercive hysteresis at 150 K (above the blocking temperature) is characteristic of superparamagnetic particles. Fig. 6 shows the hysteresis loops at 15 K of γ-Fe_2O_3-silica annealed at different temperature. The observed magnetic behavior confirms that γ-Fe_2O_3 nanoparticles embedded in a silica shell remain stable until 1273 K and are in agreement with X-ray diffraction data. When the field is reduced, the magnetization M_r, known as the remnant magnetization at H = 0, remained identical until 1273 K. At 1473 K, the very weak signal observed was attributed to the transformation of the ferrimagnetic γ-Fe_2O_3 to the canted antiferromagnetic α-Fe_2O_3.

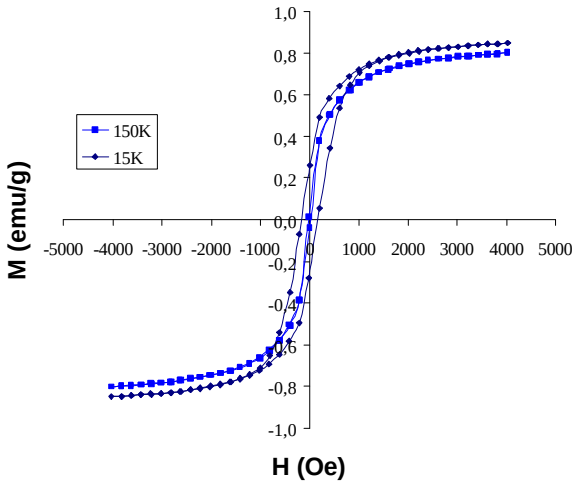

Fig. 5: Hysteresis loops at 15 K and 150 K of g-Fe_2O_3@SiO_2 nanoparticles.

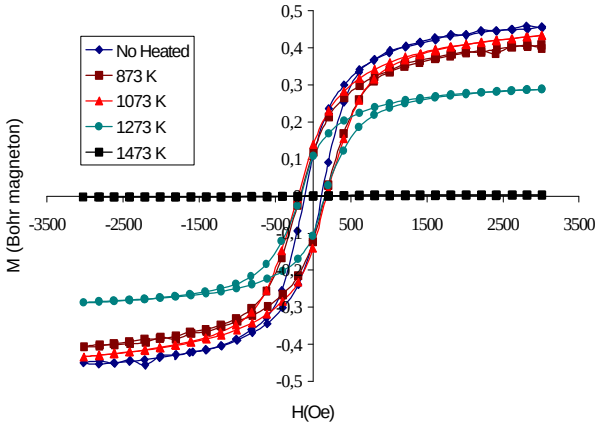

Fig. 6: Hysteresis loops at 15 K of g-Fe_2O_3@SiO_2 annealed at different temperatures.

CONCLUSION AND PERSPECTIVES

We have presented a reverse microemulsion technique, demonstrating the feasibility of synthesizing γ-Fe_2O_3@SiO_2 nanoparticles with a size of a few tens of nanometers. The initial pH of the ferrofluid seems to play an important role in the morphology of the materials and allows to control the number of magnetic cores per silica shell. These γ-Fe_2O_3@SiO_2 nanoparticles were dispersed in aqueous phase and the ZPC of the new ferrofluid was measured at pH 2.5. Maghemite nanoparticles with a silica shell may therefore be readily dispersed in water in the pH range from 5 to 11, making them stable in biological fluids. Magnetic experiments have shown that maghemite nanoparticles preserve their superparamagnetic properties, despite being embedded in silica shells.

Currently, further experiments are in progress to (i) investigate new water/AOT/Brij30®/heptane ratios in order to vary the micelle size and therefore the thickness of the silica shell and (ii) functionalize the surface of the silica shells with various alkoxysilane derivatives and then with molecules of biological and medical interest.

Concerning the silica hollow nanospheres, our study has demonstrated the possibility to obtain them through a discriminatory dissolution technique with a good correlation between the magnetic core number and the hole number. We are focusing our efforts on their potential applications as (non magnetic) drug carriers or as nanoreactors for (magnetic) materials whose synthesis in nanoparticle form is not known. For such applications, the core would be loaded with the precursor and the silica shell could act as a rigid template. It would be stable even during the high temperature treatment of solid state chemistry, and finally would be dissolved under basic conditions to release the new materials.

REFERENCES: [1] *Scientific and Clinical Applications of Magnetic Microspheres* (1997), (eds. U. Häfeli, W. Schütt, J. Teller and M. Zborowski) Plenum Press, New York. [2] R. Massart (1982) *IEEE Trans Magn* **17**:1247. [3] S. Mornet, F. Grasset, E. Duguet and J. Portier (2000) *Proceedings of the Eighth International Conference on Ferrites, Kyoto and Tokyo*, ed. by the Japan Society of Powder and Powder Metallurgy, pp 766-8. [4] E. Tronc, C. Chanéac and J.P. Jolivet (1998) *J Solid State Chem* **139**:93.

ACKNOWLEDGMENTS: The Groupe d'Intérêt Scientifique "Vectorisation *in vivo*" is gratefully acknowledged for its financial and scientific support. The authors are deeply grateful to L. Albingre for BET measurements, E. Lebraud for the in-temperature X-ray diffraction measurements and E. Sellier for carrying out the electron microscopy observations.

IRON SUBSTITUTED APATITES: A RESORBABLE BIOMATERIAL WITH POTENTIAL MAGNETIC PROPERTIES

K.A. Gross, R. Jackson, J.D. Cashion, & L.M.Rodriguez-Lorenzo

School of Physics & Materials Engineering, PO Box 69M, Monash University, VIC 3800, Australia

INTRODUCTION: Localized hyperthermia shows promise as a treatment modality for tumor eradication [1]. The most common approach, for difficult to access locations, in the body has been to manufacture a thermoseed that can be heated remotely. Ferri-magnetic materials are suitable thermoseeds that produce hysteresis heating by application of an alternating magnetic field. In addition to displaying magnetic properties for heating a material for hyperthermia also needs to be biocompatible.

Biocompatible ferri-magnetic glass ceramics have been identified as suitable candidates for hysteresis heating [2]. These glass ceramics have been based upon the ferric oxide - calcia - silica system [3-6]. Heat treatment of the glass in a reducing atmosphere nucleates the magnetite phase. Another approach has been to combine both a ferric and ferrous ions in the reactants to nucleate magnetite [7]. These glass ceramics have been optimized for hysteresis heating and are relatively stable in the body. Ideally, the most suitable thermoseed would be stable during heating and resorb at a later time. At present only biodegradable polymers have been utilized as soluble carrier materials for ferromagnetic materials [8].

The apatite structure is relatively flexible in the range of substitutional elements [9]. Previous work has indicated that the inclusion of ferrous ions during synthesis has produced an apatite structure [10]. While processing of sintered zinc, silicon, strontium substituted apatites have been investigated no information is available for iron containing apatites. This work will investigate synthesis and high temperature processing of an iron containing apatite to determine the suitability in production of a magnetite containing apatite ceramic.

METHODS: Apatites were synthesized at 37 °C by the drop-wise addition of di-ammonium hydrogen phosphate to a solution containing metal nitrate. As a reference, the first reaction employed a 1M calcium nitrate aqueous solution to produce hydroxyapatite, labeled as R1. In the second reaction, iron was added at a concentration of 10 mol. % to partially replace the calcium in the apatite, $Ca_{10}(PO_4)_6(OH)_2$ resulting in a compound designated as R2. In the third reaction, iron was added at 10 mol. % in excess to produce R3. Metal nitrate solutions mixed to a volume of 1 liter were adjusted to a pH of 9.4 with ammonium hydroxide before addition of the phosphate.

During the course of the reaction a pH stat was used to maintain the set pH level by addition of 10 vol.% of ammonium hydroxide. The precipitate was allowed to mature for 24 hours, washed with 2 liters of deionized water, filtered in a Buchner funnel and then washed with 1 liter of ethanol before drying at 80 °C. The powder cake was heat treated at 1150 °C in either air or nitrogen in a tube furnace for 3 hours.

The specific surface area was determined on the synthesized powders using the BET method. The 5 point method with nitrogen was performed using a Micromeritics Gemini 2360 (Norcross GA, USA) to determine the specific surface area.

The powders were characterised by X-ray diffraction, Fourier transform infrared and Mossbauer spectroscopy. X-ray diffraction patterns were obtained using a Rigaku Geigerflex diffractometer, using copper K_α radiation at 22.5 mA and 40 kV passing through a 0.3° receiver and 0.5° divergence slit. A scan rate of 0.5° per minute and a step size of 0.05 degrees were selected over a two theta range of 20-60°. Fourier transform infra-red spectra were recorded using the KBr pellet technique in a Perkin Elmer 1600 Series FTIR over a 400 – 4000 cm^{-1} range at a resolution of 4 cm^{-1}.

The samples were crushed with a pestle and mortar and 50 mg/cm^2 of each sample was sealed into perspex holders. The Mossbauer spectra were taken using a conventional constant acceleration waveform with calibration using α-iron.

RESULTS: The surface area of the dried hydroxyapatite, R1, was 50 m^2/g compared to a value of 70 m^2/g for the iron modified apatite powders, R2 and R3. The smaller ionic size of iron compared to calcium has aided the nucleation

process or prevented crystal growth, resulting in fine crystallites.

All apatite powders, (R1, R2 and R3) after drying indicated the same absorption peaks in the infrared spectra, Fig. 1. The presence of iron does not seem to have influenced the chemical bonding within the apatite structure.

After synthesis, both R2 and R3 appeared mud-brown compared to a white color for R1. Heating of the iron containing powders to 1150 °C resulted in a color change to red when heated in nitrogen and to gray when heated in nitrogen.

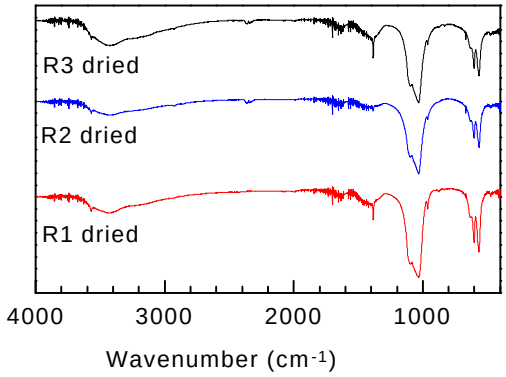

Fig. 1: Fourier transform infrared spectra of dried hydroxyapatite (R1), iron substituted hydroxyapatite (R2) and hydroxapatite with excess iron (R3).

X-ray diffraction patterns revealed a change in phase composition. When heated in air, R2 formed both tricalcium phosphate and hematite, while in nitrogen no hematite was observed, Fig. 2.

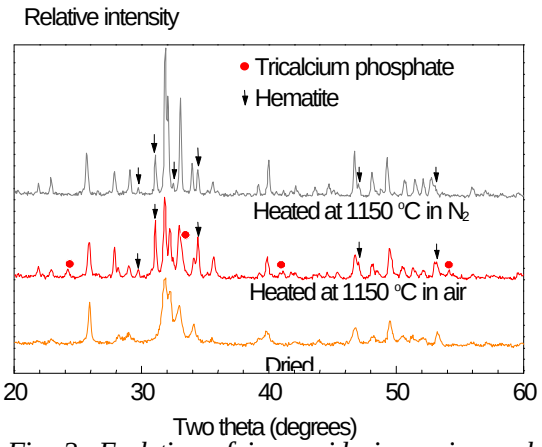

Fig. 2: Evolution of iron oxide in an iron substituted apatite (R2) upon heating in air & nitrogen.

R3 also showed the presence of hematite when heated in air and the absence of this phase when heat-treated in nitrogen, Fig. 3. A diffraction peak shift and a change in the relative peak intensities has occured. The absence of hematite in the sample heated in nitrogen, a shift in the apatite diffraction peaks and a change in relative peak intensities all suggest iron incorporation into the apatite lattice.

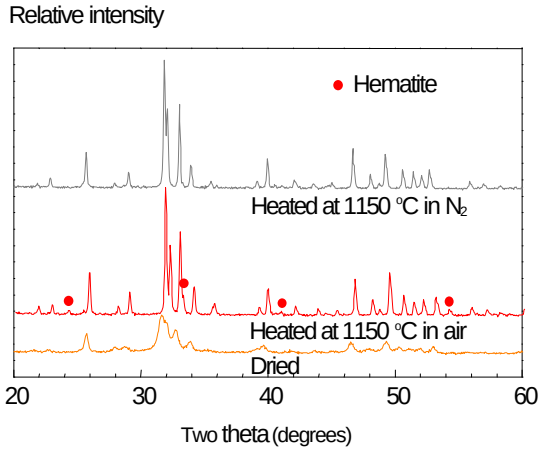

Fig. 3: Evolution of iron oxide in an apatite synthesized with excess iron (R3) and heat treated in air and nitrogen.

The room temperature spectra of R2 and R3 both showed two doublets. The dominant doublet has parameters isomer shift (IS) = 0.35(1) mm/s and quadrupole splitting (QS) = 0.74(2) mm/s with broad lines having a FWHM of nearly 0.50 mm/s. The second doublet had IS = 0.24(1) mm/s and QS = 0.30 mm/s with a good linewidth of 0.29 mm/s. The first doublet has the characteristic parameters of Fe^{3+} in octahedral coordination with oxygen and is very similar to that observed by Bauminger et al [11]. They ascribed the site to a compound similar to goethite α-FeOOH, which may be superparamagnetic since spectra taken by both groups at 85-100 K did not show any magnetic splitting. We would assign the second doublet to Fe^{3+} in the lattice and this accounted for 24% of the spectra area in R2 and 43% in R3.

After heat treatment in air, the dominant contribution to both spectra was due to hematite, α-Fe_2O_3 with a hyperfine field of 51.2(2) T. This accounted for 85% and 65% respectively of the spectral areas from the two samples. Although this is higher than the original goethite-like contribution, it does not necessarily imply that some has come from the other site since the narrower linewidth of approximately 0.30 mm/s indicates that the hematite is of much better crystallinity, and possibly larger particle size, which could lead to a higher recoilless fraction. The remainder of the area required three doublets with the best characterized one having an IS = 0.16(3) mm/s and QS = 1.6(1) mm/s. The low IS indicates that this is probably still structural but the site has been considerably

distorted from its arrangement prior to the heat treatment.

DISCUSSION: Other workers have synthesized γ-Fe_2O_3 using ferric nitrate in an aqueous solution. This involves a similar sequence of events comparable to the reaction route described in this paper. Initially, a precipitated $Fe(OH)_3$ was reported after addition of ammonium hydroxide. Calcination at 250 ^oC produced a maghemite [12]. Such low temperature processing of powder applied to the synthesized powder reported in this paper may possibly produce the magnetic maghemite phase. Despite the attractiveness of obtaining a magnetic phase, the practicality is limited since the low temperatures would not be suitable in establishing a strong, coherent body. Maghemite (γ-Fe_2O_3) is transformed to α– Fe_2O_3 between 350 and 600 ^oC [13,14]. Sintering of apatites requires a temperature of at least 1100 ^oC.

From the two compositions chosen involving ferric ions, it can be observed that a replacement of calcium with a ferric ion has resulted in decomposition to beta tricalcium phosphate. The higher solubility of tricalcium phosphate compared to hydroxyapatite unnecessarily modifies the solubility characteristic of the resulting ceramic. On this basis, an addition of iron oxide during the synthesis stage, in line with the procedure chosen to produce R3, would be the most desired. Heat treatment could then be focused on transforming the iron oxide to the desired condition while maintaining a homogeneous matrix phase.

The ability of iron to remain in the lattice depends upon the heat treatment schedule. This property is confirmed by the diffraction peak shift that suggests that the iron is not adsorbed on the surface of the crystals, but enters the crystalline structure. This can be used to an advantage whereby an initial heat treatment in conducted in nitrogen to produce a sintered body and then the atmosphere is changed to crystallize an iron oxide phase. Since hysteresis heating depends on the amount of magnetic phase in the material, it would be necessary to increase the amount of magnetite. Further work would need to experiment with higher amounts of iron addition during the synthesis stage to ascertain the influence on the stability of the apatite lattice. The oxidation state of iron could be a key factor that influences the amount of iron that can fit into the apatite lattice.

This work has shown the formation of hematite, formed in neutral or oxidizing heating conditions. The use of a reducing gas such as 10% hydrogen in carbon dioxide chosen by Kawashita et al [6] or pure hydrogen as discussed by Atalay [4], for forming magnetite in glasses, could also be selected for controlling the state of the iron oxide phase. It is believed that this would produce a magnetite containing hydroxyapatite.

The color of the heated apatite may be used to identify the type of apatite. A red has been produced from hematite and a change to gray occurs when the iron is accommodated in the lattice. This feature can be used to an advantage in determining the location of iron oxide even at the low concentrations.

A combination of ferrous and ferric ions has been used in producing magnetite in glass ceramics as described by Ebizawa et al [7]. This approach presents the correct proportion of ferrous and ferric ions required for formation of magnetite upon heating.

The resorption of hydroxyapatite is well established and it is predicted that magnetite containing apatite will dissolve at a rate dependent upon the amount of iron in the apatite lattice. For sintered hydroxyapatite, the dissolution at 37 ^oC produces about 5 ppm over a period of one hour. Heating the ceramic at temperatures required for hyperthermia will increase the solubility due to the increase in temperature and also due to the internal stress from the temperature gradient within the ceramic. These factors need to be determined as well as the relative solubility of the magnetite relative to the apatite.

CONCLUSIONS: It can be concluded that the transportability of iron is dictated by the atmosphere chosen for heat treatment. While nitrogen favours the formation of iron containing apatite, heating in air produces a hematite. Selection of a reducing atmosphere will be able to produce a finely dispersed magnetite in a biocompatible hydroxyapatite phase.

REFERENCES:

[1]M.W. Dewhirst, L. Prosnitz, D. Thrall, et al (1987) *Seminars in Oncology* **24**:616-625. [2]A.A. Luderer, N.F. Borrelli, J.N. Panzarino, et al (1983) *Radn Res* **94**:190-98. [3]Y.K. Lee, S.Y. Choi (1997) *J Mater Sci* **32**:431-36. [4]S. Atalay, H.I. Adiguzel, F. Atalay (2001) *Mater Sci & Eng - A* **304**:796-99. [5]S.H. Oh, S.Y. Choi, Y.K. Lee et al (2001) *J Biomed Mater Res* **54**:360-5. [6]M. Kawashita, H. Takaoka, T. Kokubo (2001) *J Ceram Soc Japan* **109**:39-44. [7]Y. Ebisawa, F. Miyaji, T. Kokubo et al (1997) *Biomaterials* **18**:1277-84. [8]U.O. Hafeli, S.M. Sweeney, B.A. Beresford, J.L et al (1995)

Nucl Med Biol **22**:147-55. [9]T.S.B. Narasaraju, D.E. Phebe (1996) *J Mater Sci* **31**:1-21. [10]M. Okazaki, J. Takahashi (1997) *Biomaterials* **18**:11-14. [11]E Bauminger, S Ofer, I Gedalia, et al (1985) *Calcif Tissue Int* **37**:386-89. [12]X. Ye, D. Lin, Z. Jiao, L. Zhang (1998) *J Phys D: Appl Phys* **31**:2739-44. [13]E. Herrero, M.V. Cabanas, M. Vallet-Regi (1997) *Solid State Ionics* **101-103**:213-219. [14]G. Ennas, G. Marongiu, A. Musinu (1999) *J Mater Res* **14:**1570-75.

ACKNOWLEDGEMENTS: This work has been supported by Grant # F10017027 provided by the Australian Research Council.

PARA-MAGNETIC COMPOSITE MICROPARTICLES AS HEAVY METAL ION-EXCHANGERS

Ponpan Phanapavudhikul, J. A. Waters, E.S. Ortiz

Department of Chemical Engineering, Imperial College of Science, Technology, and Medicine, London SW7 2BY UK.

INTRODUCTION: Considerable work on the use of magnetic composite particles in the area of biosciences, medicine, and wastewater treatment has been published. However, the report on their use as ion-exchangers to remove metal cations from wastewater has been limited [1, 2]. In this work, composite particles **(CP)** have been made by combining functionalised polymer nanoparticles with microparticles of magnetite using an encapsulation process [3]. The advantage of these particles is that they provide a very large area per unit volume. The polymer was mainly of acrylic composition and was designed to include components that would give the particles colloidal stability. The polymer particles carried carboxylic groups to function as ion-exchange entities; they were made from solution-polymer by replacing the solvent phase with water. The derived composite particles included a magnetite core to facilitate separation from the aqueous phase applying a magnetic field. Association between the polymer particles and the magnetite particles was achieved by mixing at a pH range in which the former particles carried a net negative surface charge whilst the other particles carried a net positive charge [3]. To enhance this electrostatic, opposite charge attraction, the magnetite particles were coated with a cationic polymeric surfactant before they were mixed with the polymer particles. The dispersion of composite particles was heated to a temperature in excess of the glassy transition temperature of the polymer which was found to be around 70 ºC, anticipating that the polymer particles should spread over the magnetite to form a polymeric layer. The process is schematically illustrated Figure 1. The performance of the composite particles as ion-exchangers was investigated in the separation and recovery of selected heavy metal cations (e.g. Zn^{2+}, Cu^{2+}, Ni^{2+}, Cr^{3+}) in a batch reactor at laboratory scale.

METHODS:

Chemical and Reagents

Azo-bis (4 cyanovaleric acid), azo-bis (2-2 methyl propionamide dihydrochloride), methacryloyloxy ethyl trimethyl ammonium chloride (QMa, 75% in water), N-vinyl pyrrolidone (VP), vinyl acetate (VA), methyl methacrylate (Mma), butyl acrylate (Ba), acrylic acid (AA), and magnetite (Fe_3O_4 with particles sizes < 5 um) were obtained from Aldrich Chemical Company. Methoxy poly(ethylene glycol) methacrylate (MeOPEGMa) was kindly supplied as a 50 % solution in water by International Speciality Chemicals Limited. Ethyl acetate and ethanol (96%) were purchased from BDH. The general purpose grade metal salts used (BDH) were $Cu(NO_3)_2.3H_20$, $ZnSO_4.7H_20$, $CrCl_3.6H_20$, and $Ni(NO_3)_2.6H_2O$. HCl (1N) and NaOH (1N) were used to adjust pH. Distilled water was used throughout.

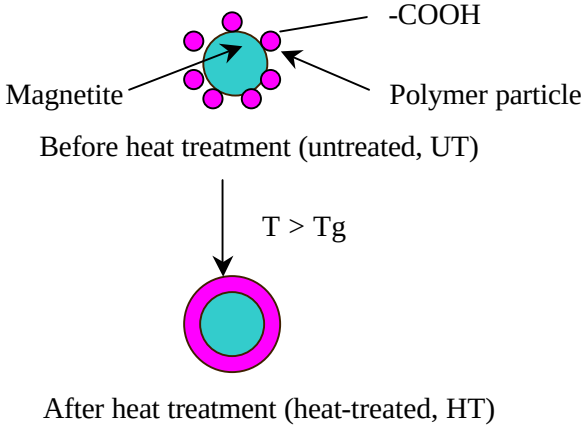

Fig. 1: Schematic representation of the encapsulation of composite particles.

Experimental

Preparation of cationic polymeric surfactant

Cationic polymeric surfactant was produced by solution terpolymerisation of vinyl acetate, vinyl pyrrolidone, and methacryloyloxy ethyl trimethyl ammonium chloride using azobismethyl-propionamidine dihydrochloride as an initiator. The proportions of monomers used in the preparation (by solution polymerisation) of the cationic surfactant were VA/VP/QMa 34/21/45 (%wt). A mixture of ethanol and water was used as a solvent.

Preparation of anionic polymer particles

The polymer was made by solution tetrapolymerisation of MeOPEGMa, Mma, Ba, AA in the proportions 15/69/34/5 (%wt) respectively. A mixture of ethyl acetate and ethanol was used as a solvent. The solution

polymer was converted into colloidally-stable particles by a two-step process: the ethyl acetate was displaced by distillation during addition of further ethanol; the ethanol was subsequently substantially displaced by addition of water and distillation. The particles exhibited steric, colloidal stability arising from the MeOPEGMa components.

Preparation of composite particles

Ten g of magnetite was initially mixed with 300 mL of a 20% wt cationic surfactant solution for 16 hours at pH 8 using ball-milling. A ceramic pot containing different sizes of stainless steel beads was used for this purpose. The coated particles were washed several times with water. The particles were magnetically separated from an aqueous phase after each wash by placing a strong magnet under the container. Any nonmagnetic particles were removed with the wash liquid. The particles were dried overnight in a fume cupboard. The dried surfactant coated particles were added to a dispersion of the polymer particles (3% weight content) at pH 8. The resulting composite particles were stored and used as slurry whose solid content was found to be 0.03 g/L. To prepare composite particles as ion exchangers in the form of H^+ and H^++Na^+, they were further treated with 5 % HCl solution to remove ionised impurities. The particles were then converted into H^++Na^+ -form by treatment with 5% NaOH solution and washed with distilled water until pH 10 was reached. Under this condition, it was found that only 20% Na^+ displacement was achieved. The slurry of composite particles was heat-treated at 80 °C, which was above the Tg of the polymer particles.

Particle Characterisation

The zeta-potential of surfactant coated magnetite, polymer particles, and composite particles was determined by using a Malvern Zetamaster at room temperature. The pH of a range of samples was altered by adding a very small amount of acid and alkaline solutions containing 2 mmoles of HCl with 3 mmoles of NaCl and 2 mmoles of NaOH with 3 mmoles of NaCl .

The size distribution of polymer particles was measured by photon correlation spectroscopy (Malvern Autosizer S4700); laser diffraction (Malvern Mastersizer 2000) was used for the composite particles.

The glass-transition temperature of polymer particles was measured by a differential scanning calorimeter (Perkin Elmer DSC pyris1) at a heating rate of 10 °C/min. The samples of polymer particle dispersions had been cast on a dish and dried at room temperature in a dessicator for 2 weeks.

The morphology of surfactant-coated magnetite and composite particles was observed with a scanning electron microscope (SEM, JEOL T-220A). The samples for SEM work were dried at room temperature under an air flow and then ground with a mortar to break up agglomerations.

Metal ions sorption experiments**:**

The characteristics of composite particles are presented in Table 1.

Table1. Properties of composite particles.

Physical form	Aggregates (~7μm diameter) in slurry
Exchange characteristics	
Functional group	$-COO^-$
Counter ion	H^+ , H^++Na^+
Carboxylic groups content* (mmol/g dry composite particles)	0.217
Operating condition	
pH	5-7
Temperature (ºC)	20
Regenerant (strong acid)	1 N. aq.

* The polymer carboxylic groups content was measured by gas chromatography.

These experiments were carried out with composite particles which had not been heat-treated.

Capacity studies

Metal cations sorption from the single-metal aqueous solutions was investigated in batch sorption-equilibrium experiments. Selected metal cations were Zn^{2+}, Cu^{2+}, Ni^{2+}, Cr^{3+}. In sorption isotherm studies, aqueous metal cation solutions with different concentrations in the range 0-25 mmol/L were mixed with 10 mL of the slurry of the particles in 500 mL conical flasks at pH 5.5. The solutions were made up to 50 mL for each concentration. The flakes were shaken for 30 minutes at 400 osc./min using a flask shaker. This sorption time was expected to be more than sufficient for the system to reach equilibrium, because the separate experiments had indicated that the process was almost instantaneous. After sedimentation of the particles had been induced by applying a magnetic field, the supernatant was filtered through 0.45 μm membrane filters. The quantity of metal cations sorbed on the particles was determined by atomic absorption spectroscopy, based on the differences in the metal cation concentrations before and after introduction of the particles.

Competitive sorption of metal cations from their mixture was also investigated in a batchwise form. A solution (500mL) containing different amounts of each metal cation was mixed with 2.5 mL slurry of the particles in a 2L beaker. The mixture was agitated by a three-blade impeller driven by a variable speed motor at 250 rev./min, at pH 5. Initial concentrations of metal cations were 0.078 mmol/L for Cu^{2+}, 0.076 mmol/L for Zn^{2+}, 0.096mmol/L for Cr^{3+}, and 0.088 mmol/L for Ni^{2+}.

Influence of the counter ions on the exchange with Zn^{2+} at different pH.
A ratio (R) was defined as follows.

$$R = Zn^{2+} \text{ in the solution (mmol)} / \text{COOH or COOH+Na (mmol)}$$

The R ratios were 1/4, 1/8, 1/16 for both forms. The experiments were conducted in the same manner as in the sorption isotherm section. The initial Zn^{2+} concentration was kept constant at 0.076 mmol/L. The pH ranged from 5 to 7.

Recovery and re-use of the composite particles
In an extraction experiment, 0.3 g of the composite particles were loaded into a solution of Zn^{2+}, initial concentration = 0.31 mmol/L, with R = ¼ at pH 7. After extraction, the composite particles were recovered by treatment with 50 mL of 1M. HCl aq. Kinetics studies indicated that 3 hours contact was in excess of the required time to reach equilibrium. At the end of the experiment, the amount of Zn^{2+} in the solution was measured. 10 cycles of consecutive extraction and stripping were carried out.

RESULTS AND DISCUSSION:
Particle characterisation

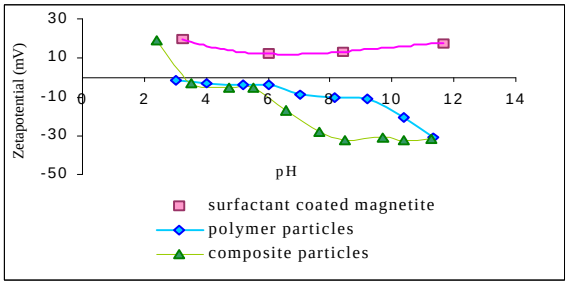

Fig. 2: Variation of surface charge with pH.

Figure 2 shows the result of the zeta-potential examination of cationic surfactant-coated magnetite, polymer particles, and composite particles at different pH values. As anticipated the presence of cationic surfactant on magnetite whose isoelectric point is around 6.5 shifted the surface charge of magnetite into the positively-charged region at alkaline pH. The charge of polymer particles tended to lie in the negatively charged region at all pHs. The negative charge of polymer particles increased with pH values due to ionisation of the carboxylic groups from both the initiator and acrylic acid. The zeta-potential characteristics of the composite particles resembled those of polymer particles rather than those of surfactant-coated magnetite. This confirmed that surfactant-coated magnetite was covered with the polymer particles.

The sizes of the polymer particles were found to be in the range of 50 to 70 nm. The particle size analyser gave the sizes of aggregates of composite particles to be less than 7 µm.

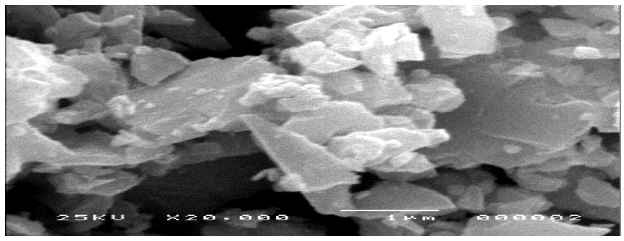

Fig. 3a: SEM micrograph of surfactant-coated magnetite.

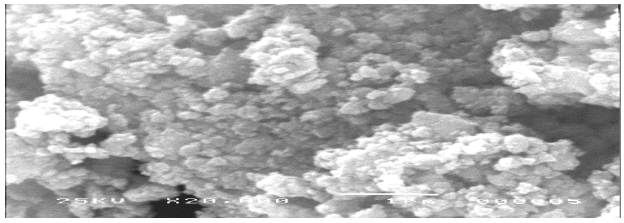

Fig. 3b: SEM micrograph of UT composite particles.

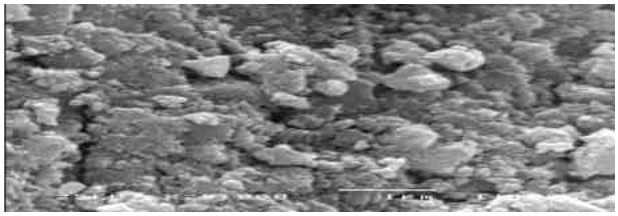

Fig. 3c: SEM micrograph of HT composite particles.

Scanning electron micrographs (Fig. 3a, 3b, 3c) show that the particles were not uniform and were aggregated. Surfactant coated magnetite exhibited a smooth surface (Fig. 3a). The composite particles (Fig. 3b) had a rough surface due to the presence of the polymer particles. The composite particles after heat treatment (Fig. 3c) provided a smoother and less nodular surface than those before heat treatment, as expected.

Capacity studies

Experimental results showed that the process was almost instantaneous, yielding complete removal when the initial concentrations of heavy metals were very low (0.015-0.076 mmol/L). Considering the ratio of mmoles of metal extracted to the mmoles of carboxylic groups in the amount of particles used, the maximum values were found in using single metal solutions: 4.42 for Cu^{2+}, 3.87 for Cr^{3+}, 2.12 for Ni^{2+}, and 1.94 for Zn^{2+}. These ratios are higher than the stoichiometric ratio, suggesting that ion exchange is not the only mechanism of metal extraction. With the multicomponent solution, the relative amount of the different cations extracted was consistent with the above results, i.e. $Cu^{2+} > Cr^{3+} > Ni^{2+} \sim Zn^{2+}$.

Influence of the counter ions on the exchange with Zn^{2+} at different pH values.

Table 2 shows the removal percentages of Zn^{2+} as a function of the R ratio. It showed that the choice of counter ions had an influence on the exchange capacities at all investigated pH values, especially in acidic solution. H^++Na^+-form tended to have higher affinity for Zn^{2+}. This finding could be explained in terms of the degree of dissociation of carboxylate group, which is heavily dependent on pH and counter ions. Decreasing the R ratio value (increasing in the number of active groups) led to an increase in Zn^{2+} removal. Nevertheless, complete removal could not be achieved even with a relatively large excess of counter ions (R=1/16, pH=7). In terms of the surface complexation model, one part of H^+ counter ions is situated in the diffuse layer where the exchange occurs and the other is specifically connected to the surface (in the Stern layer) where it is difficult for Zn^{2+} to reach, in the case of weak acid exchangers. This led to a decrease in available active sites [4].

Table 2. Removal percentages of Zn^{2+} as a function of the R ratio (initial Zn^{2+} concentration kept constant at 0.076 mmol/L, T=20 °C).

		% removal		
pH	Particles	R=1/16	R=1/8	R=1/4
5	H^+form	6	3	1
5	H^++Na^+form	17	8	6
6	H^+form	52	36	27
6	H^++Na^+form	62	39	23
7	H^+form	92	92	84
7	H^++Na^+form	93	93	87

Recovery and Reuse

Figure 5 clearly indicates that heavy metals could be repeatedly adsorbed and stripped without significant loss in the loading capacity of the composite particles.

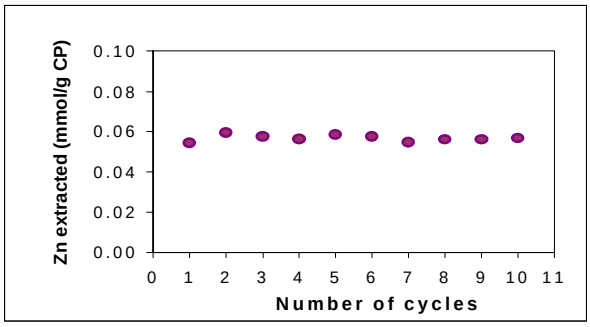

Fig. 5: The extraction performance of the composite particles as a function of the number of cycles (initial Zn^{2+} concentration for each cycle was 0.31 mmol/L, at pH 7).

CONCLUSIONS:

The metal cations sorption process on composite particles is almost instantaneous, yielding complete removal when the initial concentrations of heavy metals are very low. H^+-form composite particles appeared to be less efficient than H^++Na^+-form ones under the experimental conditions studied. Consecutive loading and stripping showed the feasibility of the composite particles for metal cation extraction.

REFERENCES:

[1]M.D. Kaminski, L. Nunez (1999) Journal of magnetism and magnetic materials **194**:31. [2]M.D. Kaminski, L. Nunez (2000) Separation Science and Technology **35**:2003. [3]R. H. Ottewill, A. B. Schofield, J. A. Waters, and N. St. J. Williams (1997) Colloid Polym Sci **275**:274-283; R. H. Ottewill, A. B. Schofield and J. A. Waters (1998) J. Disp. Sci. & Techn. **19**:1151-1162. [4]S. Lacour, J. C. Bollinger, B. Serpaud, et al (2001) Analytica Chimica ACTA **428**:121-132.

ACKNOWLEDGEMENTS:

We wish to express our thanks to the British Council for the Overseas Research Award to one of us (P. P.).

MAGNETOELECTRONICS, MAGNETIC LABELS AND BIOMOLECULAR DETECTION

M.M. Miller[1], J.C. Rife[1], C.R. Tamanaha[2], P.E. Sheehan[1], M. A. Piani[3], S.P. Mulvaney[1], M. Tondra[4], and L. J. Whitman[1]

[1]Naval Research Laboratory, Washington, DC 20375, USA
[2]Geo-Centers, Inc., Fort Washington, MD, USA [3]NOVA Research, Inc., Alexandria, VA, USA
[4]Nonvolatile Electronics, Eden Prairie, MN USA

INTRODUCTION: The Bead Array Counter (BARC) is a magnetic-label-based system for the detection of biomolecules. Central to this system is a microfabricated sensor chip containing giant magnetoresistance (GMR) magnetic field sensors. The third-generation sensor chip (BARC III) shown in Fig. 1 consists of 64 probe sites with a sensing area of approximately 30,000 μm^2 per site. Currently, BARC is configured as a "DNA-chip" that detects the presence of magnetically-labeled DNA samples.

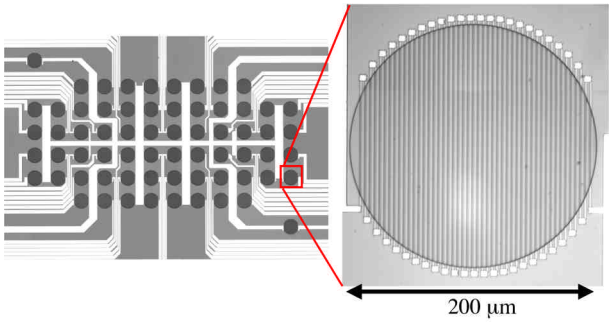

Fig. 1: A micrograph of the BARC III chip containing 64 sensor areas (dark circles). On the right is an expanded view of an individual sensor.

METHODS: The BARC III chips are an evolution of a lower density prototype (BARC II) chip that has been described elsewhere [1]. Briefly, thiolated, single-stranded DNA capture probes are arrayed on a gold surface above the embedded GMR sensors. An assay is performed by flowing biotinylated DNA samples over the probe areas and hybridization with the complementary probes occurs. Streptavidin-coated magnetic microbeads (2.8 µm diameter Dynal M-280) are then introduced into the flow cell and bind to the biotin at the hybridized DNA spots. The immobilized microbeads are detected by the GMR sensors.

The BARC III chip represents a compromise in which the sensor detection threshold was sacrificed for a nearly 10-fold increase in sensing area/probe and an 8-fold increase (to 64) in the number of probes over that of the BARC II. While BARC II was capable of detecting a single Dynal M-280 microbead, BARC III has a detection threshold of about 15 microbeads. Nevertheless, we have demonstrated the ability to detect 30-mer samples of anthrax lethal factor (ALF) at concentrations as low as 10 fM in about 30 minutes.

DISCUSSION: Currently the electronic noise background (~15 beads) is below the chemical "noise" background (~50 beads) due to non-specific binding. Furthermore, the magnetic variability [1,2] within a sample of the Dynabeads makes ensemble averaging necessary; i.e., single-bead detection is unreliable. As the chemical background is lowered the electronic detection threshold will become a greater issue and must be addressed. Simply substituting solid, soft-ferromagnetic labels such as NiFe for the polymer-ferrite composite labels will yield a 10-fold increase in magnetoelectronic sensitivity due to larger effective magnetization [1]. Additionally, these ferromagnetic labels will be magnetically uniform [1]. With a narrowly defined range of label diameters single-bead detection will be meaningful. We are currently developing techniques for sizing and functionalizing these materials for this purpose.

Finally, it has been shown that improved signal-to-noise can be realized when the sensors have lateral dimensions comparable to those of magnetic labels [3]. However, as sensor dimensions are reduced, magnetostatic barriers become increasingly important and magnetic sensitivity is compromised [4]. Using solid ferromagnetic labels and more efficient sensor designs utilizing ring-shaped structures that are currently being developed for non-volatile computer memory should further enhance the magnetoelectronic sensitivity as well as increase the number of different biomolecules that can be simultaneously detected [4]. Such an approach provides a reasonable path to a robust, massively-arrayed biosensor.

REFERENCES: [1]M.M. Miller *et al* (2001) J. Magn. Magn. Mat. **225**, 138. [2]D.R. Baselt *et al* (1998) Biosens. Bioelectron. **13**, 731. [3]M. Tondra et al (2000) J. Vac. Sci. **A18**, 1125. [4]J.J. Krebs (1996) J. Appl. Phys. **79**, 6087. [5]US Patent Application 09/497,754.

METAL-POLYMER HYBRID MICROCHANNELS FOR MICROFLUIDIC HIGH GRADIENT SEPARATIONS

M.D. Ward, J. Quan, P.Grodzinski

Motorola Labs, Tempe, AZ 85284, USA

INTRODUCTION: Microfluidic devices have long promised to revolutionize the diagnostic world by providing high throughput small volume automated assays at an affordable price. To date however, microfluidic technology has not fully delivered on its promise. It is still difficult to integrate individually successful microfluidic devices into a single automated sample to answer device.

One difficult integration to achieve is front end sample processing such as cell or nucleic acid purification with back end amplification or analysis. Central to this problem is that typical microfluidic devices operate with fluid volumes of less than 10 microliters and unprocessed sample volumes are in the range of milliliters. This discrepancy cannot be ignored for many clinically important rare targets such as bacteria during sepsis or disseminated tumor cells in peripheral blood. Typical microfluidic sample volumes are unlikely to contain extremely rare targets (1). Efficient processing of large sample volumes (>1ml) is required to capture enough of these rare targets for analysis. Immunomagnetic separation is a very attractive solution to this problem because of its ability to rapidly, efficiently and selectively separate targets present in complex biological fluids.

Many magnetic label manufacturers now offer products that can bind to important targets or to primary antibodies to these targets. Large particulate super paramagnetic particles on the order of ~1-5 um diameter can be easily manipulated in relatively weak magnetic fields, but smaller sub-micron particles require strong gradient fields. The smaller particles offer important advantages in speed and efficiency of target labeling (2), but they complicate device design. In order to fully take advantage of magnetic separation in the microfluidic environment, inexpensive, easily integrated devices capable of forming high magnetic gradients must be developed.

The ability of such devices to replace conventional biological protocols has already been demonstrated by Immunicon's innovative CPAS (formerly Celltracks) system (3). The system uses sputtered micron sized magnetic lines and CD-ROM technology for optical detection and is designed to replace the functions of much more expensive cell analysis such as flow cytometry.

The devices we present here can also be used for direct optical analysis of rare targets, but they were designed to act as a sample preparation unit for further microfluidic processing by genetic amplification and hybridization devices. They consist of sub-millimeter iron or nickel-iron matrix elements fabricated into acrylic and polycarbonate substrates that geometrically concentrate external magnetic flux to form the necessary magnetic gradients. Initial prototypes used randomly distributed iron beads as matrix elements (Fig. 1).

Although results achieved in these structures were encouraging, difficulties in the manufacture of reproducible devices prompted the exploration of alternative more controllable and more easily manufactured designs. Preliminary results for laser machined electroplated devices are promising. For these devices magnetic gradients can be precisely controlled by manipulating the size and or shape of the matrix elements.

In both designs, targets are collected at the walls of the channel where they can by washed or otherwise processed in a flow stream. The channels can concentrate milliliter volumes greater than 200 fold in just a few minutes and can be integrated with other polymer based downstream microfluidic amplification and analysis devices. Trapping of bacteria, mammalian cells and target antibodies are shown.

METHODS: *Device fabrication*. Iron sphere device prototypes consisted of 50-300 um diameter iron spheres (Starmet, Concord, MA) imbedded by compression molding into acrylic or polycarbonate channels. Channels in both acrylic and polycarbonate structures were formed by laser cutting desired channel shapes in 100um thick double sided tape (3M, St. Paul, MN). Acrylic channels were covered with microscope cover glass to facilitate epi-fluorescent microscope viewing. For polycarbonate structures two iron sphere containing sheets were taped together.

Plated prototype devices were made using a 40 W CO_2 laser engraving system (Universal Laser

Systems, Scottsdale, AZ). Laser machined acrylic sheets were sputtered with a gold seed layer prior to plating in a low temperature nickel-iron bath (4). Plating thickness was typically 100 um. Channels were formed using cut tape and cover slips. Samples were pumped through all devices using a micro peristaltic pump (Instech, Plymouth Meeting, PA) fitted with silicon tubing and barbed connectors. 10mm x 10mm x 5 mm thick Neodymium magnets (magnetized through the thickness), were placed on the device surface to generate the external magnetic field. Devices with matrix elements on both top and bottom were fitted with N to S facing magnets on either side of the device. Glass covered channels were fitted with magnets only on the matrix (opaque) side. A substantially uniform magnetic field of ~ 0.7 T was observed in channels with magnets on both sides and a variable field of ~0.2-0.4 T was observed at the surface of channels with a single magnet.

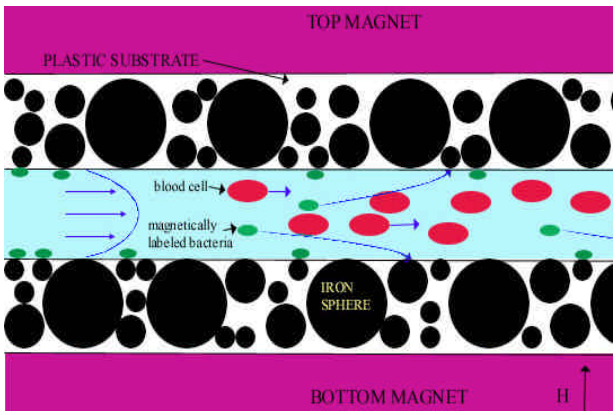

Fig. 1: Schematic of the structure containing spherical matrix elements on both top and bottom of the channel.

Target capture protocols. Citrated sheep blood (Colorado Serum Company) was diluted 1:1 with phosphate buffered saline (PBS)/5mM EDTA pH 7.4 and inoculated with 100-500 cfu of E.coli K12 per ml. 10ul of anti-E. coli biotinylated polyclonal antibody (Virostat, Portland Maine) was incubated with the sample for 15 minutes at room temperature on a rotary mixer. 20 ul of colloidal super paramagnetic streptavidin microbeads (Miltenyi Biotec GmbH, Bergisch Gladbach, Germany) were added and another 15 minute incubation was performed. Samples were pumped through the devices at various flow rates. Fractions were collected and plated overnight on LB agar. Capture efficiency was determined by comparing the number of colonies in a given volume pumped through the device with the magnets alternately off and on.

A GFP expressing line of E. coli K12 was used to generate fluorescent images. In imaging experiments a much higher density of ~100,000 cfu per ml was used.

Rabbit white blood cells were captured using anti-CD45 monoclonal antibody conjugated to FITC (Molecular Probes, Eugene, OR) and anti-mouse IgG1 super paramagnetic microbeads (Miltenyi Biotec). Rabbit blood was diluted 1:1 with PBS/EDTA and incubated with primary antibody for 15 min as before. 40 ul of microbeads were incubated as before for magnetic labeling. For capture of IgG the anti-CD45-FITC antibody was incubated with anti-mouse IgG1 microbeads for 5 minutes in PBS/EDTA.

RESULTS: *Capture of bacteria.* Plating experiments of E.coli inoculated blood demonstrated that large sample volumes could be concentrated in minutes with relatively high recovery rates. About 50% recovery was obtained at the maximum tested average flow rate of ~19mm/s. This corresponded to ~350 ul/min in the device tested. Epi-fluorescent video of magnetically labeled GFP expressing E. coli was used to visually confirm the capture of E.coli at the surface of imbedded matrix elements.

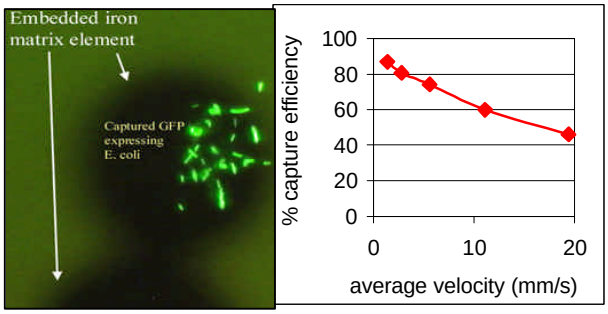

Fig. 2: Epi-fluorescent image of magnetically labeled GFP expressing E. coli captured at the surface of an imaging device (left). Graph showing capture efficiency vs. average flow velocity in polycarbonate devices with 100 um channel height (right).

Capture of Mammalian cells and IgG. Preliminary studies of capture of these targets in ridge structures demonstrated that they could be captured in high velocity flow streams and localized onto the tips of the saw-tooth ridge elements. Although capture rates were not quantified, sample flow at the inlet and outlet were observed through the epi-fluorescent microscope The majority of labeled cells were depleted from the flow stream at flow velocities up to 4mm/s. Similar results were observed in both sphere imbedded and plated ridge structures.

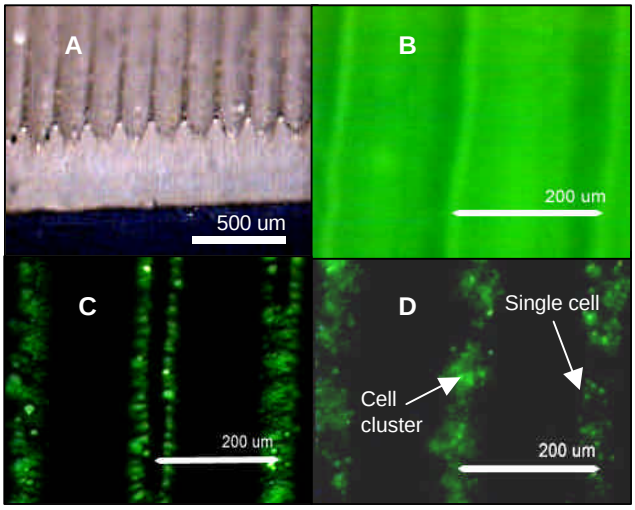

Fig 3: Laser machined acrylic ridge structure prior to electroplating (A). Ni-Fe ridge device with fluorescein labeled CD45 antibody coupled to IgG1 specific magnetic beads prior to separation(B). Same device after separation. Fluorescence is focused on the ridges(C). Similar device after separation of white blood cells using the fluorescent anti-CD45 antibodies(D).

DISCUSSION & CONCLUSIONS: The efficient capture and concentration of rare targets for downstream analysis is an important problem facing the advancement of microfluidic diagnostics. The devices presented here demonstrate that this problem can be effectively and inexpensively addressed with metal-polymer hybrid microchannels. The ability to selectively capture labeled targets in a relatively high velocity flow stream permits the rapid concentration and purification necessary to analyze rare targets on a microfluidic scale.

While initial prototypes using imbedded iron spheres demonstrated efficient separation of bacteria from whole blood, the desire for highly reproducible and manufacturable structures led to the design of Ni-Fe plated ridge devices that promise to replace the initial prototypes. The plated prototypes shown here are limited by the laser used. It has low resolution (~100um) and the features sculpted tend to be somewhat rough. With the application of more sophisticated fabrication technology however, the features can be resolved to the lithographical level. This kind of resolution would enable precise control of magnetic gradient properties. Larger features can produce more global gradients that can attract targets from further distances while smaller features can produce extremely high local gradients. Combining these features could result in devices capable of capturing very weakly labeled targets in high flow rate devices. It would also permit high flexibility in designing for capture of different targets e.g. large and small cells viruses or macromolecules. Although a direct quantitative comparison of the capture rate for bacteria vs. mammalian cells was not done, it was obvious from the microscope studies that mammalian cells are more difficult to capture. Although mammalian cells are larger particles, their smaller surface to volume ratio gives them a lower overall volume magnetic susceptibility upon labeling. Their larger size also makes them more subject to drag forces from the velocity profile of the channel flow. Channels with greater heights can reduce this susceptibility but the matrix magnetic gradients tend to fall off very rapidly with distance from the channel surface.

Future studies will focus on integration with downstream components, optimization of ridge structures and quantitative testing with relevant models and actual clinical samples.

REFERENCES: [1] L.J. Krica, *Microchips, Bioelectronic Chips and Gene Chips* in Biochip Technology (eds J. Cheng and L.J. Krica) Harwood Academic Publishers, p. 4. [2]S. Miltenyi. et. al. (1990) *J Cytometry* **11,** 231-8. [3]Chalmers, J. et. al. (1998) *Biotechnol Prog* **14,** 141-8. [4] G.A. Di Bari (2000) *Nickel Alloys, Cobalt, and Cobalt Alloys* in Modern Electroplating (eds. M. Schlesinger and M. Paunovic) John Wiley & Sons, Inc. pp. 561-564.

ACKNOWLEDGEMENTS:
This research was funded in part by NIST contract #1999011104A and DARPA contract #MDA972-01-3-0001. Special thanks to Joe Bonnano and Dale Ganser for their help in the development of the initial prototype device.

HIGH SENSITIVITY SENSORS FOR THE LOCALIZATION OF MAGNETIC MICROSPHERES

G. Durin, G. de Milato, A. Stantero, & M. Coïsson

Istituto Elettrotecnico Nazionale Galileo Ferraris, str. delle Cacce 91, 10135 Torino, Italy

INTRODUCTION: In recent years, a large number of different clinical applications of magnetic microspheres has been proposed, mainly connected to disease treatments. On the contrary, only a few authors have proposed to use nanoparticles for the reliable detection and localization of tumors. The simple idea is to inoculate a certain quantity of particles and use a high sensitivity sensor to locate them. One of the most promising methods appears to be the detection of susceptibility artifacts in magnetic resonance, as proven recently in rats [1]. As a matter of fact, the drawback of this methodology is related to the use of a magnetic resonance setup together with the high magnetic field required for particle alignment. All these facts can seriously limit the spreading and clinical use of this type of technique.

In principle, an alternative and less-expensive method would be the detection of the small dc field produced by an ensemble of *interacting* superparamagnetic nanoparticles. Commercial superparamagnetic microbeads, such as the ones used in cell separation, are small enough to remain dispersed and thus do not interact. After the application and subsequent removal of an external field, they do not show any residual magnetic field (usually called remanence). Establishing when a particle ensemble can produce a detectable remanence is not easy, because many different parameters, such as particle size and distance to the detector, contribute to the particles' interaction. We are presently investigating such a complex issue by considering different particle concentrations and measuring hysteresis loops up to 1.5 T with a vibrating sample magnetometer.

The magnetic field produced by the particle ensembles is negligible with respect to the magnetic field of the earth and other magnetic disturbances. Therefore, the use of a sensor with high background reduction and insensitivity to spatially constant external fields is thus necessary. One of the most promising solutions to this problem is the use of a gradient field detector based on the magneto-impedance properties of magnetic wires [2,3].

METHODS: Some families of magnetic wires show large variations of impedance when small external fields are applied. In particular, we have investigated the properties of an amorphous $Co_{68.25}Fe_{4.5}Si_{12.25}B_{15}$ wire having a diameter of 110 μm, properly annealed under dc current to improve the magneto-impedance response (Fig. 1) [4]. As seen in fig. 1, the wire sensitivity is a non-uniform function of the field. It is worth noting that around H~300 A/m, the curve is approximately linear: in particular, we obtained a percentage sensitivity of $0.3/Am^{-1}$. Working around this field by using a suitably designed solenoid integrated into the sensor, any external constant field of some tens of A/m or lower (e.g. earth field) does not influence the magneto-impedance response of the wire. The response is thus insensitive to any fluctuation of background field. We are currently investigating other types of magnetic wires and different thermal treatments in order to maximize the overall field sensitivity of the sensor.

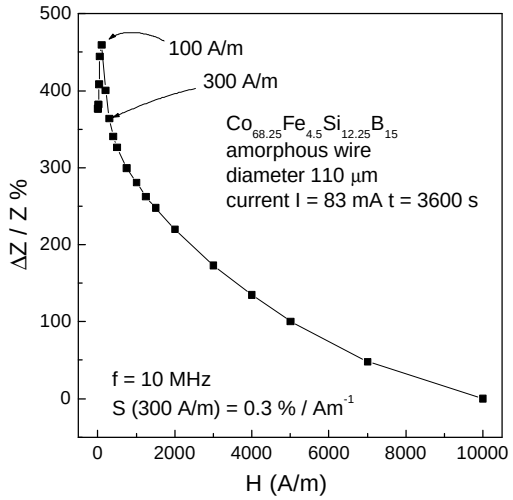

Fig. 1: Magneto-impedance response of an amorphous $Co_{68.25}Fe_{4.5}Si_{12.25}B_{15}$ wire annealed under dc current. The sensitivity around the working point of 300 A/m is also reported.

A detailed description of the electrical circuit of the sensor can be found in [2]. Briefly, a couple of short magnetic wires are aligned at a distance of a few centimeters, and fed by a 10 MHz ac voltage. Non-uniform magnetic field sources produce different impedance variations in the wires: the sensor circuit is able to produce a dc voltage proportional to the field gradient. In our system, two 3 mm magnetic wires are glued on a small bar at a distance of about 3 cm. In this configuration, if the field source is approximately a magnetic dipole 1 cm far from the first wire (which is reasonable in

most applications), the second farthest wire will measure a field of less than 3% with respect to the former. This means that the signal measured by the sensor is approximately the field produced by the magnetic source.

This type of configuration cannot only detect a small magnetic source such as a particle ensembles, but also identify it with good accuracy. In fact, considering the distribution of the measured field in a plane, it is possible to calculate the position and the dipole moment of the source with good approximation. The measurement requires that the field be relatively close to the source over a grid of uniformly spaced points of a plane. In order to calculate position and intensity of the source, we then need to solve a typical 'inverse problem'. To this end, we have developed a proper code for optimal localization, using the methodology of biomagnetism for current dipole localization [5-6]. The code is reasonably fast, and permits a localization of the source with an approximation sufficient for any possible clinical application.

DISCUSSION & CONCLUSIONS: The sensor we are currently using is reasonably simple and stable. Measurements in a RF shielded room showed no significant improvements. Therefore, no particular environment is required for its practical use.

Apart from the studies on particle ensembles, we are currently considering the use of the sensor for the localization of *known* magnetic sources which have been previously inserted in a human body. These sources can be small ferromagnetic markers, previously magnetized under fields of a few tesla, with a known residual dipole moment. They can be used in clinical application where it is necessary to localize the site of previous operations, even in the case of large time delay. In particular, it represents a simpler and valid alternative to the use of damaging techniques, such as radiography or endoscopy.

REFERENCES:

[1] C.W. Jung, J.M. Rogers, E.V. Groman (1999) *J. Magn. Magn. Mat.* **194**:210-216.

[2]T. Uchiyama et al. (1997) *IEEE Trans. Magn.* **33**:4266-4268.

[3]K. Bushida et al. (1996) *IEEE Trans. Magn.* **32**:4944-4946.

[4]L. Brunetti, M. Coisson, P. Tiberto, F. Vinai, *J. Magn. Magn. Mat.* (in press).

[5]F. Brauer, G. Stroink (1985) *IEEE Trans. Biom. Eng.* **32**:386-391

[6]G. Stroink (1987) *Physics in Medicine & Biology: the Biomagnetic Inverse Problem*, **32**:53-58.

TUNING THE SP TO FM TRANSITION OF COBALT NANOPARTICLES IN VIEW OF BIOMEDICAL APPLICATIONS

V. F. Puntes, W. J. Parak and A. P. Alivisatos

UC Berkeley, College of Chemistry, Berkeley, CA 94720, US

Magnetic nanoparticles are a powerful and versatile diagnostic tool in biology and medicine. Bound to a suitable antibody, they are used to label specific molecules, structures or microorganisms. Established techniques such as magnetic cell separation use magnetic field gradients to manipulate and isolate magnetically-labeled cells. More recently, magnetic immunoassay techniques have been developed in which the magnetic field generated by the magnetically-labeled targets is detected directly with a sensitive magnetometer. In addition, drug delivery and contrast enhancement in MRI would benefit from a simple reproducible chemical synthesis of monodisperse magnetic nanoparticles.

In general, the use of magnetic particles for biological and medical applications has been intense and focused on iron oxides.

At the present point, development of better techniques would require better-controlled nanoparticles. Two possible approaches are either improving synthesis of the iron oxide nanoparticles or changing the magnetic material. Synthesis of iron oxides often shows low reproducibility (due to the complex oxygen chemistry), polycrystallinity and low control. T. Hyeon *et al.* [1] recently showed the synthesis of monodisperse Fe_2O_3 nanoparticles. Even if the results are remarkable, still, Fe_2O_3 is a weak ferrimagnetic material, while Co (and Fe and Ni and their alloys) is ferromagnetic and has shown an outstanding capacity of shape control, perhaps thanks to the particular epsilon crystal structure [2], which is more complex than the conventional hexagonal and cubic compact faces, while keeping the magnetic properties almost unchanged.

The magnetic transition from the superparamagnetic (SP) to ferromagnetic (FM) state of the magnetic susceptibility and coercivity is determined at the synthesis. Depending on the desired properties, different magnetic behavior is requested. For example, Chemla *et al*. [3] recently showed a method for ultra-high sensitivity immunoassays where monodisperse SP nanoparticles are needed. Many tests reveal the presence of a molecule or disease-causing organism by detecting the binding of an antibody to the target. When antibodies labeled with magnetic nanoparticles bind to the target on a surface, brief exposure to a magnetic field causes these probes collectively to give off a strong magnetic signal. Meanwhile unbound antibodies tumble about in all directions producing no net signal. For a 20 nm Fe_2O_3 particle, Neel relaxation (bound particles) is about 1 s while Brownian relaxation (unbound particles) is about 1 μs [3]. This last property makes it possible to read the results without first washing away any probes that fail to find their target.

Besides, weakly FM particles capable of self-assembly in solution would be useful for dynamically changing the local concentration of molecules linked (conjugated) to the nanoparticles surface.

The general requirements would often be of magnetic particles displaying a large magnetic susceptibility, while keeping interparticle interactions low so they do not agglomerate.

Progress has been made recently by Riffle and Rutnakornpituk (micelle-grown cobalt nanoparticles of 10 nm diameter). Other groups have also developed magnetic nanocrystal synthesis [4]. In this paper we present the synthesis of monodisperse cobalt ferrofluids with controlled size and shape. The synthesis is carried out in non-polar solvents, necessary for the size and shape control. Recent developments in the solubilization of this nanoparticles in aqueous solutions are commented.

By modifying the volume or the shape, and therefore the shape anisotropy, the SP to FM transition can be modified. In addition, by partially oxidizing the particles, coercivity may be increased (for passive sensor purposes) thanks to the exchange between CoO and Co. Surface chemistry, like absorption of CO may also modify magnetic properties.

The particles are obtained by rapid pyrolysis of Co carbonyl in dichlorobenzene in the presence (about 1%) of surfactants (carboxylic acids, phosphonic acids and amines), which controls the crystal growth, and therefore, the size and shape of the particles; solubilizes the particles; avoids agglomeration; and protects them (but not fully) against oxidation. In the presence of oleic acid and trioctyl phospine oxide, spherical monodisperse particles are obtained (Fig.1).

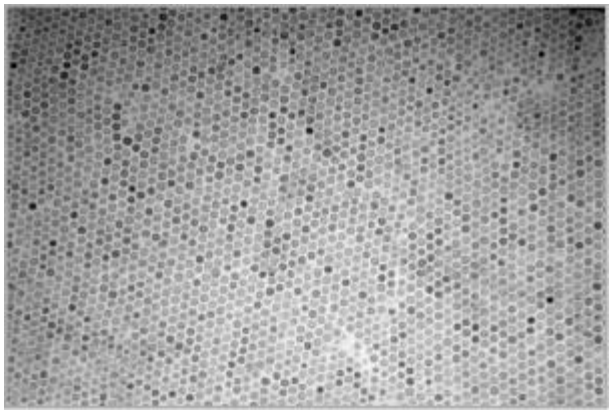

Fig.1: TEM picture of 10 nm Co nanoparticles

A concentrated solution of $Co_2(CO)_8$ (0.40 to 0.80 g in 2-3 ml of o-dichlorobenzene anhydrous) was injected in an o-dichlorobenzene anhydrous refluxing bath (15 ml, T=181° C). All reactions were conducted under Ar following standard airless procedures using commercially-available pure reactants. Macroscopic amounts (10^{16} particles/ml) of monodispersed nanoparticles were thus obtained. The decomposition and nucleation occurs instantaneously upon injection. The lifetime of atoms in solution is short leading to the simultaneous formation of many small metal clusters (nuclei). Control of the bath temperature and the surfactant composition modifies the strength of the metallic particle-organic molecule bonding. Thus, by controlling the precursor-to-surfactant ratio, the reaction temperature and injection time, the size of the spherical particles can be controlled and varied between 3 to 16 nm (Fig.2).

Small magnetic particles are single domain, i.e., all the atomic magnetic spins of the particle are coupled in the same direction and the particle behaves as a single magnetic dipole. Depending on anisotropy, size and temperature, the magnetic dipole of the particles will be free to rotate (superparamagnetism) or will be blocked in the anisotropy direction (ferromagnetism). In the first case, the time average of the magnetic moment of the particle is zero. The relation between anisotropic energy and thermal energy is $KV=k_BT$ (where K is the anisotropy constant, V is the particle volume, k_B is the Boltzmann constant and T is the temperature), determines the transition between the SP and the FM regime. Once the particles become FM, magnetic interactions among them start to play a crucial role following the relation between magnetic interaction and thermal energy $2\mu^2/a^3 = k_BT$ (where μ is the magnetic dipole moment and a is the particle diameter).

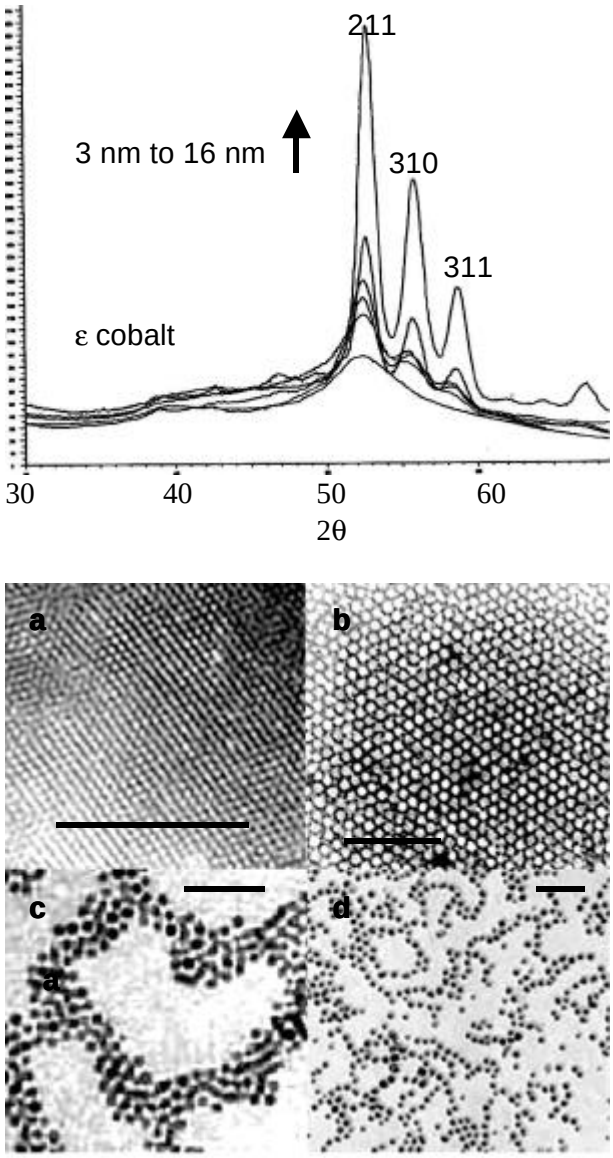

Fig.2: XRD and TEM as a function of particle size. The XRD peaks increases in intensity and become narrower as the size of the crystal domain increase. All bars are 100 nm.

Thus, due to strong dipole-dipole interactions, large nanocrystals form closed loops in order to minimize the magnetostatic energy (Fig.2d). In the transition range, a mixture of hexagonal monolayer and closed loops is observed (Fig.2c) suggesting that in this case, the SP-FM transition is taking place at room temperature for particles with sizes around 12 nm, as supported by low susceptibility magnetization measurements (not shown).

In addition to the volume, the shape may be modified to obtain objects with anisotropies up to an order of magnitude higher than the crystal anisotropy, shifting considerably the SP-to-FM transition to lower temperatures for a constant particle volume.

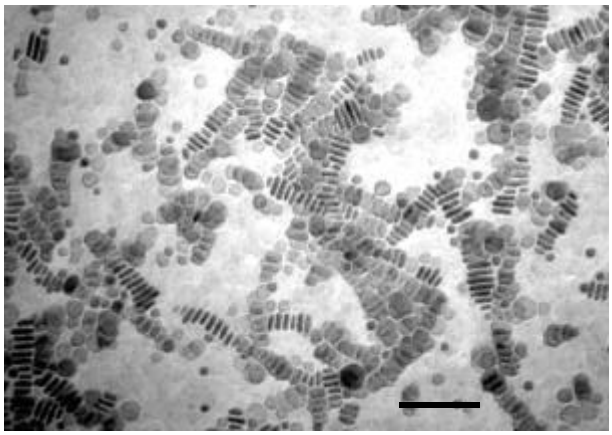

Fig.3: TEM picture of Co nanodisk-shaped crystals. The bar is 100 nm.

By mixing small amounts of amines to the surfactant mixture, Co nanodisks have been synthesized (Fig.3). And, as previously, the diameter may be modified (Fig.4). These crystals show a strong anisotropy and spontaneous self-assembly into large ribbons. Thus, when these particles are introduced in solution, they will find each other, and so will any molecule that is attached to them.

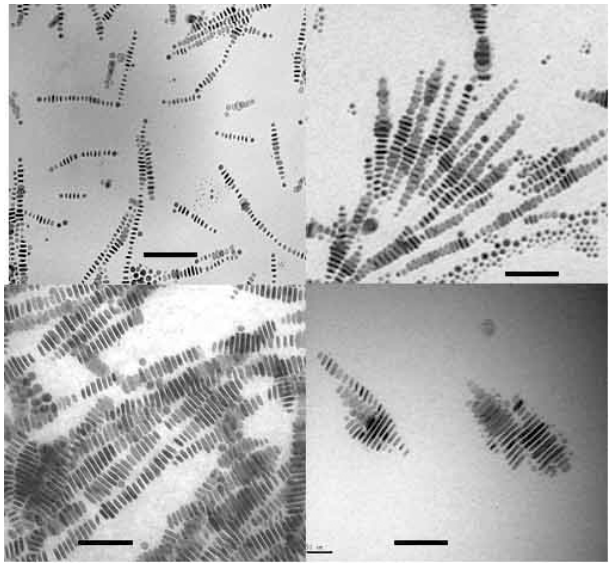

Fig. 4: Co nanodisks of different average diameters. The bars are 100 nm.

It is often desirable to have particles which interact strongly between themselves or with an external field, but not so much that they collapse and precipitate. Also desirable are large SP particles which give a large signal without interacting.

As an example of tuning the magnetic properties, small disk-shaped particles will show a FM behavior for much smaller magnetic moments than the corresponding spheres, thus they will have a weak tendency for self-assembly, so they may be easily redispersed (by agitation, sonication or slight T increase). Once the particles are far apart, the re-call interactions will be small, and independent tests may be performed before letting them slowly self assemble again. Assemblies of large disks will attach strongly and may be easily collectively transported by an external field. Large spherical particles may be useful for cell separation and drug delivery, and small ones may be useful for ultra-fast detection and labeling.

Proof of the quality and magnetic character of the samples yielded by this approach comes from observations of the spontaneous self-assembly of the nanocrystals, as well as from the formation of unique superstructures, such as chains and ribbons of disks. All sizes and shapes self-assemble into superstructures as a colloidal solution is allowed to evaporate slowly in a controlled atmosphere. A drop of the colloids (2% weight of particles) was placed on a carbon-coated TEM grid at room temperature and slowly evaporated (in a covered watch glass). The use of high boiling solvents (like o-dichlorobenzene), allows slow evaporation at RT, which permits the particles to diffuse to their lowest energy sites during evaporation, producing well-defined super-structures. The final arrangement of the nanocrystal assembly is driven by the balance of surface tension, van der Waals forces, and magnetic interactions among SP or FM particles.

Spherical particles self-assemble into hexagonal 2D superlattices (Fig.1). This assembly is determined by the size of the crystals and the thickness of the coating layer (~ 2 nm). Higher initial concentrations lead to 3D self-assemblies where the particles in the second layer occupy sites determined by the hexagonal arrangements.

As the particle diameter is increased, the magnetic moment - and thus, the interparticle interactions - increase. For 12 nm SP particles, their large moment leads to strong repulsive interactions that help to order the solid particles on the microscope grid, as the sample is dried. Thus, the largest and most ordered self-assemblies are found for the larger SP particles. However, when the volume further increases, particles become FM at room temperature and begin forming chains as previously commented.

In addition, particles oxidize progressively inwards when O_2 is bubbled through the solution. By controlling the oxygen rate, the thickness of the CoO layer may be regulated. CoO is antiferromagnetic and Co is FM. It has been repeatedly observed that as adjacent layers of FM

and AFM form, CoO-Co core-shell structures display an increase in coercivity (memory) and a shift of the hysteresis loop after cooling the sample under an applied field due to exchange interactions. This parameter may also be used to finely tune the properties of the desired particles.

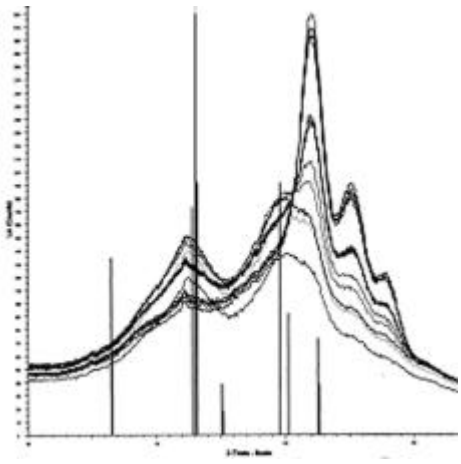

2θ

Fig. 5: XRD of a progressive Co nanoparticle oxidation. Vertical lines correspond to CoO peaks.

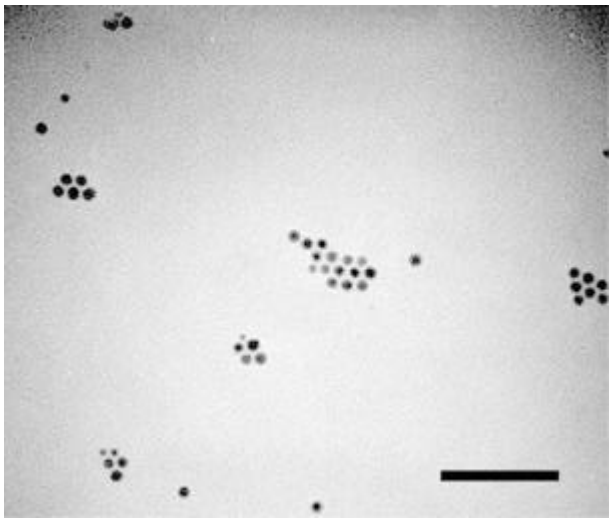

Fig. 6: TEM of CoO-Co particles. CoO appears as a lighter ring around a dark core (due to electron density differences).

These particles are completely insoluble in water and, moreover, they are attacked and rapidly transformed into $Co(OH)_2$. There is an intense effort to solubilize such particles into aqueous solutions for biomedical techniques. Up to now there are four main approaches: i) growing epitaxially another metallic shell which will protect the particle and make it soluble (such as Au or Pt), ii) wrapping the particles with a polymer consisting of hydrophobic and hydrophilic sections, iii) growing amorphous silica around the particle and, iv) attaching a surfactant molecule, like a sugar, that will make the particle water soluble.

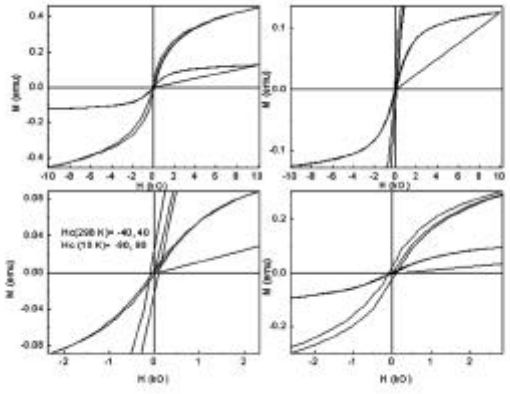

Fig. 7. Hysteresis loop at low T after field cooling at 1 Tesla, showing an increase of the coercivity and shift in the x-axis for samples which have been oxidized (by bubbling O_2 into the solution).

In conclusion, promising results in nanocrystal synthesis may assist the development of magnetic nanosensors and nanoactuators, first *in vitro* and then *in vivo*, for all the existing techniques applicable to magnetic carriers, as well as new ones to come.

REFERENCES: [1]T. Hyeon, Su Seong Lee, Jongnam Park, Yunhee Chung, and Hyon Bin Na (2001) *J. Am. Chem. Soc.* **124**: 12798-801. [2]Puntes VF, Krishnan KM, Alivisatos AP *Science* (2001) **291**:2115-7. [3]Y. R. Chemla, H. L. Grossman, Y. Poon, R. McDermott, R. Stevens, M.D. Alper, and J. Clarke (2000) *PNAS* **97**: 14268-72. [4]Stevenson, J.P.; Rutnakornpituk, M.; Vadala, M.; Esker, A.R.; Charles, S.W.; Wells, S.; Dailey, J.P.; Riffle, J.S. *J. of Mag. and Mag. Mater.* (2000) **225**:47-58; S. Sun, C. B. Murray, *J. Appl. Phys.* 85, 4325 (1999); C. Petit, A.Taleb, P. Pileni, J. Phys. Chem. 103, 1805 (1999); J. S. Yin, Z.L. Wang, *Phys. Rev. Lett.* (1997) **79**:2570; S. Sun, C. B. Murray, D. Weller, L. Folks, A. Moser (2000) *Science* **287**:1989; J. R. Thomas, *J. Appl. Phys.* (1966) **37**: 2914; D. P. Dinega, M. G. Bawendi, *Angew. Chem. Int. ed.* (1999) **38**:1788; T. Ould Ely, C. Amiens, B. Chaudret, *Chem. Mater.* (1999)**11**:526

AKNOWLEDGEMENTS: This work was supported by the NIH National Center for Research Resources, Grant Number 1 R01 RR-14891-01 through the U.S. Department of Energy under Contract No. DE-AC03-76SF00098.

European Cells and Materials Vol. 3. Suppl. 2, 2002 (pages 132-134) ISSN 1473-2262

SINGLE DOMAIN MAGNETS IN BIO-MEDICAL APPLICATIONS

Mladen Barbic

Department of Applied Physics, California Institute of Technology 200-36, Pasadena CA 91125

INTRODUCTION: Miniaturizing mechanical, optical, magnetic, and electronic components is part of a MEMS research effort, with the goal of reducing the size of operating laboratory systems into sub-millimeter or even sub-micron dimensions. There are several factors that make magnetic components attractive for use in MEMS and bio-medical applications. Magnetic components can generally create larger forces at a larger distance than their electrostatic counterparts. Since magnetic devices are responsive to magnetic fields and field gradients generated by the current carrying wires, they also tend to be of low input impedance. In the sub-micron size range, magnetic objects are often in the single domain state where the magnetization can only be in two possible stable states. This fact can be exploited in a variety of applications if the challenges in fabrication can be overcome. Single domain magnets are by default permanent magnets, and require no energy to be magnetized by outside sources. Their small size also translates into large gradient magnetic fields that can be generated, and therefore large magnetic forces that can be applied. Additionally, the fact that the single domain magnets are permanently magnetized allows for both attractive and repulsive forces to be utilized. Based on these principles, several applications of single domain magnets to various technologies will be presented, including magnetic micro-manipulation of individual magnetic beads with micron resolution, micro-manipulation of single domain magnets and development of micro-fluidic micro-motors, utilization of magnetostatic interaction for micro-magnetic tweezers, and ultra-high gradient magnetic separation systems.

MAGNETIC MICROMANIPULATION OF INDIVIDUAL MAGNETIC BEADS: We recently introduced a new micromanipulation technique that utilizes integrated micro-coils and magnetic micro-tips for localized positioning of micron-sized magnetic objects [1]. The magnetic manipulator is shown in Fig. 1, and is fabricated by winding a 25 μm diameter copper magnet wire around a 50 μm diameter soft-ferromagnetic wire. The usual winding design consists of two coil layers with 6-8 turns each. In order to create high field gradients, soft ferromagnetic wire is electrochemically etched into a sharp probe in aqueous 40% sulfuric acid solution at 3 V. The tip

Figure 1

is then positioned in the vicinity of the coil, as seen in Fig. 1, in order to be maximally magnetized by the coil fields. The micro-tweezer's tip was placed on a mechanical stage for positioning the tip above the viewing lens of the microscope. The coil component of the manipulator was connected to a programmable constant current source for tunable operation of the device. The samples to be manipulated were placed inside a rectangular cross section quartz capillary tube with 40 μm capillary wall thickness. White light illumination was coupled to the capillary tube from a 1 mm diameter optical fiber connected to a white light source. The capillary tube containing the magnetic particles was placed between the tip and the lens, and the micro-tip was positioned within several microns of the outside capillary tube surface.

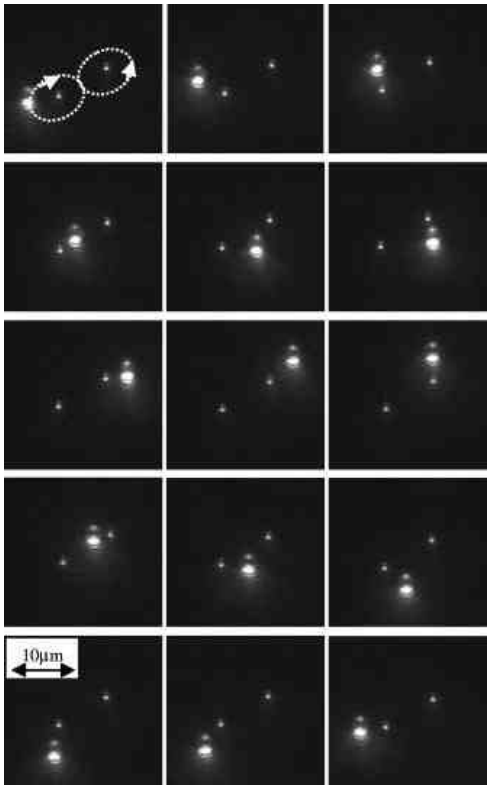

Figure 2

Figure 2 shows a composite of successive images of the magnetic bead manipulated so as to trace a "figure eight" around the non-magnetic beads. The non-magnetic polystyrene beads in the figure are 10 μm apart, and we are able to achieve sub-micron positioning resolution. One should also note the high dark background contrast in Figure 2 due to the illumination method used in the micromanipulation technique. Although the tip of the micromanipulator is very close to the particle, there is no observable scattered light from the manipulator tip, due to the total internal reflection at the outside capillary surface. Forces of 10 pN and sub-micron positioning control were demonstrated on the 2.8 μm diameter superparamagnetic beads.

ELECTRO-MAGNETIC MICRO-FLUIDIC MICROMOTOR


Figure 3

Manipulation of magnetic objects by the micro-manipulator described in the previous section was extended to applying torques and forces on a magnetic single domain particle inside a fluid, acting as a micro-fluidic micro-motor. Magnetic micro-motors with sub-millimeter dimensions have previously been fabricated by semiconductor processing techniques. We miniaturized and simplified the micro-motor design by arranging three micro-manipulator coils and tips into an equilateral triangle arrangement, as shown in Figure 3. This device acted as the three-phase stator of the micro-motor positioned outside of the fluid, while an individual single domain particle placed in a fluid acted as the rotor. The rotor was a cylindrical nickel particle, 40 μm long and 1 μm in diameter, and is fabricated by electro-deposition of nickel into a porous nano-channel glass membrane.

The electric currents through the three micro-coils were sinusoidally driven at a 120 degree phase difference in respect to each other (three-phase motor). This arrangement of the currents provided the sinusoidal attractive and repulsive forces to be applied to the magnetic rotor, resulting in the rotational motion of the single domain particle.

Figure 4 shows the composite sequence of images demonstrating one full rotation of the rotor.

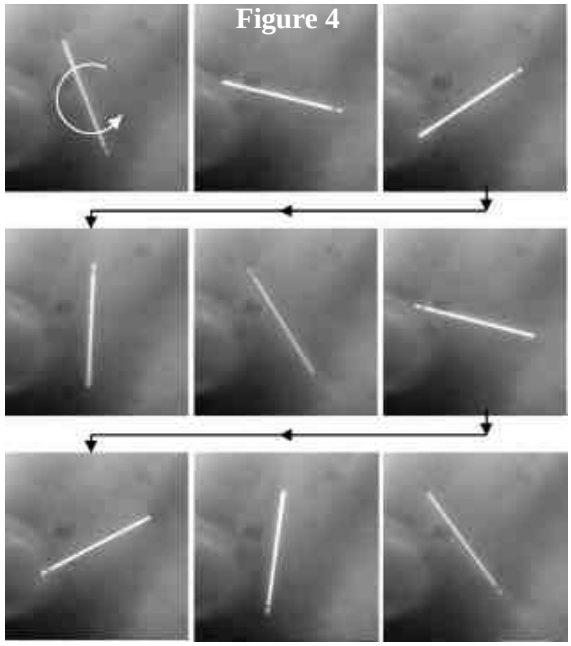
Figure 4

MAGNETIC MICRO-WIRE MAGNETO-STATIC TWEEZERS

Manipulation of magnetic micro-wires in fluid environments described in the previous section was extended into a regime where magneto-static interaction between two micro-wires is utilized for the construction of a magneto-mechanical tweezers system. The opposite poles of the micro-wires are attracted to each other, and form a natural clamping system. Figure 5 shows a sequence of images where the two magnetic nickel wires, 9 micro-meters long and 250 nm in diameter, are closed by the magnetic micro-manipulator.

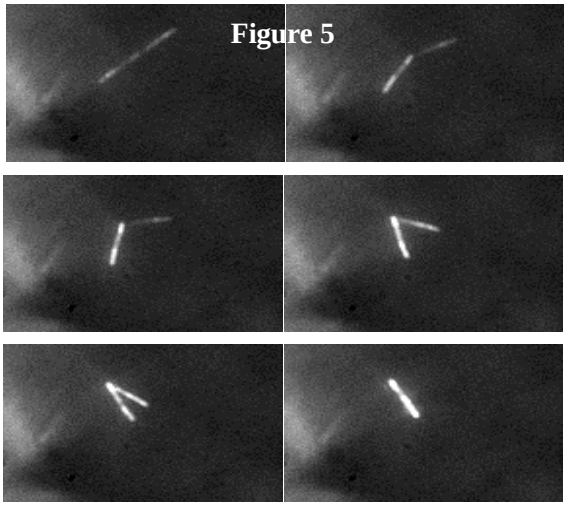
Figure 5

We developed several methods of opening and closing magnetostatic nanowire tweezers using hysteresis properties of this coupled magnetic

system as well as using the localized manipulator of Figure 1.

ULTRA-HIGH GRADIENT MAGNETIC SEPARATION

In the described uses of magnetic wires in micro-fluidic applications, the magnetization of the wires has always been along the wire long axis. However, the wire can be a source of strong gradient fields along the entire length of the wire if the external field is used to orient the magnetization perpendicular to the wire long axis. This principle is often used in ultra-high gradient magnetic separation applications where a fluid of interest is passed through a magnetized wire mesh. A nano-porous membrane partially filled with magnetic wires can provide a potentially superior template for magnetic separation in bio-medical applications.

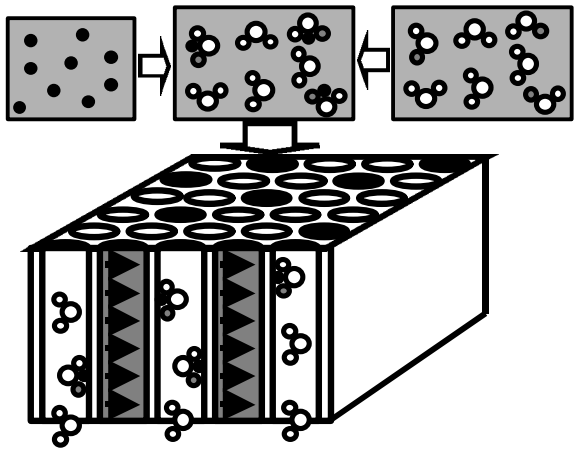

Figure 6

Figure 6 shows a simple example of applying a magnetic separation filter. The magnetic beads on the left are engineered to bind to the specific biological system (molecules, proteins, viruses, bacteria) and are mixed with the biological solution of interest on the right. After the binding process, the solution is passed through the partially filled ultra-high gradient magnetic separation filter. An external magnetic field is applied parallel to the filter surface in order to magnetize the ferromagnetic cylinders perpendicular to the wires' long axis. Inside the filter, the biological system bound to the magnetic bead is trapped on the walls of the capillaries while the unbound units are passed though. The trapped particles can later be released by removing the external magnetic field.

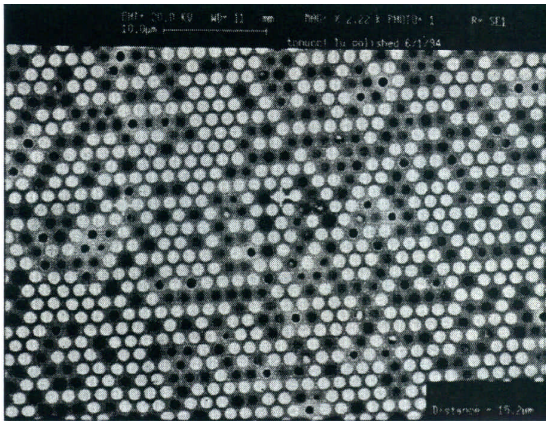

Figure 7

Figure 7 shows an example of a partially filled porous membrane that could be used for the described purpose.

REFERENCES: M. Barbic, J. J. Mock, A. P. Gray, and S. Schultz, *Applied Physics Letters* **79**, 1897 (2001). M. Barbic, J. J. Mock, A. P. Gray, and S. Schultz, *Applied Physics Letters* **79**, 1399 (2001). M. Barbic *Journal of Magnetism and Magnetic Materials* (in press 2002).

ACKNOWLEDGEMENTS: I am indebted to Jack Mock and Andrew Gray for technical help, Robert O'Barr for preparation of magnetic particles, Ron Tonucci for providing the plating template membranes, and Prof. Sheldon Schultz for use of laboratory equipment and space. This work was supported by the grants form NSF DMR9724535, NIH PHS H601959-02, and ONR (DARPA) N00014-00-1-0632.

ENRICHMENT AND BIODISTRIBUTION OF A MAGNETICALLY TARGETED DRUG CARRIER

Ch. Alexiou, Ch. Bergemann,[1] R. Schmid, P. Hulin, A. Schmidt, R. Jurgons, W. Arnold, F.G. Parak[2]

Department of Otolaryngology, Head and Neck Surgery, Klinikum rechts der Isar, Technical University of Munich, 81675 Munich; [1]Chemicell, 10777 Berlin; [2]Physics-Department E 17, Technical University of Munich, 81675 Munich, Germany

INTRODUCTION: Biocompatible ferrofluids are superparamagnetic nanoparticles, that may be used as a delivery system for anticancer agents in locoregional tumor therapy, called "magnetic drug targeting." Through this form of target directed drug application, one attempts to concentrate a pharmacological agent at its site of action in order to minimize unwanted side effects in the organism and to increase its loco-regional effectiveness [1]. Ferrofluids have been used in medicine since the 1960's for magnetically controlled metallic thrombosis of intracranial aneurysms [2] and magnetically guided selective embolization of the renal artery in case of a renal tumor [3], for example. Ferrofluids have also been used as a contrast agent for MRI in the diagnostic evaluation of liver and spleen tumors [4]. Furthermore ferrofluids have been used for a specific cell separation method called "immuno-magnetic cell separation" for the early detection of cancer [5], and have also been an important subject in the development of an implantable artificial heart [6].

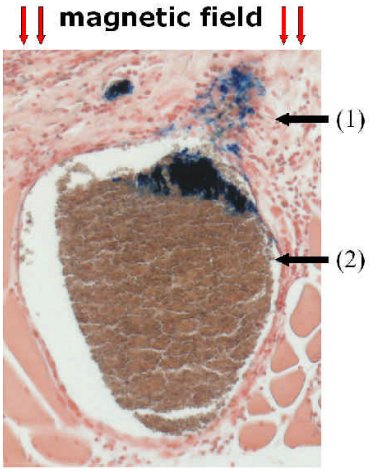

Fig. 1: Section of the tumor removed after treatment with ferrofluids stained with Prussian blue. The orientation of the ferrofluid to the gradient of the magnetic field is clearly visible in the tumor tissue (1) and in the vascular lumen (2).

MATERIALS AND METHODS: The ferrofluids used in the experiments were obtained from Chemicell (Berlin, Germany; German patent application no. 19624426.9) and consisted of a colloidal dispersion of iron oxides and hydroxides. The particles were surrounded by starch polymers for stabilization under various physiological conditions and to allow ionic binding to chemotherapeutic agents or to form a complex with iodine [7].

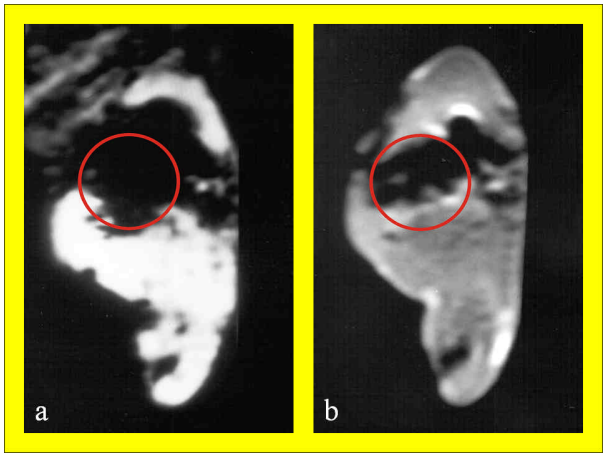

Fig. 2: Magnetic resonance imaging of rabbit's left hind limb following intraarterial ferrofluid application; (a) T2-weighted, (b) T1-weighted imaging technique.

The ferrofluids were injected into the tumor supplying artery (femoral artery) of tumor bearing rabbits (squamous cell carcinoma at the medial portion of the hind limb). An external magnetic field was focused on the tumor for 60 min. Enrichment of ferrofluids in tumor tissue was documented in vivo by histological analysis (five µm thick paraffin sections of the tumor were cut and stained with Prussian Blue) (Fig. 1) and by magnetic resonance imaging (T1- and T2-weighted MRI) using an electro-magnetic field with a strength of 1.7 Tesla (Fig. 2). Biodistribution was studied semi-quantitatively by the use of ^{123}I-labeled nanoparticles focused by an external magnetic field (permanent magnet) of 0.6 Tesla (Fig. 3), and quantitatively with radioactive ^{59}Fe-ferrofluids using an external magnetic field of 1.7 Tesla (electromagnet) (Fig. 4).

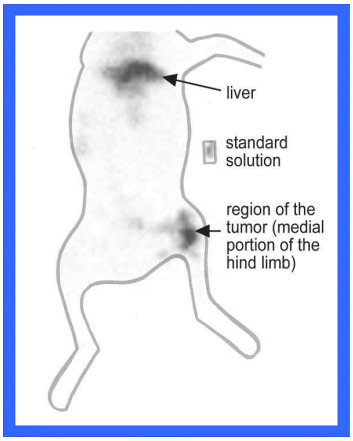

Fig. 3: Enrichment of ^{123}I-labeled nano-particles in the region of interest (VX2-tumor) after "Magnetic Drug Targeting." This image was taken 10 minutes after application, still showing stable concentration of ferrofluids in the tumor region.

Sedimentation characteristics of ferrofluids were investigated in vitro. A ^{125}I-ferrofluid suspension was incubated in 96-well-plates in magnetic field strengths of 0, 0.2 and 0.4 Tesla. Activities of the upper and the lower phases were determined (Fig. 5).

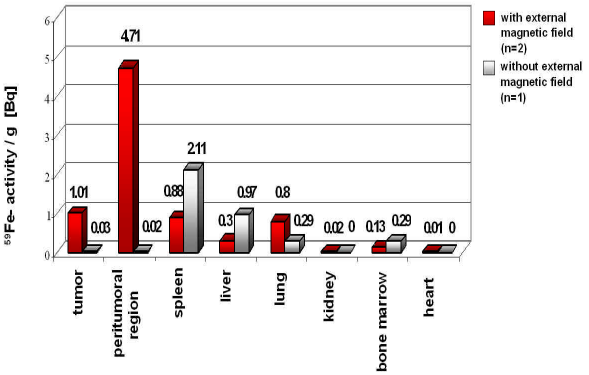

Fig. 4: Radioactive ^{59}Fe-distribution 60 minutes after intraarterial application.

RESULTS: In histological investigations, we could demonstrate enrichment of ferrofluids in tumor tissue (Fig. 1). MRI investigation revealed a definitive extinction of signal in the area of the tumor, which was caused by the enrichment of ferrofluids due to the magnetic field (Fig. 2). The scintigraphically detected ^{123}I-signal has been shown to be significantly higher in the magnetically focused region compared to application without magnetic field (Fig. 3).

^{59}Fe-ferrofluids could be concentrated in the tumor area by a factor of 235 using an external magnetic field compared to the absence of a magnetic field. In vitro studies using ^{125}I-labeled ferrofluids showed sedimentation to be dependent on magnetic field strength (Fig. 5). No sedimentation was found with gravitation alone (triangles). By using permanent magnets a logarithmic dependency was observed. The fraction of sedimentation was not doubled by doubling the strength of the magnetic field.

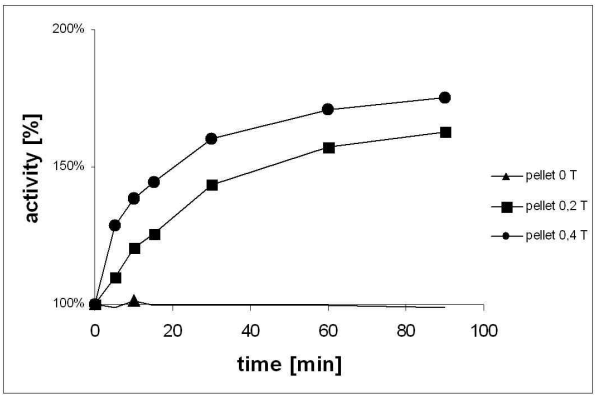

Fig. 5: Activity of sedimentary ^{125}I-labeled nanoparticles in dependence on magnetic field strength and time in the lower phase.

DISCUSSION & CONCLUSIONS: Besides conventional investigation (i.e. histological cross sections and MRI), the biodistribution studies with radioactive labeling showed enrichment of ferrofluids targeted by a focused magnetic field and also, semi-quantitatively and quantitatively, a high and selective concentration in the tumor region. In vitro data indicate a strong dependency of sedimentation on the magnetic field strength.

REFERENCES: [1]C. Alexiou, W. Arnold, R.J. Klein, et al. (2000) *Locoregional cancer treatment with magnetic drug targeting,* Cancer Res. **60**:6641-6648. [2]J.F. Alksne, A. Fingerhut, R. Rand (1966) *Magnetically controlled metallic thrombosis of intracranial aneurysm,* Surgery **60**:212-218. [3]S.K. Hilal, W.J. Michelsen, J. Driller, et al. (1974) *Magnetically guided devices for vascular exploration and treatment,* Radiology **113**:529. [4]R. Weissleder, P.F. Hahn, D.D. Stark, et al. (1987) *MR imaging of splenic metastases: ferrite-enhanced detection in rats, AJR* **149**:723. [5]J.E. Hardingham, D. Kotasek, R.E. Sage, M.C. Eaton, V.H. Pascoe (1995) *Detection of circulating tumor cells in colorectal cancer by immunobead-PCR is a sensitive prognostic marker for relapse of disease, Molecular Medicine* **1**:789-794. [6]Y. Mitamura, T. Wada, K. Sakai (1992) *A ferrofluidic actuator for an implantable artificial heart, Artif.*

Organs Oct; **16**(5):490-5. [7]A.S. Lübbe, C. Bergemann, H. Riess, et al. (1996) *Preclinical experiences with magnetic drug targeting: tolerance and efficacy, Cancer Res.* **56**:4686.

ACKNOWLWDGEMENTS: This study was supported by the Margarethe Ammon Foundation, Munich, grants from the Technical University of Munich, Germany and the German Research Community (DFG, AL552-1).

PHYSICAL CHARACTERISTICS OF POLYMER MICROSPHERES, FILLED WITH MAGNETITE NANOPARTICLES

R.A. Ali-zade

Institute of Physics Azerbaijan National Academy of Sciences, 370143 Baku, Azerbaijan

INTRODUCTION: Polymer magnetic microspheres (PMMS) have been synthesized from collagen and polystyrene [1,2]. Four types of magnetite nanoparticles with average particle sizes of 9.48±0.15 (I), 7.7±0.15 (II), 7.3±0.07 (III) and 5.48±0.11 (IV) nm respectively have been used as magnetic filler. PMMS was synthesized in three sizes of 255.49±1.55, 179.09±1.49, 46.92±7.33 μm with narrow size distributions. Figure 1 shows PMMS filled with sample IV magnetite nanoparticles (PMMS-IV).

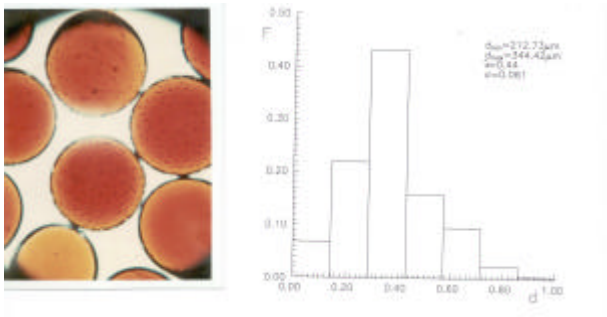

Fig. 1: Microphotography of PMMS-IV (left) and size distribution of PMMS-IV (right).

The object of the present work is to investigate the physical characteristics, structure and mechanism of magnetization of PMMS.

METHODS: *Determination of concentration of magnetite nanoparticles.* Density of polymer microspheres without magnetite nanoparticles (PMS) and with magnetite nanoparticles (PMMS) is determined by following formulas:

$$r_{PMS}=r_1V_1/V_{PMS}+r_2V_2/V_{PMS} \quad (1)$$

$$r_{PMMS}=r_1V_1/V_{PMMS}+r_2V_2/V_{PMMS}+r_3V_3/V_{PMMS} \quad (2)$$

where r_{PMS}, r_{PMMS}, r_1, r_2, r_3 are the density of PMS, PMMS, polymer matrix (collagen, polystyrene), carrier medium and magnetite, respectively. V_{PMS}, V_{PMMS}, V_1, V_2, V_3 are the volume of PMS, PMMS, polymer matrix (collagen, polystyrene), carrier medium and magnetite, respectively. r_{PMS} =1.0597 g/cm^3, r_1=1.1608 g/cm^3, r_2=0.9982 g/cm^3, r_3=5.24 g/cm^3.

The concentration of carrier medium in PMMS is determined as $j_2=V_2/V$ and consequently we obtained $j_2=(r_{PMS}-r_1)/(r_2-r_1)$. We substituted the value of φ_2 to (2) and receive $j_3=(r_{PMS}-r_{PMMS})/(r_3-r_2)$ for the concentration of magnetite nanoparticles in PMMS.

The density of PMS and PMMS is determined on the basis of measurement of mass of fixed number of PMS and PMMS in a Mettler HE20 sedimentometer. The density is determined as $r=M/V$, where M, V are total mass and volume of microspheres.

Preparation of section of PMMS for electron microscopy investigation. PMMS was deprived of water by consequently transferring to 50, 60, 70, 80 and 96% ethanol for 20 min each, followed by 1 h in acetone. Then PMMS was transferred to solution of mixture I-acetone = 1:3; 1:1; 3:1. Mixture I consists of DMP=57:0.67, where mixture is 54(812 EPON):36(DDSA):24(MNA). PMMS were sectioned to about 50 nm in a LKB UM IV Ultrotome.

Measurement of magnetic susceptibility of individual PMMS. Magnetic susceptibility of individual PMMS was determined on the base analysis of velocity of movement of microspheres under gradient magnetic field, created with ferromagnetic cylinder, placed in uniform magnetic field. Apparatus for determination of magnetic susceptibility of PMMS and mathematical formula for its calculation has been described in [3].

RESULTS: Structure of PMMS and size of magnetite nanoparticles in PMMS was carried out by electron microscopy (Figure 2).

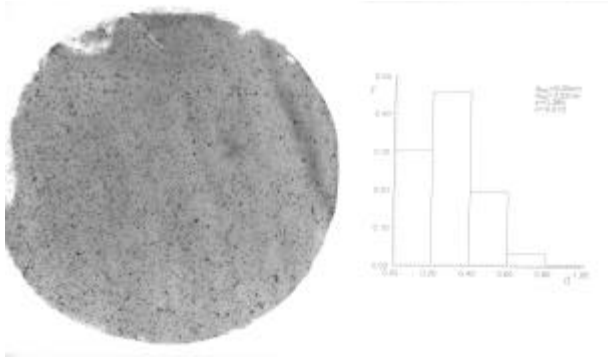

Fig. 2: Microphotography of sectioned PMMS-IV (left) and size distribution of enclosed magnetite nanoparticles-IV (right).

The magnetite nanoparticles are homogeneously distributed throughout the polymer matrix. The

average distance between magnetite nanoparticles, as determined by EM sections of PMMS-IV is 17.4 nm. Determination of average diameter of magnetite nanoparticles before and after filling into PMMS-IV is shown. No change in size of the magnetite nanoparticles takes place, and there are no aggregates formed during microsphere synthesis. Figure 2 also shows the size distribution of magnetite nanoparticles.

Magnetic susceptibility of 120 individual PMMS with concentration of magnetite nanoparticles equal to j_t=0.013 at H=206.4 kA/m was determined. The average value of magnetic susceptibility of PMMS equaled to $4.79 \cdot 10^{-3}$.

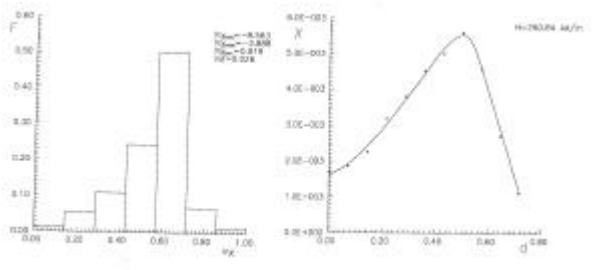

Fig. 3: Distribution of PMMS-IV versus logarithmic value of magnetic susceptibility (left), and dependence of magnetic susceptibility on the diameter of PMMS-IV (right).

Figure 3 (left) shows the histogram of distribution versus the logarithmic value of magnetic susceptibility of PMMS. Agreement of histogram of distribution on diameter and logarithmic value of magnetic susceptibility of PMMS has been investigated by χ^2 criterion method. It is shown that 95% agreement is presented and correspondingly the dependence between diameter and magnetic susceptibility of individual PMMS exists. In preliminary calculations, a coincidental value of magnetic susceptibility of PMMS with certain diameter has been discarded by 4th-D and Q methods. The dependence of magnetic susceptibility of PMMS-IV on diameter has been determined and is presented in Figure 3 (right).

We suggest that the magnetization of PMMS occurs by magnetization of the sum of sections magnetic moment of PMMS, which consists of magnetic moment of chains formatted along an external magnetic field. Value of magnetic moment of chain depends on the magnetic moment and the number of magnetite nanoparticles. At a small diameter of PMMS-IV, magnetization occurs by magnetization of all chains. At larger diameters of PMMS, the number of magnetite nanoparticles in chains is increased and chains are destroyed.

We investigated the magnetic susceptibility of PMMS at different concentration of magnetite nanoparticles j_m=0.0007, 0.001, 0.003, 0.008, 0.01 to exam our hypothesis about magnetization of PMMS at small diameter. Our results show that at small concentrations of magnetite nanoparticles, the magnetic susceptibility of PMMS-IV is a leaner function of concentration ($\chi = 0.69 \cdot \varphi_m - 0.52 \cdot 10^{-3}$). The value of magnetic susceptibility is increased with increasing concentration of magnetite nanoparticles.

At increasing diameters of PMMS-IV, chains of magnetite nanoparticles are destroyed. The length of chains depends on the magnetic field and the energy interaction between magnetite nanoparticles. The number of magnetite nanoparticles with average diameter d=5.48 nm, localized in diameter of PMMS-I d=304.36, 314.51, 324.13 μm at concentration of nanoparticles j_t =0.0258 is equal to 17913, 18510, 19076 respectively. The number of magnetite nanoparticles in chaines determined by formula in [4] is equal to 16130, 13096, 14310 respectively. As shown, the real value of magnetite nanoparticles is larger than the value determined by formula in [4]. Thus, at big diameters of PMMS occurs a transformation of chains to clusters with decreased magnetic susceptibility.

DISCUSSION & CONCLUSIONS: The analysis of our experimental results shows that magnetite nanoparticles are homogenously localized in PMMS. Magnetization of PMMS at small diameters occurs by magnetization of chains of magnetite nanoparticles, located along the diameter of microspheres. At larger diameters of PMMS, the chains are converted to clusters, with consequently decreased values of magnetic susceptibility.

REFERENCES: [1] S.I. Turkin, Yu.V. Lukin, E.A. Markvichyeva, et.al, (1989) *Method of preparation of collagen microcarriers. A.S. N 1486515, Moscow, USSR.*. [2] S.I. Turkin, Yu.V. Lukin, E.A. Markvichyeva, et al (1990) *Method of preparation of magnetic microcarriers. A.S. N 1567623, Moscow, USSR.*. [3]Yu.A. Plyavinsh, E.Ya. Blum (1983) Magnitnaya gidrodinamika, **4:**3. [4] M.P. Shiliomis (1974) *UFN*, 112, 427.

DOXORUBICIN MEDIATED FREE IRON RELEASE FROM FERRITIN MAGNETOPARTICLES IS ENHANCED AT HIGHER TEMPERATURES: IMPLICATIONS FOR CANCER THERAPY

M. Babincová[1], V. Altanerová[2], È. Altaner[2], Z. Baèová[1], P. Babinec[1]

[1]Department of Biophysics and Chemical Physics, Comenius University, Mlynská dolina F1, 842 48 Bratislava, Slovakia [2]Cancer Research Institute, Slovak Academy of Sciences, Vlárska 7, 833 91 Bratislava, Slovakia

INTRODUCTION: One of the principal forms in which iron is stored in living organisms are magnetic nanoparticles of hydrated iron oxide of the composition $5Fe_2O_3.9H_2O$ bound by an apoferritin protein shell. These iron containing proteins, i.e. ferritins, play an important role in the regulation of free iron within the cell. Mobilization of iron from ferritin requires reduction of ferric Fe(III) iron to ferrous Fe(II) iron and several reductants have been identified. Among them are also some antitumor anthracycline drugs. The anthracycline antibiotic doxorubicin (adriamycin®) has been in use for more than 30 years for the treatment of a variety of malignancies such as those arising in the breast, bile ducts, endothelial tissue, the esophagus and liver, osteosarcomas, and soft-tissue sarcomas [1]. Despite the extensive and long-standing clinical utilization of this drug, its mechanism of action is not clear. A number of different mechanisms have been proposed, including intercalation into DNA, free radical formation with consequent DNA damage, DNA cross-linking and inhibition of topoisomerase II [2]. Tritton and Yee [3] reported that doxorubicin (DOX) coupled to insoluble agar beads that cannot traverse the membrane was more toxic than free drugs, and as an alternative hypothesis direct membrane-mediated effects were proposed for the DOX toxicity. Due to the fact that DOX was found to stimulate iron release from ferritin in the presence of P450 reductase and NADPH [4] and because reduced Fe^{2+} is required for oxidative damage of membrane lipids, we have in this paper investigated DOX mediated iron mobilization at various temperatures. We were stimulated by an experimental finding that DOX efficacy is enhanced at higher temperatures [5], explained by a possibly higher permeability of cells.

MATERIAL AND METHODS:

1. Chemicals

Horse spleen ferritin, ferrozine NADPH, TBA, and trichloric acid were obtained from Sigma (St. Louis, USA). NADPH-cytochrome P-450 reductase isolated from rat liver microsomes was kindly supplied by Dr. P. Sourivong. Other chemicals were from commercial sources and were of the highest analytical grade.

2. Iron release assay

Iron concentration was determined by the spectrophotometric measurement of the iron-ferrozine complexes [7]. Reaction mixture containing ferritin (100 μg/ml), ferrozine (1.0 mM), NADPH-cytochrome P-450 reductase (0.2 U) and DOX (1 mM) was preincubated at various physiological temperatures (36-42 °C) and the reaction was initiated by the addition of NADPH (0.7 mM). The absorbance at 562 nm (the absorption coefficient of iron-ferrozine complex is 27 900 M^{-1} cm^{-1}) was measured against a blank containing the same reaction mixture except NADPH using spectrophotometer Specol 210 (Carl Zeiss, Jena, Germany).

3. Lipid peroxidation measurement

The extent of lipid proxidation was determined by measuring TBA-reactive substances (TBARS) [8]. The reaction mixture described above was augmented with phosphatidylcholine liposomes (5 μmol/ml) and 30 min after NADPH addition 0.5 ml of it was added to 2 ml TBA reagent consisting 15 % trichloric acid 0.375 % TBA and 0.5 HCl and heated in 100 °C water bath for 15 min. After cooling in ice-cold water, the mixture was centrifuged at 1250 × g for 10 min. The absorbance of the supernatant at 535 nm was read against a blank containing 2 ml TBA and 1 ml distilled water. The concentration of TBARS was calculated using the molar absorption coefficient 156000 M^{-1} cm^{-1}.

RESULTS AND DISCUSSION: Figure 1 shows that the presence of DOX actually release iron from horse spleen ferritin and that the release at 42 °C is almost 4 times higher than at 36 °C. We have further investigated lipid peroxidation which occurred when phospholipid liposomes were incubated with ferritin, DOX, and other reagents for 30 min. The formation of TBARS increased 8-fold at 42 °C as compared with 36 °C (Fig. 2).

The potential involvement of free radical generation in the cytotoxicity of the anthracyclines (both in terms of antitumor effects and cardiotoxicity) is complex and confusing. There is no question that under appropriate conditions the chemistry of the anthracyclines lends itself to the generation of reactive free radicals. The quinone structure permits DOX to act as electron acceptors in reactions mediated by oxoreductive enzymes including cytochrome P-450 reductase. The addition of the free electron converts the quinones to semiquinone free radicals, which may induce free radical injury to DNA as well as membranes. The problem is that the required DOX concentrations are substantially lower than clinically relevant concentrations.

The analysis of a new mechanism proposed in our study clearly demonstrated that the damage of membrane lipids due to their peroxidation may be a key element of the DOX cytotoxic effect by iron mobilized from ferritin (as has been found [6], ferritin levels in tumors are substantially higher than in the normal tissue) and moreover it offers a theoretical rationale for the combination of DOX chemotherapy with local hyperthermia for more effective treatment of tumors.

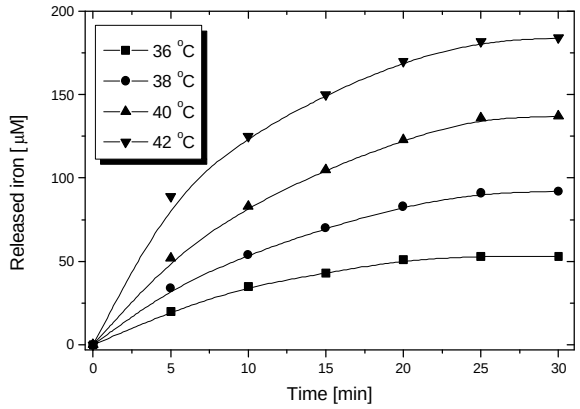

Fig. 1: Time course of iron release from ferritin by 1 mM doxorubicin at various temperatures.

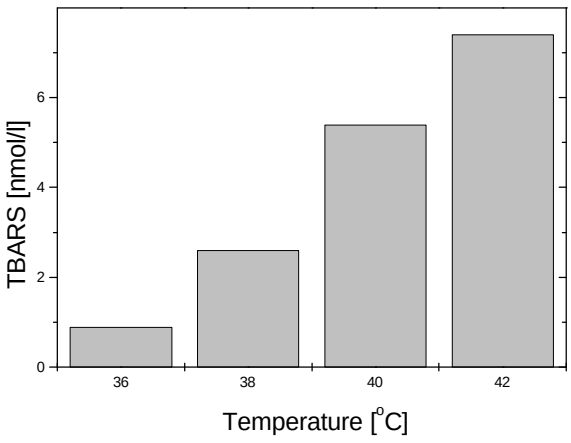

Fig. 2: *Lipid peroxidation of phosphatidyl-choline liposomes induced by doxorubicin in the presence of ferritin at various temperatures.*

REFERENCES: [1] G.P. Murphy, W. Lawrence and R.E. Lenhard, (1995) *American Society Textbook of Clinical Oncology*, American Cancer Society, Atlanta, GA. [2] D.A. Gewirtz (1999) *Biochem Pharmacol* **57**: 727-41. [3] T.R. Tritton and G. Yee (1982) *Science* **217**:248-50. [4] E.T. Craig and S.D. Aust (1986) *Arch Biochem Biophys* **248**:684-689. [5] G.M. Hahn, J. Braun and I. Har-Kedar (1975) *Proc Natl Acad Sci USA* **72**:937-40. [6] J. Blatt, D. Huntley and P.K. Eagon (1990) *Cancer Biochem Biophys* **11**:169-76. [7] R.F. Boyer, T.W. Grabill and R.M.Petrovich (1988) *Anal Biochem* **174:**17-22. [8] J.A. Buege and S.D. Aust (1987) *Methods Enzymol* **52**:302-10.

ACKNOWLEDGEMENTS: This work was supported by VEGA grant No. 1/9179/02.

COLLOIDAL – CHEMICAL LAWS OF INTERACTIONS OF MAGNETIC FLUID PARTICLES WITH SURFACES OF NATURAL FIBERS

Felix S. Bayburtskiy*[1], Irina I. Senatskaya*[1], Alexander S. Skorovarov[1], Valeriy A. Boldyrev[1], Nilkolay A. Brusentsov[2], Lyubov Kh. Komissarova[2], Vasiliy A. Razumovskiy[2].

[1]*All-Russian Research Institute of Chemical Technology, Kashyrskoye shosse 33, Moscow, 115320.*
[2]*Blokhin Oncological Research Center RAMS, Kashirskoe shosse 24, Moscow 115478 Russia.*

INTRODUCTION: The interaction of magnetic fluids (MF) with an extraneous phase (including particles, fiber and tissue) can break the aggregation stability of a magnetic phase and cause sedimentation. Coagulation of magnetic fluid particles on a surface of an extraneous phase occurs spontaneously, that is at the expense of power resources of the system. The contact of natural fibers and tissues with magnetic fluids allows the coating of their surface with magnetic layers and gives them magnetic properties. Our investigations [1-3] are devoted to study this phenomenon. The preparation of metal particle films and strings from polymeric materials is possible by introducing particles of these metals in a polymeric phase during the stage of fiber formation. This method cannot be applied to fibers of natural origin, as the thermal or chemical influence on them will result in their irreversible destruction. The modification of a surface by coagulation [4,5] allows creating biologically compatible magnetic strings and filters based on these strings.

MATERIALS: MF were prepared by the peptization method, using various types of stabilization.

Table 1. MF characteristics.

MF	$\rho \cdot 10^{-3}$ kg/m^3	Ñ, (%)	$D_1 \cdot 10^9$ m	$D_2 \cdot 10^9$ m
1	1,11	11, 4	12	60
2	1,17	14, 3	12	200

MF	$S_S \cdot 10^{-3}$ m^2/kg	$\eta \cdot 10^3$ Pa · c	B, G	$B_S \cdot 10^3$ G · m^3/kg
1	96	7	102	92
2	100	16	94	81

r – Density of MF; C – concentration of a magnetic phase (mass); D_1, D_2 – diameters of magnetic particles without or with the thickness of a stabilizing surfactant or polymer layer; S_S – specific surface of magnetic particles; h – viscosity of MF; B – magnetic properties of MF; B_S – specific magnetic properties of MF.

MF_1 contained spherical magnetite particles (Fe_3O_4) stabilized in aqueous medium by the anionic surfactant sodium oleate (70 g/l). MF_2 contained spherical γ–Fe_2O_3 particles stabilized in aqueous medium by the polymer dextran (200 g/l). The MF choice is based on the fact that MF_1 is widely used in laboratory and industrial investigations, and that MF_2 is of interest in biology and medicine (Table 1). The chosen natural fibers and their properties are given in Table 2.

Table 2. Fiber characteristics.

Natural fiber	Albumen	$\rho \cdot 10^{-3}$ kg / m^3	$S_S \cdot 10^{-3}$ m^2 / kg
Wool	Keratin	1300	950
Catgut	Collagen	1440	700

r – Density of MF; S_S – specific surface of fibers.

METHODS: The basic physico-chemical parameters of the colloidal systems were analyzed as follows. The *density* of magnetic fluids and natural fibers was determined with a picnometer. The *concentration* of particles was determined gravimetrically. The *size and specific surface* of the magnetic particles were examined by means of line ultramicroscopic and photon-correlation spectrometer (Malvern model 4300, England). The *specific surface* of natural fibers was determined by adsorption of nitrogen by the BET method. The *viscosity* of magnetic colloids was determined with a scanning rotational rheometer Low - Shear 30. The *magnetic properties* were investigated with a ferrograph 1.033 (FRG). The *sedimentation stability* of prepared magnetic colloids was investigated in a centrifuge at 6000 rpm for 1h. The *electrostatic surface properties* of magnetic fluids and natural fibers were investigated by electrophoresis and electroosmosis, using a background electrolyte of 0.013 Ì KCl solution and correcting the ðÍ with 0.027 Ì HCl and 0.0178 Ì KOH. The investigation of MF particle coagulation on the surface of natural fibers was carried out optically with a photocolorimeter KFK – 2 after direct contact of the magnetic fluids (1.0 kg/m^3) with fibers.

The aggregation stability of MF with positively and negatively charged particles at a pH between 6 to 8 and with or without electrolytes was investigated. The binding kinetics was investigated

with or without electrolytes, using different amounts of fibers with modified or unmodified surfaces. For the initiation of slow MF coagulation, 0.05 M HCl and NaOH solutions were used. The surface modifiers for the fibers were anionic surfactants (sodium dodecylbenzensulphonate (sulphonol), sodium carboxymethylcellulose (Na–CMC)) and cationic surfactants (dodecylammonium chloride (DACl), dodecyl dimethyl benzene ammonium chloride (cathamine)).

RESULTS AND DISCUSSION: The MF – fiber interactions take place within 5 days (Fig. 1 and 2) and can be explained by good particle stabilization by the surfactants and polymers. The coagulation of highly dispersed magnetic particles on a firm surface is shown in two processes: direct interaction of MF particles with points on a surface and interaction of MF particles with particles and their aggregates fixed on a surface. These processes proceed simultaneously, but at various speeds. The degree of fiber coating can be predetermined by regulating the two involved processes. The MF cooperates with all macrophases, but to different extents. The initial ratio of cooperating phase surfaces determined in parameter q is very important:

$$q = S_{1S} \cdot m_1 / S_{2S} \cdot m_2 \quad (1)$$

where S_{1S}, S_{2S} are the values of specific surfaces of magnetic particles and fibers (m^2/kg), m_1, m_2 are the masses of the magnetic phase and fibers (kg).

The coagulation kinetics depends on the mass of the entered fiber at constant concentrations of MF (Figure 1).

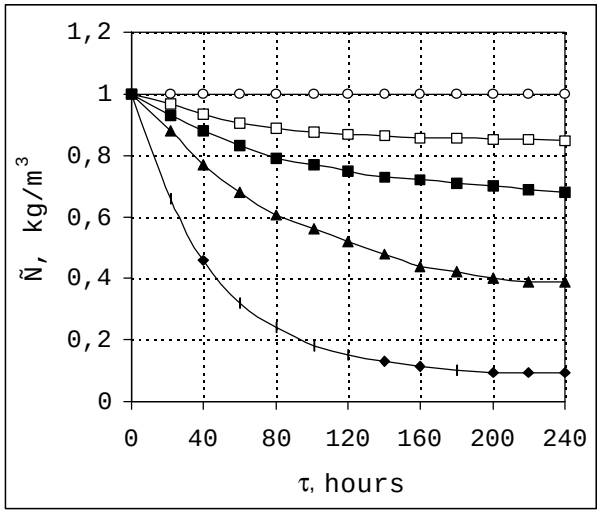

Fig. 1. Kinetics of particles MF_1 coagulation on a fiber (wool) at various q:
without added electrolyte
with added electrolyte
MF_1 with electrolyte in contact to a fiber
q = 0.02; q = 0.10; q = 0.20

The surface condition of the fiber is also very important (Figure 2). The process proceeds most effectively when cationic surfactants (DACl and cathamine) are present.

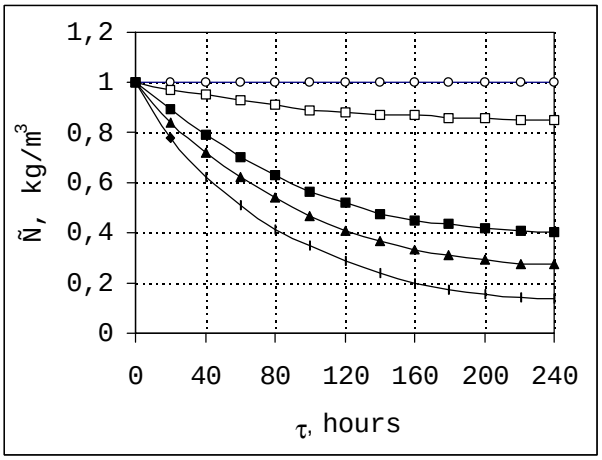

Fig. 2. Kinetics of particles MF_1 coagulation on a fiber (wool) at q = 0.10:
without added electrolyte
with added electrolyte
MF1 with electrolyte in contact to a fiber
in contact with a fiber modified by DACl
in contact with a fiber modified by cathamine

It proves to be true by dependences of quantity fixed on fibers magnetic coagulum from equilibrium concentration of a magnetic phase in solutions MF, achieved to time of the termination of process (Figures 3 and 4). They look like curves leaving on a plateau, with the further rise upwards, that testifies to formation on a surface of fibers mono- and polylayers of magnetic particles structures.

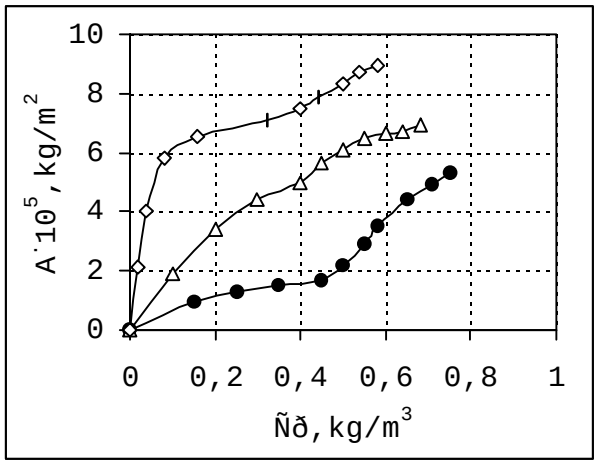

Fig. 3. Amount of magnetic coagulum A from MF1 fixed on a fiber (wool) at different equilibrium concentrations Cp.

We received similar results using catgut (data not shown).

The presented results will allow choosing the conditions to fine-tune a fiber coating with mono- or multi-layers of magnetic particles.

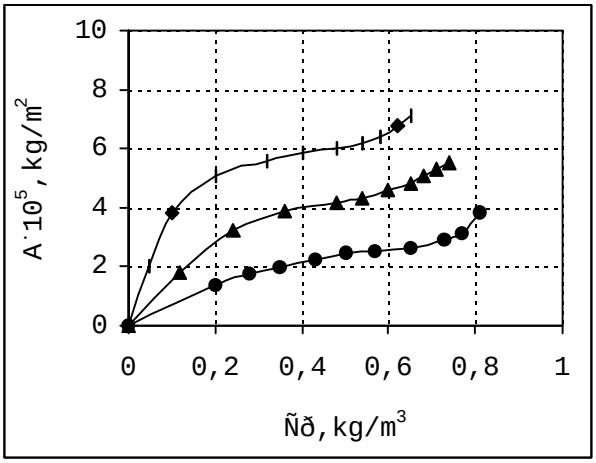

Fig. 4. Amount of magnetic coagulum A from MF_2 fixed on a fiber (wool) at different equilibrium concentrations Cp.

ðèãå fiber; fiber modified with:

DACl; cathamine;

sulphonol; Na-CMC.

The aggregation stability of a magnetic fluid is disturbed near a fiber. The level of this process is determined by experimental conditions such as ðÍ. Driving forces of interaction between MF particles and a fiber are the differences of superficial forces at the borders between "particle of a magnetic phase - medium" and "surface of a fiber - medium". The electrostatic surface properties of magnetic fluid particles and fibers depend on the pH, as shown with zeta-potential measurements (Figures 5 and 6).

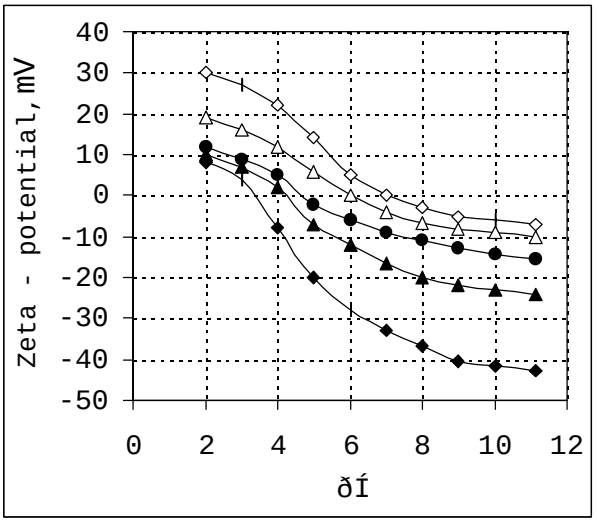

Fig. 5. Change of zeta - potential of a natural fiber (wool) with ðÍ.

In the investigated range of ðÍ 6 to 8, particles MF_1 are charged negatively and MF_2 are charged positively, whereas the fibers are charged negatively. To achieve higher coagulation rates for particles MF_1 on fibers, it was thus necessary to reduce the negative charge. This was achieved by preliminary modification of their surface with DACl or cathamine. Similarly, an increase of positive charge on the MF_2 particles by treatment with sulphonol or Na–CMC led to increased coagulation on the fibers.

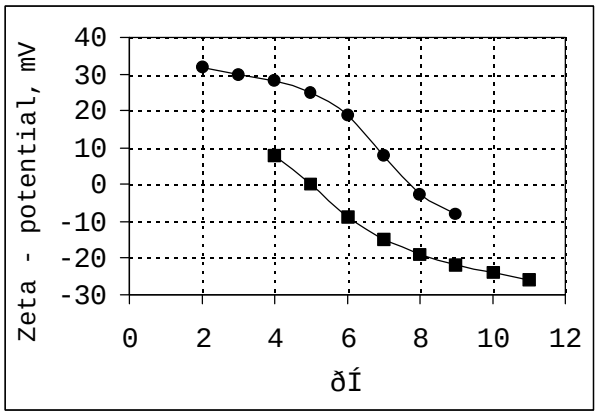

Fig. 6. Zeta - potential of a MF at different ðÍ's.
MF_1; MF_2.

The difference between the zeta-potential of fibers and MF particles was thus increased during neutralization, as seen by the process of coagulation.

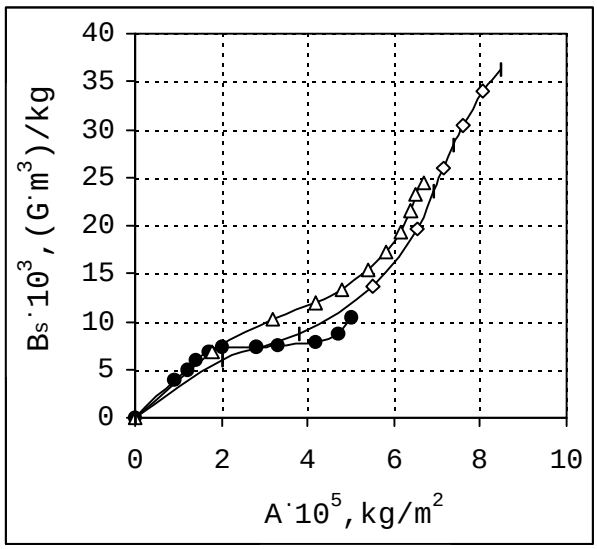

Fig. 7. Dependence of magnetic properties of a fiber B_S (wool) on the amount of magnetic coagulum A after contact with MF_1.

The magnetic properties of the fibers changed considerably depending on the way of treating the surfaces with surfactants (Figures 7 and 8). Cationic surfactant pretreated fibers (DACl or cathamine) show increased adsorption of MF_1

particles stabilized with sodium oleate (Figure 7). A similar effect is seen between fibers and dextran-stabilized MF_2 particles (Figure 8).

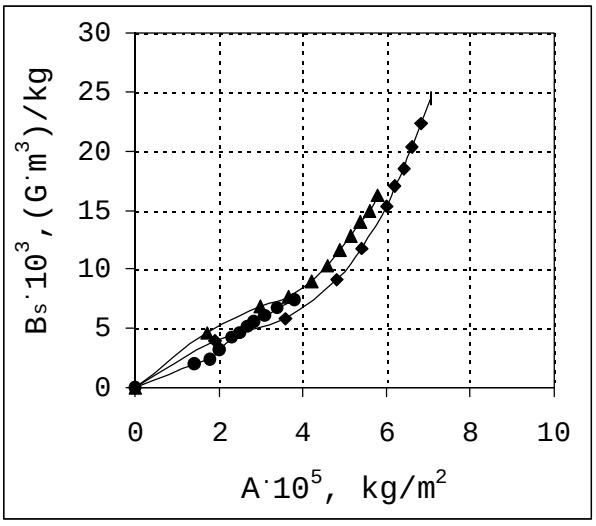

Fig. 8. Dependence of magnetic properties of a fiber B_S (wool) on the amount of magnetic coagulum A after contact with MF_2 .

We observed a sharp increase of the magnetic fiber properties after modifying them with the anionic surfactants sulfonol and Na-CMC. The difference between the electrostatic surface forces in the system "magnetic fluid – fiber" is the basis of process coagulation. A future direction is the investigation of influence of temperature and stirring on coagulation kinetics. Our work is the basis for the coating of fiber surfaces with magnetic particles.

CONCLUSIONS: The coagulation process depends on the fiber quantity and its surface properties. Modification of the fiber surfaces with surfactants changes their electrostatic properties, which is a precondition for the effective formation of layers of magnetic particles. The magnetic fiber coating initially is modest, but increases considerably after preliminary treatment with surfactants.

REFERENCES: [1] M.A. Lunina, L.V. Nikitin, F.S. Bayburtskiy and L.S. Mironova (1998) *The International Conference on Colloid Chemistry and Physical-Chemical Mechanics*, Moscow, Russia, Book of Abstracts, p.353. [2] O.A. Kuznetsov, N.A. Brusentsov, A.A. Kuznetsov, N.Yu. Yurchenko, N.E. Osipov, F.S. Bayburtskiy (1999) *J. Magn. and Magn. Mater.* **194**:83-89. [3] F.S.Bayburtskiy and N.A.Brusentsov (1999) *Pharm. Chem. J.* **33**:57-61. [4] M. A. Lunina, M. R. Kiselyov, I.I. Senatskaya and F. S. Bayburtskiy (2000) *The 9th International Plyos Conference on Magnetic Fluids*, Plyos, Russia, Book of Abstracts, p.7-11. [5] F. S. Bayburtskiy, I. I. Senatskaya, V. V. Tarasov, L. V. Nikitin, N. A. Brusentsov and V. A. Razumovskiy (2001) *The 9th International Conference on Magnetic Fluids*, Bremen, Germany, Book of Abstracts.

BIOMONITORING BY COMBINATION OF IMMUNOMAGNETIC SEPARATION AND DIRECT EPIFLUORESCENCE FILTER TECHNIQUE

Elke Boschke,[1] J. Steingroewer,[1] S. Ripperger,[2] E. Klingner,[3] T. Bley[1]

[1]Institute of Food Processing and Bioengineering, Dresden University of Technology, D-01062 Dresden; [2]Institute of Process Engineering and Environmental Engineering; [3] IBN Gesellschaft für Industielle Forschung und Technologie mbH, Dresden

INTRODUCTION: Traditional microbiological methods have proved to be slow and insensitive in controlling the quality and microbiological safety of perishable products. There is a need for more rapid, sensitive and specific methods that will facilitate product release and identify hygiene and safety problems more rapidly so that corrective action can be taken. Several new methods that use a variety of different principles have been developed (overview see [1, 2]). These include the direct epifluorescence filter technique (DEFT) [3-6].

DEFT is performed by homogenisation of samples. This procedure is supported by a Stomacher device followed, if demanded, by enzymatic disintegration of the homogenate (see below). The sample is further processed by prefiltration through a 5µm pore nylon filter and passage of the filtrate through a 0.2µm pore black polycarbonate filter to collect and concentrate microorganisms. These are subsequently stained with fluorochrome and prepared for following examination and counting by epi-fluorescence microscopy.

Depending on the components of the food samples analyzed, a disadvantage of DEFT is that one may get microscopic images which cannot be evaluated because particles of the food sample can be collected on the filter along with the microorganisms. The prefiltration through a nylon filter with pores smaller than 5µm can prevent this occurring but one cannot be sure that all microorganisms pass the prefiltration module. Thus, the number of detectable bugs in the epifluorescence microscope will not map reality. We set out to isolate microorganisms from these heterogeneous suspensions by combination of DEFT and immunomagnetic separation reducing levels of background particles. Magnetic particle-based technology [7] offers distinct advantages for the rapid processing of large numbers of cells.

MATERIALS AND METHODS: Dried apricots and figs were used in the experiments. 10g of fruits were mixed with 90mL of phosphate buffered solution (PBS) in a ´400´ Closure Bag (Seward) and homogenised in a Stomacher device (Seward Lab System) for 10 minutes.

Uncoated paramagnetic, polysterene, Tosyl-activated (450T) beads (4.5 µm) (DYNAL) and/or enzyme mixtures were added. Beads were resuspended and washed in appropriate buffer and stored at 4°C before use. A wide number of enzyme preparations (Novo Nordisk; Erbslöh; Röhm) with corresponding activities was tested.

Disassembly of the structure of fruit particles was followed by measuring the decrease of particle size with a Helos laser diffraction system (Sympatec).

RESULTS: Mixtures of cellulases, hemicellulases and pectinases were used to disintegrate fruit particles remaining after homogenizing.

By help of those enzymes the amount of small particles in the suspension increased after treatment (Fig. 1).

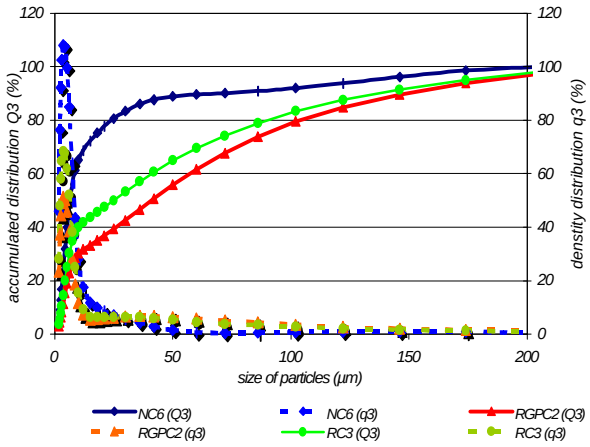

Fig. 1: Particle size in a fig probe after treatment with cellulase preparations.

Best results were achieved with the following enzyme mixtures.

Table 1. Optimum quantity of enzymes.

	fig	apricot
amylase	0.5 % RA5	0.5 % RA5
pectinase	5.0 % EP2	5.0 % NGP3
cellulase	2.0 % NC6	4.0 % RGC4
other supplements	none	2.0 % NGP2

Experiments concerning recovery rate of magnetic beads from fruit pulp are documented in Fig. 2.

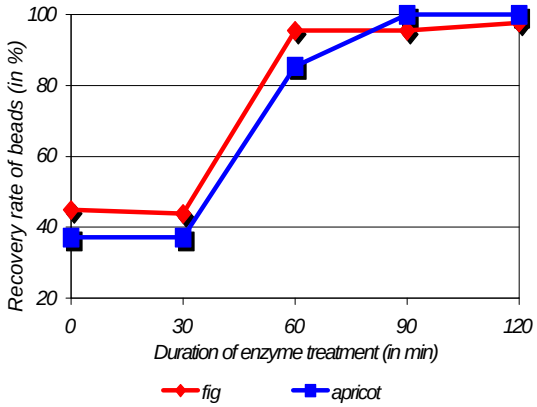

Fig. 2: Recovery rate of magnetic beads after enzymatic treatment.

It was clearly shown that beads cannot be isolated completely from the probes without sufficient enzyme treatment. Only after incubation for a period of between 60 and 90 minutes at 45°C could more than 95% of beads be recovered from the fruit pulp by magnetic processing.

Enzyme treatment studies and studies with magnetic beads in fruit pulps gave confidence that the combination of DEFT and Magnetic particle-based technology can lead to sensitive, specific and rapid methods, which can be directly applied to food samples.

An aim of further experiments is to evaluate the coating of the beads with related antibodies, or other highly specific ligands such as lectins, against relevant microorganisms. The results will be shown at the conference.

REFERENCES: [1]J. Baumgart (1999) *Möglichkeiten und Grenzen aktueller mikrobiologischer Schnellverfahren zur Lebensmitteluntersuchung und Hygienekontrolle.* in HY-PRO '99 International Exhibition and Conference. Wiesbaden: VDE VERLAG GMBH. [2]D.Y.C. Fung (1994) *Rapid methods and automation in food microbiology: A review.* Food Reviews International, **10**(3):357-375. [3]G.L. Pettipher (1987) *Detection of low numbers of osmophilic yeasts in creme fondant within 25 h using a pre-incubated DEFT count.* Appl. Microbiol. **4**:95-98. [4]R.P. Betts, et al (1988) *The detection of irradiated foods using the Direct Epifluorescent Filter Technique.* J. Appl. Biotechnol. **64**:329-335. [5]I. Walls, J.J. Sheridan and P.N. Levett (1989) *A rapid method of enumerating microorganisms from beef, using an Acridine Orange Direct Count Technique.* Irish J. Food Sci. & Technol. **13**:11. [6]R.P. Betts (1998) *Rapid enumeration of viable microorganisms by staining and direct microscopy.* Lett. Appl. Microbiol. **9**:199-202. [7]M.J. Payne, et al (1992) *The use of immobilized lectins in the separation of Staphylococcus aureus, Escherichia coli, Listeria and Salmonella spp. from pure cultures and foods.* J. Appl. Bacteriology **73**(1):41-52. [8]J. Porter, et al (1998) *An evaluation of lectin-mediated magnetic bead cell sorting for the targeted separation of enteric bacteria.* J. Appl. Microbiol. **84**(5):722-732.

EMULSION/AGGREGATION TECHNOLOGY: A PROCESS FOR PREPARING MICROSPHERES OF NARROW POLYDISPERSITY

P. Burns, P. Gerroir, H. Mahabadi, R. Patel, & D. Vanbesien

The Xerox Research Centre of Canada, Mississauga, ON, L5K 2L1, Canada

INTRODUCTION: Processes of preparing microspheres that enable control of well-defined particle characteristics such as size, size distribution, and functionality are becoming increasingly important for a variety of applications. However, either the particle size range that is achievable, or the types of materials that can be utilized in the process limit some of the current methods of microsphere preparation. The development of new methods for the preparation of microspheres that broaden the design space would therefore be an asset.

Of particular interest for certain applications is the preparation of particles in the micron-size range. This size of particles is typically prepared via dispersion or suspension polymerization techniques [1]. For suspension polymerization, control of particle size distribution can be difficult range because of the mechanical factors that control the particle size. In dispersion polymerization limitations arise due to the types of materials that will work in the process, thus one is limited to using particular solvents, or monomer/solvent combinations. Thus, a less complicated and more controlled process for preparing microspheres of good size distribution would be beneficial.

This paper describes a new process for preparing micron-sized polymeric microspheres with narrow particle size distribution. It is called the Emulsion/Aggregation (EA) technology and was originally developed for the controlled growth of particles for electrophotographic applications. The process involves the growth of microspheres from nanometer size constituents, such as polymer and pigments, through careful control of chemical and physical conditions.

METHODS: The Emulsion/Aggregation process (Figure 1) begins with the preparation of nanometer sized polymer particles stabilized in water using various techniques. These particles are on the order of 10-300 nm in size. A variety of resin types are possible including styrene-based materials, acrylates, polyesters etc.

The second step involves the growth of the nanometer-sized particles by mixing in deionized water in the presence of an aggregating agent. It is at this stage that other ingredients can be incorporated into the particle by adding them as water based dispersions. All of the components are homogenized to ensure effective mixing and continuous mixing is utilized throughout the growth process. Once the desired particle size is reached, the growth process is terminated.

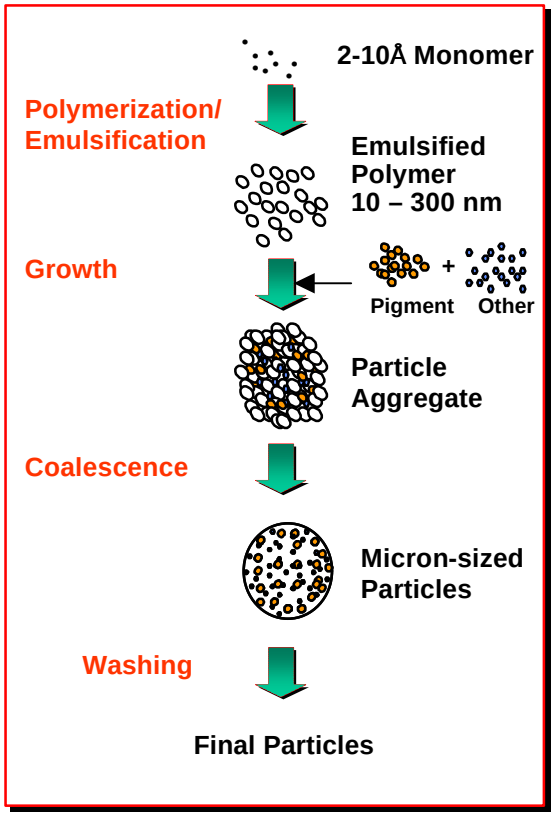

Fig. 1: Microsphere preparation by the emulsion aggregation process

Depending on the resin type utilized, the particles generated at this stage are either already spherical or require further treatment to coalesce into spheres. Once the microspheres are formed they can be isolated from the water and washed to remove the various ions and surfactants used in the process.

RESULTS: The EA process enables control of particle size and size distribution. As particles grow, the particle size increases with time as shown in Figure 2a. It is also during this phase that the particle size distribution narrows as illustrated in Figure 2b. A narrow particle size distribution is achieved using the EA process and a typical size distribution curve is shown in Figure 3. The geometric standard deviation based on volume is less than 1.25.

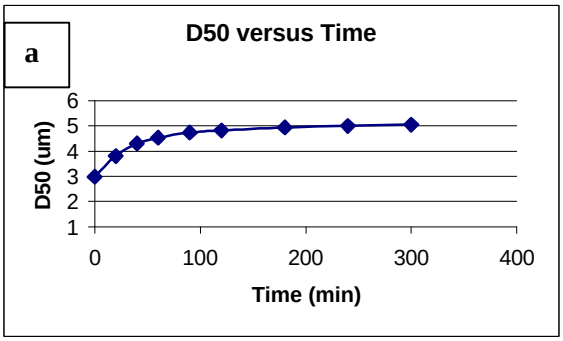

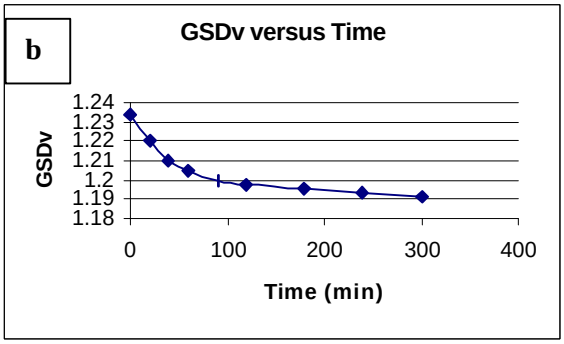

Fig.2: Particle Size (a) and Geometric Standard Deviation (b) as a function of growth time.

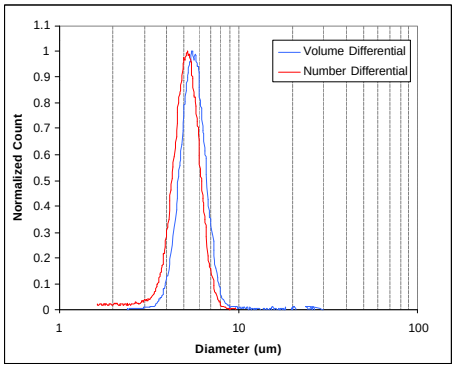

Fig.3: Particle Size of final particle as measured on a Coulter Counter instrument.

The ability to obtain narrow particle size distributions is driven by the growth kinetics and balance between the forces binding the particles together and the shear forces that erode aggregated particles. Figure 4 illustrates how the growth process proceeds from individual particles, to a gel network, to individual aggregates that continue to grow with time.

The particles produced in this process can vary in shape depending on process conditions. For the styrene-based case, the conditions can be adjusted such that a non-spherical or completely spherical particle is obtained. Figure 5a shows final particles with an irregular morphology. In 5b the particles are completely spherical.

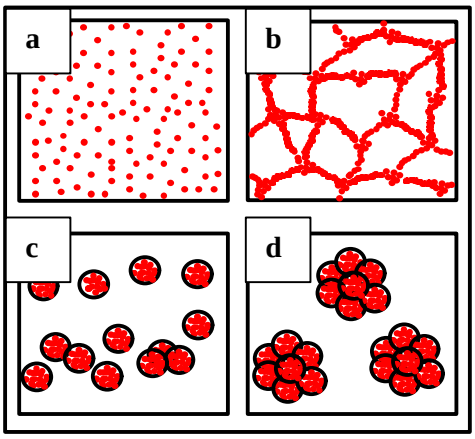

Fig.4: Mechanism of growth. a) Emulsified resin particles. b) Nucleation of Primary Particles. c) Primary particles. d) Final particles.

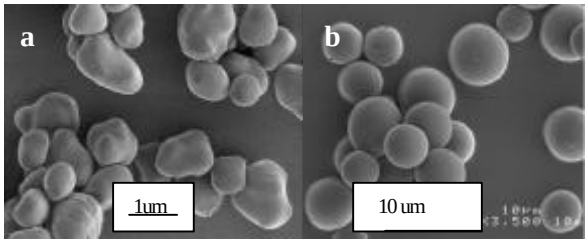

Fig.5: SEM of particle during EA process. a) Final irregular particles. b) Final spherical particles.

The Emulsion/Aggregation process is particularly suited to the incorporation of nanometer-sized pigments. This has been demonstrated in the application to toner materials for electrophoto-graphic applications. Dispersions of pigments in water are mixed with the emulsified resin and the process is carried out in the same manner.

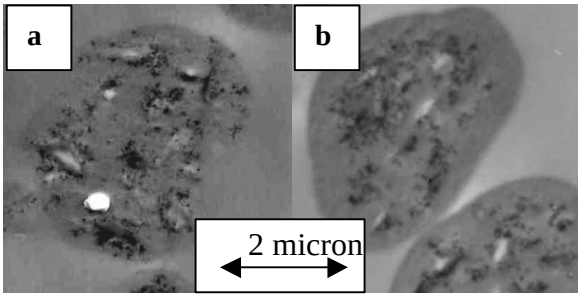

Fig. 6: TEM images of a) particle containing pigment throughout the particle, and b) particle with surface pigment covered by resin.

Cross sections of particles that contain pigment show that the pigment is fairly evenly distributed throughout the particle. It is possible to add additional latex to cover surface pigment. Figure 6 shows TEM's of particles with and without additional latex added to cover surface pigment.

CONCLUSIONS: The Emulsion/Aggregation technology is a process which has been developed for the preparation

of micron-sized polymeric particles that enables the control of particle size, shape and size distribution. This process offers an alternate route to microspheres of narrow polydispersity. The process yields particles with geometric standard deviations of below 1.2 with well-controlled structures. A variety of resin types can be used in this process and other materials such as pigments can be incorporated into the particles.

REFERENCES: [1]R. Arshady, (1992) *Colloid Polym Sci 270:717-732*.

ACKNOWLEDGEMENTS: The entire Xerox group Emulsion Aggregation Technology team members have contributed to the development of this process and are acknowledged for their efforts.

A THEORETICAL APPROACH OF SUCCIMER COMPLEXATION AT THE SURFACE OF FERRITE NANOPARTICLES IN ORDER TO IMPROVE THE SYNTHESIS OF BIOCOMPATIBLE MAGNETIC FLUIDS

A. F. C. Campos, F. A. Tourinho, T. A. P. G. Cotta & J. Depeyrot

Complex Fluids Group, Universidade de Brasília, Brazil

INTRODUCTION: Currently, magnetic carrier technology is widely used for biological and biomedical purposes such as cell sorting, drug vectoring, contrast agents in magnetic resonance imaging (MRI), and oncological treatment. Many applications of these materials are based on specific receptor-efector complexes where the latter is coupled with coated iron oxide particles. The receptor is located on the outer monolayer of the membrane and the effector is bonded to the particle surface through non-toxic chelating agents like meso-2,3-dimercaptosuccinic acid (DMSA). Moreover succimer is also a polyfunctional Brönsted acid leading to five species, including amphoteric ones, whose amounts vary strongly with pH. It is therefore surprising that until now, the speciation diagram of DMSA has not been taken into account in the nanoparticle surface complexation mechanism of spinel ferrite-based magnetic fluid. On the other hand, it has been shown very recently [1] that magnetic fluids behave as a mixture of a strong acid (bulk dispersion) and a weak diprotic acid (nanoparticle surface). In this model, the charge of the particle surface, responsible for the colloidal stability of electric double layered magnetic fluids (EDL-MF), is obtained through the aquation reaction of metal ions and the following hydrolysis reactions:

$$\equiv MOH_2^+ + H_2O \overset{pK_1}{\rightleftharpoons} \equiv MOH + H_3O^+_{(aq)}, \quad (1)$$

$$\equiv MOH + H_2O \overset{pK_2}{\rightleftharpoons} \equiv MO^- + H_3O^+_{(aq)}. \quad (2)$$

Such equilibria lead to three kinds of superficial sites where most of them are MOH_2^+ in strong acidic medium, MO^- in strong basic medium, with MOH being the intermediate amphoteric sites (where M = superficial metal). pK_1 and pK_2 are the thermodynamic constants of each respective chemical equilibrium. Then, the surface charge densisity σ_0 results from a proton transfer mechanism between the particle surface and the bulk dispersion. Therefore, the analysis of equilibria (1) and (2) allows the determination of the pH dependence of the surface charge density, and σ_0 is given by [1]:

$$s_0 = \frac{F}{A}V\left(\frac{10^{-2pH} - 10^{-(pK_1+pK_2)}}{10^{-2pH} + 10^{-(pH+pK_1)} + 10^{-(pK_1+pK_2)}}\right)C_T, \quad (3)$$

where F is the Faraday constant, A is the total surface area of particles, and V is the volume of the dispersion. The total concentration of surface sites C_T and the dissociation constants can be easily obtained using simultaneous potentiometric and conductimetric titrations.

The aim of the present work is to explore the surface – DMSA complexation in order to improve the synthesis of biocompatible magnetic fluids. In this context, using our formalism of Brönsted complex equilibria involving amphoteric species, we first obtain the quantitative pH dependence of the superficial density of charge for the case of EDL-MF based on cobalt ferrite nanoparticles. Then, the speciation diagram for charged sites of particle surface is coupled with that of DMSA in order to analyse the mechanism of surface – DMSA complexation. Finally, we propose a surface reaction which leads to the maximum complexation rate.

METHODS: The elaboration of EDL-MF sample was carried out using the usual procedure. $CoFe_2O_4$ oxide nanoparticles were prepared through hydrothermal coprecipitation of aqueous solutions of $Co(NO_3)_2$-$FeCl_3$ in alkaline medium. Then the particles were peptized in acidic medium by adjustment of the ionic strength, resulting in stable sols of high quality. The mean nanoparticle size was determined by X-ray diffraction recorded from dry powder samples, obtained by evaporation of the liquid carrier, and was found to equal 12.0 nm. Simultaneous potentiometric and conductimetric titrations of 40 mL of the ferrofluid dispersion (volume fraction $\Phi = 1.46\%$, corresponding to 1.7×10^{22} particles per m^3) were performed using a titrant solution of 0.106 mol L^{-1} sodium hydroxide. All titrations were repeated two times. The potentiometric readings were obtained with a pH meter (Metrohm 713) using a glass double-junction electrode, while the conductivity was measured with a conductometer (Metrohm 712). Both apparatus were gauged using appropriate templates. From the simultaneous titration curves, the Henderson-Hasselbalch equation was used to determine the pK´s corresponding to both equilibria (1) and (2). Moreover C_T was calculated using the mass balance. Then, the speciation diagram of surface sites was obtained. In the case of DMSA, the molar ratio for each species was determined using pK values from the literature [2].

RESULTS & DISCUSSION: Fig.1 shows the pH dependence of the surface charge density for the cobalt ferrite EDL-MF sample. The saturation value is equal to 0.326 C m^{-2} which corresponds to approximately one charge per 0.5 nm^2 or about 905 sites per particle. This is in excellent agreement with reported values [3]. At pH values of around 3.5 and 10.5, σ_0 reaches the maximum positive and negative values, respectively, and the particle surface is charge saturated. This agrees with ultrastable magnetic sols obtained experimentally in acidic or basic media. However, for extreme values of pH, the high ionic strength does not allow stable ferrofluid dispersions, although the particle surface is charge saturated.

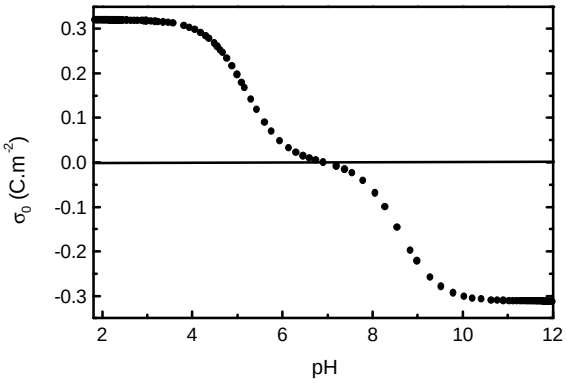

Fig. 1: pH dependence of the superficial density of charge for EDL-MF sample.

In the pH range corresponding to physiological medium, the superficial charge density approaches zero and the ferrofluid dispersion flocculates showing that uncoated particles cannot be used for biological purposes.

Table 1 lists the experimentally determined thermodynamic constants associated with the equilibria between the particle surface and the bulk dispersion. The molar ratio values of particle surface sites can then be calculated and plotted as function of pH as shown in Fig. 2. This speciation diagram gives a quantitative description of the particle surface illustrating the domains of protonation of surface sites. At low (high) pH values in acidic (basic) medium (typically $pH \leq 3.5$ and $pH \geq 10.5$), the particle surface is charge saturated. For small pH ranges around the pK values, Fig. 2 shows the coexistence of charged and neutral sites.

Table 1. pK_1 and pK_2 values and the modulus of the maximum superficial density of charge for the EDL-MF sample.

pK_1	pK_2	$\lvert\sigma_0^{MAX}\rvert$ (C m^{-2})
5.2	8.6	0.326

Close to the neutral region (physiological medium), the molar ratio of charged sites strongly decreases, and, contrary to the expected result, the cobalt ferrite ferrofluid solution does not present any point of zero charge since the molar ratio of the amphoteric sites does not reach the unity value. However, an isoelectric point is found and is readily related to the equilibrium constants for the surface sites species.

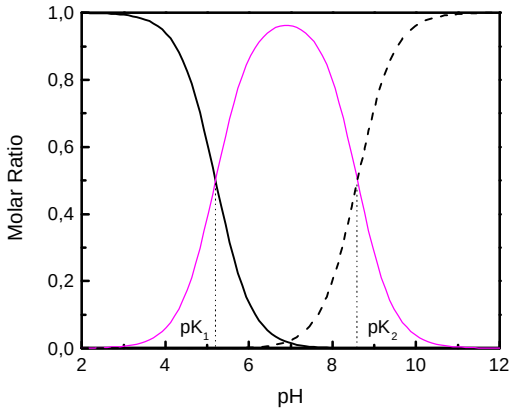

Fig. 2: Speciation Diagram of particle surface sites.

¾ MOH_2^+; ¾ MOH; - - - MO^-

Table 2 lists the pK values corresponding to the equilibria involving the five DMSA species often abbreviated H_4L, H_3L^-, H_2L^{2-}, HL^{3-} and L^{4-}. The first and second steps in the dissociation process involve successive loss of protons from the two carboxylic groups; the third and fourth steps involve dissociation of the protonated thiol groups.

Table 2. Values of equilibrium constants of meso 2,3 - dimercaptosuccinic acid [2].

pK_{C1}	pK_{C2}	pK_{S1}	pK_{S2}
2.71	3.43	9.65	12.05

The eight curves plotted as a function of pH in Fig. 3 show the five molar ratios for DMSA containing species coupled with the three curves for nanoparticle superficial sites. Since the first two constants of DMSA are of the same order of magnitude, it suggests that the first two protons dissociate from opposite ends of the molecule. As a consequence of their physical separation, the negative charge created by the first dissociation does not greatly affect the removal of the second proton. Thus, around pH = 3 the three first DMSA species coexist. The dissociation of the other two protons, relative to the thiol groups, is more difficult since they are much closer to the negatively charged carboxylate ions created by the initial dissociation.

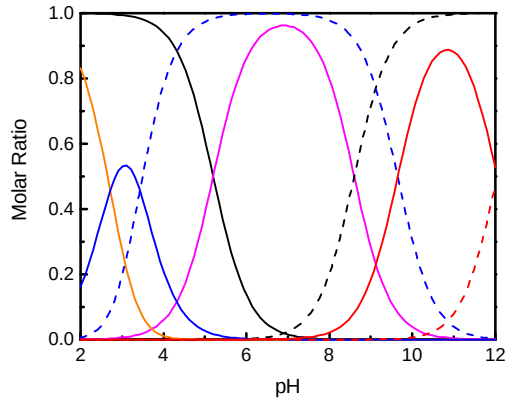

Fig. 3: Coupled speciation Diagrams of superficial sites and DMSA

¾ MOH_2^+; ¾ MOH; - - - MO^-

¾ H_4L; ¾ H_3L^-; - - - H_2L^{2-}; ¾ HL^{3-}; - - - L^{4-}

Moreover, it is well known that carboxylate acid groups form remarkably stable chelates with many metal ions in solution [4]. In this context, the elaboration of DMSA-coated magnetic nanoparticles by complexation of superficial metal ions should be controlled by the pH which also monitor the superficial density of charge. Then, it is therefore necessary to analyze the coupled speciation diagrams of particle superficial sites and DMSA. Based on the free metal ion complexation equilibrium, the most probable surface reaction can be written as:

$$\equiv MOH_2^+ + \text{Ligand} \rightleftharpoons \equiv M^+ - \text{Ligand} + H_2O \quad (4)$$

since the exchange of ligand for OH superficial groups is thermodynamically less favored [4]. In alkaline medium, both particles and DMSA ions are negatively charged (see Fig. 3) and no complexation would occur. From these considerations, one can easily conclude that the best pH to coat magnetic nanoparticles by DMSA is around 3. Although the pH range of the maximum molar ratio for MOH_2^+ superficial sites goes from strong acid medium to pH = 3, H_3L^- and H_2L^{2-} only reach their maximum values for this pH. Once the DMSA is coated to the particle surface, the stability of the magnetic sol in biological buffers is obtained through the H_2L^{2-} species whose one end is bonded to the surface and the other ensures the charge.

CONCLUSIONS: Magnetic fluids behave as a mixture of a strong acid and a weak diprotic acid. The thermodynamic constants of the chemical equilibria involved between the bulk dispersion and the nanoparticle surface are experimentally determined. Then, the pH dependence of the nanoparticle surface charge density of EDL-MF based on cobalt nanoparticles is obtained. From the coupled speciation diagrams of both particle surface and DMSA one can predict the optimal pH for DMSA surface complexation and colloidal stability in physiological medium.

REFERENCES: [1]A.F.C. Campos, F.A. Tourinho, G.J. da Silva, M.C.F.L. Lara and J. Depeyrot (2001) *Eur Phys J E* **6**:29-35. [2]G. Crisponi, F. Cristiani, V.M. Nurchi, R. Pinna, M.J.T. Estévez (1999) *Polyhedron* **18**:3257-3262. [3]F.A. Tourinho, R. Franck, R. Massart (1990) *J. Mater. Sci.* **25**:3249. [4]R.Pribil (1982) *Applied Complexometry*, Pergamon.

ACKNOWLEDGEMENTS: The authors thank the Brazilian Agencies (CAPES, CNPq and FAP-DF) for their financial support.

MAGNETOLIPOSOME EVALUATION USING CYTOMETRY AND MICRONUCLEUS TEST

V. A. P.Garcia [1] L. M. Lacava [1] S. Kückelhaus [1] R. B. Azevedo [1] M. F. Da Silva [2] P. C. Morais [2] M. De Cuyper [3] & Z. G. M. Lacava [1]

[1] *Instituto de Ciências Biológicas, Universidade de Brasília, 70910-900, Brasília-DF, Brazil*

[2] *Universidade de Brasília, Instituto de Física, Núcleo de Física Aplicada, 70919-970 Brasília-DF, Brazil*

[3] *K.U. Leuven Campus Kortrijk, Interdisciplinary Research Center, E. Sabbelaan 53, B-8500 Kortrijk-Belgium*

INTRODUCTION: A large number of applications of magnetic nanoparticles (MNPs) in the biotechnology and biomedicine field still remain to be devised. In particular, MNPs covered with bio-mimetic materials, as for instance magnetoliposomes (MLs) [1], do offer a wide range of new opportunities. MLs consist of magnetic nanoparticles wrapped by a phospholipid bilayer, problably presenting lipid molecules oriented in a similar way to that observed in biological membranes [2]. These biocolloidal structures can be successfully applied for several purposes, as for instance in drug-delivery systems, magnetic resonance imaging markers for cancer diagnosis, and thermal cancer therapy [3]. The present study reports on several *in vivo* biological tests carried out with a ML sample developed as a precursor of more complex thermal cancer therapy systems.

MATERIALS AND METHODS: DMPG (dimyristoulphosphatidyl-glycerol) and DMPC (dimyristoylphosphatidyl-choline) were obtained from Avanti Polar Lipid Products (Birmingham, Alabama, USA). Lipid dispersions were prepared by ultrasonication of DMPG (10%) and DMPC (90%) at 37 °C. Magnetite (Fe_3O_4) nanoparticles with a diameter of approximately 14 nm were prepared by co-precipitation of $FeCl_2$ and $FeCl_3$ in the presence of an excess of ammonia, and subsequently coated with lauric acid to obtain a stable dispersion. Upon co-incubation and dialysis of this so-called water-adapted magnetic fluid in the presence of DMPG-DMPC vesicles, the laurate coat is replaced by phospholipid molecules. During incubation and dialysis for 2-3 days of this water-based magnetic fluid in the presence of preformed sonicated phospholipid vesicles, ML (named DMPC-ML) are formed and subsequently captured from solution with high-gradient magnetophoresis [1,2]. Female Swiss mice were studied: control animals (n = 5) were not treated. In the experimental group adult female Swiss mice were endovenously treated with a bolus dose of 100 µL of DMPC-ML ($1.8x10^{15}$ particles/mL). Blood cytometry experiments [3,4] were carried out 1, 6, 12, 24, and 48 hours and also 14 and 28 days after DMPC-ML administration. Imprints of peripheral blood cells were made in glass slides, stained by Wright-Giemsa and five hundred cells per each animal were scored for the cytometry. The data were analyzed by the statistical Scheffe test (ANOVA, $p < 0.05$). The micronucleus (MN) test [4] was performed 12, 24, and 48 hours after DMPC-ML administration to evaluate ML genotoxic and cytotoxic effects [5,6]. Clastogenic drugs induce MN, a chromosome fragment left in the cell after the expulsion of the main nucleus during maturation of erythroblasts to erythrocytes in bone marrow of mammals. Anucleated polychromatophilic erythrocytes (PCEs) are normally less than 30 hours old and stain differently from normochromatophilic erythrocytes (NCEs). Cytotoxicity is revealed when the %PCE obtained by [PCE/(PCE + NCE)]×100 is far from the normal expected value (50%). Differences of MN rates and %PCE between spontaneous and DMPC-ML treated cells were tested for significance using the Mann-Whitney test with $p < 0.05$. As far as we know this study reports for the first time MN tests performed after ML treatments.

RESULTS: Our characterization data showed that DMPC-ML has an average bilayered structure diameter of 20 nm containing 13.27 mg magnetite/mL and 10.24 µmol phospholipid/mL, and thus a phospholipid/magnetite ratio of 0.77 µmol/mg. The DMPC-ML treatment caused no animal death during the 28 days of experiment. Cytometry analysis provided the differential counting of lymphocyte, neutrophil, monocyte, and eosinophil populations. As far as the monocyte and eosinophil populations are concerned, data from the DMPC-ML-treated animals were not different from those of the control group (data not shown). Neutrophil population starts to increase 1 hour after DMPC-ML treatment (Fig. 1), reaching its maximum value 6 hours after ML administration. However, 12 hours after DMPC-ML treatment, the neutrophil population had already decreased in the peripheral blood. From 24 hours until 28 days after administration the cell frequencies are the same as in the control animals. Simultaneously to the neutrophil population increase the lymphocyte population presented a maximum decrease 6 hours after DMPC-ML treatment. Further, 24 hours after DMPC-ML treatment the proportion of lymphocytes in blood returned to control values (see Fig. 1). At the tested concentration, DMPC-ML treatment presented no significative increase in the MN frequency on PCE (Table 1) or NCE (data not shown) on bone marrow along the experiment. There was observed a tendency of MN induction only after 24 hours of ML treatment. The percentage of polychromatophilic cells (see Table 1) presented a significant decrease 24 hours after the DMPC-ML treatment.

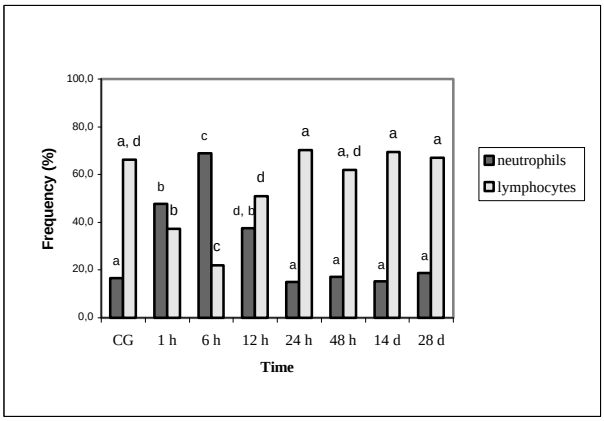

Fig. 1: Effects of DMPC-ML (100 mL of 1.82´10[15] particle/mL) on the blood cytometry of mice; a-d different letters show statistical differences found in the same cell type frequency ($p < 0.05$); CG = control group.

Table 1. Effects of DMPC-ML on micronucleus induction and percentage of polychromatophilic cells as a function of time treatment.

Group	MN PCE	% PCE
Control	2.9	39.8
ML-12h	2.2	30.3
ML-24h	3.7	21.1*
ML-48h	2.4	26.7

MN, micronucleus (%); PCE, polychromatophilic cell; %PCE = [PCE/(PCE + NCE)] × 100; *, statistically different from control group ($p < 0.05$).

DISCUSSION & CONCLUSIONS: The cell population changes detected by blood cytometry analysis revealed an inflammation process that may be considered as a normal host response to the presence of foreign species [4]. The observation of no blood cell population changes 24 hours after the DMPC-ML treatment suggests that a slight instead of a severe inflammation process took place. The absence of MN induction in bone marrow cells revealed that DMPC-ML has no genotoxic effect. Nevertheless, the ML treatment presented a slight cytotoxic effect revealed by the decrease of %PCE on bone marrow cells 24 hours after the ML treatment. This cytotoxic effect is problably related to the slight increase in the MN induction observed after the same period of time. Based on these data we conclude that DMPC-ML is reasonably biocompatible and may be considered as a precursor for magnetothermocytolysis purposes. Further evidence for this conclusion is supported by the fact that no morphological alterations were observed in several organs examined, even when ML is detected by magnetic resonance experiments, after DMPC-ML administration.

REFERENCES: [1] J.W.M. Bulte, M. De Cuyper, D. Despres et al. (1999) *J Magn Magn Mater* **9**, 329-335. [2] M. De Cuyper and M. Joniau (1988) *Eur Biophys J* **15**:311-9. [3] Z.G.M. Lacava, R.B. Azevedo, L.M. Lacava et al. (1999) *J Magn Magn Mater* **194**:90-5. [4] M.L.L. Freitas, L.P. Silva, R.B. Azevedo et al. (2002) *J Magn Magn Mater*. In press.

ACKNOWLEDGEMENTS: This work was partially supported by the Brazilian agencies CNPq/PIBIC, FINATEC, and CAPES and by the Flemish *Fonds voor Wetenschappelijk Onderzoek*.

SYNTHESIS AND PATTERNING OF MAGNETIC NANOSTRUCTURES

L. Fu[1], V.P. Dravid[1], K. Klug[1], X. Liu[2] and C.A. Mirkin[2]
[1] Dept. of Materials Science and Engineering, Northwestern University, Il, 60208
[2] Dept. of Chemistry, Northwestern University, Il 60208

The recent developments in biocompatible, functionalized magnetic nanoparticles show considerable promise for both enhanced and novel applications in biomedical and diagnostic fields, ranging from targeted drug delivery to MRI contrast enhancement. Magnetite (Fe_3O_4) and related oxides, which are chemically stable, nontoxic, non-carcinogenic and have attractive magnetic properties, have been pursued for many years [1,2]. As an alternative, we are also exploring synthesis and properties of graphite or SiO_x encapsulated superparamagnetic (ESP) nanoparticles. The ESP nanoparticles provide exciting prospects of not only biocompatibility but also the robust protection of inert graphite coating, which permits encapsulation of otherwise toxic high magnetic moment metals/alloys such as Ni-Pd, FePt, Co-Sm [3-5].

In our group, two approaches have been applied to synthesize magnetic nanoparticles. Magnetite, magnetic ferrites, Co, FePt nanoparticles were prepared by standard wet chemical method but using procedural and surface chemical control for narrow size distribution. Graphite and SiOx encapsulated Ni/Co/Fe nanoparticles were prepared by arc evaporation and the CVD coating approach [3, 6-8].

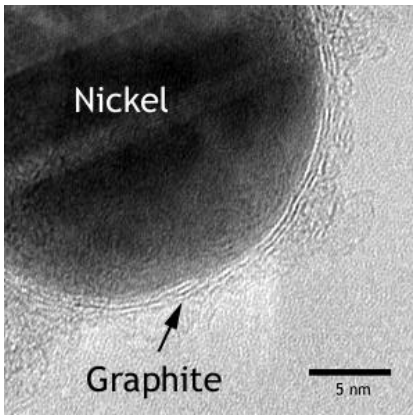

Fig. 1. TEM image of graphite encapsulated Ni nanoparticle.

Figures 1 to 3 show the morphology of the nanoparticles of graphite encapsulated Ni and SiO_x, encapsulated Ni nanoparticles and monodispersed Fe_3O_4.

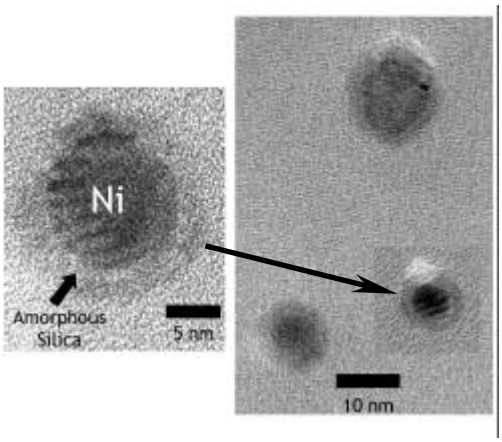

Fig. 2. TEM images of silica encapsulated Ni nanoparticles.

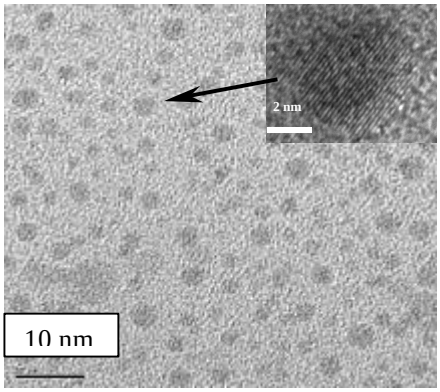

Fig. 3. TEM images of monodispersed magnetite (Fe_3O_4) nanoparticles.

The magnetic properties of monodispersed magnetite nanoparticles have been measured by SQUID (Figures 4 and 5). The results indicated that the monodispersed magnetite nanoparticles show superparamagnetic behavior at room temperature. The blocking temperature decreased with increasing strength of the magnetic field.

There has been considerable interest in developing methods for patterning nanostructured magnetic particles because of their potential applications for biomarkers and biosensors. Herein we present a new and straightforward strategy, based on Dip-pen nanolithography (DPN), for preparing nanometer scale magnetic structures with precise feature size control [9,10].

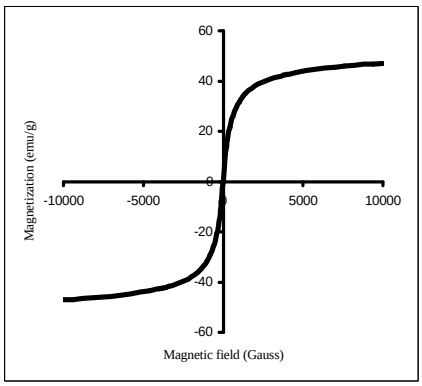

Fig. 4. Fe_3O_4 nanoparticles magnetization.

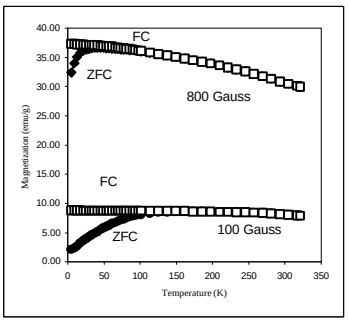

Fig. 5. Zero-field cooled and field cooled measurements at different magnetic fields.

To confirm the concept, nano-scale Fe_3O_4 and $MnFe_2O_4$ have been patterned successfully via Dip-pen nanolithograpgy. Figures 6 and 7 show the patterns of the magnetic nanostructures. Patterning of metal nanoparticles with precise control will be done later in the project. The objective is to use biochemical markers (e.g. DNA/proteins) as templates for nanoparticle assembly and vice versa.

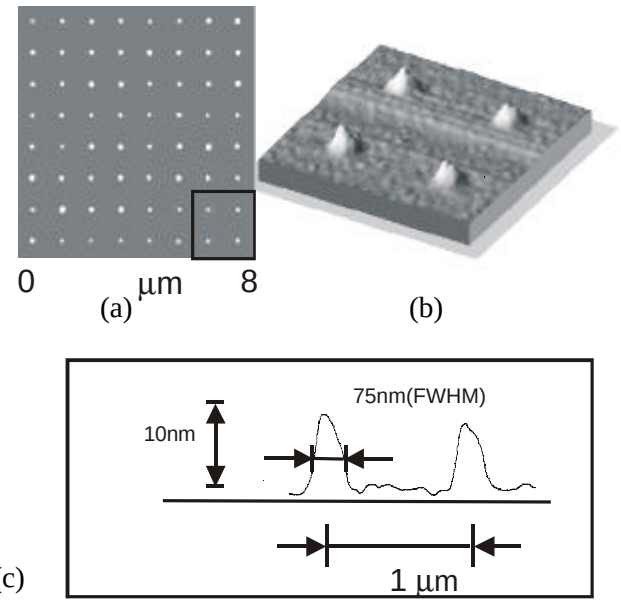

Fig. 6. An array of magnetite dots patterned by Dip-pen nanolithography. (a) AFM topography image of the dots. (b) Three dimension topography image for a selective area (marked square). (c) Cross section topography of the dots.

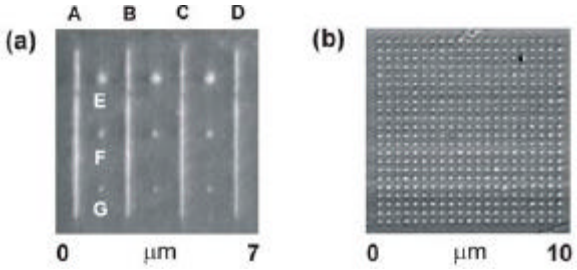

Fig. 7. Manganese ferrite nanostructures patterned via Dip-pen nanolithography. (a) AFM image of patterned dots and line. (b) AFM image of an array of dots.

In summary, metal, nonmetal and encapsulated magnetic nanoparticles have been synthesized by chemical and arc evaporation methods. We have presented a versatile new method for generating magnetic nanostructures down to sub-100 nm with precise control, allowing a major step towards biodiagnostics at nanoscale.

REFERENCES: [1]B. Bonnemain (1998) J. Drug Targeting 6:167. [2]U. Hafeli, W. Schutt, J. Teller, et al, *Scientific and Clinic Applications of Magnetic Microspheres*, Plenum Press, New York, 1997. [3]L. Fu, V.P. Dravid and D.L. Johnson (2001) *Applied Surface Science* **181**:173-178. [4]W.F. Parron, J. Kim, B.S. Jacobson (1985) *Biochem. Biophys., Acta* **83**:816. [5]P.K. Gupta, C.T. Hung (1989) *Life Sci.* **44**:175. [6]X.W. Li, A. Gupta, V.P. Dravid et al. (1998) *Applied Physics Letters* **73**: 3282-3284. [7]V.P. Dravid, J. J. Host, et al. (1995) *Nature* **374**: 602-602. [8]Hwang, J. H., V. P. Dravid, et al. (1997) *Journal of Materials Research* **12**: 1076-1082. [9]S. Hong, J. Zhu, C.A. Mirkin (1999) *Science*, **283**:661. [10]X. Liu, L. Fu, V.P. Dravid et al (2002) *Advanced Materials*, **14**: 231-234.

NOVEL BIOCOMPATIBLE MAGNETIC FLUIDS

C. Gansau[1], N. Buske[1], C. Gross[2] and W. Weitschies[2]

[1] *Berlin Heart AG, Wiesenweg 10, D-12247 Berlin, Germany*
[2] *Ernst-Moritz-Arndt-University, Institute of Pharmacy, Jahnstr. 17, D-17487 Greifswald, Germany*

INTRODUCTION: Biocompatible magnetic fluids (MF) are composed of homogeneously dispersed magnetic core/shell nanoparticles in physiological aqueous carriers. The core material is mostly magnetite/maghemite and the non-magnetic shells are made of biocompatible or even biodegradable organic molecules. Typical shell materials are polysaccharides [1] such as dextran and starch. They can be modified by carboxy groups, dimercaptosuccinic acid or other reactive components.

MF are increasingly used in medical diagnostics and therapy as well as in biotechnology.

MF with a novel biocompatible shell:
A new generation of biocompatible MF [2] are presented composed of magnetic nanoparticles that are coated with cyclodextrin (CD). CD is formed by 6, 7 or 8 glucose units as a cycle (Fig. 1). These cycles generate subnanometer pores of 0.5-0.8 nm diameter.

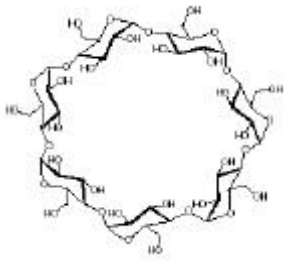

Fig. 1: Structure of b-cyclodextrin

Inclusion products with small molecules or components of molecules can be formed by incorporation into these pores [3]. Furthermore, the cyclodextrin shell can be functionalized in order to conjugate bioactive molecules such as antibodies.

METHODS: The preparation procedure has been divided into the following steps: First, carboxymethylated (CM) α-, β- and γ-CD were prepared by well-known methods [4]. The degree of substitution (DS) can be varied, but mostly in a range of 0.8 to 1.2 CM per glucose unit.
Then, magnetite nanoparticles were synthesized by co-precipitation with ammonia, and in a next step coated with carboxylated cyclodextrins (CM-CD). The CM-CD-MF were synthesized in high yields with iron concentrations of 5-10 % (w/w). Even higher concentrated MF were obtained after evaporation of the solvent.

The core size of the magnetic particles was determined by TEM (CM20 FEG Philips). The hydrodynamic size of the nanoparticles and their zeta potential were determined by photon correlation spectroscopy (PSC) using a Coulter N4 plus, and a Zetasizer 3000HS. Magnetization curves were obtained using coupled transformer spoils as the sensor. The saturation polarization Js and the initial susceptibility was evaluated from magnetization curves.
For the determination of the Fe(II) and Fe(III) concentration the particles were dissolved in hydrochloric acid and titrated with $KMnO_4$ and $Na_2S_2O_3$, respectively.

RESULTS: All measurements were executed with CM-β-CD (degree of substitution = 0.9) and the corresponding magnetic fluid, respectively.

The magnetic measurements (Fig. 2) yielded a very high saturation polarization that corresponded to 18 % (v/v) magnetite in the magnetic fluid.

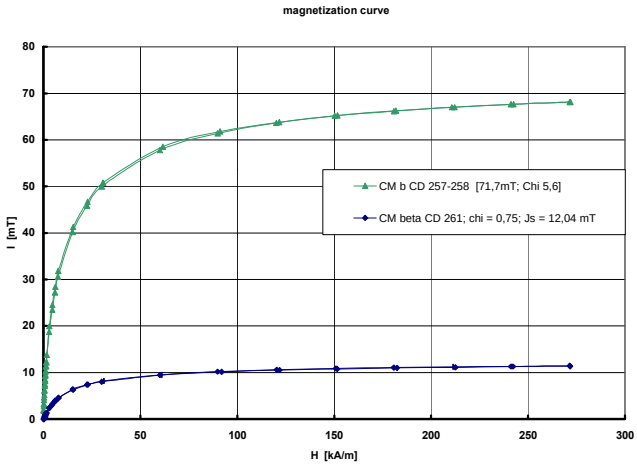

Fig. 2: *Magnetization curve of a high and low concentrated CM-b-CD-MF. Calculated saturation polarisation Is = 71.7 mT (12 mT) and initial susceptibility c = 5.6 (0.75) of the high (low) concentrated CM-b-CD- MF.*

The core particle size was determined by electron micrographs (Fig. 3). A mean particle diameter of 10.3 nm with the shown particle size distribution was found.

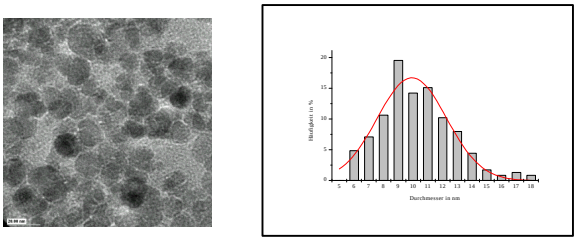

Fig. 3: Electron micrograph and particle size histogram of stabilized CM-b-CD-magnetite particles.

The zetapotential measurement (Fig. 4) showed that the diluted particles are negatively charged with a relatively high zeta potential of –30 to –50 mV in a pH range of 4-10 (titration with HCl and NaOH). This corresponds to the good colloidal stability of the particles.

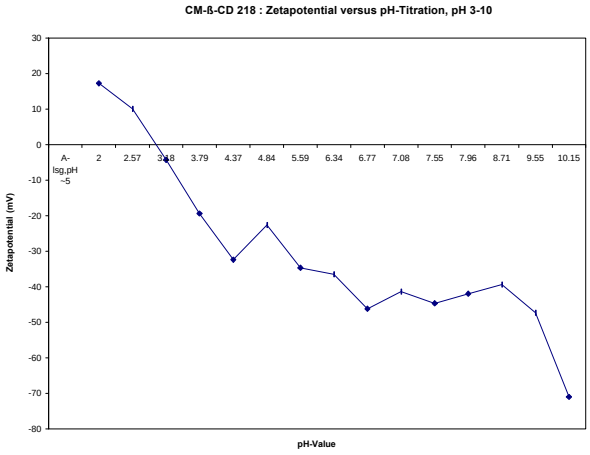

Fig. 4: Zetapotential vs. pH of CM-b-CD-MF

An average PCS hydrodynamic diameter of 65 nm of the very diluted *CM-b-CD-MF at pH = 7* with a polydispersity index of 0.22 was observed.

PCS measurements of the same CM-β-CD-MF at different pH were also executed (Fig. 5).

The hydrodynamic size of stable particles is 60-70 nm. But at strong acidic conditions the particles are not stable. Agglomerates were formed with higher PCS-values.

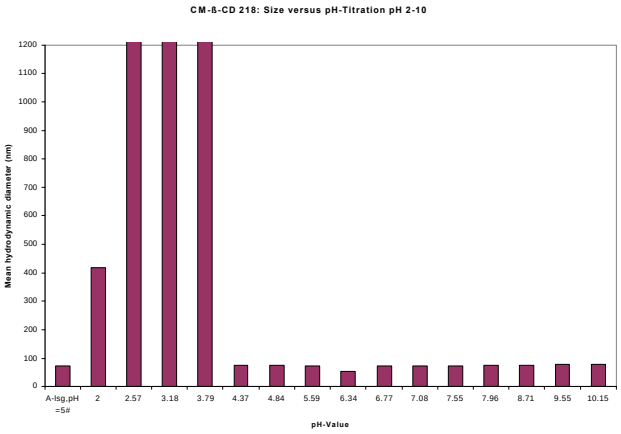

Fig. 5: Mean hydrodynamic diameter (PCS) versus pH-titration, pH 2-10, titrated with HCl and NaOH.

CONCLUSIONS: Novel magnetic fluids (MF) composed of nanosized magnetic iron oxide cores coated with biocompatible cyclodextrines (CD) and carboxylated cyclodextrins (CM-CD) were successfully prepared.

CM-β-CD-MF of high colloidal stability over a pH range of 4-10 in water and with magnetite volume concentration up to 18 % (v/v) (Js 71.7 mT) were synthesized. An average core size of the core/shell-particles of 10.3 nm with a size distribution ranging from 6 to 16 nm, and an average hydrodynamic diameter of 65 nm with a polydispersity index of 0.22 was observed.

The novel MF are intended for use in clinical and biochemical applications.

REFERENCES: [1] Th. Goetze, C. Gansau, N. Buske, M. Roeder, P.Görnert and M. Bahr *Biocompatible Magnetic Core/Shell Nanoparticles* 9. International Conference of Magnetic Fluids (2001) to be published in JMMM, in press. [2] C. Gansau, T. Götze and N. Buske: DE-patent pending 10154016.7. [3] W. Saenger, Angew. Chem. 92, 343-361 (1980). [4] S. Maruno, M. Hasegawa, EP 0928809A1 (1997).

DEVELOPMENT OF IMMUNOMAGNETIC REAGENTS FOR HUMAN HEMATOPOIETIC CELL SORTING

E. Golenkina [1], P. Ivanov [1], D. Blochin [1], V. Filippov [2], O. Yershov [3]

[1] Blokhin Memorial Cancer Research Center, RAMS, Moscow, Russia [2] Research Institute of Chemical Physics, RAS, Moscow, Russia, [3] Research Institute of Chemistry and Technology of Hetero-organic Compounds, Moscow, Russia

INTRODUCTION: Immunomagnetic separation is generally recognized as one of the most specific, reliable and fastest techniques to isolate cell subpopulations from complex cell mixtures.

The objective of our work was to develop the immunomagnetic reagent for human haematopoietic cell sorting. To this end monosized, superparamagnetic microspheres were generated and completely characterized. The conditions to conjugate monoclonal antibodies to the particles surface were optimized. The selection technique with the obtained immunomagnetic particles was further worked out.

METHODS: *Preparation and characterization of magnetic polystyrene microspheres (MPM):* Magnetite (Fe_3O_4) prepared by the reaction of Fe(II) and Fe(III) with the ammonia aqueous solution was dispersed at organic solvent enriched with nonionic surfactant to obtain stable colloidal solution. Polystyrene magnetic particles with surface hydroxyl groups were prepared by the method of emulsifying polymerization of copolymers and magnetite ferrocolloid. Briefly, styrene (20 g), divinyl-benzene (2g) and magnetite ferrocolloids (4,5 g) in styrene were emulsified in 400 ml of distilled water containing 0.25% SDS and agitated well for 10 min at room temperature. The mixture was ultrasonicated for 30 sec (frequency 22 kHz, power 40 W/cm^2). To perform polymerization 100 ml of 1% potassium peroxysulphate in distilled water was added and stirred at 60 ^{o}C for 24 h followed by incubation at 70 ^{o}C for 1 h. After reaching room temperature they were centrifuged at 500 g for 15 min. The sediment was resuspended in SDS and the magnetic particles concentrated in the magnetic field of a permanent magnet of magnetic intensity 2000 oersted for 30 min. SDS treatment was carried out twice. MPM were filtered with a Millipore 3 ìm filter and resuspended in SDS for a final concentration of 10 mg/ml.

Particles were analyzed by transmitted-light microscopy. Size distribution was estimated by laser correlation spectroscopy. Magnetic properties (saturation and residual magnetization) were determined by magnetometry (Bruker, USA).

To increase the protein-binding capacity magnetic support was activated by *p*-toluenesulfonyl chloride. MPM were washed with water, water : dioxane (3:1, v:v), water : dioxane (1:3), dried dioxane. Wet weight treated particles (1g) were put into a round-bottomed flask containing 200 mg of tosyl chloride dissolved in 2 ml dioxane. Pyridine was added slowly under stirring. After 1 hour, the MPM were washed with dioxane and transferred back to water gradually. Activated particles were stored at 4 ^{o}C until being used.

Binding of antibodies to the particles: Ammonium sulfate precipitation was used to obtain immunomagnetic conjugates murine IgG monoclonal antibodies (MoAbs) against human lymphocyte antigens CD3 (clone ICO-90), CD4 (clone ICO-86), CD8 (clone ICO-31) and CD20 (clone ICO-180) raised and purified from ascites fluids. Searching for optimal conjugation conditions we used varying buffer solutions (0.025M borate-buffered saline, pH 8.5; 0.05M carbonate-buffered saline, pH 9.5; 0.05M and 0.015M phosphate-buffered saline, pH 7.4). Then we studied kinetics of immunoglobulin binding by altering the reaction time from 30 min to 24 h. Generally, to prepare conjugates 10 mg of corpuscular magnetic support (approximately 5x10^8 beads) were incubated with 200 ìg MoAbs in a total volume of 1 ml buffer solution at 4 ^{o}C under gentle rotation. Microspheres were then collected and washed twice using a magnetic field. Unoccupied protein-binding sites were then blocked with 0.05M PBS containing 2% human serum albumin for 12 h at 4 ^{o}C under gentle rotation. Antibody-coated magnetic particles were resuspended to a concentration of 10 mg/ml (approx. 5x10^8 particles per ml) with 0.01M PBS containing 2% human serum albumin (HSA) and 0.05% NaN_3 and stored at 4 ^{o}C until being used.

Separation of cells: Peripheral blood mononuclear cells (PBMC) from normal donors were isolated by density centrifugation on a Ficoll Paque gradient.

Generally, immunomagnetic selection (depletion) of antigen-positive lymphocytes was carried out as follows: immunomagnetic particles were washed twice with 0.01M PBS (pH 7.4) using a magnetic field. 10x10^6 PBMC in 1 ml of 2mM EDTA in 0.01M PBS containing 0.5% HSA were added to the collected particles to obtain an estimated 3:1 bead : target cell ratio. The resuspended mixture was incubated for 30 min at room temperature under gentle rotation. The bead/cell complexes were retained by the permanent magnet whereas unbound cells were removed by four washes with 0.01M PBS. To evaluate depletion effectiveness flow cytometric analysis was carried out by direct immunofluorescence on samples from PBMS both before and after selection and on unbound cells (negative fraction). Data acquisition and analysis were assessed on a FACScan using FACScan research software (Becton Dickinson & Co.).

To determine an optimal quantity of immobilized MoAb magnetic beads conjugated with anti-CD3 and anti-CD20-antibodies that were known to have bound 4, 7, 10 and 12 ìg of antibody per 1 mg of support were used, the results obtained were analyzed for different processing variables.

RESULTS: *MPM preparation and analysis:* Our preparation method for the magnetic polystyrene microspheres formed spherical particles (Fig. 1). Laser correlative spectroscopy showed that the particles had a mean diameter of 1.0 ìm (var. from 0.3 to 2.0 ìm) with size homogeneity of more than 90%.

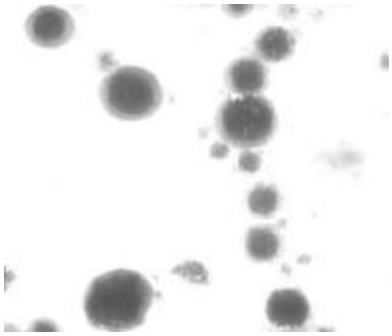

Fig. 1: Transmitted-light microscopy of synthesized magnetic polystyrene particles.

Estimated basic magnetic properties are given in Table 1. Due to the insignificant residual magnetization, MPM can be repeatedly collected in a magnetic field and thereafter easily redispersed.

Table 1. Measured magnetic characteristics of MPM synthesized.

Remanent magnetization, Gs cm^3/g	Saturation magnetization, Gs cm^3/g
1.2	25

The saturation magnetization of 25 Gs cm^3/g enabled the rapid concentration of the MPM using a permanent magnetic field of 2000 Oe.

Coupling of antibodies to the particles: MPM did not bind MoAbs when incubated in 0.05M carbonate-buffered saline at pH 9.5. The maximum protein-binding capacity was less then 2 ìg MoAbs per mg particles when 0.025M borate-buffered saline at pH 8.5 or 0.05M phosphate-buffered saline at pH 7.4 were used. We elicited 0.015M PBS at pH 7.4 to be best for immunoglobulin coupling to the particles. In this way, 10-15 ìg MoAbs per mg particles could be immobilized after incubation of the MoAbs/MPM mixture for 24 h.

When studying the kinetics of immunoglobulin coupling we discovered that the binding rate was not the same for different MoAbs (Fig. 2).

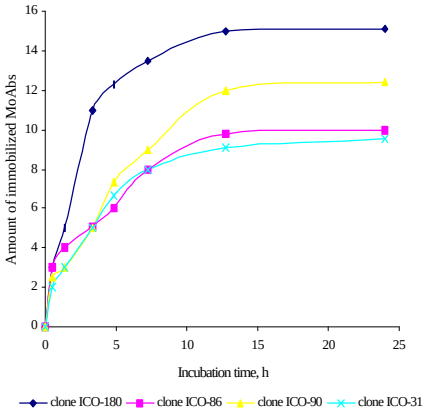

Fig. 2: Rates of IgG immobilization on MPM surface. Amounts of immobilized immuno-globulines (ìg per 1 mg support) (Y) were measured as a function of interaction time (h) (X) for different MoAb clones.

The optimal antibody-binding capacity as determined by subsequent immunomagnetic selection was found to be 7-10 ìg MoAb per mg particles. The required incubation time was averaged to be 10 hours for conjugating with clones ICO-90, ICO-86, ICO-31, and not more than 6 hours for clone ICO-180.

Immunomagnetic cell selection (depletion): Our primary concern was to determine an optimal amount of MoAbs that should be immobilized on the particles' surface. For this purpose, a series of $CD3^+$-lymphocytes depletions were carried out. As noted before, immunomagnetic anti-CD3 conjugates with 4 to 12 ìg IgG per mg support were used. There proved depletion grade to be estimably influenced by the level of coupled MoAbs, the other conditions (i.e. source PBMC, beads per cell ratio, incubation time and temperature) being equal. The antibody binding capacity of 4 ìg/mg was apparently deficient because in this case immunomagnetic selection failed to eliminate $CD3^+$ target-cells. The maximum antibody binding capacity of 12 ìg per mg support for clone ICO-90 was also not optimal, because excess IgG split out easily and blocked CD3 receptors on target cells interfering with bead/cell complexes formation. The latter was detected by staining of unbound cells after selection with FITC labeling sheep anti-mouse $F(ab)_2$. The most efficient was the depletion with MPM covered with MoAbs in concentration 7 to 10 ìg. Negative selection in those cases resulted in depletion of 97% $CD3^+$-lymphocytes MoAbs (Fig. 3). Data were verified by $CD20^+$-lymphocyte depletion. We used MPM conjugated with anti-CD20 MoAbs (clone ICO-180) at concentrations 4, 10 and 15 ìg per mg of support. IgG ICO-180 concentrations of 10 ìg/mg were optimal, providing a depletion rate of 96% (Fig. 4).

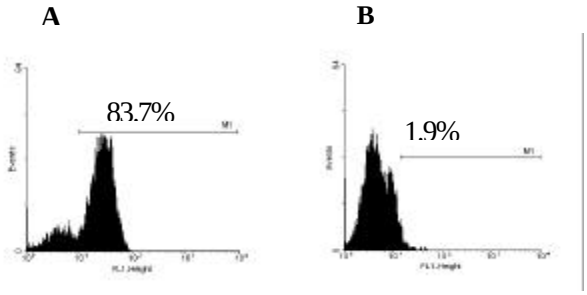

Fig. 3: Negative selection of $CD3^+$-lymphocytes from human PBMC using MPM conjugated with MoAbs anti-CD3 (clone ICO-90) (8 ìg IgG per mg support). Cells are stained with CD3 FITC. A: PBMS before selection. B: negative fraction after immunomagnetic depletion.

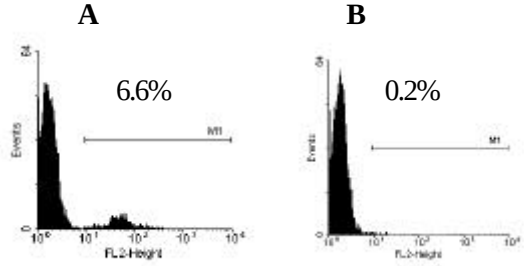

Fig. 4: Negative selection of $CD20^+$-lymphocytes from human PBMC using MPM conjugated with MoAbs anti-

CD20 (clone ICO-180) (10 ìg IgG per mg support). Cells are stained with CD20 PE. A: PBMS before selection. B: negative fraction after immunomagnetic depletion.

For further experiments immunomagnetic particles covered with MoAbs anti-CD4 (clone ICO-86) and anti-CD8 (clone ICO-31) were used at a concentration of 8 ìg/mg. Immunomagnetic separations with these conjugates eliminated 95-97% of antigen positive cells from an initial PBMC suspension (data not shown).

DISCUSSION & CONCLUSIONS: Polystyrene magnetic microspheres were prepared from copolymers and magnetic iron oxide employing the method of emulsifying polymerization. The resulting particles were 1µm in diameter, the homogeneity level was better than 90%. Microspheres possessed insignificant magnetic remanence and showed superparamagnetic behavior. To provide active surface groups MPM were activated by *p*-toluenesulfonyl chloride.

Optimal immunoglobulin coupling for the particles was performed in 0.015M PBS at pH 7.4 at 4 ^{o}C with gentle rotation. The interaction time should be determined for each MoAb clone because the immobilization rate is not constant. To achieve the optimal amount of surface-bound IgG, which was estimated to be 7-10 ìg MoAbs per mg support, conjugation times had to be 6 h for clone ICO-180, and 10 h for clones ICO-90, ICO-86 and ICO-31. Both deficient and excessive immunoglobulin coupling was proven to be inadvisable. Immunospecific conjugates against human lymphocyte antigens CD3, CD4, CD8 and CD20 were consequently generated. Immunomagnetic separation with these conjugates is able to eliminate about 97% of antigen positive cells from an initial PBMC suspension.

We believe that the developed immunomagnetic reagents will be useful in laboratory and clinical practice. They might be especially useful for the removal of tumor cells from bone marrow before autologous transplantation (in patients with B- or T-cell lymphomas). They also could be applied for T-lymphocyte purging of bone marrow before allogeneic transplantation to avoid development of graft versus host disease

REFERENCES: K. Nilsson, K. Mosbach (1980) *Eur. J. Biochem.* **112**:397-402. A. Rembaum, S. Margel (1979) *Br. Polym. J.* **10**:275-280. E.A. Golenkina, P.K. Ivanov, E.R. Polosukhina, O.N. Donskaya (2000) *High Medical Technologies, Materials of the V Russian Oncological Congress* 243-244

CHARACTERIZATION OF A FERROFLUID BY ATOMIC FORCE MICROSCOPY AND PHOTON CORRELATION SPECTROSCOPY AFTER MAGNETIC FRACTIONATION

C. Groß[1], K. Büscher[2], E. Romanus[1], C.A. Helm[2] & W. Weitschies[1]

[1]Institute of Pharmacy, *University of Greifswald, Jahnstr. 17, D-17487 Greifswald, Germany*
[2]Institute of Applied Physics, *University of Greifswald, Jahnstr. 16, D-17487 Greifswald, Germany*

INTRODUCTION: Ferrofluids are colloidal solutions of magnetic nanoparticles in a carrier fluid. The nanoparticles consist of a ferri- or ferromagnetic core that is stabilized against aggregation by a shell based on various materials such as citrate ions or fatty acids. Ferrofluids are increasingly used for biological and medical applications, such as high gradient magnetic separation techniques [1], magnetic drug targeting [2], magnetic hyperthermia [3], contrast agents for Magnetic Resonance Imaging [4] and measurement of the relaxation of magnetic nanoparticles [5]. In all of these medical and biological applications the carrier fluid is water-based, while iron oxides (magnetite or maghemite) are predominantly chosen as core materials due to their proven biodegradability and low toxicity [6]. In order to avoid aggregation under physiological conditions (i.e., physiological pH values and salt concentrations), the nanosized magnetic cores are usually stabilized by shells derived from biocompatible polymeric carbohydrates such as dextrans or starch [7, 8].

In technical applications, concentrated ferrofluids are commonly used to obtain a “fluid magnet” with strong bulk magnetic properties, e.g. a high saturation magnetization. In contrast, in most medial and biological applications, the bulk magnetism of the ferrofluid is only of minor importance. Here, the properties of the individual nanoparticles contained in the fluid are more relevant. These properties include a high relaxation signal for nanoparticles used as contrast agents and a high magnetic moment for nanoparticles used as drug carriers in magnetic targeting or as separation devices in high gradient magnetic separation techniques.

It is well known, that the nanoparticles in ferrofluids produced by classical chemical syntheses display a rather broad particle size distribution [9]. This size distribution may either be due to variations of the core size, the thickness of the coating, or different stages of agglomeration (Fig. 1). In principle, the size of the magnetic cores can differ, whilst the thickness of the stabilizing coating remains constant (Fig. 1a) or is also variable (Fig. 1b). Furthermore, the size of the magnetic cores may be rather constant, but some of the individual nanoparticles agglomerated during the synthesis, resulting in stable agglomerates with constant (Fig. 1c) or variable (Fig. 1d) thickness of the polymeric coating. Thirdly, the particle sizes may also vary due to the agglomeration of coated nanoparticles during storage (Fig. 1e, 1f).

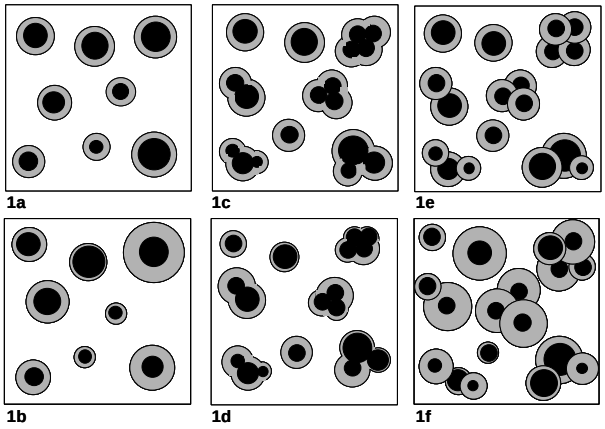

Fig. 1: Models for the origin of the nanoparticle size distribution in ferrofluids.

It was the aim of this study to investigate the size distribution of the magnetic nanoparticles in a water-based ferrofluid. For this purpose, a magnetic fractionation was performed and the fractions were characterized by atomic force microscopy (AFM) and photon correlation spectroscopy (PCS).

MATERIALS & METHODS: A water based ferrofluid (DDM 128N, Meito Sangyo, Japan) consisting of magnetic nanoparticles with a core of iron oxide and a shell of carboxydextran (M_r about 2000) were magnetically fractionated by stepwise reduction of the electromagnetic field from 6 A (1 T) to zero field using an electromagnet (Bruker B-MN 90/30) and magnetic separation columns (MACS Cell Separation Column LS, Miltenyi Biotec). A detailed description of the fractionation procedure is given elsewhere [9]. In brief, the separation columns were fixed between the pole shoes of the electromagnet and rinsed with 2 ml of buffer solution (phosphate buffered saline, pH 7.4). Then, at the highest current (6 A), 500 µl of the ferrofluid was added. The column was rinsed with the buffer solution until the eluate was clear (6 A

fraction). Then the field was reduced and the next eluate was gathered. This procedure was repeated until zero current was applied. Then, the column was removed from the magnet and the remaining nanoparticles were eluated with buffer solution and gathered (fraction "out of magnet").
The iron content of each fraction was determined by chemical analysis [10]. The hydrodynamic diameter of the nanoparticles was measured by PCS (ZetaSizer 3000HS, Malvern). Furthermore, fractions were also investigated by AFM in the tapping mode (Multimode-AFM with Nanoscope IIIa-controller, Digital Instruments) after electrostatic adsorption of the nanoparticles onto polyetheleneimine modified mica [11]. The particle diameters were determined from the height images. Furthermore the magnetic relaxation signals of the freeze dried fractions were measured at room temperature using a LTS SQUID gradiometer system described elsewhere [12] and calculated as magnetic relaxation signal (in pT) per molar content of iron (in µmol) in the fractions.

RESULTS: The hydrodynamic diameters of the different fractions and the original ferrofluid as well as the particle diameters determined by AFM are given in Table 1.

Table 1: Mean particle diameters of magnetically fractionated nanoparticles measured by PCS and AFM and the magnetic nanoparticle relaxation signal.

Fraction	AFM (nm)	PCS (nm)	Magnetic relaxation signal (pT/µmol Fe)
Original	20	61	15
4 A	6	14	0
1 A	7	15	0
0.25 A	10	22	0
0.125 A	10	29	0
0.06 A	13	36	9
0.015 A	13	44	58
0 A	24	46	79
Out of magnet	29	66	167

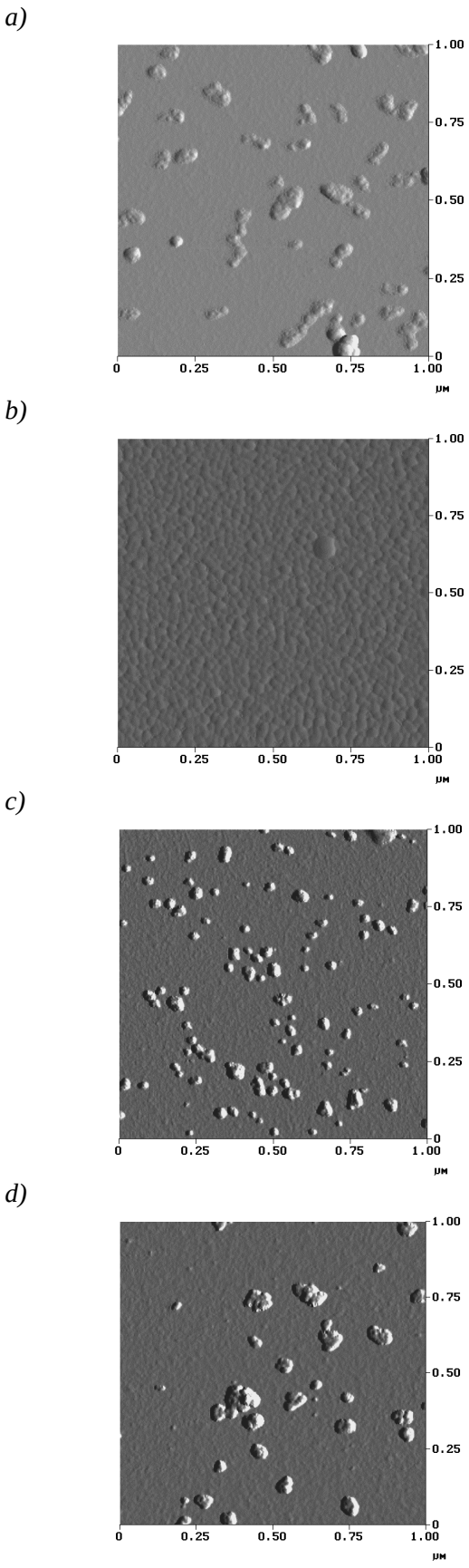

Fig. 2: AFM-amplitude images of the (a) original ferrofluid, and the fractions gathered at (b) 4 A, (c) 0.125 A and (d) 0 A. The surface coverage is diffusion controlled.

The fraction gathered at 6 A could not be evaluated by PCS, as the count rate was below the critical limit, indicating a very small particle size, that is mostly due to dissolved carboxydextran. The mean particle sizes as determined by PCS increase continuously from the fractions gathered at 4 A to the fraction that was finally rinsed after removal of the column from the magnet (fraction: "out of magnet"). This increase in the mean particle diameters could also be observed by AFM.

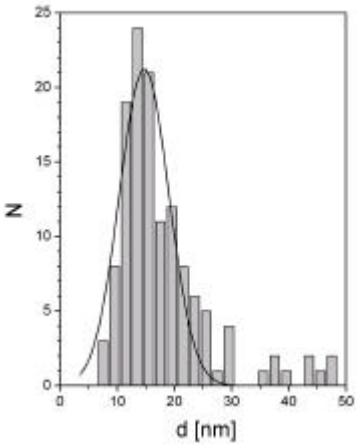

Fig. 3: Histogram of the particle size distribution of the original ferrofluid before fractionation as determined from the AFM-amplitude image with overlaid Gauss curve.

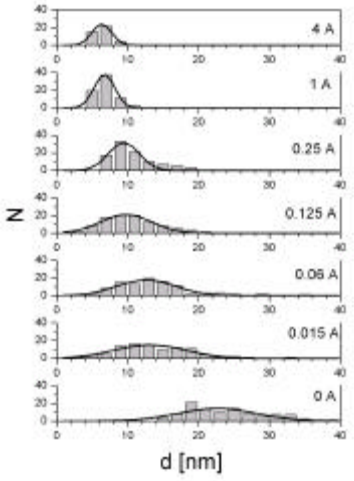

Fig. 4: Histograms of the particle size distributions of fractions of a ferrofluid as determined from AFM-amplitude images.

A magnetic nanoparticle relaxation signal could only be found for the factions gathered below 0.125 A, whilst the strength of the magnetic signal increases with decreasing current and increasing particle size.

In the AFM-amplitude image of the original ferrofluid before fractionation (Fig. 2a) single nanoparticles and agglomerates are present. The nanoparticles gathered at 4 A are free of agglomerates (Fig. 2b). They form an adsorption layer on the mica surface. In contrast, the fractions gathered at lower currents (Fig. 2c and 2d) are predominantly formed by agglomerates with increasing diameters. The histograms of the particle size distributions of the original ferrofluid (Fig. 3) and the fractions (Fig. 4) show, that the particle size distribution broadens with increasing particle size.

DISCUSSION & CONCLUSIONS: During magnetic fractionation the magnetic nanoparticles are separated according to their magnetic moments. As the magnetic moment of a single domain magnetic nanoparticle is proportional to the amount of magnetic material, i.e. the volume of the magnetic core, only particles with very small core sizes pass the column at high magnetic field strengths, i.e. high applied currents. This could be confirmed by the AFM and the PCS measurements. The immeasurable signal in the magnetic nanoparticle relaxation measurements reconfirms this result, as the magnetic relaxation signal of single domain particles is also strongly dependent on the particle size [13].

The AFM images show, that the larger nanoparticles are mostly agglomerates of small nanoparticles. It can be ruled out, that these agglomerates had been formed during the fractionation process or that they are artifacts derived from the preparation of the AFM samples, as the mean hydrodynamic diameter of the reunified fractions was found to be nearly identical to the mean hydrodynamic particle diameter determined before fractionation (65 nm versus 61 nm).

The magnetic relaxation signals measured for fractions gathered at low currents indicate, that some nanoparticles with relatively large core diameters are also present, but they are only representing a minor proportion.

The comparison of the mean particle sizes determined by AFM and PCS further indicates, that the mean diameters yielded by PCS measurements are mostly determined by large particles that are present in the sample. This is due to the fact that the PCS signal derived from nanoparticles with diameters far below the laser wavelength (in our case 630 nm) is dominated by Rayleigh diffraction. In Rayleigh diffraction, the intensity of the signal depends on the diameter of the particle, specifically the diameter raised to the power of six.

With respect to the different models presented for the origin of particle size distributions in Fig. 1, we conclude, that the investigated ferrofluid will most probably be described by Fig. 1c, although the model in Fig. 1d cannot be ruled out entirely.

Knowledge about the inner structure of magnetic nanoparticles with larger diameters may have great implications for their biological or medical applications. This can be explained with the following example: Two magnetic nanoparticles with identical particle diameters consist either of an agglomerate of a number of small magnetic cores or one single magnetic core. Assuming that the magnetic particles will not interfere magnetically without the presence of an external magnetic field, the magnetic moment of the agglomerate will be low or even zero in the absence of an external magnetizing field, as the magnetic moments of the individual cores will be statistically distributed. In the presence of an external field, the directions of the magnetic moments will align in the direction of this field and generate a strong magnetic moment. In contrast, the strength of the magnetic moment of the nanoparticle composed of one magnetic core will be independent of the external magnetic field, only its orientation will be influenced by the external field. Therefore, in applications where no or only weak external magnetic fields will be applied, the nanoparticle composed of several magnetic cores will not provide a magnetic force, whilst in applications where strong magnetic fields are applied, the two nanoparticles will yield comparable magnetic forces. In order to use magnetic nanoparticles in biological or medical applications it is therefore important to know which properties of magnetic nanoparticles are needed and which kind of nanoparticles are really present in the ferrofluid.

REFERENCES: [1]A. Radbruch, B. Mechtold, A. Thiel, S. Miltenyi and E. Pfluger (1994) *High-gradient magnetic cell sorting* Methods Cell Biol **42**: 387 [2]A.S. Lübbe, C. Alexiou and C. Bergemann (2001) *Clinical applications of magnetic drug targeting* J Surg Res **95**: 200-206 [3]A. Jordan, P. Wust, H. Fähling, W. John, A. Hinz and R. Felix (1993) *Inductive heating of ferrimagnetic particles and magnetic fluids: physical evaluation of their potential of hyperthermia* Int. J. Hyperthermia **9**: 51-68 [4]D. Pouliquen, H. Perroud, F. Calza, P. Jallet and J.J. Le Jeune (1992) *Investigation of the magnetic properties of iron oxide nanoparticles used as contrast agent for MRI* Magn. Reson. Med. **24** :75-84 [5]W. Weitschies, R. Kötitz, T. Bunte and L. Trahms (1997) *Determination of relaxing or remanent nanoparticle magnetization provides a novel binding specific technique for the evaluation of immunosassays* Pharm. Pharmacol. Lett. **7**: 5-8 [6]F. Kopp, M. Laniado, F. Dammann, F. Stern, E. Gronewaller, T. Balzer, C. Schimpfky and C.D. Claussen (1997) *MR imaging of the liver with Resovist: safety, efficacy and pharmacodynamic properties* Radiology **204**: 749-756 [7]L.M. Lacava, Z.G. Lacava, M.F. Da Silva, O. Silva, S.B. Chaves, R.B. Azevedo, F. Pelegrini, C. Gansau, N. Buske, D. Sabolovic and P.C. Morais (2001) *Magnetic resonance of a dextran-coated magnetic fluid intravenously administered mice* Biophys J **80:** 2483-2486 [8]A.S. Lübbe, C. Bergemann, W. Huhnt, T. Fricke, H. Riess, J.W. Brock and D. Huhn (1997) *Preclinical experiences with magnetic drug targeting: tolerance and efficacy* Cancer Res **57**: 3063-3065 [9]T. Rheinländer, J. Justiz, A. Haller, R. Kötitz, W. Weitschies and W. Semmler (1999) *Dynamic properties of fractions yielded by magnetic fractionation of magnetic fluids* IEEE Trans. Magn. **35:** 4055-4057 [10]E.-G. Jäger, K. Schöne and G. Werner (1981) *Lehrwerk Chemie – Arbeitsbuch 5, Elektrolytgleichgewichte und Elektrochemie,* Deutscher Verlag für Grundstoffchemie, p. 266 [11]J. Schmitt, P. Mächtle, D. Eck, H. Möhwald and C.A. Helm (1999) *Preparation and Optical Properties of Colloidal Gold Monolayers* Langmuir **15**: 3256 [12]L. Warzemann, J. Schambach, P. Weber, W. Weitschies, R. Kötitz (1999) *LTS SQUID gradiometer system for in vivo magnetorelaxometry* Supercond. Sci. Technol. **12** 953-955 [13]L. Néel (1955) *Some Theoretical Aspects of Rock-Magnetism* Adv. Phys. **4**, 191-243

ACKNOWLEDGEMENTS: This research project is supported by the Deutsche Forschungsgemeinschaft DFG (WE 2555/1) and He 1616/10-1

HIGH GRADIENT MAGNETIC SEPARATION ORDERED MATRICES

Gh. Iacob[1], Al. D. Ciochina[2], & O. Bredetean[2]

[1]*National Institute of Research & Development for Technical Physics, Iasi, Romania*
[2]*University of Medicine and Pharmacy, Iasi, Romania*

INTRODUCTION: Magnetic separation is a complex physical process based on the magnetic phenomena and the magnetic properties of the substances. Several separation procedures are known: separation according to magnetic susceptibility, magnetohydrostatic separation, magnetohydrodynamic separation, separation using eddy currents. The principle of separation by magnetic susceptibility consists in the different action of the magnetic force upon the components of a mixture in competition with other forces, such as drag force, gravity or friction force. Within the separation by magnetic susceptibility procedures, the high gradient magnetic separation (HGMS) technique has a special place because of the practical necessity of capturing very small particles with low magnetic properties from the fluids. The HGMS direct and indirect (also called magnetic seeding) techniques were applied to purify kaolin clay, desulphurize coal, process rare metals ores, treat water polluted with heavy metal ions, organic substances or microorganisms, treat water from conventional and nuclear power plants, treat urban waste water, purify industrial gas etc.

The magnetic separation of some biological entities that have intrinsic magnetic properties (red blood cells, "magnetic" bacteria) can be described as *a direct separation method*, because the magnetic force is directly applied on the entity that has to be separated. For this reason we are considering that the magnetic carrier technique (by which there are manipulated non-magnetic entities bound to magnetic particles) is *an indirect separation method.*

DISCUSSION: The main factor in the magnetic separation is the magnetic force, F_m. The general expression of F_m acting on a paramagnetic particle, which has the magnetization linearly proportional to the applied magnetic field is

$$F_m = m_0 V_p (c_p - c_L) H \tilde{N} H \qquad (1)$$

where V_p is the particle volume, χ_p - the particle susceptibility, χ_L - the fluid susceptibility and $\tilde{N}H$ is the magnetic field gradient. As one can see, F_m depends on $\tilde{N}H$, so in order to obtain a high value of magnetic force it is necessary to create a high

gradient magnetic field. There are two different means to obtain a high gradient magnetic field. One possibility is a special design of the polar pieces (edges, peaks etc.) that limit the separation volume. In this case, $\tilde{N}H$ value is often strong enough to capture or to deviate the small sized paramagnetic particles that are placed at a relatively long distance from the polar pieces. The other possibility is by adding some small and easily magnetizable ferromagnetic elements (wires, balls etc.) within the separation volume. The role of these elements is to create high local gradients of the magnetic field (of the order $\sim 10^5$ kOe/m); these gradients allow the appearance of very intense magnetic forces with short-range action. This setup of ferromagnetic elements that disturb the background magnetic field forms a HGMS matrix that is the characteristic component of a HGMS separator [1]. The most used matrices are made from thin wires obtained from soft magnetic alloys (i.e. Fe-Ni alloy). The wires can be disorderly packed or can be arranged in an ordered net. The ordered matrices have some advantages compared to the random ones: they have a constant packing factor throughout the entire volume, the local fluid velocity variations are small and the removal of the captured particles is easier.

A HGMS ordered matrix could be made in three flow - capture variants: transversal configuration (T) for which the fluid flow, the magnetic field and the wires are reciprocally perpendicular; longitudinal configuration (L) for which the fluid flow and the magnetic field are parallel with each other and perpendicular to the wires; axial configuration (A) for which the flow and the collecting wires are parallel and the magnetic field is transversal (Figure 1).

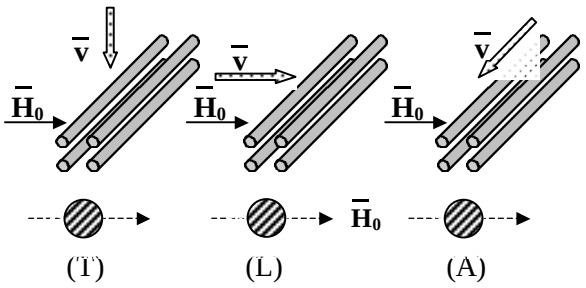

Fig. 1: Flow – capture configurations for HGMS ordered matrices: transversal (T), longitudinal (L) and axial (A).

In essence, a magnetized ferromagnetic wire can capture a paramagnetic particle if F_m is at least equal to the drag force (one could neglect the gravity force). As can be seen in Figure 1, the particles are captured in two regions of attraction situated around the axis parallel to the direction of the applied field H_0 and form deposits that have an approximately fan shaped section.

Usually, one could vary the force F_m by increasing or decreasing the applied field H_0 and the drag force by changing the average fluid flow velocity.

For a ferromagnetic wire – paramagnetic particle system there is another possibility to modify the force F_m. It consists in the different alignments of the wire to the direction of the applied magnetic field H_0. In this case, the force F_m on a particle is:

$$F_m = (4/3)\,(\pi b^3 a^2\,\chi_p\,M_S\,H_0 / r_S^3)\,\sin^2\alpha \quad (2)$$

where b is the particle radius, a the wire radius, χ_p the particle susceptibility, r_s the distance between the wire axis and the particle and $\acute{a}$ the angle between the wire and the H_0 direction [2].

The relation (2) shows clearly that F_m depends on $\acute{a}$; consequently, in order to modify the magnetic force between the wire and the particle, it is enough to modify the angle between the wire and the applied field H_o direction (Figure 2).

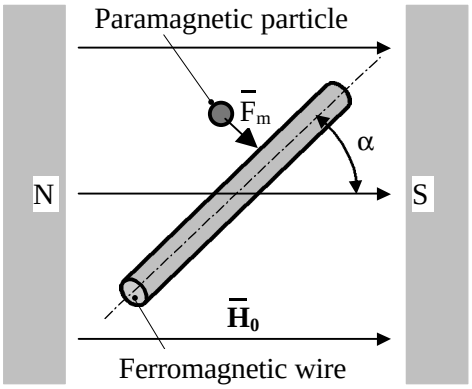

Fig. 2: System of a ferromagnetic wire and a paramagnetic particle: F_m depends on the α angle.

APPLICATIONS: Figure 3 shows a possible practical application of the relation (2). A HGMS ordered matrix (configuration T) made from parallel wires is placed in a background magnetic field H_0. The matrix must have the wires perpendicular to the field H_0 direction ($\acute{a} = 90^0$) in order to capture the particles from the fluid. It is not necessary to cancel the applied magnetic field H_0 to remove the captured particles. A simple rotation of the matrix so the wires become parallel to the H_0 direction ($\acute{a} = 0^0$) will lead to the cancellation of F_m and, as a consequence, to the detachment of the particles from the wires. Another advantage is that one could use permanent magnets as magnetic field source [3].

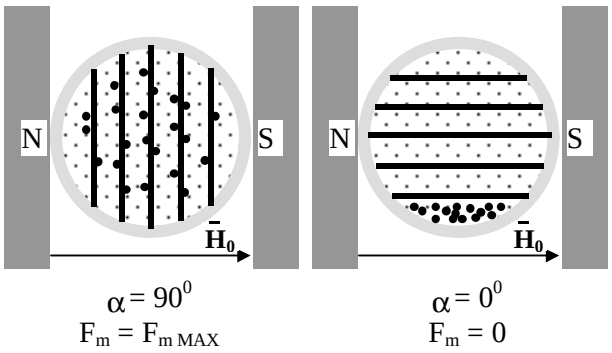

Fig. 3: The capture and the removal of the paramagnetic particles in a HGMS ordered matrix.

Such an ordered HGMS matrix, manufactured from thin ferromagnetic wires (25-60 ìm diameter) covered (or not) with a biocompatible coat (glass) and placed in the gap of a magnetic circuit excited by NdFeB magnets, could be a magnetic separator for sorting magnetic beads (1-3 ìm) in biological assays.

One could also obtain the concentration of the magnetic entities with or without intrinsic magnetism by magnetic deviation under F_m action in which case the laminar flow is an essential condition for the separation.

Adequate ferromagnetic elements situated within the separation volume can disturb on a short distance the flow trajectory stronger compared to the disturbance obtained on the same distance when the magnetic field gradient is generated by external polar pieces. In this case, the laminar flow is not an essential condition.

A magnetic separator that can be used to concentrate the paramagnetic microparticles is schematically shown in Figure 4. The HGMS ordered matrix consists of some parallel plans of wires (see in section in Figure 4b) situated also parallel to the magnetic poles. The wires from the same plan make two identical nets that form an angle (10^o-30^o) with the central vertical axis. Under the dominant action of the magnetic forces determined by the wires, the magnetic particles are

deviated laterally and down and finally evacuated through two lateral collector tubes [4].

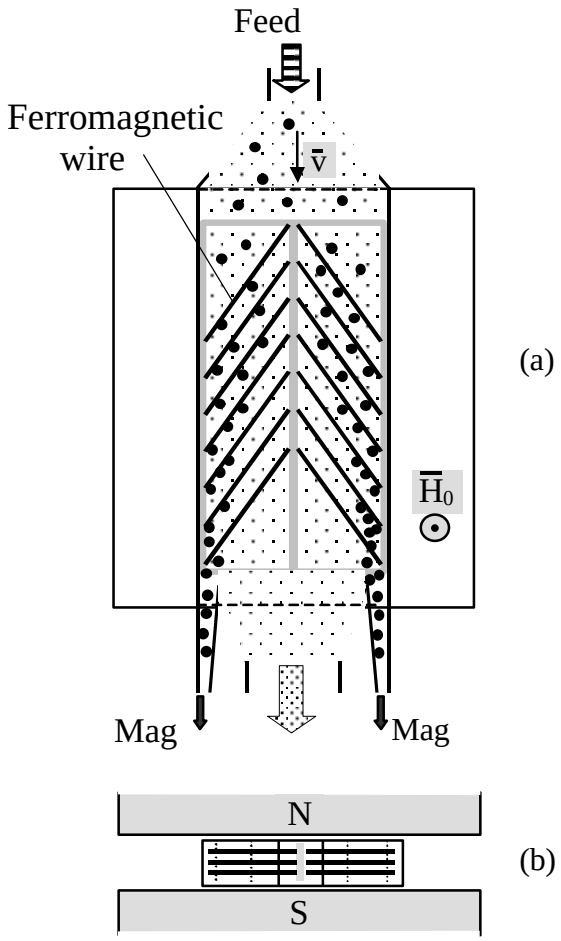

Fig. 4: Magnetic sorter with HGMS matrix used to concentrate paramagnetic particles: (a) longitudinal section, (b) transversal section.

We realized an experimental set-up of a magnetic separator as shown in Figure 5. This separator is made from a magnetic circuit excited by a pair of NdFeB magnets; a HGMS matrix is placed in the gap in axial configuration (A).

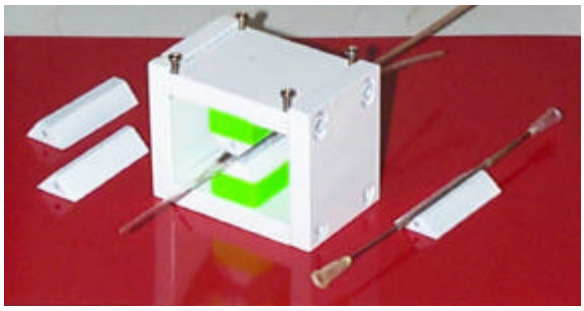

Fig. 5: Experimental set-up of a magnetic separator with axial HGMS matrix.

The matrix has an active length of 40 mm and consists of amorphous magnetic metallic wires covered by a glass coat (total diameter of 36 ìm).

The magnetic field background can vary by moving the upper polar piece or by using polar pieces of different shapes (up to H_{max} = 12.6 kOe). The magnetic separator was manufactured for experiments of capturing with high efficiency low paramagnetic microparticles from flowing fluids.

CONCLUSIONS: In some cases, the magnetic separation process can be improved by using HGMS ordered matrices, because they promote the appearance of short-range intense magnetic forces that are able to capture or to deviate more efficiently low paramagnetic microparticles or biological entities with induced paramagnetism.

REFERENCES: [1] N. Rezlescu, V. Badescu, E.B. Bradu, and Gh. Iacob (1984), *High Gradient Magnetic Separation* in Physical Principles of Magnetic Separation of Materials, Romanian Academy Press, pp. 46-80. [2] Gh. Iacob and N. Rezlescu, (1997), *IEEE Trans. Magn.*, **33**, pp. 4445-48. [3] Gh. Iacob and N. Rezlescu, (1997), Patent no. RO 112090 B1. [4] Gh. Iacob and N. Rezlescu, (1998), Patent no. RO 113814 B1.

European Cells and Materials Vol. 3. Suppl. 2, 2002 (pages 170-171) ISSN 1473-2262

MAGNETOGRAVIPHORESIS OF STATOLITHS AND ASSESSMENT OF VISCOELASTICITY OF THE *CHARA* CYTOPLASM

O.A. Kuznetsov, K.H. Hasenstein

Biology Department, University of Louisiana at Lafayette, *LA 70504-2451*

INTRODUCTION: The viscosity of the cytoplasm is crucial for many cellular functions but has not been reliably measured. We measured *in vivo* the viscoelastic properties of the cytoplasm by inducing movements of statoliths [1-6, 14] ($BaSO_4$-containing vesicles [13]) by ponderomotive forces in High Gradient Magnetic Fields (HGMF) and gravity [7-11].

MATERIALS & METHODS: Statoliths are denser and more diamagnetic than the cytoplasm. They can be displaced by HGMF with a dynamic factor $grad(H^2/2)$ of up to $1.9 \cdot 10^{10}$ Oe^2/cm in a custom experimental setup. We measured the HGMF-induced forces on statoliths using magnetograviphoresis of extracted statoliths. For this purpose five rhizoid cells were placed in a 25 µl drop of aqueous 0.01% SDS and the statoliths were released by severing the rhizoid tip with a scalpel. The density and viscosity of the SDS solution differed from to that of distilled water by less than 0.5%. The resulting suspension was collected into a 100 µm ID capillary. The shear forces during uptake separated the statoliths from cytoplasmic residue. The capillary was sealed at both ends and positioned between magnetic poles. The dynamic factor of the magnetic field was either zero or $1.9 \cdot 10^{10}$ Oe^2/cm. The movement of the particles in the capillary was video-recorded and analyzed by a custom analysis program from the video signal. Individual statolith trajectories were used to calculate their velocity.

Tips of actively growing *Chara* rhizoids were positioned near the upper edge of the same 175 µm gap between magnetic poles that were used for *in vitro* measurements (Fig. 1). The movements of individual statoliths inside the cells in HGMF and gravity were measured.

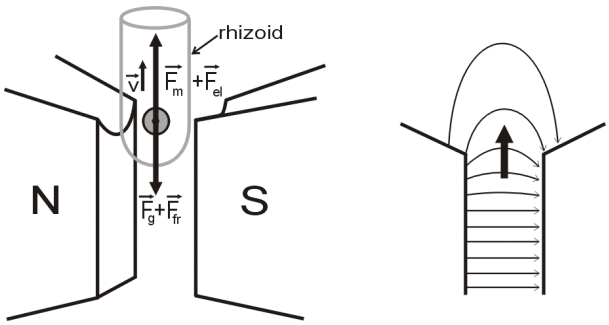

Fig. 1. Schematic representation of the magnetic system used for intracellular magnetophoresis of statoliths in Chara rhizoids (left). The statoliths are affected by gravity (F_g), and by the elastic force (F_{el}) of the cytoskeleton. Near the upper edge of the gap diamagnetic statoliths will be pushed up by the ponderomotive magnetic force (F_m). Moving statoliths also experience viscous frictional force (F_{fr}). The distribution of the magnetic field in the gap between the magnetic poles is shown on the right. The bold arrow indicates the direction of the ponderomotive force acting on diamagnetic statoliths.

RESULTS & DISCUSSION: Based on the sedimentation and the upward velocity in the presence of a HGMF, the difference in magnetic susceptibilities and densities between the extracted statoliths and medium (æ/ ñ) was calculated to be $1.3 \pm 0.2 \cdot 10^{-7}$ $emu/(g/cm^3)$. This value corresponds to the data for $BaSO_4$ particles, suggesting that the statoliths contain a significant amount of $BaSO_4$. The force induced by a magnetic gradient of $1.9 \cdot 10^{10}$ Oe^2/cm on *Chara* statoliths was estimated to be 2.4 times stronger, than the gravity force acting on them. The apparent cytoplasmic viscosity in intact rhizoids was about 0.1 Poise, comparable with previous estimations [15]. The contribution of the actin cytoskeleton to cytoplasmic viscoelasticity was assayed before and after application of the actin depolymerizer Latrunculin-B. This drug caused cessation of growth, sedimentation and partial clumping of statoliths. Statoliths in Latrunculin-treated rhizoids can be displaced by HGMF significantly higher than in intact rhizoids (Fig. 2). Analysis of individual statoliths movement indicated 40% increase in apparent cytoplasmic viscosity but elimination of elasticity.

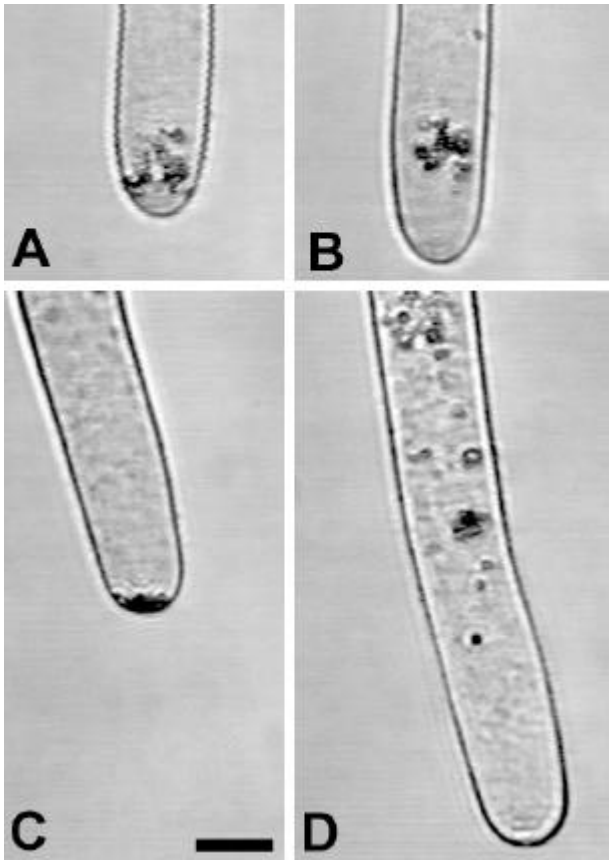

Fig. 2: Vertical displacement of statoliths in HGMF. The initial distribution in untreated rhizoids shows statoliths at a discrete distance from the apex (A). After 12 minutes of HGMF application the statoliths moved upward (B). Longer application of the field did not substantially increase the displacement. Statoliths in a rhizoid treated with 1 :m latrunculin B sedimented to the rhizoid apex and the rhizoid stopped growing (C). In such rhizoids a much greater displacement of statoliths was possible (D). Bar = 25 :m.

REFERENCES: [1]M. Braun and A. Sievers (1993) *Protoplasma* **174**: 50-61.
[2]M. Braun and A. Sievers (1994) *Eur. J. Cell Biol.* **63**: 289-298.
[3] M. Braun (1997) *Planta* **203**: S11-S19.
[4]M. Braun and G. Wasteneys (1998) *Planta* **205**: 39.
[5]B. Buchen et al (1991) *Protoplasma* **165**, 121-126.
[6]B. Buchen et al (1993) *Protoplasma* **172**, 38-42.
[7]A.A. Kuznetsov and O.A. Kuznetsov (1989) *Biofizika* **35**, 835-840.
[8]O.A. Kuznetsov and K.H. Hasenstein (1996) *Planta* **198**, 87-94.
[9]O.A. Kuznetsov and K.H. Hasenstein (1997) *Magnetophoretic Characterization of the Plant Gravity Receptor*. in Scientific and Clinical Applications of Magnetic Carriers. (eds. U. Häfeli, W. Schütt, J. Teller, M. Zborowski) Plenum Press, New York, NY, pp. 429-444.
[10]O.A. Kuznetsov et al (1999) *Plant Physiol*. **119**, 645-650.
[11]O.A. Kuznetsov, and K.H. Hasenstein (2001) *Adv. Space Res.* **27**(5): 887-892.
[13]A. Sievers, and M. Schmitz (1982) *Ber. Deut. Bot. Ges*. **95**, 353-360.
[14]A. Sievers et al (1996) *TIPS* **1**, 273-279.
[15]P. Todd (1994) *Adv. Space Res.* **14**, 121-124.

ACKNOWLEDGEMENT: Supported by NASA grants NAG10-0190 & NAG2-1423.

PREPARATION OF MAGNETO-VESICLES WITH DOPE/DDAB LAYERS

Kezheng Chen and Weili Luo

Department of Physics, University of Central Florida, Orlando, FL 32816

INTRODUCTION: Biocompatible magneto-vesicles have very good dispersibility in aqueous solution, as well as affinity to the cell and will be very useful in drug delivery and hyperthermia as magnetic carriers [1-3]. Vesicles with Dioleoyl phosphatidylethanolamine (DOPE) and dimethyl dioctadecylammonium bromide (DDAB) as bilayers and magneto-vesicles consisting of the same bilayers, with magnetite nanoparticles as cores, were prepared by the sonication method. The morphologies and size distributions of DOPE/DDAB vesicles and magneto-vesicles were characterized by AFM.

METHODS: A series of DOPE/DDAB in chloroform stock solution was mixed at different concentration ratios. The mixture of phospholipids was dried under nitrogen in a flask and was desiccated in vacuum overnight to remove the residual solvent in the dried film. A drop of magnetic fluid was added to the dried film and the sample was incubated for 2 hours. The vesicle suspension was sonicated to clarity for 40 min in a sonicator. The resulting solution of magnetic vesicles was stored at 4°C.

RESULTS AND CONCLUSION: The vesicles with different concentration ratios of DOPE and DDAB were prepared at different temperatures and pH values. We found that the aqueous vesicle suspension with DOPE to DDAB ratio of 1:1 is very stable. With DOPE/DDAB (1:1, wt.%) as surfactant magneto-vesicles were synthesized using magnetite nanoparticles (D_m = 9 nm, Fig.1) as the cores.

From AFM measurements, the size distributions of vesicles and magneto-vesicles can be described by a log-normal function [4]. The average sizes of vesicles and magneto-vesicles are 316 nm and 311 nm, respectively.

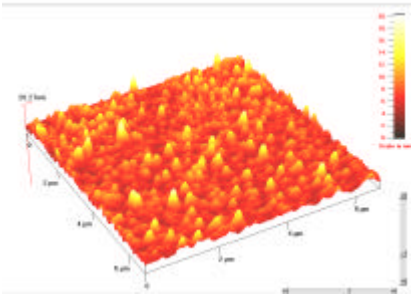

Fig. 1: AFM image of magnetic nanoparticles.

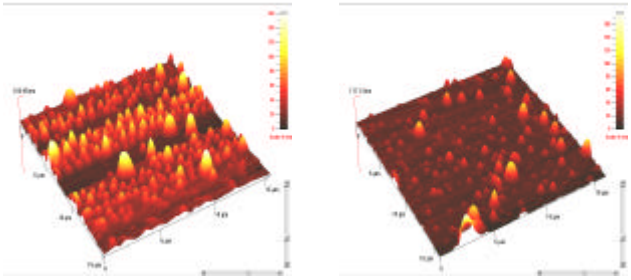

Fig. 2: AFM images of DOPE/DDAB (1:1, wt%) vesicles (left) and magneto-vesicles (right).

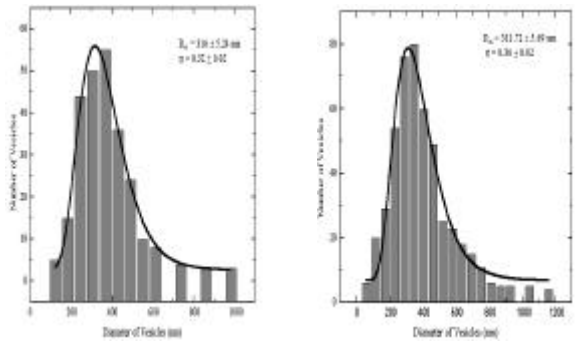

Fig. 3: Size distributions of DOPE/DDAB (1:1, wt%) vesicles (left) and magneto-vesicles(right).

REFERENCES: [1] C. Sangregorio, J.K. Wiemann, C.J. O'Connor, et al (1999) *J Appl Phys* **85**(8): 5699-5701. [2]A.A. Kuznetsov, V.I.Filippov, R.N. Alyautdin, et al (2001) *J Magn Magn Mater* **225**:95-100. [3] M.Shinkai, M.Yanase, M.Suzuki, et al (1999) *J Magn Magn Mater* **194**:176-184. [4] R.A. Buhrman, C.G. Granqvist (1976) *J Appl Phys* **47**:2200-2219.

ACKNOWLEDGEMENTS: This work is partially supported by a US NSF NIRT grant.

SYNTHESIS AND CHARACTERIZATION OF MAGNETITE NANOPARTICLES EMBEDDED IN COPOLYMER MICROSPHERES

P.C. Morais [1], V.K. Garg [1], A.C. Oliveira [1], R.B. Azevedo [2], D. Rabelo [2] & E.C.D. Lima [3]

[1] *Universidade de Brasília, Instituto de Física, Núcleo de Física Aplicada, 70919-970 Brasília-DF, Brazil*

[2] *Universidade de Brasília, Instituto de Ciências Biológicas, Departamento de Genética e Morfologia, 70910-900 Brasília-DF, Brazil*

[3] *Universidade Federal de Goiás, Instituto de Química, 74001-970 Goiânia-GO, Brazil*

INTRODUCTION: In recent years the design and synthesis of nanometer-scaled magnetic structures have been the focus of intense investigation, particularly because the unusual or enhanced properties of such materials [1]. As far as the size and size-dispersity control is concerned, the tendency of isolated magnetic nanostructures to aggregate into bigger clusters during the synthesis process, driven by particle-particle interaction (e.g. magnetic dipole and Van der Waals) and/or reduction in energy associated with the high surface-to-volume ratio, has represented a critical obstacle. Iron oxide-based nanoparticles can be conveniently synthesized and maintained as stable single units using a variety of polymer templates, though it is quite clear that the chemical route, the nature of the polymer matrix, and the polymer morphology strongly affect the composition of the end product.

Magnetic polymer-based spheres have lately been considered as an important material in the biotechnology industry, for cell separation [2] and DNA extraction [3] for example. In particular, mesoporous polymeric templates can be produced as micron-sized spheres that allow *in-situ* chemical synthesis of nanosized ferrite particles with adjustable magnetic properties and mass density [4]. Both parameters are extremely important in the composite engineering for targeting of tumor cells, among others [5]. The fine-tuning of the physical parameters, e.g. net magnetic moment and density of the composite, can be realized through several cycles (*N*) of chemical synthesis. Once the composite spheres are dispersed in the blood and bound to a particular biological structure the resulting complex can be efficiently trapped in a high magnetic field gradient device for later removal. In the present study Mössbauer spectroscopy (MS) and transmission electron microscopy (TEM) were used to characterize the iron oxide-based nanoparticles precipitated in mesoporous styrene-divinylbenzene (Sty-DVB) microspheres.

METHODS: Six composite samples were chemically prepared using the Sty-DVB template immersed in $FeSO_4$ aqueous solution (bath solution) at 30 mmol/L. The Sty-DVB copolymer used was synthesized by suspension polymerization in the presence of inert diluents. The porous structure in the dry polymer template presents an average pore diameter of about 13 nm. The swelling behavior of the copolymer in heptane indicates the presence of collapsed pores, which could not be detected through mercury intrusion porosimetry and surface area measurements. The porous structure in the swollen state can be considered to be preferentially mesoporous due the expansion of the collapsed pores. The sulfonated copolymer presented ion exchange capacity (dry resin) of about 4.8 mmol H^+/g. The polymeric matrix was characterized through the apparent density (0.44 g/cm^3), fixed pore volume (0.44 cm^3/g), surface area (140 m^2/g), toluene regain (1.52 cm^3/g), heptane regain (1.24 cm^3/g), % volume swelling in toluene (100 %), and % volume swelling in heptane (58 %).

Each chemical cycle in the composite synthesis follows a four step experimental procedure. Firstly, the mixture was first stirred for 1 hour at room temperature. Second, the iron-loaded polymer particles were separated by filtration and washed thoroughly with water until no ferrous ion was detected in the eluent. Third, the oxidation of the ferrous ion was performed in alkaline medium following the standard recipe used in the synthesis of magnetite micro-crystals from ferrous ion in aqueous solution. Fourth, the obtained black composite was filtered, washed with water until the pH of the eluent was neutral, and dried at 60 ◦C. The described procedure was performed up to six times in order to obtain composite samples with increasing amount of magnetic material.

Transmission electron micrographs were obtained from the dried composite samples using a Jeol 100CXII instrument. Typically, 3 mg of the composite sample was frozen in liquid nitrogen and ground to fine powder. The powder obtained was dispersed in 3 ml of n-propanol and droplets of the

dispersion were placed on top of the copper grid coated with palladium and carbon films. Transmission Mössbauer spectra were recorded at 77 and 300 K, using a MCA (256 channels) and a Wissel constant acceleration transducer coupled to a 50 mCi ^{57}Co/Rh source. Each plastic sample holder (1.7 cm diameter) contained 80 mg of uniformly distributed and pressed sample. The spectra were least square fitted using two sextets.

RESULTS & DISCUSSION: Typical particle size histograms obtained from the TEM micrographs are shown in Figure 1, for N = 1, 3, and 5 chemical cycle composite samples. The histograms were curve-fitted using the log-normal distribution function:

$$P(D) = \frac{\exp(-2\sigma^2)}{D_m \sigma \sqrt{2\pi}} \exp\{-\ln^2(D/D_m)/2\sigma^2\}, \quad (1)$$

where D_m is the mean particle diameter and σ is the standard deviation.

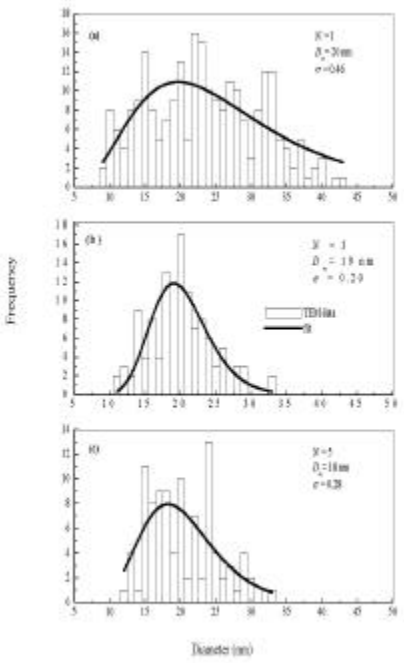

Fig. 1: Typical particle size histograms (TEM data) of magnetite nanoparticles, for (a) N = 1, (b) N = 3, and (c) N = 5. The solid lines represent the best fit of the data using the log normal distribution function.

Whereas the mean particle diameter slightly decreases from 20 nm (1 cycle sample) down to 17 nm (6 cycle sample) the standard deviation shows a considerable decrease from 0.46 $\pm$ 0.06 (1 cycle sample) to 0.23 $\pm$ 0.02 (6 cycle sample). At the same time, the amount of iron incorporation in the polymeric template, increases from 8.25 % (1 cycle sample) up to 29.2 % (6 cycle sample), as obtained from atomic absorption measurements (data not shown). The experimental data suggest that both template morphology and bath solution concentration determine the mean particle diameter, whereas cycling narrows the particle size distribution and increases mass incorporation.

Typical Mössbauer spectra (N = 1, 3, and 5) of the synthesized black composite samples, at 77 and 300 K, are shown in Figures 2(a) and 2(b), respectively. Note that the Mössbauer spectra were curve-fitted using two sextets, as expected from bulk magnetite crystals, at 77 and 300 K. Though the curve fitting procedure is quite good for all spectra analyzed, the presence of a very small fraction of a paramagnetic phase may change the fitted values of the isomer shift with respect to the standard values.

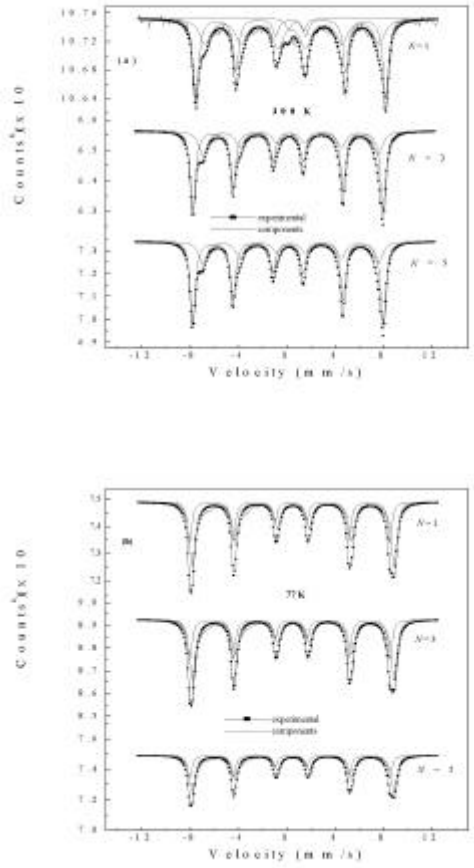

Fig. 2: Typical Mössbauer spectra of magnetic nanoparticles for (a) N = 1, 3, and 5, at room temperature and (b) N = 1, 3, and 5, at liquid nitrogen temperature.

Table 1 shows the Mössbauer parameters (average values), obtained from all the recorded Mössbauer

spectra, as well as the corresponding standard Mössbauer parameters from bulk magnetite [6].

Table 1. The average values of the internal fields (H ± 3kOe) obtained from the composite samples (N = 1 through 6) and the standard magnetite data, at 77 and 300 K.

	T(K)	*H* (kOe) [Fe^{3+}(Tet)]	*H* (kOe) [$Fe^{2+/3+}$(Oct)]
Composite	77	522	509
Standard	77	514	499
Composite	300	484	458
Standard	300	493	460

CONCLUSIONS: Magnetite (Fe_3O_4) nanoparticles have been synthesized by alkaline oxidation in mesoporous sulfonated styrene-divinylbenzene copolymer template, and several iron-loading treatments of the polymer matrix to increase the amount of iron magnetic material have been used. The synthesized nanoparticles have been characterized by Mössbauer spectroscopy and transmission electron microscopy as magnetite.

REFERENCES: [1]Fanyao Qu and P.C. Morais (2000) *J. Phys. Chem. B* **104**:5232-5236. [2]J. Chatterjee, Y. Haik, and C.-J. Chen (2001) *J. Magn. Magn. Mater.* **225**:21-29. [3]J. Oster, J. Parker, and L. Brassard (2001) *J. Magn. Magn. Mater.* **225**:145-150. [4]D. Rabelo, E.C.D. Lima, A.C. Reis, W.C. Nunes, M.A. Novak, and P.C. Morais (2001) *Nano Lett.* **1**:105-108. [5]S. Sieben, C. Bergemann, A. Lübbe, B. Brockmann, and D. Reschelieit (2001) *J. Magn. Magn. Mater.* **225**:175-179. [6]E. Kuzmann, S. Nagy, A. Vértes, T.G. Weiszburg, and V.K. Garg (1998) *Geological and mineralogical applications of Mössbauer spectroscopy* in *Nuclear Methods in Mineralogy and Geology: Techniques and Applications*. (eds A. Vertes, S. Nagy, and K. Süvegh) Plenum Press, pp. 285-376.

ACKNOWLEDGEMENTS: This work was supported by the Brazilian agencies CTPETRO, and CNPq.

ON ESTIMATION OF A CHARACTERISTIC SIZE OF AGGREGATES IN SUSPENSION OF NANODISPERSED MAGNETICS FROM THE DECAY CURVES OF TRANSMITTED LIGHT INTENSITY WHEN REMOVING THE APPLIED MAGNETIC FIELD

O.M. Mykhaylyk[1], A.K. Dudchenko[1], Yu.V. Pridatchenko[2] & E.Yu. Taran[2]

[1]*Inst. Appl. Problems Physics & Biophysics, PO Box 355, 252001 Kyiv, Ukraine*

[2]*Taras Schevchenko National Kyiv Univ, Kyiv, Ukraine*

INTRODUCTION: Suspensions of magnetic particles are always aggregated [1, 2] and become optically anisotropic when subjected to a magnetic field; in particular, an increase (or sometimes decrease) in light transmission parallel to the applied magnetic field is observed. The large magnetically-induced optical anisotropies can be explained by the orientation or aggregation into the strings of large aggregates that are already present in the absence of the magnetic field [1]. Microscopically-visible strings of the order of 1μm have been reported [3]. The strings can be several particles (chains) thick [1]. Estimation of the characteristic size of aggregates (effective magnetic moment of aggregates or strings) in suspension is rather important for magnetic carriers for scientific and clinical applications. The aim of the work is to estimate the characteristic size of aggregates in suspensions of nanodisperse magnetite and iron from decay curves of transmitted light intensity when removing the applied magnetic field.

METHODS: Experiments were done with suspensions of magnetite and stabilized metal iron in physiological solution (0.05 g/l, average particles core size of 25 nm and 80 nm, respectively). Electron micrographs are given in *Fig. 1*.

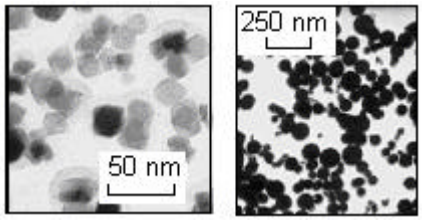

Fig. 1: Electron micrographs of nanodispersed magnetite (left) and iron (right) samples.

Preparation and characterization of the materials were published elsewhere [4]. Magnetic field H=20 Oe was applied along the optical axis of the red light 2 minutes after sonication of suspensions and removed after approaching the steady state. Light transmission decay curves (represented in *Fig. 2*, curve a) were registered and analyzed.

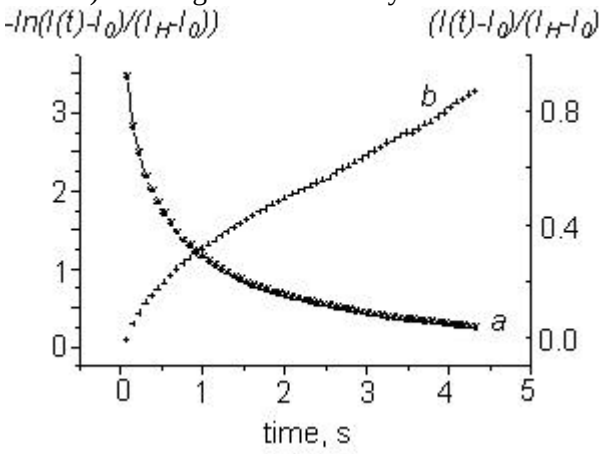

Fig. 2: Relative alteration of transmitted light intensity (a) and the same value in logarithmic coordinates (b) as a function of time after removal of the external magnetic field H=20 *Oe for a suspension of nanodispersed iron with mean particles size of about 80 nm, T=300 K.* I_H *and* I_0 *are transmitted light intensities in the magnetic field* H *applied along the optical axis and at* H=0*, respectively.*

RESULTS AND DISCUSSION: We are treating the medium as a diluted suspension of magnetic particle aggregates in Newtonian fluid. Aggregates of magnetic particles are considered as rigid bars with zero buoyancy. We assume that they are sufficiently large to interact with dispersion medium as hydrodynamic bodies, that they are sufficiently small for their orientation to be determined, and that by rotational Brownian movement they possess a temporary magnetic moment p and are oriented in an applied magnetic field H. To derive the equations, which determine the orientation of suspended aggregates, we have made use of the structural approach common for rheology of similar systems with no regard for hydrodynamic and magnetic interaction between strings.

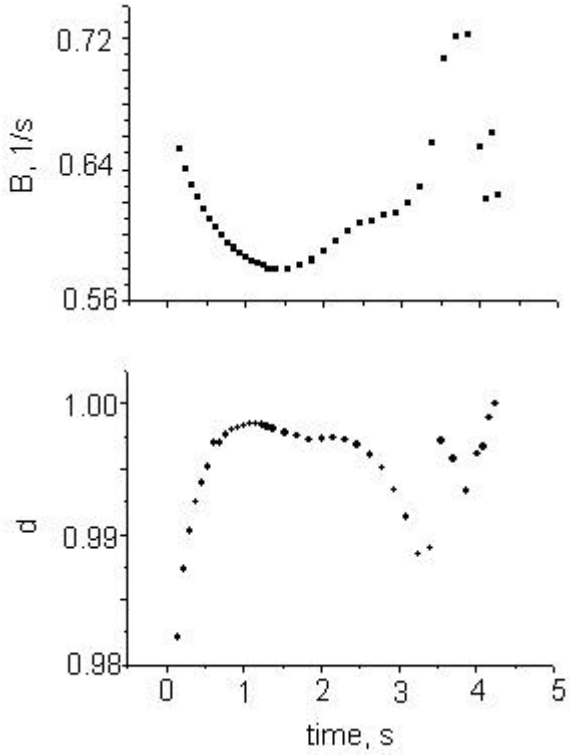

Fig. 3. The slope (B) of the line b from Fig. 2 and the coefficient of determination (d) as a function of the starting time point for regression analysis.

Taking into account hydrodynamic forces, rotational Brownian movement and moment of forces of the external magnetic field, rotational movement of aggregates is defined by the following equation

$$\dot{n}_i = D_r a\,(h_i - h_l n_l n_i) - D_r \frac{\P \ln F}{\P n_i}. \qquad (1)$$

Here $a = pH / kT$, where p is the aggregate magnetic moment, H is the magnetic field, k is the Boltzmann constant, T is the temperature, n_i is the unit vector directed along the symmetry axis of a suspended aggregate, h_i is the unit vector directed along the external magnetic field, F is the distribution function of angular positions of aggregate symmetry axes of aggregates, $D_r = kT / f_p$ is the rotational Brownian diffusion coefficient of aggregates, f_p is the rotational friction coefficient of aggregates with respect to an axis perpendicular to the main axis of an aggregate, $\dot{n}_i$ is the local time derivative of n_i.

The distribution function F in the phase space of n_i coordinates satisfies the equation:

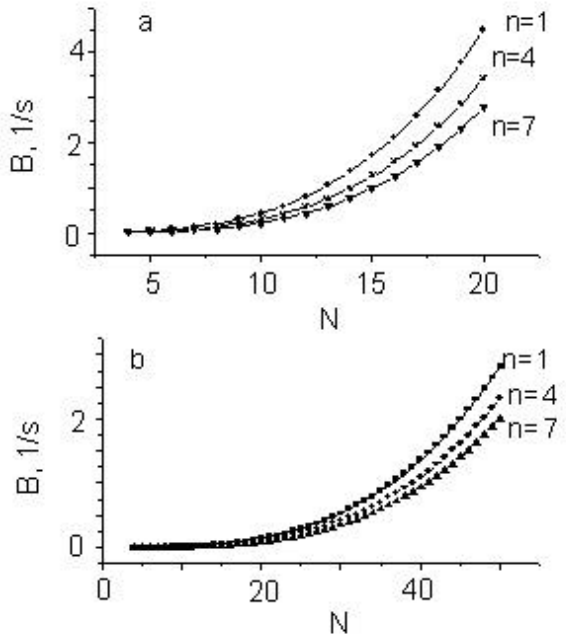

Fig. 4. Calculated from Eq. (6), the maximum rotation relaxation time of magnetic particle aggregates (t_1=1/B*) after removing of the external magnetic field as a function of average number of particles in a chain* N *depending upon the number of chains (n) in a "string" for particles with mean outer diameters of 80 nm (a) and 25 nm (B), in water medium, T=300 K;* q *was taken to be* N, N/2 *and* N/3 *for n=1, n=4 and n=7, respectively.*

$$\frac{\P F}{\P t} + \frac{\P}{\P t}(F\dot{n}_i) = 0, \qquad (2)$$

where t is the time.

For coinciding directions of the steady magnetic field and the light beam realized in the experiment, equation (2) with account for (1) can be represented as follows:

$$\frac{\P F}{\P t} = \frac{D_r}{\sin q}\frac{\P}{\P q}(\sin q \frac{\P F}{\P q} + a \sin^2 qF), \qquad (3)$$

where q is the angle between the external magnetic field and n_i vector. In the external magnetic field the orientation of aggregates is characterized by the stationary distribution function

$$F(q) = \frac{1}{4p}\frac{a}{sha} e^{a \cos q}$$

Table 1.

Sample	t_s, s	$B=\frac{1}{t_1}$, 1/s	d	N(n=1)	N(n=4)	N(n=7)
M3	1.0	0.5545	0.987	44	46	49
S7	1.38	0.579	0.998	15	17	18

as the solution of Eq. (3) at $\frac{\partial F}{\partial q}=0$. Upon removing the field, a reorientation of aggregates occurs, and at $a \ll 1$, the distribution function F is defined by $\frac{\partial F}{\partial q}\neq 0$ as

$$F(q,t)=\frac{1}{4p}[1+a\cos q e^{-\frac{t}{t_1}}] \qquad (4)$$

where

$$t_1=\frac{1}{2D_r} \qquad (5)$$

is the characteristic decay time of the orientation of aggregates.

When a is large, higher terms of the expansion of F in a containing an infinite series of relaxation times

$t_i=\frac{1}{i(i+1)D_r}$, $i\geq 1$, should be taken into account.

As $t_1 > t_i$ $(i\geq 2)$, formula (4) holds true at t and a sufficiently large. The existence of a long linear region at large t on experimental curves plotted in logarithmic coordinates (Fig. 2, curve b) supports this treatment and enables one to estimate the maximum relaxation time t_1, and hence, geometric parameters of an aggregate, taking into account the well-known expression for the rotational diffusion coefficient of rigid bars:

$$D_r=kT\frac{3\ln(2q)-0.8}{phL^3}, \qquad (6)$$

where h is the dynamic coefficient of liquid viscosity, L is aggregate length and q is the aggregate length/diameter ratio.

To choose a linear region of the curve (Fig.2, curve b) for the calculation of t_1, the dependence of the coefficient of determination d and the slope $B=\frac{1}{t_1}$ on the starting time point t_s within the linear regression model, were analyzed. Here, $d=1-\frac{S_r^2}{S^2}$, where S_r^2 is the sum of squared differences between the y-values estimated for points and their actual values, and S^2 is the total sum of squares (the sum of squared differences between the actual y-values and the average of the y-values). We note that t_s was chosen at the maximum of the determination coefficient (Fig. 3).

Table 1 shows obtained values of t_s, t_1, d and the corresponding aggregate lengths for various numbers of chains in a string (Fig. 4) for two examined samples of magnetic nanoparticles. Aggregates were estimated to be 44, 46 and 49 particles in length (1.1, 1.15 and 1.33μm) for magnetite and 15, 17 and 18 particles in length (1.1, 1.15 and 1.33μm) for iron, assuming strings of 1, 4 and 7 chains, respectively.

CONCLUSIONS: The physical model and equations derived for the distribution function of angular positions of the symmetry axes of aggregates enable one to estimate the rotational Brownian diffusion coefficient and, hence, the characteristic size of aggregates in suspensions of magnetic nanoparticles from decay curves of the transmitted light intensity when removing the applied magnetic field.

REFERENCES: [1]P.S. Scholten and J.A.P.Felius (1990) *J Magn Magn Mater* **85**: 107-113. [2]D.A. Krueger (1980) *IEEE Trans Magn* **Mag-16**: 251-253. [3]C.F.Hayes (1975) *J Colloid Interface Sci* **52**: 239-243. [4]O.M. Mykhaylyk, O. N. Razumov, A.K.Dudchenko et al (1997) *Use of ESR, Mössbauer spectroscopy and SQUID-magnetometry for the characterization of magnetic nanoparticles on the base of metal iron and its implications in vivo* in Scientific and Clinical Applications of Magnetic Carriers (Eds. U. Häfeli, W. Schütt, J. Teller and M. Zborowski) Plenum Press, pp 277-298.

European Cells and Materials Vol. 3. Suppl. 2, 2002 (pages 179-180) ISSN 1473-2262

APPLICATION OF MAGNETIC DEVICES AND SORBENTS IN GASTROINTESTINAL SURGERY

A.A. Kuznetsov[1], N.N. Kanshin[2], L.A.Piruzyan[3], V.M. Chikov[1], G.S. Nechitailo[1], & O.A. Kuznetsov[1,4]

[1] Institute of Biochemical Physics, Russian Academy of Sciences, 117977 Moscow, Russia; [2] N.V.Sclifosovsky Scientific Research Institute of Emergency Medicine, Moscow, Russia; [3] Center for Theoretical Problems of Physical and Chemical Pharmacology, Russian Academy of Sciences, Moscow, Russia; [4] University of Louisiana at Lafayette, LA 70504-2451, USA

INTRODUCTION: We have been working on application of magnetomechanical forces in abdominal surgery since 1971 [1-7] and continue our work in this area.
Significant difficulties in gastrointestinal surgery are caused by non-sterility of the inner surfaces of gastrointestinal tract organs and their contents. The common task during such surgery is formation of anastomoses: joining incised hollow organs while preserving connectivity of their internal cavities. Such connections should be hermetic and the joined organs should touch each other only with their sterile serous (outer) surfaces. The situation is complicated even further by the relatively thin and mechanically weak walls of many of the organs. Imperfect connections lead to numerous complications: inflammations, non-hermeticity, impassibility and peritonitis. Several technologies of seamless connections of hollow organs have been developed over the last decades to overcome these difficulties, including different glues and various mechanical devices, which connect the tissue using elastic forces, forming so-called compressing anastomoses. Each of these methods has advantages and disadvantages, but the problem of flimsiness of such joints remains to be solved because of difficulties in providing hermeticity, sterility of joints and matching of serous membranes.

MATERIAL AND METHODS: We solve these problems using magnetic devices based on permanent magnets. The principle scheme of the operation is illustrated in Fig. 1. The typically ring-shaped devices are inserted inside the hollow organs being connected. The magnetic elements are mutually attracted to each other, squeezing tissues between them. A hermetic seal is formed, and the passibility of the gastrointestinal tract is maintained. The patient can eat immediately after operation.
Tissues squeezed between the elements necrose in 7-10 days and inoculation of serous membranes of the jointed organs occurs along the outer (external) perimeter of the elements. After necrosis of the squeezed tissues the pressing elements are separated and excreted from the organism through the natural way.

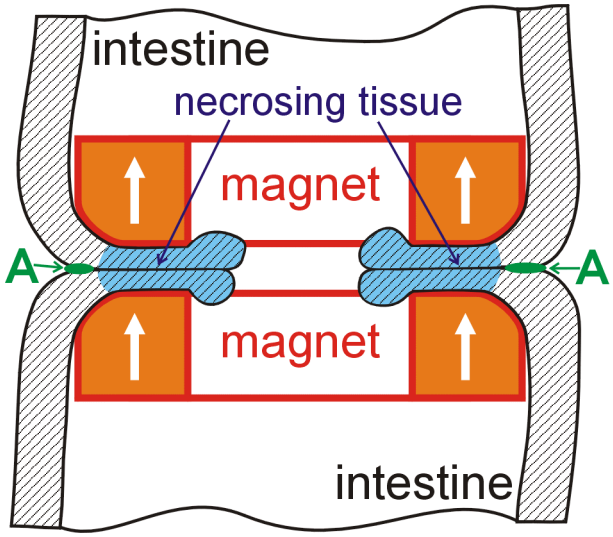

*Fig. 1. Scheme of joining hollow organs using ring-shaped magnetic devices. **A** indicates the zone of tissue growth and anastomosis formation. White arrows indicate magnetization direction.*

We designed and tested many types of pressing magnetic elements (Fig. 2): rigid and elastic, of different sizes and shapes (rings, prisms, rhombi), with special arrangements for tissue fixation, etc. Typically multi-polar magnetic systems were used, since they can be made elastic and provide sufficient force with minimal size and weight. We used SmCo and NdFeB permanent magnets, imbedded in a silicone plastic to provide biocompatibility and elasticity. Surgical techniques of the magnetic device applications for different types of operations were also developed.

52 mongrel dogs were used in pre-clinical trials. Two to four anastomoses were performed on each of the animals. Kinetics of tissue compression between the magnetic elements and the following necrosis, as well as tissue regeneration and joint formation, was studied. Histological studies were also performed.
Clinical trials of the magnetic devices were performed on more than 100 patients at the N.V.Sclifosovsky Moscow Scientific Research Institute of Emergency Medicine.

Fig. 2. Magnetic devices used for forming anastamoses of hollow organs of abdominal cavity. Scale is in centimeters.

RESULTS AND DISCUSSION: Both pre-clinical and clinical data indicate good quality of the anastomoses formed by the magnetic devices and the ease of use of the later.

The animal experiments have shown, that necrosis and rejection of the tissues squeezed by the magnets is not a mechanical amputation, but a complex biophysical process. The pressed tissue loses blood supply, and the oxygen-starved cells are partially destroyed by the pressure and die of both hypoxia and mechanical damage. The products of cell destruction moving from the zone of pressure stimulate the active rejection of the dead tissues by the organism (including immune reactions). The more intensive is the pressing force, the faster the rejection. It was found, that tissue regeneration occurs mostly in the zone of moderate pressure at the periphery of the magnetic devices. A mathematical model of the first stages of the pressing process was suggested. Its predictions correlated well with experimental data.

Detailed morphological and histological investigations demonstrated the absence of any harmful influence of the magnetic field on the joined tissues and organs.
The presence of high-gradient magnetic field at the site of operation allows the organization of a targeted drug delivery, either through the bloodstream (this could be beneficial for antibiotics, for example) or through the gastrointestinal tract. We conducted successful experiments of targeted delivery of catalases (for faster dead tissue destruction) conjugated with ferro-carbon particles through the gastrointestinal tract.

Clinical trials of the magnetic devices were successfully performed at the N.V. Sclifosovsky Moscow Scientific Research Institute of Emergency Medicine during operations on various parts of the human gastrointestinal tract, including gullet, esophagus, stomach, duodenum, bile ducts, large and small intestine, and rectum. Magnetic elements were also successfully applied in urology. Overall more than 100 patients were treated. All operations were successful, with low occurrence of mild after-operation complications. A high quality of anastomoses was observed: an absence of scars or narrow spots and a low occurrence of inflammations. After separation of the magnetic devices no artificial objects (threads, stitches, etc.) remained in the patients' organism. Surgeons easily learned the technique and found it to be convenient. Application of the magnetic devices reduced the duration of the operation and lowered the requirements for the surgeon qualification. All these factors increase the reliability of the operation and reduce the risk of complications.

REFERENCES.

[1]A.A. Kuznetsov, N.N. Kanshin & L.A. Piruzyan (1971) Method of hollow organs tissue connection. USSR patent # 2111068/28-13 3/9/1971. [2]N.N. Kanshin, L.A. Piruzyan & A.A. Kuznetsov (1973) Method of hollow organs tissue connection. USSR patent #211068/28-13 1/15/1973. [3]N.N. Kanshin, L.A. Piruzyan, A.A. Kuznetsov, V.M Gleizer & A.A. Hutoryansky (1975) Device for tissue connection. USSR patent #873506 3/19/1975. [4]A.A. Kuznetsov, N.N. Kanshin & N.K. Permyakov (1975) Studies of the tissue compression process. (in Russian) *Archive of Pathology* **8**: 37-42. [5]A.A. Kuznetsov, L.A. Piruzyan, R.A. Djalagonia & N.N. Kanshin (1977) Method of hollow organs tissue connection. USSR patent #2505398 12/11/1977. [6]L.A. Piruzyan, N.N. Kanshin, N.K.Permyakov, A.A. Kuznetsov, R.A. Djalagonia & V.M. Chikov (1979) On the tendencies of the processes of tissue compression and regeneration during the formation of 'seamless' anastomoses of hollow organs of the gastro-intestinal tract. (in Russian) *Izvestia AN SSSR, Biology* **1**: 13-17. [7]N.N. Kanshin, A.A. Kuznetsov, V.A. Lipatov, A.I. Hamidov & I.A. Gus'kov (1983) Device for forming anastomoses of hollow organs. USSR patent #1142926 4/8/1983.

MAGNETIC NANOSENSORS FOR DNA ANALYSIS

J. Manuel Perez, L. Josephson, & R. Weissleder

Center for Molecular Imaging Research, MGH-Harvard Medical School, 149 13th Street, Boston, MA 02129 USA

INTRODUCTION: Sensitive and cost-effective biosensors are required for the high throughput detection of DNA in un-modified biological samples and potentially even *in vivo*. To facilitate these studies, we have developed biocompatible magnetic nanoparticles capable of detecting specific DNA sequences upon structured self-assembly of the disperse nanoparticles into a stable assembly (clusters). This target-induced assembly occurs with a concomitant change in the proton relaxivity of neighboring water molecules, rendering these nanoparticles as magnetic nanoswitches capable of sensing DNA as a function of changes in water relaxivity. We have shown that these magnetic nanoparticles can be used to read out complementary DNA sequences and that the resulting changes in water relaxivity can be detected by NMR. The developed system could be useful as generic biosensors in a variety of other applications such as affinity ligand determination for rapid magnetic resonance imaging of arrays, as probes for magnetic force microscopy, and potentially, for *in vivo* imaging.

METHODS:

Synthesis of magnetic nanosensors. A dextran-coated iron oxide colloid was cross-linked with epichlorohydrin, and treated with ammonia to yield amino-derivitized, cross-linked iron oxide nanoparticles (CLIO-NH_2), as described [1]. These superparamagnetic nanoparticles were further derivatized with the cross-linking agent N-succinimidyl 3-(2-pyridyldithio)propionate (SPDP) to yield 2 pyridyldithiopropionate-derivitized CLIO (CLIO-SPDP). The CLIO-SPDP preparation had an iron concentration of 2.8 mg Fe/mL and an average of 48 pyridyl disulfide groups per particle. CLIO-SPDP (3 mg of Fe in 0.1 M phosphate buffer, pH 8.0) was reacted with the corresponding alkanethiolooligonucleotide (HS-$(CH_2)_6$-CGC-ATT-CAG-GAT or TCT-CAA-CTC-GTA-$(CH2)_3$-SH) and incubated overnight at room temperature. The next day the mixture was applied to a magnetic separation column (Miltenyi Biotec, Auburn, CA) equilibrated with 0.1 M phosphate buffer, pH 7.5, and the retained material was washed with phosphate buffer to remove any non-bound oligonucleotide. To recover the purified conjugate, the column is removed from the magnet and the material is eluted with buffer. The pooled volume, containing either CLIO-S-S-$(CH_2)_6$-CGC-ATT-

CAG-GAT (P1) or TCT-CAA-CTC-GTA-$(CH2)_3$-S-S-CLIO (P2), had an iron concentration of 0.58 mg of Fe/mL and 3 oligonucleotides per particle, on average [2] .

Synthesis of Target Oligonucleotides. The complementary (TAC-GAG-TTG-AGA-ATC-CTG-AAT-GCG), and non-complementary (ATG-CTA-AAT-GAC-GAC-TGC-CCA-CAT) oligonucleotides were synthesized on a 50-nmol scale using standard phosphoramidite chemistry. Stock solutions (10 OD per mL) were prepared by resuspending the sample in deionized water.

Relaxation Times (T2) Measurements. The T2 relaxation times of P1, P2 or P1/P2 (10 ug Fe/mL, each) were recorded at 0.47 Tesla (Bruker NMR Minispec, Billerica, MA). To study the effect that hybridization might have on the magnetic properties of these nanoparticles, the T2 was recorded before and after addition of complementary oligonucleotide target (390 ng) to a mixture of P1 and P2 (10 µg Fe/mL, total iron). Control experiments were performed using the half-complementary and non-complementary oligonucleotides.

Atomic force microscopy. An atomic force microscope (Dimension 3100, Digital Instrument) was used to collect images of P1/P2 with and without target DNA. The samples containing either equal amounts of each nanoparticle (P1/P2) alone or with target oligonucleotide were spotted on freshly cleaved mica at a total iron concentration of 10 µg/mL. This iron concentration is identical to the one used in relaxation time measurements. Images were taken by mounting the sample on a fluid cell containing a silicon nitride cantilever (20-40 nm tip size). Images were recorded using a tapping/lift mode.

RESULTS:

The magnetic nanoparticles used in these studies consist of a 3 nm superparamagnetic iron oxide core caged with a cross-linked and aminated dextran coating, resulting in 50-nm amine derivitized magnetic nanoparticles. We coupled an average of 3 oligonucleotides per particle with sequences complementary to a target DNA

sequence. The oligonucleotide sequences attached to the nanoparticles were chosen to recognize adjacent sequences on the DNA target. For each target sequence we made two particle populations (termed P1 and P2) recognizing adjacent sequences covering 24 base pairs (Figure 1). These nanoparticles were stable in solution without precipitation for months and were present in a monodisperse state when viewed by atomic force microscopy (Figure 1a). However, upon hybridization with a target sequence, the particles oligomerized into larger assemblies of approximately 200 nm (Figure 1b). Such oligomerization was not observed when the nanoparticles were incubated with a non-complementary oligonucleotide.

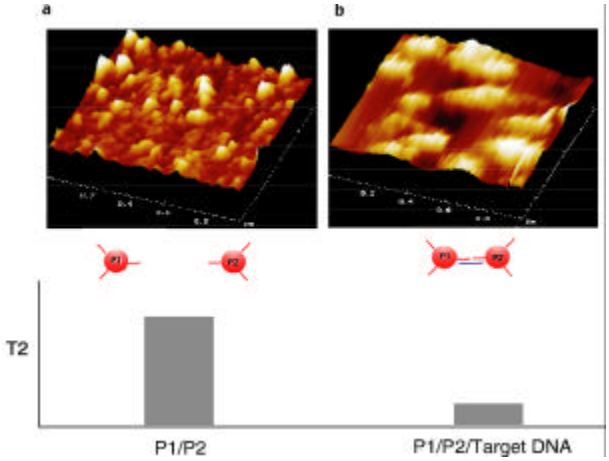

Fig. 1: Clustering of magnetic nanoparticles (P1 and P2) upon hybridization to a target DNA as shown by an AFM image of the particles before (a) and after (b) addition of target DNA. Such clustering correlates with a decrease in T2 relaxation times observed upon addition of target DNA.

These magnetic nanoparticles are potent enhancers of the spin-spin and spin-lattice relaxation process. Oligomerization of these nanoparticles (P1 and P2) into larger assemblies resulted in significant changes in the spin-spin relaxation times (T2) of neighboring water molecules as determined by relaxation measurements using a NMR bench top relaxometer. Within several minutes after oligonucleotide addition to a P1/P2 mixture (10 µg Fe/mL), the T2 relaxation times decreased by over 20 msec and remained constant. No visible precipitate formed at this concentration over a 24-hour observation period indicating that the clusters are stable in solution. When dithiothreitol (DTT) was added, T2 relaxation times returned to baseline values, as the hybridized oligonucleotides were cleaved from the nanoparticles and the particle nanoassembly was converted back to a monodisperse state. (Data not shown).

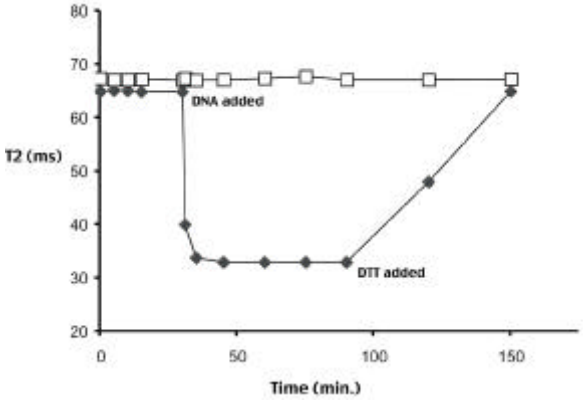

Figure 2: Time course of water T2 relaxation times for a mixture of P1 and P2 (10 µg/mL, total iron) with complementary (♦) and non-complementary target oligonucleotide (•).

CONCLUSION: We have shown that the hybridization-induced assembly of magnetic nanoparticles results in a decrease in the spin-spin relaxation time of neighboring water protons. Using a simple bench top NMR relaxometer (0.47T), we have observed a fast and reversible decrease in T2 relaxation time when complementary oligonucleotide is added to P1 and P2. Using this technique, we have been able to detect as low as 10 fmoles of DNA while lower amounts (0.5 fmoles) have been detected using a 1.5 T MR imager (data not shown). The developed magnetic nanosensors will have considerable applications in the detection of oligonucleotides (DNA/RNA) and studies are underway to expand the use of these nanoprobes to study other types of molecular interactions.

REFERENCES: [1]L. Josephson, C.H. Tung, A. Moore, R. Weissleder (1999) *Bioconjugate Chem.*, 10, 186-191. [2]L. Josephson J.M. Perez, R. Weissleder (2001) *Angew. Chemie Int. Ed. Engl.* **40**/**17**: 3204-3206.

ACKNOWLEDGEMENTS: This work was supported in part by a grant from the National Cancer Institute at NIH. JMP is a recipient of a fellowship from the National Cancer Institute.

INVESTIGATION OF FERROFLUIDS FOR BIOMEDICAL APPLICATION

A. Petri[1], M. Chastellain[1], H. Hofmann[1] and K. V. Rao[2]

[1] *Powder Technology Laboratory, DMX, EPFL, Lausanne, Switzerland*

[2] *Department of Material Science and Engineering, Tmfy-MSE, KTH, Stockholm, Sweden*

INTRODUCTION: The recent development of a large variety of ferrofluids has led to a range of new biomedical and diagnostic applications. A major drawback for many applications remains the lack of well-defined and well-characterized particles.

Growing attention is paid to iron oxide nanoparticles embedded in a polymer matrix. The matrix fulfills several demands: on the one hand it acts as a stabilizer, or even controls the particle formation, on the other hand it determines the physicochemical properties of the material, or allows surface functionalization.

In this study magnetic nanoparticles were prepared either in the presence of polyvinylic alcohol or were redispersed after precipitation and isolation of iron oxide powder. Aqueous suspensions of magnetic particles were obtained under identical reaction conditions by coprecipitation of Iron(III)- and Iron(II)-salts using aqueous ammonia. The suspensions were finally dialyzed against distilled water to approximately pH 6.5.

METHODS: For a better understanding of the colloidal and magnetic properties, an extensive characterization of the ferrofluids must be carried out. Three major points are discussed in this work: composition, size distribution, and first tests with human endothelial and synovial cells.

Composition: The iron oxide particles, with and without coating, were analyzed using XRD as well as FTIR. High resolution TEM measurements were also carried out to obtain qualitative information about the presence of an amorphous phase.

Size distribution: Different techniques were applied in order to obtain information about the iron oxide particle size distribution. Among these are X-ray diffraction peak broadening, TEM picture analysis, magnetic characterization techniques, photon correlation spectroscopy, or analytical ultracentrifugation. Although the obtained results are not always comparable, valuable information is provided by their interconnection.

Cell survival tests: In collaboration with the Tierspital Zuerich (Musculoskeletal Research Unit), first tests with human endothelial cells and synovial cells have been carried out. The cell survival after different time periods has been

compared for different concentrations as well as different methods of synthesis.

RESULTS: The main characterization results are summarized in the following.

Composition: XRD patterns show a large amorphous zone as well as typical peaks, which can be attributed to nanocrystalline magnetite (Fe_3O_4) or maghemite (γ-Fe_2O_3). After close examination the presence of two distinct phases is excluded, and the composition is thought to consist of a defective magnetite structure with a lattice parameter in between the one of bulk magnetite and bulk maghemite. FTIR investigations yield the same results.

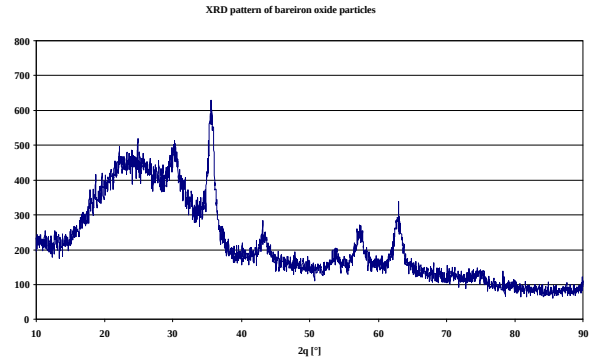

Fig. 1: XRD pattern of uncoated iron oxide nanoparicles showing a wide amorphous zone and typical inverse spinel peaks.

Size distribution: Typical monomodal distributions were found with an average size slightly smaller than 10nm.

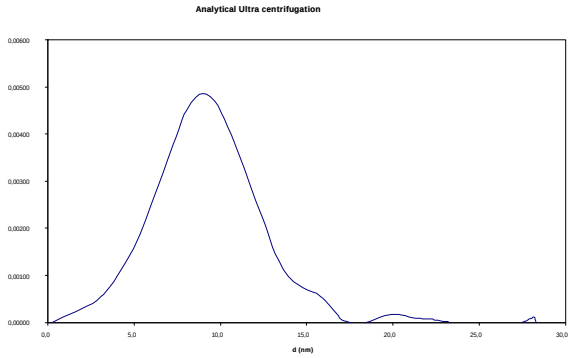

Fig. 2: AUC size distribution of bare iron oxide

The differences in size distribution determined by various methods show the necessity of combined size characterization for particles of that size. The comparison of the results also gives qualitative information about other properties such as the density or the refractive index. In particular, the spherical assumption for the particle shape proved to be satisfactory.

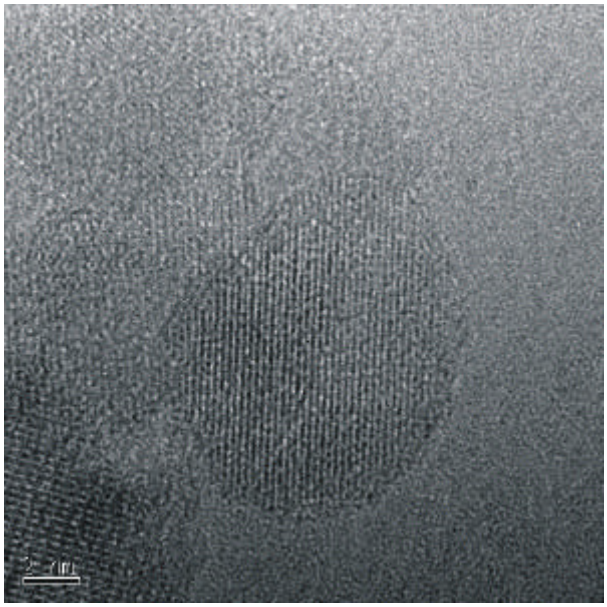

Fig. 3: High resolution TEM picture of crystalline iron oxide particles.

Cell survival tests: It could be shown that the concentration of the polymer as well as the ammonia concentration plays a very important role in the cell survival tests. As a first result it can be concluded that a minimum concentration of ammonia during the preparation of the polymer is essential for cell survival.

CONCLUSION: Ferrofluids were synthesized using PVA to ensure the colloidal stability at neutral pH. The composition, structure, and size distribution of these iron oxide particles were characterized, and the influence of the synthesis parameters was studied. After the first tests, the obtained ferrofluids seem to be non-toxic to human endothelial as well as synovial cells.

ACKNOWLEDGMENTS: This project is supported by EU - under the project NANOMAG - Magnetic Nanoparticles for Medical and Biological Diagnostics and Devices. We thank Tobias Neuberger from the Musculoskeletal Research Unit (MSRU)-Zürich for the cell analysis.

MAGNETOPHORETIC ANALYSIS OF CELLS AND MAGNETIC CARRIERS

J. Plavins

Institute of Physics, Latvian Academy of Sciences, Miera iela 32, Salaspils, LV-2169, Latvia

INTRODUCTION: Many areas in biotechnology and medicine related to cellular biology often require physical isolation of functionally-specific types of cells from biologically heterogeneous suspensions. Efficient use of magnetic methods is based, first of all, on sufficient differences in magnetic susceptibilities of biological cells and secondly, on the availability of reliable magnetic susceptibility values for all relevant cells present in a suspension. If natural magnetic properties of all blood cells except phagocytes are considered, magnetic separation methods, and in particular HGMS methods, have been successfully applied mostly to red blood cells by virtue of the presence of paramagnetic Fe atoms in intracellular hemoglobin. However, present development trends in separation technologies have highlighted massive interest in studying the differences which lie on the surface of cells by means of conjugating a wide variety of specific immunomagnetic labels to antibodies that target specific molecules on the surface of a cell, thus adding to the otherwise insufficient overall magnetic susceptibility of targeted population for subsequent magnetic enrichment or isolation using appropriate HGM or OGM separation devices [1]. To optimize the separation process it is necessary to determine magnetic susceptibility distributions of suspended populations of cells. Though more complicated than open gradient devices, the HGM systems are in a position to offer increased sensitivity and resolution for magnetic susceptibility measurements and fractionation due to the possibility of generating considerably higher magnetic field gradients.

METHODS: The magnetophoretic force $\boldsymbol{F_m}$ acting on a weakly magnetic cell or carrier in a gradient magnetic field is

$$\boldsymbol{F_m} = 1/2\ m_0\ VDc\tilde{N}\boldsymbol{H}^2 \qquad (1)$$

where m_0 is the magnetic permeability of vacuum, V is the volume of the suspended cell in question, Dc is the difference in magnetic susceptibility between the cell and the suspending medium and $\tilde{N}\boldsymbol{H}^2$ is the product of the intensity of a magnetic field $\boldsymbol{H}$ and its gradient $\boldsymbol{gradH}$ across the cell. The values of $\boldsymbol{H}$ $\boldsymbol{gradH}$ can be calculated for the ferromagnetic cylinder in a transversal magnetic field [2], and in the widely utilized directions along the magnetic field intensity $\boldsymbol{H}$ and

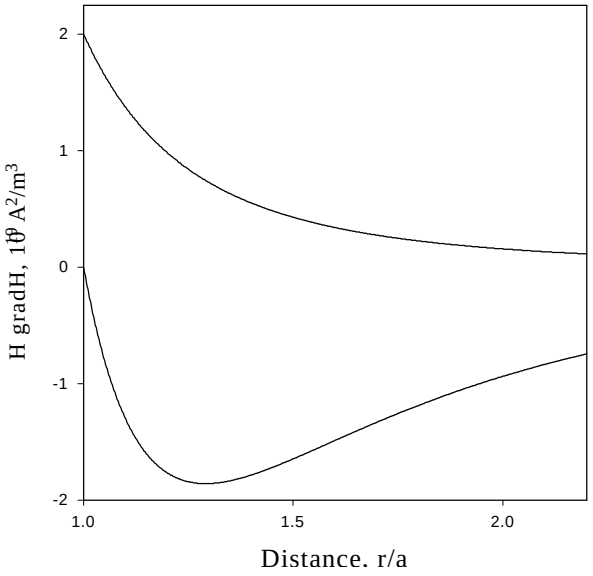

Fig. 1: H gradH as a function of the distance r/a from the surface of a magnetized stainless steel cylinder (diameter 50 mm, M_s = 1.51 x 10^5 A/m) in the direction of the field intensity $\boldsymbol{H}$ *(top curve; values are multiplied by the factor 1/10 for comparison) and perpendicular to* $\boldsymbol{H}$ *(bottom curve).*

perpendicular to $\boldsymbol{H}$, it is equal to

$$2KH^2a^2/r^3\ (Ka^2/r^2 \pm 1). \qquad (2)$$

K = 1 for $H \leq M_s/2$, whereas for $H > M_s/2$, $m_s \approx 1$ and $K \approx M_s/2H$; m_s and M_s refer to the magnetic permeability and magnetization of saturated material; a is the radius of the cylinder; and r defines the distance from the center of the cylinder. Fig.1 demonstrates that in the direction along the field F_m peaks on the surface of the cylinder; whereas, in the direction perpendicular to the magnetic field the absolute value of F_m on the surface is negligibly small and reaches the maximum value at r/a = 1.292, where it is still more than an order of magnitude smaller than the value on the surface in the direction of the field. Further away from the surface this difference levels out and drops to about 10% at r/a = 4.36.

RESULTS: The aforementioned negative gradient in the vicinity of a ferromagnetic cylinder in the direction perpendicular to a magnetic field is often used to exert a repulsive magnetophoretic force in order to perform magnetic fractionation in a continuous mode with respect to cells or carriers, which contain ferromagnetic colloidal particles or are labeled with immunomagnetic microspheres or colloidal particles. Thus, it is of practical interest to study the force profile in this direction in more detail. The trends shown in Fig.2 are calculated on the basis of expression (2).

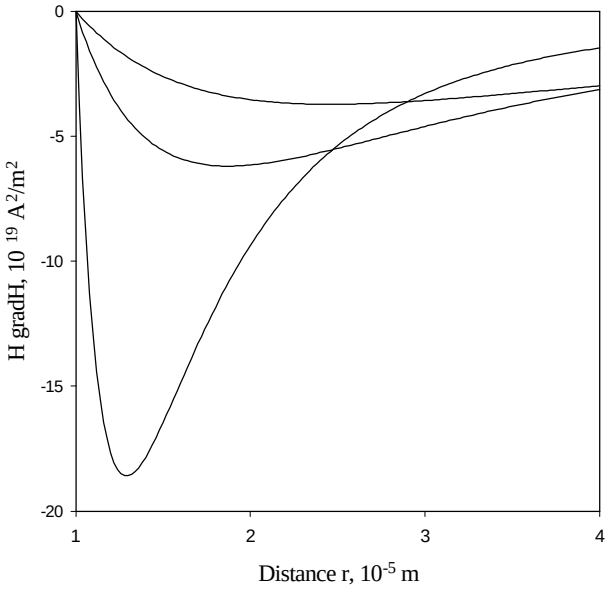

Fig. 2: Repulsive branch of H gradH as a function of the distance r from the surface of a ferromagnetic cylinder for different diameters of the cylinder (from bottom curve up: 20, 50 and 100m).

Presented curves, first of all, are indicative of marked differences in *H gradH* values in the close proximity of the peak value for different cylinder sizes. It is quite clear that the size and/or magnetic properties of cells or carriers are to be considered very carefully in order to attain an optimum balance between the intensity and the reach of the gradient of a magnetic field in the given direction.

The sensitivity of the magnetophoretic technique for measuring magnetic susceptibilities of suspended cells or carriers is considered under the assumption that the force of gravity may be neglected, and that the magnetophoretic force causing the displacement s_m of an individual cell or carrier during the act of measurement *Dt* is opposed solely by the viscous drag and thermal agitation. The translational Brownian displacements *d*, each of which is assumed to be random despite the presence of the gradient of a

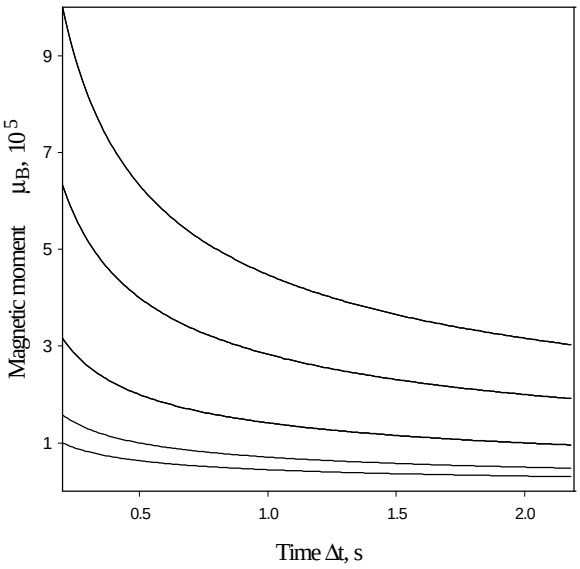

Fig. 3: The smallest difference in the magnetic moment inherent to an individual carrier/cell in Bohr magnetons m_B, the magnetophoretic technique will detect as a function of the characteristic duration of measurement Dt for different characteristic sizes of carriers/cells in the presence of HÑH = 8 x 10^{17} A^2/m^3 (from the bottom curve up: 20, 8, 2, 0.5, 0.2 mm).

magnetic field, is given by $d = D^{1/2}Dt^{1/2}$. *D* is the coefficient of translational diffusion expressed as $kT/6\pi h_0 R$, where Boltzmann constant k = 1.38 x 10^{-23} *J/K*, *T* is the absolute temperature, h_0 is the dynamic viscosity of the medium, and *R* is the radius of a carrier or cell. *D* ranges from 10^{-14} to 10^{-12} m^2/s for diameters of larger blood cells down to microcarriers still detectable by light microscopy. Assuming that for characteristic Reynolds numbers the opposing drag force equals $6\pi h_0 Rv$, where *v* is the velocity of a suspended cell/carrier, the magnetophoretic displacement, in accordance with (1), yields

$$s_m = 2m_0/9h_0\ R^2\ Dc\ ÑH^2\ Dt. \qquad (3)$$

From the above considerations it follows that the smallest difference in the relative magnetic susceptibility *Dc*, which in spite of thermal agitation in the suspending media is still detectable using a magnetophoretic technique, is proportional to parameter $Dt^{-1/2}\ R^{-5/2}$.

DISCUSSION & CONCLUSIONS: It is obvious that magnetophoretic analysis of cells and magnetic carriers using a HGM systems is a useful and

sensitive tool for measuring magnetic susceptibilities of different populations of natural or labeled biological cells. Moreover, HGM systems offer various configurations and profiles of attractive and repulsive forces, which can be efficiently applied for the batch - as well as for the continuous - mode of magnetic fractionation. By virtue of the fact that the values of each component of the product *H gradH* along the magnetophoretic trajectory keep increasing or decreasing depending upon the specific profile of the magnetophoretic force utilized in a device, this analytical tool has the potential of measuring magnetization values for different magnetic field intensities and building magnetization curves for individual cells and carriers which subsequently can be used for more in-depth analysis of magnetic properties [3]. Sizing of individual carriers combined with analyzing their respective magnetophoretic velocities makes it possible to plot the volumes of individual microspheres containing colloidal magnetic particles versus volume magnetic susceptibilities, and further application of correlation analysis to scatter plots allow the study of localization patterns of colloidal magnetic particles within an ensemble of carriers [4].

REFERENCES: [1]K.E.McCloskey, K.Comella, J.J.Chalmers, et al (2001) Biotechn.Bioeng. **75**:642-55. [2]S.J.Gill, C.P.Malone, M.Downing (1960) Rev.Sci.Instr. **31**: 1299-1303. [3]R.Ali-zade, J.Lukin, M.Maiorov, et al (1987) *Study of magnetic properties of magnetic colloid-filled polymer carriers* in 12th Riga Meeting on Magnetohydrodynamics (Russ), Zinatne Press, 91-94. [4]J.Plavins, M.Lauva, S.Krisko, et al (1985) Magnitn.Gidrodin. (Russ) 2: 130-132.

INTERACTION OF TRICYCLIC DRUGS WITH COPPER PHTHALOCYANINE DYE IMMOBILIZED ON MAGNETIC CARRIERS

M. Safarikova & I. Safarik

Laboratory of Biochemistry and Microbiology, Institute of Landscape Ecology, Na Sadkach 7, 370 05 Ceske Budejovice, Czech Republic

INTRODUCTION: During the last decades, the abuse of various drugs has increased considerably. This situation resulted in the development of different procedures for the detection and determination of the target drugs in various matrices, such as urine, serum, saliva, hair etc.

In many cases a two-stage process is generally employed for drugs of abuse testing in urine or other body fluids. At first, an appropriate screening test is used to differentiate between negative and positive samples. Various types of immunoassays can be used as screening tests. Alternatively, simple chromatographic procedures such as thin-layer chromatography (TLC) can be used for the same purpose. Results of positive screening tests are confirmed by a second technique such as gas or high-performance liquid chromatography with mass spectrometry detection (GC-MS, HPLC-MS).

The sensitivity of the instrumental techniques used for the confirmation and detailed analysis may not be sufficient to handle the samples directly, without preconcentration of the target compound(s). That's why the targets present in urine or other body fluids are usually extracted before chromatography is applied. There are two basic types of extraction procedures used namely liquid–liquid extraction (LLE) and solid-phase extraction (SPE). At present, considerable attention is being paid to SPE, mainly in the minicolumn format. Various types of adsorbents can be used, ranging from standard C18 silica to highly specific immunoaffinity adsorbents.

The separation and preconcentration of an analyte from large volumes of solution can take a lot of time using standard column SPE. Another procedure has also been developed for SPE, based on the use of magnetic or magnetizable adsorbents [1]. The procedure called magnetic solid-phase extraction (MSPE), based on the adsorption of the target analyte(s) on relatively small amount of magnetic specific adsorbent, enables to handle liter volumes of samples. In this procedure magnetic adsorbent is added to a solution or suspension containing the target analyte. The analyte is adsorbed on to the magnetic adsorbent and then the adsorbent with adsorbed analyte is recovered from the suspension using an appropriate magnetic separator. The analyte is consequently eluted from the recovered adsorbent and analyzed.

Tricyclic drugs (named after their chemical structure) form a very important group of drugs, having antidepressant, antihistaminic, antiparkinsonic etc. effects. The major effects of tricyclic antidepressants are sedation, anticholinergic effects and the ability to inhibit the uptake of noradrenaline and/or serotonin into presynaptic neurons. The major clinical use of the tricyclic antidepressants is the reduction of the symptoms of depression. Concern about these medications is a result of their extensive list of side effects and drug interactions, and also because of the ability of these medications to be misused, e.g. by a depressed and suicidal patient. Intoxication with tricyclic antidepressants, e.g., amitriptyline, may cause severe complications such as cardiac arrhythmia. Even under intensive care conditions, 2-3% of intoxicated patients still die.

Adsorbents having affinity for tricyclic drugs would be useful in the development of specific preconcentration procedures. Although tricyclic drugs usually have side chains in their molecules that could affect their planar molecular structure, specific interactions with copper phthalocyanine derivatives can be expected. Immobilized derivatives of copper phthalocyanines have found many applications in analytical, bioanalytical and environmental chemistry [2]. They are used for the separation and isolation of planar organic compounds, such as polyaromatic hydrocarbons and their derivatives with three or more fused aromatic rings [2] and triphenylmethane dyes [3]. The planar target compounds can form face-to-face hydrophobic complexes with copper phthalocyanine moiety, which has a large planar surface in the molecule.

In this work reactive copper phthalocyanine dye immobilized to silanized magnetite particles ("blue magnetite") was used as a specific magnetic adsorbent for the study of interactions with several tricyclic drugs.

METHODS: Blue magnetite (silanized magnetite particles with immobilized reactive copper phthalocyanine dye) was prepared as described recently (3). The tricyclic drugs amitriptyline (3-(10,11-dihydro-5*H*-dibenzo[a,d]cyclohepten-5-ylidene)-N,N-dimethyl-1-propanamine; for structure formula see Fig. 1), chlorprothixene (3-(2-chloro-9H-thioxanthen-9-ylidene)-N,N-dimethyl-1-propanamine), diethazine (Deparkin; N,N-diethyl-10H-phenothiazine-10-ethanamine), bisulepin (Dithiaden; N,N-dimethyl-3-thienol[2,3-c][2]benzo-thiepin-4(9H)-ylidenepropylamine hydrochloride; for structure formula see Fig. 1), prochlorperazine (2-chloro-10-[3-(4-methyl-1-piperazinyl)propyl]-10H-phenothiazine), thioridazine (10-[2-(1-methyl-2-piperidinyl)ethyl]-2-(methylthio)-10H-phenothiazine) and dothiepin (Prothiaden; 3-dibenzo[b,e]-thiepin-11(6H)-ylidene-N,N-dimethyl-1-propanamine) were obtained from Leciva, Czech Republic. The drug action is shown in Table 1.

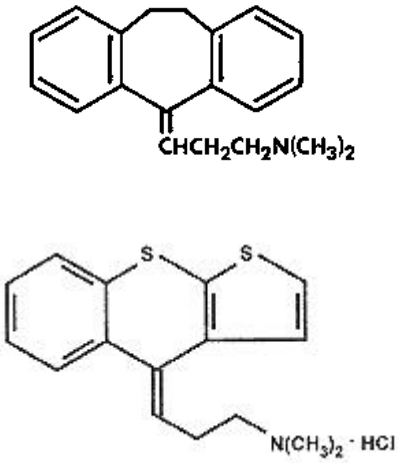

Fig. 1: Chemical structures of amitriptyline (top) and bisulepin (bottom).

The adsorption characteristics of the blue magnetite were studied in the following way. Suspensions of blue magnetite (200 μL; the settled volume of the adsorbent was 50 μL) in 15-mL test tubes were mixed with 8.8 mL of water. Then 0.01 - 1.0 mL portions of stock water solutions (1 mg/mL) of tricyclic drugs tested were added and the total volume of the suspension was made up to 10.0 mL with water. In the same manner water solutions of the tested drugs, used for the construction of the calibration curves, were prepared (instead of 200 μL of blue magnetite suspension 200 μL of water were used). The suspensions were mixed for 1 h at room temperature. Then the blue magnetite particles were separated from the suspension using a magnetic separator (MPC-1 or MPC-6, Dynal, Norway) and clear supernatants were used for the spectrophotometric measurement. The concentration of free (unbound) drug in the supernatant was determined from the calibration curve and the amount of bound drug was calculated by the difference.

The elution of the adsorbed drugs from the blue magnetite was performed using methanol as an elution agent.

RESULTS: Immobilization of reactive copper phthalocyanine dye to the silanized magnetite particles leads to the formation of the magnetically responsible affinity adsorbent with the specificity towards organic polyaromatic compounds with planar molecular structure. It was shown in preliminary experiments that the tested tricyclic drugs interacted with blue magnetite. The adsorption of tricyclic drugs to the adsorbent reached equilibrium in ca 30 min. In the following experiments the sorption of the tested drugs took place for 60 min.

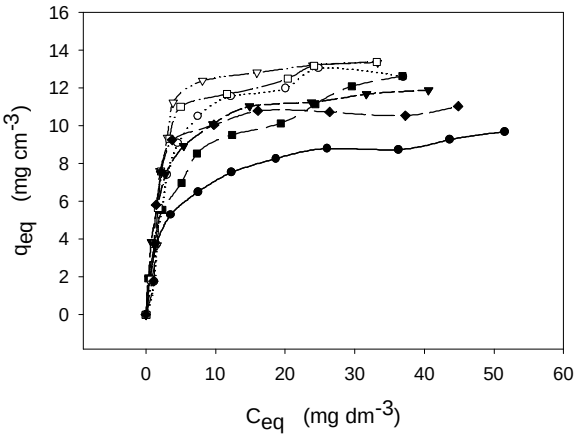

Fig. 2: Equilibrium adsorption isotherms of amitriptyline (●), bisulepin (○), chlorprothixene (▽), diethazine (■), dothiepin (▼), prochlorperazine (□) and thioridazine (◆) using blue magnetite as an adsorbent. C_{eq} – equilibrium liquid-phase concentration of the unadsorbed (free) drug (mg dm^{-3}); q_{eq} – equilibrium solid-phase concentration of the adsorbed drug (drug uptake) (mg cm^{-3}).

Equilibrium sorption isotherms for unbuffered water solutions are shown in Fig. 2. The tricyclic drugs adsorbed from water solution to immobilized phthalocyanine in a specific way. In a control

experiment when silanized magnetite was used as an adsorbent very low non-specific adsorption was observed.

The binding of tricyclic drugs to immobilized copper phthalocyanine was evaluated according to a system of classification of the solution adsorption isotherms described by Giles et al. (see Ref. 3). From Fig. 2 it can be seen that the isotherm follow the typical Langmuir adsorption pattern and belong to the class L2. It was also confirmed by the linear transformation of the data used for the construction of the adsorption isotherm (see Fig. 3).

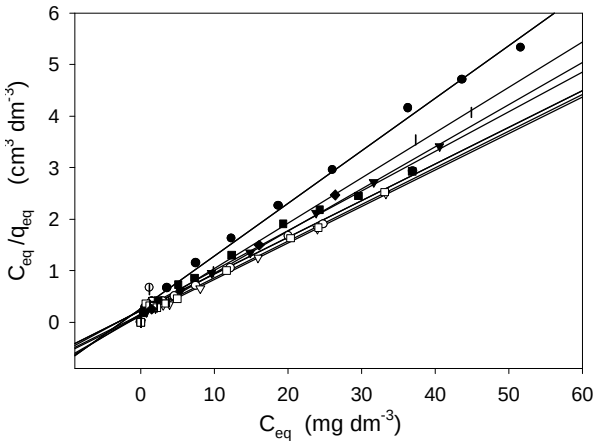

Fig. 3: Langmuir transformation of equilibrium adsorption isotherms for tricyclic drugs. The symbols and legends are the same as in Fig. 2.

Maximum adsorption capacities Q were calculated for all the drugs tested, using the linearized form of the Langmuir isotherm:

$$C_{eq} / q_{eq} = 1 / b.Q + C_{eq} / Q \qquad (1)$$

where q_{eq} is the amount of drug adsorbed per unit of adsorbent ("adsorbed drug"), C_{eq} is the concentration of drug remaining in solution at equilibrium ("free drug"), Q is maximum adsorption capacity (number of mol or g of drug adsorbed per unit of adsorbent, forming a continuous monolayer on adsorbent surface) and b is a constant.

The obtained values are shown in Table 1.

The adsorbed tricyclic drugs have been eluted with methanol; approximately 40 – 50 % of bound drugs were eluted.

The presence of molecular interaction between a drug and copper phthalocyanine derivative can be observed using a spectroscopy study. Fig. 4 shows visible absorption spectra of copper phthalocyanine (spectrum 1), amitriptyline (spectrum 2) and their mixture (spectrum 3). A significant shift of the phthalocyanine peak at 666 nm to a longer wavelength (difference ca 11 nm) is seen, indicating such interactions.

Table 1. Maximum adsorption capacities of the blue magnetite for the tricyclic drugs. Q is calculated using the settled volume of the magnetic adsorbent (mg mL^{-1}) while Q' is calculated using the dry weight of the adsorbent (mg g^{-1}).

Drug	Drug action	Q	Q'
Amitriptyline	Antidepressant	9.8	30.1
Chlorprothixene	Neuroleptic	14.2	43.6
Diethazine (Deparkin)	Antiparkinsonic	13.0	39.9
Bisulepin (Dithiaden)	Antihistaminic	14.0	43.0
Prochlorperazine	Neuroleptic	14.1	43.3
Dothiepin (Prothiaden)	Antidepressant	11.4	35.0
Thioridazine	Neuroleptic	11.4	35.0

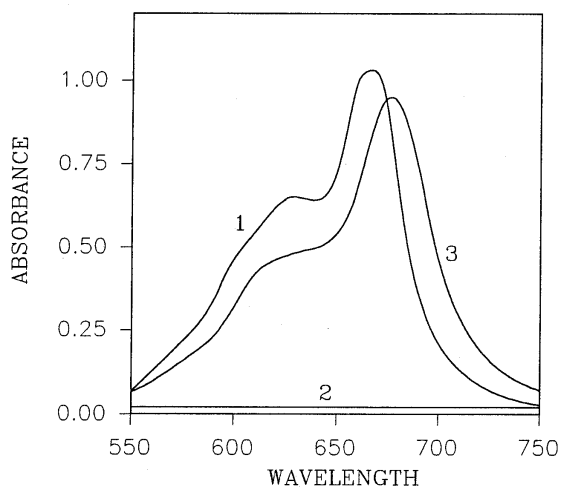

Fig. 4: Visible absorption spectra of copper phthalocyanine (spectrum 1), amitriptyline (spectrum 2) and their mixture (spectrum 3).

DISCUSSION & CONCLUSIONS: As can be seen from the results, immobilized copper phthalocyanine derivative specifically interacts with all tricyclic drugs tested. It was found that other drugs with more fused rings and a side chain in the molecular structure can also be adsorbed to the mentioned adsorbent. For example lisuride (N'-[(8α)-9,10-didehydro-6-methylergolin-8-yl]-N,N-diethylurea) was adsorbed with the maximum adsorption capacity Q = 14.6 mg mL^{-1} (other data not shown). This phenomenon can be used to isolate the target drugs from various samples using magnetic solid-phase extraction [1]. MSPE enables preconcentration of low amounts of free target compounds from a relatively large volume of the sample. As described recently, crystal violet and malachite green (both dyes being possible carcinogens) present in water in concentrations 1 ng mL^{-1} have been successfully preconcetrated from one liter of water using the same affinity adsorbent [4]. Due to the magnetic properties of the adsorbent the preconcentration process can be also performed in samples containing suspended solids.

The specific interaction between tricyclic drugs (and most probably with their metabolites with intact tricyclic structure) may enable specific preconcentration of this important group of drugs from various biological matrices and thus simplify the subsequent analysis using appropriate analytical procedures such as high performance liquid chromatography.

REFERENCES: [1] M. Safarikova and I. Safarik (1999) *J Magn Magn Mater* **194:** 108-112. [2] H. Hayatsu (1992) *J Chromatogr* **597**:37-56. [3] I. Safarik, M. Safarikova, and N. Vrchotova (1995) *Coll Czech Chem Commun* **60:** 34-42. [4] I. Safarik and M. Safarikova (2002) *Water Res* **196:** 196-200.

ACKNOWLEDGEMENTS: The research is a part of ILE Research Intention No. AV0Z6087904. The experimental work was supported by the NATO Linkage Grant No. LST.CLG.977500), Ministry of Education of the Czech Republic (grant project No. OC 523.80) and Grant Agency of the Czech Academy of Sciences (Project No. S6087204).

MAGNETIC SOLID-PHASE EXTRACTION OF TARGET ANALYTES FROM LARGE VOLUMES OF URINE

M. Safarikova & I. Safarik

Laboratory of Biochemistry and Microbiology, Institute of Landscape Ecology, Na Sadkach 7, 370 05 Ceske Budejovice, Czech Republic

INTRODUCTION: Analysis of urine is often used to detect the presence or determine the concentration of various biologically active compounds or xenobiotics. Urine has become the preferred specimen since many compounds can be detected for longer time periods in urine than in blood. Furthermore, urine collection does not require phlebotomy, and urine is typically an ample and stable sample. In most cases the concentration of target analytes is low and thus the analytes have to be preconcentrated before the application of an appropriate analytical procedure.

There is a wide range of preconcentration procedures available that can be used individually or sequentially according to the complexity of the samples, the nature of the matrix, the analytes, and the instrumental techniques available. The use of an extraction technique is common in the pretreatment of most types of sample. Both liquid-liquid and solid-phase extraction procedures are widely used for the urine analytes analysis.

A great increase in the use of solid-phase extraction (SPE) as a preconcentration step has occurred recently. Solid-phase extraction can effectively handle small samples using only small volumes of organic solvents and very simple equipment (usually a small column and a syringe). In some cases, however, it is needed to extract very low amounts of the target analytes from larger volumes of samples. In this case standard SPE requires additional equipment such as solid-phase extraction vacuum manifolds.

Recently a new extraction procedure, called magnetic solid-phase extraction (MSPE), has also been developed [1]. This procedure based on the adsorption of the target analyte on relatively small amount of magnetic specific adsorbent enables to handle liter volumes of samples. Using MSPE with subsequent elution very low concentrations in ppb (μg/L) range of some compounds can be detected. There are two main advantages of this procedure when compared with standard column SPE. At first, it is the possibility to perform the extraction steps in a very simple way, without the need of expensive equipment, even using larger amount of sample (up to 1000 mL of liquid can be manipulated without problems). At second, MSPE can be performed not only in solutions, but also in suspensions. This is a general advantage of magnetic separation techniques due to the fact that majority of accompanying impurities are diamagnetic and do not interfere with magnetic particles during the magnetic separation step.

The use of MSPE in urine analysis was tested using silanized magnetite particles with immobilized reactive copper phthalocyanine dye (C.I. Reactive Blue 21; see Fig. 1) as an affinity ligand. This ligand interacts specifically with polyaromatic hydrocarbons having three or more conjugated rings [2] and with diamino- and triaminotriphenylmethane dyes [3]. This adsorbent can thus be used for the preconcentration of various compounds with proven or suspected carcinogenic properties [2].

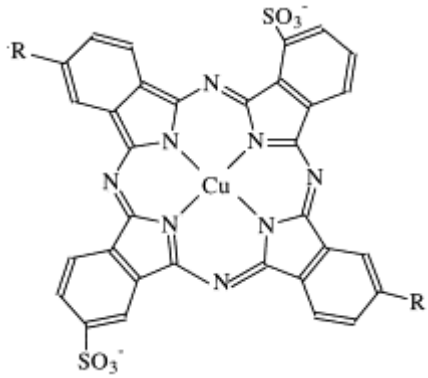

Fig. 1: Possible structure of the C.I. Reactive Blue 21. R – reactive linker arms of the following structure:
$SO_2NHC_6H_4SO_2CH_2CH_2OSO_3H$

For experiments crystal violet (Basic Violet 3, CI 42555; also known as gentian violet or hexamethylpararosaniline chloride; chemical structure is shown in Fig. 2) was used as a model analyte. This dye belongs into the letter group of compounds interacting with copper phthalocyanine derivative. Because of its potential cancerous

property FDA put this dye on the Food and Drug Administration's (FDA's) priority list for drugs that need analytical methods development.

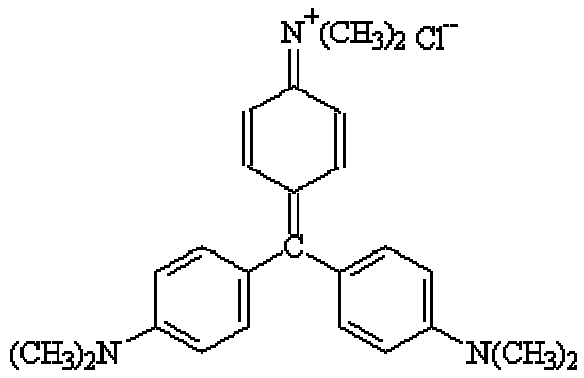

Fig. 2: Chemical structure of crystal violet

Concern about the health risks and carcinogenicity associated with the use and contact with various dyes and other xenobiotics requires a routine laboratory method to be developed to monitor the presence of target dyes and dye metabolites in body fluids. In this paper we demonstrate the use of MSPE for the preconcentration of a model dye (crystal violet) from human urine. Due to the fact that this dye exhibits high extinction coefficient (112,000 $M^{-1}cm^{-1}$ at 590 nm) subsequent spectrophotometric detection can easily be performed.

METHODS: In model experiments fine magnetite particles with immobilized reactive copper phthalocyanine dye (blue magnetite) were used as an affinity adsorbent. Blue magnetite was prepared in a similar way as described recently [3]. Iron(II,III) oxide (10 g; Aldrich, USA) was suspended in 5 % nitric acid and boiled in a closed vessel at 100 ºC for 60 minutes. After thorough washing with distilled water, 40 mL of 10 % water solution (pH 4.0) of 3-aminopropyl-triethoxysilane (Sigma, USA) were added to the sedimented magnetite. The suspension was mixed in a water bath at 80 ºC for 4 h. Then the silanized magnetite was thoroughly washed with water, suspended in 200 mL of water and mixed with 4 g of Ostazin turquoise V-G (C.I. Reactive Blue 21; produced by Spolek pro chemickou a hutni vyrobu, Usti nad Labem, Czech Republic) and 12 g of sodium chloride. The suspension was warmed to 70 ºC and 15 min later 10 g of anhydrous sodium carbonate were added. The suspension was stirred at 70 ºC for 4 h and then the mixture was left overnight at ambient temperature without mixing. The blue magnetite particles were thoroughly washed with water and the remaining free dye was removed using an extraction with methanol in a Soxhlet apparatus. The extracted particles were then repeatedly washed with methanol – 2 % acetic acid (50:1, v/v). The washed blue magnetite particles were stored in water at 4 ºC. The dry weight of 1 mL of the settled blue magnetite was 322 mg. The copper phthalocyanine content of the blue magnetite was ca 80 μmol per g of the dry adsorbent (determined from elemental analysis for copper using a PU 7450 ICP spectrometer (Pye-Unicam, England) after mineralization of blue magnetite with concentrated nitric acid).

Various volumes of human urine (usually 100 mL or more; obtained from healthy male donors) were spiked with various amounts of crystal violet and subsequently 400 μL of water suspension of magnetic adsorbent (corresponding to 100 μL of sedimented adsorbent) was added. The suspension was stirred for 3 – 4 hours at room temperature. After that magnetic particles were captured to the bottom of the beaker or flask using an appropriate magnet or flat magnetic separator and urine was poured off taking care not to lose the adsorbent. The adsorbent was washed several times with water and transferred into a test tube (test tube magnetic separators MPC-1 or MPC-6 from Dynal, Norway were used for magnetic separation). After washing and removing all water 1.5 mL of methanol – 2 % acetic acid (50:1, v/v) solution was added to the adsorbent. The elution proceeded for ca 20 minutes. The eluate was used for the spectrophotometric measurement when the position of the crystal violet peak was verified using a crystal violet standard.

RESULTS: Crystal violet was used as a model dye in order to test a new preconcentration procedure MSPE (magnetic solid-phase extraction) for the detection and determination of low concentration of target analytes in urine. The procedure was developed for standard spectrophotometers having the possibility to record spectra in visible region of light and for use of standard semi-microcuvettes (working volume ca 1.5 ml).

In previous experiments magnetic carrier with immobilized copper phthalocyanine dye (blue magnetite) efficiently adsorbed chromatic form of crystal violet from water solutions [3]. Nevertheless this dye can also be separated from other liquid samples, such as urine. It was shown in preliminary experiments that majority of the tested dye (added

in amounts 0.25 - 1 μg into 100 mL of urine) was adsorbed on blue magnetite in approximately 120 min; further prolongation of the incubation time did not improve the dye adsorption and subsequent recovery (data not shown). This incubation period (ca 2 hours) was used in all further experiments.

Fig. 3 shows an example of eluates spectra obtained after MSPE of crystal violet from male urine. It can be seen that very low amounts of the dye can be detected spectrophotometrically. After MSPE clearly visible peak of crystal violet can be found at the concentration 0.5 μg/100 mL urine (i.e., 5 ppb) and even at the half concentration (2.5 ppb). It corresponds to the concentration of crystal violet 6 - 12 nmol/L. The samples showing a peak corresponding to that one of crystal violet (with the maximum at ca 585 - 590 nm) can be considered as presumptive positive and the presence of crystal violet can be verified e.g. using a HPLC procedure.

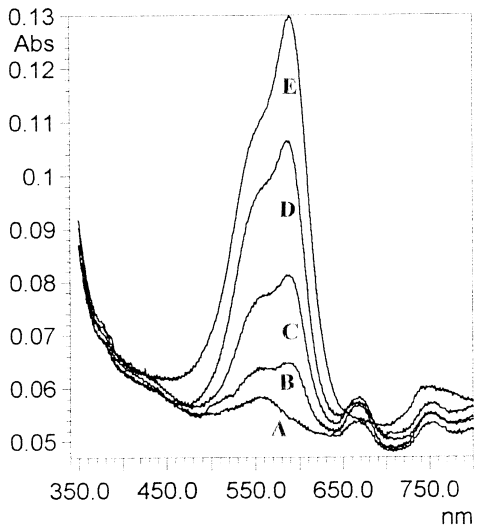

Fig. 3: Spectra of a standard and eluates (1.5 mL) after magnetic solid-phase extraction of crystal violet from 100 mL of male urine. A – control sample (unspiked urine); B – urine spiked with 0.25 mg of crystal violet; C – urine spiked with 0.5 mg of crystal violet; D – urine spiked with 1.0 mg of crystal violet; E – crystal violet (1.0 mg per 1.5 mL of the elution solution).

The recovery of crystal violet was ca 60 – 75 % depending mainly on the batch of magnetic affinity adsorbent used for the MSPE. The reproducibility of the technique was determined from five replicate measurements for one concentration (1.0 μg per 100 mL of urine) of crystal violet. The typical relative standard deviation of the adsorption and elution efficiencies (measured as the absorbance of the eluate at the peak maximum) was 9.3 %.

DISCUSSION & CONCLUSIONS: Isolation and preconcentration of compounds present in solutions or suspensions in very low concentrations belongs to the basic operations in analytical, bioanalytical and environmental chemistry. The aim of this work was to develop a simple and ready to use procedure for the preconcentration and subsequent detection or determination of low concentrations of target analytes in urine. Crystal violet was chosen as a model compound because it belongs (together with e.g. malachite green) to a group of compounds that are linked to an increased risk of cancer [4]. This dye is commonly used for many purposes (e.g. such as an antimicrobial or antifungal agent) nevertheless its use has already been controlled in some individual member states within the European Community.

The results confirmed the applicability of MSPE procedure for a treatment of biological samples, specifically urine. Using MSPE low concentrations (5 ppb) of the native dye (in a chromatic form) can be detected spectrophotometrically. Of course, different situation can be expected if the dyes (or other xenobiotic compounds) enter the human body and their metabolic modification takes place. Rapid metabolic conversion of crystal violet to the colorless leuco form can be expected followed by its slow release into urine. The leuco form cannot be simply separated using the described procedure. An appropriate oxidizing process may lead to the conversion of leuco form into the chromatic form of crystal violet, which could then be separated and subsequently detected using the described procedure. The optimized oxidation / preconcentration procedure for the detection of metabolically modified crystal violet will be studied soon.

It can be supposed that MSPE can also be used for the preconcentration of other xenobiotics from urine provided that suitable affinity ligands (e.g., antibodies) will be available. MSPE could thus be efficiently used as a simple screening and preconcentration procedure that can be followed by a more precise chromatography analysis in case suspected urine samples are found. Currently we test other types of magnetic adsorbents (both specific and non-specific ones) which could be used for magnetic solid-phase extraction of various xenobiotics from human urine.

It can also be expected that MSPE could be used for the isolation and preconcentration of important minority biologically active compounds directly from urine and other body fluids such as blood and milk.

REFERENCES: [1] M. Safarikova and I. Safarik (1999) *J Magn Magn Mater* **194:** 108-112. [2] H. Hayatsu (1992) *J. Chromatogr* **597:** 37-56. [3] I. Safarik, M. Safarikova and N. Vrchotova (1995) *Collect Czech Chem Commun* **60**: 34-42. [4] J.J. MacDonald and C.E. Cerniglia (1984) *Drug Metab Dispos* **12:** 330-336.

ACKNOWLEDGEMENTS: The research is a part of ILE Research Intention No. AV0Z6087904. The experimental work was supported by the NATO Collaborative Linkage Grant No. LST.CLG.977500, Ministry of Education of the Czech Republic (Project No. OC 523.80) and Grant Agency of the Czech Academy of Sciences (Project No. S6087204).

MAGNETIC RESONANCE OF DEXTRAN- AND DMSA-COATED MAGNETITE-BASED MAGNETIC FLUIDS: PARTICLE INTERACTION INVESTIGATION

J.G. Santos [1], N. Buske [2], C. Gansau [2], & P.C. Morais [1]

[1] *Universidade de Brasília, Instituto de Física, Núcleo de Física Aplicada, 70919-970 Brasília-DF, Brazil*

[2] *Berlin Heart AG, Wiesenweg 10, D-12247 Berlin, Germany*

INTRODUCTION: Magnetic resonance (MR) has been successfully used to investigate different aspects of ionic and surfacted magnetic fluids (MFs). Most of the experimental data refer to the MR from the core nanoparticle instead of from doping species intentionally introduced in the MF sample. The effects of the particle concentration, nanoparticle size, coating agents, ionic strength, and temperature upon the resonance linewidth or/and resonance field have been investigated in the last ten years. Very recently, however, investigation of the kinetic disposition of biocompatible magnetic fluids (BMFs) endovenously administered in mice has been performed using MR experiments [1]. However, to be used as an analytical technique while probing nanosized magnets in living beings and biological materials, the analysis of the resonance spectra has to be previously performed in a wide range of nanoparticle concentration, say from 10^{12} to 10^{17} cm^{-3}. This is particularly important because specific tissues and cells may, under certain conditions, concentrate nanosized particles either internally in the cell or externally attached to the cell membrane. Aggregation of magnetic nanoparticles in a small cluster or in a chain-like structure is expected to change the MR lineshape or even to cause MR line splitting. In the present study a systematic investigation of the resonance spectra of BMFs is carried out at room temperature and in the concentration range of 2×10^{13} to 5×10^{16} particle/cm^3.

METHODS: The two biocompatible magnetic fluids used in this study are based on magnetite nanoparticles (9.4 nm in average diameter) coated with dextran and DMSA (dimercaptosuccinic acid). After precipitation, magnetite nanoparticles were surface-coated to produce stable BMF samples at physiological pH and salinity. Typical sample preparation routine can be found in Ref. [2]. Room temperature resonance measurements were performed using a commercial spectrometer (Bruker ESP-300) tuned around 9.421 GHz.

RESULTS & DISCUSSION: Figure 1 shows the room-temperature resonance spectra (first derivative of the absorption curve) of dextran-coated (sample BMF1) and DMSA-coated (sample BMF2). Magnetic resonance spectra of the samples containing high, intermediate, and low particle concentrations are reasonably well described by one single resonance line, differently of typical resonance spectra observed in ionic MFs.

Open and full circles in Fig. 2 represent the room-temperature resonance field (H_R) versus resonance linewidth (ΔH_R) of samples BMF1 and BMF2, respectively. Dashed and solid lines in Fig. 2 represent the best numerical fit of H_R versus ΔH_R according to [3]:

$$H_R = A(\Delta H_R)^2 \quad , \qquad (1)$$

where A is a fitting parameter. Note the stronger resonance field deviation between the two sets of data at higher values of the resonance field, i.e. at lower nanoparticle concentration.

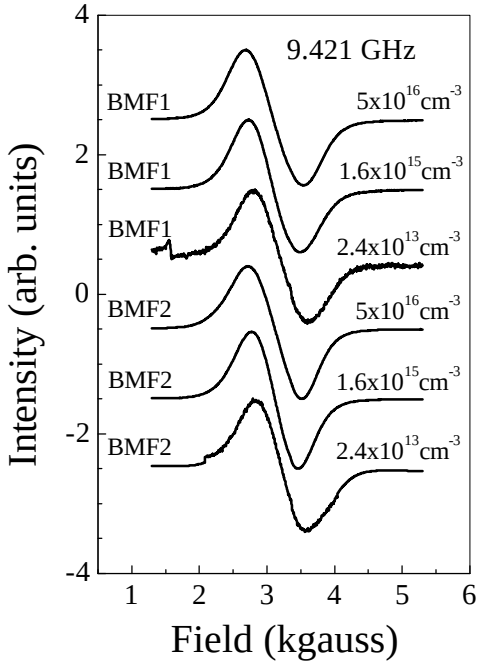

Fig. 1: Typical room-temperature magnetic resonance spectra taken from samples BMF1 and BMF2, at different particle concentrations.

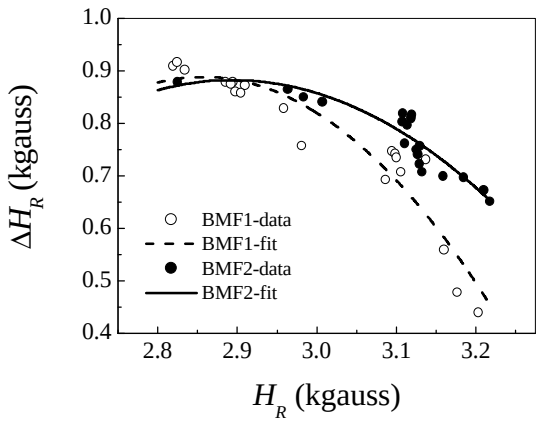

Fig. 2: Resonance field versus resonance linewidth for samples BMF1 and BMF2. Dashed and solid lines represent the best fit of the data according to Eq. (1).

Figure 3 shows the resonance field (H_R) versus the inverse of particle concentration (1/C) for the two samples investigated. Solid lines in Fig. 3 represent the best fit of H_R versus 1/C, according to the model described in Ref. [1]. The description of H_R versus 1/C starts with the basic resonance equation, i.e. $H_{EFF} = w_R/g$, where H_{EFF} is the effective field at the resonance center, w_R is the microwave frequency, and g is the gyromagnetic ratio. At low particle concentration the effective field is mainly a combination of the external field (H_E), the anisotropy field (H_K), and the demagnetizing field (H_D) [4]. Only the demagnetizing field depends upon C. At the resonance condition, $H_E = H_R$, the basic resonance equation is rewritten as $H_R = w_R/g - H_K - H_D$. The demagnetizing field of an assembly of isolated spherical nanoparticles in a magnetically inert matrix, however, is given by $H_D = (4\pi/3)[(1/p) - 1]M$, where M is the magnetization associated to the magnetic nanoparticle and p is the volumetric packing fraction of the nanoparticle in the matrix [5]. Note that the relationship between p and C is $p = \pi DC/6$, where D is the nanoparticle diameter. Therefore, at the low-concentration end the relationship between H_R and C would be written as $H_R = H_0 + K_1/C$, where H_0 and K_1 are fitting parameters. The data in Fig. 3, however, shows a linear relationship between H_R and 1/C only at nanoparticle concentrations below about 10^{14} cm^{-3}. Above 10^{14} cm^{-3} particle-particle (dipole) interaction plays a key role in the H_R versus 1/C curve, as revealed by the abrupt change of the H_R versus 1/C slope.

Inclusion of the particle-particle interaction in the description of the H_R versus 1/C curve is realized via the relationship between the shift of the resonance field and the shift in the resonance linewidth, as described in Eq. (1) [3]. However, the linewidth shift has been successfully described by $\Delta H_R = BC\tanh(K_2 + K_3C^2)$ [6]. The K_3C^2 term describes the dipole-dipole interaction at the higher end of nanoparticle concentration, as discussed in Ref. [6]. The resonance field now reads:

$$H_R = H_0 + K_1/C - B^2C^2\tanh^2(K_2 + K_3C^2) \quad , \quad (2)$$

where H_0, B, and K_j (j = 1, 2, 3) are fitting parameters. In Fig. 3 the solid lines represent the best fit of the data in the full range of particle concentration, i.e. according to Eq. (2). The ratio of the K_3 values for BMF1 and BMF2 (0.91) indicates that dipole-dipole interaction is roughly the same for both samples. However, the ratio of the B values for BMF1 and BMF2 (1.3) indicates that particle-particle coupling, due to the coating molecular layer, is quite different in both samples. Finally, the ratio of the K_1 values for BMF1 and BMF2 (0.88) indicates that the particle-core diameter (effective values) is slightly different in both samples.

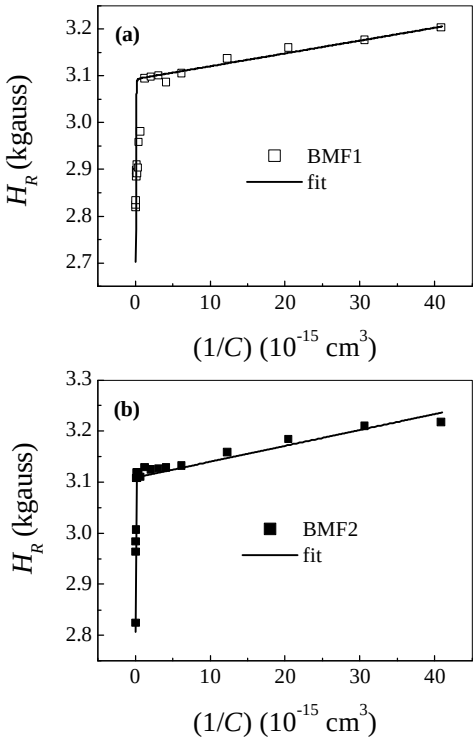

Fig. 3: Resonance field versus the inverse of particle concentration for samples (a) BMF1 and (b) BMF2.

CONCLUSIONS: In summary, magnetic resonance has been used to investigate magnetic fluids based on magnetite nanoparticle coated with two biocompatible molecular species (dextran and DMSA). Whereas the resonance field shift by about

the same amount in both samples, the shift in the resonance linewidth in the dextran-coated sample is twice the shift observed in the DMSA-coated sample. This aspect would favor the use of the DMSA-coated MF sample to probe biodistribution after injection in animals. In particular, concentration of DMSA-coated magnetite nanoparticles in specific organs could be signaled through line splitting in MR measurements.

REFERENCES: [1]L.M. Lacava, Z.G.M. Lacava, M.F. Da Silva, O. Silva, S.B. Chaves, R.B. Azevedo, F. Pelegrini, C. Gansau, N. Buske, D. Sabolovic, and P.C. Morais (2001) *Biophys. J.* **80**:2483-2486. [2]D. Günther and N. Buske (1993) DE patent Nr. 4325386. [3]K. Nagata and A. Ishihara (1992) *J. Magn. Magn. Mater*. **104**:1571-1573. [4]A.F. Bakuzis, P.C. Morais, and F. Pelegrini (1999) *J. Appl. Phys.* **85**:7480-7482. [5]E. Kneller (1969) *Fine particle theory* in Magnetism and Metallurgy (eds A.E. Berkowitz and E. Kneller), Academic Press, pp. 365-471. [6]P.C. Morais, M.C.F.L. Lara, A.L. Tronconi, F.A. Tourinho, A.R. Pereira, and F. Pelegrini (1996) *J. Appl. Phys.* **79**:7931-7935.

ACKNOWLEDGEMENTS: This work was partially supported by the Brazilian agencies CNPq and CAPES.

INNOVATIVE AUTOMATED NUCLEIC ACID ISOLATION BY THE KEY USE OF MAGNETIC SILICA PARTICLES

Vidar Skagestad, Evy Reitan , Robin Stacy, Arne Deggerdal, Tine Thorbjørnsen, Hege Hardersen, Erik Hornes and Lars Kilaas*

*GenoVision A.S., Frysjaveien 40, 0884 Oslo, Norway; *Particle Solutions AS, Richard Birkelandsv. 2B, 7491 Trondheim, Norway*

INTRODUCTION: Reproducible isolation of highly pure DNA is critical to successful downstream analyses such as routine diagnostic testing, genetic screening, forensics, research and animal testing among others. Reproducibility may be increased by automating time consuming, labor intensive steps. Automation has the additional advantage of allowing for high throughput downstream analyses. We have developed three workstations, GenoM-48 GenoM-96 and GenoM-6, for automated isolation of nucleic acids from a wide range of sample types. The workstations are closed, fully walk-away systems. GenoM-48 isolates from 6-48 samples per run and GenoM-96 from 8-96 samples per run. GenoM-6 isolates from 1-6 samples per run. Sample volumes range from 25-350 µl. The workstations use magnetic particle-based technology as the solid phase for capturing and purifying the nucleic acids. This allows for rapid washing procedures and produces highly pure nucleic acids.

METHODS: GenoVision has recently developed a second generation of reagents for the nucleic acid (NA) isolation which maintains the high quality of the isolated material but in general increases the total yield compared to our first products. In this poster, we would like to present results of nucleic acid isolations on the basis of this new chemistry. The examples will include NA isolations from a variety of starting materials including fresh and frozen tissue biopsy, blood, cultured cells, and dried blood from filter membrane cards.

All the isolations are based on the use of chaotropic agents (GTC, GuHCl) for lysis and binding, chaotropic agents/alchols for washing and pure water for elution of the isolated NA.

Fig. 1: GenoM-48 for automated isolation of nucleic acids (6-48 samples per run).

RESULTS: Tables 1 and 2 show typical isolated DNA and RNA, respectively, from a variety of different samples, all isolated on the GenoM-48. The elution volumes (in which the NA is isolated) differ typically from 100 to 300 ul.

Table 1. Isolated DNA from a variety of samples on the GenoM-48. Comparing old and new kits.

Sample volume/material	Old kit (µg)	New kit (µg)
Whole blood 100µl	1.1-3.1	1.7-3.0
Whole blood 200µl	2.4-5.2	3.5-6.0
Whole blood 350µl	-	5.0-10
50µl buffy/1x10^8 cells		6-10
75µl buffy/1x10^8 cells		8-12
100µl buffy/1x10^8 cells	4.4-6.3	10-15
2x10^6 Hl60 cells	-	6-9
Porcine muscle/60 mg	-	8-9
Rat liver/20 mg	-	6-10

Table 2. Isolated total RNA from cultured cells on the GenoM-48. Comparing old and new kits. Typical values.

Cell samples	Old kit	New kit
2x10^6 Jurkat	6-8 µg	8-12 µg
2x10^6 Bjab	7-9 µg	10-12 µg
2x10^6 HL60	13-15 µg	22-28 µg
4x10^6 HL60	-	45-50 µg

DISCUSSION & CONCLUSIONS: Although the old NA isolation kit gives excellent quality of isolated DNA (ratio 280/260 = 1.8) and RNA (ratio 280/260 ca 1.9), the yield for some applications are in the lower acceptable range.

With the new chemistry, we have improved the yields of isolated NA's without compromising the quality (DNA: ratio 280/260 ca 1.87 and RNA: 280/260 ca 2.0). In addition, the second generation kits allow for larger input volumes of samples, and the isolated yield of NA in general shows an improved linearity with respect to sample input

REFERENCES: For more information on GenoVision and its products (handboks etc), please consult www.genovision.com.

SYNTHESIS OF MAGNETIC CLUSTER NANOPARTICLES

A. Suslov

University of California, Santa Barbara, CRSS Lab.- ERC Building 6740, Cortona Dr., Goleta, CA 93117, USA

INTRODUCTION: The existing chemical and physical methods [1-4] of producing nanoparticles do not allow synthesizing nanoparticles in the size range of about 1 nm with high degree of certainty. The nanoparticles must possess pre-designed physical and chemical properties, such as: size, composition, charge, magnetic momentum, etc, which are necessary in a number of technological applications.
The presented article describes synthesis of nanoparticles in the air performed due to the heterogeneous condensation of iron atoms on ions. The size range is about 1nm.

METHODS: The general concept of the proposed method for the controlled synthesis of cluster nanoparticles (CNP) having pre-designed physical and chemical properties is as follows:

> realization of the exclusively heterogeneous condensation, which occurs on ions; creation of the premeditated required correlations of the condensed molecules' concentrations *(Nm)* to the amount of condensation nuclei – ions, *(Ni) : Nm / Ni* . The control of transferring atoms and ions, participating in the CNP synthesis is carried out by the external electromagnetic fields.

To accomplish this objective, a well-known phenomenon – facilitation and stabilization of heterogeneous condensation of substance molecules on ions was employed [5,6]. Investigators mentioned that stabilization and termination of the particles' growth (their size is about 1 nm) were observed in the course of condensation [7].
The effect of the charge of a condensation nucleus on the process of trapping the surrounding molecules (i.e., condensation) can be explained in terms of polarization of the neighboring substance molecules by the Coulomb field of the condensation nucleus (ion). The induced dipoles of these molecules are attracted by the heterogeneous electric field of the condensation nucleus. It continues till $W >> kT$. Here W stands for the energy of attraction of the polarized molecules by the Coulomb field of the condensation nucleus and kT defines the thermal energy of molecules. It should also be noted that the Coulomb field of an ion effects the chemical and physical properties of the nanoparticle being synthesized. Hence, when moving in the heterogeneous electric field of an ion, an electric axis of the polarized molecule (dipole) will orient by the normal onto the ion's surface. It implies a certain geometric configuration of the synthesized nanoparticle during the condensation process. The simultaneous superimposing of the external magnetic fields onto the condensation process, results in the configuration of the magnetic moments of the condensed molecules. The combination of the above-mentioned processes advances the controlling physical and chemical properties of the nanoparticles being synthesized.
To verify the above stated ideas, an experimental investigation aimed at synthesizing CNP with the pre-designed physical and chemical properties, i.e. size, charge, magnetic momentum, etc, was carried out. This process was performed in the air according to the following technological sequence on a setup consisting of: – ion generators; – Ohmic furnaces; - measuring dish; – differential mobility analyzer (DMA); – electrostatic precipitator (ESP); – rotation meters; – electrometers; – power supply units with high and low voltage; – gas aspiration units.
The air supplied by the compressor (through the system of highly and roughly purifying filters and through a receiver) passes into the ion generator. The generators operate using the corona discharge and may generate a definite concentration of ions $(N \sim 10^6 - 10^7\ cm^{-3})$ with a pre-designed polarity. Having passed through the ion generators, the air goes to the furnaces having spirals made of iron wire with the diameter 0.1 cm and could achieve temperatures up to $T \sim 1200^0\ C$. Afterwards the air is advanced into a metal dish ($2r = 6cm$ and $h = 50\ cm$). To control the parameters of the generated media, DMA or ESP were introduced into this dish.

Upon high temperatures of the spirals, there occurs the active realization of the phase transfer "solid body – vapor" of iron atoms, which later condense onto the artificially generated condensation nuclei – ions (created by the ion generators) and further form nanoparticles. The condensation occurs in the external fields: the Coulomb field of an ion; the magnetic field, created by the current from the spirals and achieving the values of $H \approx 4 \cdot 10^4 A/m$. We also controlled the transfer of the electricity carriers, which participated in the nanoparticles' synthesis. It was realized with the help of the external electrical field, which was generated between the spiral and the walls of the furnace. The parameters (concentration, charge, mobility, sizes of the generated ions and of the synthesized nanoparticles) were registered by a differential mobility analyzer. The size of the synthesized nanoparticles was analyzed at an AFM. The trapping of the synthesized nanoparticles was carried out in the electrostatic precipitator [8]. To detect the magnetic properties of the synthesized CNP we carried out photo registering of their velocity in water under the effect of the external heterogeneous magnetic field and by employing the phenomenon of opalescence [9].

RESULTS: Measuring of the particles' spectra (the dependency of the sizes of particles on their concentration) was carried out on the DMA At first, a single-mode spectrum with particles' sizes characteristic of insignificantly clusterized O_2^- ions in the air has been obtained. During this process only the generator of ions was functioning. A two-mode spectrum for the negatively charged particles and the three-mode spectrum for the positively charged particles have been obtained in the course of the subsequent measurement of the spectra when both generators and the furnaces were working and iron atoms were being generated. It caused the increase of the particles' sizes, which confirms their condensation growth, i.e., the clusterization of condensation nuclei – ions. The first mode showed the presence of mildly clusterized particles with the sizes ~ 0.5 nm. The particles' sizes for the second mode were ~ 1nm and for the third ~ 1.7 nm. While measuring the size spectrum of the particles, only the positively charged particles were registered, whereas ion generators were not functioning and only furnaces were working *(T~900^0 C)*. It resulted in obtaining a three-mode size spectrum. The range of particles' sizes was repeated for each of modes under various operating regimes of the setup. The only factors being slightly changed were the width of the modes and the concentration of the particles. When the external electric field was superimposed on the synthesis process and when the potential on the spirals was positive, the form of the size spectrum of the synthesized particles changed and, starting with the 60 V potential, the spectrum became one-mode and the particles' size was about 1 nm. Further increase of the potential (90 V) at first increased the concentration of particles and then (at ~100 V) caused the widening of the mode. The ions' generators were not working and only positive charges of these particles were registered.

The work of the corona discharge generators and the supply of the negative potential onto the heating spiral also resulted in changing the form of the size spectrum of the particles. Therefore, when the potential on the spiral was negative (-112 V), we registered a clear two-mode spectrum, containing charges of only negative particles. When the potential value of the spiral was still negative and changed into (-90 V), we observed one-mode size spectra of both positively and negatively charged particles with the size of about 1 nm .

DISCUSSION & CONCLUSIONS: The obtained results of the measurements can be interpreted in terms of the analyzed elementary processes occurring on the phase interface " hot metal – air". Heating the metal staring from certain temperature will cause thermal emission of electrons from the metal surface as well as thermal emission of positive ions of metal atoms and a more active sublimation of metal atoms. The particles, which escaped from this metal, move into the kinetic zone without any interactions. The particles started to interact with air molecules and with one another on the kinetic zone boundary, where $l \approx 6 \cdot 10^{-8} m$ (the mean value of an ion and an electron path). Thus, electrons, which interact with oxygen, create ions O_2^-, and if they interact with iron atoms, they produce negative ions of iron. Eventually, as the time, characteristic for such reactions is

$t \sim 10^{-8}$ sec, there exist three ions O_2^-, Fe^- and Fe^+, which are real nuclei of condensation for the neutral atoms of Fe. The presence of these nuclei may explain the three modes appearing during the synthesis of CNP. The fact that only positive particles are present, is interpreted in terms of a possible thermal emission from the negatively charged particles, sited close to the hot surface, i.e. at $T \sim 900^0$ C. Superimposing of the external electric fields causes the selection of the condensation nuclei – ions – depending on the potential sign on the spirals. Hence, when the potential is positive, the electric field collect negative ions and gathers them onto the spiral, thus causing the appearance of a one-mode size spectrum of the synthesized particles. When the potential on the spiral is negative, the generated electric field attracts positive charges (ions) to the surface of the spiral and repels the negative ones. Thus, the synthesis of nanoparticles occurs on two condensation nuclei – ions of O_2^- and of Fe^-, which causes a two-mode size spectrum of nanoparticles. The possibility to generate exclusively negative charges is explained by the attraction of the positive particles produced close to the spiral. It is also possible to generate exclusively negative nanoparticles on the negative ions, which were pushed out by the electric field into the "cold" zone of the gas. The thermal emission from the nanoparticles surface is not realized in this "cold" zone.

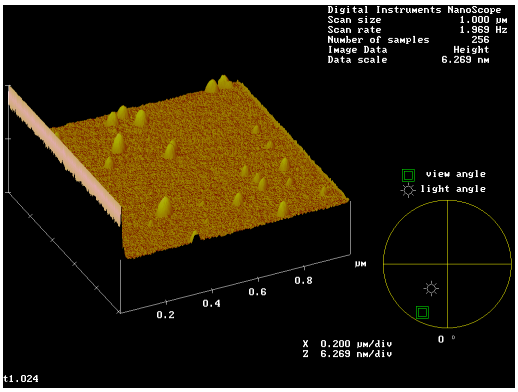

Fig. 1: AFM view of cluster nanoparticles.

The investigation has also shown an active movement of the synthesized CNP in the heterogeneous magnetic fields. This fact confirms the existence of the non-compensated magnetic momentum in CNP. Estimations based on measurements (diffusion coefficient) and calculations of the number of the clusterizing molecules in the synthesized nanoparticle, showed that the density of the particles is the same for Fe_3O_4 particles. The characteristic look of the synthesized particles is given in Figure 1.

In conclusion we would like to state that the above-analyzed approach to synthesizing CNP in the air, enables to synthesize nanoparticles in the size range of ~ 1 nm. with a great degree of certainty. The produced particles will possess various physical and chemical properties. Controlling the synthesis by electric fields enables to change the sizes of nanoparticles, the signs of their charges, and the value of their magnetic parameters.

REFERENCES [1]. H. Gleiter " Structure and Properties of Nanometer-Sized Materials", *Phase Transitions*, 1990, v.24-26, pp.15-34 . [2] M.Magnusson, et. al. "Gold Nanoparticles: Production, Reshaping and Thermal Charging", *J. of Nanoparticle Research* 1:243-251 (1999). [3] K. Yagi, M. Tokuda, T. Kobayashi and T. Kishita *1999 International Symposium on Micromechatronics and Human Science*, pp.157-162 (1999). [4] M.H.Nayfeh (2000), *J. Applied Physics Letters*, (U.S. patent pending). [5] L.Kip. et. al. J. Chem. Phys. **6**, 264 (1938). [6] C.T.R. Wilson. *Phil. Trans. Poy.Soc.*, 193, 289 (1899). [7] A.G. Amelin *Theoretical Basis of the Fog Formation During Vapor Condensation*. Moscow, 1972, p.304. (In Russian). [8] J. Dixkens and H. Fissan *Development of an Electrostatic Precipitator for Off-Line Particle Analysis*, Aerosol Science and Technology 30: 438-453 (1999). [9] D. Fridregsberg *Curs Colloidnoy chemistry*, Leningrad, 1974, p. 350 (In Russian).

THE POTENTIAL OF QUADRUPOLE MAGNETIC FIELD-FLOW FRACTIONATION FOR DETERMINING PARTICLE MAGNETIZATION DISTRIBUTIONS

P. Stephen Williams,[1] Lee R. Moore,[1] Jeffrey J. Chalmers,[2] & Maciej Zborowski[1]

[1] *Dept. of Biomedical Engineering, The Cleveland Clinic Foundation, Cleveland, OH 44195, USA*
[2] *Dept. of Chemical Engineering, Ohio State University, Columbus, OH 43210, USA*

INTRODUCTION: In recent years, Zborowski and co-workers [1,2] have developed the flow-through quadrupole magnetic separator (QMS) for isolating or enriching specific biological cell types for the purposes of medical diagnostics or therapy. In this system the quadrupole magnet produces a radially symmetric magnetic field. The flow channel has a thin annular geometry and is mounted concentrically in the field. Using an annular inlet flow splitter, a cell sample suspension is introduced close to the inner channel wall and pure suspending fluid introduced at the outer wall. Particular cell types, mobilized by labeling with immunospecific magnetic nanoparticles, are driven toward the outer channel wall as they are carried along the channel by the overall flow of suspending fluid. The mobilized cells are divided from the remaining cells by an annular splitter at the channel outlet. The theory for the annular channel operation [3] was based upon that previously developed for the parallel-plate systems invented by Giddings [4,5].

We have made use of the experience gained in developing this magnetic cell sorting system to develop quadrupole magnetic FFF. Magnetic FFF may be used to characterize particulate magnetic materials, such as the immunospecific particles used for labeling cells for magnetic separation. The principles of quadrupole magnetic FFF are explained below, and preliminary experimental results are presented.

THEORY: Field-flow fractionation (FFF) is a particle separation technique that takes place in a flow of suspending fluid in a thin channel. A field is applied across the channel thickness, perpendicular to the direction of flow. The particles to be separated interact with the field to a greater or lesser extent and are driven into the slower moving fluid close to one of the walls. Due to back diffusion from the resultant region of higher concentration next to the wall, a steady-state concentration profile is established for each (monodisperse) fraction of the sample. The diffusion rate of submicron-sized particles allows a fast exchange of particles within the thickness of the steady state distribution. Generally, the stronger the interaction of the particles with the field, the thinner will be the steady-state distribution, and the more time that particles spend in the slowest moving streams next to the wall. Therefore, with the imposition of flow, an elution of the sample takes place with the particles that interact weakly with the field being carried to the channel outlet first, followed by particles that interact more and more strongly with the field. A consideration of the fluid flow velocity profile and the theory yielding steady-state particle distribution within this profile allows the prediction of elution time for a given strength of particle-field interaction. Conversely, an elution profile may be converted to a distribution in the sample property that interacts with the field. In the case of magnetic FFF, this yields a distribution in particle magnetic moment.

The velocity profile in an annulus is given by

$$v(\rho) = 2 < v > (1 - \rho^2 - A_2 \ln\rho) / A_1 \qquad (1)$$

in which $<v>$ is the mean fluid velocity, ρ is the ratio of radial distance from the axis to the radius r_o of the outer wall, A_1 and A_2 are functions of ρ_i, the ratio of inner wall radius r_i to r_o. These are given by

$$A_1 = 1 - \rho_i{}^2 + A_2 \qquad (2)$$

$$A_2 = (1 - \rho_i{}^2) / \ln\rho_i \qquad (3)$$

It may be shown that the steady-state concentration profile for magnetically saturated particles in the quadrupole field is given by

$$c(\rho) = c_o \exp\left(-\frac{1}{\lambda} \frac{(1-\rho)}{(1-\rho_i)} \right) \qquad (4)$$

in which c_o is the concentration at the outer wall, and λ is the ratio of thermal energy kT to the work required to move a particle against the magnetic force from r_o to r_i. The value of λ is given by

$$\lambda = \frac{kT}{V_m M_s B_o} \frac{1}{(1-\rho_i)} \qquad (5)$$

in which V_m is the volume of magnetic material in the particle, M_s is the saturation magnetization of the material, and B_o is the magnetic induction at the outer wall.

The fast exchange of particles by diffusion across the thickness of a steady-state distribution leads to equalized sampling of velocity streamlines, and the migration of a small sample plug of monodisperse particles as a coherent zone along the length of the channel. The ratio of the velocity of such a zone to the mean fluid velocity is known as the retention ratio. The zone velocity corresponds to a weighted average of the stream velocities over the annular cross section, with the weighting being proportional to local particle concentration. The retention ratio is therefore given by

$$R = \frac{v_p}{< v >} = \frac{< cv >}{< c >< v >} \qquad (6)$$

where v_p is the zone velocity, and the angle-brackets defines a quantity averaged over the annular cross section:

$$< x >= \frac{2\pi \int_{r_i}^{r_o} r\, x(r)\, dr}{2\pi \int_{r_i}^{r_o} r\, dr} = \frac{s \int_{\rho_i}^{1} \rho\, x(\rho)\, d\rho}{(1-{\rho_i}^2)} \qquad (7)$$

Therefore,

$$R = \frac{\int_{\rho_i}^{1} \rho\, c(\rho)\, v(\rho)\, d\rho}{< v > \int_{\rho_i}^{1} \rho\, c(\rho)\, d\rho} \qquad (8)$$

The retention ratio is therefore a function of both λ and ρ_i. Fig. 1 shows the dependence of R on λ for ρ_i of 0.5 and 0.9.

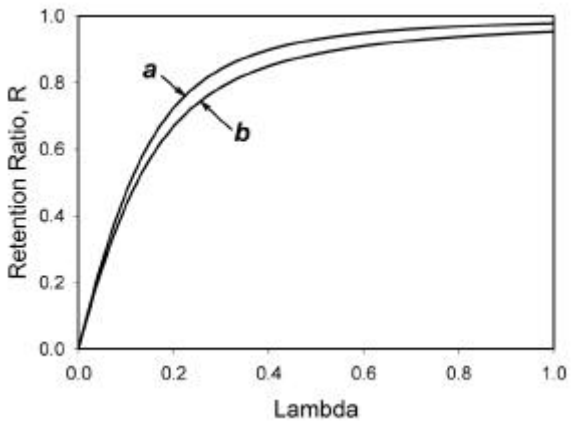

Fig. 1: Plots of Retention Ratio, R, versus l for a) r_i = 0.9, and b) r_i = 0.5.

METHODS: A schematic of the quadrupole magnetic FFF channel and magnet is shown in Fig. 2. The sample and suspending fluid are delivered to the channel and collected at the channel outlet via a set of radial tubes at each end of the core rod. In this figure the channel thickness is exaggerated for clarity. It is, in fact, just 0.0508 cm in thickness, with a radius of 0.743 cm (so that r_i = 0.932), and length between inlet and outlet radial tubes of 14.6 cm.

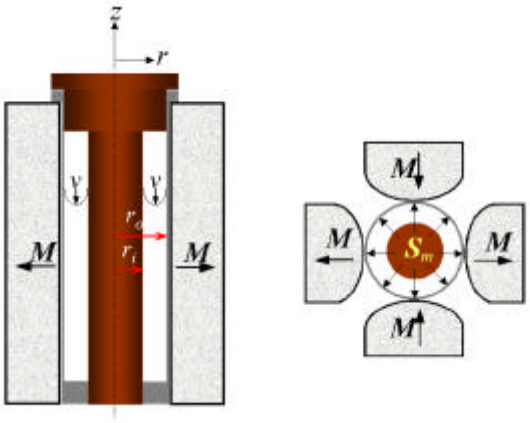

Fig. 2: Schematic diagram of the quadrupole magnetic FFF channel, shown in mid-axial section on the left and radial section on the right.

The quadrupole magnet was determined to exhibit a magnetic induction of 1.32 T at the inner wall of the channel cylinder.

A sample injection valve (Reodyne, Model 7725i) and syringe pump (Harvard Apparatus, Pump Model PhD2000) were used to introduce the sample and drive it through the channel. The pump was programmable, which allowed for the "stop-flow relaxation" of the sample once it was carried onto the channel. During this short interruption of flow, prior to the elution step, the sample particles attain their steady state distributions across the channel thickness. A HyperQuan VUV-10 HPLC detector (HyperQuan Inc., Colorado Springs, CO) was used to detect eluting particles.

RESULTS: A 33µL sample of unconjugated MACS beads (Miltenyi Biotec, Bergisch Gladbach, Germany) was introduced to the channel. Following a stop-flow time of 5 minutes, the sample was eluted at 1.0 mL/min. The sample was eluted in the presence of the magnetic field and with the channel removed from the magnet. The elution profiles (fractograms) are shown in

Fig. 3. The magnetic field is seen to cause the retardation of particle elution. This is consistent with the expectations for elution via the mechanism of magnetic FFF.

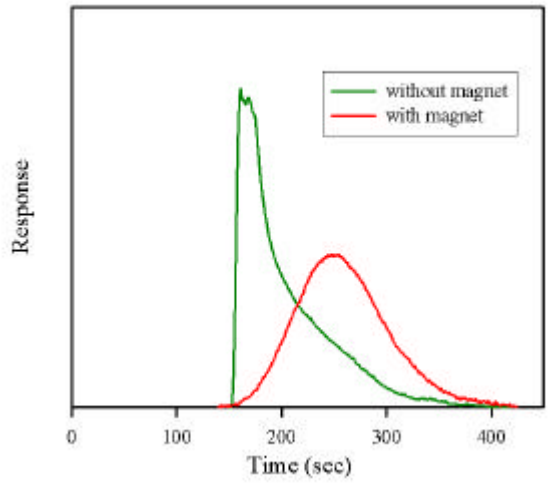

Fig. 3: Elution profiles (fractograms) for unconjugated MACS bead samples in the presence and absence of the quadrupole magnetic field.

DISCUSSION & CONCLUSIONS: MACS beads are expected to have a magnetic content approximately equivalent to a 10nm magnetite core (Miltenyi literature), although the polydispersity must be considered unknown. They are coated with dextran and have an overall diameter of about 50nm. (This overall size was confirmed in our laboratory by diffusion measurements.) If we assume a saturation magnetization of 480 kA/m for the magnetite, the expected mean λ would be approximately 0.18 for our system, corresponding to a retention ratio of about 0.6 (see Fig. 1). This is consistent with the moderate level of retention observed for the sample in the presence of the magnetic field. The moderate level of retention for this sample unfortunately does not allow us to extract any meaningful conclusions regarding their polydispersity of magnetic content.

The results, although preliminary, are an encouraging indication that quadrupole magnetic FFF will prove to be a powerful characterization tool for magnetic nanoparticles.

REFERENCES: [1]M. Zborowski, L.R. Moore, L. Sun, and J.J. Chalmers (1997) *Continuous-flow magnetic cell sorting using soluble immuno-magnetic label* in Scientific and Clinical Applications of Magnetic Carriers: An Overview (eds. U. Häfeli, W. Schûtt, J. Teller, M. Zborowski), Plenum Press, New York, pp. 247-260. [2]M. Zborowski, P.S. Williams, L. Sun, L.R. Moore, and J.J. Chalmers (1997) *Cylindrical SPLITT and quadrupole magnetic field in application to continuous-flow magnetic cell sorting*, J. Liq. Chromatogr. & Rel Technol. **20**:2887-2905. [3]P.S. Williams, M. Zborowski, and J.J. Chalmers (1999) *Flow rate optimization for the quadrupole magnetic cell sorter*, Anal. Chem. **71**:3799-3807. [4]J.C. Giddings (1992) *Optimization of transport-driven continuous SPLITT fractionation*, Sep. Sci. Technol. **27**:1489-1504. [5]J.C. Giddings (1985) *A system based on split-flow lateral-transport thin (SPLITT) separation cells for rapid and continuous particle fractionation*, Sep. Sci. Technol. **20**:749-768.

ACKNOWLEDGEMENTS: This work was supported by NIH grant CA 62349 to M.Z. and by NSF Grant 0125657 to P.S.W.

A GENERALIZED METHOD FOR MAGNETITE NANOPARTICLE STERIC STABILIZATION UTILIZING BLOCK COPOLYMERS CONTAINING CARBOXYLIC ACIDS

K.S. Wilson[1], L.A. Harris[1], J.D. Goff[1], J.S. Riffle[1] and J.P. Dailey[2]

[1]*Department of Chemistry, Virginia Tech, Blacksburg, VA 24061 USA*
[2]*Department of Ophthalmology, Case Western Reserve University, Cleveland, OH, USA*

INTRODUCTION: Magnetic nanoparticles that display high saturation magnetization and high magnetic susceptibility are of great interest for medical applications. Nanomagnetite is particularly desirable because it displays strong ferrimagnetic behavior, and is less sensitive to oxidation than magnetic transition metals such as cobalt, iron, and nickel. For *in-vivo* applications, it is important that well-defined organic coatings surround the nanomagnetite particles. It is rationalized that this will prevent any aggregation of the nanoparticles *in-vivo*, and may also enable efficient excretion and protection of the body from toxicity.

Magnetite nanoparticles can be prepared by co-precipitating iron (II) and iron (III) chloride salts in the presence of ammonium hydroxide at pH 9-10. Oleic acid is known to effectively stabilize dispersions of nanomagnetite in nonpolar solvents [1,2]. Stabilization occurs because the carboxylic acid group covalently reacts with the surface of the magnetite and the aliphatic chain extends out into the nonpolar solvent, preventing aggregation of the particles by a steric (entropic) mechanism. One goal of this work has been to develop a generalized methodology for stabilizing nanomagnetite dispersions using well-defined, non-toxic, block copolymers, so that the resultant magnetite-polymer complexes can be used in a range of biomedical materials. Our objectives have included: (1) Understanding what types of polymer structures bind irreversibly to magnetite at the physiological pH and what block lengths are desirable, (2) Tailoring polymer block lengths to maximize the concentration of bound magnetite, yet preserve good dispersion and (3) Designing copolymers with both hydrophilic and hydrophobic tail blocks to enable dispersion in different types of carrier fluids.

Triblock copolymers with controlled concentrations of carboxylic acids were designed as steric stabilizers for magnetite nanoparticle dispersions. The materials are comprised of hydrophilic, hydrophobic or amphoteric tail blocks to enable dispersion in media with various polarities, and central segments containing the carboxylic acid groups for anchoring to the nanomagnetite surfaces. A range of compositions involving poly(ethylene oxide) hydrophilic tail blocks have been investigated having averages of 3, 5, and 10 carboxylic acid-containing repeat units in the central, polyurethane anchor segment. Tail block lengths in this series have included 2000, 5000 and 15000 g/mol poly(ethylene oxide) oligomers which flank the central segments. Poly(dimethylsiloxane) hydrophobic tail blocks and amphoteric poly(dimethylsiloxane)-b-poly(ethyloxazoline) tail blocks have been studied as a means for preparing hydrophobic dispersions. In all cases, the carboxylic acid groups were reacted into the central block to provide binding sites for the nanomagnetite particles (Figure 1). It is important that the carboxylic acid binding groups are closely located in the copolymer as opposed to being randomly distributed along the chains to afford the desired particle-polymer morphologies (Figure 2).

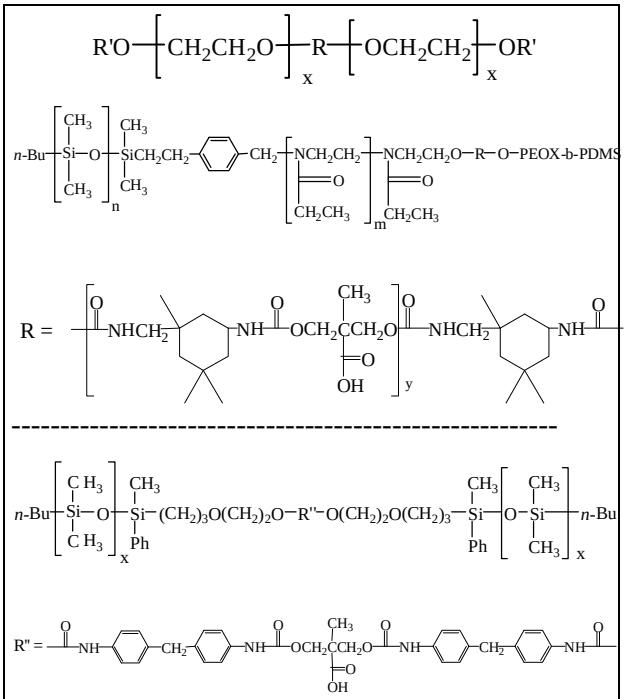

Fig. 1: PEO-COOH (top); PDMS-PEOX-COOH (middle); PDMS-COOH (bottom) where R' is a methyl or t-butyl, x = 44, 112 or 340.

METHODS: Sterically stabilized, neutral nanomagnetite dispersions were prepared by first forming the magnetite particles, then stabilizing the particle surfaces. A procedure for preparing a stabilized magnetite composition using a PEO-COOH triblock copolymer with 2000 g/mol M_n PEO endblocks and an average of three carboxylic acids in the central segment (2k-3-2k) is provided.

This composition utilizes 34.9 wt. % Fe_3O_4 charged to the reaction. All solutions (water, base and polymer/CH_2Cl_2) were carefully deoxygenated prior to use with ultrahigh purity dry nitrogen for a minimum of 30 minutes to avoid unwanted oxidation.

The first step of the reaction sequence involves forming magnetite nanoparticles in anaerobic conditions at ambient temperature. Aqueous solutions of $FeCl_3 \cdot 6H_2O$ (0.389 M, 2.0 g) and $FeCl_2 \cdot 4H_2O$ (0.195 M, 0.736 g) reagents were prepared separately under N_2 and syringed into a 3-necked, 250-mL, roundbottom flask equipped with a mechanical stirrer and pH electrode connected to a pH meter. The fittings for the apparatus were attached with vacuum-tight adapters to maintain an inert nitrogen environment. NH_4OH (50% v/v aqueous) was quickly syringed into the flask until a pH of 9.5 was reached (~10 mL) with rapid stirring (60 rpm) immediately after the aqueous iron salts addition. The solution quickly turned black indicating formation of the magnetite. The nucleation and growth of magnetite particles were allowed to occur for 30 minutes with stirring under a N_2 atmosphere.

After this, the steric stabilizer solution comprised of the PEO-COOH copolymer dissolved in CH_2Cl_2 (2 g polymer in 25 mL CH_2Cl_2) was syringed into the flask and allowed to react with the magnetite for 30 minutes with stirring (pH ~ 8.5–9). The CH_2Cl_2 solvent was subsequently removed with a strong N_2 flow (~2 h) and the resulting polymer-magnetite nanoparticle aqueous suspension was neutralized with dilute HCl (25 % v/v aqueous) to a pH ~ 6.5–7.

The resulting stable dispersion was transferred to a dialysis membrane (Spectra pore 7, MWCO 1000) and dialyzed against water for three days, refreshing the dialysis water twice/day. Particle aggregates in the salt-free magnetite ferrofluids were removed by centrifuging for 30-minute time intervals where the sediment was discarded and the process was repeated until no precipitation was observed in the bottom of the centrifuge tube. This generally required centrifuging the magnetite for 3 – 5 intervals.

The method for preparing magnetite dispersions using the nonpolar stabilizers, such as PDMS-COOH or PDMS-PEOX-COOH, is similar. Interfacial interactions allow for the magnetite to be extracted into the organic phase in these dispersions.

RESULTS AND DISCUSSION:

Synthesis of magnetite dispersions. Magnetite nanoparticles were synthesized by co-precipitating aqueous $FeCl_2$ and $FeCl_3$ salt solutions at room temperature under N_2 with a hydroxide base. The stoichiometric molar ratio of Fe^{2+}/Fe^{3+} was 0.5 to achieve quantitative conversion. All solutions were deoxygenated prior to use and reacted immediately to minimize oxidation of the Fe^{2+} species [3,4]. The two iron salts were dissolved separately and combined with vigorous mixing, just prior to base addition, and the base was quickly syringed into the flask with rapid stirring (~ 1–3 s) to a pH of 9.5–10. This produced a stable nanomagnetite dispersion in water, electrostatically stabilized with ammonium ion double layers.

Two slightly different methods for coating the nanomagnetite with the polymer stabilizers were used, depending on the solubility of the polymers in water. Numerous groups have previously reported that if carboxylic acid functional groups are present in the iron oxide solution during magnetite synthesis, the crystallization process to form the cubic inverse spinel crystalline structure of magnetite is greatly inhibited, and magnetite does not form [5,6].

The copolymer stabilizers which contained the hydrophilic poly(ethylene oxide) tail blocks were soluble in the aqueous iron salt solutions, so these copolymers were not added until after the magnetite nanoparticles had formed. The polymers were introduced to the aqueous magnetite particle dispersions as solutions in dichloromethane, a step which produced two-phase mixtures. Since these copolymers are soluble in both the aqueous and organic phases in this case, they partition between the two phases. It is not yet clear whether the stabilizer must be located within the aqueous phase to efficiently react with the particles, or whether a substantial portion of the coating reaction can take place at the water-solvent interface, and it is recommended that further attention be given to this issue as the work progresses. Following reaction of the magnetite-polymer complex for 30 minutes in the two-phase mixture, the dichloromethane was removed with a strong N_2 purge to transfer all of the polyethylene oxide based stabilizer into the water phase. It should be noted that if stirring is stopped at this stage, the magnetite settles out of solution. This suggests that the carboxylate groups are not yet irreversibly bound to the surface of the magnetite. The pH of the reaction mixture was subsequently lowered to pH 6.5 – 7 by titrating with acid, whereupon stable dispersions were obtained.

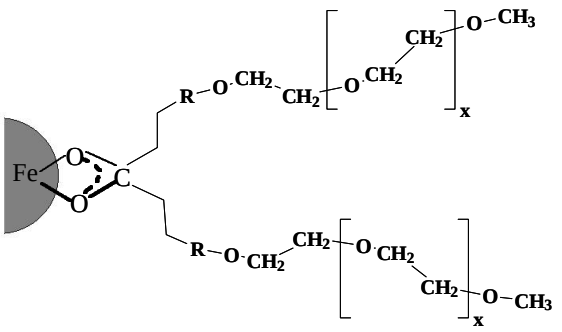

Fig. 2: Carboxylic acid groups of the central segment of a PEO-COOH copolymer bound to the surface of magnetite in an aqueous dispersion.

The hydrophobic and amphoteric stabilizers which contained poly(dimethylsiloxane) tail blocks were insoluble in the aqueous iron salt solutions. Hence, these polymers were added to the aqueous iron salt solutions in dichloromethane to produce a two-phase mixture before magnetite was formed. Subsequently, the base was added to the multiphase reaction to crystallize and precipitate the nanomagnetite in the aqueous phase (while the polymer was present in the organic phase). This process results in the coated magnetite being extracted into the organic phase. Subsequently, the mixtures were neutralized and the organic phase was dialyzed and centrifuged to remove any minor concentrations of aggregates that may have formed. Again, the locus of coating reaction is unknown and warrants further study. Interestingly, only the amphoteric copolymers with the hydrophobic poly(dimethylsiloxane) block connected to a hydrophilic poly(ethyloxazoline) block were able to efficiently "reach" into the aqueous phase and coat the magnetite. Table 1 shows clearly that if the hydrophilic block is not present (e.g., PDMS-COOH in table 1), only minimal concentrations of magnetite become coated.

Aqueous dispersion stabilities of the magnetite nanoparticles coated with the hydrophilic poly(ethylene oxide) containing block copolymers were investigated as a function of pH. Results suggest that the magnetite coating process should be conducted at pH of 8 -10, then the dispersions should be neutralized. Stable dispersions were observed only at pH 7 and below. At neutral and lower pH, the carboxylate group chemisorbs onto the surface of magnetite, and sterically stabilizes the dispersions (figure 2). This provides stable dispersions at physiological pH's which are not sensitive to ionic strength or pH changes.

Transmission electron photomicrographs of all of the samples show magnetite particles ~10 nm in diameter. Magnetite crystalline structure was confirmed by powder X-ray diffraction and electron diffraction. The magnetite nanoparticles appear to be single crystals.

Magnetic properties of these polymer-magnetite nanoparticle systems were investigated by vibrating sample magnetometry in the solid state. The saturation magnetization was determined from the plateau region of the magnetization displayed by the sample in the presence of an externally applied field varied from 8000 Oe to –8000 Oe. The magnetization data was quantified in terms of magnetite using elemental analysis to determine the concentration of iron in the materials (Table 1).

Table 1. Magnetic properties of polymer stabilized magnetite nanoparticles.

Sample	Conc. Fe_3O_4 charged (wt. %)	Conc. Fe_3O_4 obtained (wt. %)	M_S/g sample (emu/g)	M_S/g Fe_3O_4 (emu/g)
2k PEO-COOH	35	23	17	74
5k PEO-COOH	46	30	20	66
PDMS-*b*-PEOX-COOH	30	26	17	68
PDMS-COOH	30	3.9	1.6	40

Experimental saturation magnetization values for magnetite nanoparticles reported in the literature range from 30–60 emu/g, whereas bulk magnetite can theoretically be as high as 92 emu/g [7,8]. Thus, the response of the magnetite nanoparticles described herein compare favorably with previous materials. The lower magnetizations for the nanoscale particles have been attributed to surface effects.

The concentration of magnetite in these materials has not yet been maximized, and TEM photomicrographs suggest there are significant amounts of excess polymer remaining in the samples. It will be necessary to eliminate the excess polymer to achieve higher magnetite concentrations, and hence higher M_S per gram of sample. It is clear that the minimum tail block length investigated thus far can be reduced further, which should enable the concentration of magnetite relative to polymer to be raised further.

CONCLUSIONS: The magnetite is formed first by aqueous coprecipitation of di- and trivalent iron salt solutions in a nitrogen environment and stabilized afterwards. The magnetite particles formed are ~10 nm in diameter, independent of the polymer stabilizer used because they were formed prior to stabilization. Stable dispersions were achieved at neutral pHs with all of the hydrophilic poly(ethylene oxide) based polymer stabilizers. Powder X-ray diffraction patterns of these systems suggest the magnetite crystalline structure for all samples.

The saturation magnetization of these ~10 nm polymer-coated particles are ~66–74 emu/g Fe_3O_4. Such behavior is high for magnetite nanoparticles, and suggest "good quality" magnetite. However, the maximum concentration of magnetite achieved thus far results in a saturation magnetization of only ~ 20 emu/g, and TEM suggests that there is a significant excess of polymer remaining. Thus, one key aspect of our continuing work will be to

maximize the magnetite/polymer concentration, yet maintain stable dispersions.

Nanomagnetite stabilization using the nonpolar PDMS-COOH and PDMS-*b*-PEOX-COOH stabilizers provided significantly different results. The PDMS-*b*-PEOX-COOH stabilizer was able to incorporate more than ten times more magnetite per gram than the PDMS-COOH stabilizer. It is proposed that the hydrophilic PEOX block facilitates the reaction with the magnetite surface. The presence of the hydrophilic PEOX block adjacent to the carboxylic acid groups makes the carboxylic acid groups more available for reaction with the magnetite in the aqueous phase.

REFERENCES: [1]S. S. Papell, O. C. Faber, in *NASA Technical Note, Vol. (NASA-TN-D-4676)*, **1968**, p. 25pp. [2]R. Massart, *IEEE Transactions on Magnetics* **1981**, *Mag-17*, 1247. [3]R. M. Cornell, U. Schertmann, *Iron Oxides in the Laboratory; Preparation and Characterization.*, VCH, Weinheim, **1991**. [4]N. M. Gribanov, E. E. Bibik, O. V. Buzunov, V. N. Naumov, *Journal of Magnetism and Magnetic Materials* **1990**, *85*, 7. [5]G. S. R. Krishnamurti, P. M. Huang, *Clays and Clay Minerals* **1991**, *39*, 28. [6]P. M. Huang, M. K. Wang, in *Advances in Geoecology, Vol. 30* (Eds.: K. Auerswald, H. Stanjek, J. M. Bigham), International Development Centre, Ottawa, **1997**, pp. 241. [7]T. Sato, T. Iijima, M. Sekin, N. Inagaki, *Journal of Magnetism and Magnetic Materials* **1987**, *65*, 252. [8]V. Pillai, D. O. Shah, *Journal of Magnetism and Magnetic Materials* **1996**, *163*, 243.

ACKNOWLEDGEMENTS: The authors gratefully acknowledge the collaboration of R. Claus (Virginia Tech) for his help in characterizing the magnetic behavior of the materials. The financial support of Carilion Biomedical Institute and DARPA-AFOSR is greatly appreciated.